

# Wideband Propagation Measurements for Personal Communication Systems

*Gregory Theodore Martin*

B.E.(Honours) University of Melbourne, M.E. (Distinction) University of Canterbury,  
MIEE, Chartered Electrical Engineer

June 2000



A thesis submitted to the School of Communications and Informatics  
Faculty of Engineering and Science  
Victoria University of Technology  
in accordance with the requirements for  
the degree of Doctor of Philosophy

23/24859

FTS THESIS  
621.38411 MAR  
30001006995064  
Martin, Gregory Theodore  
Wideband propagation  
measurements for personal  
communication systems

---

# ABSTRACT

The propagation channel is a vital but invisible part of any wireless communications system. As wavelengths get shorter, multipath effects become more pronounced, causing small scale fading in narrowband channels, and inter-symbol interference in wideband systems because of delay spread in the channel impulse response. Multipath propagation becomes more pronounced as the wavelength decreases, and at the frequencies around 2GHz assigned for 3rd. generation cellular 'phones and personal communication services, multipath is pervasive, and very dependent on the built environment and topography. Multipath makes non-line-of-sight (NLOS) operation possible, but also introduces a degree of randomness and unpredictability which complicates radio system design. System designers, and researchers pursuing improved methods of communicating information need realistic channel statistics and models to progress.

At the start of this thesis project, no wideband outdoor propagation data had ever been published for the Australian environment. The primary objective of the project was to develop and build wideband channel-sounding instrumentation operating at 1.89GHz, and to investigate propagation conditions in a variety of cities and locations, to allow the comparison of multipath behaviour in the Australian environment with results from overseas countries. This aim has been met.

A novel portable wideband vector channel sounder was successfully developed and used in measurement campaigns in four Australian cities. The high resolution (10 nanoseconds) mode of the sounder also allowed indoor propagation effects to be studied. Methods for measuring and interpreting radio channels vary widely, but the results from this program indicate that Australian propagation conditions fit midway into the overseas results surveyed.

Results are given both as cumulative distributions, and in a new way as 'propagation signatures'. The validity of ray tracing for indoor and out-door micro-cells has been tested against measurement showing large discrepancies at times.

Internal diversity in CDMA systems has been studied, resulting in a new empirical law, relating diversity order to system bandwidth and the propagation environment.

---

## Acknowledgements

During a sabbatical visit to the *University of Bristol* in 1991, I was introduced to wideband channel sounding by Professor Joe McGeehan and Dr. Mark Beach, and given the opportunity to assist in a field measurement program at 1.87 GHz being conducted by the university for *Hutchison Microtel* (now renamed *Orange*). Helping Richard Davies and Simon Swales was not only good fun, but I also learnt a lot about current RF design, and the black art of propagation measurement. Simon and Rich generously ensured that I was fully included in the social life of the Comms Lab (*CCR, Centre for Communications Research*), which greatly enriched my stay in Bristol. I am grateful to Joe and Mark for pointing out that Australia offered virgin territory for wideband propagation work, resulting in my enrolment for this part-time PhD program in 1992 when I returned to *Victoria University of Technology*. I would like to thank Professor McGeehan for his help and encouragement as my PhD co-supervisor, and for making me very welcome at Bristol on subsequent visits to the *CCR*. Many people have helped to make Bristol feel like a home away from home, and I would like to thank all in the *CCR* and the *Department of Electrical and Electronic Engineering*, especially Chris Simmonds, Steve Allpress, Ross Wilkinson, Andy Nix, Geoff Hilton, George Tsoulas, Georgia Athanasiadou, Tom Busby, and all the workshop staff, for their technical help and friendship. Special thanks also to Dr. Andy Nix for many helpful comments on a draft of Chapter 4, and to Dr. Mark Beach for reading drafts of Chapters 1 to 6, and offering many constructive comments.

My supervisor at *Victoria University of Technology*, Professor Mike Faulkner, has developed a vigorous research group at *VUT*, and has provided a good climate for research, facilitated funding, and given me technical help and advice with aspects of signal processing. Professor Faulkner also suggested many worthwhile improvements after reading a draft of the entire thesis. Thanks, Mike!

This protracted PhD program has paralleled my marriage to Sue, and the life of our son Harry, who has so far never known a dad not preoccupied with problems of RF hardware design or channel modelling. Sue has helped and encouraged me immensely, running the family while I have been fully occupied with this PhD project and a full time lecturing job, assisting with propagation measurements, and proof reading all of this document. I would like to deeply thank Sue, and our children Steve, Kathy and Harry, for their tolerance and patience.

Finally I would like to thank my father, Theo, for a lifetime of interest in my education, and for always encouraging me to go further and try harder.



---

## Publications

1. G.T.Martin, "Distortion using a Sliding Correlator", 10th. Virginia Tech Symposium on Wireless Personal Communications, Blacksburg Virginia, USA, June 2000.
2. G.T.Martin, "Propagation Signatures to Characterize Wideband Environments", 10th. Virginia Tech Symposium on Wireless Personal Communications, Blacksburg Virginia, USA, June 2000.
3. Gregory Martin, "Wideband Channel Sounding Dynamic Range using a Sliding Correlator", Published in the Proceedings of the 51st. IEEE Vehicular Technology Conference (VTC'2000-Spring), Tokyo, Japan, May 2000, pages 2517-2521.
4. Gregory T. Martin and Michael Faulkner, "Useable CDMA Diversity Order At Various System Bandwidths For In-Building Propagation". Published in the Proceedings of the 3rd. ACTS Mobile Communications Summit, Rhodes, Greece, June 1998, Volume 2, pages 892-896.
5. G.T.Martin and M.Faulkner, "1.9 GHz Measurement-based Analysis of Diversity Power versus the Number of RAKE Receiver Tines at Various System Bandwidths". Published in the Proceedings of the 8th. IEEE International Symposium on Personal, Indoor and Mobile Radio Communications (PIMRC'97), Helsinki, Finland, September 1997, Volume 3, pages 1069-1073.
6. G.T.Martin and M.Faulkner, "PCS Ray Characteristics Between Multiple Floors of a Concrete Building". Published in the Proceedings of the 47th. International IEEE Conference on Vehicular Technology (VTC'97), Phoenix USA, May 1997, Volume 3, pages 1400-1404.
7. G.T.Martin and M.Faulkner, "Wide Band PCS Propagation Measurements in Four Australian Cities". Published in the Proceedings of the 10th.International IEE Conference on Antennas and Propagation (ICAP'97), Edinburgh UK, 14-17 April, 1997, Volume 2, pages 199-203.
8. G.T.Martin and M.Faulkner, "Wide Band Propagation Measurements and Ray Tracing Simulations at 1890 MHz.". Published in the Proceedings of the 4th IEEE International Conference on Universal Personal Communications (ICUPC'95), November 6-10, 1995 Tokyo Japan, pages 283-287
9. G.T.Martin, M.Faulkner and M.A.Beach\*, "Comparison of Delay Spread Measurements with Ray Tracing Simulations at 1890 MHz.". Published in the Proceedings of the 6th. IEEE International Conference on Personal, Indoor and Mobile Communications (PIMRC'95), September 27-29, 1995 Toronto Canada. (\* *University of Bristol*). Volume 3, pages 1156-1160.
10. G.T.Martin and M.Faulkner, "Wideband Propagation at 1890 MHz. in an Indoor Multistorey Concrete Building". Presented at the Workshop on Applications of Radio Science (WARS'95), June 25-27, 1995, Canberra, Australia.
11. G.T.Martin and M.Faulkner, "Delay Spread Measurements at 1890 MHz in Pedestrian Areas of the Central Business District in the City of Melbourne". Published in the Proceedings of the IEEE 44th. Vehicular Technology Conference (VTC'94), Stockholm, Sweden, June 8-10, 1994. Volume 1, pages 145-149.
12. G.T.Martin, "A Fast Variable Parameter Pseudo Noise Generator". Published in the Proceedings of the First International Workshop on Mobile and Personal Communication Systems, University of South Australia, Adelaide, Australia. November 12-13, 1992, pages 223-229.
13. S.A.Allpress, M.A.Beach, G.Martin, C.M.Simmonds, "An Investigation of RAKE Receiver Operation in an Urban Environment for Various Spreading Spectrum Bandwidth Allocations". Published in the Proceedings of the IEEE 42nd. Vehicular Technology Conference (VTC'92), Denver USA, May 1992.

- 
14. R.I.Davies, S.C.Swales, C.Simmonds, G.Martin, M.A.Beech and J.P.McGeehan, "Time Dispersion Measurements Undertaken at 1.87 GHz for Hutchison Microtel", Centre for Communication Research, Department of Electrical and Electronic Engineering, University of Bristol (UK), December 1991.
  15. G.T.Martin, "Wideband Channel Sounding Final Report , for Ericsson Australia Pty. Ltd.", December 1995.
  16. G.T.Martin, "Wideband Channel Sounding Progress Report No.2, for Ericsson Australia Pty. Ltd.", December 1994.
  17. G.T.Martin, "Wideband Channel Sounding Progress Report No.1, for Ericsson Australia Pty. Ltd.", April 1994.

# Symbols

## CHAPTER 2

$T_s$	the period of the baseband data symbol, or the period of one bit of data
$ds_{rms}$	rms delay spread
$BW_s$	the bandwidth of the transmitted information after modulation
$BW_c$	coherence bandwidth
$BW_D$	Doppler spread
$v$	velocity of the mobile, metre/sec
$f_c$	carrier frequency
$\lambda_c$	carrier wavelength metre
$c$	speed of light meter/sec
$f_D$	Doppler shift Hz
$T_c$	coherence time
$\mu$	mean value
$\sigma$	standard deviation
$I_0$	zero-order modified Bessel function of the first kind
$v_M$	magnitude of the dominant path
$K_{factor}$	K factor
$K_m$	modified K factor
$\alpha_w$	shape factor for the Weibull distribution
$\alpha_n$	lognormal shape parameter
$\sigma_r$	most probable value of the Rayleigh distribution
$\mu_p$	Poisson variance
$P_r$	available power at the receiving antenna
$P_t$	power supplied to the transmitting antenna
$L$	path loss in dB
$G_r$	gain of the receive antenna
$G_t$	gain of the transmit antenna
$f$	the frequency in Hz
$f_{MHZ}$	the frequency in MHz
$D$	distance in metres
$D_{km}$	distance in kilometres.
$h_t$	height of the transmit antenna
$h_r$	height of the receive antenna
$x(t)$	bandpass signal
$u(t)$	complex lowpass equivalent of a bandpass signal $x(t)$
$A(t)$	amplitude of the bandpass signal
$\phi(t)$	phase of the bandpass signal
$u_I(t)$	in-phase component
$u_Q(t)$	quadrature component
$h(t, \tau)$	complex impulse response where $\tau$ is delay
$t$	time seconds
$\tau$	delay seconds
$\nu$	Doppler shift Hz
$\alpha_h$	horizontal angle of arrival
$\alpha_v$	vertical angle of arrival
$\alpha_D$	angle of arrival in 3D space (angle between mobile velocity vector and radio ray)
$q$	slope factor for exponential power delay profile
$T$	time for exponential power delay profile to reach threshold level
$\rho$	reflection coefficient
$\tau$	excess delay

---

$P_\tau$	power at excess delay $\tau$
$P_0$	power in strongest ray
$D_{avg}$	average delay
$M_0$	zero order moment of the power delay profile
$M_1$	first order moment of the power delay profile
$M_2$	second order moment of the power delay profile
$D_{max}$	maximum excess delay

## CHAPTER 3

$\Delta f$	difference in chip frequencies between sliding sequences
$f_{PNt}$	chip frequency of transmitter PN sequence
$f_{PNr}$	chip frequency of receiver PN sequence
$k$	sliding correlator time scaling factor
$N$	PN sequence length
$t_{ref}$	time reference
$t_{r(m)}$	next clock transition in the receiver PN sequence
$t_{x(n)}$	next clock transition in the transmitter PN sequence
$t_{chip}$	receiver chip period in ns
$\tau_{max}$	maximum excess delay in $\mu s$
$y$	windowing factor
$R_{alias}$	maximum range in km to a reflecting object without ambiguity
$t_{measure}$	time to complete an unsynchronised channel sounding measurement, in ms
$T_{measure}$	time to complete a continuous mode channel sounding measurement, in ms
$f_{-3dB}$	correlation filter -3dB cutoff frequency in KHz
$f_D$	maximum measurable Doppler frequency, Hz
$v$	maximum channel sounder velocity in km/h, based on Doppler resolution
$f_c$	channel sounder carrier frequency, Hz.
$c$	velocity of light in free space, metre/s
$q$	a slope constant
$k_B$	Boltzmann's constant
$T_{abs}$	absolute temperature in degrees Kelvin
$BW_{Hz}$	system bandwidth in Hz
$N_{thermal}$	thermal noise in watts

## CHAPTER 4

$error_{rms}$	rms error measure of difference between measured and ray tracing delay spreads
$ds_{measured}$	measured delay spread
$ds_{XRay}$	X-Ray simulated delay spreads
$m$	number of measurements
$D_{avg}$	average excess delay
$ds_{rms}$	rms delay spread
$a_{pos}$	exponential PDP slope in dB/ns before peak
$a_{neg}$	exponential PDP slope in dB/ns after peak
$T_{neg}$	negative excess delay for PDP to reach threshold value before peak power
$T_{pos}$	excess delay for PDP to fall to threshold value after peak power
$r$	uniform density of rays per ns prior to PDP peak power
$p$	uniform density of rays per ns after PDP peak power
$W$	threshold window in dB, relative to PDP peak power

**CHAPTER 6**

$P_{total}$	total profile power
$n$	number of strongest rays used
$P_n$	the tine power, which is the sum of peak powers in the strongest $n$ rays or peaks
$P_{used}$	ratio of tine power to total power
$\alpha$	environment factor
$BW_{MHz}$	system bandwidth in MHz
$N_{tines}$	the number of tines, rounded to the nearest integer
$ds_{median}$	median instantaneous rms delay spread

**APPENDIX A**

$f_{VCO}$	phase locked loop output frequency
$f_{comp}$	phase comparison frequency
$f_{ref}$	reference frequency
$f_{step}$	synthesiser frequency step size
$R$	reference divider ratio
$P$	prescaler ratio
$M$	first programmable divider ratio
$M_{minimum}$	minimum value of $M$
$A$	second programmable divider ratio
$B$	overall programmable divider ratio
$K_\phi$	PFC gain in volt/radian
$K_{VCO}$	VCO gain in radian/sec/volt
$K_{amp}$	buffer amplifier voltage gain
$\omega_n$	loop natural frequency in radian/second
$\zeta$	damping factor
$A_{high}$	amplitude of the high PN signal
$A_{low}$	amplitude of the low PN signal
$G(c)$	PN signal envelope
$\tau_1$	PN chip duration, <i>high</i> state
$\tau_2$	PN chip period

**APPENDIX B**

$N_{receiver}$	total receiver noise figure
$N_{bp}$	insertion loss of the bandpass filter
$N_c$	insertion loss, antenna cable and connectors
$N_a$	noise figure, receiver low noise amplifier
$\delta$	skin depth
$f$	frequency Hz
$d$	conductor diameter
$R_{dc}$	DC conductor resistance
$R_{ac}$	AC or high frequency conductor resistance due to skin effect
$\Delta_{rms}$	rms surface roughness
$\rho_{eff}$	effective resistivity
$IL_{db}$	bandpass filter insertion loss in dB
$Q_l$	resonator loaded Q
$Q_u$	resonator unloaded Q
$q$	normalised Q for the resistively loaded first and last resonator
$N_{order}$	filter order
$K_{couple}$	filter coefficient of coupling

---

$k_{norm}$	interdigital filter normalised coefficient of coupling
$d$	interdigital filter resonator rod diameter
$h$	interdigital filter enclosure width
$C$	interdigital filter axial spacing between adjacent parallel resonator rods
$d/h$	interdigital filter normalised rod diameter
$C/h$	interdigital filter normalised rod spacing
$f_0$	interdigital filter centre frequency
$BW_{3dB}$	interdigital filter bandwidth
$e/h$	interdigital filter normalised end wall spacing
$Z_0$	interdigital filter impedance of the end resonators
$R$	interdigital filter resistive load
$l$	interdigital filter tap distance from the grounded end of a resonator
$BW'$	fractional filter bandwidth
$t_{delay}$	filter group delay
$\phi$	phase shift

---

# Abbreviations

2D	two dimensional
3D	three dimensional
A-D	analogue to digital
AH	amp-hours
ASIC	application specific integrated circuit
CCR	Centre for Communications Research (University of Bristol)
CDF	cumulative distribution function
CDMA	code division multiple access
CMOS	complementary metal oxide silicon
CoDiT	code division testbed
dB	decibels
dBc	power in decibels relative to carrier power
dBm	power in decibels relative to one milliwatt
dBV	voltage in decibels relative to one volt
DIP	dual in-line package
DSP	digital signal processing
DSSS	direct sequence spread spectrum
ECL	emitter-coupled logic
EMC	electromagnetic compatibility
ETSI	European Telecommunications Standards Institute
EXOR	exclusive-or logic function
FET	field effect transistor
FMCW	frequency modulated continuous wave
FPLMTS	future public land mobile telephone system
GHz	gigahertz
GPS	global positioning system
GSM	global system for mobile
IEEE	Institute of Electrical and Electronics Engineers
IF	intermediate frequency
IMT-2000	international mobile telecommunications 2000
IQ	in-phase, quadrature
LAN	local area network
LC	inductance-capacitance
LCD	liquid crystal display
LED	light emitting diode
LO	local oscillator
LOS	line of sight
MHz	megahertz
MMIC	monolithic microwave integrated circuit
MPRG	Mobile and Portable Radio Group (Virginia Tech.)
$\mu$ s	microseconds

---

ms	milliseconds
NLOS	non-line of sight
ns	nanoseconds
PCS	personal communication systems
PDF	probability distribution function
PDP	power delay profile
PFC	phase-frequency comparator
PLL	phase lock loop
PN	pseudo noise
Q	quality factor
QWSSUS	quasi-wide sense stationary uncorrelated scattering
RACE	Research in Advanced Communications in Europe
RC	resistor-capacitor
RCO	ripple carry out
RF	radio frequency
rms	root mean square
RSSI	received signal strength indicator
SAW	surface acoustic wave
SCR	silicon controlled rectifier
SLA	sealed lead-acid
SNR	signal to noise ratio
SPICE	simulation program for integrated circuit evaluation
TTL	transistor-transistor logic
UHF	ultra high frequency
UMTS	universal mobile telecommunications system
US	uncorrelated scattering
VCO	voltage controlled oscillator
VHF	very high frequency
VNA	vector network analyser
VSWR	voltage standing wave ratio
VTS	Vehicular Technology Society
VUT	Victoria University of Technology
WCDMA	wideband code division multiple access
WLAN	wireless local area network
WSS	wide sense stationary
WSSUS	wide sense stationary uncorrelated scattering



# Contents

## Chapter 1 - Introduction

1.	Introduction .....	1-1
1.1	Mobile Communications .....	1-1
1.2	Original Contributions .....	1-1
1.3	Thesis Outline.....	1-2

## Chapter 2 - The Fading Channel

2. 1	Small Scale and Large Scale Fading .....	2-1
2. 1.1	Large Scale Fading .....	2-1
2. 1.2	Small Scale Fading .....	2-2
2. 1.3	Definitions .....	2-2
2. 1.3.1	Symbol Period $T_S$ .....	2-2
2. 1.3.2	Rms Delay Spread $ds_{rms}$ .....	2-2
2. 1.3.3	Transmitted Bandwidth $BW_S$ .....	2-2
2. 1.3.4	Coherence Bandwidth $BW_C$ .....	2-2
2. 1.3.5	Doppler Spread $BW_D$ .....	2-3
2. 1.3.6	Coherence Time $T_C$ .....	2-4
2. 1.4	Flat Fading .....	2-4
2. 1.5	Frequency-selective Fading .....	2-5
2. 1.6	Slow fading .....	2-5
2. 1.7	Fast Fading .....	2-5
2. 1.8	Fading Summary .....	2-5
2. 2	Narrowband and Wideband Channels .....	2-6
2. 3	Statistical Distributions .....	2-6
2. 3.1	Gaussian (or Normal) Distribution .....	2-7
2. 3.2	Rayleigh Distribution .....	2-7
2. 3.3	Ricean or Nakagami-n Distribution .....	2-7
2. 3.4	Nakagami-m Distribution .....	2-8
2. 3.5	Weibull Distribution .....	2-8
2. 3.6	Lognormal Distribution .....	2-9
2. 3.7	Mixed Distributions: Suzuki Distribution .....	2-9
2. 3.8	Stacy Distribution .....	2-9
2. 3.9	Poisson Distribution .....	2-10
2. 4	Path Loss Models .....	2-11
2. 4.1	Free Space .....	2-11
2. 4.2	Plane Earth (2-Ray model) .....	2-11
2. 4.3	IEEE VTS Committee on Radio Propagation .....	2-13
2. 4.4	Models for Built-up Areas .....	2-15
2. 4.5	Level Crossing Rate and Average Fade Duration .....	2-15
2. 5	Narrow Band Measurements - Example.....	2-16
2. 5.1	Instrumentation .....	2-17
2. 5.2	Signal Strength Results .....	2-18
2. 5.2.1	Building Penetration Loss .....	2-20
2. 5.3	Level Crossing Rate .....	2-22

2. 6	Wideband Channels . . . . .	2-23
2. 6.1	Introduction . . . . .	2-23
2. 6.2	Bandpass to Lowpass Equivalence . . . . .	2-24
2. 6.3	Time Domain Description . . . . .	2-24
2. 6.4	Bello System Functions . . . . .	2-25
2. 6.5	Angle of Arrival . . . . .	2-26
2. 6.6	Wide Sense Stationary (WSS) Channels . . . . .	2-27
2. 6.7	Uncorrelated Scattering (US) Channels . . . . .	2-27
2. 6.8	Wide Sense Stationary Uncorrelated Scattering (WSSUS) Channels . . . . .	2-28
2. 6.9	Quasi-Wide Sense Stationary Uncorrelated Scattering (QWSSUS) Channels . . . . .	2-28
2. 7	Measures of Time Spread . . . . .	2-28
2. 7.1	Average or Mean Delay $D_{avg}$ . . . . .	2-28
2. 7.2	Rms Delay Spread $ds_{rms}$ . . . . .	2-29
2. 7.3	Maximum Excess Delay $D_{max}$ or 15 dB Delay Window . . . . .	2-31
2. 7.4	K Factor $K_{factor}$ . . . . .	2-31
2. 7.5	Proposed Modified K factor $K_m$ . . . . .	2-32
2. 8	Thresholds . . . . .	2-33
2. 8.1	Rms Delay Spread Sensitivity to Threshold . . . . .	2-34
2. 8.1.1	The Exponential Power Delay Profile . . . . .	2-34
2. 8.1.2	A Measured Power Delay Profile . . . . .	2-36
2. 8.1.3	Courtyard Measurement Series <i>vutrv</i> . . . . .	2-38
2. 8.1.4	Sydney Outdoor Measurement Series <i>sydb</i> . . . . .	2-39
2. 8.2	Conclusions - Variation of Delay Spread with Threshold . . . . .	2-40
2. 9	Conclusions. . . . .	2-40
2. 10	References - Chapter 2 . . . . .	2-42

## Chapter 3 - Channel Sounding

3. 1	Wideband Sounding Techniques . . . . .	3-2
3. 1.1	Pulse Sounders . . . . .	3-3
3. 1.2	Pulse Compression Sounders . . . . .	3-4
3. 1.3	The Sliding Correlator . . . . .	3-4
3. 1.4	Frequency Domain Sounders . . . . .	3-5
3. 1.5	Chirp Sounders . . . . .	3-5
3. 1.6	The Cox Sounder . . . . .	3-6
3. 1.7	Improvements to the Cox Architecture . . . . .	3-6
3. 1.8	Takeuchi Sounder . . . . .	3-7
3. 2	Sliding Correlator Simulations . . . . .	3-8
3. 2.1	Introduction. . . . .	3-8
3. 2.1.1	Dynamic Range of PN Sequences . . . . .	3-8
3. 2.1.2	Previous work . . . . .	3-9
3. 2.1.3	Other Factors Limiting Dynamic Range . . . . .	3-10

---

3.2.2	Sliding Correlation Algorithm .....	3-10
3.2.2.1	Number of Calculations - New Algorithm ....	3-12
3.2.2.2	Parameters Degraded by Sliding .....	3-13
3.2.3	Illustrative Simulation Results for N=63 .....	3-13
3.2.4	Correlation peak N=1023.....	3-15
3.2.5	Correlation Peak Widening.....	3-16
3.2.6	Correlation Peak Power .....	3-17
3.2.7	Simulation of Channel Sounder PDPs .....	3-17
3.2.8	Dynamic Range from Simulations .....	3-19
3.2.9	Comparison with Johnson.....	3-20
3.2.10	The Integrating Filter .....	3-21
3.2.11	Comparison of Measured and Simulated PDPs .....	3-24
3.2.12	Sliding Correlator Design.....	3-25
3.2.12.1	Fix Chip Period $t_{\text{chip}}$ .....	3-25
3.2.12.2	Specify Maximum Excess Delay $t_{\text{max}}$ .....	3-26
3.2.12.3	Specify the Required Dynamic Range .....	3-26
3.2.12.4	Calculate the Measurement Time $T_{\text{measure}}$ ....	3-26
3.2.12.5	Example .....	3-26
3.3	The VUT Channel Sounder .....	3-27
3.3.1	Portability .....	3-27
3.3.2	General Description .....	3-27
3.3.3	Signal levels .....	3-28
3.3.4	Transmitter Description .....	3-29
3.4	Receiver Description .....	3-30
3.4.1	Weight.....	3-31
3.4.2	Power Consumption .....	3-31
3.4.3	Frequency Standards.....	3-32
3.4.4	Bandpass Filters .....	3-32
3.4.4.1	Frequency Response .....	3-32
3.4.4.2	Impulse Response .....	3-33
3.4.5	Receiver Signal and Noise Power Budget .....	3-35
3.5	Channel Sounder Parameters .....	3-38
3.5.1	Free-running .....	3-38
3.5.2	Continuous or Coherent .....	3-40
3.5.3	Windowed.....	3-42
3.6	Synchronizing PN sequences .....	3-43
3.6.1	Wheel Trigger.....	3-44
3.7	Back-to-back Tests .....	3-45
3.7.1	Back-to-back Tests with the Artificial Channel .....	3-47
3.7.1.1	Indoor Mode .....	3-47
3.7.1.2	Outdoor Mode .....	3-47

---

---

3. 7.2	Back-to-back Straight Through Tests . . . . .	3-48
3. 7.2.1	Indoor Mode . . . . .	3-48
3. 7.2.2	Over a 1 Metre Air Path . . . . .	3-48
3. 7.2.3	With 130 dB Attenuation . . . . .	3-49
3. 7.2.4	Example of an Indoor Mode PDP . . . . .	3-49
3. 7.2.5	Outdoor Mode . . . . .	3-50
3. 7.2.6	Calibration - Outdoor Mode . . . . .	3-50
3. 7.2.7	RF Power Amplifier Linearity . . . . .	3-51
3. 8	Software . . . . .	3-52
3. 8.1	Offset Removal . . . . .	3-52
3. 9	Antennas . . . . .	3-53
3. 9.1	Discone antenna . . . . .	3-53
3. 9.2	Halfwave J antennas . . . . .	3-54
3. 10	Conclusions . . . . .	3-54
3. 11	References . . . . .	3-55

**Chapter 4 - Indoor Measurements**

4. 1	Ray Tracing Simulations and Measured Values . . . . .	4-2
4. 1.1	Ray Launching and Image Source Methods . . . . .	4-2
4. 1.2	The Environment Database . . . . .	4-3
4. 1.3	Ray Tracing Validation . . . . .	4-4
4. 1.4	X-Ray . . . . .	4-5
4. 1.5	MCS™ Microcell Communication Simulator . . . . .	4-6
4. 1.6	Wall Types and Estimated Electrical Properties . . . . .	4-7
4. 1.7	Measurements . . . . .	4-8
4. 1.8	Single Point Measurement . . . . .	4-9
4. 1.9	Corridor Route . . . . .	4-10
4. 1.9.1	Convergence of X-Ray Simulations - Power . . . . .	4-11
4. 1.9.2	Convergence of X-Ray Simulations - Delay Spread . . . . .	4-12
4. 1.9.3	Comparison of X-Ray Values with Measurements - Delay Spread . . . . .	4-14
4. 1.9.4	High Delay Spread Example . . . . .	4-15
4. 1.9.5	Medium Delay Spread Example . . . . .	4-16
4. 1.9.6	Applying a Range Limit . . . . .	4-17
4. 1.10	Campus Courtyard Measurements . . . . .	4-20
4. 1.10.1	Convergence of X-Ray Simulations on Route <i>nv</i> - Power . . . . .	4-22
4. 1.10.2	X-Ray Simulations on Route <i>nv</i> - Delay Spread . . . . .	4-23
4. 1.10.3	MCS™ Simulations on Route <i>nv</i> - Delay Spread . . . . .	4-24
4. 1.10.4	Convergence of X-Ray Simulations on Route <i>m</i> - Power . . . . .	4-25
4. 1.10.5	X-Ray Simulations on Route <i>m</i> - Delay Spread . . . . .	4-26
4. 2	Multipath Propagation Between Floors . . . . .	4-28
4. 2.1	Introduction . . . . .	4-28
4. 2.2	Delay Spread Versus Path Loss . . . . .	4-31

---

4. 2.3	Average Delay versus Delay Spread . . . . .	4-33
4. 2.4	Number of Rays in Each Power Delay Profile . . . . .	4-35
4. 2.5	Number of Paths Sorted Into Power and Time Bins . . . . .	4-39
4. 3	Conclusions . . . . .	4-40
4. 4	References - Chapter 4 . . . . .	4-41

## Chapter 5 - Outdoor Measurements

5. 1	Adelaide . . . . .	5-2
5. 1.1	Hotel Adelaide, First Floor . . . . .	5-3
5. 1.2	Hotel Adelaide, Sixth Floor Roof . . . . .	5-3
5. 1.3	Adelaide - Victoria Square . . . . .	5-3
5. 1.4	Adelaide - Results . . . . .	5-4
5. 1.4.1	rms Delay Spread . . . . .	5-4
5. 1.4.2	Average Delay . . . . .	5-4
5. 1.4.3	15dB Delay Window . . . . .	5-5
5. 1.4.4	K Factor . . . . .	5-5
5. 2	Melbourne . . . . .	5-6
5. 2.1	Melbourne - Bourke Street Mall, and Flinders Street . . . . .	5-6
5. 2.2	Melbourne - City Arcades . . . . .	5-6
5. 2.3	Melbourne - Delbridge Street Balcony . . . . .	5-7
5. 2.4	Melbourne - Delbridge Street Roof . . . . .	5-7
5. 2.5	Melbourne - Results . . . . .	5-8
5. 2.5.1	rms Delay Spread . . . . .	5-8
5. 2.5.2	Average Delay . . . . .	5-8
5. 2.5.3	15dB Delay Window . . . . .	5-9
5. 2.5.4	K Factor . . . . .	5-10
5. 3	Canberra . . . . .	5-10
5. 3.1	Canberra - O'Connor Residential Area . . . . .	5-11
5. 3.2	Canberra - Dundas Court . . . . .	5-11
5. 3.3	Canberra - Results . . . . .	5-12
5. 3.3.1	rms Delay Spread . . . . .	5-12
5. 3.3.2	Average Delay . . . . .	5-13
5. 3.3.3	15dB Delay Window . . . . .	5-13
5. 3.3.4	K Factor . . . . .	5-14
5. 4	Sydney . . . . .	5-14
5. 4.1	Sydney - University of Technology Sydney . . . . .	5-16
5. 4.2	Sydney - Results . . . . .	5-16
5. 4.2.1	rms Delay Spread . . . . .	5-16
5. 4.2.2	Average Delay . . . . .	5-17
5. 4.2.3	15dB Delay Window . . . . .	5-17
5. 4.2.4	K Factor . . . . .	5-18
5. 5	High And Low Antennas . . . . .	5-18
5. 6	A Novel Graphic Propagation Environment Signature . . . . .	5-19
5. 6.1	The Presentation Problem . . . . .	5-19
5. 6.2	The Propagation Signature . . . . .	5-19

---

5.7	Results Summary .....	5-26
5.8	Conclusions .....	5-27
5.9	References .....	5-31

## Chapter 6 - RAKE Diversity

6.1	Multipath Diversity .....	6-2
6.2	RAKE Receivers .....	6-2
6.3	Propagation Data .....	6-3
6.4	Measurement Environments .....	6-4
6.5	Receiver .....	6-4
6.6	Filtering .....	6-4
6.7	Thresholds .....	6-5
6.8	Tine Power and Total Power .....	6-6
6.9	Outdoor Results .....	6-6
6.10	Number of Tines Plots .....	6-9
6.11	Initial Tine Number Model - Outdoor .....	6-11
6.12	Indoor Results .....	6-12
6.12.1	Group 1 Plot .....	6-13
6.12.2	Group 2 Plots .....	6-15
6.13	Initial Tine Number Model - Indoor .....	6-16
6.14	Model Summary .....	6-18
6.15	Incorporating Delay Spread .....	6-18
6.16	Final Tine Number Model .....	6-20
6.17	Comparisons - Models and Measurements .....	6-20
6.17.1	Comparison with the <i>Ericsson</i> Model .....	6-20
6.17.2	Comparison of Models with Outdoor Measured Data ..	6-21
6.17.3	Comparison of Models with Indoor Measured Data ...	6-22
6.18	Conclusions .....	6-23
6.19	References - Chapter 6 .....	6-24

## Chapter 7 - Conclusions and Future Work

7.1	Conclusions .....	7-1
7.2	Future Work .....	7-1
7.3	References .....	7-1

## Appendix A - Transmitter Hardware

A.1	Frequency Standards .....	A-2
A.2	UHF Frequency Synthesizers .....	A-2
A.2.1	Loop Bandwidth and Phase Noise .....	A-3
A.2.2	Prescalers .....	A-4
A.2.3	Fixed Prescaling .....	A-4
A.2.4	Dual-Modulus Prescaling .....	A-4
A.2.5	Minimum Divider Ratio .....	A-5
A.2.6	Loop Design .....	A-5
A.2.7	Open Loop Bode Plot .....	A-7
A.2.8	Voltage Controlled Oscillator .....	A-8
A.2.9	Circuit Schematics .....	A-8
A.2.10	Synthesizer Performance .....	A-10
A.2.11	Future Improvements .....	A-13
A.3	VHF Synthesizer .....	A-14
A.3.1	Performance .....	A-17
A.4	Frequency Dividers .....	A-17
A.5	PN Generator .....	A-18
A.5.1	Design .....	A-18
A.5.2	Circuit Techniques .....	A-19
A.5.3	Logic .....	A-20
A.5.4	ECL Techniques .....	A-20
A.5.5	Power Supplies .....	A-21
A.5.6	Feedback Paths .....	A-21
A.5.7	Address Switching .....	A-21
A.5.8	Input Clock .....	A-22
A.5.9	Variable Chip Rate .....	A-22
A.5.10	All Zero State .....	A-23
A.5.11	Synchronisation Pulse .....	A-23
A.5.12	Start Pulse .....	A-24
A.5.13	Evaluation .....	A-25
A.5.14	Clock BreakThrough .....	A-26
A.5.15	Maximum Chip Rate .....	A-29
A.5.16	Acknowledgement .....	A-30
A.6	Mixer .....	A-30
A.7	Power Amplifier .....	A-31
A.8	Power Supplies - Transmitter .....	A-32
A.8.1	Step-up Regulator For Driver Amplifier .....	A-33
A.8.2	Low Dropout +12 volt Regulator .....	A-33

A.8.3	Supply Supervision .....	A-35
A.9	References - Appendix A .....	A-36

## Appendix B - Receiver Hardware

B.1	Receiver Portability .....	B-1
B.2	Bandpass Filter .....	B-2
B. 2.1	Losses .....	B-3
B. 2.1.1	Skin Effect .....	B-3
B. 2.1.2	Radiation .....	B-5
B. 2.2	Filter Technologies .....	B-6
B. 2.2.1	Ceramic Filters .....	B-7
B. 2.2.2	Microstrip and Stripline Filters .....	B-7
B. 2.2.3	Helical Filters .....	B-7
B. 2.2.4	Comblined Filters .....	B-8
B. 2.2.5	Interdigital Filters .....	B-8
B. 2.3	Filter Design .....	B-9
B. 2.4	Filter Design Parameters: .....	B-11
B. 2.5	Filter Design: .....	B-11
B. 2.6	Experimental Filters .....	B-12
B. 2.6.1	Tinplate Filter .....	B-12
B. 2.6.2	Circuit Board Filter .....	B-12
B. 2.7	Centre Frequency .....	B-13
B. 2.8	Other Effects - Bandwidth Shrinkage .....	B-13
B. 2.9	Other Effects - Tap Position .....	B-14
B. 2.10	Filter Tuning .....	B-14
B. 2.11	Filter Construction .....	B-14
B. 2.12	50 MHz Filter .....	B-16
B. 2.13	200 MHz Filter .....	B-17
B. 2.14	Measured Performance for 50 MHz Filter .....	B-18
B. 2.15	Group Delay .....	B-19
B. 2.16	Measured Performance for 200 MHz Filter .....	B-20
B. 2.17	Summary of Measured Filter Performance .....	B-21
B.3	Low Noise Amplifiers .....	B-22
B. 3.1	Stage One .....	B-22
B. 3.2	Stage Two .....	B-23
B.4	Frequency Multiplier .....	B-24
B.5	Bessel Integrators .....	B-26
B. 5.1	Design of Bessel filters .....	B-27
B. 5.2	Frequency Response and Gain Matching .....	B-31
B. 5.3	Group Delay .....	B-32



B.6	$I^2 + Q^2$ Display .....	B-34
B.7	Power Supplies - Receiver .....	B-35
B.8	Modifications to Synchronise PN Sequences .....	B-38
B. 8.1	Introduction .....	B-38
B. 8.2	PN Counter .....	B-39
B. 8.3	PN Preset .....	B-39
B. 8.4	Reset Switch .....	B-40
B. 8.5	Other Modifications .....	B-40
B. 8.6	Wheel Trigger .....	B-41
B. 8.6.1	Auto Setting .....	B-42
B. 8.6.2	Manual Setting .....	B-43
B. 8.6.3	Wheel Counter Settings (Auto) .....	B-43
B. 8.6.4	Examples .....	B-44
B. 8.7	PN Preset Counter .....	B-44
B.9	References - Appendix B .....	B-45

Appendix C - Antennas

C. 1	Discone Antenna .....	C-1
C.1.1	Discone Antenna Matching .....	C-2
C.1.2	Discone Antenna - Polar Pattern in Azimuth .....	C-3
C.1.3	Discone Antenna - Polar Pattern in Elevation .....	C-4
C. 2	Halfwave J Antennas .....	C-5
C.2.1	Halfwave J Antenna Matching .....	C-5
C.2.2	Halfwave Antenna - Polar Pattern in Azimuth .....	C-6
C. 3	Antenna Mounting .....	C-7
C.3.1	Backpack Receiver Unit .....	C-7
C.3.2	Vehicle Roof Mount - Magnetic Base .....	C-7
C.3.3	Camera Tripod Mount .....	C-8
C.3.4	Car Tow Bar Mount .....	C-8
C.3.5	Portable Mast .....	C-9
C. 4	References - Appendix C .....	C-10

Appendix D - Software

D.1	DAQ3 .....	D-1
D.2	CONVRTG2 .....	D-2
D.3	DELAYG4 .....	D-2
D.4	AVERAGEG, AVERAGEA .....	D-2

D.4.1	AVERAGEG.....	D-2
D.5.1	AVERAGEA.....	D-3
D.6	PLOTG2.....	D-4
D.7	RAYS, RAYS1, RAYS20.....	D-5
D.7.1	.PTH File.....	D-5
D.7.2	.RAY File.....	D-6
D.7.3	.STS File.....	D-6
D.7.4	Example of a filebaseS.PTH Output File.....	D-8
D.7.5	Example of a filebase.PKE Output File.....	D-9
D.7.6	Example of Part of a filebase.RAY Output File.....	D-9
D.7.7	Example of a filebase.STS Output File.....	D-10
D.7.8	Example of part of a filebase.PA Output File.....	D-10
D.7.9	Example of Part of a filebase.PT Output File.....	D-11
D.7.10	Example of Part of a filebase.NA Output File.....	D-11
D.7.11	Example of Part of a filebase.NT Output File.....	D-12
D.8	RAYSORT.....	D-13
D.9	RAYBIN, RAYBIN1.....	D-14
D.9.1	.TBN File.....	D-15
D.9.2	RAYBIN1.....	D-15
D.9.3	Example of a filebase.TBN Output File.....	D-16
D.10	ELIPSE.....	D-16
D.12	RMSIM Family.....	D-17
D.13	RAKE Family.....	D-20

## Appendix E - Measurement Locations

E.1	Adelaide - Victoria Square.....	E-2
E.2	Adelaide - Hotel Adelaide First Floor.....	E-5
E.3	Adelaide - Hotel Adelaide Roof.....	E-7
E.4	Melbourne - Bourke Street Mall.....	E-12
E.5	Melbourne - 300 Flinders Street, 13th. Floor.....	E-13
E.6	Melbourne - City Arcades.....	E-14
E.7	Melbourne - North Fitzroy Balcony.....	E-15
E.8	Melbourne - North Fitzroy Roof.....	E-17
E.9	Canberra - City Hill.....	E-23
E.10	Canberra - O'Connor Suburban.....	E-27
E.11	Canberra - Dundas Court.....	E-29
E.12	Sydney - McMahon's Point.....	E-32
E.13	Sydney - McMahon's Point, Second Series.....	E-35
E.14	Sydney - University of Technology, Broadway.....	E-38

# Figures

## Chapter 2 - The Fading Channel

FIGURE 2.1	Doppler shift experienced by a moving vehicle .....	2-3
FIGURE 2.2	Summary of fading conditions.....	2-6
FIGURE 2.3	Interrelationship between statistical distributions.....	2-10
FIGURE 2.4	2-Ray propagation model.....	2-12
FIGURE 2.5	Map showing base station location .....	2-16
FIGURE 2.6	Instrumentation for signal strength measurement.....	2-18
FIGURE 2.7	Level 7 building D - part of route showing small scale fading.....	2-18
FIGURE 2.8	Level 7 building D, north-south route. ....	2-19
FIGURE 2.9	Level 5 building D, north-south route .....	2-19
FIGURE 2.10	Level 3 building D, north-south route .....	2-19
FIGURE 2.11	Signal strength statistics on different floors.....	2-21
FIGURE 2.12	Normalised level crossing rate relative to moving dB average. ....	2-22
FIGURE 2.13	Densely tapped delay line model .....	2-25
FIGURE 2.14	Relationship between the impulse response and the delay-Doppler function .....	2-26
FIGURE 2.15	Angle of arrival in three dimension space .....	2-26
FIGURE 2.16	A measured power delay profile showing level threshold.....	2-29
FIGURE 2.17	Measures of time spread .....	2-31
FIGURE 2.18	Power delay profile examples: (a) low K factor (b) medium K factor (c) high K factor. ....	2-32
FIGURE 2.19	Relation between modified K factor $K_m$ and K factor .....	2-33
FIGURE 2.20	Idealised exponential power delay profile .....	2-35
FIGURE 2.21	Normalised delay spread versus threshold for an exponential power delay profile .....	2-36
FIGURE 2.22	Idealised power delay profile with multiple clusters of scatterers.....	2-36
FIGURE 2.23	Measured instantaneous PDP showing an exponential envelope .....	2-37
FIGURE 2.24	rms delay spread versus threshold for measured PDP <i>vutrv97</i> with a range threshold of 950 ns .....	2-37
FIGURE 2.25	CDF of rms delay spread versus threshold - Victoria University campus measurement series <i>vutrv</i> .....	2-38
FIGURE 2.26	CDF of rms delay spread versus threshold - Sydney outdoor measurements. ....	2-39
FIGURE 2.27	Detail of CDF of rms delay spread versus thresholds from -10 dB to -25 dB for Sydney outdoor measurements. ....	2-39
FIGURE 2.28	Delay spread variation with threshold .....	2-40

## Chapter 3 - Channel Sounding

FIGURE 3.1.	Summary of wideband sounding techniques .....	3-2
FIGURE 3.2.	Relative popularity of channel sounding techniques .....	3-6
FIGURE 3.3.	Cox receiver sliding correlator sounder architecture.....	3-6
FIGURE 3.4.	Modified Cox receiver (after Demery) .....	3-7
FIGURE 3.5.	Takeuchi sounder receiver architecture .....	3-7
FIGURE 3.6.	New algorithm - principle of operation .....	3-11
FIGURE 3.7.	Illustration of the new algorithm .....	3-11

FIGURE 3.8.	Simulations for $N=63$ , $k/N = 0.51$ to 50 .....	3-14
FIGURE 3.9.	Correlation peak detail for $N=1023$ , various $k$ .....	3-15
FIGURE 3.10.	Correlation power in dB for $N=1023$ , various $k$ .....	3-16
FIGURE 3.11.	Correlation peak width versus $k/N$ , $N = 1023$ .....	3-16
FIGURE 3.12.	Correlation peak power versus $k/N$ .....	3-17
FIGURE 3.13.	Simulated sliding correlator performance for $N$ and $k$ values used in the VUT channel sounder .....	3-18
FIGURE 3.14.	Simulated dynamic range, for $k/N$ values of 0.5 to 50 .....	3-19
FIGURE 3.15.	Sliding correlator dynamic range design curves .....	3-20
FIGURE 3.16.	Comparison with Johnson, $N = 127$ .....	3-21
FIGURE 3.17.	Active filters used in the SPICE simulation .....	3-22
FIGURE 3.18.	Integrating filter frequency response - Four different filters each with cutoff frequency $\approx 2.5$ kHz .....	3-22
FIGURE 3.19.	Filter time response with input from ideal correlator .....	3-23
FIGURE 3.20.	Effect of various correlation filters .....	3-24
FIGURE 3.21.	Simulated and measured PDPs showing similar dynamic ranges. $N=1023$ , $k=5000$ , receiver input for measured response = $-73$ dBm .....	3-25
FIGURE 3.22.	Detail of correlation peaks shown in Figure 3.21 .....	3-25
FIGURE 3.23.	Backpack receiver unit .....	3-27
FIGURE 3.24.	Channel sounder transmitter - block diagram .....	3-29
FIGURE 3.25.	Channel sounder receiver - block diagram .....	3-30
FIGURE 3.26.	Measured frequency response of bandpass filters .....	3-33
FIGURE 3.27.	Passband detail - bandpass filters measured response .....	3-33
FIGURE 3.28.	Measured impulse response of single bandpass filters .....	3-34
FIGURE 3.29.	Best-case channel sounder impulse response based on two cascaded 50 MHz filters convolved with the PN autocorrelation function .....	3-35
FIGURE 3.30.	Receiver noise model .....	3-36
FIGURE 3.31.	Receiver noise floor and signal overload levels .....	3-38
FIGURE 3.32.	Receiver on trolley with distance triggering wheel .....	3-45
FIGURE 3.33.	Artificial channel time response (using HP8510C) .....	3-45
FIGURE 3.34.	Back-to-back testing via an artificial channel .....	3-46
FIGURE 3.35.	Channel sounder response with artificial channel, 100 MHz chip rate, $N=1023$ , $k=20,000$ , receiver input = $-73$ dBm .....	3-47
FIGURE 3.36.	Channel sounder response with artificial channel, 25 MHz chip rate, $N=1023$ , $k=5,000$ , receiver input = $-80$ dBm .....	3-47
FIGURE 3.37.	Impulse response of the Channel Sounder, 100 MHz chip rate, $N=1023$ , $k=20,000$ receiver input = $-73$ dBm .....	3-48
FIGURE 3.38.	Response over a 1 metre air path, indoors .....	3-48
FIGURE 3.39.	Impulse response via cable and 130dB attenuator .....	3-49
FIGURE 3.40.	Example of an indoor mode PDP, rms delay spread 48 ns, threshold $-15$ dB .....	3-49
FIGURE 3.41.	Back-to-back resolution in outdoor mode, 25 MHz chip rate .....	3-50
FIGURE 3.42.	Back-to-back calibration for outdoor and indoor modes .....	3-51
FIGURE 3.43.	Measured RF power amplifier linearity with DSSS signal .....	3-51
FIGURE 3.44.	Dynamic range improvement with new offset removal scheme .....	3-53

## Chapter 4 - Indoor Measurements

FIGURE 4.1	Victoria University of Technology Footscray campus - aerial view showing measurement locations .....	4-9
FIGURE 4.2	Single point ray tracing .....	4-10

FIGURE 4.3	Receiver route along corridor .....	4-10
FIGURE 4.4	D Block Level 7 corridor .....	4-11
FIGURE 4.5	X-Ray simulated receiver power for various combinations of reflections, wall transmissions, and diffractions.....	4-11
FIGURE 4.6	Median and standard deviation of X-Ray simulated receiver power in dB for all combinations of parameters used .....	4-12
FIGURE 4.7	X-Ray rms delay spread for various numbers of reflections .....	4-13
FIGURE 4.8	X-Ray rms delay spread for various numbers of wall transmissions .....	4-13
FIGURE 4.9	X-Ray rms delay spread for various numbers of reflections and diffractions ..	4-14
FIGURE 4.10	Measured rms delay spread.....	4-14
FIGURE 4.11	Scattering ellipse for high delay spread measurements .....	4-15
FIGURE 4.12	Measured average PDPs along corridor AA.....	4-16
FIGURE 4.13	Scattering ellipses for medium delay spread example.....	4-16
FIGURE 4.14	Measured average PDPs (Section AA) after range limit application .....	4-17
FIGURE 4.15	Delay spread from measurement and ray tracing .....	4-18
FIGURE 4.16	Comparison of measured and simulated rms delay spreads .....	4-18
FIGURE 4.17	Distributions of average measured, X-Ray best configurations, and MCST <sup>TM</sup> in the long corridor Section AA of route.....	4-20
FIGURE 4.18	Campus plan, showing two outdoor routes in the courtyard area.....	4-21
FIGURE 4.19	VUT Campus showing overhead walkways.....	4-21
FIGURE 4.20	Victoria University of Technology campus route <i>nv</i> , showing overhead structures .....	4-22
FIGURE 4.21	X-Ray simulated receiver power for route <i>nv</i> .....	4-23
FIGURE 4.22	X-Ray and measured rms delay spread for route <i>nv</i> .....	4-24
FIGURE 4.23	MCST <sup>TM</sup> and measured rms delay spread for route <i>nv</i> .....	4-24
FIGURE 4.24	Distributions of average measured, X-Ray and MCST <sup>TM</sup> ray tracing delay spreads for route <i>nv</i> .....	4-25
FIGURE 4.25	The location of route <i>m</i> .....	4-26
FIGURE 4.26	X-Ray simulated receiver power for route <i>m</i> .....	4-26
FIGURE 4.27	X-Ray and measured rms delay spread for route <i>m</i> .....	4-27
FIGURE 4.28	MCST <sup>TM</sup> and measured rms delay spread for route <i>m</i> .....	4-27
FIGURE 4.29	Distributions of average measured, X-Ray and MCST <sup>TM</sup> delay spreads over route <i>m</i> .....	4-28
FIGURE 4.30	Level 7 route, showing transmitter location near windows .....	4-29
FIGURE 4.31	Delay spread CDFs for different transmitter locations - Level 7.....	4-30
FIGURE 4.32	Delay spread CDFs for different floors of building.....	4-31
FIGURE 4.33	Delay spread versus path loss factor - Level 7 with transmitter on the same floor.....	4-31
FIGURE 4.34	Delay spread versus path loss factor - Level 5 with transmitter two floors above.....	4-32
FIGURE 4.35	Average delay versus delay spread - Level 7.....	4-33
FIGURE 4.36	Relation between average delay and delay spread - Level 5 .....	4-34
FIGURE 4.37	Illustrating a PDP with high $D_{avg}/ds_{rms}$ ratio .....	4-35
FIGURE 4.38	CDF of number of rays in one PDP on Levels 7, 5, 4 and 3 .....	4-36
FIGURE 4.39	Average total rays per PDP vs. threshold, and building floor.....	4-37
FIGURE 4.40	Approximations to average total rays per PDP .....	4-37
FIGURE 4.41	Exponential power delay profile.....	4-38
FIGURE 4.42	Average number of rays per PDP sorted by power and delay .....	4-39

Chapter 5 - Outdoor Measurements

FIGURE 5.1	Victoria Square transmitter site.....	5-3
FIGURE 5.2	Adelaide - CDFs of rms delay spread.....	5-4
FIGURE 5.3	Adelaide - CDFs of average delay.....	5-4
FIGURE 5.4	Adelaide - 15dB delay window.....	5-5
FIGURE 5.5	Adelaide - CDFs of K factor.....	5-5
FIGURE 5.6	Antenna on Delbridge Street balcony, looking north east.....	5-7
FIGURE 5.7	Roof antenna at Delbridge Street.....	5-7
FIGURE 5.8	Melbourne - CDFs of rms delay spread.....	5-8
FIGURE 5.9	Melbourne - CDFs of average delay.....	5-8
FIGURE 5.10	Melbourne - 15dB delay window, showing long delays.....	5-9
FIGURE 5.11	Melbourne - 15dB delay window with detail at lower delays.....	5-9
FIGURE 5.12	Melbourne - CDFs of K factor.....	5-10
FIGURE 5.13	City Hill transmitter site.....	5-11
FIGURE 5.14	Roof-top antenna - Dundas Court.....	5-12
FIGURE 5.15	Canberra - CDFs of rms delay spread.....	5-12
FIGURE 5.16	Canberra - CDFs of average delay.....	5-13
FIGURE 5.17	Canberra - CDFs of 15dB delay window.....	5-13
FIGURE 5.18	Canberra - CDFs of K factor.....	5-14
FIGURE 5.19	View from North Sydney (McMahons Point) across Sydney Harbour to the high-rise city.....	5-14
FIGURE 5.20	McMahons Point transmitter site in relation to the city.....	5-15
FIGURE 5.21	McMahons Point transmitter site, on 4th. floor balcony.....	5-15
FIGURE 5.22	Sydney CDFs of rms delay spread.....	5-16
FIGURE 5.23	Sydney CDFs of average delay.....	5-17
FIGURE 5.24	Sydney CDFs of 15dB delay window.....	5-17
FIGURE 5.25	Sydney CDFs of K factor.....	5-18
FIGURE 5.26	Presentation example - distribution of rays over time and power bins.....	5-19
FIGURE 5.27	Adelaide propagation signatures.....	5-21
FIGURE 5.28	Melbourne City propagation signatures.....	5-22
FIGURE 5.29	Melbourne suburban propagation signatures.....	5-23
FIGURE 5.30	Canberra propagation signatures.....	5-24
FIGURE 5.31	Sydney propagation signatures.....	5-25
FIGURE 5.32	Comparison of delay spread statistics.....	5-26

Chapter 6 - RAKE Diversity

FIGURE 6.1	Filtered power delay profile (file <i>sydb18</i> ).....	6-5
FIGURE 6.2	Melbourne - 1.25 MHz bandwidth.....	6-7
FIGURE 6.3	Melbourne - 8 MHz bandwidth.....	6-7
FIGURE 6.4	Sydney - 1.25 MHz bandwidth.....	6-8
FIGURE 6.5	Sydney - 8 MHz bandwidth.....	6-8
FIGURE 6.6	Number of tines - Melbourne.....	6-9
FIGURE 6.7	Number of tines - Adelaide.....	6-10
FIGURE 6.8	Number of tines - Sydney.....	6-10
FIGURE 6.9	Level 7 D Block - LOS.....	6-13
FIGURE 6.10	Level 7 D Block - NLOS and LOS.....	6-13
FIGURE 6.11	Level 6 D Block - NLOS.....	6-14
FIGURE 6.12	Level 7 D Block - NLOS.....	6-14
FIGURE 6.13	Level 5 D Block - NLOS.....	6-15
FIGURE 6.14	Level 4 D Block - NLOS.....	6-15

FIGURE 6.15	Level 3 D Block - NLOS .....	6-16
FIGURE 6.16	Finding environment constants for the indoor model .....	6-17
FIGURE 6.17	Distribution of rms delay spreads for each model environment factor .....	6-19
FIGURE 6.18	Comparison of <i>Martin</i> and <i>Ericsson</i> models .....	6-21
FIGURE 6.19	Comparison of models with outdoor measured data .....	6-22
FIGURE 6.20	Comparison of models with indoor measured data .....	6-23

## Appendix A - Transmitter Hardware

FIGURE A.1	Transmitter electronics .....	A-1
FIGURE A.2	Phase lock loop block diagram .....	A-3
FIGURE A.3	Loop filter .....	A-6
FIGURE A.4	Loop filter design at 1.89 GHz .....	A-6
FIGURE A.5	Open loop Bode plot for 1890 MHz phase locked loop .....	A-7
FIGURE A.6	Z-Com C-600M measured VCO transfer function .....	A-8
FIGURE A.7	PLL programmable counter schematic .....	A-9
FIGURE A.8	Phase frequency comparator and loop filter .....	A-10
FIGURE A.9	VCO and output amplifier .....	A-10
FIGURE A.10	PLL phase noise .....	A-11
FIGURE A.11	Spectrum of 1890 MHz synthesizer at 10 MHz span .....	A-12
FIGURE A.12	Spectrum of 1890 MHz synthesizer at 40 kHz span .....	A-12
FIGURE A.13	Spectrum at 1890 MHz showing $\pm 200$ kHz spurs .....	A-13
FIGURE A.14	Spectrum at 1690 MHz showing $\pm 200$ kHz spurs .....	A-13
FIGURE A.15	PLL design parameters .....	A-15
FIGURE A.16	Open loop Bode plot for 100 MHz phase locked loop .....	A-16
FIGURE A.17	VHF Synthesizer circuit schematic .....	A-16
FIGURE A.18	VHF synthesizer single sideband phase noise .....	A-17
FIGURE A.19	Frequency divider circuit schematic .....	A-18
FIGURE A.20	Variable length PN generator - block diagram .....	A-19
FIGURE A.21	Clock preamplifier and ECL translator .....	A-22
FIGURE A.22	Block diagram - variable clock .....	A-23
FIGURE A.23	PN generator clock and power supply schematic .....	A-24
FIGURE A.24	Spectrum showing clock spurs .....	A-25
FIGURE A.25	PN generator circuit schematic .....	A-25
FIGURE A.26	PN spectrum fine detail .....	A-26
FIGURE A.27	PN output waveform .....	A-27
FIGURE A.28	Clock break through at first null - PN generator No.1 .....	A-28
FIGURE A.29	PN generator No.1 spectrum with 20 MHz clock .....	A-29
FIGURE A.30	PN generator No.1 spectrum with 80 MHz clock .....	A-29
FIGURE A.31	Double balanced SRA-2000 bi-phase modulator .....	A-30
FIGURE A.32	Bi-phase modulation action .....	A-30
FIGURE A.33	Transmitter power arrangements .....	A-32
FIGURE A.34	Step-up switching regulator for the RF driver amplifier .....	A-33
FIGURE A.35	High current regulator block diagram .....	A-34
FIGURE A.36	High current 12V regulator .....	A-34
FIGURE A.37	Low-dropout regulator performance .....	A-35
FIGURE A.38	Power supply supervision LEDs .....	A-35

**Appendix B - Receiver Hardware**

FIGURE B.1	Receiver electronics.....	B-1
FIGURE B.2	VUT channel sounder receiver and data acquisition equipment in portable backpack configuration.....	B-2
FIGURE B.3	Front end noise considerations .....	B-2
FIGURE B.4	Prototype low pass filter parameters.....	B-5
FIGURE B.5	Filter insertion loss versus bandwidth, unloaded $Q$ , and order $N_{order}$ .....	B-6
FIGURE B.6	Plan view showing filter dimensions .....	B-9
FIGURE B.7	Tinplate experimental filter.....	B-12
FIGURE B.8	Effect of resonator rod diameter .....	B-13
FIGURE B.9	Filter construction detail .....	B-15
FIGURE B.10	Filter design spreadsheet - 50 MHz bandwidth .....	B-16
FIGURE B.11	Filter with top plate removed (connector taps incomplete) .....	B-16
FIGURE B.12	Side elevation of 50 MHz filter, showing dimensions.....	B-17
FIGURE B.13	Design spreadsheet for the 200 MHz filter.....	B-17
FIGURE B.14	Side elevation of the 200 MHz filter .....	B-18
FIGURE B.15	Measured frequency response for 50 MHz filter (serial 001).....	B-18
FIGURE B.16	Group delay for 50 MHz filter (serial 001).....	B-19
FIGURE B.17	Measured passband group delay for 50 MHz filter (serial 001).....	B-19
FIGURE B.18	Measured frequency response for 200 MHz filter (serial 001).....	B-20
FIGURE B.19	Passband detail (1 dB/division) for 200 MHz filter (serial 001) .....	B-21
FIGURE B.20	Frequency response of ZEL-1724LN low noise amplifier .....	B-22
FIGURE B.21	Circuit schematic of low noise amplifier .....	B-23
FIGURE B.22	Measured response of boxed INA low noise amplifier .....	B-23
FIGURE B.23	Multiplier block diagram .....	B-24
FIGURE B.24	Multiplier 100 MHz and 200 MHz - circuit schematic .....	B-25
FIGURE B.25	Phase noise versus frequency offset at 200 MHz .....	B-25
FIGURE B.26	Bessel integrators circuit schematic.....	B-27
FIGURE B.27	Bessel integrators frequency response (SPICE simulations).....	B-29
FIGURE B.28	Bessel integrators group delay (SPICE simulations).....	B-29
FIGURE B.29	Bessel integrators group delay (SPICE simulations).....	B-30
FIGURE B.30	Group delay error with nearest preferred value components for 3 kHz filter .....	B-30
FIGURE B.31	Bessel integrators measured frequency response.....	B-31
FIGURE B.32	Measured difference in dB gains, I Channel - Q Channel .....	B-32
FIGURE B.33	3 KHz filters, measured phase difference I and Q channels .....	B-33
FIGURE B.34	3 kHz filters, measured % delay difference I and Q channels .....	B-33
FIGURE B.35	$I^2+Q^2$ squarer and adder circuit .....	B-34
FIGURE B.36	$I^2+Q^2$ squarer and adder performance .....	B-35
FIGURE B.37	Receiver switching supplies.....	B-36
FIGURE B.38	Receiver power supply arrangement.....	B-37
FIGURE B.39	Receiver power supply tagstrip.....	B-38
FIGURE B.40	PN counter .....	B-39
FIGURE B.41	TTL to ECL interface for presetting PN generator.....	B-40
FIGURE B.42	Modified receiver divider .....	B-41
FIGURE B.43	10 MHz buffer.....	B-41
FIGURE B.44	Wheel trigger electronics .....	B-42
FIGURE B.45	Receiver on a trolley - with wheel trigger .....	B-42
FIGURE B.46	Range switch (C1, C2) settings.....	B-43



**Appendix C - Antennas**

FIGURE C.1    Discone antenna - cross section view .....C-1

FIGURE C.2    Discone - measured VSWR .....C-2

FIGURE C.3    Discone azimuth polar pattern at three frequencies .....C-3

FIGURE C.4    Discone elevation pattern at three frequencies .....C-4

FIGURE C.5    Discone on test in the anechoic chamber at the University of Bristol.....C-4

FIGURE C.6    Halfwave 1890MHz J antenna.....C-5

FIGURE C.7    Halfwave J antenna - measured VSWR.....C-6

FIGURE C.8    J antenna azimuth polar pattern at three frequencies - roof mount  
                  model in plastic tube .....C-6

FIGURE C.9    J antenna - roof mount version .....C-7

FIGURE C.10    Tow bar mount in use.....C-8

FIGURE C.11    Portable light weight mast .....C-9

**Appendix E - Measurement Locations**

FIGURE E.1    Adelaide - Victoria Square site, showing receiver locations .....E-2

FIGURE E.2    Hotel Adelaide - transmitter on first floor (map 1).....E-5

FIGURE E.3    Hotel Adelaide - transmitter on first floor (map 2).....E-7

FIGURE E.4    Hotel Adelaide - transmitter on roof (map 1) .....E-10

FIGURE E.5    Hotel Adelaide - transmitter on roof (map 2) .....E-11

FIGURE E.6    Hotel Adelaide - transmitter on roof (map 3) .....E-11

FIGURE E.7    Melbourne - Bourke Street mall, and Flinders Street transmitter sites.....E-12

FIGURE E.8    Melbourne - city arcades, showing measurement locations .....E-14

FIGURE E.9    Melbourne - Delbridge Street balcony receiver locations .....E-17

FIGURE E.10    Melbourne - Delbridge Street roof measurement locations.....E-18

FIGURE E.11    Canberra - City Hill measurement locations.....E-23

FIGURE E.12    Canberra - O'Connor suburban residential area .....E-27

FIGURE E.13    Canberra - Dundas Court light industrial area .....E-29

FIGURE E.14    Sydney - McMahons Point, showing measurement locations .....E-34

FIGURE E.15    McMahons Point transmitter site in relation to the city.....E-35

FIGURE E.16    Sydney - University of Technology Sydney measurement locations .....E-38

# Tables

## Chapter 2 - The Fading Channel

TABLE 2.1.	Definitions of Distributions (from Ref.[2.12]) .....	2-10
TABLE 2.2.	Summary of models - VTS Radio Propagation Committee Ref.[2.15] .....	2-14
TABLE 2.3.	Building penetration loss on different floors .....	2-20
TABLE 2.4.	Summary of some published building penetration loss values .....	2-21
TABLE 2.5.	Three Denver buildings - penetration loss .....	2-22
TABLE 2.6.	Maximum normalised level crossing rates .....	2-23
TABLE 2.7.	Median delay spread ratio summary .....	2-41

## Chapter 3 - Channel Sounding

TABLE 3.1.	Ideal dynamic range of maximal length sequences .....	3-9
TABLE 3.2.	Channel sounder weights .....	3-31
TABLE 3.3.	Power consumption.....	3-32
TABLE 3.4.	Measured channel sounder impulse response in outdoor mode compared with best-case values.....	3-35
TABLE 3.5.	Parameters using free-running PN sequences.....	3-40
TABLE 3.6.	Channel sounder parameters - continuous measurement.....	3-42
TABLE 3.7.	Channel sounder parameters - windowed PN sequences.....	3-43

## Chapter 4 - Indoor Measurements

TABLE 4.1	Wall Types and Properties .....	4-8
TABLE 4.2	rms error over measured route for various X-Ray configurations, and for EDX MCS™ sorted from best to worst .....	4-19
TABLE 4.3	rms error values for route <i>nv</i> .....	4-25
TABLE 4.4	rms error values for route <i>m</i> .....	4-28
TABLE 4.5	Delay spread on different floors, with transmitter on Level 7 .....	4-30
TABLE 4.6	Number of rays per PDP .....	4-36
TABLE 4.7	Comparison between measured and ray tracing delay spreads.....	4-40

## Chapter 5 - Outdoor Measurements

TABLE 5.1	Summary of results for high antennas .....	5-27
TABLE 5.2	Summary of results for low antennas .....	5-27
TABLE 5.3	Australian measurements compared with other published results.....	5-29
TABLE 5.4	Australian measurements compared with other published results (continued)	5-30
TABLE 5.5	Explanation of abbreviations used in Tables 5.3 and 5.4.....	5-30

## Chapter 6 - RAKE Diversity

Table 6.1	Outdoor propagation data .....	6-4
Table 6.2	Number of tines versus bandwidth - outdoor data .....	6-11
Table 6.3	Number of tines from the model compared with outdoor data.....	6-12
Table 6.4	Number of tines - Group 1 INDOOR - model [measured] .....	6-17
Table 6.5	Number of tines - Group 2 INDOOR - model [measured] .....	6-18
Table 6.6	Summary of model application.....	6-18
Table 6.7	Comparison of $\alpha$ values from EQ.6.5 with empirical values .....	6-19

**Appendix A - Transmitter Hardware**

TABLE A.1	M-100 rubidium oscillator specifications .....	A-2
TABLE A.2	PLL parameters.....	A-7
TABLE A.3	VCO specifications .....	A-8
TABLE A.4	UHF synthesiser performance .....	A-10
TABLE A.5	PN generator feedback tappings .....	A-21
TABLE A.6	PN Generator Synch Patterns .....	A-24
TABLE A.7	Measured clock break-through .....	A-28
TABLE A.8	SRA-2000 data.....	A-31
TABLE A.9	RF Power amplifier specifications, model No. ANP-0113S, serial No. 4310, WESSEX Electronics.....	A-31
TABLE A.10	Batteries - transmitter.....	A-33

**Appendix B - Receiver Hardware**

TABLE B.1	Resistivity of metals.....	B-3
TABLE B.2	Butterworth low pass parameters $g(0)=g(N+1)=1$ .....	B-5
TABLE B.3	Loaded Q.....	B-6
TABLE B.4	Butterworth normalised parameters $N_{order} = 7$ .....	B-11
TABLE B.5	Measured filter performance.....	B-21
TABLE B.6	ZEL-1724LN specifications .....	B-22
TABLE B.7	Multiplier spurious outputs .....	B-26
TABLE B.8	8 pole Bessel filter parameters.....	B-27
TABLE 9.	Bessel filter component values .....	B-28
TABLE B.10	Measured filter group delay .....	B-32
TABLE B.11	DIP switch aliases for C1, C2 settings.....	B-44
TABLE B.12	Example DIP switch settings .....	B-44
TABLE B.13	PN counter DIP switch settings .....	B-45

**Appendix D - Software**

TABLE D.1	DAQ3.....	D-1
TABLE D.2	CONVRTG2 .....	D-2
TABLE D.3	DELAYG4 .....	D-2
TABLE D.3A	AVERAGEG .....	D-3
TABLE D.4	AVERAGEA .....	D-4
TABLE D.5	PLOTG2.....	D-5
TABLE D.6	RAYS .....	D-7
TABLE D.7	RAYS1 .....	D-12
TABLE D.8	RAYS20 .....	D-13
TABLE D.9	RAYSORT .....	D-14
TABLE D.10	RAYBIN .....	D-15
TABLE D.10A	ELIPSE .....	D-17
TABLE D.11	SUMMARY OF SIMULATION PROGRAMS .....	D-19
TABLE D.12	RMSIM2 .....	D-19
TABLE D.13	RAKE Turbo Pascal FILES SUMMARY .....	D-20
TABLE D.14	MATLAB SCRIPTS SUMMARY .....	D-21
TABLE D.15	BINFILEM.....	D-21
TABLE D.16	RAKE.....	D-22
TABLE D.17	RAKEMATX .....	D-22
TABLE D.18	RAKEMATC .....	D-23
TABLE D.19	ASCMAT .....	D-23

---

TABLE D.20	gtmfilt.m (MATLAB script) .....	D-24
TABLE D.21	gtmdata.m (MATLAB script) .....	D-24
TABLE D.22	gtmdatff.m (MATLAB script).....	D-25
TABLE D.23	gtmclean.m (MATLAB script).....	D-25
TABLE D.24	gtmhires.m (MATLAB script) .....	D-26

# Chapter 1: Introduction

## 1. INTRODUCTION

This chapter introduces the thesis project, and discusses the important role of the propagation channel as a component of wireless systems. Evolving third generation personal communications systems are introduced, emphasising the need for knowledge of propagation behaviour in planing and designing successful systems.

The original contributions of this project are explained, followed by an outline of the organisation of the thesis.

### 1. 1 Mobile Communications

Linking the receiver and the transmitter, the propagation channel is an essential part of any radio system.

Personal communication systems (PCS), operating in frequency bands around 1.9 GHz, are third generation systems in the rapidly evolving climate of personal and mobile telecommunications.

These services promise considerably more than voice traffic. With much wider bandwidths than existing first and second generation systems, possible facilities include high speed data, email, internet access, video and remote camera, and wireless information and shopping services.

With wideband systems such as wideband code division multiple access (WCDMA), the final configuration of services will evolve with the imagination of service-providers and users, because the technology is approaching a stage where almost anything seems possible.

No matter which mobile services are in use, at the physical level the wireless system handles streams of digital signals. And the signal is subject to all the vagaries of the multipath propagation channel, which behaves in a environment-dependent, but seemingly random manner.

### 1. 2 Original Contributions

Much activity in wideband propagation research has occurred in the northern hemisphere - in Europe, the USA, and Japan. Although Australia has the second highest take-up rate for new mobile 'phone subscribers (after Scandinavia), and has a unique rural environment, and cities different enough from other countries to merit attention, no published Australian outdoor wideband propagation measurements existed when this project commenced,

and none have appeared since.

The main original contributions of this work are:

1. development of the first self-contained and portable wideband high resolution vector channel sounder (not requiring a synchronising cable)
2. a full simulation of the sliding correlator, using a novel algorithm allowing long sequence lengths and very slow sliding rates, without the computation time becoming impossibly long. The simulations illustrate the important role of correlation noise, and show how correlation noise is often the dominant factor in determining channel sounder dynamic range.
3. the measurement of wideband channel statistics at 1.89 GHz, in different environments in four Australian cities - Adelaide, Melbourne, Canberra and Sydney.
4. a graphic way of presenting a summary of a large number of instantaneous delay spread measurements which characterise a particular propagation environment - the 'propagation signature'.
5. publication of an empirical relationship giving a guide to the number of CDMA diversity branches or 'tines' which should be used, as a function of system bandwidth and an environment constant. The number of tines was found to be proportional to the square root of the system bandwidth, and proportional to the square root of the median instantaneous rms delay spread. The relationship can be applied to both indoor and outdoor propagation.

## 1.3 Thesis Outline

Chapter 2 covers background propagation theory, beginning with a discussion of fading and definitions of the categories of fading.

Statistical distributions used in propagation are introduced, and it is shown how many of these functions nest together, as special cases of other distributions.

Some of the more popular narrowband path-loss models are discussed.

To illustrate flat-fading, some signal strength measurements inside a building are presented, and by comparison with signal strengths outside the building, building penetration loss is deduced.

Finally, wideband channels are discussed, and measures of time-dispersion are defined, including a proposed variation on the K factor, termed the *modified K factor*. Some of the measures have been applied to channel sounding data in later chapters.

Chapter 3 surveys alternative approaches to wideband channel sounders, and the merits of each method. This leads into a description of the *Victoria University of Technology* (VUT) sounder, and the parameters of the sliding correlator. An investigation of correlation distortion in the sliding correlator, using (possibly) a new simulation algorithm, is used to provide both insights into this popular technique, and design information.

Chapter 4 begins with a study of the comparison between indoor measurements and ray-tracing simulations. Evidence of multipath rays from well outside the building has been

found. Time-dispersion and the number of rays on different floors of a multistorey building is measured, showing a large increase in delay spread when the transmitter is on a different floor.

The outdoor measurement program, the main objective of this project, is documented in Chapter 5. Channel statistics are presented in several forms: rms delay spread, average delay, maximum delay, and K factor.

In Chapter 6, data from indoor and outdoor measurements described in Chapters 4 and 5, is analysed to investigate the relationship between the number of diversity branches used in a RAKE receiver, and the fraction of the total available signal power utilized, as a function of system bandwidth. A simple empirical relationship has resulted from this study.

A detailed description of the design of the channel sounder transmitter makes up Appendix A. Channel sounder receiver hardware is documented in appendix B.

The antennas are discussed in appendix C. Dimensions of antennas used with the channel sounder are given, together with standing wave ratio (VSWR) plots, and polar plots.

In the course of this project, a lot of software has been written for processing of the measured data. A summary of the functions of each program is included in appendix D.

Appendix E describes all the locations used for outdoor measurements, using detailed maps, and locality lists.

---

# Chapter 2: The Fading Channel

## 2. INTRODUCTION

Aspects of radio propagation theory are outlined in this chapter. Although much of this material is well established in the literature, summarizing it here provides a useful background for the work to follow which is presented in this thesis.

Fading is a term describing changes in the received signal amplitude and phase, leading to changes in the signal power envelope.

Types of fading are discussed, and various statistical distributions used to describe signal fading in narrowband channels are introduced and defined. The physical basis which leads to these distributions is considered. Inter-relationships between many of the distributions, where some functions are special cases of more general distribution expressions, are clarified.

The study of fading is illustrated with some measurements demonstrating narrowband small scale fading, and building penetration, for the 900 MHz band used by the GSM system.

A summary of the most widely used of the many empirical path loss models is presented.

The wideband channel is introduced, and signal dispersion effects are described. Measures of signal time dispersion, relating to the measurements presented in later chapters, are defined and discussed.

The importance of a defined threshold level for the calculation of rms delay spread is given a new emphasis, and considered in detail.

## 2. 1 Small Scale and Large Scale Fading

### 2. 1.1 Large Scale Fading

A receiver traveling over a large area (distances  $>$  many tens of wavelengths), may move from line of sight (LOS) to non-line of sight (NLOS) positions, or into areas where additional obstructions (for example, buildings) intrude into the propagation path. Under these conditions, *large scale fading* is observed. The amplitude of the signal is usually found to be lognormally distributed, and this sort of fading is also called lognormal shadow fading {Ref.[2.10]}.



## 2. 1.2 Small Scale Fading

At the receiver antenna in a multipath environment, the arriving signal is the vector sum of all significant rays in three dimensional space. Amplitudes, phases and angles of arrival of the rays are randomly distributed. If the receiving antenna moves to a new position, the vector sum will change. Large changes for small amounts of movement can occur. In one position all rays might happen to reinforce, giving a peak in the spatial signal amplitude, while just half a wavelength distant, signal cancellation may develop, giving a deep signal null. This fading effect is a spatial phenomenon, related to interference patterns in the signal field. If the receiver is moving, the spatial fading appears as a time variation of the signal. As large changes in the signal can occur within a small area of movement, this effect is termed *small scale fading*. Large scale and small scale fading should not be confused with slow and fast fading {Ref.[2.51]}.

Small scale fading may be subdivided into flat fading and frequency-selective fading on the basis of multipath time delay spread, and into fast fading and slow fading, based on Doppler spread. This results in four categories of small scale fading.

## 2. 1.3 Definitions

### 2. 1.3.1 Symbol Period $T_s$

Symbol period  $T_s$  is the period of the baseband data symbol, or the period of one bit of data.

### 2. 1.3.2 Rms Delay Spread $ds_{rms}$

Rms delay spread is the square root of the second central moment of the channel power delay profile, and gives a measure of the channel time dispersion. The definition of delay spread is discussed more fully later in this chapter (paragraph 2.7.2).

### 2. 1.3.3 Transmitted Bandwidth $BW_s$

Transmitted bandwidth  $BW_s$  is the bandwidth of the transmitted information after modulation.

### 2. 1.3.4 Coherence Bandwidth $BW_c$

Coherence bandwidth  $BW_c$  is a measure of the bandwidth over which a channel can be considered to have a flat frequency response, or the bandwidth over which spectral integrity is maintained. It is defined as the frequency spacing between two single frequency carriers which have a correlation function  $\geq 0.5$ . Coherence bandwidth is related to delay spread.

Ref[2.51] gives:

$$BW_c \approx \frac{1}{5ds_{rms}} \quad (\text{EQ 2.1})$$

Ref [2.52] gives:

$$BW_c \approx \frac{1}{2\pi ds_{rms}} \quad (\text{EQ 2.2})$$

Coherence bandwidth is also defined in terms of a correlation  $\geq 0.9$  by some authors.

### 2. 1.3.5 Doppler Spread $BW_D$

Doppler shift is the well known phenomenon where the apparent frequency of a source is modified by relative motion of the source and the receiver.

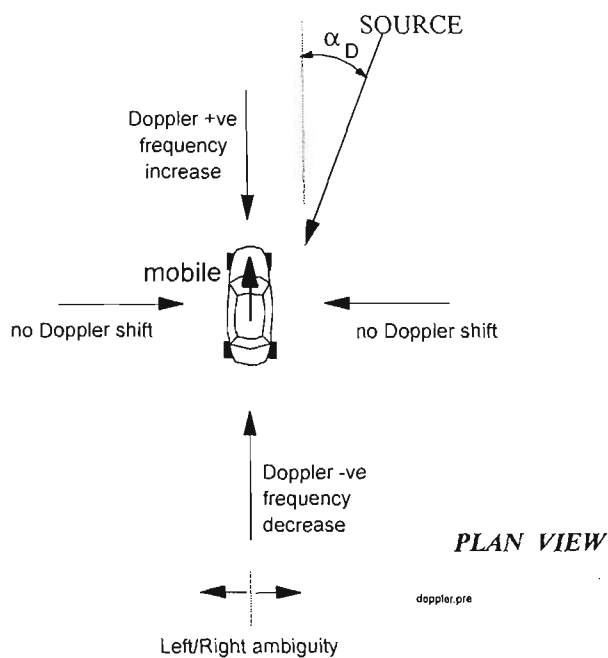


**FIGURE 2.1 Doppler shift experienced by a moving vehicle**

The vehicle shown in Figure 2.1 suffers Doppler shift  $f_D$  given by:

$$f_D = \frac{v}{\lambda_c} \cos \alpha_D = \frac{vf_c}{c} \cos \alpha_D \quad (\text{EQ 2.3})$$

Where  $f_c$  is the carrier frequency, carrier wavelength in metres is  $\lambda_c$ ,  $c$  metre/sec is the speed of light, and angle  $\alpha_D$  is the angle between the mobile vehicle velocity vector  $v$  and the incident radio ray. Doppler spread  $BW_D$  is the width of the Doppler spectrum, and is a measure of the frequency dispersion caused by relative motion of the receiver and transmitter. The Doppler spectrum extends from  $f_c - f_D$  to  $f_c + f_D$  hence:

$$BW_D = (f_c + f_D) - (f_c - f_D) = 2f_D \quad (\text{EQ 2.4})$$

Moving scatterers within the radio channel environment, principally moving motor vehicles, can create Doppler spread, even if the receiver is stationary. And if the receiver is moving, other moving vehicles can increase the expected Doppler spread by up to a factor of three {Ref.[2.53]}.

Interpreting frequency as rate of change of phase, allows the Doppler effect to be formulated in units of phase change per unit distance  $\left(\frac{\Delta\phi}{\Delta x}\right)$ , independent of velocity. This is useful for converting static phase shift measurements to Doppler shift, and for plotting Doppler shift in a normalised, velocity-independent form.

$$\frac{\Delta\phi}{\Delta x} = 2\pi \frac{\cos\alpha_D}{\lambda_c} \quad (\text{EQ 2.5})$$

Figure 2.1 shows a plan view of a Doppler scenario in three dimensions. Other rays are also arriving at various elevation angles, and these also experience Doppler shifts, provided there is a resolved component of the ray in the direction of relative motion. Note the left/right ambiguity, which must be accounted for when basing angle of arrival measurements on Doppler data.

### 2.1.3.6 Coherence Time $T_c$

Coherence time  $T_c$  is a representation of the time over which the channel impulse response remains unchanged. It is defined as the time interval between two consecutive signals which have a correlation function  $\geq 0.5$ .

Coherence time is inversely related to Doppler shift. In Ref[2.52], coherence time in terms of Doppler shift is given by the following approximate expression:

$$T_c \approx \frac{9}{16\pi f_D} \quad (\text{EQ 2.6})$$

## 2.1.4 Flat Fading

Fading effects caused by multipath propagation are categorised into *flat fading* and *frequency-selective fading*. These effects are position dependent, and occur even without motion between receiver and transmitter.

For two carrier frequencies sufficiently close together, each path will have approximately the same electrical length for the two frequencies, so amplitude and phase variations will be similar. The channel frequency response will be flat, and the transmitted spectrum will be received without any spectral distortion. This condition of flat fading occurs if the transmitted bandwidth is much less than the coherence bandwidth, and if the symbol period is much greater than the rms delay spread. That is:

$$BW_S \ll BW_c \text{ and } T_s \gg ds_{rms} \quad (\text{EQ 2.7})$$

A flat fading channel will be referred to simply as a *flat channel*.

## 2.1.5 Frequency-selective Fading

As the frequency separation of two carriers is increased, a point is reached where the behavior at one carrier frequency becomes uncorrelated with behavior at the second frequency, because phase shifts along each multipath at the different frequencies become quite different. The decorrelation, and the extent of the phase shifts, increases with increasing delay spread. This results in the amplitudes and phases of the received signal differing from the transmitted signal, giving spectral distortion. A constant amplitude carrier will experience a fluctuating amplitude at the receiver as the frequency changes. This effect is termed *frequency-selective fading*, and the channel is referred to as a *frequency-selective channel*.

Frequency-selective fading occurs when the transmitted bandwidth exceeds the coherence bandwidth, and the symbol period is less than the rms delay spread:

$$BW_s > BW_c \quad \text{and} \quad T_s < ds_{rms} \quad (\text{EQ 2.8})$$

## 2.1.6 Slow fading

Slow fading and fast fading pertain to the rate of change of the channel impulse response relative to the symbol duration, and result from motion between the receiver and transmitter, or more specifically, the Doppler spread of the channel.

Slow fading occurs when the channel impulse response changes more slowly than the symbol duration, and the transmitted bandwidth is much greater than the Doppler spread.

$$T_s \ll T_c \quad \text{and} \quad BW_s \gg BW_D \quad (\text{EQ 2.9})$$

## 2.1.7 Fast Fading

Fast fading happens when the channel impulse response changes rapidly over one symbol duration; that is, when the symbol time is greater than the channel coherence time, and the transmitted bandwidth is less than the Doppler spread.

$$T_s > T_c \quad \text{and} \quad BW_s < BW_D \quad (\text{EQ 2.10})$$

## 2.1.8 Fading Summary

In summary, flat and frequency-selective fading are determined by the extent of multipath, and are position dependent, but not motion dependent fading effects. Slow and fast fading relates to the temporal rate of change of channel characteristics in comparison with the transmitted symbol duration, and this sort of fading requires both multipath, and movement,

such that a finite Doppler spread exists. The Doppler spread may be caused by a relative velocity between the receiver and transmitter, and/or the motion of other objects which can perturb the radio channel multipath environment. Transitions between the different fading categories are not abrupt, but rather overlap and merge into each other.

The resulting four possible channel descriptions are depicted in Figure 2.2, which follows a similar diagram in Ref[2.51].

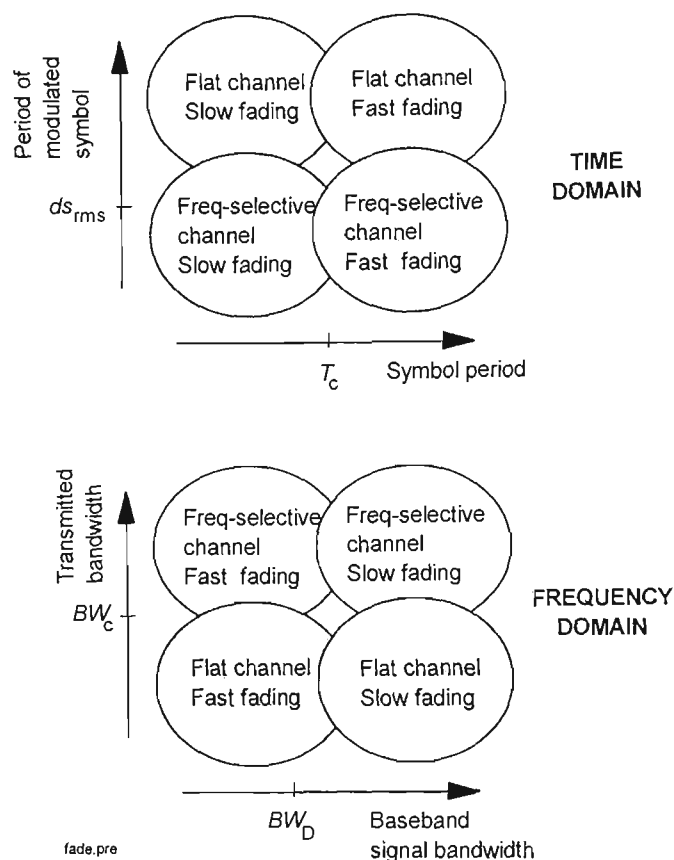


FIGURE 2.2 Summary of fading conditions

## 2. 2 Narrowband and Wideband Channels

The classification of a channel as narrowband or wideband depends on the relationship between the multipath time dispersion of the channel and the period of the transmitted information symbol (or the inverse of the modulated signal bandwidth).

A channel is classed as narrowband if flat fading prevails, and wideband if frequency-selective fading occurs.

Narrowband channel measurements have traditionally used a single carrier frequency, and measured the amplitude of the received signal envelope, whereas wideband measurements use a signal in the form of a narrow impulse, or a spread spectrum or swept frequency, equivalent to a wide transmitted bandwidth, and measure an approximation to the impulse response of the channel.

## 2.3 Statistical Distributions

The envelope of the received signal in a narrowband (flat fading) channel, or in one time bin of a wideband channel, shows a certain amplitude distribution over a small scale area. For a number of similar strength randomly distributed signal components arriving at the receiver, the signal envelope follows a Rayleigh distribution. If one path is dominant, the distribution becomes Ricean. Other mixed distributions have been formulated, and often these reduce to Rayleigh or Ricean distributions as special cases.

This section briefly introduces a number of statistical distribution functions used in propagation work, and shows the similarities and inter-relationships between these distributions.

### 2.3.1 Gaussian (or Normal) Distribution

The Gaussian probability distribution function (PDF) is:

$$P(r) = \frac{1}{\sqrt{2\pi}\sigma} \exp\left(-\frac{(r-\mu)^2}{2\sigma^2}\right) \quad (\text{EQ 2.11})$$

where  $\mu$  is the mean, and  $\sigma$  the standard deviation. The importance of the Normal distribution stems from the implications of the Central Limit Theorem.

### 2.3.2 Rayleigh Distribution

Where the receiver is located in a uniform scattering environment with no LOS or dominant path, the signal envelope is found to follow a Rayleigh distribution. All arriving signal vectors or rays are assumed to have approximately the same amplitude, with a phase distribution which is uniform over 0 to  $2\pi$ . The Rayleigh PDF is given by {Ref.[2.1], Ref.[2.2]}:

$$P(r) = \frac{r}{\sigma_R^2} \exp\left[-\frac{r^2}{2\sigma_R^2}\right] \quad (\text{EQ 2.12})$$

The most probable value (the Rayleigh parameter) is  $\sigma_R$ , and the mean and variance are given by  $\sigma_R\sqrt{\frac{\pi}{2}} = 1.253\sigma_R$  and  $\sigma_R^2\{2 - \frac{\pi}{2}\}$  respectively.

### 2.3.3 Ricean or Nakagami- $n$ Distribution

Adding a strong or dominant ray to the approximately uniform scattered rays of the Rayleigh distribution leads to the Ricean or Nakagami- $n$  distribution, developed independently by Nakagami and by Rice, {Ref.[2.3], Ref.[2.4], Ref.[2.5], Ref.[2.2]}:

$$P(r) = \frac{r}{\sigma_R^2} \exp\left[-\frac{r^2 + v_M^2}{2\sigma_R^2}\right] I_0\left(\frac{rv_M}{\sigma_R^2}\right) \quad \text{for } (r \geq 0) \quad (\text{EQ 2.13})$$

here  $I_0$  is the zero-order modified Bessel function of the first kind,  $v_M$  is the magnitude of the dominant path, and  $\sigma_R^2$  is proportional to the power of the scattered Rayleigh components. If  $v_M \rightarrow 0$  or if  $v_M^2 \ll r^2$  the dominant ray disappears, and EQ 2.13 reverts to the Rayleigh distribution.

A  $K_{factor}$  may be defined as equal to the ratio of the power in the dominant ray, to the power in the scattered rays, where:

$$K_{factor} = \frac{v_M^2}{2\sigma_R^2} \quad (\text{EQ 2.14})$$

### 2.3.4 Nakagami- $m$ Distribution

The Nakagami- $m$  distribution is a more general distribution, which reduces to the Rayleigh or the one-sided Normal distribution in particular cases, and which can also approximate the Ricean, and the lognormal distributions.

The Nakagami- $m$  PDF is given by {Ref.[2.3], Ref.[2.2]}:

$$P(r) = \frac{2m^m r^{2m-1}}{\Gamma(m) \Omega^m} \exp\left[-\frac{mr^2}{\Omega}\right] \quad \text{for } (r \geq 0) \quad (\text{EQ 2.15})$$

where  $\Gamma(m)$  is the gamma function defined by the integral:

$$\Gamma(m) = \int_0^{\infty} x^{m-1} \exp(-x) dx \quad (\text{EQ 2.16})$$

For  $m=1$  this reduces to the Rayleigh distribution, and for  $m=1/2$  it reduces to the one-sided Normal (or Gaussian) distribution.

### 2.3.5 Weibull Distribution

Introduced originally in relation to investigation of the strength of materials, the Weibull distribution has no obvious physical interpretation in terms of radio propagation. It has, however, been found to provide a good fit to the fading channel in some circumstances, for example, radar sea clutter at low grazing angles {Ref.[2.6], Ref.[2.7], Ref.[2.8], Ref.[2.9], Ref.[2.2]}. The Weibull PDF is given by:

$$P(r) = \frac{\alpha_w b}{r_0} \left(\frac{br}{r_0}\right)^{\alpha_w-1} \exp\left(-\left(\frac{br}{r_0}\right)^{\alpha_w}\right) \quad (\text{EQ 2.17})$$

where  $\alpha_w$  is a shape factor,  $b = \sqrt{(2/\alpha_w) \Gamma(2/\alpha_w)}$  and  $r_0$  is the rms value of  $r$ . This reduces to the Rayleigh distribution when  $\alpha_w = 1/2$ , and to the exponential distribution when  $\alpha_w = 1$ .

## 2.3.6 Lognormal Distribution

Shadowing resulting in large scale fading (sometimes mistakenly called slow fading), or a gradual variation of the local mean, has been found to follow a lognormal distribution {Ref.[2.10]}, where  $\log(r)$  has a Normal or Gaussian distribution. In a multipath situation, the signals reaching the receiver have typically undergone multiple reflections. Signal losses at each reflection or scattering multiply to give the total signal loss, and this multiplicative process leads to a lognormal distribution, just as the central limit theorem indicates that an additive process results in a normal distribution. The lognormal distribution is given by {Ref.[2.2]}:

$$P(r) = \frac{1}{\sqrt{2\pi}\sigma r} \exp\left(-\frac{(\ln r - \mu)^2}{2\sigma^2}\right) \quad \text{for } (r \geq 0) \quad (\text{EQ 2.18})$$

## 2.3.7 Mixed Distributions: Suzuki Distribution

Consider a signal which after undergoing multiple scattering, arrives in the vicinity of the receiver with a lognormal distribution, and is then expanded into a number of approximately equal paths by local scatterers. Each local path has approximately the same amplitude, similar excess delays, and random uniformly distributed phase, and derives from a parent with a lognormal distribution. The resulting distribution can be described by a combination of the lognormal and Rayleigh distributions {Ref.[2.11], Ref.[2.10]}:

$$P(r) = \int_0^\infty \frac{r}{\sigma^2} \exp\left(\frac{-r^2}{2\sigma^2}\right) \frac{M}{\sigma \alpha_n \sqrt{2\pi}} \exp\left(\frac{-\log(\sigma/\sigma_0)}{2\alpha_n^2}\right) d\sigma \quad (\text{EQ 2.19})$$

where  $\alpha_n$  is the lognormal shape parameter, and  $\sigma$  is the most probable value of the Rayleigh distribution, and  $M = \log e$

## 2.3.8 Stacy Distribution

It has been shown in Ref.[2.12] that the exponential distributions used in radiowave propagation (including the Rayleigh, Ricean, Nakagami- $m$ , Weibull, and one-sided Gaussian discussed above), are all particular cases of the Stacy distribution {Ref.[2.13]}. Note that the log and mixed distributions are not included in this generalization.



TABLE 2.1. Definitions of Distributions (from Ref.[2.12])

Type	Distribution	PDF	Conditions
m = 1	gamma	$Ax^n \exp (-x/b)$	n = n
m = 1	Erlang	$Ax^n \exp (-x/b)$	n+1 = PI*
m = 1	chi-squared	$Ax^n \exp (-x/b)$	b = 2, 2(n+1) = PI*
m = 2	Nakagami-m	$Ax^n \exp (-x^2/b^2)$	n = n
m = m	Stacy	$Ax^n \exp (-x^m/b^m)$	n = n
m = m	Weibull	$Ax^{m-1} \exp (-x^m/b^m)$	n = m-1
n = 0	exponential	$A \exp (-x/b)$	m = 1
n = 0	one-sided normal	$A \exp (-x^2/b^2)$	m = 2
n = 0	generalised exponential	$A \exp (-x^m/b^m)$	m = m
n = 1	Rayleigh	$Ax \exp (-x^2/b^2)$	m = 2
n = 1	generalised Rayleigh	$Ax \exp (-x^m/b^m)$	m = m

\*PI means “a positive integer”

Territory occupied by a number of these distributions is depicted in Figure 2.3.

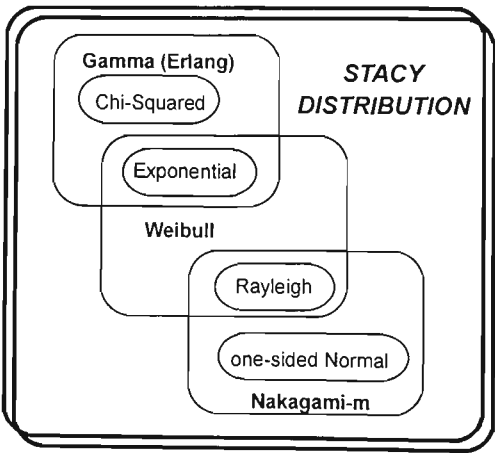


FIGURE 2.3 Interrelationship between statistical distributions

2. 3.9 Poisson Distribution

The Poisson distribution has application in predicting the occurrence of isolated events in a continuum of time. It can be used to fit the arrival times of scattered rays in a multipath radio environment. The Poisson distribution is given by {Ref.[2.14]}:

$$P(r) = \frac{\mu_p^r}{r!} \exp (-\mu_p) \qquad (\mu_p > 0)$$

(EQ 2.20)

where the expected or average number of occurrences of an event = variance =  $\mu_p$

## 2.4 Path Loss Models

Many have sought the Holy Grail of a universal propagation model, and the past is littered with myriad attempts to solve this problem. Path loss models attempt to predict signal strengths over large scale distances.

The starting point for a path loss model is propagation in free space, which gives a lower bound for the value of path loss.

### 2.4.1 Free Space

Energy radiating unimpeded from an isotropic point source spreads with a spherical wavefront, so the power density in terms of power per unit area is diluted by the inverse square of the distance from the source, as the size of the sphere grows. The ratio of available power at the receiving antenna to the power supplied to the transmitting antenna  $P_r/P_t$  is given by {Ref.[2.10]}:

$$\frac{P_r}{P_t} = G_t G_r \left( \frac{c}{4\pi f D} \right)^2 \quad (\text{EQ 2.21})$$

or in terms of path loss  $L$  dB where  $L = 10 \log \frac{P_t}{P_r}$ ,

$$L = 10 \log_{10} G_t + 10 \log_{10} G_r - 20 \log_{10} f - 20 \log_{10} D + 147.6 \quad (\text{EQ 2.22})$$

using isotropic antennas, the path loss becomes:

$$L_{\text{isotropic}} = -32.44 - 20 \log_{10} f_{\text{MHz}} - 20 \log_{10} D_{\text{km}} \quad (\text{EQ 2.23})$$

where  $G_t$  and  $G_r$  are the gains of the transmit and receive antennas respectively,  $c$  is the velocity of light,  $f$  is the frequency in Hz,  $f_{\text{MHz}}$  is the frequency in MHz,  $D$  is distance in metres, and  $D_{\text{km}}$  is distance in kilometres. Free space propagation is usually assumed if the first Fresnel zone is clear of any reflecting surfaces or obstructions.

### 2.4.2 Plane Earth (2-Ray model)

Free space propagation seldom occurs, because usually there are reflecting surfaces in the region of the propagation path. The simplest situation involving reflection is propagation over the reflecting earth, where the signal at the receiver is the resultant of the direct or free space ray, and a ground-reflected ray. At large distances, the curvature of the earth affects the geometry of the problem. Distances used with cellular mobile radio are small enough that curvature can be neglected, and the earth can be treated as a horizontal plane. The reflection coefficient is a complex quantity, and depends on the dielectric properties of the earth (which vary greatly from seawater to dry rocky ground), and also on the angle of incidence, and the

polarization. At grazing incidence, the reflection coefficient  $\rho \approx -1$ , for both horizontal and vertical polarization. For plane earth propagation where the distance  $D$  is much greater than the heights of the transmit and receive antennas,  $h_t$  and  $h_r$ , the ratio of received to transmitted power is given by {Ref.[2.10]}:

$$\frac{P_r}{P_t} = G_t G_r \frac{(h_t h_r)^2}{D^4} \quad (\text{EQ 2.24})$$

Note that the power ratio is independent of frequency, and follows an inverse fourth-power relationship with distance, which gives a much more rapid decay of power (12 dB less power for each doubling of distance or -40 dB for each decade) than in the free space case.

In log form for isotropic antennas, for comparison with EQ 2.23, the 2-ray grazing angle equation becomes:

$$L_{\text{isotropic}} = 20 \log_{10} h_t + 20 \log_{10} h_r - 40 \log_{10} D \quad (\text{EQ 2.25})$$

A plot of the 2-ray model receiver to transmitter power ratio, for frequency = 1890 MHz, transmitter antenna height = 20 metre and receiver antenna height = 1.5 metre, with asymptotes showing the inverse square law and inverse fourth power law {Ref.[2.10]} is shown in Figure 2.4.

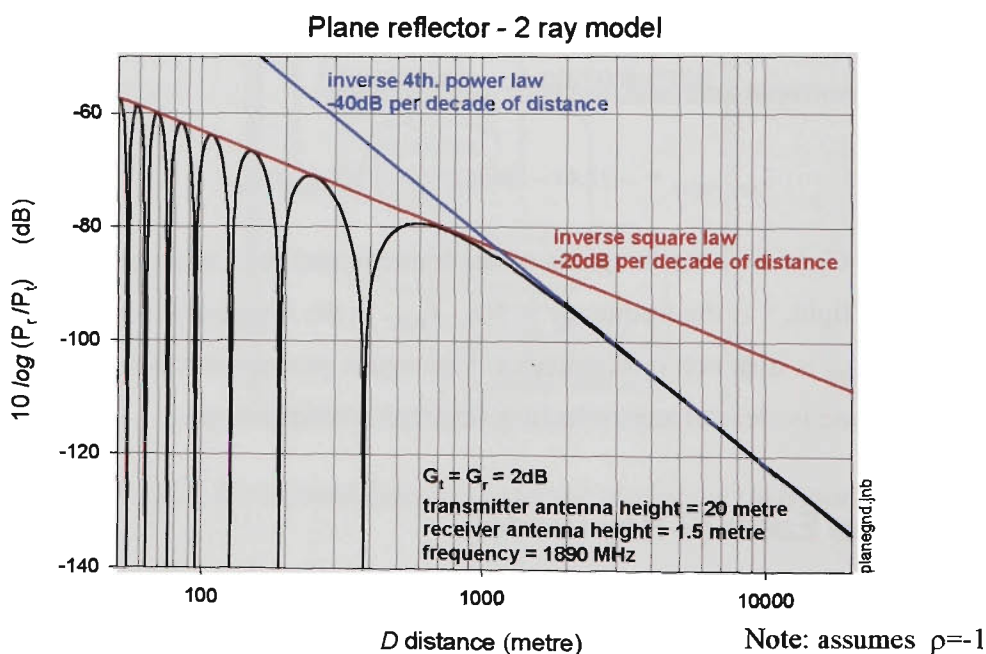


**FIGURE 2.4 2-Ray propagation model**

The 2-ray model can be extended to include more rays, for example to six rays {Ref.[2.2]}. A NLOS model with an initial path loss slope of 20dB/decade, a step loss (a corner loss) at a break-point, then a path loss slope of approximately 40dB/decade has been found to fit experimental data in some cases {Ref.[2.2]}.

Path loss behavior showing a break-point, where the slope changes from  $-10n_1$  dB/decade of distance, to  $-10n_2$  dB/decade where  $n_1$  and  $n_2$  can take a range of values, has been frequently observed.

### 2.4.3 IEEE VTS Committee on Radio Propagation

In 1988, the IEEE Vehicular Technology Society (VTS) Committee on Radio Propagation published the result of five years of deliberation on radio propagation models for the cellular radio band, in a paper titled, "Coverage Prediction for Mobile Radio Systems Operating in the 800/900 MHz Frequency Range" {Ref.[2.15]}.

Models included large area terrain models, and models more suited to small cells in built-up areas. Some models have a theoretical basis, although many are empirical models attempting to generalise from specific measurements and observations. Various correction or adjustment factors are commonly appended. Some models are presented in analytical form, some as graphs, charts, nomograms or slide rule calculators (all now of course rendered obsolete by advances in technology), and some as algorithms embodied in computer software.

A summary of features of the models considered by the IEEE committee is attempted in Table 2.2.

Most of the models listed in Table 2.2 apply to large area propagation over irregular terrain, for distances up to the order of 200 km, and are not suitable for small cells covering built-up areas dominated by building clutter. The starting point for one group of theory based approximate models is diffraction over a hill or ridge, which is treated as a knife-edge, combined with free space path loss plus possible ground reflections on each side of the hill, leading to a four-ray model. Treating the hill as an infinitely thin knife-edge is inaccurate, unless the radius of the hill top is very small compared with the wavelength. An excess loss correction can be added to the theoretical knife-edge loss to allow for rounded hills {Ref[2.10], Ref.[2.29], Ref.[2.30]}. Tree cover on the hill top modifies the loss further, and can be allowed for by another correction factor. The path loss caused by multiple knife-edges becomes mathematically complicated, so approximate methods based on various geometric constructions are used in models which attempt to treat more than one knife-edge.

The *Bullington* model represents irregular terrain as a single fictitious knife-edge. In the *Epstein-Peterson* method {Ref.[2.31]}, losses from multiple knife-edges are added, using knife heights obtained from a geometric construction. Other models of this type include the *Japanese Atlas* method {Ref.[2.32]}, the *Deygout* method {Ref.[2.33]}, and the *Giovanelli* treatment {Ref.[2.34], Ref.2.10}. Diffraction calculations based on the *Epstein-Peterson* method are also used in the *JRC* model {Ref.[2.35], Ref.[2.36]}, the *Blomquist-Ladell* model {Ref.[2.37]}, and the *Longley-Rice* models.

TABLE 2.2. Summary of models - VTS Radio Propagation Committee Ref[2.15]

Model	Ref.	Freq (MHz)	Equation	Features
Bullington	2.16		$L=139.1-20\log h+40\log D$	T,H,D,FS,GD,GR,HD
Egli	2.18	90-1000		D,GR
Carey	2.19	450-1000	$L=110.7-19.1\log h+55\log D$ for $8 \leq D < 48$ $L=91.8-18\log h+66\log D$ for $48 \leq D < 96$	D
Tech Note 101	2.20			T,F,H,D,FS,GD,GR,HD,BP
R-6602-LM	2.21			D
Longley-Rice point-point	2.22	>20		T,H,D,FS,GD,GR,HD
Longley-Rice area	2.22			D,FS,GD,GR
Okumura	2.23	150-2000		T,F,H,D,FS,GD,HD
TIREM	2.24	40-20GHz		T,H,D,FS,GD,GR,HD
General Electric slide-rule	2.25			D,FS,GD,GR
Lee	2.26		$L=142.3-20\log h+36.8\log D$	T,H,D,GR,HD
CCIR Rp.567	2.27	900		D,FS,GD,BP
Bertoni-Walfish	2.28	900	$L=147.2+A-18\log(h-h_b)+38\log D$ $A= -9 \text{ dB for example given}$	T,B,D,FS

$L$ =path loss (dB)     $h$ =base station antenna height (m)     $h_b$ =building height (m)     $D$ =distance (km)

- T    terrain data

B    building data

F    foliage data

H    hill shape

D    distance

FS    free space
- GD    diffraction- smooth earth

GR    reflection- smooth earth

HR    reflection- hills

HD    diffraction- hills

BP    building penetration

key for  
features given  
limited or  
extensive  
treatment in  
the model.

Weissberger {Ref[38]} produced equations based on empirical data, for paths blocked by trees in leaf, with dense foliage in dry condition. Using measurements from 90 MHz to 1GHz, the Egli model {Ref[2.39]}, uses an inverse fourth power law equation, multiplied by an empirical chart-based correction factor. Another example of a chart-based method is the CCIR model {Ref.[2.40]}, compiled from statistical analysis of data collected in many countries, and particularly applicable to rolling, hilly land. A second chart provides a terrain irregularity correction factor. The British Broadcasting Corporation developed the BBC model {REF.[2.41]} to plan UHF television services. This uses diffraction approximations, with a clutter-loss correction factor for clutter at the receiver end.

More recently (1997), a report published by the IEEE Vehicular Technology Society

Propagation Committee {Ref.[2.48]} has made recommendations for a two dimensional physical propagation model. This recommendation followed evaluation of nine different proposed models against extensive propagation measurement data obtained in the USA. The recommended model is the *Anderson 2D* physical model. This requires an accurate terrain database. The model first determines if the path is LOS or NLOS. If it is LOS, path loss is based on the free space value plus a ground reflection weighted according to how significantly the first Fresnel zone is obstructed. If NLOS, path loss is based on knife edge diffraction loss where a succession of obstacles is replaced by two knife edges, one at the start, and the other at the end of the obstructed region. An extra term is also included to allow for Fresnel zone obstruction prior to the first knife edge, and after the last knife edge {Ref.[2.49]}.

## 2.4.4 Models for Built-up Areas

Shadowing effects of buildings, and the guiding of propagation paths along street canyons are features of built-up areas. Models often include an environment classification, such as “suburban” or “urban”, leading to problems when the model is applied away from its home town, because usually the environment descriptions are not precisely defined. Attempts to overcome this are discussed in Ref.[2.10].

*Young* {Ref.[2.42]} used measurements between 150 MHz and 3700 MHz in New York to plot cumulative distribution curves of path loss. These are found to follow an inverse fourth power law, strongly modified by a large clutter factor. *Allsebrook and Parsons* {Ref.[2.43]} and *Ibrahim and Parsons* {Ref.[2.44]} also found the fourth power law useful for models to fit measurements in several British cities. One of the best known urban path loss models is due to *Okumura* {Ref.[2.23]}, and uses charts based on measurements in the Tokyo area. *Hata* {Ref.[2.45]} used Okumura’s charts to formulate equations from the empirical data, with some minor limitations. These equations allow easy computation of the model.

Other urban models published include those by *Lee* {Ref.[2.26]}, *McGeehan and Griffith* {Ref.[2.46]}, and *Atefi and Parsons* {Ref.[2.47]}.

Various computer software models are now available commercially, such as *Planet*® by Mobile Systems International, and network planning tools marketed by EDX. An example of European work towards a computer propagation prediction and radio network planning tool is described in Ref.[2.40]. All mobile phone operators now either use commercial tools, or in many cases have developed proprietary software to facilitate their network planning.

## 2.4.5 Level Crossing Rate and Average Fade Duration

As explained in Section 2.3, the narrow band signal amplitude over a small area can be described with one of the statistical distributions, such as the Rayleigh distribution.

Other parameters which can be obtained from narrow band multipath measurements include the *level crossing rate*, and the *average fade duration* {Ref.[2.10], pages 125-130}. A normalised level crossing rate is defined as the number of times per wavelength of travel that the signal strength drops below a specified level. The average fade duration is the average of the intervals during which the signal is below the specified threshold. This can also be normalised and expressed in terms of wavelengths. Dividing by the mobile velocity gives the denormalised fade duration in units of time. Levels are usually relative to a localised mean or median signal strength.

## 2.5 Narrow Band Measurements - Example

To illustrate aspects of narrow band propagation such as small scale fading, and level crossing rate, and as an example of building penetration around 900 MHz, measurements have been made on different floors of a multi-storey concrete and brick building with an external transmitter. The university engineering school, on the south west corner of the *Victoria University of Technology* Footscray campus was the scene of these measurements.

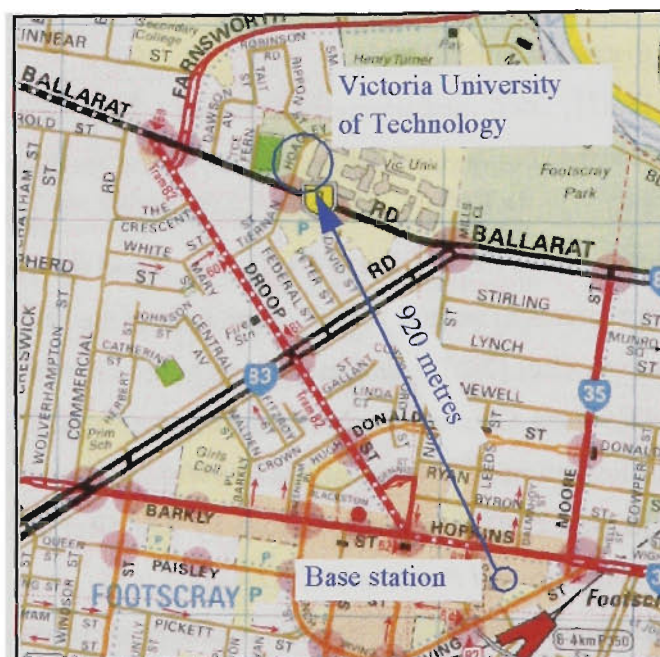


FIGURE 2.5 Map showing base station location

A broadcast channel on 945.200 MHz, transmitting from an *Optus* GSM base station approximately 920 metres to the south of the campus provided a constant signal (Figure 2.5).

Within the building, signal strength measurements were made on identical north-south routes approximately 70 metres long in a central corridor, on the top floor (Level 7), two floors lower (Level 5), and another two floors lower at ground level (Level 3). Turning ninety degrees to the corridor route, and heading east, a 20 metre route just outside the south side of the building, along the north side of Ballarat road on the footpath (ground level), was



also measured. This provided the reference outdoor signal level statistics for comparison with indoor signal strengths, required to deduce the building penetration loss.

## 2.5.1 Instrumentation

A commercial communications receiver (*Icom* R7100) and serial port interface unit (*Icom* CAV-15) were used to log received signal strength indication (RSSI) readings to a notebook computer via the RS232 port. Trolley mounted and battery powered, receiver travel distance was measured by a wheel and optical encoder, and logged through the computer parallel port (Figure 2.6). Each pulse from the wheel encoder initiated storage of a RSSI value, giving approximately 32 readings per wavelength.

Calibration of the system was done using an HP8648B signal generator and two Lucas 30 dB fixed attenuators. The receiver was calibrated with and without the internal 20 dB attenuator, although this attenuator was not used during the RSSI measurements. Plotting RSSI units against receiver input level in dBm gave a characteristic closely approximating (within  $\pm 0.5$  dB) two straight line segments, with a break-point at -77 dBm. The calibration characteristic can be written as:

$$\text{for RSSI} < 68 \quad \text{dBm} = -95 + (\text{RSSI} - 24) \frac{23}{56} \quad (\text{EQ 2.26})$$

$$\text{for RSSI} \geq 68 \quad \text{dBm} = -77 + (\text{RSSI} - 68) \frac{27}{95} \quad (\text{EQ 2.27})$$

A measured  $20 \pm 0.01$  metre run generated  $2010 \pm 1$  counts. Wavelength at 945.2 MHz is 0.3174 metre, giving 31.9 counts per wavelength. The vertically polarized quarter wave dipole antenna was mounted 1.6 metre above floor level. Measurements were made in the evening when the building was deserted, moving the trolley down the length of the corridor at a slow walking pace.

The distance measuring wheel, counter electronics, antenna, and the software for logging RSSI values to the computer, were put together by a final year undergraduate student undertaking a project supervised by the author. The measurements were made by the author, assisted by the student. Data processing, and analysis, was done by the author.



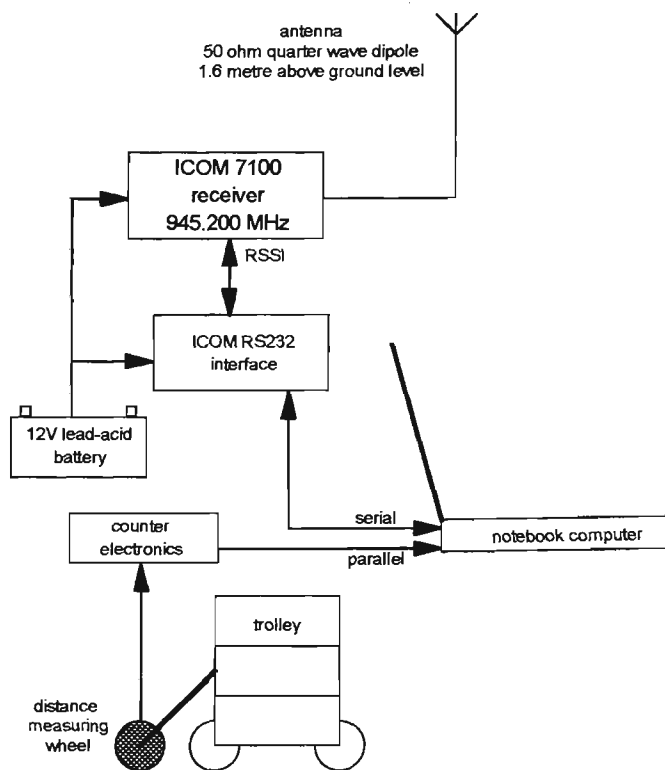


FIGURE 2.6 Instrumentation for signal strength measurement

2. 5.2 Signal Strength Results

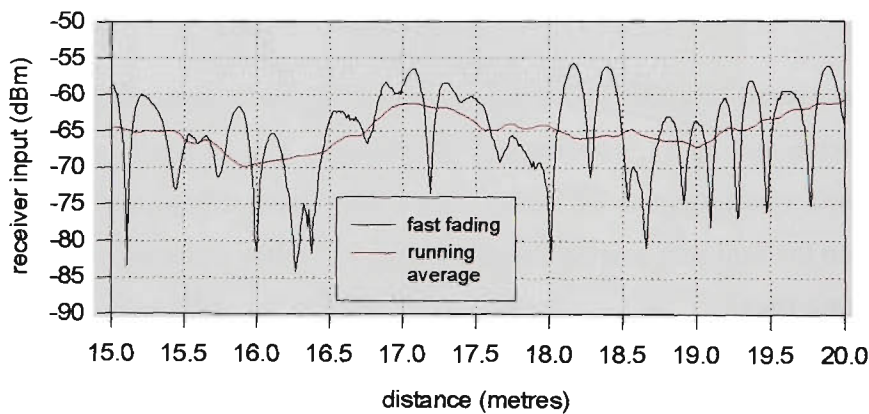
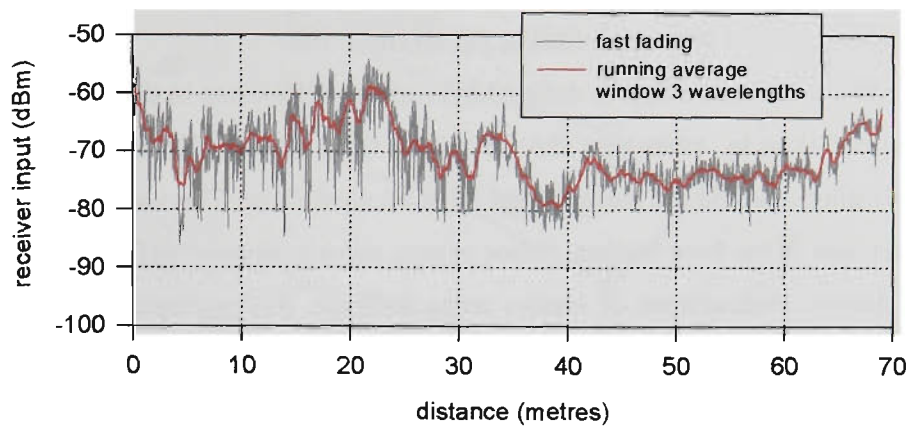
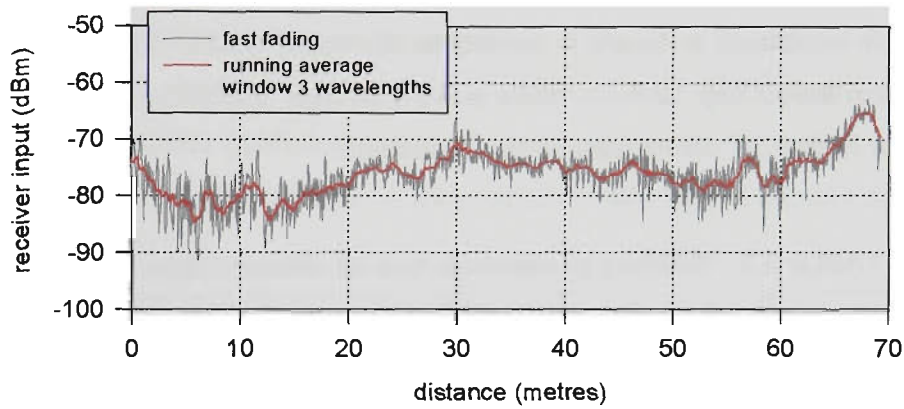


FIGURE 2.7 Level 7 building D - part of route showing small scale fading

Figure 2.7 shows a short section of the corridor route, illustrating the small scale fading structure with nulls of over 25dB. Measurements over the full corridor length on different floors are shown in Figures 2.8, 2.9, 2.10



**FIGURE 2.8** Level 7 building D, north-south route.



**FIGURE 2.9** Level 5 building D, north-south route

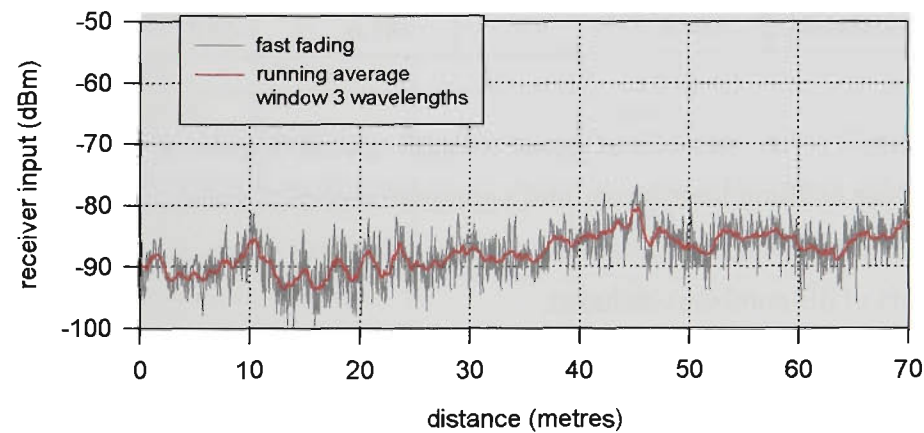


**FIGURE 2.10** Level 3 building D, north-south route

These signal strength plots (Figures 2.8, 2.9, 2.10) show small scale fading along each route, with running averages (using a 3 wavelength window) plotted in red. The average signal strengths increase at higher floor levels, being greatest on the top floor (Level 7).

2. 5.2.1 Building Penetration Loss

*Molkdar* {Ref.[2.67]}, and *Barry and Williamson* {Ref.[2.69]} include useful reviews of published literature on building penetration loss.

Building penetration loss is defined here as the difference in the dB mean signal level at ground level (taken by averaging the dB values over all sample points) outside the south end of the building, and the dB mean signal level on each floor. The south side of the building faces the direction of the base station. Other papers use a variety of definitions for penetration loss, which makes comparisons of results more difficult. For example, *Walker* {Ref.[2.61]} used an outside reference based on a dB average of the signal measured around the closest route to all the outside walls of the building. The practise of averaging dB values (rather than linear power) is widely used, for example see Ref.[2.61] and Ref.[2.68].

Taking the mean and standard deviation of the dB values of signal strength for levels 7, 5, 3, and outside the building at the south end, gives the values summarised in Table 2.3.

Penetration loss is most severe on the ground floor at 20.3 dB, and improves (i.e. the signal strength increases) as height is gained on the upper floors. Ascending two floors to Level 5 reduces the loss by 10.8 dB, while moving another two floors up to Level 7 (the top floor) gives a further 5.7 dB increase in signal strength.

:

TABLE 2.3. Building penetration loss on different floors

Location	dB mean	db standard deviation	minimum dB	maximum dB	building penetration loss dB
Level 7	-70.4	5.7	-86.4	-54.3	3.8
Level 5	-76.1	4.4	-91.3	-62.5	9.5
Level 3	-86.9	4.5	-100.3	-67.6	20.3
Outside	-66.6	5.7	-85.6	-53.1	-

Figure 2.11 shows a plot of signal strength against floor level, showing greater signal power at higher building floor levels, and a comparison with the street level values outside the building. The minimum, maximum, and average dB power values are shown, with  $\pm 1\sigma$  error bars (in terms of dB numbers) included.

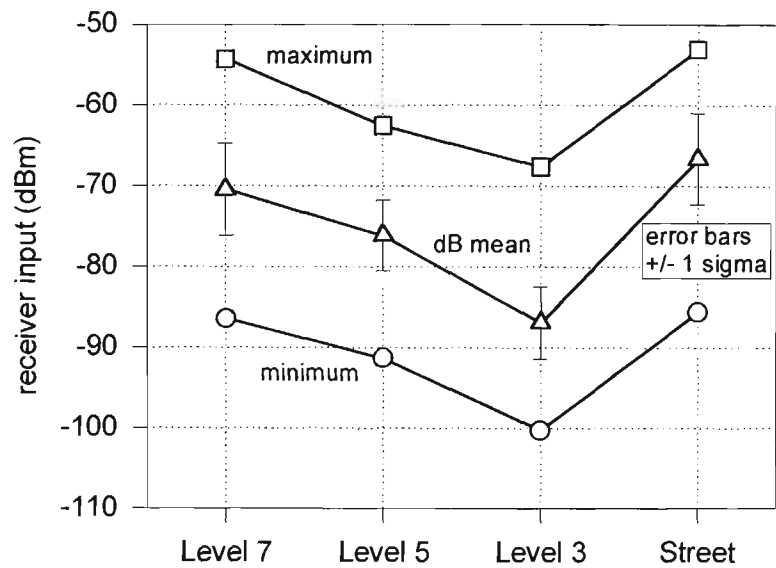


FIGURE 2.11 Signal strength statistics on different floors

The mean penetration loss on the ground floor (Level 3) is 20.3 dB, and this reduces on average by 5.4 dB per floor over the next two higher floors, and 2.9 dB per floor over the two highest floors. Other published results for penetration loss generally show the signal increasing in strength on higher floors. A summary of results from a number of other publications is given in Table 2.4.

TABLE 2.4. Summary of some published building penetration loss values

Author Reference	City	Antenna height (metre)	Range (metre)	Freq (MHz)	Penetration Loss (dB)	
					Average	change/floor
Walker 1983[2.61]	Chicago (urban)			800	18	-1.9
Turkmani 1987[2.63]	Liverpool			896.5	11.6	-2
Toledo 1992[2.64]	Liverpool	40	180 to 350	900	14.2	-1.4
Tanis 1993[2.65]	Philadelphia	57, 136		880	19.2	-1.2
Aguirre 1994[2.66]	Denver	5	200	912	12.5	
(Lee) <sup>#</sup> 1995[2.60]	Tokyo			800	26	-2.7
Martin 1999	Melbourne	25 (approx)	920	945	20.3	-5.4* -2.9**

<sup>#</sup> Lee does not disclose the source of these figures

\* for first 2 floors  
\*\* for second 2 floors

The figures in Table 2.4 often result from averaging of widely differing values. However, the penetration loss on the ground floor measured here is comparable with other published figures, but the change in penetration loss per floor over the first two floors is greater than other researchers have found. Over the next two higher floors, the change in penetration loss of -2.9 dB/floor is comparable with several other published studies {Refs.[2.60], [2.61], [2.63]}.

Different buildings, in different locations with respect to the transmitter, can give quite different penetration loss values. Table 2.5 illustrates this point, with results for three different buildings, reported by Aguirre {Ref.[2.66]}.

TABLE 2.5. Three Denver buildings - penetration loss

Number of floors	Age	Construction	Penetration Loss		
			Ground floor	change 2 floors up	change 4 floors up
19	new	glass clad	18 dB	-2 dB	5 dB
15	65 years	stone, small windows	18.5 dB	-11.5 dB	- 4.5 dB
50	new	concrete, large windows	10 dB	+11 dB	+12 dB

2. 5.3 Level Crossing Rate

The level crossing rate, and the average fade duration were defined in Section 2.4.5. Normalised level crossing rates obtained from the measurements are plotted in Figure 2.12.

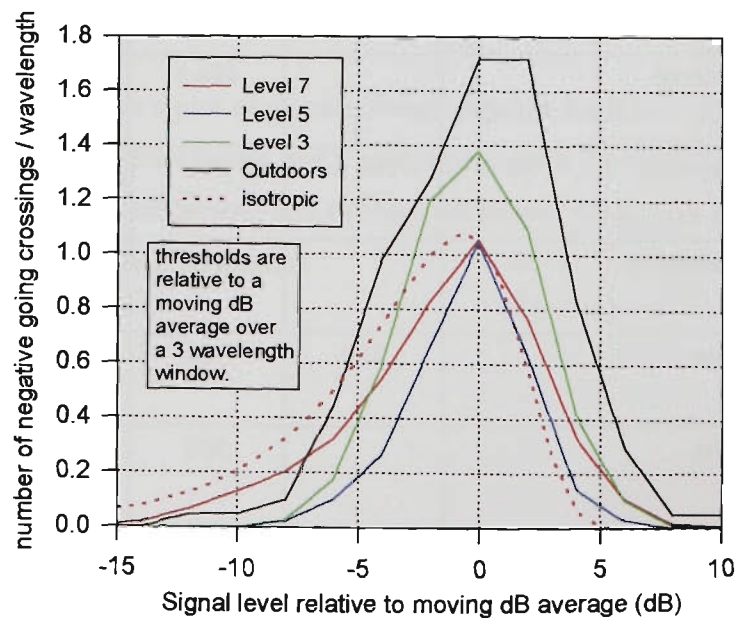


FIGURE 2.12 Normalised level crossing rate relative to moving dB average.

Results in Figure 2.12 have been calculated with the threshold level changing in 2 dB steps. The threshold is relative to the local running dB mean, over a window of 3 wavelengths. The theoretical curve for isotropic, or Rayleigh, propagation is included for comparison.

A free space or single ray model would give a level crossing rate of zero. Under conditions of isotropic (Rayleigh) scattering, Ref.[2.10] gives a peak value of 1.08, while a two ray model gives a rate of 2 level crossings per wavelength. Table 2.6 summarizes the peak values taken from Figure 2.12, and includes the theoretical values for comparison.

TABLE 2.6. Maximum normalised level crossing rates

	Measured	Theoretical
Free space	-	0
Level 7	1.05	-
Level 5	1.05	-
Isotropic	-	1.08
Level 3	1.38	-
Outdoors (Level 3)	1.72	-
Two rays	-	2

The inference is that outdoor ground level measurements indicate propagation approaching the two ray model, while Level 3 indoors shows behaviour part way between isotropic and the two ray limit. Double glass doors at the south end of Level 3 north-south corridor route face towards the base station, and wall attenuation would be expected to reduce the strength of scattered rays coming from east and west sectors. Levels 5 and 7 both give a measured peak value slightly on the free space or “one ray” side of isotropic behaviour. On these floors, antenna height is above most of the adjacent single storey buildings between the receiver and the base station, so propagation is line-of-sight, apart from the intervening walls of building D.

## 2. 6 Wideband Channels

### 2. 6.1 Introduction

A radio channel is described as wideband if frequency-selective fading occurs, or the coherence bandwidth is less than the channel bandwidth.

The radio channel can be treated as a linear filter with time-variant properties. Input and output parameters can be considered in the time or frequency domains (time, delay, frequency, Doppler shift), which results in four equivalent versions of the channel transmission function.

The weakly stationary or wide-sense stationary channel has channel correlation func-

tions which are invariant with time, or in other words, the fading statistics do not change over a short time interval. The uncorrelated scattering channel is one where rays from scattering elements with different path delays are uncorrelated. Combining these two channel definitions, the wide-sense stationary channel in the time domain, and the uncorrelated scattering channel in the time-delay domain, results in the wide sense stationary uncorrelated scattering (WSSUS) channel, which exhibits both uncorrelated delay spread and uncorrelated Doppler shifts {Ref.[2.10]}.

## 2. 6.2 Bandpass to Lowpass Equivalence

Using the complex lowpass equivalent signal allows the study of communications systems without the tedious mathematics involved in handling signals modulated onto a sinusoidal carrier.

In Chapter 2 of Ref.[2.52], the complex lowpass equivalent  $u(t)$  of a bandpass signal  $x(t)$  with a carrier frequency of  $f_c$  is derived as:

$$x(t) = \text{Re}\{u(t) e^{j2\pi f_c t}\} \quad (\text{EQ 2.28})$$

This shows that if  $u(t)$  and  $f_c$  are known then the bandpass signal  $x(t)$  is completely described. If the signal information is contained in the amplitude  $A(t)$  and phase  $\phi(t)$  of the bandpass signal,  $u(t)$  may be expressed in terms of in-phase and quadrature components  $u_I(t)$  and  $u_Q(t)$  given by:

$$u_I(t) = A(t) \cos\phi(t) \quad (\text{EQ 2.29})$$

$$u_Q(t) = A(t) \sin\phi(t) \quad (\text{EQ 2.30})$$

## 2. 6.3 Time Domain Description

A linear system is specified in the time domain by the complex time-impulse response {Ref.[2.10]}. Radio channels are time-variant, principally because of movement of the mobile station, but also because signal scatterers in the radio environment may be moving, so the impulse response is also time varying. Representing the radio channel as a time-variant linear filter with complex impulse response  $h(t, \tau)$ , where  $\tau$  is delay, the complex output  $z(t)$  of the filter is obtained by convolution:

$$z(t) = \int_{-\infty}^{+\infty} u(t - \tau) h(t, \tau) d\tau \quad (\text{EQ 2.31})$$

In physical terms,  $h(t, \tau)$  gives the channel response at time  $t$  resulting from an impulse excitation  $\tau$  seconds previously. Equation 2.31 represents the channel as an infinite number of stationary, shimmering scatterers, each with a gain fluctuation  $h(t, \tau)d\tau$ , producing

rays in the delay range  $(\tau, \tau + d\tau)$ . The physical channel is constrained to have zero output prior to the first input signal, with negligible echo signals arriving after time  $T$ , so the infinite integration limits in equation 2.31 should be altered to  $(0, T)$ . Expressing equation 2.31 as a summation with the physically realisable limits gives:

$$z(t) = \Delta t \sum_{\eta=0}^m u(t - \eta \Delta \tau) h(t, \eta \Delta \tau)$$

(EQ 2.32)

Equation 2.32 leads to the well known densely tapped delay line model for the wideband radio channel, illustrated in Figure 2.13.

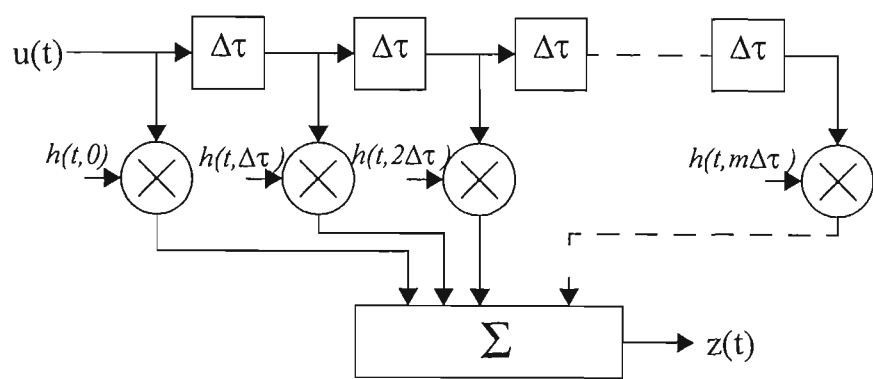


FIGURE 2.13 Densely tapped delay line model

Each path in this model represents a resolvable incoming delayed ray, and the summation of all these rays gives the time-spread output  $z(t)$  of the channel.

### 2. 6.4 Bello System Functions

*Bello* {Ref.[2.70]} developed a set of eight symmetrical functions to describe linear time-variant channels. Four of these functions are duals of the other four, and each group of four are related by Fourier transform operations {Ref.[2.10], Ref.[2.52]}. Using terminology from Ref.[2.52] , which has a clear treatment of this topic, the four system variables are: *time*  $t$  seconds, *frequency*  $f$  Hz, *delay*  $\tau$  seconds, and *Doppler shift*  $\nu$  Hz. A full description of a system requires two of these variables, one from each Fourier pair. There are twelve permutations of two variables selected from four, but four of the permutations consist of variables from the same Fourier pair (namely  $t, \nu$ ;  $\nu, t$ ;  $\tau, f$ ; and  $f, \tau$ ), leaving eight system functions remaining. For a moving terminal, time  $t$  may be related to position, or distance along a route.

The first set of four *Bello* functions comprise: (i) the impulse response  $h(t, \tau)$ , which is measured directly by wideband time-domain channel sounders, (ii)  $T(f, t)$ , measured by narrowband single frequency sounders, (iii)  $H(f, \nu)$ , measured by wideband frequency-domain sounders, and (iv)  $S(\tau, \nu)$ , the delay-Doppler function, used to illustrate simultaneous time and



frequency dispersion. The relationship between the impulse response and the delay-Doppler function is shown in Figure 2.14.

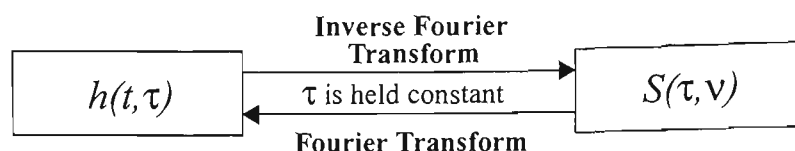


FIGURE 2.14 Relationship between the impulse response and the delay-Doppler function

## 2.6.5 Angle of Arrival

The impulse response signal voltage from the receiver antenna completely describes the radio channel in terms of phase, amplitude, time delay, and the rate of change of these with time. However, it does not contain all the information about the signal arriving at the antenna. The missing parameter is full disclosure of the angle of arrival of each ray. Doppler shift, obtained from the delay-Doppler function, allows the angle between an incoming ray and the velocity vector of the mobile to be deduced, but not the angle between the plane common to the incoming ray and the velocity vector, and the horizontal plane. In other words, left/right and up/down ambiguities exist unless additional angle of arrival information is obtained. The three dimensional angle of arrival requires two variables to describe it, such as the horizontal angle of arrival  $\alpha_h$  and the vertical angle of arrival  $\alpha_v$ . Both angles can range from 0 to  $2\pi$ . These angles are defined in Figure 2.15. Hence each tap in the delay line model (Figure 2.13) also requires an angle parameter for a complete description of the incoming signal.

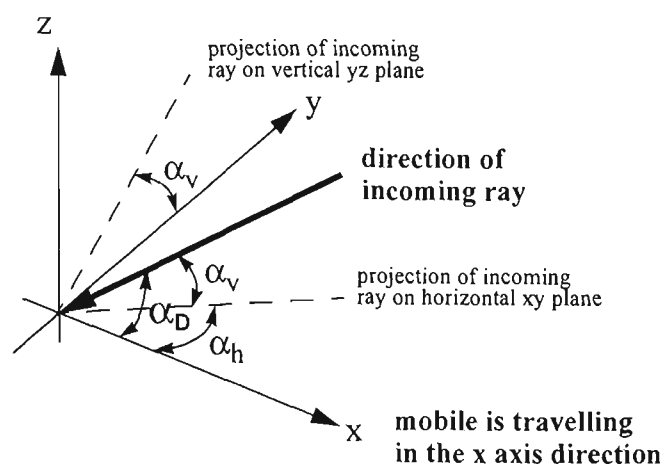


FIGURE 2.15 Angle of arrival in three dimension space

The *Clarke* two-dimensional omnidirectional scattering model {Ref.[2.71]} assumes that incoming rays are vertically polarised plane waves, which all lie in the horizontal plane. Rays arrive with random phase uniformly distributed over 0 to  $2\pi$ , and all angles of arrival are equally likely, so that  $\alpha_v = 0$  and the probability density function for the horizontal arrival

angle is  $p(\alpha_h) = 1/2\pi$

Clarke's model leads to a U-shaped Doppler spectrum, extending from  $f_c - f_D$  to  $f_c + f_D$  (see EQ. 2.4), with infinite power spectral density at the edges. Measured Doppler spectra agree with this fairly well, except at the edges, indicating that most incoming rays have small angles  $\alpha_v$ . Aulin {Ref.[2.72]} extended the model by allowing a spread of values for arrival angle  $\alpha_v$  in the vertical plane, with an abrupt-edged probability density function. Parsons {Ref.[2.10], chapter 5} has improved the model further using a smooth probability density function for  $\alpha_v$ . The resulting Doppler spectrum is similar in shape to Clarke's, except at the band edges, which have more realistic finite power spectral density values.

It is interesting to note that if two-dimensional measurements of angle of arrival based on Doppler or phase shift are performed in the horizontal plane, the left/right ambiguity can be overcome by taking measurements at different  $y$  values, but if we assume a possible range for the vertical arrival angle of say  $\alpha_v = \pm 30^\circ$ , the horizontal angle can, at best, only be determined to an accuracy of  $\pm 30^\circ$ . Angle of arrival measurements using a rotating highly directional antenna do not suffer from this problem.

## 2.6.6 Wide Sense Stationary (WSS) Channels

In order to model the radio propagation channel as a statistical process, some restrictions must be made to the class of statistical channel used, to make the characterisation feasible.

A random process  $f(x, t)$  is stationary if it has statistical properties independent of time. The joint probability density function of the process consisting of values at an arbitrary number  $N$  of time instants  $t_1, t_2, t_3, \dots, t_N$  is denoted by  $f_X(x_1, t_1; x_2, t_2; x_3, t_3; \dots, x_N, t_N)$ , and imparts all the information about the random process which is known. If this  $N$ -fold joint probability density function does not depend on the time origin used for the sampling, the random process is described as *strictly stationary*. Often the  $N$ -fold joint probability density function is not completely known, or is very difficult to verify {Ref.[2.58]}.

A *wide sense stationary (WSS)* or *weakly stationary* process has a less stringent stationarity definition, requiring only that the average statistics described by the process mean and process autocorrelation be independent of absolute time, and depend only on time difference. A *WSS* process may be used to characterise a propagation channel exhibiting time dispersion.

## 2.6.7 Uncorrelated Scattering (US) Channels

A channel where the attenuation and phase for different path delays are uncorrelated is termed an *uncorrelated scattering* channel in the delay variable, or alternatively is described as a *WSS* channel in the frequency variable. The *US* channel and the *WSS* channel

are duals. A *US* channel characterises a propagation process showing frequency dispersion.

## 2.6.8 Wide Sense Stationary Uncorrelated Scattering (WSSUS) Channels

A hybrid channel displaying both *WSS* and *US* characteristics, and termed the *wide sense stationary uncorrelated scattering channel*, provides the simplest class of channel in the statistical sense exhibiting both time and frequency dispersion.

## 2.6.9 Quasi-Wide Sense Stationary Uncorrelated Scattering (QWSSUS) Channels

A radio channel might satisfy the restrictions of a *WSSUS* channel over short intervals of time, and over a restricted bandwidth, but fail the requirements over longer times and larger bandwidths. This channel may be characterised as quasi-wide sense stationary uncorrelated scattering (*QWSSUS*) over small intervals of time and frequency, such that the significant scatterers do not change appreciably. The small scale statistics can then be averaged over a number of these small intervals, leading to a two stage model.

## 2.7 Measures of Time Spread

All wideband measurements undertaken for this thesis have been done with the transmitter stationary, and the receiver also stationary or quasi-stationary. The *VUT channel sounder* measures the instantaneous complex impulse response, implying that the channel is stationary for the duration of the measurement. Emphasis has been placed on the measurement of time dispersion. No attempt has been made to measure Doppler shift or angle of arrival; these areas remain for future extensions of the propagation work.

Obtained from the complex impulse response, the power delay profile (PDP) is a plot of received power as a function of excess delay. Figure 2.16 shows a measured PDP. A variety of single number parameters can be extracted from the power delay profile to describe the channel statistics. Measures used in this project are defined and discussed in this section.

### 2.7.1 Average or Mean Delay $D_{avg}$

Average delay  $D_{avg}$  is defined as:

$$D_{avg} = \frac{\int_0^{\infty} \tau P_{\tau} d\tau}{\int_0^{\infty} P_{\tau} d\tau} \quad (\text{EQ 2.33})$$

where  $\tau$  is the excess delay, and  $P_\tau$  is the power at  $\tau$

The zero and first moments of the power delay profile are denoted by  $M_0, M_1$  respectively, defined as:

$$M_0 = \int_0^\infty P_\tau d\tau \quad (\text{EQ 2.34})$$

$$M_1 = \int_0^\infty \tau P_\tau d\tau \quad (\text{EQ 2.35})$$

The average excess delay has been defined in equation 2.33 above. In terms of moments, it is given by:

$$D_{avg} = \sqrt{\frac{M_1}{M_0}} \quad (\text{EQ 2.36})$$

A threshold is applied to power values before calculating  $D_{avg}$ . See Figure 2.16.

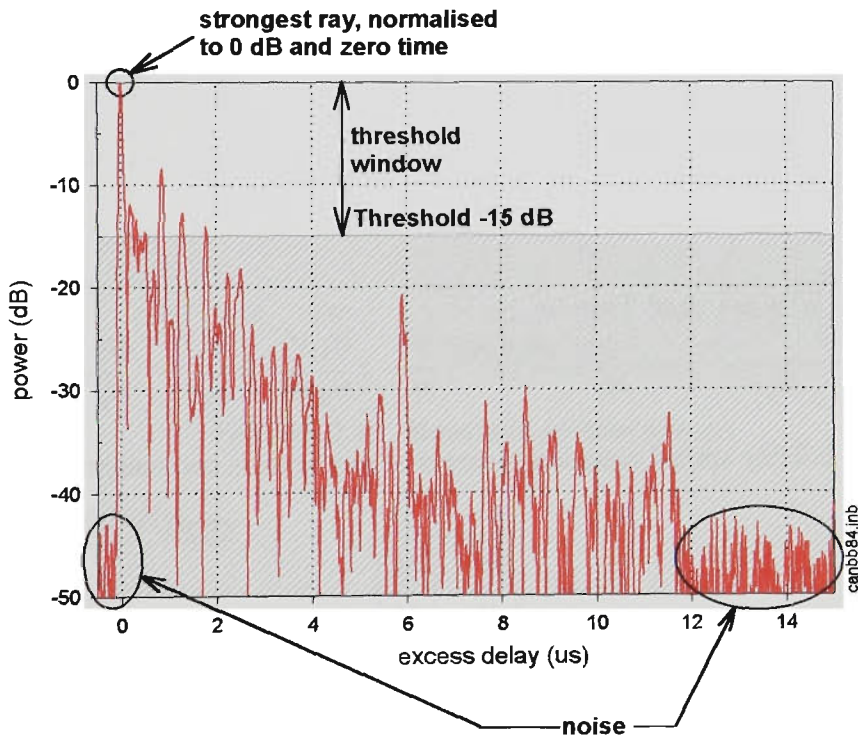


FIGURE 2.16 A measured power delay profile showing level threshold

## 2.7.2 Rms Delay Spread $ds_{rms}$

The root mean square delay spread is the square root of the second central moment of the power delay profile, and is a widely used measure of time dispersion.

Rms delay spread (or simply, delay spread)  $ds_{rms}$  is given by {Ref.[2.10]}:

$$ds_{rms} = \sqrt{\frac{\int_0^{\infty} (\tau - D_{avg})^2 P_{\tau} \partial\tau}{\int_0^{\infty} P_{\tau} \partial\tau}} \quad (\text{EQ 2.37})$$

The second moment of the power delay profile is denoted by  $M_2$  and defined as:

$$M_2 = \int_0^{\infty} \tau^2 P_{\tau} \partial\tau \quad (\text{EQ 2.38})$$

Delay spread can be expressed in terms of moments.

$$(ds_{rms})^2 = \frac{\int_0^{\infty} (\tau - D_{avg})^2 P_{\tau} \partial\tau}{\int_0^{\infty} P_{\tau} \partial\tau} = \frac{\int_0^{\infty} (\tau^2 - 2\tau D_{avg} + D_{avg}^2) P_{\tau} \partial\tau}{M_0}$$

$$= \frac{\left( \int_0^{\infty} \tau^2 P_{\tau} \partial\tau \right)}{M_0} - \frac{2D \left( \int_0^{\infty} \tau P_{\tau} \partial\tau \right)}{M_0} + D^2 = \frac{M_2}{M_0} - 2 \frac{M_1}{M_0} \frac{M_1}{M_0} + \left( \frac{M_1}{M_0} \right)^2 = \frac{M_2}{M_0} - \left( \frac{M_1}{M_0} \right)^2$$

This form of the delay spread equation in terms of moments is convenient for computation

$$ds_{rms} = \sqrt{\frac{M_2}{M_0} - \left( \frac{M_1}{M_0} \right)^2} \quad (\text{EQ 2.39})$$

The program *DELAYG4* computes average delay and delay spread {refer to Appendix D} from measured power delay profiles, and includes provision for applying a power threshold and a range threshold. See Figure 2.17. All samples with values less than the power threshold are set to zero, which is necessary to prevent noise inflating the delay statistics, as will be discussed in the next Section, 2.8.

A correction for the self-delay spread of the channel sounder is included:

$$\text{corrected rms delay spread} = \sqrt{(\text{rms delay spread})^2 - (\text{self-delay})^2} \quad (\text{EQ 2.40})$$

Self-delay is taken as the computed rms delay spread of the single impulse obtained during back-to-back testing of the sounder (see Chapter 3).

Choice of the reference for zero time affects the average delay value, but not the delay spread. Zero time is set at the first arriving above-threshold ray, and excess delay is referenced to this point.

### 2.7.3 Maximum Excess Delay $D_{max}$ or 15 dB Delay Window

The maximum excess delay is defined as the time interval between the first occurring ray exceeding the threshold level, and the last occurring ray exceeding the threshold level. For a threshold level of -15 dB, this quantity is also called the *15 dB delay window* (Figure 2.17).

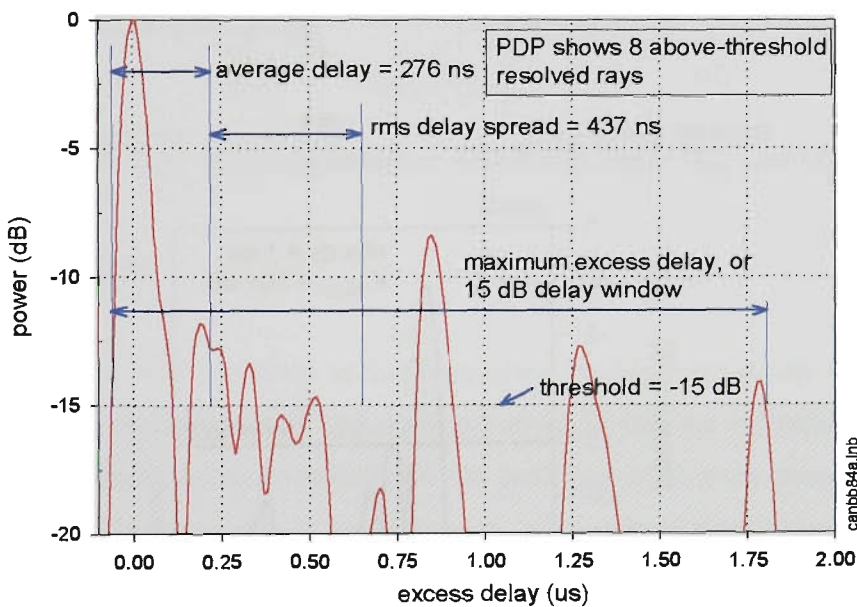


FIGURE 2.17 Measures of time spread

### 2.7.4 K Factor $K_{factor}$

Inspired by the Ricean  $K$  factor,  $K_{factor}$  is defined as the ratio of the power in the strongest ray  $P_0$  to the sum of the powers in all other above-threshold rays, where the ratio is expressed as a dB value.

$$K_{factor} = 10 \log \left( \frac{P_0}{\sum_{i=1}^n P_i} \right) \text{ dB for } P_i > P_{threshold} \quad (\text{EQ 2.41})$$

To calculate  $K_{factor}$  from a measured power delay profile, the individual resolved rays in the profile are identified, and the peak value of each ray is used to calculate the power of

that ray.

For a single ray power delay profile, the bottom line of this expression is zero, making  $K_{factor}$  infinite. To allow plots of  $K_{factor}$ s and  $K_{factor}$  distributions, the value of  $K_{factor}$  is clipped at 30 dB in this thesis.

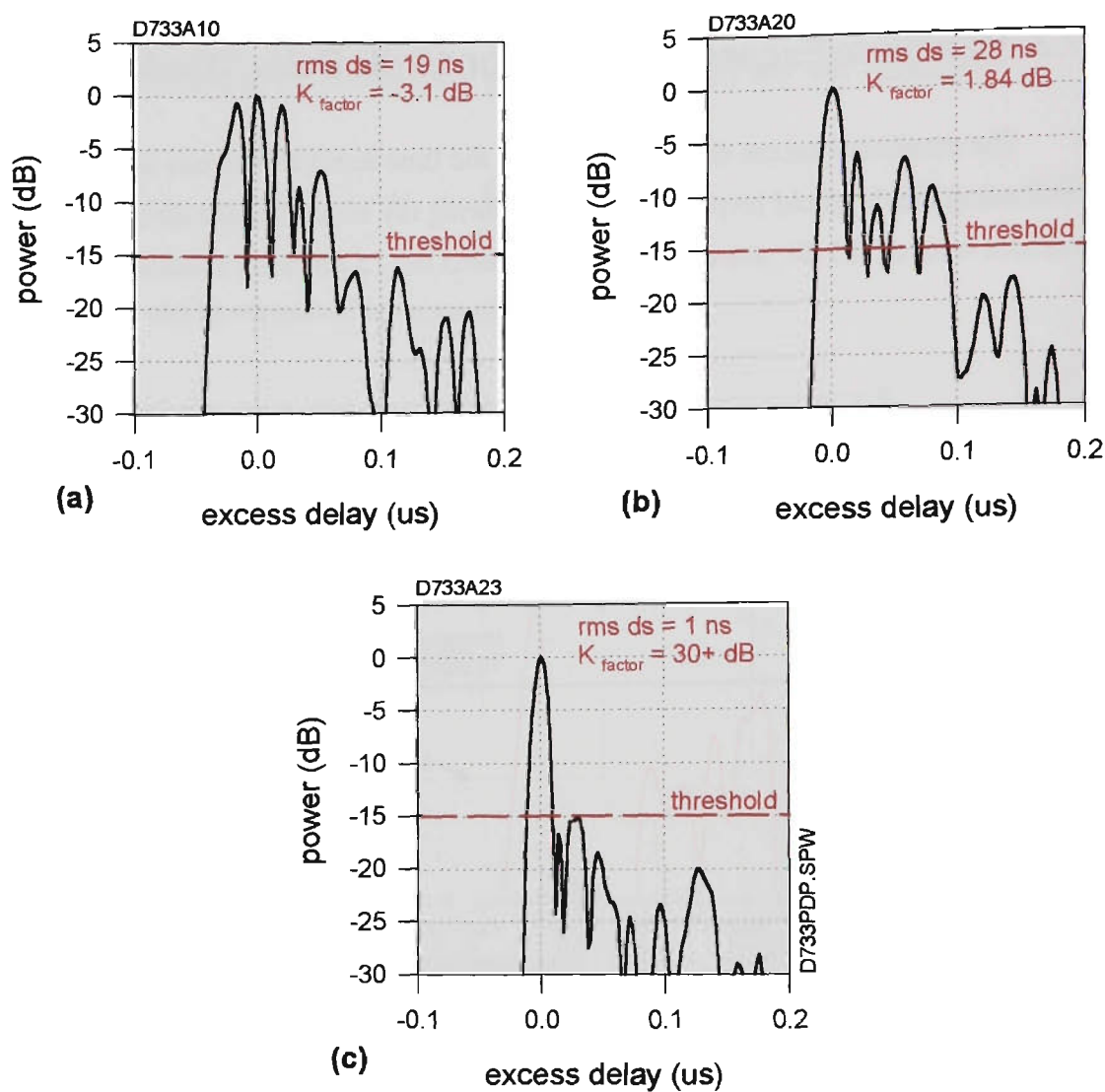


FIGURE 2.18 Power delay profile examples: (a) low  $K$  factor (b) medium  $K$  factor (c) high  $K$  factor.

### 2. 7.5 Proposed Modified K factor $K_m$

To overcome the problem mentioned above, where  $K_{factor}$  goes to infinity when only one above-threshold ray is resolvable (which is not an uncommon occurrence), a modified measure which approaches unity instead of infinity, is proposed.

The modified K term  $K_m$  is defined as the dB ratio of the power in the strongest ray, to the sum of the powers in all (above threshold) rays. Then for a single ray profile,  $K_m = 0$  dB, and for a profile with  $n$  equal power rays,  $K_m = -10 \log (n)$ . For small power ratios,  $K_m$  and  $K_{factor}$  converge. This is illustrated in Figure 2.19.

$$K_m = 10 \log \left( \frac{P_0}{\sum_{i=0}^n P_i} \right) \text{ dB for } P_i > P_{threshold} \tag{EQ 2.42}$$

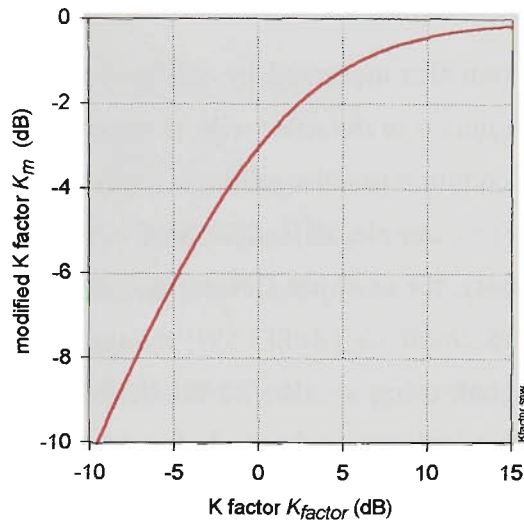


FIGURE 2.19 Relation between modified *K factor*  $K_m$  and  $K_{factor}$

2. 8 Thresholds

The objective of this section is to demonstrate the high sensitivity of delay spread measurements to the threshold level imposed, and to argue that for *equipment-independent* measurements, a defined threshold relative to the peak power in each power delay profile (PDP) must be used. In the course of the argument, a theoretical single exponential PDP is employed as an example - but this is not intended to imply that such a simple PDP can be used to model the complexity of real world measured PDPs.

Instrumentation and physical limitations dictate that measured wideband channel soundings will have a restricted dynamic range. At the top end, the dynamic range is limited by available transmitter output power, and by receiver overload points. At the low signal end, the noise floor, and low level spurious signals set the limit. The noise floor arises from thermal noise, phase noise and jitter in signal sources and synthesisers, and correlation noise. Spurious signals can originate from intermodulation and harmonic distortion, mixer spurious products, and IQ demodulator imbalance products.

Reported results of wideband channel sounders rarely demonstrate much better than a 40 dB dynamic range (see Chapter 3), and in low signal areas this can degrade to 20 dB or worse. Many parameters influence this generalisation, but for typical sliding correlator sounders it proves to be a good guideline.

To prevent noise and spurious components from being confused with genuine low level delayed signals and inflating the value of channel parameters, it is essential to apply a



threshold, to slice the noise floor. All power values below the threshold are set to zero, and then no longer contribute to the channel statistics. As the threshold must include a generous safety margin, some legitimate signal data is also inevitably discarded, thus making calculated channel parameters dependent on the threshold value. Some measures, in particular rms delay spread, where power terms are weighted by the square of a delay term, are very sensitive to the threshold value.

To allow channel statistics measured by different workers to be meaningfully compared, *the same threshold, applied in the same way*, is important.

Unfortunately it is common practise amongst many authors to define a threshold with respect to the noise floor. For example, in Ref.[3.28], *Driessen* uses a threshold, “just above the noise level”. Other authors, for example *Devasirvatham* {Ref.[3.8]}, say nothing about a threshold. On the other hand, *Bultitude* {Ref.[2.59]} recognizes the importance of a threshold relative to the strongest signal, using a value 28 dB below the peak. *Karlsson* {Ref.[2.56], [2.57]} also fixes the threshold relative to the peak, but uses different values of either -26 dB or -30 dB in particular circumstances.

Relative to the wanted signal, the noise floor varies from measurement to measurement. If defined relative to the noise floor, the threshold will also vary from one measurement to the next.

The noise floor also varies between channel sounders, so relating the threshold to the noise floor makes the measured channel statistics *equipment dependent*. If the threshold is tied to the noise floor, the effective threshold (relative to the strongest ray) and hence also the calculated rms delay spread, will vary as the transmitter power is varied. This makes the measured channel statistics *transmitter power dependent*.

If propagation researchers do not mention use of a threshold, either some unspecified default threshold is in effect being used, or worse, calculation of channel parameters includes noise and spurious components. This makes it difficult to evaluate measurements from different sources in any accurate or meaningful way - only approximate comparisons can be made.

The correct way to define the threshold is relative to the peak value of the power delay profile. If this is normalised to 0 dB, the threshold level is given as a negative dB value relative to 0 dB.

In this project, a threshold level of -15 dB has been adopted. Defining the threshold in this way makes the measured channel parameters *equipment independent*, and *transmitter power independent*.

## 2. 8.1 Rms Delay Spread Sensitivity to Threshold

### 2. 8.1.1 The Exponential Power Delay Profile

Measured PDPs are often found to have an envelope which approximately follows an exponential slope, resulting from the inverse power law path attenuation with increasing dis-

tance, with excess delay proportional to distance. Plotting power on a logarithmic axis, the exponential slope becomes a linear slope. Such an idealised PDP is shown in Figure 2.20. The parameter  $q$  is a slope constant.

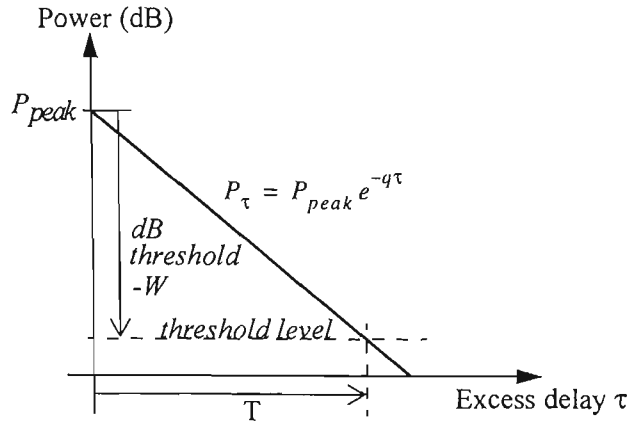


FIGURE 2.20 Idealised exponential power delay profile

Using equations 2.34, 2.35, 2.38, and 2.39, the rms delay spread  $ds_{rms}$  for the exponential power delay profile can be calculated as a function of the time  $T$  corresponding to a chosen threshold as:

$$ds_{rms} = \frac{1}{q} \frac{1}{(e^{-qT} - 1)} \sqrt{(e^{-qT} - 1) [e^{-qT} (q^2 T^2 + 2(1 + qT)) - 2] - [1 - e^{-qT} (1 + qT)]^2} \quad (\text{EQ 2.43})$$

$$\text{In the limit, as } T \rightarrow \infty \text{ then } ds_{rms} \rightarrow \frac{1}{q} \quad (\text{EQ 2.44})$$

The parameters  $q$  and  $T$  are related to the threshold window magnitude  $W$  dB by:

$$qT = \frac{W}{4.343} \quad (\text{EQ 2.45})$$

The *normalised rms delay spread* for a particular threshold is defined as the ratio of the delay spread calculated at that threshold, to the delay spread calculated with a threshold at  $-\infty$  dB.

The *normalised rms delay spread*  $\rightarrow 1$  as the *threshold*  $\rightarrow -\infty$  dB. A plot of *normalised delay spread* as a function of *threshold* is shown in Figure 2.21. At a threshold of -15 dB, as used throughout this thesis, the *normalised delay spread* is 77.3% of the limiting value, and the slope (sensitivity) of delay spread is 3.8 % per dB of threshold change

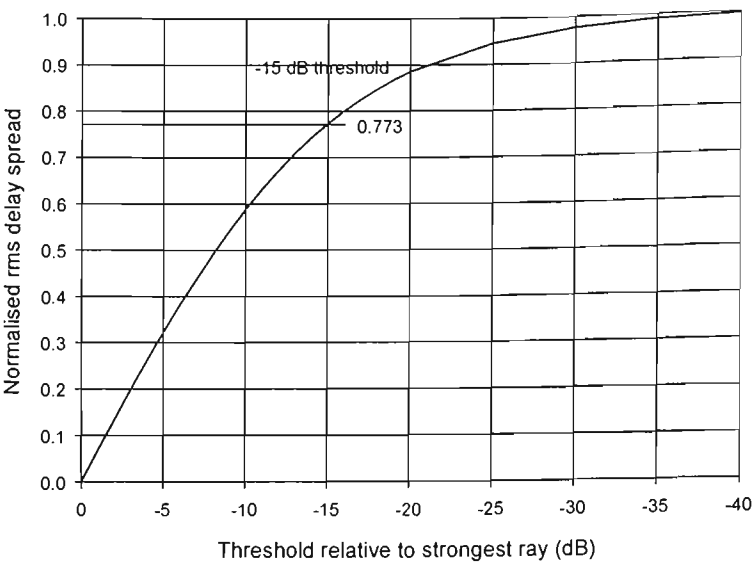


**FIGURE 2.21** *Normalised delay spread versus threshold for an exponential power delay profile*

In many cases where multiple clusters of distant scatterers are present, the PDP is better represented by a series of components with exponential slopes, such as depicted in Figure 2.22. With this sort of PDP, step increases in the delay spread will occur as the threshold is lowered and progressively includes rays at long delays, increasing the sensitivity of delay spread to the threshold.

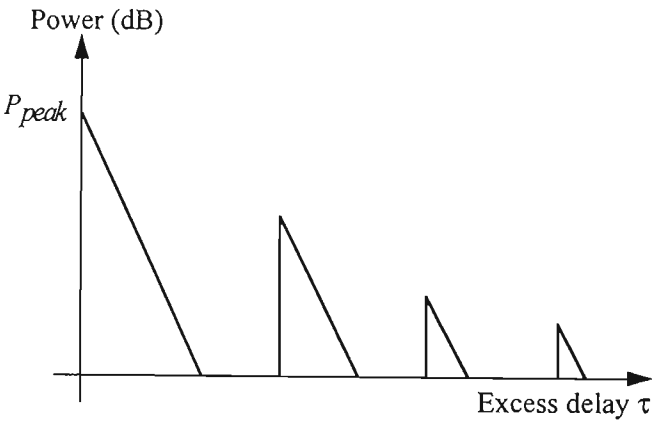


**FIGURE 2.22** *Idealised power delay profile with multiple clusters of scatterers*

**2. 8.1.2 A Measured Power Delay Profile**

Figure 2.23 shows a measured PDP which fits a single exponential envelope with a slope of approximately -37 dB/microsecond. This profile was measured in the *Victoria University of Technology* courtyard, using the channel sounder in 10 ns resolution mode (*indoor mode*), and shows about 40 rays. If measurement resolution was increased, more rays would be revealed. On the other hand, lower resolution sounding would tend to fill in between rays,

giving a PDP looking more like a continuous smooth function, approaching the exponential envelope.

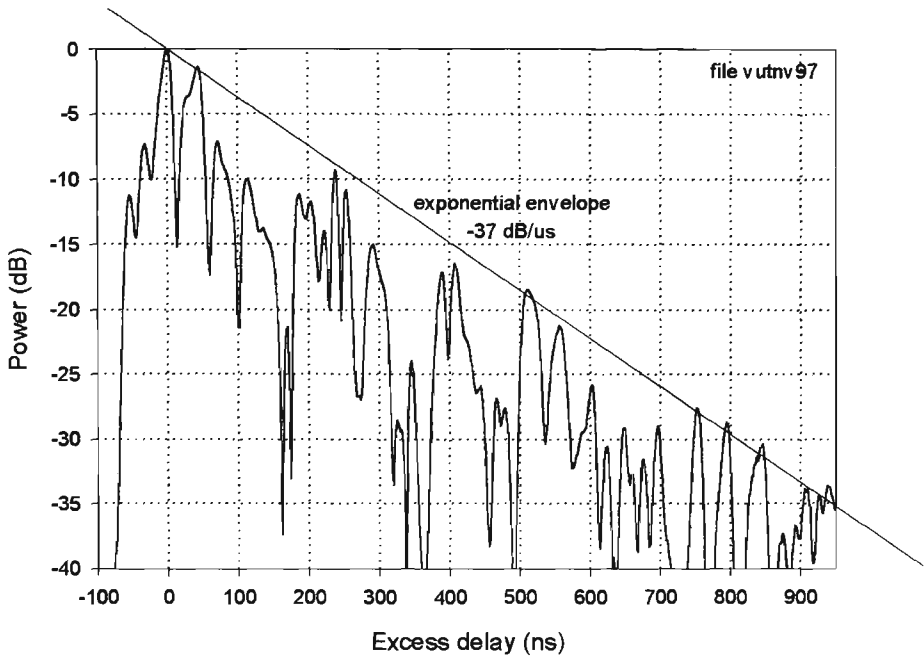


**FIGURE 2.23** Measured instantaneous PDP showing an exponential envelope

Calculating the rms delay spread for the measured profile shown in Figure 2.23 using a series of different thresholds, gives the result shown in Figure 2.24. A range threshold of 950 ns was applied, so only the part of the profile shown in Figure 2.23 is used in calculating the delay spread, with no contribution from possible scatterers at longer delays.

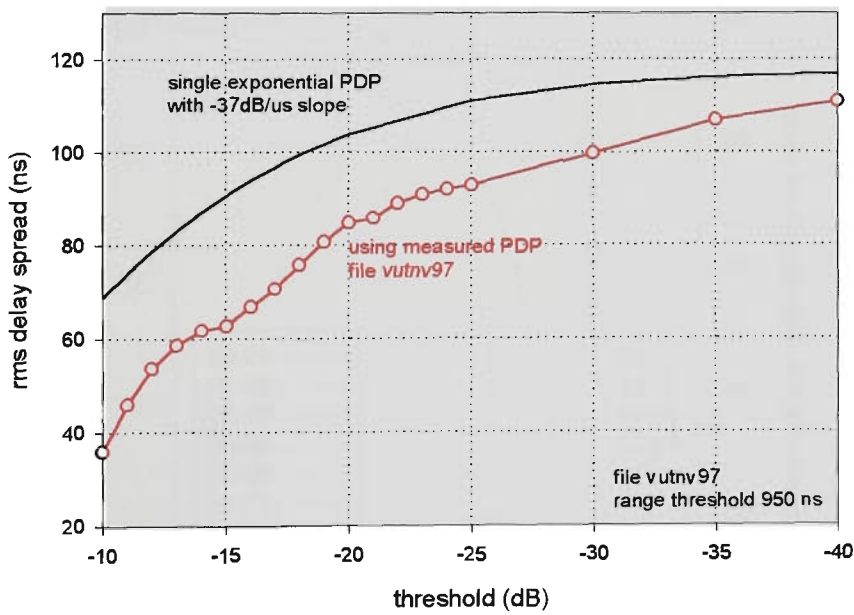


**FIGURE 2.24** rms delay spread versus threshold for measured PDP *vutnv97* with a range threshold of 950 ns

A slope of  $-37 \text{ dB}/\mu\text{s}$  is equivalent to  $q = 8.519$ , giving a limiting delay spread  $ds_{rms} = 1/q = 117.4 \text{ ns}$  (see Figure 2.24). Note that in calculating this theoretical limiting value for

an exponential PDP, no range threshold is implied (but indeed the contribution from the portion below  $-40$  dB is negligible as Figure 2.24 shows). The delay spread calculations on the measured profile use a range threshold of 950 ns, and also have contributing rays preceding the strongest ray

The curve shows slope changes and kinks as additional discrete rays become included in the calculation. The slope or sensitivity around  $-15$  dB, calculated as the slope of a straight line segment from  $-14$  dB to  $-16$  dB, is  $3.9\%$ /dB. Normalising the delay spread to 117.4 ns, gives a *normalised delay spread* of  $94.5\%$  at  $-40$  dB (compared with  $99.6\%$  for an exponential PDP), and  $53.8\%$  at  $-15$  dB (compared with  $77.3\%$  for an exponential PDP). In Figure 2.23, the measured PDP has ray peaks which lie on the exponential PDP, but some time bins contain no rays, and on average the power is always less than for the exponential PDP. Because of this, the measured delay spread will be less than for the exponential PDP.

### 2.8.1.3 Courtyard Measurement Series *vutnv*

Taking the whole series of *Victoria University of Technology* courtyard measurements series *vutnv* (203 instantaneous power delay profiles), and plotting a family of delay spread cumulative distribution function (CDF) curves for different thresholds ranging from  $-40$  dB to  $-10$  dB in steps of 5 dB, gives Figure 2.25.

Curves for thresholds from  $-10$  dB to  $-30$  dB are reasonably parallel, and spaced approximately uniformly, whereas the  $-35$  dB and  $-40$  dB threshold distributions diverge to show some very high delay spread values, suggesting that noise and spurious components are coming into play.

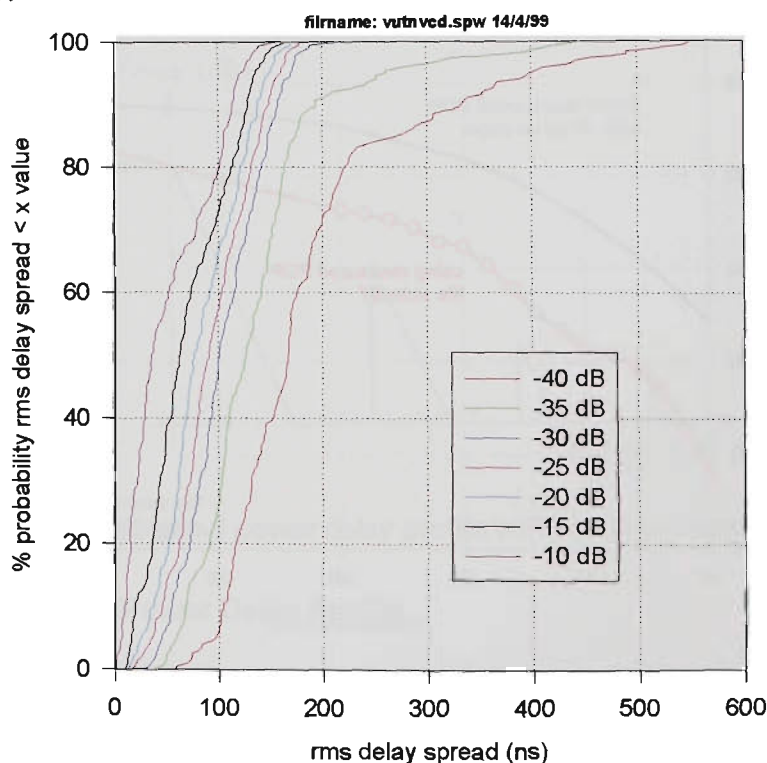


FIGURE 2.25 CDF of rms delay spread versus threshold - *Victoria University* campus measurement series *vutnv*

2. 8.1.4 Sydney Outdoor Measurement Series *sydb*

Distributions of instantaneous delay spreads as a function of threshold for outdoor measurements performed in *Sydney* (see Chapter 5, section 5.5.1, for more detail) as a function of threshold are shown in Figures 2.26 and 2.27..

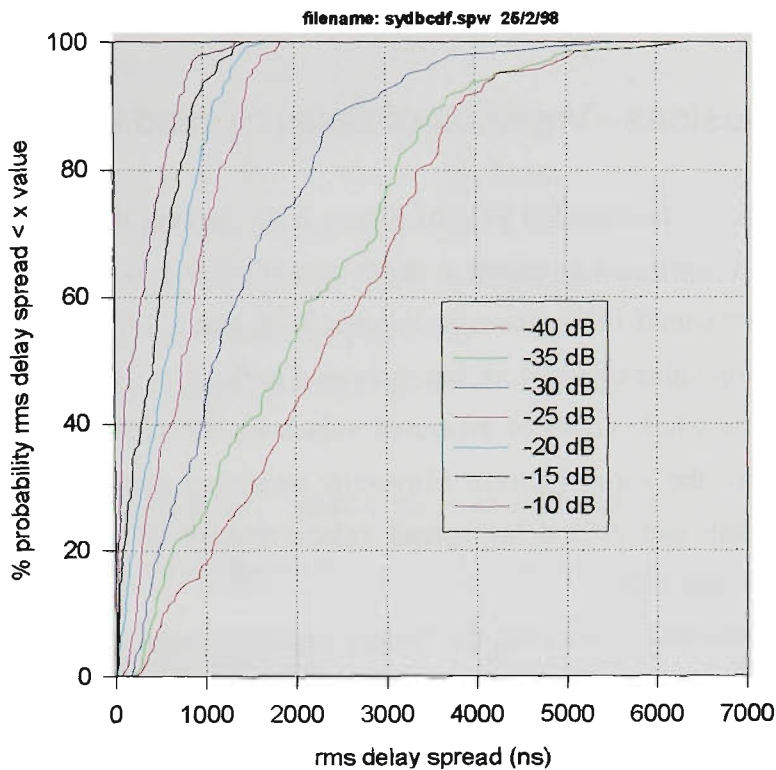


FIGURE 2.26 CDF of rms delay spread versus threshold - *Sydney* outdoor measurements.

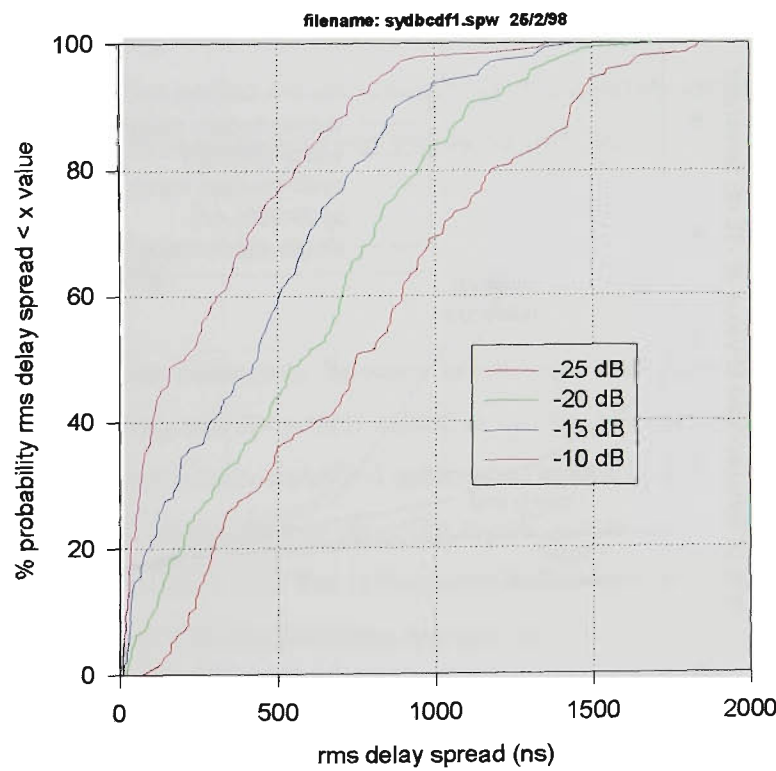


FIGURE 2.27 Detail of CDF of rms delay spread versus thresholds from -10 dB to -25 dB for *Sydney* outdoor measurements.

For thresholds from -10 dB to -20 dB, the distribution curves increment in a fairly evenly spaced manner. Figure 2.27 shows an expanded plot covering this range.

At lower thresholds, -25 dB to -40 dB, the appearance of the distribution curves becomes more erratic, particularly indicating the emergence of some high delay spread values, again suggesting the influence of noise and spurious components

## 2.8.2 Conclusions - Variation of Delay Spread with Threshold

For the single exponential PDP of Figure 2.20, varying the threshold from -15 dB to  $-\infty$  dB results in a maximum variation in delay spread of 29.4 % (relative to the value at -15 dB). Using the measured PDP shown in Figures 2.23, and 2.24, the delay spread variation, assuming a limiting value of 117.4 ns, has increased to 86 %.

Taking the whole series of measured values for the *sydb Sydney* outdoor city measurements, and for the *vutnv Victoria University* courtyard measurements and plotting the variation of median and 90% delay spread values relative to -15 dB, as the threshold is changed, gives Figure 2.28.

As the threshold is lowered, the *Sydney* measurements show a greater increase than the *Victoria University* group. *Sydney* measurements used a high antenna (on the 23rd. floor of a tall building, see Chapter 5, section 5.5.1) covering the downtown city area which has many tall buildings, giving plenty of scope for low power rays at large excess delays. On the other hand, the *Victoria University* measurements used a low antenna, and covered a confined courtyard area surrounded by relatively tall buildings (see Chapter 4, section 4.1.10).

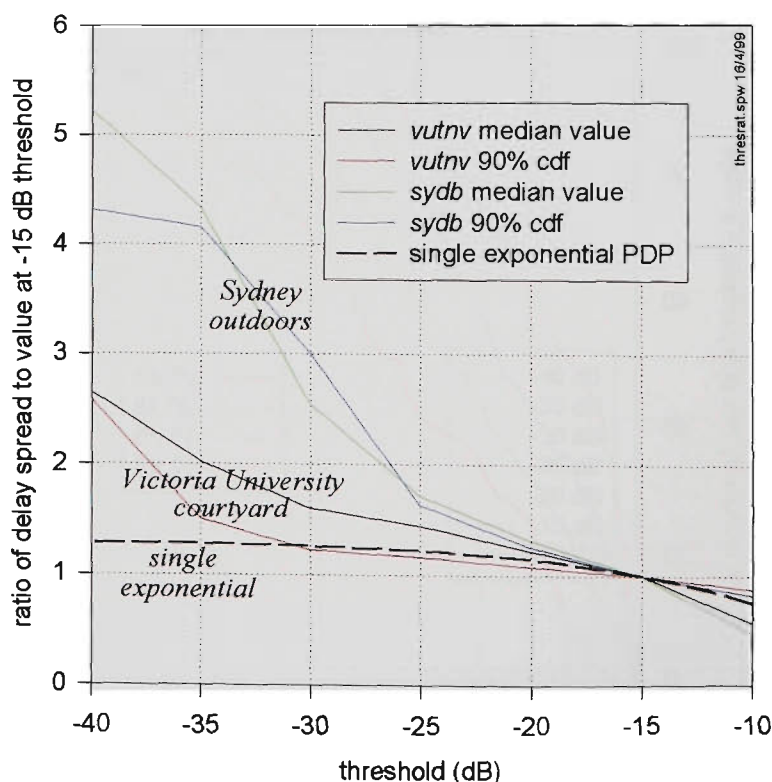


FIGURE 2.28 Delay spread variation with threshold



The increase in delay spread ratio as the threshold is lowered is approximately at a constant rate to a threshold of -30 dB for the *Victoria University* measurements, and to a threshold of -25 dB for the *Sydney* measurements. At lower thresholds, the rate of increase of delay spread ratio rises. The ratio of median value at -40 dB threshold to median value at -15 dB threshold reaches 5.22 for *Sydney*, and 2.65 for *Victoria University*. Evaluating the single exponential PDP, the ratio of delay spreads at two different thresholds is independent of the exponential slope. This curve is also plotted in Figure 2.28. While the exponential PDP shows a reasonable match to the 90% CDF courtyard measurements down to thresholds of -30dB, the *Sydney* outdoor measurements show much higher delay spread sensitivity to threshold than that modelled by a single exponential PDP. A multiple exponential PDP model, already mentioned, may fit the outdoor measurements better.

A summary of the changes in delay spread with threshold is given in Table 2.5.

TABLE 2.7. Median delay spread ratio summary

Threshold	Increase in Median Delay Spread relative to value at -15 dB threshold		
	Victoria University	Sydney	single exponential PDP
-25 dB	144 %	171 %	122 %
-40 dB	265 %	522 %	129 %

Section 2.8 has emphasised the sensitivity of rms delay spread measurements to the threshold used, and has stressed the necessity for a defined threshold relative to the peak power in each PDP. Using such a threshold makes measurements independent of receiver noise levels and transmitter output power, and allows meaningful comparison with measurements from other researchers using the same threshold definition.

## 2.9 Conclusions

In this chapter the distinction between small scale and large scale fading, fast and slow fading, and flat fading and frequency selective fading, has been explained. Narrowband and wideband channels have been classified in terms of fading behavior.

Statistical distributions used to describe signal parameters, most usually the signal amplitude, have been defined, and the relationship between these distributions discussed, pointing out that some distribution functions are special cases of more general distributions.

Classical path loss models, ranging from free space to built-up area models, have been surveyed. Some of these models, embedded in software tools, and enhanced with specific three dimensional terrain data, form the basis of current computer aids used for network planning.

Issues of fading, and building penetration loss, have been illustrated using narrow-



band measurements in a university building. Ground floor penetration loss of 20.3 dB is similar to values in other published work. Two floors up, the penetration loss reduces to 9.5 dB, then to 3.8 dB a further two floors higher. The change per floor over the first two floors is greater than other published values found, while over the next two higher floors, the value of -2.9 dB/floor is comparable to some published values.

By examining the peak value of level crossing rate, the nature of the multipath propagation can be deduced. On the upper floors, propagation behavior is slightly on the free-space or one-ray side of isotropic or Rayleigh behavior. On the ground floor within the building, conditions depart from Rayleigh towards a two-ray model. Outside the building at ground level, propagation more strongly approaches the two-ray model.

Wideband statistical channel definitions and parameters have been discussed, and the role of angle of arrival in signal description examined.

Measures of time spread including average delay, rms delay spread, maximum excess delay or delay window, K factor, and a new proposed measure termed modified K factor, have been defined, and illustrated in terms of actual signal power delay profiles. Some of these parameters will be used in later chapters to summarize the results of channel sounding measurements.

Finally, the importance of using a threshold level, defined relative to the strongest ray, has been stressed. The sensitivity of delay spread to the threshold level has been investigated, to emphasize the necessity of a defined threshold level.

## 2.10 References - Chapter 2

- [2.1] Lord Rayleigh, "On the Resultant of a Large Number of Vibrations of the Same Pitch and Arbitrary Phases", *Phil. Mag.*, Vol.10, pp.73-78, 1880, Vol.27, No.27, June 1889, pages 460-469.
- [2.2] N. Hashemi, "Propagation Modeling for PCS System" Tutorial Notes, IEEE 4th. Int. Conf. on Universal Personal Communications, Tokyo, Nov 1995.
- [2.3] M. Nakagami, "The m-distribution: a general formula of intensity distribution of rapid fading", *Statistical Methods in Radio Wave Propagation*. Editor: W.C. Hoffman, Pergamon, 1960.
- [2.4] S.O. Rice, "Mathematical Analysis of Random Noise", *Bell System Technical Journal*, Vol.23, 1944, pages 282-332.
- [2.5] S.O. Rice, "Statistical Properties of a Sine Wave Plus Random Noise", *Bell System Technical Journal*, Vol.27, Jan. 1948, pages 109-157.
- [2.6] W. Weibull, "A Statistical Theory of the Strength of Materials", *Ingeniors Ventenskaps Akademiens Handligar*, Stockholm, 1939.
- [2.7] W. Weibull, "A Statistical Distribution Function of Wide Applicability", *J. Appl. Mech.*, Vol.18, 1951, pages 293-297.
- [2.8] F.A. Fay, J. Clarke and R.S. Peters, "Weibull Distribution Applied to Sea-clutter", *IEE Conf. Publ.* 155, 1977, pages 101-103.

- 
- [2.9] K.D. Ward, "Compound Representation of High Resolution Sea-clutter", *Electronics Letters*, Vol.17, No.16, 1981, pages 561-563.
- [2.10] J.D. Parsons, "The Mobile Radio Propagation Channel", Pentech Press, London, 1992.
- [2.11] H. Suzuki, "A Statistical Model for Urban Radio Propagation", *IEEE Trans. COM-25*, 1977, pages 673-680.
- [2.12] J. Griffiths & J.P. McGeehan, "Interrelationship Between Some Statistical Distributions used in Radio-wave Propagation", *IEE Proceedings*, Vol.129, No.6, December 1983, pages 411-417.
- [2.13] E.W. Stacy, "A Generalisation of the Gamma Distribution", *Annal. Math. Stat.*, Vol.33, 1962, pages 1187-1192.
- [2.14] Christopher Chatfield, "Statistics for Technology", Chapman and Hall, 3rd.Ed., 1983, pages.69-74.
- [2.15] IEEE Vehicular Technology Society Committee On Radio Propagation, "Coverage Prediction for Mobile Radio Systems Operating in the 800/900 MHz Frequency Range", *IEEE Trans. on Vehicular Technology*, Vol.37, No.1, February 1988, pages 3-72.
- [2.16] K. Bullington, "Radio Propagation above 30 Megacycles", *Proc. IEE*, Vol.35, 1947, pages 1122-1136.
- [2.17] Kenneth Bullington, "Radio Propagation for Vehicular Communications", *IEEE Transactions on Vehicular Technology*, Vol.VT-26, No.4, November 1977, pages 295-308.
- [2.18] J. Egli, "Radio Propagation above 40 Mc. over Irregular Terrain", *Proc. IRE*, Vol.45, 1957, pages 1383-1391.
- [2.19] R. Carey, "Technical Factors Affecting the Assignment of Facilities in the Domestic Public Land Mobile Radio Service", Report R-6406, FCC, Washington DC., 1964.
- [2.20] P.L. Rice, A.G. Longley, "Transmission Loss Predictions for Tropospheric Communication Circuits", NBS Tech. Note 101, U.S. Govt. Printing Office, Washington DC, May 1966.
- [2.21] J. Damelin, W.A. Daniel, H. Fine and G. Waldo, "Development of UHF Propagation Curves for TV and FM Broadcasting", Report R-6602, FCC, Washington, DC., 1966.
- [2.22] A.G. Longley and P.L. Rice, "Prediction of Tropospheric Radio Transmission over Irregular Terrain. A Computer Method - 1968", ESSA Tech. Report ERL 79-ITS 67, U.S. Govt. Printing Office., July 1968.
- [2.23] Y. Okumura et al., "Field Strength and its Variability in VHF and UHF Land-Mobile Radio Service", *Rev. Elec. Commun. Lab.*, Vol.16, 1968, pages 825-873.
- [2.24] "Master Propagation System (MPS 11) User's Manual", U.S. Dept. Comm. Nat. Telecom. Information Service, NTIS Acc. No. PB-173971.
- [2.25] General Electric, "Range and Transmitter Power Calculator", Mobile Radio Department, Lynchburg, VA., 1977.
- [2.26] W.C.Y. Lee, "Mobile Communications Engineering", McGraw-Hill, New York, 1982.
- [2.27] "Methods and Statistics for Estimating Field Strength Values in Land Mobile Services Using 30 MHz", CCIR Plenary Assembly Report 567-2, Geneva, 1982.

- [2.28] H.L. Bertoni and J. Walfisch, "A Diffraction Based Theoretical Model for Prediction of UHF Path Loss in Cities", Proc. AGARD Conf. Terrestrial Prop. Charac. in Modern Systems, Ottawa, 1986, pages 8.1-8.9.
- [2.29] K. Hacking, "Propagation Over Rounded Hills", BBC Research Report RA-21, 1968.
- [2.30] H.T. Dougherty and L.J. Maloney, "Applications of Diffraction by Convex Surfaces to Irregular Terrain Situation", Radio Science, Vol.68-D, No.2, 1964, pages 284-305.
- [2.31] J. Epstein and D.W. Peterson, "An Experimental Study of Wave Propagation at 850 MC", Proc. IRE, Vol.41, No.5, 1953, pages 595-611.
- [2.31A] R. Edwards and J. Durkin, "Computer Prediction of Service Area for VHF Mobile Radio Networks", Proc. IRE, Vol.116, No.9, 1969, pages 1493-1500.
- [2.32] "Atlas of Radiowave Propagation Curves for Frequencies Between 30 and 10,000 Mc/s", Radio Research. Lab., Ministry of Postal Services, Tokyo, Japan, 1957, pages 172-179.
- [2.33] J. Deygout, "Multiple Knife-edge Diffraction of Microwaves", IEEE Trans. Antennas and Propagation, Vol.14, No.4, 1966, pages 480-489.
- [2.34] C.L. Giovaneli, "An Analysis of Simplified Solutions for Multiple Knife-edge Diffraction", IEEE Trans. on Antennas and Propagation, Vol.32, No.3, 1984, pages 297-301.
- [2.36] C.E. Dadson, "Radio Network and Radio Link Surveys Derived by Computer from a Terrain Data Base", NATO-AGARD Conference Pub. CPP-269, 1979.
- [2.37] A. Blomquist and L. Ladell, "Prediction and Calculation of Transmission Loss in Different Types of Terrain", NATO-AGARD Conference Pub. CP-144, 1974, pages 32.1-32.17.
- [2.38] M.A. Weissberger, "Critical Summary of Models for Predicting the Attenuation of Radio Waves by Trees", ED-TR-81-10, EMC Analysis Center, Annapolis, MD, USA, 1982.
- [2.39] J.J. Egli, "Radio Propagation Above 40Mc Over Irregular Terrain", Proc. IRE, Vol.45, 10, 1957, pages 1383-1391.
- [2.40] CCIR XV Plenary Assembly, "Methods and Statistics for Estimating Field Strength Values in the Land Mobile Services using the Frequency Range 30MHz to 1GHz", Report 567, Vol.5, 1982.
- [2.41] J.H. Causebrook, "Computer Prediction of UHF Broadcast Service Areas", BBC Research Dept. Report 1974/4, 1974.
- [2.42] W. Rae Young, Jr., "Comparison of Mobile Radio Transmission at 150, 450, 900 and 3700 Mc", Bell System Technical Journal, Vol.31, November 1952, pages 1068-1085.
- [2.43] K. Allsebrook and J.D. Parsons, "Mobile Radio Propagation in British Cities at Frequencies in the VHF and UHF Bands", Proc. IEEE, Vol.124, 2, 1977, pages 95-102.
- [2.44] M.F. Ibrahim, J.D. Parsons, "Signal Strength Prediction in Built-up Areas. Part 1: Median Signal Strength", Proc. IEE, Part F, Vol.130, 5, 1983, pages 377-384.
- [2.45] Masaharu Hata, "Empirical Formula for Propagation Loss in Land Mobile Radio Services", IEEE Trans. on Vehicular Technology, Vol.29, No.3, August 1980, pages 317-325.
- [2.46] J.P. McGeehan, J. Griffiths, "Normalised Prediction Chart for Mobile Radio Reception", 4th. Int. Conf. on Antennas and Propagation, IEE Conf. Pub. No.248, 1985, pages 395-399.
- [2.47] A. Atefi, J.D. Parsons, "Urban Radio Propagation in Mobile Radio Frequency Bands", Comms 86, IEE Conf. Pub. No.262, 1986, pages 13-18.

- 
- [2.48] IEEE VTS Propagation Committee and Telecommunications Industry Association (TIA) Personal and Mobile Communication Section TR8 WG8.8 Technology Compatability Committee, "A Report on Technology Independent Methodology for the Modeling, Simulation and Empirical Evaluation of Wireless Communications System Performance in Noise and Interference Limited Systems Operating on Frequencies Between 30 and 1500 MHz", Version 20, 1997.
- [2.49] H.R. Anderson, "New 2D Physical EM Propagation Model Selected", IEEE Vehicular Technology Society News, Vol.44, No.3, August 1997, pages 15-22.
- [2.50] P. Calegari, F. Guidic, P. Kuonen, "Urban Radio Network Planning for Mobile Phones", EPFL Supercomputing Review, November 1997, pages 4-10.
- [2.51] Theodore S. Rappaport, "Wireless Communications - Principles and Practice", IEEE Press, New York, Prentice Hall PTR, New Jersey, 1996. ISBN 0-13-461088-1
- [2.52] Raymond Steele, "Mobile Radio Communications", Pentech Press, London, 1992.
- [2.53] L.J. Millott, "Mobile Radio Channel Modelling", PhD Thesis, Monash University, Melbourne, September 1994.
- [2.54] Peter F. Driessen, "Multipath Delay Characteristics in Mountainous Terrain at 900 MHz" Proceedings of the IEEE 42nd. Vehicular Technology Conference, 1992. pages 520-523.
- [2.55] Daniel M.J. Devasirvatham, "Time Delay Spread and Signal Level Measurements of 850 MHz Radio Waves in Building Environments", IEEE Transactions on Antennas and Propagation No.11, November 1986, pages 1300-1305.
- [2.56] Peter Karlsson, "Indoor Radio Propagation for Personal Communications Services", PhD Thesis, Deptment of Applied Electronics - Lund Institute of Technology, March 1995, pages 1-132.
- [2.57] Peter Karlsson, Henrik Borjesson and Torleiv Maseng, "A Statistical Multipath Propagation Model Confirmed by Measurements and Simulations in Indoor Environments at 1800 MHz", Personal, Indoor and Mobile Radio Communications Conference 1994, pages 149-155.
- [2.58] Roger E. Ziemer and Roger L. Peterson, "Introduction to Digital Communication", Chp.2, Macmillan Publishing Company, New York, 1992.
- [2.59] Robert J.C. Bultitude, Pierre Melancon, Hatim Zaghloul, Gerald Morrison, Marjo Prokki, "The Dependence of Indoor Radio Channel Multipath Characteristics on Transmit/Receive Ranges", IEEE Journal on Selected Areas in Communications, Vol.11, No.7, September 1993, pages 979-990.
- [2.60] Willian C.Y. Lee, "Mobile Cellular Telecommunications", 2nd. Ed. McGraw-Hill, Inc. 1995, pages 417-420.
- [2.61] E.H. Walker, "Penetration of Radio Signals Into Buildings in Cellular Radio Environment", Bell System Technical Journal, Vol.62, No.9, 1983, pages 2719-2735.
- [2.62] A.M.D. Turkmani, J.D. Parsons, and D.G. Lewis, "Radio Propagation into Buildings at 441, 900 and 1400 MHz.", Proceedings of the Fourth International Conference on Land Mobile Radio, December 1987, pages 129-138.
- [2.63] A.M.D. Turkmani, J.D. Parsons and D.G. Lewis, "Measurement of Building Penetration Loss on Radio Signals at 441, 900 and 1400 MHz.", Journal of Electronic and Radio Engineers (IERE), Vol.58, No.6, 1988, pages S169-S174.
- [2.64] A.F. de Toledo and A.M.D. Turkmani, "Propagation Into Buildings at 900, 1800 and 2300 MHz.", Proceedings of the IEEE 42nd. Vehicular Technology Conference, 1992, pages 633-636.
-

- 
- [2.65] William J. Tanis II and Glen J. Pilato, "Building Penetration Characteristics of 880 MHz. and 1922 MHz. Radio Waves", Proceedings of the IEEE 43rd. Vehicular Technology Conference, New Jersey USA, 1993, pages 206-209.
- [2.66] Sergio Aguirre, Lynette H. Loew and Yeh Lo, "Radio Propagation Into Buildings at 912, 1920, and 5990 MHz. Using Microcells", Proceedings of the 3rd. IEEE International Conference on Universal Personal Communications, 1994, pages 129-134.
- [2.67] D. Molkdar, "Review on Radio Propagation Into and Within Buildings", IEE Proceedings-H, Vol.138, No.1, February 1991, pages 61-73.
- [2.68] D.C. Cox, R.R. Murray and A.W. Norris, "Measurements of 800 MHz Radio Transmission Into Buildings With Metallic Walls", Bell System Technical Journal, November 1983, pages 2695-2717.
- [2.69] P.J. Barry and A.G. Williamson, "Modelling of UHF Radiowave Signals Within Externally Illuminated Multi-storey Buildings", Journal of the Institution of Electronic and Radio Engineers (IERE), Vol.57, No.6(supplement), November/December, 1987, pages S231-S240.
- [2.70] P.A. Bello, "Characterization of Randomly Time-invariant Linear Channels", IEEE Transactions on Communications Systems, Vol.CS-11, December 1963, pages 360-393.
- [2.71] R.H. Clarke, "A Statistical Theory of Mobile Radio Reception", Bell System Technical Journal, Vol.44, 1968, pages 957-1000.
- [2.72] T. Aulin, "A Modified Model for the Fading Signal at a Mobile Radio Channel", IEEE Transactions on Vehicular Technology, Vol.VT-28, No.3, 1979, pages 182-203.
-

---

# Chapter 3: Channel Sounding

## 3. INTRODUCTION

A survey of wideband channel sounding techniques and a discussion of the relative advantages of each approach begins this chapter, leading on to a description of the sliding correlator channel sounder (*the VUT sounder*) instrumentation, and antennas used in the thesis.

The widely used sliding correlator is demystified with the aid of extensive simulations based on a new and faster algorithm. This work shows that correlation noise, resulting from the slight difference in chip frequencies, is likely to be the major factor limiting the dynamic range of channel sounders using this method. A full design procedure for sliding correlators, based on the simulation results, is presented.

Recent modifications to synchronise PN sequences, window the correlation process, and trigger measurements from a distance logging wheel are included. Channel sounder hardware and software is covered in detail in the appendices.

Portability of the *VUT channel sounder* is novel, and the *VUT sounder* is the first and only (to the author's knowledge) sliding correlator sounder to be developed and operated in Australia. The receiver and data acquisition system can be used as a self-contained backpack, allowing measurements to be made in busy pedestrian areas, city footpaths, and stairways; places inaccessible to a vehicle or a wheeled trolley. The transmitter is also battery powered, and consists of a single box plus batteries, which can easily be moved by one person; for example it can be carried up access ladders to rooftop locations. The receiver and transmitter can be placed on trolleys for conventional indoor measurements, or used in vehicles as easily as loading holiday hand luggage.

The *VUT sounder* can operate in two modes: (i) 25 MHz chip rate, 50 MHz bandwidth, 40 ns resolution, and (ii) 100 MHz chip rate, 200 MHz bandwidth, 10 ns resolution. Mode (i) is normally used for outdoor measurements, and mode (ii) for indoor work. In either mode the PN length can be switched to 255, 511, 1023, or 2047 bits.

Limitations of the sliding correlation technique, and the trade-off between speed and accuracy, are discussed. Bandpass filters form part of the channel sounder, and the effect of the impulse response of these filters on the channel impulse response measurement is studied.

Back-to-back calibrations of the *VUT channel sounder*, via a cable and attenuator, and via a three path artificial channel, for both resolution modes of the sounder, are included in this chapter.

3.1 Wideband Sounding Techniques

Duality of the time and frequency domains provides two approaches to wideband channel sounding instrumentation. A summary of the various methods for realising a sounder in both domains is shown in Figure 3.1.

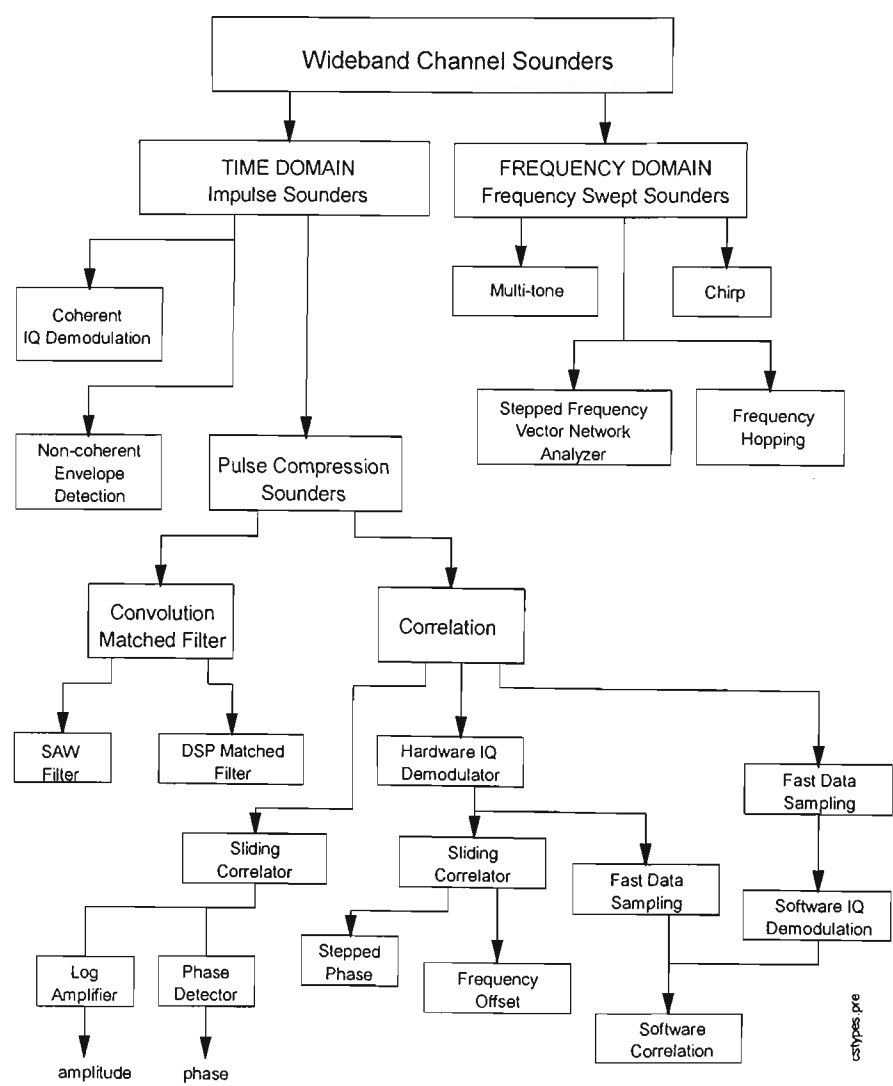


FIGURE 3.1. Summary of wideband sounding techniques

Up until the 1970s, almost all land mobile propagation research measurements con-

centrated on narrowband channels, studying path loss, and large and small-scale fading. These measurements required relatively simple equipment; transmission of a single frequency carrier, and a receiver to measure and record signal strength.

In 1949, *Young and Lacy* used a 500 ns pulse sounder with envelope detection, to measure radio channel impulse response at 450 MHz, in New York City {Ref.[3.89]}. The impulse response was displayed on an oscilloscope, continuously photographed with a movie camera as the receiver moved. The resolution of 500 ns allowed path differences down to 150 metres to be detected. This was the first published report of wideband channel sounding, but more than twenty years were to pass before any further significant activity in wideband sounding occurred. In the early 1970s, *Cox* led a *Bell Telephone Labs* team in seminal wideband sounding work, using a sophisticated direct sequence spread spectrum (DSSS) sliding correlator sounder {Ref.[3.3]}. Complex impulse response measurements at 910 MHz were performed in New York City, with sufficient phase stability to allow the first plots of the channel scattering or delay-Doppler function {Ref.[3.90]} to be published {Ref[3.1], Ref[3.2], Ref[3.4], Ref[3.5], Ref.[3.6], Ref[3.7]}. *Cox* used a modified version of equipment designed at *Bell Labs* by *H.L. Schneider* and previously used for tropospheric scatter measurements {Ref.[3.88]}. *Cox's* sounder architecture is still being used by many propagation workers, in some cases with small improvements, but essentially following the *Cox* design.

A good summary of wideband channel sounders is given in a review paper by *Parsons* in Ref[3.13]. In Ref.[3.91], *Johnson* makes a detailed study of so-called real-time wideband sounders (of course the only true real-time sounder is the pulse sounder).

### 3. 1.1 Pulse Sounders

Pulse sounders with envelope detection are the simplest type, and are also the only class of sounder giving true real-time measurements. Examples may be found in references Ref.[3.56] to Ref[3.67]. The most prolific recent proponent of the pulse method has been *Rappaport* {Ref.[3.57], Ref.[3.58], Ref.[3.59]}. Pulse sounders lack phase information, and are peak power limited. For realistic peak output power levels, the range is limited. As the bandwidth is increased (implying a shorter duration pulse), the signal-to-noise ratio (SNR) gets worse. Increasing the pulse repetition rate, or averaging the received signal over a number of pulses, improves the SNR. Pulse sounders create interference to other users of the spectrum, 'splating' across the whole bandwidth. Increasing repetition rate exacerbates the interference. The real-time advantage is to some extent lost if averaging is used. As a consequence of the real-time feature of the method, data is produced at a high rate, making data collection difficult. The early pulse sounder of *Young and Lacy* suffered from this problem; the only available technology for collecting data was optical (photographic), leaving the data in an unwieldy form discouraging detailed analysis. A further drawback is susceptibility to interference, because the receiver is wideband but has no processing gain.

If coherent sources are available at the transmitter and the receiver, it is possible to coherently demodulate the received pulses and recover phase information, giving the complex



impulse response of the channel. This complicates the instrumentation, making the pulse method less attractive, to an extent that no publications using this method have been found by the author.

### 3. 1.2 Pulse Compression Sounders

The most popular time-domain sounders use direct sequence spread spectrum modulation, making use of the autocorrelation properties of maximal-length PN sequences. At the receiver, the channel impulse response can be recovered by convolution using a matched filter, realised as a surface acoustic wave (SAW) device, or by digital signal processing (DSP). Matched filter detection is equivalent to correlation. SAW devices are inflexible, and suffer from spurious responses which limit dynamic range to 26 dB {Ref.[3.53], Ref.[3.54], or about 30 dB {Ref.[3.55]}. Alternatively, the impulse response may be recovered by correlation with an identical or nearly identical PN sequence. In advance of the correlation process, IQ demodulation may be done in hardware, or in DSP software following fast data sampling. If hardware IQ demodulation is used, correlation can then be done in DSP software following fast sampling of the I and Q signals, or in hardware using a sliding correlator.

An interesting design has been published by Takeuchi, using a log amplifier and a phase detector instead of an IQ demodulator {Ref.[3.19]}.

If phase information is not required, envelope detection can be used instead of IQ demodulation {Ref.[3.8]}.

### 3. 1.3 The Sliding Correlator

In the sliding correlator, the reference PN sequence is clocked at a slightly slower chip rate ( $\Delta f$  slower) than the transmitted sequence, which is clocked at a chip rate of  $f_{PNr}$ . Relative to the receiver reference sequence, the transmitted sequence slides past slowly from right to left (imagine looking at the two sequences on an oscilloscope). As the transmitted sequence has suffered path delays, some time will elapse before it lines up with the reference sequence, giving a correlation peak. By the time the transmitted signal reaches the receiver, it has experienced multipath delays, so the received signal is a composite of a number of delayed PN sequences, which after correlation give the multiple peaks of the power delay profile.

Sliding correlation is analogous to a down-conversion process, converting to a baseband of bandwidth  $\Delta f$ , and introduces a time-scaling effect. Complete correlation over the whole PN sequence length takes  $k$  times the sequence duration where the scale factor  $k = f_{PNr} / \Delta f$ . Excess delay is also scaled by  $k$ , which has a value typically in the range 1000 to 20,000. Time scaling eases the collection of data, which can now be done using a slow data storage method. Cox used an analogue FM tape recorder for data storage, while the VUT sounder uses an analogue to digital conversion unit and a notebook personal computer to store data to the hard disc drive.

Examples of sliding correlator sounders are described in Ref.[3.1] to Ref.[3.36], and

Ref.[3.92]. Instead of using a frequency offset for the reference sequence, a novel alternative is to use the same chip rate as for the transmitted sequence, but to continuously step the phase of the reference sequence clock. This is equivalent to a frequency offset, because frequency can be interpreted as rate of change of phase {Ref.[3.16], Ref.[3.17], Ref.[3.19]}.

### 3.1.4 Frequency Domain Sounders

The channel impulse response can be obtained by Fourier transforming the complex frequency response. The most popular method of measuring the channel frequency response is to frequency step over the desired bandwidth using a vector network analyser (VNA). Either the transmitting antenna or the receiving antenna must be located at a distance from the VNA, and connected by a cable. This limits the method to indoor measurements, and cable losses limit the spacing between antennas. A separate low noise amplifier at the receiver antenna, and/or an external power amplifier to feed the transmit antenna, can increase the range. The presence of the metallic cable also alters the propagation environment being measured, but this may be a negligible effect. The method is slow, and the channel should be stationary for the measurement duration. However, if a VNA is available, cables and antennas are all that are required to do propagation measurements. With sufficiently wide bandwidth antennas and a stationary channel, very high resolutions can be obtained, for example 0.5 ns, using 2000 MHz bandwidth in Ref.[3.74], and 1 ns in Ref.[3.78]. Frequency stepping sounders are also described in Ref.[3.73], and Ref.[3.75] to Ref.[3.81].

### 3.1.5 Chirp Sounders

Other frequency swept sounder methods include frequency hopping systems {Ref.[3.72]}, and multi-tone systems, where a large number of fixed frequency carriers are transmitted simultaneously, and received with a multi-channel receiver. No examples of multi-tone sounders have been found in the literature. The chirp method, using a linear frequency modulated sweep, also called frequency modulated continuous wave (FMCW), and popular in radar applications, has some adherents. This method has been used by *Salous* {Ref.[3.70], Ref.[3.71]}, and a range of chirp sounders has also been successfully developed by *Norwegian Telecom* {Ref.[3.68], Ref.[3.69]}. A significant recent example of this method is the *RUSK ATM* vector channel sounder developed at the *University of Ilmenau, Germany* {Ref.[3.105]}, and offered as a commercial product by *MEDAV GmbH* {see their website at [www.medav.de](http://www.medav.de)}. In standard form this high performance sounder has a bandwidth of 120 MHz from 5140 to 5260 MHz, and multiplexes the receiver over an 8 element antenna array, allowing direction of arrival to be calculated.

Based on the reference list included with this chapter (admittedly this only covers a fraction of published work on the subject), some feel for the relative popularity of the various methods may be gained. This is illustrated in Figure 3.2.

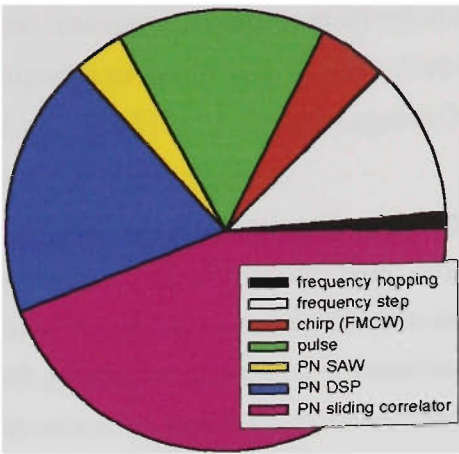


FIGURE 3.2. Relative popularity of channel sounding techniques

3. 1.6 The Cox Sounder

A block diagram of the *Cox* sounder {Ref.[3.1]} is shown in Figure 3.3.

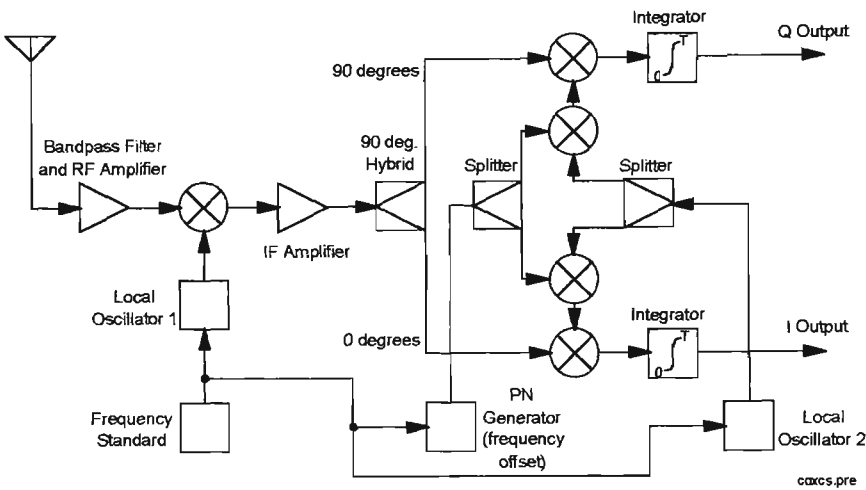


FIGURE 3.3. *Cox* receiver sliding correlator sounder architecture

3. 1.7 Improvements to the Cox Architecture

In the transmitter, *Cox* performed the bi-phase modulation at a 70 MHz intermediate frequency (IF), then mixed the modulated waveform up to the output 910 MHz RF frequency. Omitting the IF stage and directly modulating the RF carrier with the PN code simplifies the transmitter.

In the modified receiver, the sliding correlation and mixing down to the first IF can be performed prior to IQ demodulation, resulting in a narrowband first IF, with signal bandwidth equal to twice  $\Delta f$ . The integrating filter for the correlation process is the IF bandpass filter. For the IQ demodulator, the 90° hybrid splitter is moved to the second local oscillator. Because this is a single fixed frequency, more accurate quadrature splitting can be achieved. The 0° splitter operates on the IF signal, which spreads over the narrow IF bandwidth. These modifi-

cations are described by *Demery* in Ref.[3.11]. The modified receiver block diagram is shown in Figure 3.4

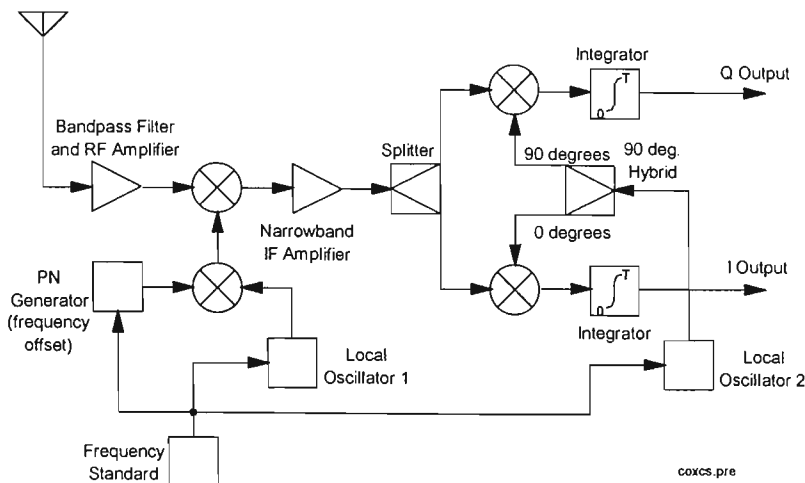


FIGURE 3.4. Modified *Cox* receiver (after *Demery*)

3. 1.8 *Takeuchi* Sounder

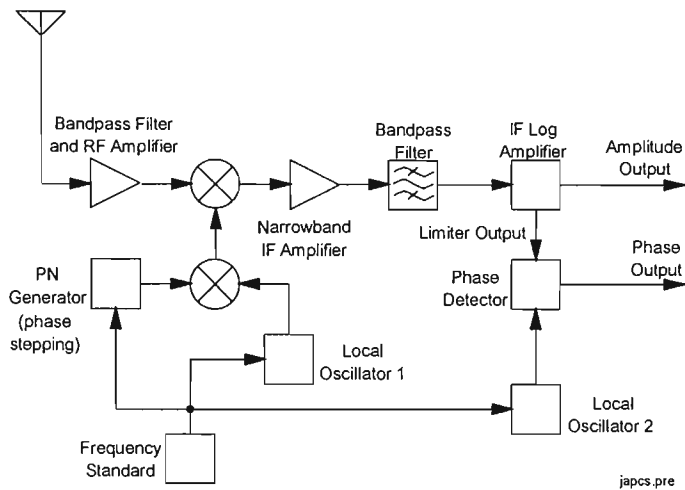


FIGURE 3.5. *Takeuchi* sounder receiver architecture

Instead of using an IQ demodulator, *Takeuchi* {Ref.[3.19]} used a log amplifier and phase detector to obtain complex signal information. The front end of the sounder follows the *Demery* scheme. Low cost log amplifiers such as the *Analog Devices AD606* are now available, making this approach very attractive. The *AD606* operates up to 50 MHz, with a dynamic range of 70 dB, and provides a limiter output with a phase accuracy of  $\pm 3^\circ$  (at 10.7 MHz). This method avoids the imbalance and spurious problems caused by the mixers and splitters comprising the IQ demodulator, and so may allow an improvement in sounder dynamic range. As an added advantage, the log output gives the power delay profile, useful for monitoring during propagation measurements, or for demonstrating channel sounder operation.

## 3.2 Sliding Correlator Simulations

### 3.2.1 Introduction

Simulations of the sliding correlator presented in this section show that, compared with the autocorrelation function of a PN sequence of length  $N$ , dynamic range is dramatically degraded even when the difference in chip periods is very small.

The simulation in this thesis uses a new algorithm, largely overcoming the computation limitation which in the past has restricted simulation attempts to short PN sequences. This work explains why the dynamic range achieved with practical channel sounders is always much less than that for the autocorrelation function of the PN sequence employed - an observation which many researchers have previously attributed in vague terms to “system noise”.

Results are presented for dynamic range, correlation peak amplitude and time width, as  $k$  and  $N$  are varied. Simulation results for dynamic range are similar to the actual dynamic range achieved with the *VUT channel sounder*, illustrating that for all but weak received signals, impulse response noise is dominated by correlation noise. Moreover, the appearance of the noise floor in measured power delay profiles is reminiscent of the simulated profiles.

Using insights obtained from these simulations, a complete design technique for the sliding correlator sounder is described in Section 3.2.11.

The simulation work is extended to compare the time domain response effect of various lowpass integrating filters following the sliding correlator. Filters simulated include:

1. single pole RC filter.
2. two pole Butterworth filter.
3. eight pole Butterworth filter.
4. eight pole Bessel filter.

#### 3.2.1.1 Dynamic Range of PN Sequences

Maximal length PN sequences are well known to have excellent autocorrelation properties {Ref.[3.95]}. With the correlation peak normalised to 1, the spurious or sidelobe correlation value for a sequence length of  $N$  is  $-1/N$ , resulting from the disparity between the number of ones and zeros in the sequence. Dynamic range, defined as the difference between the magnitude of the correlation peak and the magnitude of the maximum spurious correlation value, is equal to  $N$ , or  $20\log_{10}(N)$  dB. Ideal autocorrelation dynamic ranges for  $N$  varying from 2047 to 63 are shown in Table 3.1

TABLE 3.1. Ideal dynamic range of maximal length sequences

Sequence length $N$	Dynamic range (dB)
2047	66.2
1023	60.2
511	54.2
255	48.1
127	42.1
63	36.0

Most researchers using the popular sliding correlator method tacitly assume that cross-correlation of the receiver and transmitter PN sequences yields approximately the same result as the autocorrelation of the transmitted sequence. It seems to be a widespread belief that the sliding correlator will approximate the ideal dynamic range, subject to low system noise levels. *Cox* {Ref.[3.1]} notes that the sliding correlator gives the autocorrelation function of the PN sequence, provided  $k$  is sufficiently large. Concerned primarily with correlation peak fidelity (ideally triangular), *Cox* uses  $N=511$ , and says that  $k=5000$  produces a good correlation with only slight distortion, whereas distortion is considerable when  $k=1000$ . *Parsons* {Ref.[3.90], p.230} states that the dynamic range equals the ideal value, “ignoring the effects of system noise”.

3. 2.1.2 Previous work

*Benvenuto* {Ref.[3.96]} published a mathematical treatment of the sliding correlator in 1984. This impressive analysis seems to be relatively unknown, and is seldom referenced by other authors. For example, *Benvenuto* is overlooked by *Johnson* {Ref.[3.91]}. In his paper, *Benvenuto* evaluates correlation amplitude and dynamic range at several points. These agree with simulated values presented later in this section, and *Benvenuto*’s values are superimposed on graphs in Fig.3.12 and Fig.3.14.

*Talvite and Poutanen* {Ref.[3.85]} have given a mathematical analysis of the sliding correlator, with results shown for  $N=63$  and  $k=1000, k=2000$ . *Street and Edwards* {Ref.[3.84]} used an analysis very similar to Ref.[3.85], to illustrate a scheme claimed to eliminate self-noise. Results are shown for  $N=15, k=1000$ . No results for longer sequences were given.

*Johnson* {Ref.[3.91]} has simulated the sliding correlator at baseband for short sequences, up to  $N=127$ . Longer sequences would have taken too long with the simulation method used. Because the PN sequences are clocked at slightly different rates, using *Johnson*’s method, the signal must be sampled sufficiently frequently to ensure at least one sample occurs during the time difference between the chip periods. Each chip of the slower (receiver) sequence must thus contain  $(k+1)$  samples. The complete PN sequence then contains  $N(k+1)$  samples. The simulation is allowed to run until the entire receiver sequence has slid past the

transmitter sequence. To slide by one chip, we need to calculate for  $k/N$  sequences. So to slide through a complete sequence of  $N$  chips, this must be repeated  $N$  times, or in other words, for a total of  $k$  sequences. Hence the correlation must be done at a total of  $k(k+1)N \approx k^2N$  samples. For a constant  $k/N$  ratio, the number of samples to correlate at is proportional to  $N^3$ . If  $N=127$  and  $k/N=20$ , correlation must be computed for approximately  $0.8 \times 10^9$  samples. Results for dynamic range (called processing gain in Ref.[3.91]) are given in graph form for  $N=7$ ,  $N=15$ ,  $N=31$ ,  $N=63$  and  $N=127$ , and for up to  $k=2540$  for the longest sequence (requiring correlation at  $0.8 \times 10^9$  samples), and as a table for  $N=63$  to a maximum of  $k=3150$  (involving correlation at  $0.6 \times 10^9$  samples). Such short sequences are of little practical use for high resolution channel sounding, because of their limited ambiguity range. However, using this method, a sequence length of  $N=2047$ , with  $k/N=10$ , would require correlation at  $8.6 \times 10^{11}$  sample points.

Although quite valid, this simulation approach is a “brute-force” method, limited because of the long computation times involved as  $N$  and  $k$  values increase.

### 3. 2.1.3 Other Factors Limiting Dynamic Range

Other factors which may restrict channel sounder dynamic range include receiver front-end noise, mixer spurious products, phase noise of signal sources (local oscillators, PN generator clocks), IQ demodulator amplitude and phase imbalance, and analogue-digital converter dynamic range.

Simulations of the effect of receiver signal to noise ratio (SNR) on dynamic range are described in Ref.[3.37]. For  $N=255$  (ideal autocorrelation dynamic range 48.1 dB), the dynamic range is 27 dB when SNR= 0 dB, increasing to 44 dB for SNR = 20 dB, and to 47 dB for SNR = 40 dB. This assumes no degradation from any other effect.

Phase noise raises the noise floor and reduces dynamic range. All signal sources in the system will contribute to the aggregate phase noise. Using  $N=127$ , a double sideband phase noise standard deviation of  $10^\circ$  reduces the dynamic range to 30 dB {Ref.[3.97]}. This paper includes a simulation over part of a 127 chip sequence.

In Ref[3.41] the authors state that in order for the dynamic range to exceed 40dB, IQ demodulator balance should be better than  $1^\circ$  in phase and 0.1dB in amplitude.

Evidently, achieving a dynamic range of 40dB or better in a channel sounder requires stringent performance from all the RF hardware.

## 3. 2.2 Sliding Correlation Algorithm

Instead of sampling the PN sequences, the new algorithm used here is akin to the action of an analogue correlator.

The desired length transmitter PN sequence is software generated, and stored in a one dimensional array. All time values are in units of chip periods. The array index provides the time coordinate, and the array value gives the PN value (1 or 0) following the previous clock transition. Feedback taps used to generate the PN sequences are the same as the taps used in the channel sounder hardware (see Appendix A).

The receiver PN sequence is derived from the transmitter sequence by multiplying all time values by  $1 + \frac{1}{k}$ . The result is stored in a two dimensional array, as pairs of time and PN value numbers.

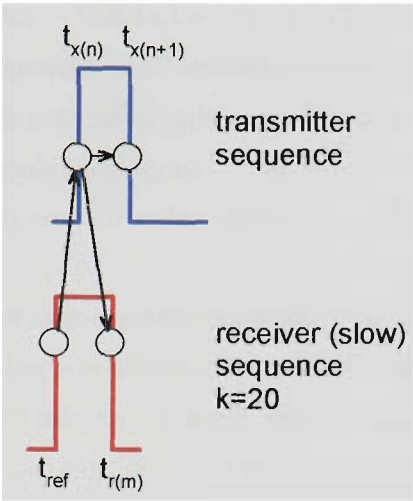


FIGURE 3.6. New algorithm - principle of operation

The first time value (or clock transition) in the receiver sequence is temporarily designated as the time reference  $t_{ref}$  (see Figure 3.6). The next clock transition in the receiver sequence  $t_{r(m)}$  is then found, and the next clock transition in the transmitter sequence,  $t_{x(n)}$ , is also located. These transitions are compared in time to determine which comes first, namely  $t_{x(n)}$  in this case, as  $t_{x(n)} < t_{r(m)}$ .

The sequences are correlated over the interval  $t_{ref}$  to  $t_{x(n)}$  by comparing the receiver sequence value after  $t_{ref}$  with the transmitter sequence value prior to  $t_{x(n)}$ . If the sequence values are equal (both 0, or both 1) a variable *correlated* is incremented by  $1 \times (t_{x(n)} - t_{ref}) = (t_{x(n)} - t_{ref})$ . If the values are unequal, which is the case here, a variable *uncorrelated* is incremented by  $(t_{x(n)} - t_{ref})$ . The time reference then becomes  $t_{x(n)}$ , and the whole process repeats, and this continues until the entire receiver sequence has been worked through.

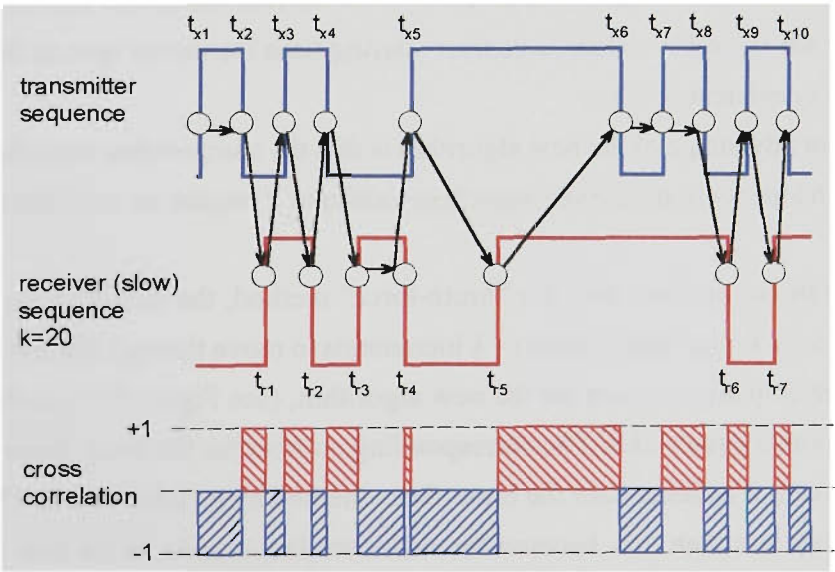


FIGURE 3.7. Illustration of the new algorithm



The movement of the  $t_{\text{ref}}$  point through the sequences is illustrated in Figure 3.7. Areas representing correlated regions are shaded in red, and uncorrelated areas are shaded in blue. After the complete receiver sequence has been worked through, the correlation value over the whole sequence is obtained as (*correlated* - *uncorrelated*), equivalent to subtracting total blue areas from total red areas. This corresponds to an ideal integrate-and-dump integration process. Figure 3.7 over-simplifies the process slightly. Actually every clock transition is examined, even if the PN sequence value does not change. At this stage, the simulation has produced the correlation value for one particular initial time of the receiver sequence.

The starting point of the receiver sequence is then moved by a small amount, for example 0.1 chips, and the complete calculation is repeated. In this way the whole  $N$  chips of the sequence can be worked through, leading to a plot of correlation as a function of initial chip offset of the receiver sequence. Alternatively, just the area within a few chips of the correlation peak, or indeed any desired region of the sequence, may be simulated. The final result consists of a series of snapshots for different positions of the receiver sequence relative to the transmitter sequence.

To allow the initial offset of the receiver sequence to range from prior to the peak correlation position, to a whole sequence length after the correlation peak, the transmitter sequence consists of two repeated sequences, plus the last 50 chips of a sequence added to the beginning, and 50 chips from the start of a sequence added to the end, so storing  $50+2N+50 = 2N+100$  chips in the transmitter sequence array.

### 3. 2.2.1 Number of Calculations - New Algorithm

For *Johnson's* method, the increment in the sequence starting time is  $N/k$  chips, for example equal to 0.1 chips if  $k/N=10$ . As  $k/N$  increases the increment becomes smaller.

The new algorithm allows the user to select the increment in sequence starting time, independent of  $k/N$ . This may involve some approximation when  $k/N$  is large, and a coarse starting time increment is used. For a given  $k/N$ , the correct increment can be calculated and used; however for large  $k/N$  values, a coarser starting time increment speeds the computation, and still yields consistent results.

A major advantage of the new algorithm is that the computation time for each snapshot correlation is independent of  $k$ . Even very high values of  $k$  require no increase of computation time.

For a fair comparison with the “brute-force” method, the starting time increment will be made equal to  $N/k$ , requiring  $N/(N/k) = k$  increments to move through the full sequence. Two correlations per chip are required for the new algorithm, (see Figure 3.7), so the total number of correlation points equals  $2kN$ . The corresponding number for the brute-force method is  $k^2N$ , so the new algorithm is faster than the brute-force method by a factor of  $k/2$ . The advantage is actually probably less than this, because for each correlation point in the new algorithm, several operations are performed.

### 3.2.2.2 Parameters Degraded by Sliding

The main impacts of the small difference in chip periods necessary for the sliding effect, in order of importance, are:

1. a reduction in dynamic range because of increased correlation noise
2. a time widening of the correlation peak, leading to a slight reduction in resolution
3. a reduction in the correlation peak amplitude

Of these, the reduction of dynamic range has the most impact on channel sounder performance. Reduction in the correlation peak amplitude is minor, and can be compensated by an increase in gain elsewhere, and the correlation peak widening is minor for typical  $k/N$  values. These effects are quantified in sections 3.2.5 and 3.2.6.

### 3.2.3 Illustrative Simulation Results for $N=63$

Illustrating the degradation as  $k/N$  is reduced, a series of simulated power delay profiles are shown in Figure 3.8 for a sequence length of  $N=63$  chips. This short sequence was chosen to improve the visibility of detail in the profiles.

The increase in noise floor, and the reduction in the correlation peak amplitude as  $k$  is increased, can be clearly seen.

PN Sequence Length = 63

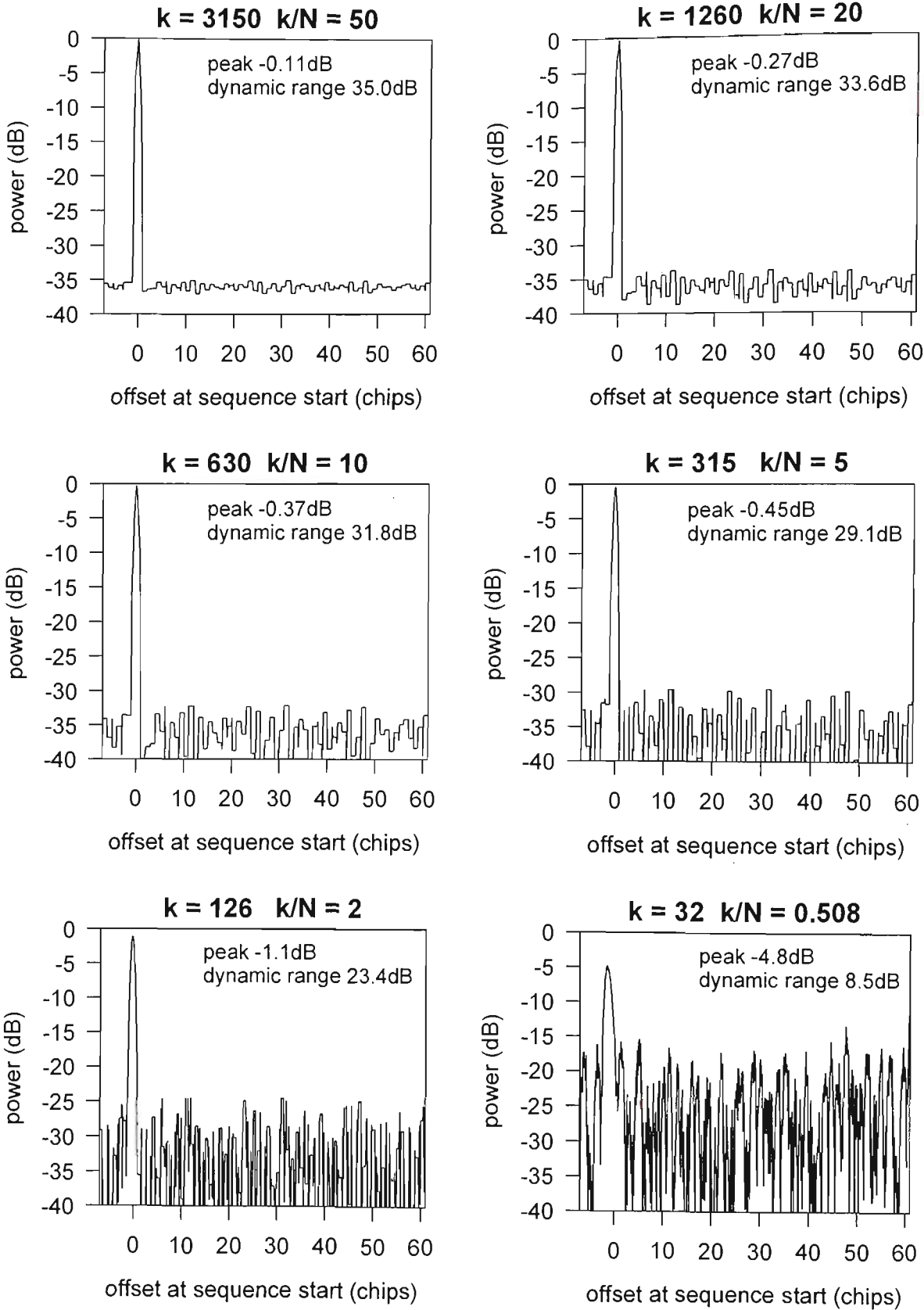


FIGURE 3.8. Simulations for  $N=63$ ,  $k/N = 0.51$  to 50

3.2.4 Correlation peak  $N=1023$

Figure 3.9 shows plots of the correlation peak region for a sequence length of  $N=1023$ , for various  $k$  values. As  $k/N$  reduces, the correlation peak reduces in amplitude, increases in width, and occurs for an earlier offset of sequences. The earlier offset balances the sequence time distortion about the centre of the sequence. The increase in correlation noise away from the peak is also evident.

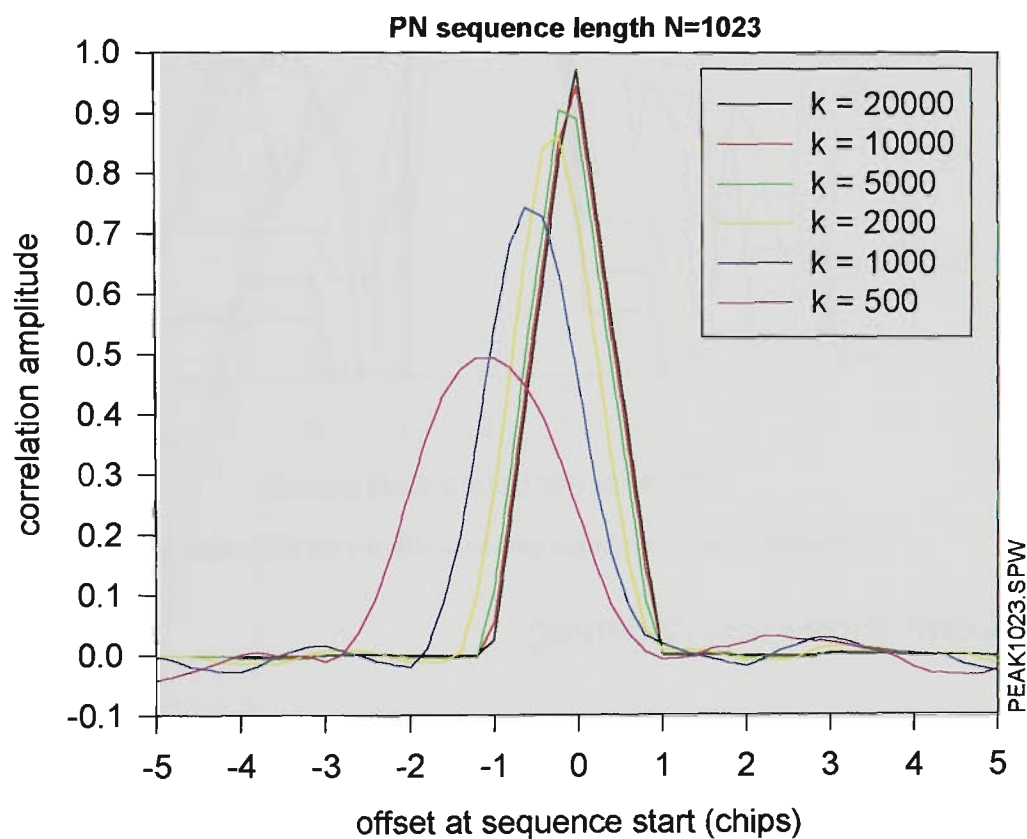


FIGURE 3.9. Correlation peak detail for  $N=1023$ , various  $k$

Correlation noise sidelobes become more obvious if Figure 3.9 is rescaled to plot power in dB on the vertical axis. This is shown in Figure 3.10.

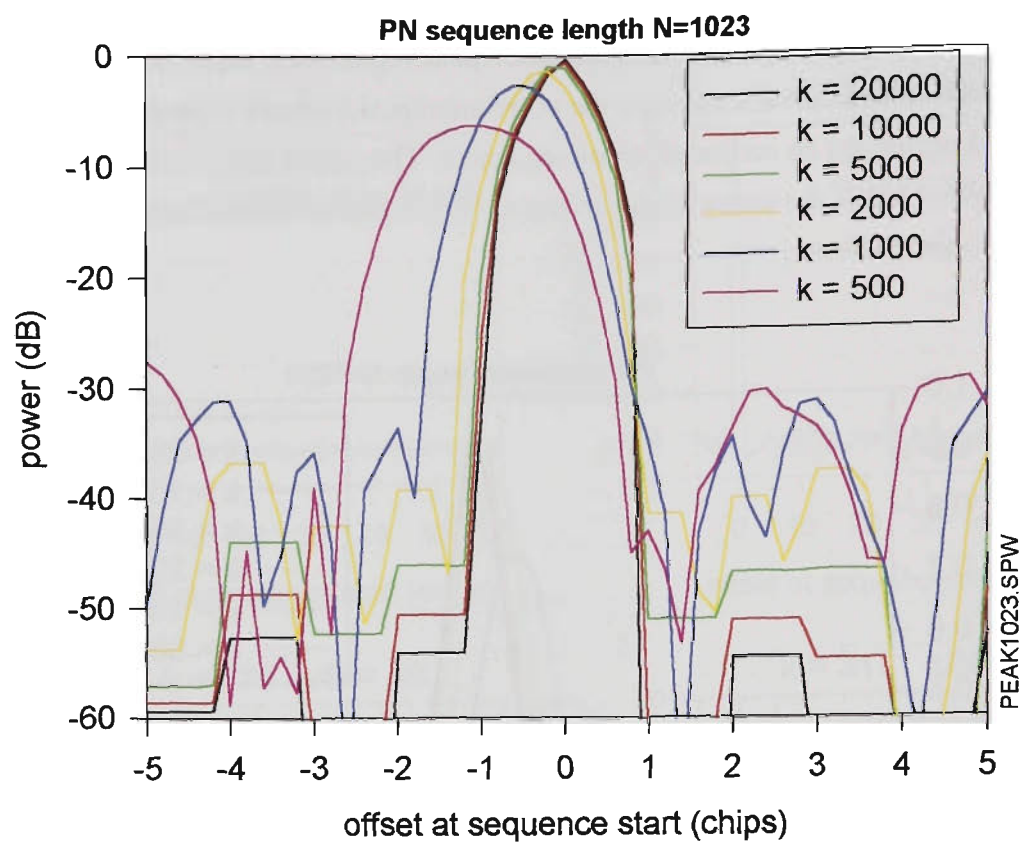


FIGURE 3.10. Correlation power in dB for  $N=1023$ , various  $k$

3. 2.5 Correlation Peak Widening

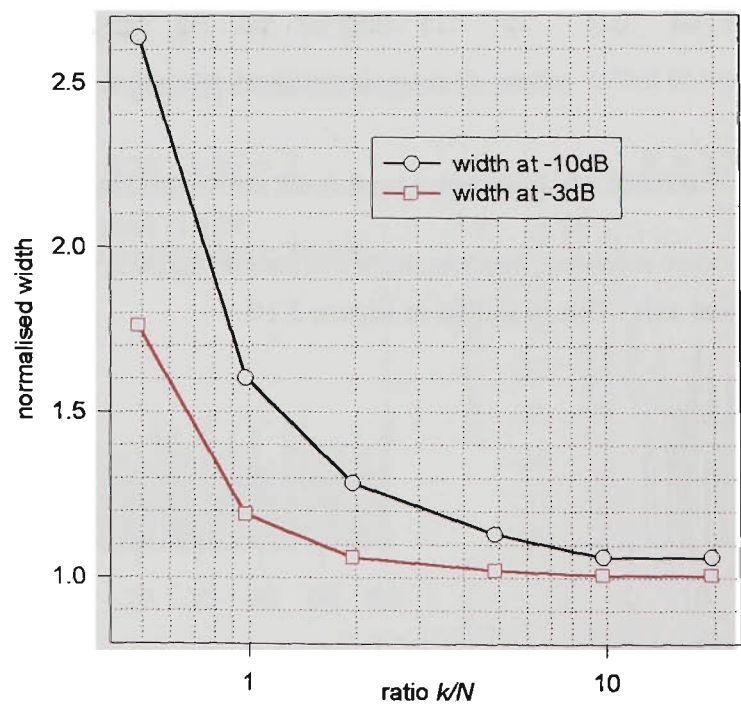


FIGURE 3.11. Correlation peak width versus  $k/N$ ,  $N = 1023$

The widening effect is minor, provided  $k/N > 2$ , or  $k > 4000$  for  $N = 1023$

### 3. 2.6 Correlation Peak Power

As  $k/N$  reduces, the correlation peak amplitude decreases. Expressed as power normalised to the ideal autocorrelation peak power, the degradation in peak power is plotted in Figure 3.12.

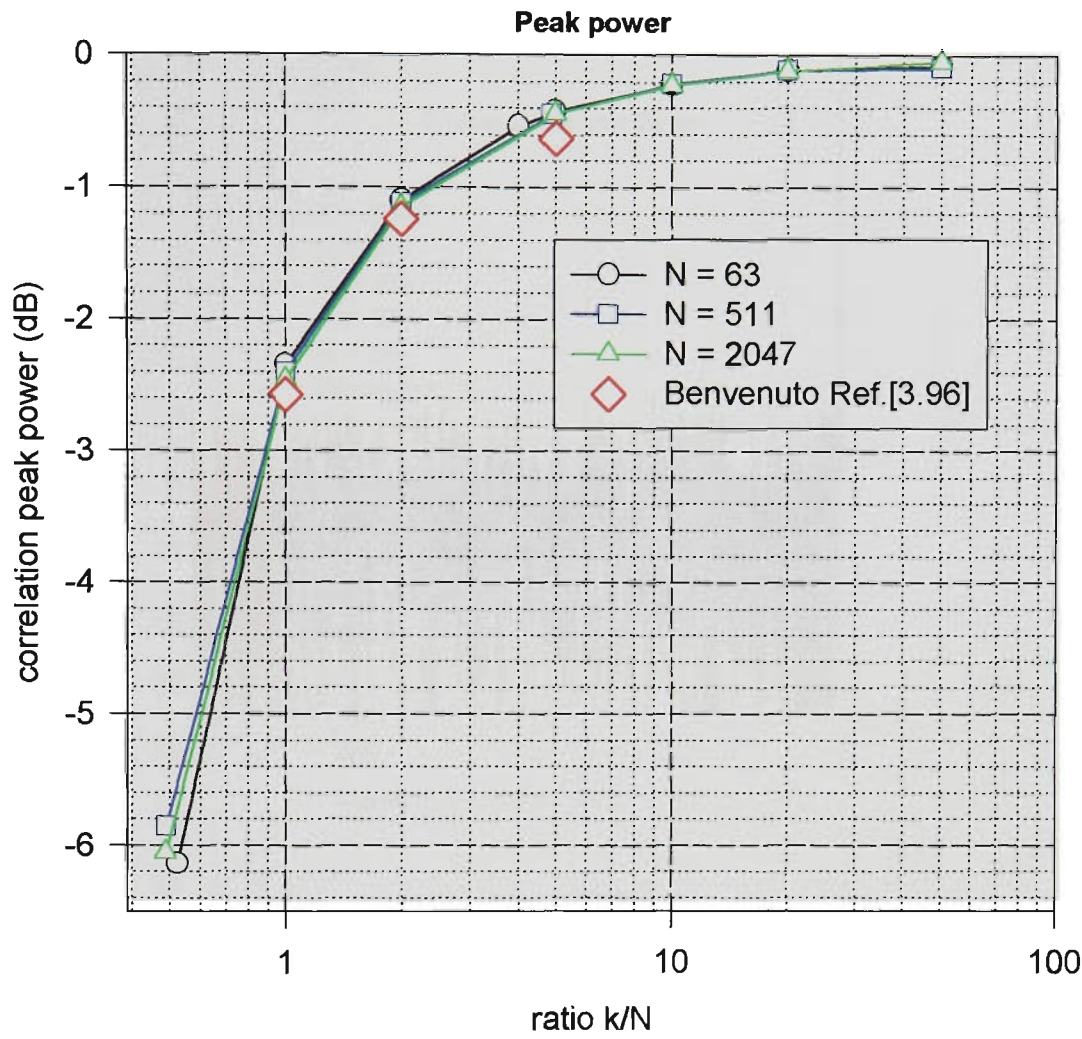


FIGURE 3.12. Correlation peak power versus  $k/N$

Figure 3.12 shows that the reduction in correlation peak amplitude depends on  $k/N$  but is independent of  $N$ . This agrees with *Benvenuto*’s theoretical treatment {Ref.[3.96]}, and the three values calculated by *Benvenuto* are plotted in Figure 3.12. These agree within  $< 0.2\text{dB}$  with the simulated values.

### 3. 2.7 Simulation of Channel Sounder PDPs

Figure 3.13 shows 80% of the sliding correlator power delay profile (PDP) for the parameter values used for the *VUT channel sounder* measurements presented in this thesis. The simulation uses an integrate and dump filter, and shows that for this method of integration, the best dynamic range which can be expected from the channel sounder is just over 40dB when  $k=5000$  (the *outdoor measurement* configuration) and just over 50dB when  $k=20000$  (the *in-*



*door measurement* configuration). Achievement of these figures would imply that other degrading mechanisms (system noise, IQ imbalance, etc.) must be negligible, resulting in performance being dominated by sliding correlation noise.

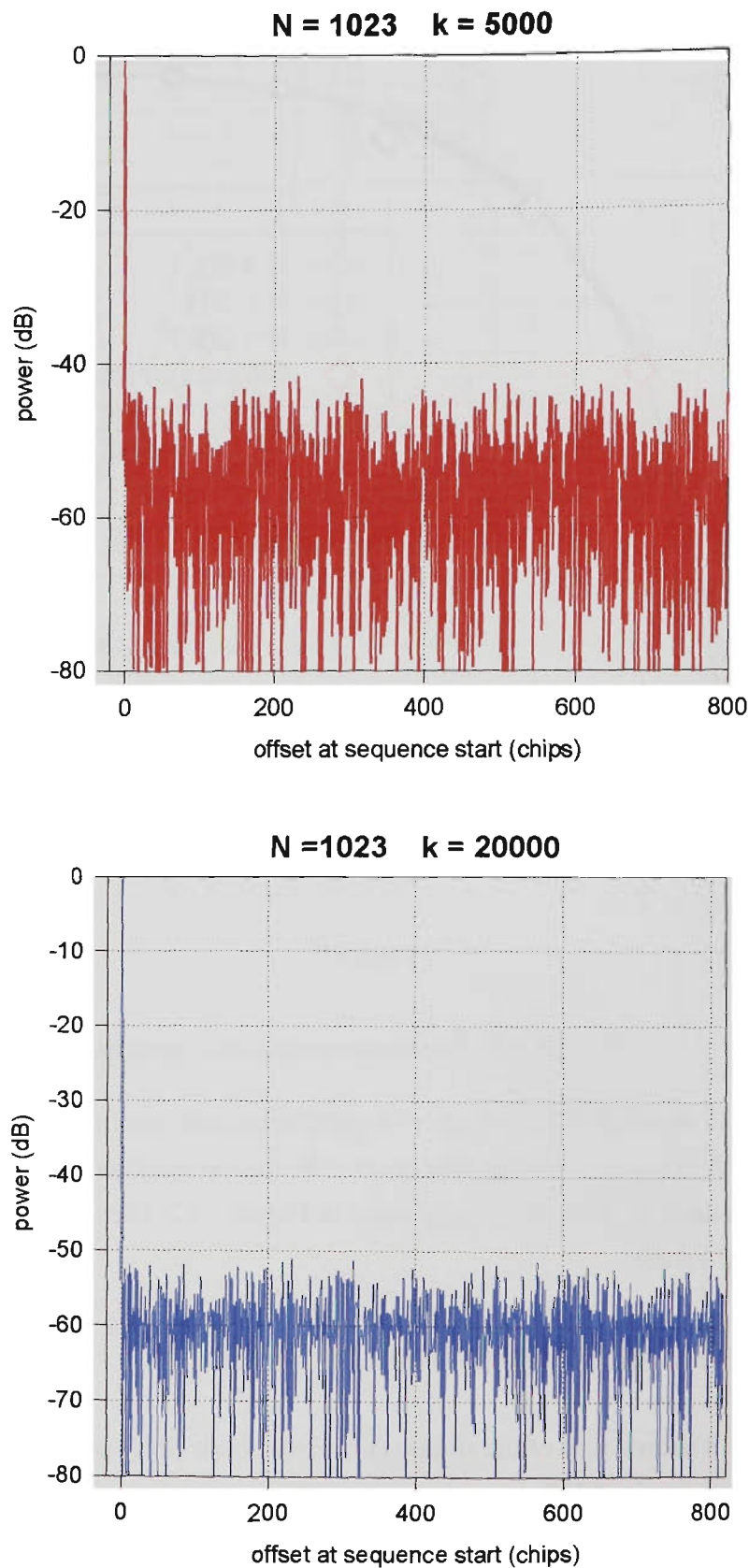


**FIGURE 3.13. Simulated sliding correlator performance for  $N$  and  $k$  values used in the *VUT channel sounder***

### 3. 2.8 Dynamic Range from Simulations

The new algorithm has allowed simulations at sequence lengths up to 2047, and at values of  $k$  up to over 100,000. Dynamic range is calculated as the difference between the correlation peak, and the maximum instance of correlation noise. A summary of results for  $N$  between 63 and 2047 and  $k/N$  between 0.5 and 50, is presented in Figure 3.14.

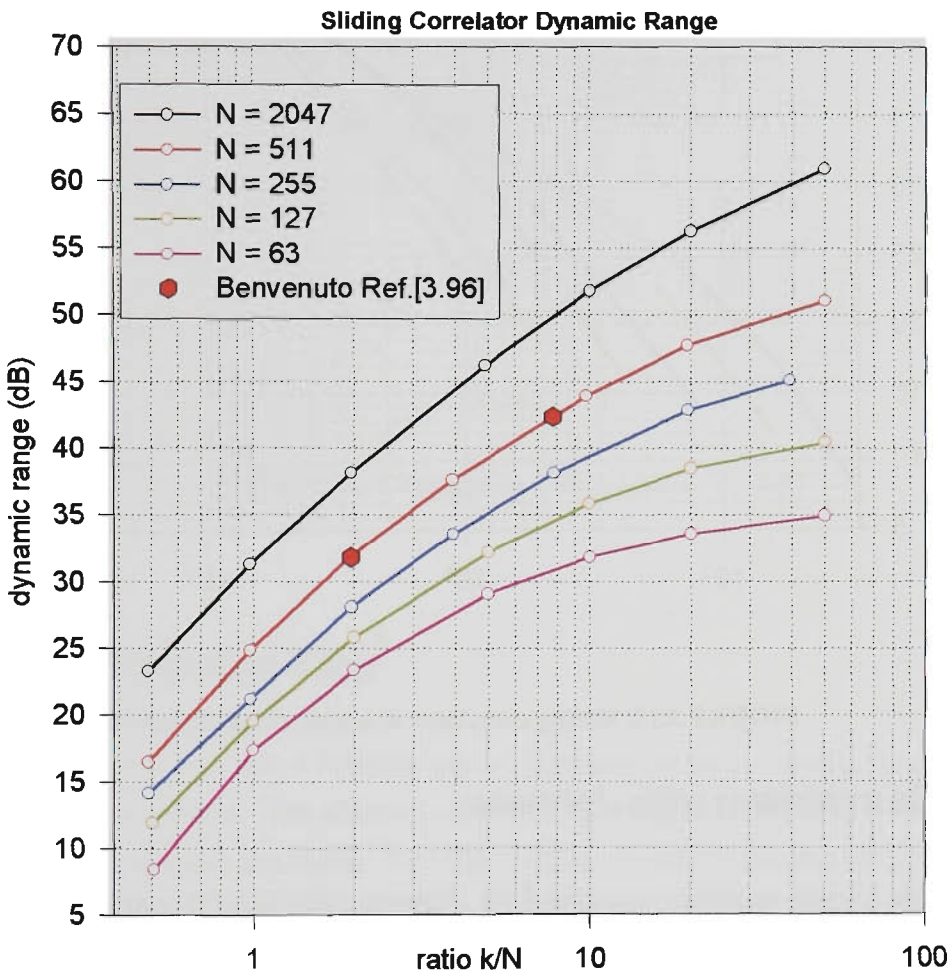


FIGURE 3.14. Simulated dynamic range, for  $k/N$  values of 0.5 to 50

*Benvenuto* {Ref.[3.96]} has calculated values at two points for the  $N=511$  sequence. These points are plotted in Figure 3.14, and show excellent agreement with simulated results.

Replotting these results in terms of  $k$  results in the family of curves shown in Figure 3.15. These will be used as the basis for the complete sliding correlator design method, described later in Section 3.2.12.



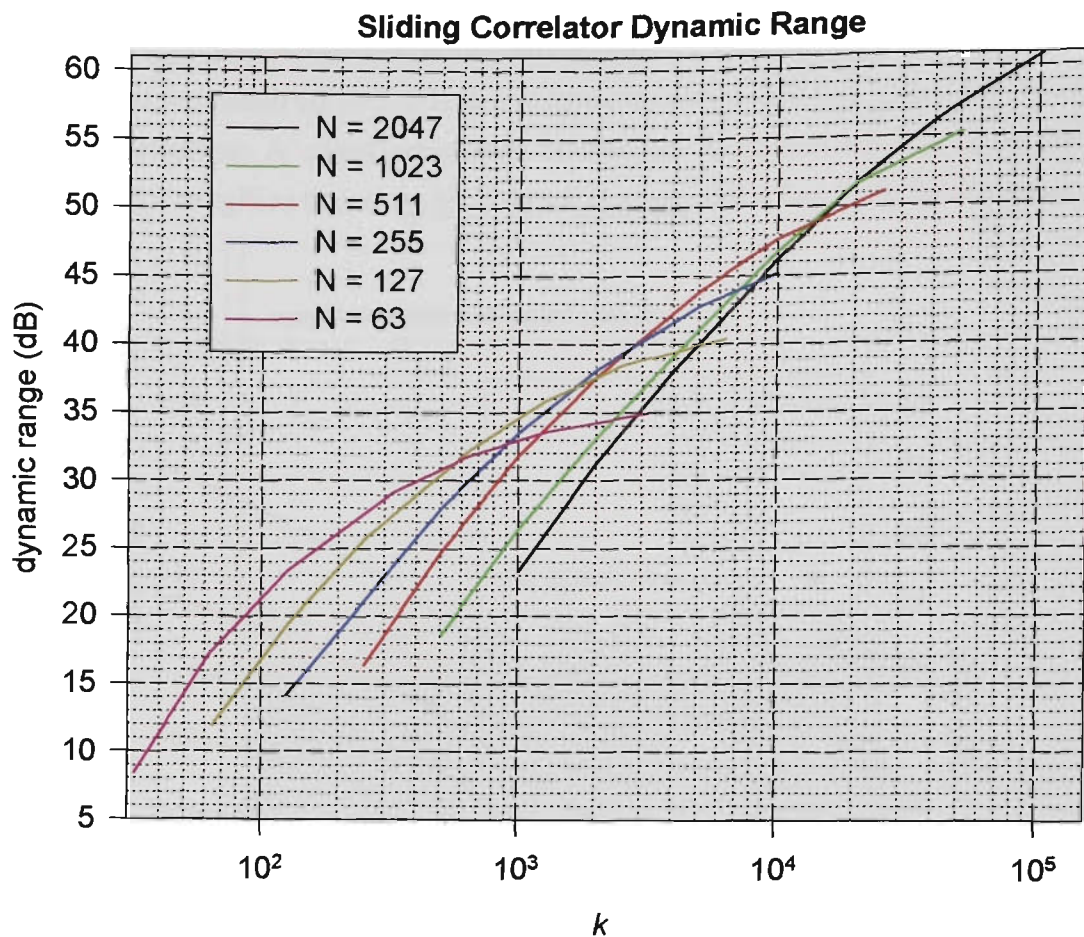


FIGURE 3.15. Sliding correlator dynamic range design curves

### 3.2.9 Comparison with *Johnson*

The longest sequence simulated by *Johnson* {Ref.[3.91]} was  $N=127$ , because the computation time become unacceptably extended for longer sequences. A comparison of simulations using the new algorithm with *Johnson*'s results for  $N=127$ , displays reasonable agreement. See Figure 3.16.

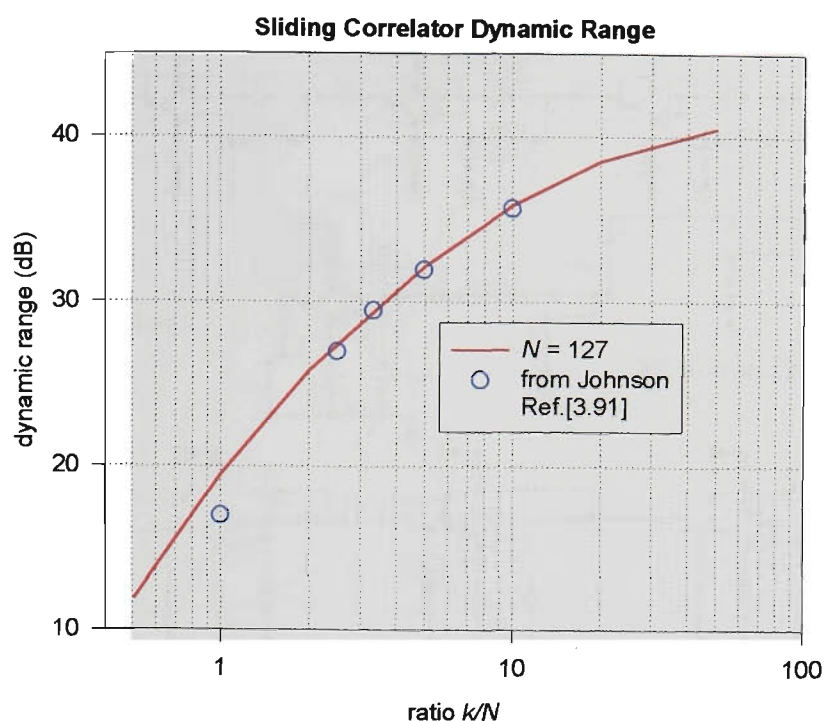


FIGURE 3.16. Comparison with Johnson,  $N=127$

### 3.2.10 The Integrating Filter

In the channel sounder, a lowpass active filter performs the integrating function following the sliding correlator. The effect of different filter alignments is shown in this section, using a *SPICE* time-domain simulator. The *SPICE* input waveform consists of the output from the sliding correlator simulator, using the piecewise-linear input signal feature available with *SPICE*.

By using a waveform produced by the simulator, and passing this through an active filter, the result in the time domain is equivalent to using a single filter with a response equal to the convolution of the ideal integrate-and-dump filter and the active filter. In the real channel sounder, only the active filter exists to perform the integration. Assuming that the convolved filter response is dominated by the active filter, the approach used in this section is valid.

Circuits used for the various filters are shown in Figure 3.17. All filters were adjusted to have approximately equal passband gain, and approximately equal -3dB cutoff frequencies of 2.5 kHz. Filter frequency responses are shown in Figure 3.18, and the time distortion inflicted upon the ideal triangular autocorrelation signal by each filter type is shown in Figure 3.19.

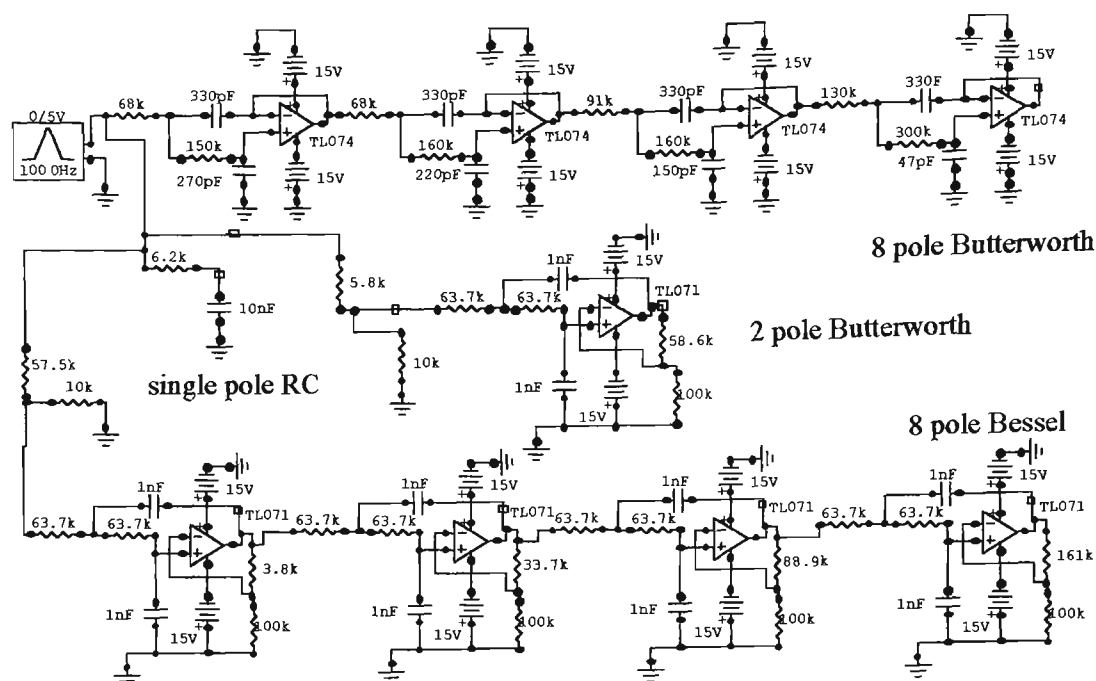


**FIGURE 3.17. Active filters used in the *SPICE* simulation**

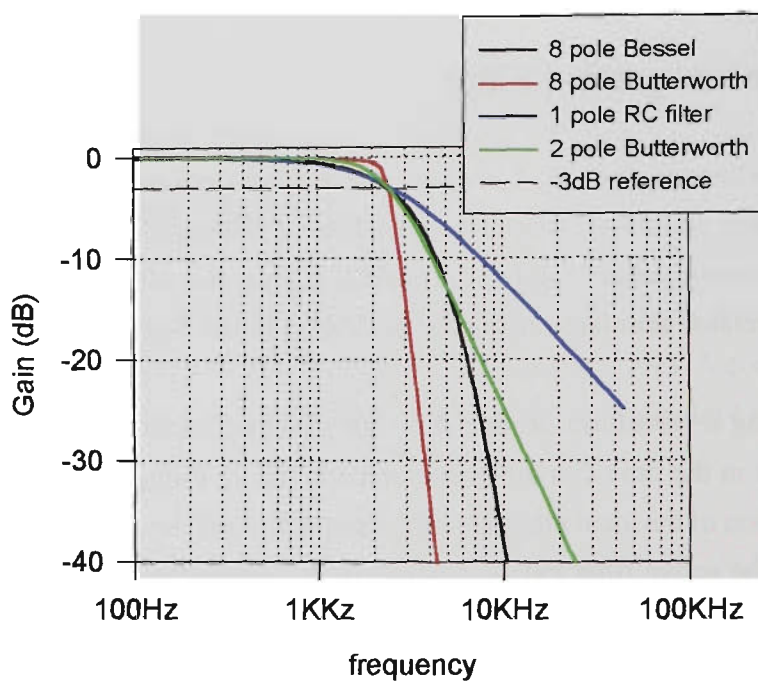


**FIGURE 3.18. Integrating filter frequency response - Four different filters each with cutoff frequency  $\approx 2.5$  kHz**

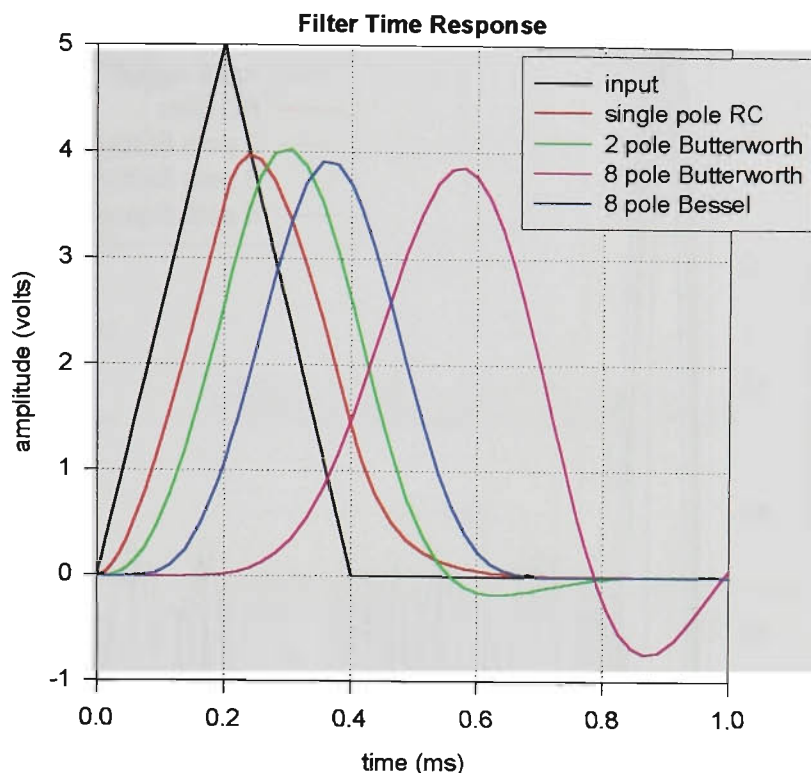


**FIGURE 3.19. Filter time response with input from ideal correlator**

From Figure 3.19, it is evident that both Butterworth filters are unacceptable, causing ringing which destroys the dynamic range of the correlation peak. The 8-pole Bessel filter causes the least time distortion, with no ringing, but some smoothing of the discontinuities in the input signal. The very simple passive single-pole RC filter spreads low level values of the input pulse trailing edge, skewing the pulse, but otherwise looks almost as good as the 8-pole Bessel filter.

Using part of the simulator output for  $N=1023$ ,  $k=5000$ ,  $k/N=4.89$  as the filter input signal, the effect of the different filters on the PDP, and on the dynamic range, is clearly illustrated in Figure 3.20. This shows the unsuitability of Butterworth filters, contrasted with the fidelity of the 8-pole Bessel, and the single-pole RC filter. Although the simplicity of the passive RC filter is appealing, time-domain fidelity is not the only consideration in choosing a filter. The filter, in addition to integrating the sliding correlator signal, also acts as an antialiasing filter preceding A-D conversion, including attenuating the high level PN chip frequency signal to negligible levels. The cutoff slope of the passive RC filter is insufficient to prevent aliasing.

Typically, the channel sounder output is sampled at 25ks/s per channel when in *indoor mode* (100MHz chip rate), or 20ks/s per channel when in *outdoor mode* (25MHz chip rate) - refer to Table 3.3. Both modes use the 8-pole Bessel filter, with nominal cutoff frequency of 2.5kHz. To maintain a dynamic range of  $\geq 40\text{dB}$  in *outdoor mode*, the antialiasing filter must provide an attenuation of at least 40dB at half the sampling frequency, viz. 10kHz. From Figure 3.18, it can be seen that the 8-pole Bessel filter just meets this requirement, whereas the passive RC filter is only down by approximately 12dB at 10kHz, well short of the requirement. Thus temporal fidelity, together with anti-aliasing capability, are the basis for the choice of an 8-



pole Bessel filter in the *channel sounder*.

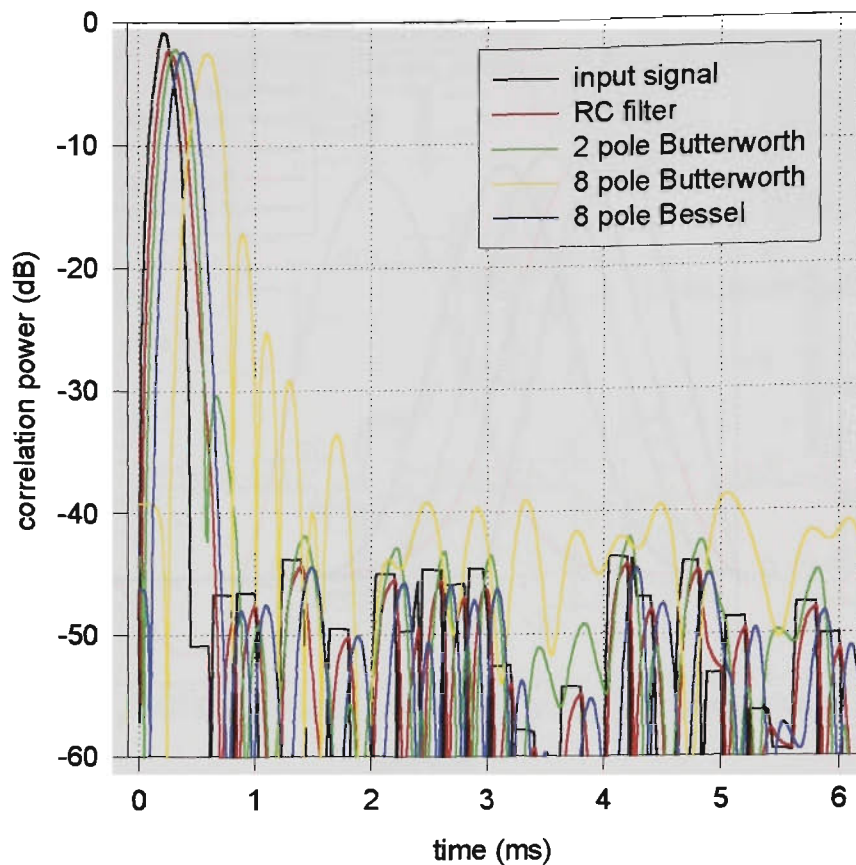


FIGURE 3.20. Effect of various correlation filters

### 3. 2.11 Comparison of Measured and Simulated PDPs

Figure 3.21 shows a comparison of a PDP simulated for a sliding correlator, and a measured PDP obtained from a back-to-back test using the *VUT channel sounder*, with a receiver input of -73dBm. The simulated result assumes an ideal integrate-and-dump filter, and does not include any allowance for the actual filters and band limiting effects encountered in the *channel sounder*. These effects broaden the measured correlation peak, shown in more detail in Figure 3.22. Note that the measured correlation peak has been normalised to 0 dB, whereas the simulated peak shows the gain loss relative to the autocorrelation function.

Dynamic range illustrated in the back-to-back test matches the simulated result, and so achieves the maximum possible with the sliding parameters chosen. Correlation noise does not exactly match in time, with more noise components apparent in the measured result. Possibly other noise sources are contributing spurious and noise components.

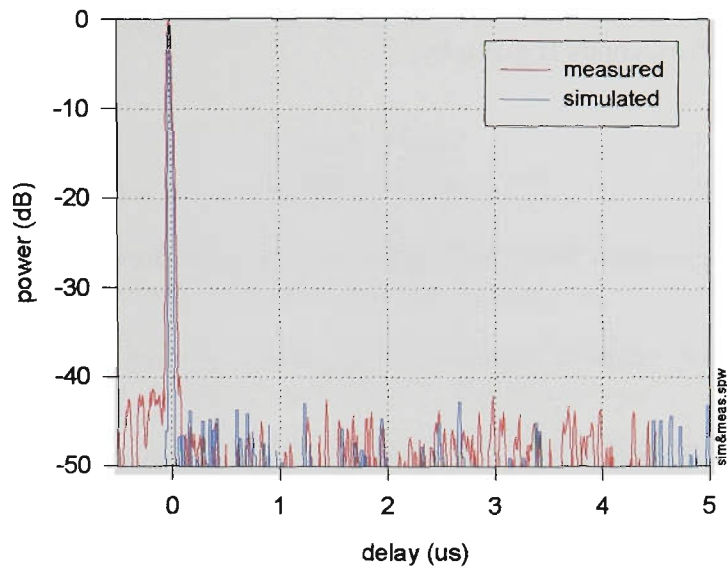


FIGURE 3.21. Simulated and measured PDPs showing similar dynamic ranges.  $N=1023$ ,  $k=5000$ , receiver input for measured response =  $-73\text{dBm}$ .

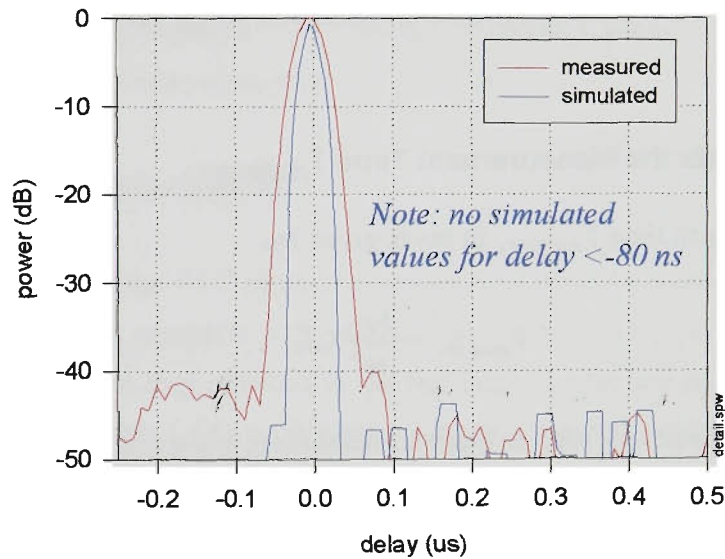


FIGURE 3.22. Detail of correlation peaks shown in Figure 3.21

3. 2.12 Sliding Correlator Design

In this section, a systematic method for designing sliding correlators is presented.

3. 2.12.1 Fix Chip Period  $t_{chip}$

The receiver chip period  $t_{chip}$  ns determines the channel sounder resolution, and is taken as the fundamental parameter.

### 3. 2.12.2 Specify Maximum Excess Delay $\tau_{max}$

$\tau_{max}$  in microseconds is given by:

$$\tau_{max} = \frac{t_{chip} N}{1000} = \frac{t_{chip} yN}{1000} \quad (\text{EQ 3.1})$$

where  $y$  is a window factor between 0 and 1, used if the PN sequence is reset prematurely.

The ambiguity range or alias range  $R_{alias}$  in km. is given by EQ. 3.9 (page 3.39), and is independent of  $y$ .

From EQ. 3.1 and EQ. 3.9, determine  $N$ , and  $y$  if windowing is used.

### 3. 2.12.3 Specify the Required Dynamic Range

$N$  has already been chosen. Use Figure 3.15 to determine  $k$  for the desired dynamic range.

The effect on correlation peak amplitude and width can be determined from Figures 3.12 and 3.11.

### 3. 2.12.4 Calculate the Measurement Time $T_{measure}$

Measurement time  $T_{measure}$  in ms is given by:

$$T_{measure} = \frac{Ny k}{10^6} t_{chip} \quad (\text{EQ 3.2})$$

Further parameters, such as Doppler resolution, and maximum channel sounder velocity, may be calculated using equations from Section 3.4.

### 3. 2.12.5 Example

Suppose  $t_{chip} = 40$  ns, the desired maximum excess delay  $\tau_{max}$  is 10  $\mu$ s, and all of the PN sequence is used ( $y = 1$ ). The desired dynamic range is >30 dB.

From the excess delay requirement,  $N=250$ , so choose  $N=255$  which will give  $\tau_{max} = 10.2$   $\mu$ s, and  $R_{alias} = 1.53$  km.

Consulting Figure 3.15 for  $N=255$ , choose  $k=1000$ , which gives a maximum possible dynamic range of 34 dB. The measurement time  $t_{measure}$  is 10.2 ms. Figure 3.11 shows that the correlation peak is widened by 17% at -10dB, and from Figure 3.12, the peak power is reduced by 0.6dB. Both these changes are relative to the ideal autocorrelation peak.

## 3.3 The VUT Channel Sounder

### 3.3.1 Portability

Prior to this thesis project, existing wideband channel sounders had generally been bulky, and often required the use of one or more items of commercial laboratory instrumentation, such as synthesised signal generators and digital sampling oscilloscopes, and consequently had very limited portability {Ref.[3.94], Ref.[3.22]}. Weight, bulk, power consumption and the unwieldiness of multiple boxes has limited the use of such equipment to laboratory trolleys or motor vehicles. In 1997, the *Mobile and Portable Radio Group (MPRG)*, a long standing and very active propagation research group at Virginia Polytechnic Institute and State University, reported that the development of a portable self-contained channel sounder was underway, with sponsorship from *Tektronix®* {Ref.[3.93]}. Meanwhile, the *VUT portable channel sounder* designed for this thesis project had been completed and in use since early 1994, and was described in Ref.[3.92]. To the author's knowledge, the *VUT sounder* was the first self-contained, portable wideband channel sounder not requiring a reference cable, to be developed and deployed for outdoor wideband propagation measurements.

### 3.3.2 General Description

From the outset, the *VUT channel sounder* has been developed as a portable self-contained unit. The receiver, complete with power source and antenna, can be carried by one person as a backpack unit. A tray attached to the backpack frame, and positioned in front of the operator, carries a portable LCD oscilloscope (*Fluke ScopeMeter®*) for monitoring the received signal, a 12 bit analogue to digital unit, and a notebook computer for data acquisition. A small panel of indicator LEDs attached to the tray and visible to the operator, monitors the health of the various supply voltages. The antenna is mounted on a tube on the side of the backpack, and positioned just above the operator's head level.

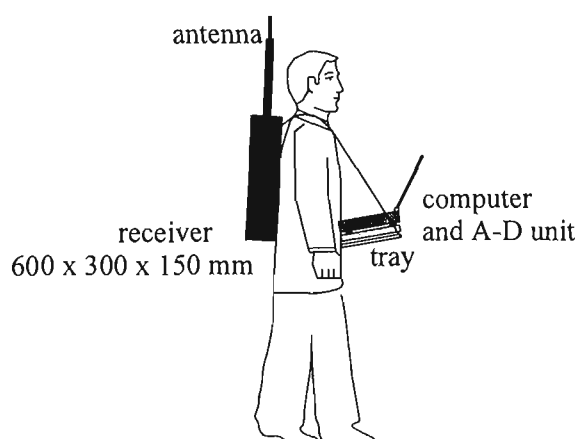


FIGURE 3.23. Backpack receiver unit



Portability allows measurements to be made in any location accessible to a pedestrian, such as pedestrian malls, narrow lanes blocked to traffic, shopping arcades and pedestrian pavements. Indoor locations inaccessible to a trolley, such as stairwells, can also be covered.

The transmitter is housed in a 19" case, and powered by an external 12V 7AH sealed lead-acid (SLA) battery, and a larger (automotive size, approximately 45AH) 12V lead-acid battery. An attenuator, and a *Bird*® wattmeter are also used. A low-loss coaxial cable connects the output to the antenna, mounted on a mast. The transmitter is intended for use at a fixed location and, unlike the receiver, is not designed to be carried by a pedestrian. However, with battery power, it is self-contained, and quick to set up. It has been used in the following situations: (i) in a car boot, with the antenna on a mast mounted on the towbar, allowing low-antenna city measurements to be carried out with the car parked in the city centre at a kerbside parking meter, (ii) outdoors sitting on the ground, with the antenna on a 5 metre portable free-standing mast, (iii) in a building or on a building roof with a long cable to an antenna mast on the roof, (iv) indoors, or on a balcony, with the antenna on a camera tripod on the balcony.

### 3.3.3 Signal levels

The channel sounder does not use automatic gain control. To keep the signal within an acceptable range:

1. the transmitter power output can be adjusted using an attenuator preceding the output amplifiers, and read from the *Bird*® wattmeter.
2. receiver gain can be adjusted using a switched attenuator located between the antenna and receiver input.

The first method requires two operators, in radio contact (UHF citizen band transceivers have been used). The second method requires only one operator, provided the location is sufficiently secure to allow the transmitter to be left running unattended. Transmitter power is set and left constant, and the receiver attenuator is varied. Receiver output is monitored on the portable *Fluke ScopeMeter*® LCD digital oscilloscope, set to give a polar display of the receiver I and Q outputs.

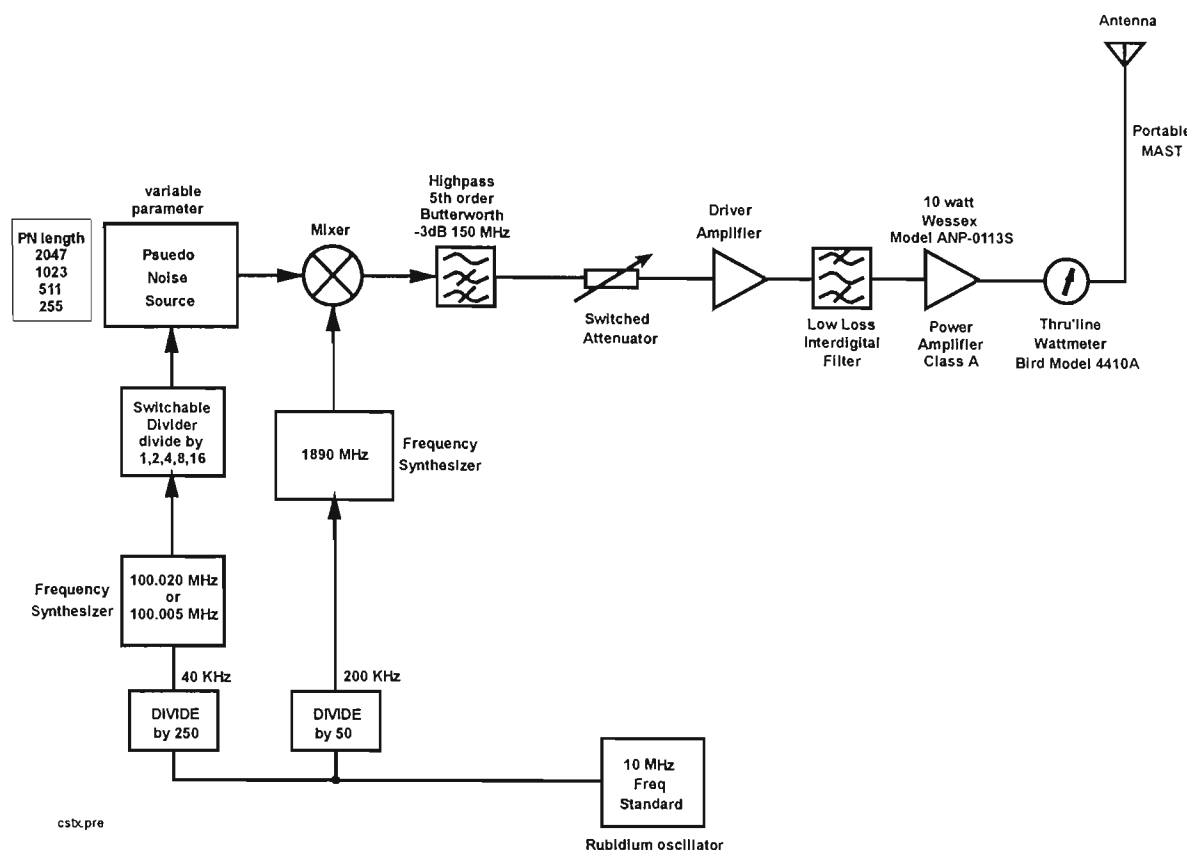


FIGURE 3.24. Channel sounder transmitter - block diagram

3. 3.4 Transmitter Description

A detailed description of the transmitter hardware design is given in Appendix A. Figure 3.24 shows a block diagram of the transmitter. Two frequency synthesizers are included. A VHF synthesiser for the PN clock is set to 100.020 MHz and followed by a  $\times 4$  stage for *outdoor mode* measurements, or 100.005 MHz for *indoor mode* measurements. This gives a time scaling factor  $k = 5000$  for the outdoor 40 ns resolution setting, or  $k = 20,000$  for the indoor 10 ns resolution setting. A UHF synthesiser at 1890 MHz generates the RF carrier. An emitter-coupled logic (ECL) PN generator bi-phase modulates the carrier, which passes through a highpass filter, then an (external) switched attenuator used to adjust the transmitter output power, to the driver amplifier and final power amplifier. An interdigital filter precedes the final amplifier, and defines the transmitted bandwidth to nominally 50 MHz for *outdoor mode* measurements, or 200 MHz for the *indoor mode*. The change in bandwidth is made by swapping SMA connectors to a different filter. The final amplifier operates in class A, and is very linear. An external wattmeter monitors the RF output power.

3. 4 Receiver Description

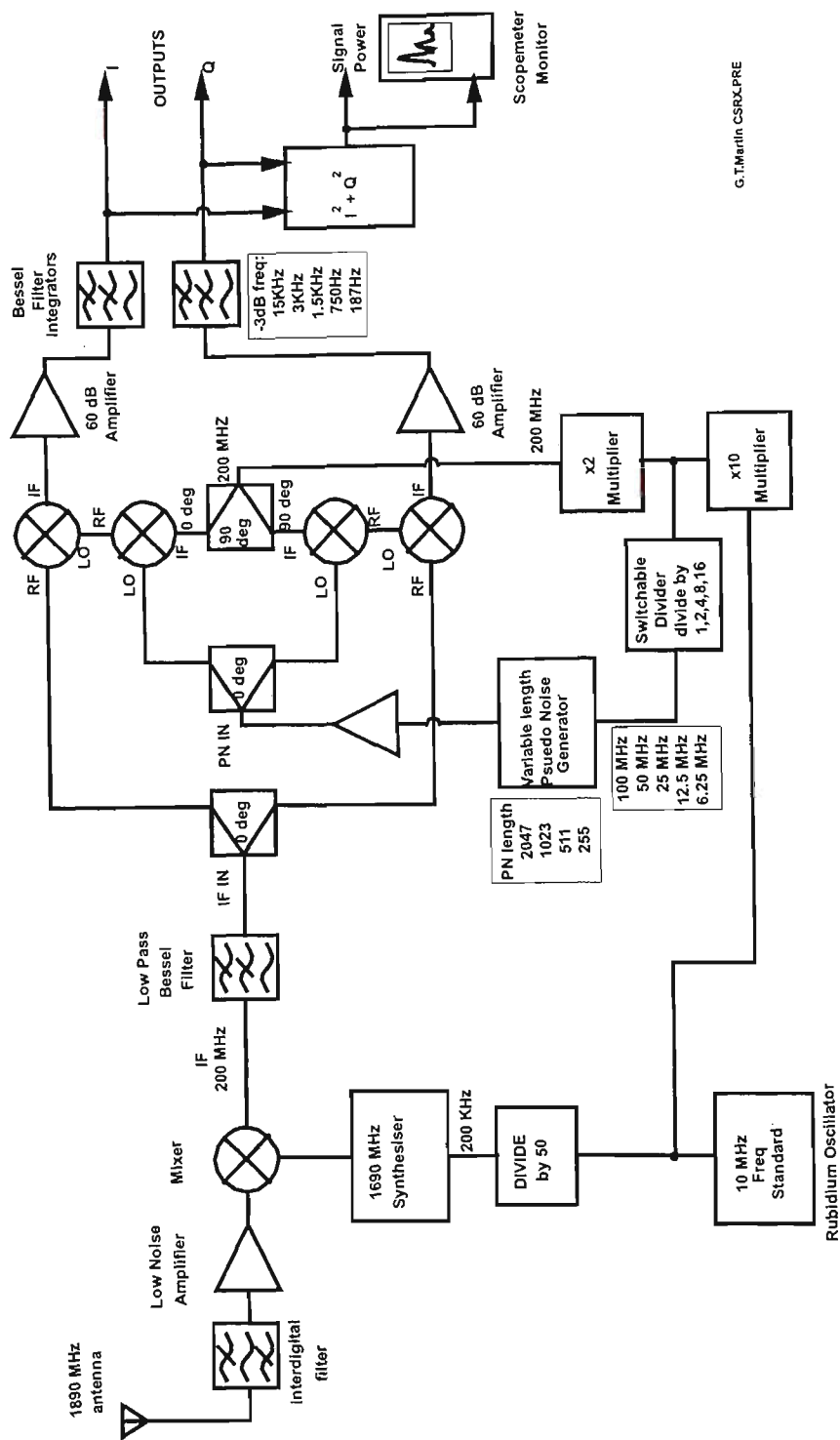


FIGURE 3.25. Channel sounder receiver - block diagram

Appendix B covers a full discussion of the receiver hardware. A block diagram of the receiver is shown above in Figure 3.25. The architecture follows that of the sounder used at the *University of Bristol* {Ref.[3.22], Ref.[3.35]}. The design uses a wideband IF (bandwidth up to 200 MHz), centered on 200 MHz. The IQ demodulator places the 90° hybrid splitter in the fixed frequency second local oscillator path, following the *Demery* design, and performs the sliding correlation down to baseband. Correlation integration is done by lowpass active RC filters, with a Bessel characteristic to preserve fidelity in the time domain. The 100 MHz PN gen-

erator clock is produced by multiplying up from the 10 MHz rubidium reference, and a further  $\times 2$  stage provides the 200 MHz second local oscillator. Multiplication gives signal sources with much lower phase noise than obtained with phase-locked loops. PN sequence lengths of 255, 511, 1023, 2047 can be selected with a front panel switch, and the PN chip rate clock can also be switched to 100, 50, 25, 12.5 or 6.25 MHz. The correlation filter cutoffs can be altered to 15 kHz, 3 kHz, 1.5 kHz, 750 Hz, or 187 Hz using a front panel switch.

### 3. 4.1 Weight

TABLE 3.2. Channel sounder weights

Receiver	Receiver, batteries, pack-frame, tray	20 kgm
	<i>Daqbook100</i> ® A-D converter unit	2.2 kgm
	Notebook computer	3 kgm
	<i>ScopeMeter</i> ®	1.8 kgm
	<b>TOTAL</b>	<b>27 kgm</b>
Transmitter	19" rack unit case	17 kgm
	attenuator, wattmeter	2 kgm
	auto battery (wet lead-acid)	16 kgm
	7AH SLA battery	2.5 kgm
	<b>TOTAL</b>	<b>37.5 kgm</b>

Weights of the transmitter antenna mast, and cables, have not been included in the above table. Moving the transmitter equipment from a vehicle to the site where it is to be operated takes one person three or four trips. With a total weight of 27 kgm, the backpack receiver does not go unnoticed, but is tolerable to carry for the battery operating time of about two hours. By building the receiver in a less modular way and sacrificing some flexibility, size and weight could be reduced considerably in a future model. The A-D function of the *DaqBook100*® unit has now been replaced by a tiny low power device which plugs into the PCMCIA port of the notebook, and the *ScopeMeter*® could be replaced by a receiver overload indicator, making a backpack unit of approximately half the present weight feasible.

### 3. 4.2 Power Consumption

Apart from the transmitter power amplifier, the rubidium oscillators are the largest power consumers, each requiring 1.7A at 24V during oven warm-up, and approximately 0.8A during normal operation. Warm-up to atomic locked operation takes 5 to 10 minutes, depending on ambient temperature. Initially only the rubidium oscillators are switched on, until the “rubidium-lock” LED lights, then the rest of the electronics may be switched on. Using 7AH SLA batteries and a large capacity (45AH) battery for the transmitter Battery ‘A’ which mainly supplies the power amplifier, gives an operating time of 3 to 4 hours. The wattmeter, the notebook computer and the *ScopeMeter*® have their own batteries. Operating time of the computer

battery is only one and a half to two hours, so a spare battery is carried if the measurement session is expected to be longer.

TABLE 3.3. Power consumption

		12V Battery 'A' current (A)	12V Battery 'B' current (A)	Total Power (watts)
Receiver	warm-up rubidium oscillator only	1.7	1.7	41
	after warm-up without <i>DaqBook100</i>	1.5	1.4	35
	after warm-up with <i>DaqBook100</i> on	1.8	1.7	42
Transmitter	warm-up rubidium oscillator only	1.7	1.7	41
	after warm-up, everything except power amplifier	2.2	1.3	42
	after warm-up, everything including power amplifier	8.1	1.3	113
NOTE: Battery 'A' is the one closer to ground				

3. 4.3 Frequency Standards

Rubidium oscillators are used in the transmitter and the receiver to provide very stable atomic frequency standards, sufficiently stable to allow both units to stay synchronised for a useful period of time, and to allow phase to be measured if desired. The oscillators are made by the *Ball Efratom Division*, a division of *Ball Aerospace Systems Group*, Colorado USA. The model used is the *M-100* Military Rubidium Oscillator. Being a military specification model, the unit is rugged and well suited to portable field use. The specifications are given in Appendix B.

3. 4.4 Bandpass Filters

The channel sounder uses two bandpass filters with low insertion loss, one in the front end of the receiver, and the other in the transmitter ahead of the final RF power amplifier. These filters define the RF bandwidth of the measuring system.

Two sets of filters, with nominal bandwidths of 50 MHz and 200 MHz, are used for the alternative channel sounder resolutions of 40ns (chip rate 25 MHz) *outdoor mode*, or 10ns (chip rate 100 MHz) *indoor mode* respectively. The filters are fitted with SMA connectors, and are swapped manually when the channel sounder resolution is changed. Design, construction, and performance of the filters are covered in detail in Appendix B.

3. 4.4.1 Frequency Response

Frequency response plots for the filters are shown in Figure 3.26 and Figure 3.27.

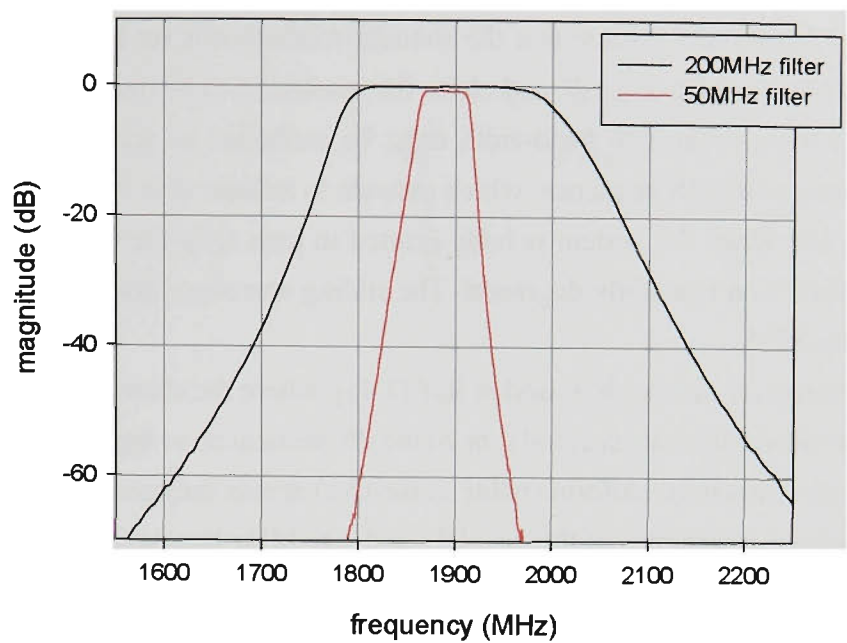


FIGURE 3.26. Measured frequency response of bandpass filters

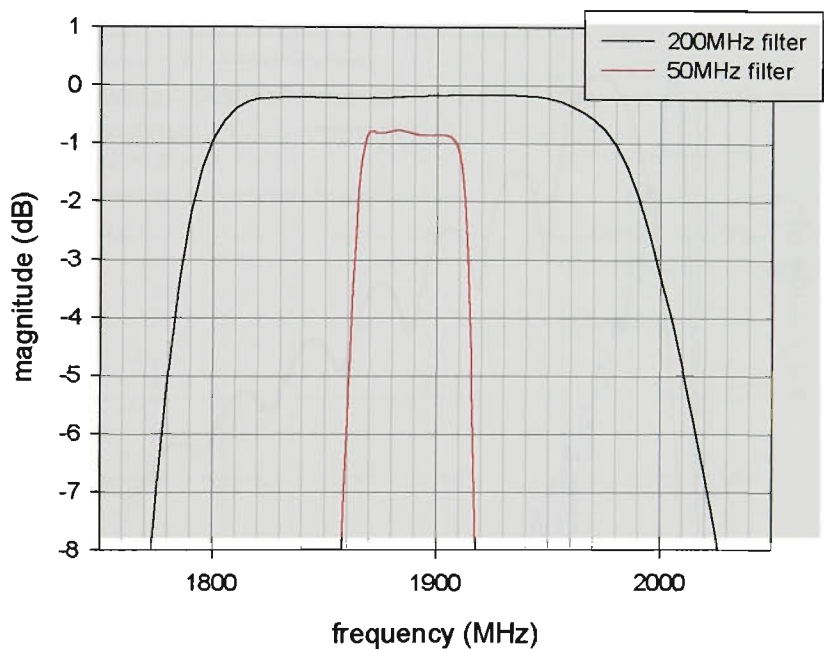


FIGURE 3.27. Passband detail - bandpass filters measured response

3. 4.4.2 Impulse Response

The system bandwidth of the sounder is primarily determined by the RF bandpass filters, and the impulse response of the bandpass filters convolves with the correlation impulse response of the PN sequence and with all other band-limited stages to give the overall impulse response of the sounder instrumentation. One bandpass filter is used at the receiver input, and a nominally identical filter is used in the transmitter at the input to the final RF power amplifier, so effectively the two filters are in cascade. Other band-limited stages, such as the receiver IF,

transmitter RF power amplifier, and the antennas, normally will all have wider bandwidths than the filters.

Many researchers assume that the sounder resolution is set by the width of the ideal triangular PN autocorrelation peak, and claim the resolution to be the inverse of the chip rate. For this to be true, the system bandwidth must be sufficient to accommodate the full  $\frac{\sin x}{x}$  shaped spectrum of the PN sequence, which extends to infinity (see Figures A.29 and A.30 in *Appendix A*). But when the system is band limited to pass only the main lobe of the PN sequence, the resolution is slightly degraded. The sliding correlator also worsens the time resolution {Section 3.2.5}.

An alternative approach is used in Ref.[3.45], where the channel sounder bandwidth is less than the width of the main spectral lobe of the PN sequence, so the PN signal spectral power density is approximately uniform (white noise-like) across the operating bandwidth.

The impulse response of the 50 MHz and 200 MHz bandwidth filters has been measured using an *HP8510C* vector network analyser, frequency sweeping over a 1000MHz span from 1400MHz to 2400MHz, then applying an inverse Fourier transform to give the time response with a resolution of approximately 1 nanosecond. The measured impulse response for both filters, normalised to 0dB, is shown in Figure 3.28.

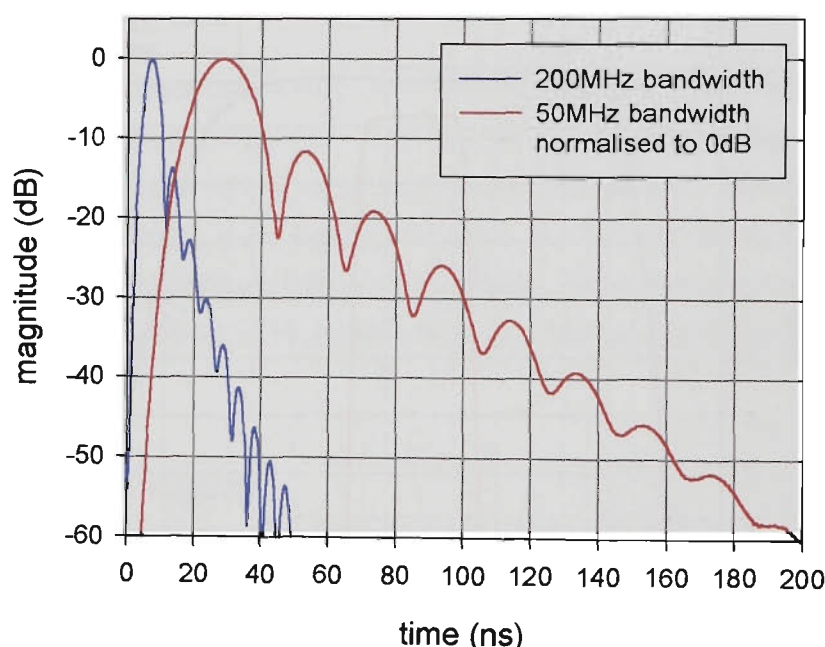


**FIGURE 3.28. Measured impulse response of single bandpass filters**

By convolving the time response of two filters and the PN autocorrelation function, a best-case version of the channel sounder impulse response is obtained. Using 50 MHz filters, the result of this procedure is shown in Figure 3.29, and from this plot, values for the time width of the *channel sounder* resolution at -3 dB, -6 dB, -10 dB and -20 dB have been obtained and compared in Table 3.4 with values measured during a back-to-back test of the sounder {shown in Figure 3.41}.

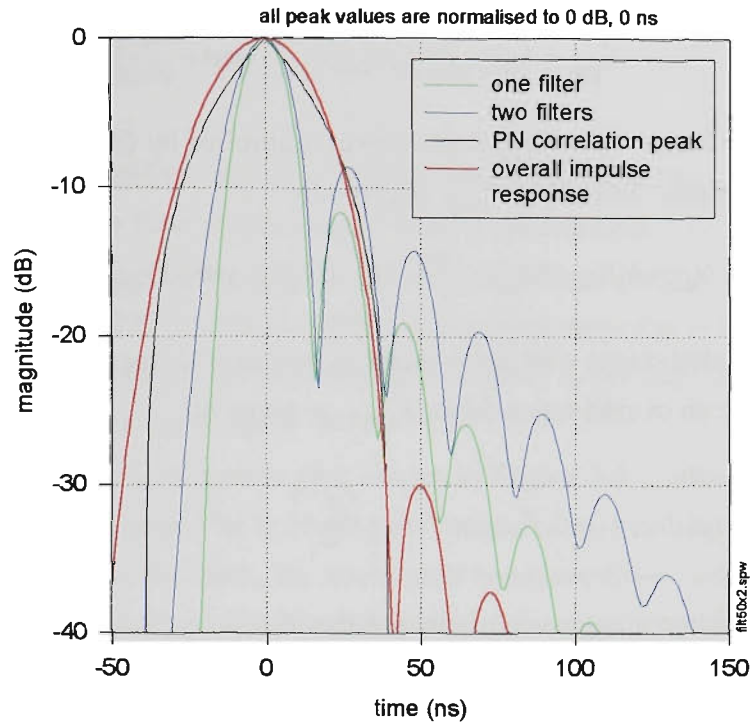


**FIGURE 3.29.** Best-case channel sounder impulse response based on two cascaded 50 MHz filters convolved with the PN autocorrelation function

**TABLE 3.4.** Measured channel sounder impulse response in outdoor mode compared with best-case values

Power (dB)	Measured time width (ns)	Two bandpass filters convolved with PN autocorrelation pulse (ns)
-3	35	32
-6	48	44
-10	63	55
-20	88	74

3. 4.5 Receiver Signal and Noise Power Budget

Receiver front-end bandwidth, throughout the RF and IF sections, is 50 MHz in *outdoor mode*, and 200 MHz in *indoor mode*. The despreading action of the sliding correlator and filter introduces considerable processing gain. Both modes use the same 3 kHz filter, giving a processing gain, equal to the bandwidth reduction factor, of 42 dB in *outdoor mode*, and 48 dB for *indoor mode*.

Thermal noise power at temperature  $T_{abs}$  and noise bandwidth  $BW_{Hz}$  is given by

$$N_{thermal} = k_B T_{abs} BW_{Hz} \text{ watts}$$

(EQ 3.3)

where  $k_B = 1.38\text{E-}23$  is Boltzman’s constant.



For an amplifier with gain  $G_{amp}$  and noise factor  $F$ , the output noise is given by

$$N_{out} = k_B T_{abs} BW_{Hz} G_{amp} F \quad \text{watts} \quad (\text{EQ 3.4})$$

$N_{out}$  is made up of the input noise power multiplied by the amplifier power gain, plus the amplifier self-noise. Self noise  $N_{self}$  is given by

$$N_{self} = N_{out} - k_B T_{abs} BW_{Hz} G_{amp} = (F - 1) k_B T_{abs} BW_{Hz} G_{amp} \quad \text{watts} \quad (\text{EQ 3.5})$$

Two cascaded stages with noise factor  $F_1$  and gain  $G_1$  for the first stage, and  $F_2$  for the second stage, have an overall noise factor  $F_{overall}$  given by:

$$F_{overall} = F_1 + \frac{F_2 - 1}{G_1} \quad (\text{EQ 3.6})$$

This well known expression indicates that the noise factor of the second stage is not very important provided the gain of the first stage is moderately high. However if the first stage is lossy or attenuating (such as a filter), it has self noise the same as a resistor but attenuates the input signal, making the noise factor the inverse of the gain. Overall noise factor is then the product of  $F_1$  and  $F_2$ , or the sum of the noise figures in decibels (see also EQ.B.1, Appendix B). Losses in the first stage of a system degrade the noise factor by the amount of the loss, but later in the system, after some signal amplification, lossy blocks have an insignificant effect on overall noise figure. Mixers (ring diode type) and splitters matched to  $50\Omega$  add thermal self noise equal to a  $50\Omega$  resistor, and attenuate input noise and input signal, but if preceded by substantial amplification, such devices have a negligible impact on system signal-to-noise ratio.

In the receiver the front-end bandwidth is large (50 MHz in *outdoor mode*), leading to high thermal noise levels. After correlation, the bandwidth is collapsed to 3 kHz, and the processing gain reduces noise correspondingly. In the signal and noise power plot shown in Figure 3.29, noise calculations use the final 3 kHz bandwidth throughout the whole system.

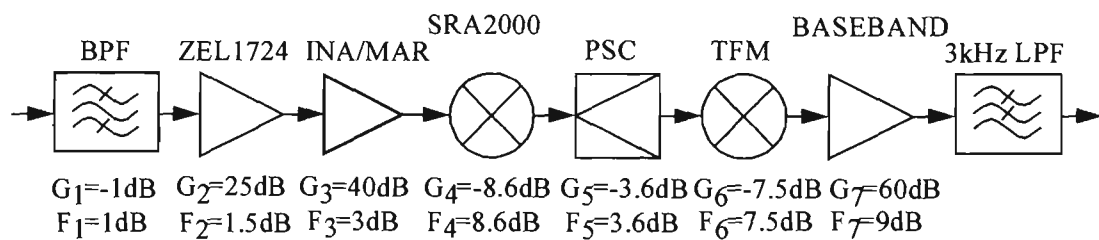


FIGURE 3.30. Receiver noise model

The overall noise figure  $F_{overall}$  for the receiver noise model shown in Figure 3.30 is given by:

$$F_{overall} = F_1 + \frac{F_2 - 1}{G_1} + \frac{F_3 - 1}{G_1 G_2} + \frac{F_4 - 1}{G_1 G_2 G_3} + \frac{F_5 - 1}{G_1 G_2 G_3 G_4} + \frac{F_6 - 1}{G_1 G_2 G_3 G_4 G_5} + \frac{F_7 - 1}{G_1 G_2 G_3 G_4 G_5 G_6} \quad (\text{EQ 3.7})$$

substituting values gives:

$$F_{overall} = 1.259 + 0.519 + 3.96 \times 10^{-3} + 2.60 \times 10^{-6} + 3.90 \times 10^{-6} + 3.20 \times 10^{-5} + 2.70 \times 10^{-4} = 2.510 \text{ dB}$$

The baseband amplifier consists of a low noise NE5534 opamp giving 60 dB gain, followed by unity gain active filter stages using a TL074 quad opamp. The NE5534 is specified for an equivalent input noise voltage of  $3.5 \text{ nV}/\sqrt{\text{Hz}}$ . The input resistance is  $50\Omega$ , producing a thermal noise voltage at  $290^\circ\text{K}$  of  $24.5 \text{ nV}$ . Equivalent input noise due to the amplifier is  $191.7 \text{ nV}$ , giving a total noise voltage referred to the input of  $193.3 \text{ nV}$ . Hence the noise figure for the NE5534 is  $193.3/24.5 = 7.89$  or 9 dB.

In the noise and signal power plot shown in Figure 3.31, noise power is followed through from the receiver input. The  $P_1$  (1 dB gain compression) overload level is also plotted, using data sheet values. At the input, the interdigital bandpass filter will handle high power levels, but has been assigned a nominal  $P_1=30 \text{ dBm}$ . At the receiver output, the baseband amplifier and active filter is matched to  $50\Omega$  at the input, but has a low impedance output interfaced to a high impedance data acquisition system, rather than a  $50\Omega$  load. Here the overload level is determined by operational amplifier voltage clipping levels, but we adopt the artifact that the output is at  $50\Omega$  for the calculation of dBm power levels.

Figure 3.31 shows the effective maximum signal-to-noise ratio at all stages through the receiver, and allows any dynamic range bottlenecks to be spotted. Working back from the output, which happens to be the limiting point for dynamic range, allows the maximum signal input of  $-71 \text{ dBm}$  to be deduced. This input signal power is the same whether it is considered to be spread over 3 kHz or 50 MHz.

The analysis ignores noise contributed from local oscillator signal sources, resulting in an optimistic or “best-case” picture. It shows a maximum output signal-to-noise ratio of 65dB, indicating that dynamic range is more likely to be dominated by sliding correlation noise (see Section 3.2.8). The corresponding maximum input signal-to-noise ratio is 68.1 dB, agreeing with the overall noise figure, referred to the input, of 2.5 dB calculated in EQ.3.7.

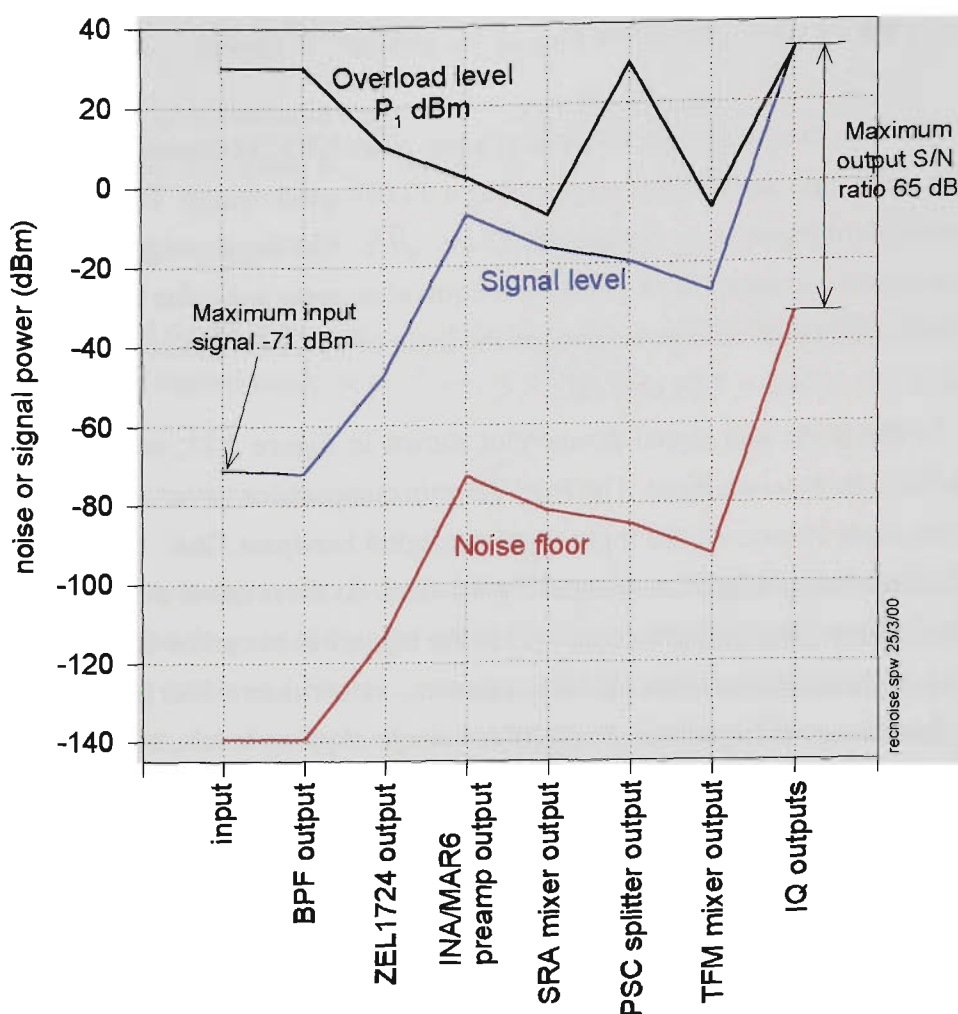


FIGURE 3.31. Receiver noise floor and signal overload levels

## 3.5 Channel Sounder Parameters

### 3.5.1 Free-running

The majority of soundings used for this thesis have been done with the PN sequences free-running, that is, with no initial synchronisation. Single, or 'instantaneous' soundings have been performed with the receiver stationary. Under these conditions, the position of the first correlation peak is not known. If data collection starts at a random time, to be certain of recording a complete impulse response, data must be gathered for twice the length of the time-scaled PN sequence.

using:

PN length  $N$   
time-scaling factor  $k$   
transmitter chip rate  $f_{PNt}$  MHz  
receiver chip rate  $f_{PNr}$  MHz  
receiver chip period  $t_{chip}$  ns  
alias range  $R_{alias}$  kilometre  
maximum excess delay  $\tau_{max}$  microseconds  
correlation filter cutoff  $f_{-3dB}$  kHz  
measurement time unsynchronised  $t_{measure}$  milliseconds  
times two sample rate/channel  $S_2$  ksamples/second

$R_{alias}$  is the maximum unambiguous range. Echoes returning from beyond that range will alias back into the preceding PN sequence period. Parameters are related as follows:

$$t_{chip} = \frac{1000}{f_{PNr}} \quad (\text{EQ 3.8})$$

$$R_{alias} = 150 \times 10^{-6} \times N \times t_{chip} \quad (\text{EQ 3.9})$$

$$\tau_{max} = \frac{N t_{chip}}{1000} \quad (\text{EQ 3.10})$$

$$f_{PNt} = f_{PNr} \left( 1 + \frac{1}{k} \right) \quad (\text{EQ 3.11})$$

$$f_{-3dB} = \frac{10^6}{2 t_{chip} k} \quad (\text{EQ 3.12})$$

$$t_{measure} = 2 \times 10^6 \times N \times t_{chip} \quad (\text{EQ 3.13})$$

$$S_2 = \frac{2 \times 10^3 \times f_{PNr}}{k} \quad (\text{EQ 3.14})$$

Typical parameters used in the indoor and outdoor modes are shown below in bold. Actual filter cutoff used is 3 kHz, but this is not critical as the Bessel characteristic rolls off slowly.

TABLE 3.5. Parameters using free-running PN sequences

Parameter	Indoor Mode	Outdoor Mode
PN length $N$ (input variable)	<b>1023</b>	<b>1023</b>
chip rate (MHz) (input variable)	<b>100</b>	<b>25</b>
time scaling ( $k$ ) (input variable)	<b>20000</b>	<b>5000</b>
No. samples/channel (input variable)	<b>12000</b>	<b>12000</b>
chip period (ns)	<b>10</b>	<b>40</b>
alias range (km)	<b>1.5345</b>	<b>6.138</b>
max. excess delay ( $\mu$ s)	<b>10.23</b>	<b>40.92</b>
transmitter PN clock (MHz)	<b>100.005</b>	<b>25.005</b>
filter cutoff (kHz)	2.5	2.5
measurement time (ms)	<b>409.2</b>	<b>409.2</b>
x2 sample rate/Ch (ks/s)	10	10
x4 sample rate/Ch (ks/s)	20	<b>20</b>
x5 sample rate/Ch (ks/s)	<b>25</b>	25
scaled sample time x4 rate (ns/samp)	2.5	<b>10</b>
scaled sample time x5 rate (ns/samp)	<b>2</b>	8
excess delay at x4 rate ( $\mu$ s)	30.0	<b>120.0</b>
excess delay at x5 rate ( $\mu$ s)	<b>24.0</b>	96.0

3. 5.2 Continuous or Coherent

Operation in the way described in Section 3.5.1 is intended for stationary measurements only. In order to measure Doppler shift, the change in phase of each ray in the impulse response as the receiver moves must be measured. Two modes are possible:

- (i) continuous data collection, where the PN sequences may be initially synchronised or unsynchronised.
- (ii) synchronising and windowing the PN sequences, and triggering measurements synchronously with the start of each window.

The maximum Doppler frequency which can be measured is half the reciprocal of the measurement time, from sampling theory. For continuous measurements, the measurement time is  $T_{measure}$  milliseconds where:

$$T_{measure} = \frac{kN t_{chip}}{10^6}$$

(EQ 3.15)

The maximum Doppler frequency  $f_D$  Hz is:

$$f_D = \frac{1000}{2T_{measure}} = \frac{500}{T_{measure}} \quad (\text{EQ 3.16})$$

Maximum channel sounder velocity  $v$  for a carrier frequency  $f_c$  Hz with velocity of light  $c$  metre/second is given by:

$$v = \frac{cf_D}{f_c} \text{ metre/second} = \frac{3.6cf_D}{f_c} \text{ kilometre/hour} \quad (\text{EQ 3.17})$$

Table 3.6 shows some typical parameters for continuous measurement operation. Using the same parameters as used in Section 3.5.1 for stationary measurements (columns 2 and 3 of Table 3.5) demonstrates the main drawback of the sliding correlator channel sounder. The maximum Doppler frequency is low, with associated very slow maximum travel speeds for the sounder receiver. This is a direct consequence of the long measurement time and the high carrier frequency (the maximum velocity at 1890 MHz is half that at 945 MHz).

However, the situation can be improved by using shorter PN sequences, and faster sliding rates. See columns 3 and 5 in Table 3.6. Maximum speeds, in terms of vehicle measurements, have now moved into a feasible range. The penalty for these changes is a reduced alias range  $R_{alias}$ , and increased correlation noise (smaller  $k$ ) and slightly increased correlation distortion. Speeding up measurement time also places more demand on the data acquisition system speed. The *VUT sounder* is restricted to a maximum sampling rate per channel of about 30 ksample/sec. with the *Daqbook100*® unit, and 100 ksamples/second with the more recent *Data Translation DT7102*® PCMCIA card.

TABLE 3.6. Channel sounder parameters - continuous measurement

Parameters		Fast Doppler		Fast Doppler
PN length $N$ (input variable)	1023	511	1023	511
chip rate (MHz) (input variable)	100	100	25	25
time scaling ( $k$ ) (input variable)	20000	2000	5000	1000
chip period (ns)	10	10	40	40
alias range (km)	1.5345	0.7665	6.138	3.066
max. excess delay ( $\mu$ s)	10.23	5.11	40.92	20.44
transmitter PN clock (MHz)	100.005	100.05	25.005	25.025
filter cutoff (kHz)	2.5	25	2.5	12.5
measurement time (ms)	204.6	10.22	409.2	20.44
x2 sample rate/Ch (ks/s)	10	100	10	50
x4 sample rate/Ch (ks/s)	20	200	20	100
x5 sample rate/Ch (ks/s)	25	250	25	125
scaled sample time x4 rate (ns/samp)	2.5	2.5	10	10
scaled sample time x5 rate (ns/samp)	2	2	8	8
maximum Doppler frequency (Hz)	2.4	48.9	1.2	24.5
maximum velocity (metre/second)	0.39	7.77	0.19	3.88
maximum velocity (km/hour)	1.40	27.96	0.70	13.98

3. 5.3 Windowed

In windowed operation, the PN sequences are reset before the sliding correlator has moved through the entire sequence length. Reset occurs after a predetermined number of frequency standard clock pulses. Initially the PN generators in the sounder transmitter and receiver are started simultaneously using a synch cable, which is then disconnected. The high stability of the frequency standards is relied upon to keep the PN resets synchronized. This is discussed in more detail in Section 3.6.

Table 3.7 shows one possible set of operating parameters.

TABLE 3.7. Channel sounder parameters - windowed PN sequences

Parameter	Value
PN length $N$	2047
chip rate (MHz)	100
time scaling ( $k$ )	20000
PN reset divide ratio	524288
distance increment (mm) (input variable)	108
chip period (ns)	10
alias range (km)	3.0705
max. excess range (metre)	393.2
max. excess delay (ns)	2621
transmitter PN clock (MHz)	100.005
reset time (ms)	52.4288
filter cutoff (kHz)	3
x4 sample rate/Ch (ks/s)	20
max. Doppler frequency (Hz)	9.54
max. speed (metre/second)	1.51
max. speed (km/hour)	5.4

Using these parameters, 800 samples/sec/channel are collected for each power delay profile, giving a maximum measurable excess delay of 2000 ns. The sample period is 50  $\mu$ s, equivalent to 2.5 ns per sample, allowing for the time scaling effect. The entire 800 samples/channel takes 40 ms to collect. Assuming the moving receiver is travelling at 0.25 metre/sec (for example using a trolley at slow walking speed), during the 10 ns resolution period of one ray, equivalent to 200  $\mu$ s after time scaling, the receiver moves 0.05 mm. A typical indoor power delay profile is contained within 150 ns, equivalent to 60 samples, or 3 ms of measurement time. During 3 ms, the receiver trolley moves 0.75 mm, or 0.00473 wavelengths. Even over the complete 800 samples, receiver travel is only 10 mm.(0.063 wavelengths) . Hence it is reasonable to treat the receiver as quasi-stationary.

### 3. 6 Synchronizing PN sequences

The transmitter and receiver each contain a *PN Preset Counter*, clocked from the 10 MHz rubidium system clocks. The count period can be set using DIP switches, over a range from 25.6  $\mu$ s to 1.678 seconds, in steps of 25.6  $\mu$ s. At the conclusion of the count period, a 50ns wide pulse, coincident with the system clock low, is used to reset the PN generator to the “all ones” state, and then restart the PN sequence.

If the transmitter and receiver *PN Preset Counters* are connected with a cable, a switch



on the transmitter unit may be used to clear and restart both counters at the same instant. Although the rubidium clocks are close in frequency, they may differ in phase by (almost) up to  $\pm 180^\circ$ , which results in a maximum difference in counter restart times of  $\pm 50$  ns. This time difference introduces a maximum uncertainty of 100 ns or 30 metres into the absolute measurement of the direct path between transmitter and receiver, further degraded by the channel sounder resolution (3 or 4 metres in *indoor mode*), and any timing jitter in the system. After the counters are synchronized, the uncertainty in the direct path distance will gradually increase with time because of relative drift between the two rubidium oscillators. For example, if the frequency difference is a constant 1 in  $10^{11}$  the error will increase by 36 ns/hour, or 10.8 metres/hour. In practice the drift will be non-constant, with a random component which should help, because the counters will be drifting closer together at times. Experience with the *sounder* operating for periods of over 2 hours has not shown any noticeable increase in drift.

The absolute measurement of the direct path distance is of secondary interest. Delay spread measurements are not affected by synchronisation drifts, provided the windowed portions of the PN sequences still substantially overlap.

Resetting the PN generators simultaneously means that at zero excess delay, the correlation peak will occur right at the start of the correlation window. However, the possible  $\pm 50$  ns difference in 10 MHz rubidium clock edges means that the correlation peak could occur prior to the start of the window. Even if the peak is initially just inside the window, the clock drift discussed above may move the peak out of the window. To reduce this problem, a delay circuit starts the transmitter PN generator approximately 70 ns after the receiver generator, at the initial synchronization. In addition, a switch debounce circuit guards against erratic behavior at initial synchronization.

At the commencement of a measurement session, after the rubidium oscillators have warmed up and phase-locked, the receiver is moved adjacent to the transmitter, and a single twisted pair cable is plugged between the transmitter and receiver. The synch press button (located on the transmitter) is momentarily pressed and released, then the twisted pair cable is removed.

### 3.6.1 Wheel Trigger

A 12 inch bicycle wheel coupled to an optical encoder giving 146 pulses/revolution, is mounted on a hinged arm, attached to the receiver trolley. Associated electronics results in a square wave output, with a period equivalent to 108 mm. of wheel travel. This square wave sets the D input of a flip-flop, which is clocked by PN generator reset pulses. The flip-flop output triggers a monostable, and the leading edge of the mono output pulse triggers the data acquisition card, to collect data corresponding to one power delay profile. Hence data acquisition is initiated at the first PN reset pulse to occur after the wheel reaches a distance increment. PN reset pulses occur every 52.4 ms, so if the trolley is travelling at 0.25 metre/sec, the maximum distance error before data acquisition begins is  $250 \times 52.4 \times 10^{-3} = 13$  mm or 0.08 wavelengths.



FIGURE 3.32. Receiver on trolley with distance triggering wheel

3. 7 Back-to-back Tests

Back-to-back tests are used to verify the correct operation of the *channel sounder*, and to measure linearity and dynamic range. Straight back-to-back tests are performed with a direct cable connection via a matched load and attenuators, from the transmitter to the receiver. An artificial channel can also be inserted. The artificial channel provides three paths with 50 ns delay between each path, and different losses in each path. The expected power delay profile consists of three peaks, separated by 50 ns. Relative to the first peak, the second peak is -4.5dB, and the third peak is -8.5dB. Time domain response of the artificial channel was verified by taking the inverse Fourier transform of a swept frequency measurement from 1400 MHz to 2400 MHz, performed on an HP8510C vector network analyser. The result is shown in Figure 3.33. Spurious responses are caused by secondary paths and mismatch reflections within the artificial channel network.

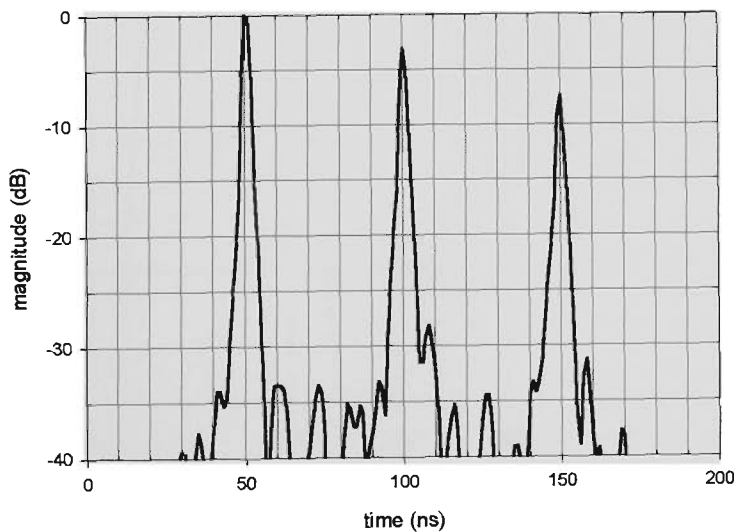
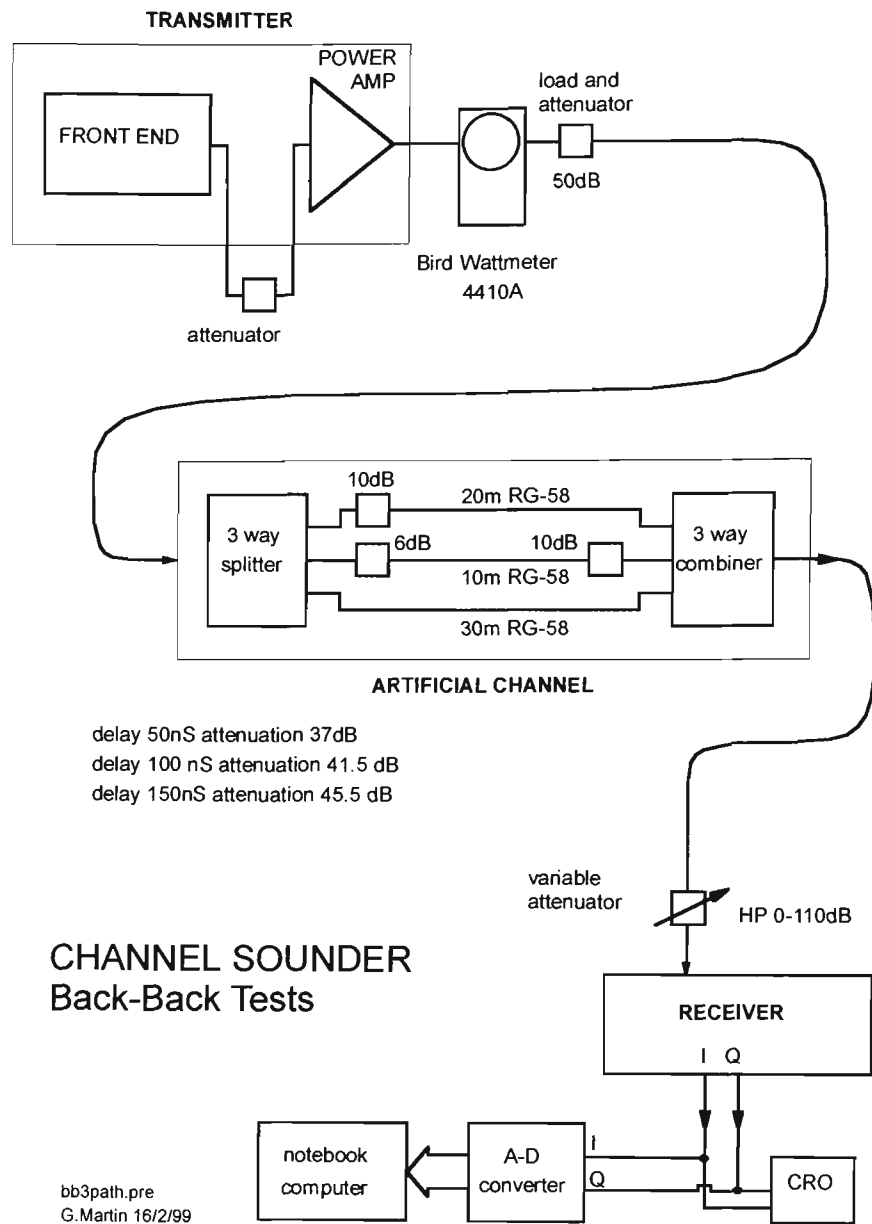


FIGURE 3.33. Artificial channel time response (using HP8510C)



**FIGURE 3.34. Back-to-back testing via an artificial channel**

### 3. 7.1 Back-to-back Tests with the Artificial Channel

#### 3. 7.1.1 Indoor Mode

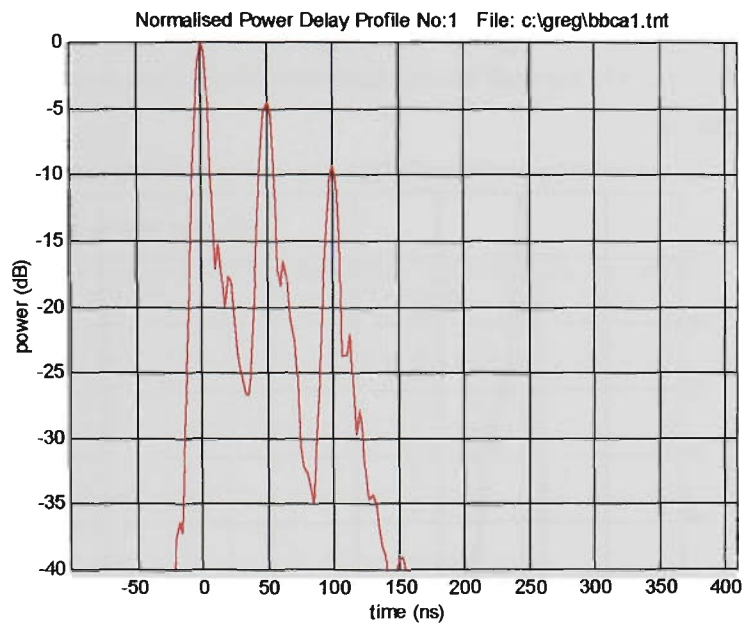


**FIGURE 3.35.** Channel sounder response with artificial channel, 100MHz chip rate,  $N=1023$ ,  $k=20,000$ , receiver input = -73dBm

Figure 3.35 shows a measured impulse response via the artificial channel. Peaks are 50 ns apart, and the relative amplitudes of the second and third peaks are -4.4 dB and -9.2 dB respectively. The width of the first peak is 12 ns at -6 dB, and 15 ns at -10 dB. Sharp spurs on the curve result from unknown spurious effects. The first spur is at -15dB, 13 ns, and the second is at -18dB, 19 ns. The spur on the second peak is at -16dB, and 13 ns (relative to the peak). In Ref[3.104] similar spurs are attributed to cable reflections.

#### 3. 7.1.2 Outdoor Mode

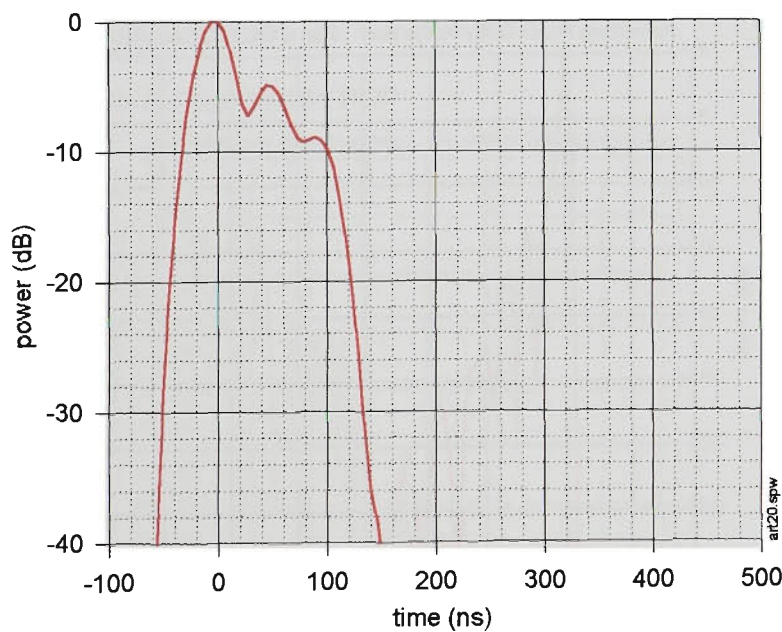


**FIGURE 3.36.** Channel sounder response with artificial channel, 25MHz chip rate,  $N=1023$ ,  $k=5,000$ , receiver input = -80dBm

In *outdoor mode* the nominal channel sounder resolution is 40 ns. Figure 3.36 shows that the three paths spaced 50 ns apart are clearly resolved, with the correct magnitudes.

### 3. 7.2 Back-to-back Straight Through Tests

#### 3. 7.2.1 Indoor Mode

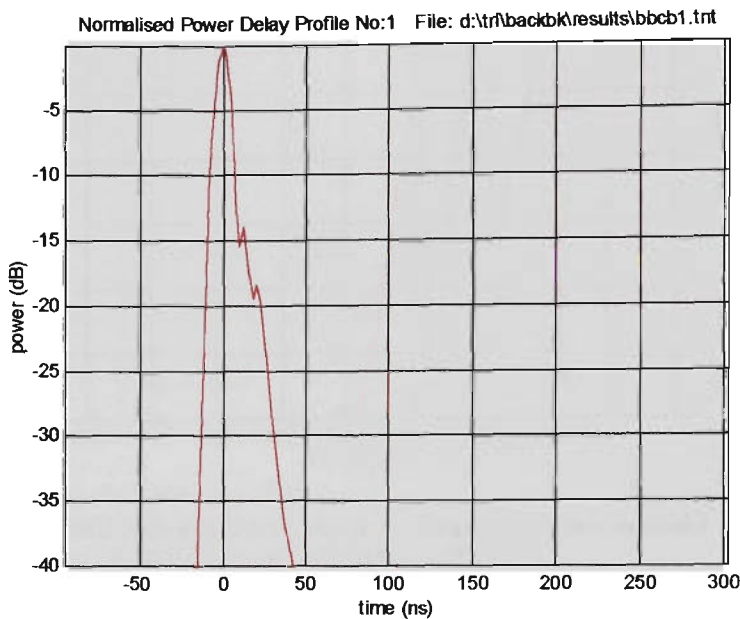


**FIGURE 3.37.** Impulse response of the *Channel Sounder*, 100MHz chip rate,  $N=1023$ ,  $k=20,000$  receiver input = -73dBm

Figure 3.37 shows the impulse response obtained with a back-to-back connection via a cable and a 100 dB attenuator. The receiver output magnitude is 1.94 volts (about 8 dB below the receiver overload level).

#### 3. 7.2.2 Over a 1 Metre Air Path

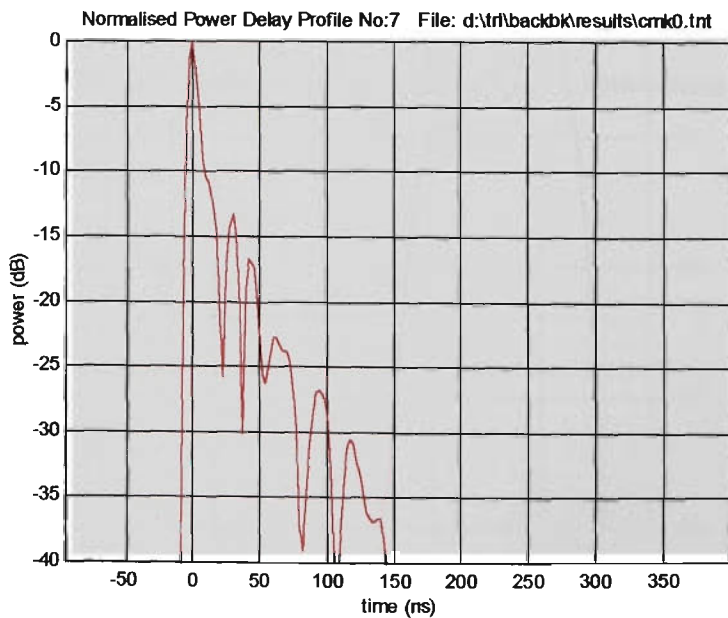


**FIGURE 3.38.** Response over a 1 metre air path, indoors

In order to include the effects of the antennas, channel measurements were made over an indoor air path of length 1 metre. The LOS ray dominates, but other paths with short excess delays are evident in the PDP shown in Figure 3.38. The time width of the LOS correlation peak is 12 ns at -6dB, and 15 ns at -10dB. These values are also obtained in cable connected back-to-back tests, indicating that the antennas do not degrade the time resolution of the measurement system.

3. 7.2.3 With 130 dB Attenuation

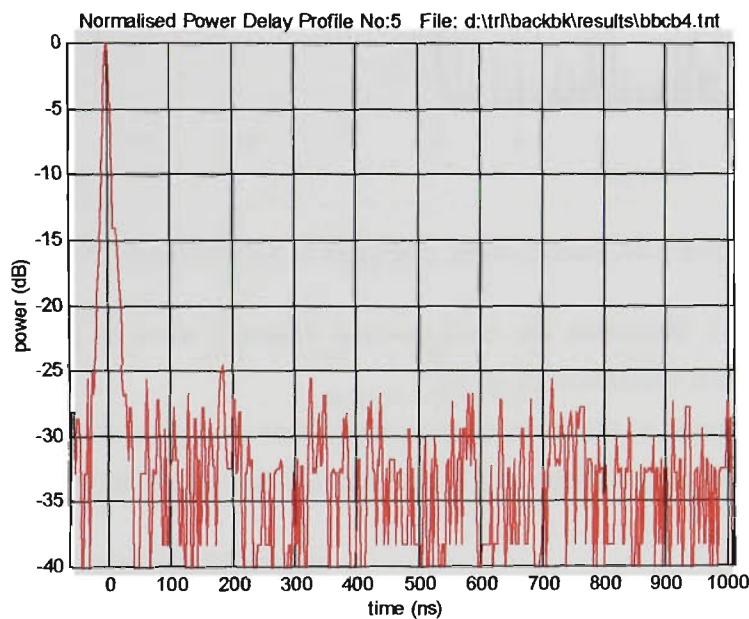


FIGURE 3.39. Impulse response via cable and 130dB attenuator

Figure 3.39 shows the response with the attenuator set to 130dB, giving a maximum receiver output of 0.06 volts. The transmitter output is 5.6 watts, hence the receiver input is -95 dBm. Output noise is dominated by thermal rather than correlation noise, with a floor about 25 dB below the peak value, or at -49 dBV, giving a dynamic range of 25 dB.

3. 7.2.4 Example of an Indoor Mode PDP

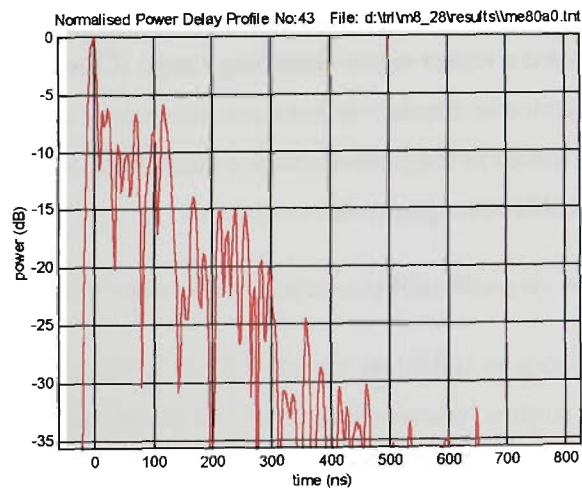
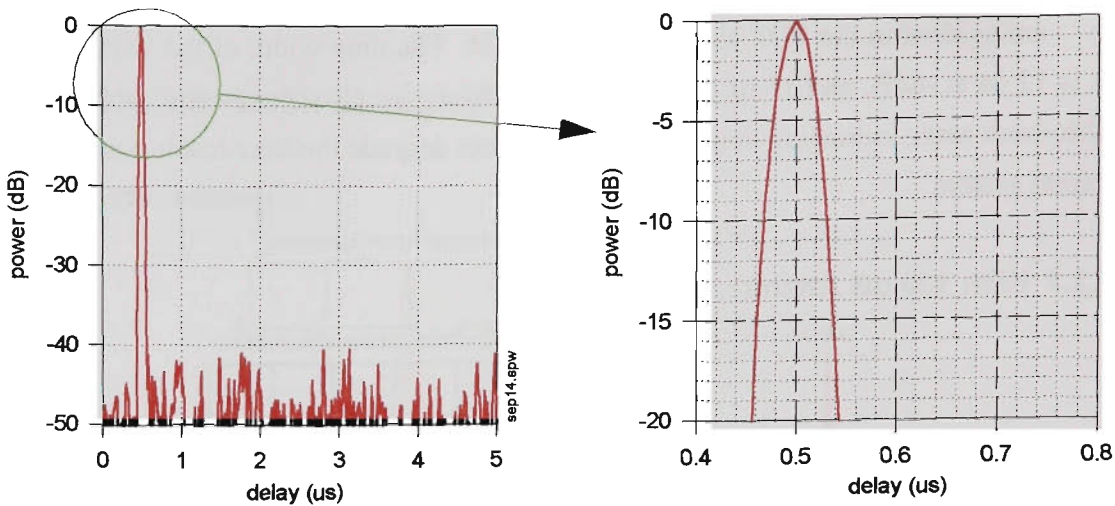


FIGURE 3.40. Example of an *indoor mode* PDP, rms delay spread 48 ns, threshold -15 dB



### 3. 7.2.5 Outdoor Mode



**FIGURE 3.41.** Back-to-back resolution in *outdoor mode*, 25 MHz chip rate

Figure 3.41 illustrates the back-to-back channel sounder performance in *outdoor mode*, with a nominal resolution of 40 ns.

Note that none of the spurs or spurious effects evident in the indoor mode occur, and the impulse response is very clean and symmetrical. Time width of the correlation peak is given in Table 3.4.

### 3. 7.2.6 Calibration - Outdoor Mode

Figure 3.42 shows receiver output voltage (dBV, volts referenced to 1 volt) as a function of receiver input power in dBm, and demonstrates the linearity of the channel sounder, which is  $\leq \pm 1$  dB down to -115 dBm. Receiver output is calculated as  $20\log_{10}\sqrt{I^2+Q^2}$  and is plotted from a number of back-to-back measurements with different attenuator settings.

The *outdoor mode* curve uses voltage values measured from an oscilloscope, so the maximum output possible is 13 volts/channel or 25 dBV. The *indoor mode* results are based on data collected using the D to A data acquisition unit, which overloads at 5 volts/channel, or 14 dBV if all of the signal is in one channel, or 17 dBV for equal I and Q signals. This indicates that the receiver would have a better signal handling range if the gain was reduced by approximately 10 dB. The difference in sensitivity between the *indoor* and *outdoor modes* may partly represent different cable losses in the back-to-back connection, as the tests were done at different times with different cable arrangements.

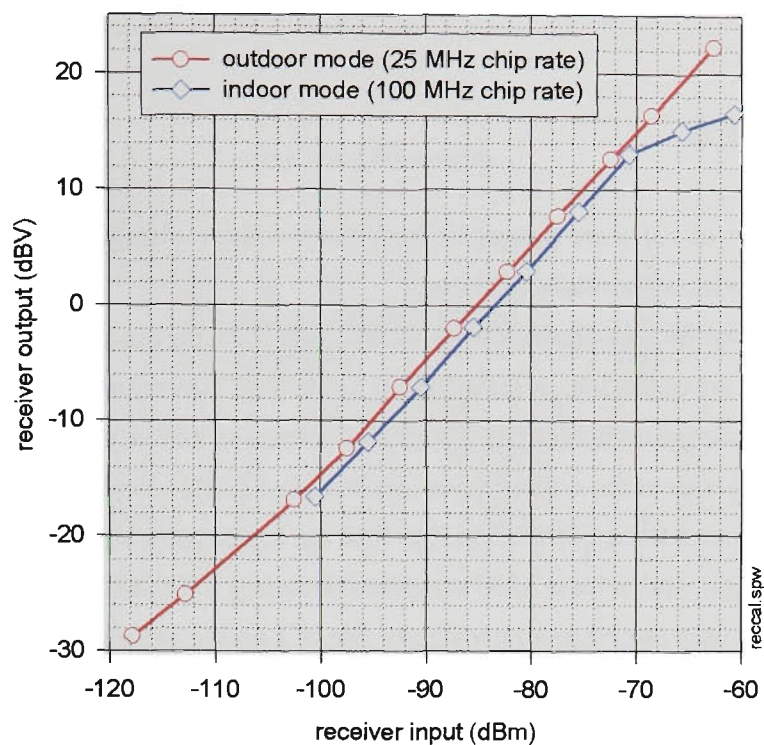


FIGURE 3.42. Back-to-back calibration for *outdoor* and *indoor* modes

3. 7.2.7 RF Power Amplifier Linearity

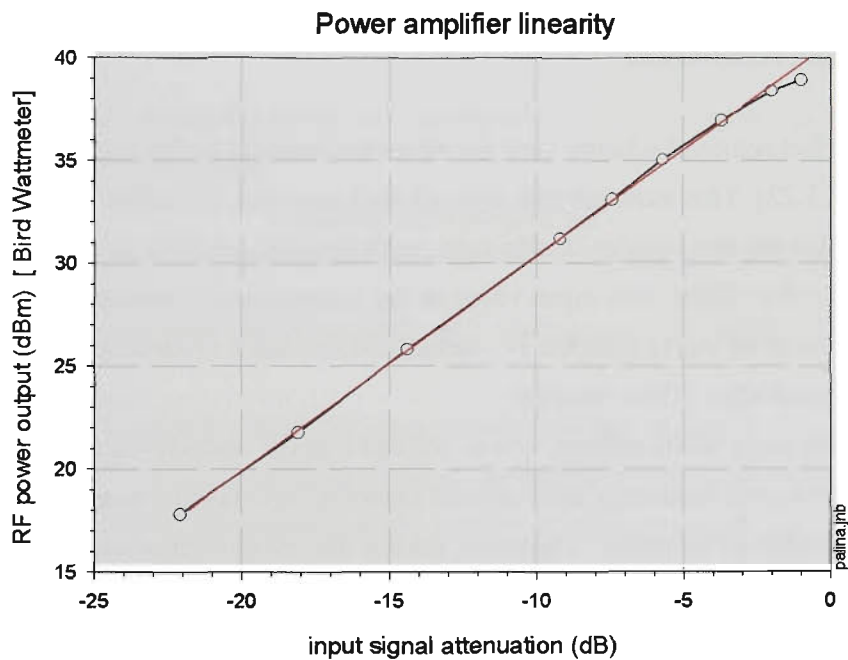


FIGURE 3.43. Measured RF power amplifier linearity with DSSS signal

Maximum power output of the RF power amplifier is specified as 40 dBm (10 watts) at the 1 dB compression point. In the *VUT channel sounder*, output power is monitored with a *Bird®* wattmeter, and the RF drive to the power amplifier is adjusted using a switched attenuator, preceding the power amplifier. To check the behavior with a wideband DSSS signal used in the channel sounder, the *Bird* power reading has been plotted against the RF power amplifier input signal level, shown in Figure 3.43. Comparing the measured curve with a straight line



(shown in red) indicates linear behavior up to an output power reading of 38 dBm, with 1 dB compression at 39 dBm output.

## 3.8 Software

A number of software programs have been written during the course of this project. Appendix D provides a summary of these.

When operating in free-running mode, for each measurement 12,000 samples per channel (I and Q) are collected, as indicated in Table 3.5. This number of samples covers more than two complete impulse responses. The data is stored as a binary file. Following the general scheme used by *Davies* at the *University of Bristol* {Ref.[3.22], Ref.[3.35]}, these files are processed (by a program called *CONVRTG2*) to find the largest power peak which has at least 499 samples preceding it, and at least 2500 samples following. This 3000 sample (per channel) section of the data is then stored to a new binary file of I and Q values, with the power peak positioned at sample 500. DC offsets are also removed from I and Q values. A further program (*DELAYG4*) calculates rms delay spreads and average delay. For plotting power delay profiles, ascii files of power can be generated, with the peak power normalised to 0 dB. Other programs identify rays and extract information such as the number of rays, and the distribution of rays as a function of excess delay. All these programs operate on batches of data files.

### 3.8.1 Offset Removal

The offset removal scheme used for all measurements in this thesis followed the method used in Ref[3.22]. This assumes that over all the I samples, the mean value is zero, and over all the Q samples the mean value is also zero, with any non-zero mean representing an offset. Hence to correct for offsets, the mean value of the I samples is subtracted from each I sample, and the mean value of the Q samples is subtracted from each Q sample. Power values for the PDP are calculated after offset removal.

At a late stage in the project, it was noticed that the underlying assumption is not true, because one strong ray extending over several samples can bias the mean I and Q values, even over a large number of samples. However, taking the mean over a section of the time delay profile where the signal is likely to consist only of random noise gives an improved estimate of the average offset, and this is a better basis for offset removal.

The new offset removal algorithm calculates I and Q means over the end 25% of the time delay data, and also excludes any sample in this range which is greater than  $\pm \frac{100}{4096}$  of full scale. The improvement is demonstrated in Figure 3.44 using data over 800 samples. Note that this exaggerates the improvement somewhat, compared with a 12,000 sample data run, where the larger number of samples will tend to dilute any bias in the means.

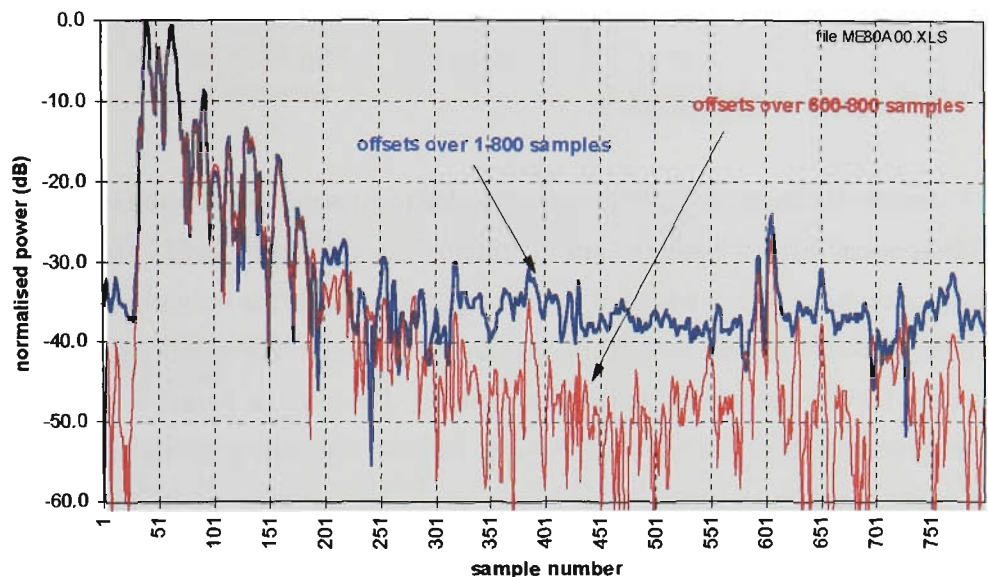


**FIGURE 3.44.** Dynamic range improvement with new offset removal scheme

Inspecting Figure 3.38 clearly shows an improvement in dynamic range of better than 5 dB. For this data each sample represents 2.5 ns. The degree of improvement with the new algorithm will depend on the particular data. All future work will use the new scheme.

### 3.9 Antennas

Two different vertically polarized antennas have been constructed for the channel sounding measurement program:

- 1. discone omnidirectional
- 2. halfwave (ground independent) omnidirectional

Measured impedance matching plots, and measured polar patterns are shown in Appendix C.

Polar patterns were measured in an anechoic chamber at the CCR, University of Bristol. Thanks are due to Dr. Geoff Hilton of the University of Bristol, for developing the excellent automated antenna measurement system, and for instruction and assistance in making the measurements.

#### 3.9.1 Discone antenna

Discone antennas provide good matching over a very wide bandwidth, and a close approximation to an ideal omnidirectional pattern. The antenna is ground-independent, and has the same gain as a halfwave dipole. Construction is not difficult, apart from the fabrication of a cone from copper sheet. The design was based on equations from Ref.[3.98], Ref.[3.99], Ref.[3.100], and Ref.[3.101]. The antenna was built on a panel-mounting N-type 50Ω connector, a convenient technique patented by T. Rappaport {Ref.[3.102]}. The only critical di-

mension is the spacing between the face of the connector and the copper disc. By empirically adjusting this, the matching can be optimised for the frequency of interest.

### 3.9.2 Halfwave J antennas

A vertical halfwave antenna, fed from a shorted quarter-wave open wire section, forms the omnidirectional ground-independent “J antenna”, described in Ref.[3.103]. The feed point along the quarter-wave line is adjusted to give a good match at the operating frequency. A balun should be used for the transition from coax to the quarter-wave matching section, but in the antennas built for this project the balun was omitted. The coaxial feeder is connected directly to the quarterwave section, using small copper clamps. Adjusting the position of the clamps alters the shunt capacitance between them and gives fine adjustment of matching. The polar pattern varies from omnidirectional by up to  $\pm 3\text{dB}$ , probably because of the unbalanced feed arrangement and external currents on the feed coaxial cable.

## 3.10 Conclusions

This chapter began with a survey of approaches to wideband channel sounding techniques with examples from the literature, and an estimate of the relative popularity of the different methods.

Based on a new simulation technique, the sliding correlator has been studied in detail, illustrating how correlation noise resulting from the small offset in chip frequencies, inherent in the sliding correlator, is the main limitation to dynamic range achievable with this method. The requirements for the correlation filter have been considered, concluding that a linear phase filter such as the Bessel alignment is required to avoid time response distortion, and a reduction in dynamic range. The correlation filter must also prevent aliasing. Typical data acquisition schemes have limited over-sampling, so an 8-pole filter is required for effective antialiasing.

The portable *VUT channel sounder* has been described, and detailed time resolution and linearity performance results based on back-to-back tests for both *indoor* and *outdoor modes*, have been presented. The effect of bandpass filters on the sounder impulse response has been considered.

Software used for processing measured data has been outlined, with a description of an improved method of software offset removal.

Antennas used with the sounder have been described.

The following chapter will show how the *VUT channel sounder* has been used to investigate indoor propagation, including an assessment of the accuracy of two different ray tracing tools, and a study of propagation between floors of a multi-storey building.

## 3.11 References

- [3.1] Donald C. Cox, "Delay Doppler Characteristics of Multipath Propagation at 910 MHz in a Suburban Mobile Radio Environment", IEEE Trans.on Antennas and Propagation, Vol.20, No.5, September 1972, pages 625-635.
- [3.2] D.C. Cox, "Time and Frequency Domain Characterizations of Multipath Propagation at 910MHz in a Suburban Mobile Radio Environment", Radio Science, Vol.7, No.12, December 1972, pages 1069-1077.
- [3.3] D.C. Cox, "Doppler Spectrum Measurements at 910 MHz Over a Suburban Mobile Radio Path", Proc. IEEE (Letters), Vol.59, June 1971, pages 1017-1018.
- [3.4] D.C. Cox, "A Measured Delay-Doppler Scattering Function for Multipath Propagation at 910 MHz in an Urban Mobile Radio Environment", Proceedings of the IEEE, April 1993, pages 479-480.
- [3.5] Donald C. Cox, "910 MHz Urban Mobile Radio Propagation: Multipath Characteristics in New York City", IEEE Trans. on Communications, Vol.21, No.11, November 1973, pages 1188-1194.
- [3.6] Donald C. Cox, "Distributions of Multipath Delay Spread and Average Excess Delay for 910-MHz Urban Mobile Radio Paths", IEEE Transactions on Antennas and Propagations, Vol.AP-23, No.2, March 1975, pages 206-213.
- [3.7] Donald C. Cox, Robert P.Leck, "Correlation Bandwidth and Delay Spread Multipath Propagation Statistics for 910 MHz Urban Mobile Radio Channels", IEEE Trans. on Communications, Vol.23, No. 11, November 1975, pages 1271-1280.
- [3.8] Daniel M.J. Devasirvatham, "Time Delay Spread and Signal Level Measurements of 850 MHz Radio Waves in Building Environments", IEEE Transactions on Antennas and Propagation, Vol.AP-34, No.11, November 1986, pages 1300-1305.
- [3.9] D.M.J. Devasirvatham, C. Banerjee, M.J. Krain, D.A. Rappaport, "Multi-frequency Radiowave Propagation Measurements in the Portable Radio Environment", IEEE International Conference on Communications, 1990, pages 1334-1340.
- [3.10] D.M.J. Devasirvatham, R.R. Murray, D.R. Wolter, "Time Delay Spread Measurements in a Wireless Local Loop Test Bed", IEEE 45th. Vehicular Technology Conference, Chicago, USA, July 1995, pages 241-246.
- [3.11] D.A. Demery, "Wideband Characterisation of UHF Mobile Radio Channels in Urban Areas", PhD thesis, University of Liverpool, January 1989.
- [3.12] J.D. Parsons, A.M.D. Turkmani and M. Khorami, "Microcellular Radio Modelling", IEE 6th. Int. Conf. on Mobile Radio and Personal Communications, December 1991, pages 182-190.
- [3.13] J.D. Parsons, D.A. Demery, A.M.D. Turkmani, "Sounding Techniques for Wideband Mobile Radio Channels: A Review", IEE Proceedings-I, Vol.138, No.5, October 1991, pages 437-446.
- [3.14] A.M.D.Turkmani, D.A.Demery & J.D.Parsons, "Measurement and Modelling of Wideband Mobile Radio Channels at 900 MHz", IEE Proceedings-I, Vol.138, No.5, October 1991, pages 447-457.
- [3.15] C. Nche, D.G. Lewis, A.M.D. Turkmani, "Wideband Characterisation of Mobile Radio Channels at 1.8 GHz", IEEE 44th. Vehicular Technology Conference, Stockholm, Sweden, June 1994, pages 1775-1779.

- 
- [3.16] L. Berggren, "Channel Sounder", Master of Science Thesis, Lund University, Sweden, 1992.
- [3.17] Peter Karlsson, Lars Olsson, "Time Dispersion Measurement System for Radio Propagation at 1800 MHz and Results from Typical Indoor Environments", Proceedings of 44th IEEE Vehicular Technology Conference, March 1994, pages 1793-1797.
- [3.18] T. Takeuchi, M.Sako, S.Yoshida, "Multipath Delay Estimation for Indoor Wireless Communication", Proc. 40th. IEEE Vehicular Technology Conference, Orlando USA, May 1990, pages 401-406.
- [3.19] Tsutomu Takeuchi, "A Wide Band Indoor Channel Sounder with High Delay Resolution", Proceedings of 44th IEEE Vehicular Technology Conference, March 1994, pages 1816-1819.
- [3.20] R. Davies, M. Bensebti, M.A. Beach, J.P. McGeehan, D.C. Rickard, "Channel Sound Measurements at 60 GHz Using Wideband Techniques with Particular Reference to Microcellular Personal Communications", IEE 5th Int.Conf.on Mobile Radio & Personal Comms., December 1988.
- [3.22] R.L. Davies, "The Measurement and Application of Multipath Propagation in the Microwave Frequencies Around 1.8 GHz", PhD Thesis, University of Bristol, UK., July 1992.
- [3.24] S.W. Wales & D.C. Rickard, "Wideband Propagation Measurements of Short Range Millimetric Radio Channels", Electronics and Communication Engineering Journal, August 1993, pages 249-254.
- [3.25] Elvinao S. Sousa, Vladan M. Jovanovic, Christian Daigneault, "Delay Spread Measurements for the Digital Cellular Channel in Toronto", IEEE Transactions on Vehicular Technology, Vol.43, No.4, November 1994, pages 837-847.
- [3.26] A.A. Arowojolu, A.M.D. Turkmani, J.D. Parsons, "Time Dispersion Measurements in Urban Microcellular Environments", IEEE 44th. Vehicular Technology Conference, Stockholm, Sweden, June 1994, pages 150-154.
- [3.27] S. Mohamed, G. Lovnes, R.H. Raekken, E. LeDoeuff, J.J. Reis, "Millimetre-wave Channel Sounding Measurements", RACE 1994, pages 663-671.
- [3.28] Peter F. Driessen, "Multipath Delay Characteristics in Mountainous Terrain at 900 MHz", IEEE Vehicular Technology Conference, 1992, pages 520-523.
- [3.29] William G.Newhall, Theodore S.Rappaport & Dennis G.Sweeney, "A Spread Spectrum Sliding Correlator System for Propagation Measurements", RF Design, April 1996, pages 40-56.
- [3.30] William G.Newhall, Kevin J.Saldanha, and Theodore S. Rappaport, "Propagation Time Delay Spread Measurements at 915 MHz in a Large Train Yard", Proc. IEEE 46th Vehicular Technology Conference Atlanta USA, April-May 1996, pages 864-868.
- [3.31] Y.L.C. de Jong, M.H.A.J. Herben, "Accurate Identification of Scatterers for Improved Microcell propagation Modelling", IEEE PIMRC, 1997, pages 645-649.
- [3.32] P.Hafezi, D.Wedge, M.A.Beach and M.Lawton, "Propagation Measurements at 5.2 GHz in Commercial and Domestic Environments", Proc. IEEE PIMRC '97 Helsinki, Vol.2, September 1997, pages 509-513.
- [3.33] A. Kato, T. Manabe, Y. Miura, K. Sata, and T. Ihara, "Measurements of Millimeter Wave Indoor Propagation and High Speed Digital Transmission Characteristics at 60 GHz.", Proc. IEEE PIMRC '97, Helsinki, Vol.1, September 1997, pages 149-154.
-

- [3.35] S.A. Allpress, M.A. Beach, G. Martin & C.M. Simmonds, "An Investigation of RAKE Receiver Operation in an Urban Environment for Various Spreading Bandwidths", IEEE Vehicular Technology Conference, 1992, pages 506-510.
- [3.36] P. Bartolome, "Temporal Dispersion Measurements for Radio Local Loop Applications", IEEE 45th. Vehicular Technology Conference, Chicago, USA, July 1995, pages 257-260.
- [3.37] Armand J. Levy, Jean-Pierre Rossi, Jean-Pierre Barbot, Jacques Martin, "An Improved Channel Sounding Technique Applied To Wideband Mobile 900MHz Propagation Measurements.", 40th. IEEE Vehicular Technology Conference, 1990, pages 513-519.
- [3.38] Rudolf Werner Lorenz & Gerhard Kadel, "Propagation Measurements Using a Digital Channel Sounder Matched to the GSM-System Bandwidth", IEEE - ICC '91, 1991, pages 548-552.
- [3.39] G. Kadel, R.W. Lorenz, "Mobile Propagation Measurements Using a Digital Channel Sounder with a Bandwidth Matched to the GSM System", IEE International Conference on Antennas and Propagation, Vol.1, 1991, pages 496-499.
- [3.40] P.C. Fannin, A. Molina, S.S. Swords, P.J. Cullin, "Digital Signal Processing Techniques Applied to Mobile Radio Channel Sounding", IEE Proceedings-F, Vol.138, No.5, October 1991, pages 502-508.
- [3.41] Peter J. Cullen, Paul C. Fannin & Albert Molina, "Wide-Band Measurement and Analysis Techniques for the Mobile Radio Channel", IEEE Trans. on Vehicular Technology, Vol.42, No.4, November 1993, pages 589-603.
- [3.42] Gerhard Kadel, "Determination of the GSM-system Performance from Wideband Propagation Measurements", IEEE Vehicular Technology Conference, 1992, pages 540-545.
- [3.43] H.J. Thomas, T. Ohgane & M. Mizuno, "A Novel Dual Antenna Measurement of the Angular Distribution of Received Waves in the Mobile Radio Environment as a Function of Position and Delay Time", IEEE Vehicular Technology Conference, 1992, pages 546-549.
- [3.44] A.M. Cloke, A.K. Prentice, "The Implementation of a Channel Estimation Scheme for the CODIT Testbed", RACE 1994, pages 678-682.
- [3.45] Robert Castle, Taberto Corvaja, Michael Lawton & Matteo Vocale, "Instantaneous Wideband Channel Sounding for 1.7 GHz PCS", IEEE PIMRIC '94, 1994, pages 1404-1409.
- [3.46] G. Kadel, "Measurement of Wideband Micro- and Macro-diversity Characteristics of the Mobile Radio Channel", IEEE 44th. Vehicular Technology Conference, Stockholm, Sweden, June 1994, pages 165-169.
- [3.47] P. LeMenn, V. Ciarletti, A. Levy, M. Sylvain, "Wide Band Characterization of the Mobile-Satellite Propagation Channel using a Helicopter", IEEE 44th. Vehicular Technology Conference, Stockholm, Sweden, June 1994, pages 924-928.
- [3.48] K.A. Stewart, G.A. Labedz, K. Sohrabi, "Wideband Channel Measurements at 900 MHz", IEEE 45th. Vehicular Technology Conference, Chicago, USA, July 1995, pages 236-240.
- [3.49] L. Dossi, G. Tartara, F. Tallone, "Statistical Analysis of Measured Impulse Response Functions of 2.0 GHz Indoor Radio Channel", IEEE International Conference on Communications, Seattle, USA, June 1995, pages 1153-1157.
- [3.50] Laura Dossi, Guido Tartara & Fiorenzo Tallone, "Statistical Analysis of Measured Impulse Response Functions of 2.0GHz Indoor Radio Channels", IEEE Journal on Selected Areas in Communications, Vol.14, No.3, April 1996, pages 405-410.

- 
- [3.51] M. Hamalainen, A. Nykanen, V. Hovinen, P. Leppanen, "Digital Stepping Correlator in a Wideband Radio Channel measurement System", IEEE Int. Symposium on Personal, Indoor and Mobile Radio Comms., Vol.3, September 1997, pages 1120-1124.
- [3.52] U. Karthaus, R. Noe, J. Graser, "High-resolution Channel Impulse Response Measurements for 'Radio in the Local Loop' ", ACTS Mobility Summit, 1997, pages 241-244.
- [3.53] A.S. Bajwa, J.D. Parsons, "Small-area Characterisation of UHF Urban and Suburban Mobile Radio Propagation", IRE Proceedings Part F, Vol.129, No.2, April 1982, pages 102-109.
- [3.54] J.S. Parsons & A.S. Bajwa, "Wideband Characterisation of Fading Mobile Radio Channels", IEE Proceedings, Vol.129, No.2, April 1982, pages 95-101.
- [3.55] Jean-Paul de Weck, Jurg Ruprecht, Boris Nemsic & Hermann Buhler, "Sounding Radio Channels for 1.8 GHz Personal Communications Systems", IEEE Vehicular Technology Conference, 1992, pages 490-493.
- [3.56] Jan Van Rees, "Measurements of the Wide-Band Radio Channel Characteristics for Rural, Residential, and Suburban Areas", IEEE Trans. on Vehicular Technology, Vol.36, No.1, February 1987, pages 2-6.
- [3.57] T.S. Rappaport & S.Y. Seidel, "900 MHz Multipath Propagation Measurements in Four United States Cities", Electronics Letters, Vol.25, No.15, July 1989, pages 956-958.
- [3.58] Theodore S. Rappaport, Clare D.M. Gillem, "UHF Fading in Factories", IEEE Journal on Selected Areas in Communications, Vol.7, No.1, January 1989, pages 40-48.
- [3.59] Theodore S. Rappaport, Scott Y. Seidel & Rajendra Singh, "900 MHz Multipath Propagation Measurements for U.S. Digital Cellular Radiotelephone", IEEE Trans. on Vehicular Technology, Vol.39, No.2, May 1990, pages 132-139.
- [3.61] Scott Y. Seidel, Theodore S. Rappaport, Sanjiv Jain, Michael L. Lord & Rajendra Singh, "Path Loss, Scattering, and Multipath Delay Statistics In Four European Cities for Digital Cellular and Microcellular Radiotelephone", IEEE Transactions on Vehicular Technology, Vol.40, No.4, November 1991, pages 721-730.
- [3.62] D.A. Hawbaker and T.S. Rappaport, "Indoor Wideband Radio Propagation Measurement System at 1.3 GHz and 4.0 GHz", Proc. 40th. IEEE Vehicular Technology Conference, Orlando, USA, May 1990, pages 626-630.
- [3.63] R. Davies, A. Simpson, J.P. McGeehan, "Propagation Measurements at 1.7 GHz for Microcellular Urban Communications", Electronics Letters, Vol.26, No.14, July 1990, pages 1053-1054.
- [3.64] R. Davies, M. Bensebti, M.A. Beach, J.P. McGeehan, "Wireless Propagation Measurements in Indoor Multipath Environments at 1.7GHz and 60 GHz for Small Cell Systems", IEEE, 1991, pages 589-593.
- [3.65] Eimatsu Moriyama, Mitsuhiro Mizuno, Yoshinori Nagata, Yukitsuna Furuya, Isamu Kamiya & Seiji Hattori, "2.6 GHz Band Multipath Characteristics Measurement in a Residential Area for Micro-cellular Systems", IEEE Vehicular Technology Conference, 1992, pages 423-426.
- [3.66] C.M.Peter Ho, Theodore S. Rappaport and M. Prabhakar Koushik, "Antenna Effects on Indoor Obstructed Wireless Channels and a Deterministic Image-Based Wide-Band Propagation Model for In-Building Personal Communication Systems", Int. Journal of Wireless Information Networks, Vol.1, No.1, 1994, pages 61-76.

- 
- [3.67] Mohamed Otmani, Michel Lecours, "Indoor Radio Impulse Response Measurements with Polarization Diversity", Proc. IEEE 46th Vehicular Technology Conference Atlanta USA, April-May 1996, pages 151-154.
- [3.68] G. Lovnes, S.E. Paulsen, R.H. Raekken, "UHF Radio Channel Characteristics - Part 1", Norwegian Telecom Report TF R 54/91, 1991.
- [3.69] Geir Lovnes, Stein Erik Paulsen & Rune Harald Raekken, "A Versatile Channel Sounder for Millimetre Wave Measurements", PIMRIC '93, September 1993, pages 382-386.
- [3.70] S. Salous, "FMCW Channel Sounder with Digital Processing for Measuring the Coherence of Wideband HF Radio Links", IEE Proceedings, Vol.133, Pt.F No.5, August 1986, pages 456-462.
- [3.71] S. Salous, N. Nikandrou, N.F. Banjj, Digital Techniques for Mobile Radio Chirp Sounders, IEE Proc. Communications, Vol.145, No.3, June 1998, pages 191-196.
- [3.72] M.P. Fitton, A.R. Nix, M.A. Beech, "Propagation Aspects of Frequency Hopping Spread Spectrum", IEEE Int. Symp. Personal, Indoor and Mobile Radio Comms., September 1997, pages 640-644.
- [3.73] P.A. Matthews, D. Molkdar, B. Mohebbi, "Direction of Arrival and Frequency Response Measurements at UHF", IEE 5th. Int. Conf. Mobile Radio and Personal Comms., Warwick UK, December 1989, pages 43-47.
- [3.74] P.F.M. Smulders & A.G. Wagemans, "Wideband Indoor Radio Propagation Measurements at 58 GHz", Electronics Letters, Vol.28, No.13, June 1992, pages 1270-1271.
- [3.75] N. Hashemi, "Propagation Modeling for PCS Systems" Tutorial Notes, IEEE 4th. Int. Conf. on Universal Personal Communications, Tokyo., November 1995.
- [3.76] S.J. Barker, J.S. Kot, K.W. Smart, "Measurement of Millimetre-wave Propagation Characteristics in Buildings", IEEE Int. Conf. on Universal Wireless Access, Melbourne, Australia, April 1994, pages 127-131.
- [3.77] H. Hashemi, D. Tholl, "Statistical Modeling and Simulation of the RMS Delay Spread of Indoor Radio Propagation Channels", IEEE Trans. Vehicular Technology, Vol.43, No.1, February 1994, pages 110-120.
- [3.78] T. Manabe, K. Taira, K. Sato, T. Ihara, Y. Kasashima, K. Yamaki, "Multipath measurements at 60 GHz for Indoor Wireless Communication Systems", IEEE 44th. Vehicular Technology Conference, Stockholm, Sweden, June 1994, pages 905-909.
- [3.79] P. Nobles, D. Ashworth, F. Halsall, "Indoor Radiowave Propagation Measurements at Frequencies up to 20 GHz", IEEE 44th. Vehicular Technology Conference, Stockholm, Sweden, June 1994, pages 873-877.
- [3.80] P. Nobles, F. Halsall, "Delay Spread and Received Power Measurements Within a Building at 2 GHz, 5 GHz, and 17 GHz", IEE 10th. Int. Conf. on Antennas and Propagation, April 1997, pages 2.319-2.324.
- [3.81] S. Guerin, Y.J. Guo, S.K. Barton, "Indoor propagation Measurements at 5 GHz for Hiperlan", IEE 10th. Int. Conf. on Antennas and Propagation, April 1997, pages 2.306-2.310.
- [3.82] M.P. Fitton, A.R. Nix, M.A. Beach, "Evaluation of Metrics for Characterising the Dispersion of the Mobile Channel", Proc. IEEE 46th Vehicular Technology Conference Atlanta USA, April-May 1996, pages 1418-1422.



- [3.83] M.P. Fitton, A.R. Nix & M.A. Beach, "A Comparison of RMS Delay Spread and Coherence Bandwidth for Characterisation of Wideband Channels", IEE- Propagation Aspects of Future Mobile Systems, October 1996,
- [3.84] A.M. Street, D.J. Edwards, "High Dynamic Range Swept Time Delay Crosscorrelator", Electronics Letters, Vol.30, No.21, October 1994, pages 1742-11744.
- [3.85] J. Talvitie and T. Poutanen, "Self-noise as a Factor Limiting the Dynamic Range in Impulse Response Measurements Using Sliding Correlation", Proc. 3rd. IEEE Int. Sym. on Spread Spectrum Tech. and Applications, Finland, July 1994, pages 619-623.
- [3.86] J. D. Balcomb, H.B. Demuth, E.P. Gyftopoulos, "A Cross-correlation Method for Measuring the Impulse Response of Reactor Systems", Nuclear Science Engineering, Vol.11, 1961, pages 159-166.
- [3.87] D. Bitzer, D. Chester, R. Ives, S. Stein, "A RAKE System for Tropospheric Scatter", Convention Record, 1965 IEEE Communications Convention, June 1965, pages 677-684.
- [3.88] C.C. Bailey, "Multipath Characteristics of Angle Diversity Troposcatter Channels", IEEE International Conference on Communications, June 1971,
- [3.89] W.R. Young, Jr & L.Y. Lacy, "Echoes on Transmission at 450 Megacycles from Land-to-Car Radio Units", Proceedings of the IRE, March 1950, pages 255-258.
- [3.90] J.D. Parsons, "The Mobile Radio Propagation Channel", Pentech Press, London, 1992.
- [3.91] I.R. Johnson, "Real-time Channel Sounding Techniques for Fixed and Mobile Communications", PhD thesis, The University of Leeds, UK, January 1992.
- [3.92] G.T. Martin, M. Faulkner, "Delay Spread Measurements at 1890 MHz in Pedestrian Areas of the Central Business District in the City of Melbourne", IEEE 44th. Vehicular Technology Conference, Stockholm, Sweden. June 1994. Vol.1, pages 145-149.
- [3.93] Keith Blankenship, Hao Xu, "Radio Channel Sounding Developments at MPRG", The Propagator, Virginia Tech. USA, Vol.8, No.2, 1997, pages 2,11,12.
- [3.94] R.I. Davies, S.C. Swales, C. Simmonds, G. Martin, M.A. Beech, J.P. McGeehan, "Time Dispersion Measurements Undertaken at 1.87 GHz for Hutchison Microtel", Centre for Communications Research, University of Bristol, December, 1991.
- [3.95] Robert C. Dixon, "Spread Spectrum Systems with Commercial Applications", 3rd.Ed., John Wiley & Sons, Inc., 1994.
- [3.96] N.Benvenuto, "Distortion Analysis on Measuring the Impulse Response of a System Using a Crosscorrelation Method", AT&T Bell Laboratories Technical Journal, Vol.63, No.10, December 1984, pages 2171-2192.
- [3.97] Jarmo Kivinen, Pertti Vainikainen, "Phase Noise in a Direct Sequence Based Channel Sounder", Proceedings of the International Symposium on Personal, Indoor and Mobile Radio Communications, Helsinki, 1997, pages 1115-1119.
- [3.98] A.G. Kandoian, "Three New Antenna Types and Their Applications", Proc. IRE, Vol.34, February 1946, pages 70-75.
- [3.99] "The ARRL Antenna Book", Section 7-17, 1994, The American Radio Relay League.
- [3.100] D.S.Evans, G.R.Jessop, "VHF-UHF Manual", Section 7.28, 3rd. Ed., 1982, Radio Society of Great Britain.

- 
- [3.101] "Reference Data for Radio Engineers", Section 25-10, 5th. Ed., 1969, Howard Sams & Co., Inc.
- [3.102] Theodore S. Rappaport, "Wide-Band Test Antennas", RF Design, April 1988, pages 37-41.
- [3.103] "The ARRL Antenna Book", Section 16-21, 1994, The American Radio Relay League.
- [3.104] Peter Karlsson, "Indoor Radio Propagation for Personal Communications Services", PhD Thesis, Department of Applied Electronics - Lund Institute of Technology, March 1995, page 38.
- [3.105] R.S.Thomas, D.Hampicke, A.Richter, G.Sommerkorn, A.Schneider, U.Trautwein, "Identification of Time-Variant Directional Mobile Radio Channels", 9th Virginia Tech. Symposium on Wireless Personal Communications, Blacksburg, USA, June 1999.

# Chapter 4: Indoor Measurements

## 4. INTRODUCTION

**Ray Tracing Simulations and Measured Values** - Ray tracing models are gaining in popularity as computing resources become cheaper. In the first part of this chapter, the advantages and drawbacks of the ray tracing approach are discussed, followed by the application of ray tracing models to indoor and enclosed outdoor propagation routes.

An attempt has been made to determine how many reflections, wall transmissions and diffractions must be used in a ray tracing model to (i) converge to consistent results, and (ii) agree with measured delay spread results over the same route.

Delay spread measurements over three different routes have been compared with ray tracing simulations for the same routes. Two ray tracing programs were used, *X-Ray* (University of Bristol) and *MCST<sup>TM</sup>* v1.0 (*EDX Engineering, Inc.*). The routes included measurements on a single floor of a large university building with the transmitter located on the same floor, and two routes in an outdoor campus courtyard area, open to the sky, but almost completely enclosed by surrounding high buildings. Measured and simulated rms delay spread values have been quantitatively compared, using an rms error measure.

Indoors, *X-Ray* agreed well with measured delay spreads, if a measurement range threshold was applied to exclude paths returning from exterior scatterers not included in the ray tracing plan, and providing at least 2 to 3 reflections and 1 to 2 onward-propagating diffractions were used. The overall average rms delay spread indoors was 24 ns, and *X-Ray* gave an rms error of 8.5 ns, while the rms error with *MCST<sup>TM</sup>* was 13.2 ns.

Outdoors, agreement was poor, possibly because a lot of the environmental complexity such as overhead structures, trees and foliage, could not be included in the simple ray tracing plan.

**Multipath Propagation between Floors** - in the second part of this chapter, measurements of rms delay spread, number of rays, and the distribution of rays in time and power, are presented for the top floor of a large concrete building, and for three lower floors, with the transmitter remaining on the top floor. For propagation between floors, both the delay spread and the

number of rays in the power delay profile (PDP) increases compared with the same-floor case.

Work described in this chapter used the *VUT channel sounder* instrumentation introduced in Chapter 3, and measures of time dispersion defined in Chapter 2. Measurements were performed using the *channel sounder* in *indoor* mode, giving a resolution of 10 ns, or 3 metres excess path length.

The comparison of ray tracing models with measured results was presented by the author at the 4th IEEE International Conference on Universal Personal Communications (ICUPC'95), November 6-10, 1995, Tokyo, Japan {Ref.[4.28]}, and at the 6th. IEEE International Conference on Personal, Indoor and Mobile Communications (PIMRC'95), September 27-29, 1995, Toronto, Canada {Ref.[4.29]}.

Work on ray propagation between multiple floors of a building was presented by the author at the 47th. International IEEE Conference on Vehicular Technology (VTC'97), Phoenix USA, {Ref.[4.30]}, and at the Workshop on Applications of Radio Science (WARS'95), Canberra, Australia, {Ref.[4.31]}.

## 4. 1 Ray Tracing Simulations and Measured Values

Ray tracing provides a deterministic method of modelling multipath propagation. Detailed information about the propagation environment, giving the location and dielectric properties of all objects and surfaces capable of reflecting, transmitting, and diffracting radio signals, is stored in a computer database in a format compatible with the ray tracing program. Applying geometric optics ray theory, and the geometric theory of diffraction, it is possible to identify all signal paths between the transmitter and receiver. Antenna directivity can be included. The amplitude, phase and time delay of each ray is computed, giving the complex impulse response of the channel with infinite bandwidth, assuming non-dispersive dielectric properties.

### 4. 1.1 Ray Launching and Image Source Methods

Two approaches to ray tracing are popular: (i) ray launching, and (ii) the image source method.

Ray launching generates a large number of rays at the transmitter, evenly distributed in direction. Each ray is followed to identify those which ultimately intersect the receiver. This "brute force" technique is an approximate method, and has a number of disadvantages: (i) for a finite number of launched rays, a point receiver may be missed, so the receiver must

be represented by a finite area, risking several specular rays being included for one actual channel path, (ii) for each new receiver location, the entire computation must be repeated, and (iii) the method is computationally demanding, limiting the complexity of the database for a given amount of computing resource.

The image source method generates images of the transmitter in permutations of dielectric surfaces. Straight lines are constructed between the receiver and the images, and the intersections of these lines with reflecting surfaces is the basis for tracing actual rays. Three dimensional (3D) tracing can be handled, by also finding images in all horizontal surfaces. The method of image sources is strictly only valid for infinite surfaces {Ref[4.1]}. However at cellular radio frequencies, reflecting surfaces are generally large compared with the wavelength, and closely approximate infinite reflectors. With this qualification, the method has several attractions: (i) it is exact in finding rays between a point transmitter and a point receiver, (ii) for a particular transmitter position, the array of images need only be calculated once, reducing the computation effort for new receiver positions, and (iii) the number of paths to be computed is much less than with the ray launching method.

These methods are discussed in Ref[4.2] and Ref[4.3]. Diffraction complicates the problem exponentially with each order of diffraction, because each diffracting edge acts like a new transmitter {Ref[4.3]}. It will be shown later in this chapter that it is important to include at least one order of diffraction to improve agreement with measured results. Adding rough surface scattering also complicates the model, but is claimed to improve accuracy significantly {Ref[4.4]}. Model accuracy depends on using a sufficiently high order of onward propagating ray interactions with dielectric surfaces, and using correct algorithms and dielectric properties for these interactions.

## 4. 1.2 The Environment Database

Ray tracing is an accurate analytical solution, but in practice has been limited by simplification of the environmental database, and by limitations in computing speed and memory. At 1890 MHz the wavelength is 159 millimetres. To specify the environment accurately (say to within one-sixteenth of a wavelength) would require a 3D resolution, and accuracy, of about 10 millimetres. Furthermore, the electrical properties and surface roughness of all objects existing in the environment should be known to the same resolution. For a realistic cell size, storage and processing of this amount of data is impractical with present technology, apart from the separate problem of gathering the information. However, even with very simplified databases of building outlines, some useful results have been reported. In Ref[4.5], the author argues that high accuracy databases are not required, because the models have limited accuracy. Unnecessary accuracy in the database increases both the cost of the database, and computing costs. Intentional simplification of the database, for example by replacing indented building walls with smooth walls, may be warranted.

Ray tracing algorithms require the building plan to be in vector form, to facilitate the calculation of intersections between rays and surfaces. Raster or pixel plans, such as those resulting from scanned maps, must first be converted to vector form, either as a pre-processing step, or within the ray tracing software.

The problem of obtaining the 3D building database is also discussed in Ref[4.5]. Traditional but costly manual methods with a human operator interpreting stereo photo maps are currently used, because automatic digital image analysis still requires extensive manual checking for quality control. Airborne automatic laser scanning mapping, using GPS (global positioning system) and inertial guidance location, may provide an affordable future solution to the database problem.

### 4.1.3 Ray Tracing Validation

Numerous authors have compared ray tracing simulations with measured results. To date, most applications of ray tracing modelling have been used to predict a local average signal strength, rather than signal time dispersion. A second order statistic such as instantaneous time delay spread is more difficult to model accurately, as it is more sensitive than average signal strength to the surroundings. Delay spreads can vary by large amounts with small position changes because small scale fading causes large alterations in the power delay profile [see Chapter 2]. Generally the basis of comparison is a sector average or overall average rather than a point-by-point or site-specific comparison. Very few papers quantify the comparison. Superimposed plots, and side-by-side plots of scattering functions, presented to allowing a subjective visual comparison, are popular.

In Ref[4.3], a two dimension (2D) plus ground ray model is used at 1.845GHz outdoors, with seven orders of reflection, or first and second order diffractions plus one reflection and one diffraction. Three different transmitter sites are used in different areas, with various receiver routes. Median values of delay spread over the whole route agree very well, with differences between 0% and 17%, although the simulation underestimates the delay spread at the high value end of the distribution, attributed to suspected paths beyond the ray tracing plan. Point-by-point delay spread comparisons along routes show worst case percentage differences ranging from 35% to 190%. Plots of single location indoor power delay profiles are given in Ref[4.2], and for the cases given, the percentage difference varies from 11% to 250%. Scatter plots of path loss and delay spread are given, with the standard deviation of path loss prediction error equal to 4.8dB, and little evident correlation for delay spread. Indoor measurements at 845MHz reported in Ref[4.6] show path loss sector averages agreeing within 2dB, except for two locations which degrade to 15dB.

Indoor measurements based on 16 profiles averaged over one metre<sup>2</sup> areas, and compared with a 3D ray tracing simulation, are described in Ref[4.7]. Average delay spreads

agree well, with a worst case percentage difference of 38%. In Ref[4.5], outdoor path loss measurements at 2GHz agree with ray tracing within  $\pm 8$ dB. In Ref[4.8], 2GHz experiments indoors averaged over a sector area of several wavelengths, underestimated measured path loss by up to 8dB. Also indoors, Ref[4.9] with a sector average over 10 metre, gave path loss agreement to within about 10dB.

At 914MHz outdoors, with a sector average of 20 wavelengths, Ref[4.10] gave path loss agreement generally within 5dB, with a worst case value of 17dB. Outdoors at 1900MHz and including diffraction, Ref[4.11] describes 8 spot measurements on two campuses. One PDP is shown, with a delay spread percentage difference of 93%, and the comment that the other sites had, "considerable error". Path loss error over the 8 sites had a standard deviation of 4.2dB. Measurements in several European cities at 890MHz and 945MHz with sector averages over 10 or 20 metres, gave 6dB path loss error in one case, and about 10dB in the other {Ref[4.12], Ref[4.13]}.

In summary, the literature indicates that ray tracing can produce agreement with measured path loss to the order of 10dB, whilst agreement with delay spread can range from, at best, the order of 20%, to no apparent agreement at all. Another aspect to this is the question of repeatability of measurements. Delay spread measurements made over apparently the same route, but on different occasions, have limited repeatability. This factor alone can cause percentage differences of over 100% {Ref[4.3], Ref[4.7]}.

#### 4.1.4 X-Ray

*X-Ray* is a UNIX software based ray tracing propagation model developed at the *University of Bristol* {Ref[4.15]}. In 1996, when the work described here was done, other improved ray tracing software was in development and use by researchers at *Bristol* {Ref[4.7]}. *X-Ray* was based on earlier research code, to which a user interface had been added, making it available for users not intimately familiar with the code. The *Centre for Communication Research* at the *University of Bristol* has a long and continuing interest in ray tracing models, and has played a pioneering role in understanding the potential offered by ray tracing for solving the propagation characterization problem {Ref[4.16], Ref[4.17], Ref[4.18], Ref[4.19], Ref[4.3], Ref[4.7]}.

*X-Ray* is intended for dense urban microcells of radius up to 500 metres, and is specified to be able to handle several thousand walls and corners. The program calculates the channel complex impulse response, and derives other parameters such as average power, delay spread, coherence bandwidth, and angle of arrival.

The ground is assumed to be flat, with all walls perpendicular to the ground. The ray engine, which uses electromagnetic image sources and builds an image map for each particular transmitter position, can work in partial 3D, and incorporates ray polarization, different

heights of the transmit and receive antennas, and a ground reflection. In Version 1.1 of *X-Ray*, rooftop diffraction was not implemented, because microcells usually have low antennas, below roof level. Although the ray engine works in 3D, there is no provision for building wall properties to vary with height, for example, to include a glass window part way up a concrete wall. Rays experiencing either a corner diffraction or a wall transmission are onward propagating, and may go on to further diffractions and wall transmissions. The order of onward propagating reflections, wall transmissions, and diffractions is set by the user at the start of each simulation. In practice, computer capacity places a limit on the maximum number of onward propagations possible.

A threshold level relative to the strongest received ray can be set, and then rays below this threshold window are ignored when calculating rms delay spread. Delay spread is sensitive to the threshold window size, as already discussed [Chapter 2]. A threshold window of 15 dB (meaning that only signals within 15 dB of the strongest ray are considered) was used in these *X-Ray* simulations, and the same threshold was applied to measured power delay profiles. Simplifying assumptions were made for the dielectric properties of the wall building materials.

#### 4.1.5 MCS<sup>TM</sup> Microcell Communication Simulator

Microcell Communication Simulator MCS<sup>TM</sup> is marketed by EDX Engineering, Inc., Oregon, USA {Ref[4.14]}. The MCS<sup>TM</sup> software uses image source ray tracing techniques to identify the multipath propagation arriving at the receiver. Multiple generation wall reflections, up to five, and zero or one corner diffraction may be included, but the maximum order is five, so if a diffraction occurs, reflections are reduced to four. For fixed transmitter and receiver locations, plots of the channel impulse response and angle of arrival are generated, and the rms delay spread is calculated. If a route for the receiver is specified, a plot of rms delay spread verses distance results.

A power threshold in dBm may be set, so all received rays below the threshold are ignored. However, the threshold is an absolute power level, so it cannot be related to the strongest ray (see Chapter 2). In effect the threshold window will vary for each point on the route, and in view of the sensitivity of delay spread to the threshold window size, this makes MCS<sup>TM</sup> results difficult to compare with measured values. This problem has been ignored in the comparisons done later in this chapter.

Grid study plots can also be performed. The software has other features described in the user manual {Ref[4.14]}.

Some limitations arise from the software, and from user simplification of the database information. The version of MCS<sup>TM</sup> used (v1.0, 1992) works essentially in 2D, apart from including one ground reflection. Terrain height variation is not included, and for indoor



applications, ceiling effects are not considered. Only one wall transmission of a ray is included, and this path is not onward propagating. Currently *MCS™* v2.0 for Windows® 95/NT is on the market, and this incorporates improvements such as 3D cell modelling, including terrain height variations. Version v2.0 was not available for the research described here.

The database describing the environment is a text file made up of coordinates specifying each building corner, an angle indicating the orientation of each corner, and a category for each wall section describing the electrical properties of the building material. Buildings, or internal walls and partitions, are thus described in 2D plan form as outlines. The number of wall sections and corners must not exceed 500 within the cell radius, which can be chosen as either 500 or 1000 metres. So the complexity and detail of real buildings is reduced to a simplified 2D outline. Rooftop diffraction is not included, with walls being treated as infinitely high. For the indoor case, walls are also treated as infinitely high, with no ceiling. Items such as steel fluorescent light units, which may be strong reflectors, cannot be included. Detail such as furniture, although many wavelengths in size, is not included in this study.

Note that as the name implies, *MCS™* was not marketed for indoor use, being targeted at outdoor microcell simulation.

#### 4. 1.6 Wall Types and Estimated Electrical Properties

The electrical properties (permeability, permittivity, conductivity, attenuation) used for the building wall materials are, at best, an approximate estimate. Windows within walls are difficult to include, except by the token gesture of modifying the average electrical parameters. In the case of internal partition walls, the electrical parameters are also in doubt, especially where the wall construction is non-homogeneous, such as with steel framed plasterboard walls. Some researchers have tackled this problem by “optimizing” electrical properties used in the ray tracing model, until the simulation gives the best match to measured values {Ref[4.2], Ref[4.6], Ref[4.12]}. Many workers use a single set of electrical parameters for the entire map, irrespective of the actual building materials.

The estimates below (Table 4.1) are based on anechoic chamber measurements done by other workers at the *University of Bristol*, and from results in Ref[4.20]. These values have been used for both *MCS™* and *X-Ray* simulations for the indoor route, while the campus courtyard routes use values for a single building material, namely solid reinforced concrete.

TABLE 4.1 Wall Types and Properties

Description	Surface				Wall Attenuation dB
	Conductivity S	Relative Permittivity	Roughness m	Thickness m	
reinforced concrete, half height windows	5E-4	3	2E-3	0.3	6
solid reinforced concrete	5E-3	2.7	2E-3	0.3	12
plasterboard and steel frame	5E-2	3	1E-3	0.1	4
plasterboard and timber frame	5E-3	2.7	1E-3	0.1	2
metal	9E6	1	0	0.1	100
timber door	3E-4	2	1E-3	0.03	1

4. 1.7 Measurements

The objective of this section is to investigate (i) how the ray tracing solution varies as the number of onward propagating reflections, wall transmissions and diffractions are varied, and (ii) how accurately the ray tracing simulations predict delay spreads over these specific routes, using simplified environment databases.

Measured receiver power, or path loss values, are not available as the channel sounder was primarily intended for time dispersion measurements, and has not been calibrated for power measurements. Hence no attempt has been made to compare measured and simulated power values, although this could be done in the future.

Results from two different ray tracing software programs, *X-Ray* and *MCS*<sup>TM</sup>, have been compared with measured values of rms delay spread, for one route inside a building (see Figures 4.1, 4.3, 4.4), and two different routes in an outdoor university campus courtyard area (see Figures 4.1, 4.18, 4.20, 4.25). All measurements were made with the 1890MHz *VUT channel sounder* in *indoor* mode, which gives 10 ns, or 3 metre, resolution. Indoor measurements were undertaken in the Engineering Faculty building (D Block), on the Footscray campus of *Victoria University of Technology*. Outdoor measurements were performed within the Footscray campus, in a courtyard area completely enclosed by a compact collection of buildings of irregular shape.

Indoor measurements were done on the top floor, called “Level 7”, of the *Engineering School*. This is an L-shaped building, with a central corridor, extending approximately 70 metres in the longer wing (see Figure 4.3). Side passages, large lecture rooms and labs, and small offices open off the main corridor. In the ray tracing plan, with the exception of doorways into some of the lecture rooms, only the corridor outlines are included.

The building has six floors, and is constructed of reinforced concrete, and clad in brick. The floors are suspended reinforced concrete, and 2.4 metre high false ceilings of

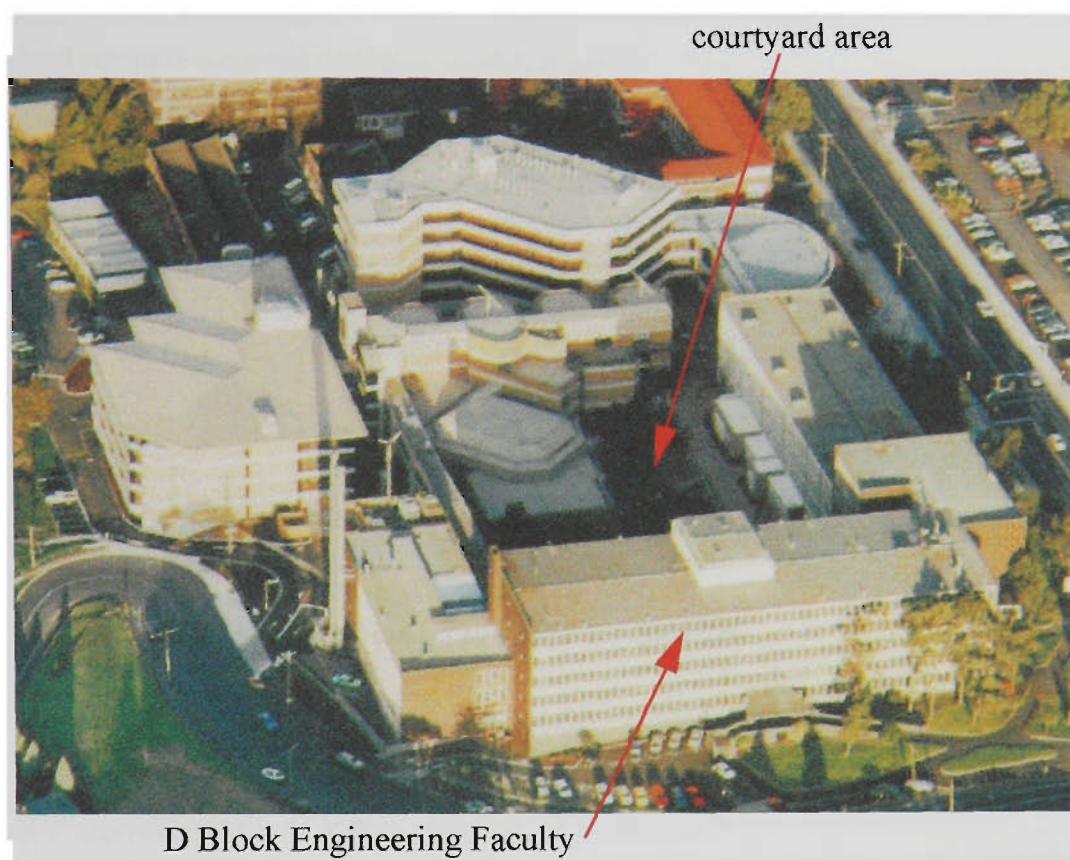


**FIGURE 4.1 Victoria University of Technology Footscray campus - aerial view showing measurement locations**

plaster acoustic tiles hang on metal rods and a light framework of galvanized iron angles, concealing a myriad of cabling. The internal partition walls in most cases are plasterboard, with either timber or galvanized steel framing. The outside walls have large areas of aluminium framed windows, extending from the ceiling to approximately half way down the wall. Various styles of internal windows are used, typically located in the upper one third of the walls. Internal doors are made of timber.

Indoor measurements were taken with the transmitter in a single location, in a side corridor which serves as a lift lobby (see Figures 4.3, 4.4). A single location non-line of sight (NLOS) measurement was performed in a nearby large lecture room, in addition to the route with the receiver following the main corridor. Most of this route was NLOS, apart from a short section adjacent to the lift lobby.

### 4.1.8 Single Point Measurement

For both the single point and route measurements, the transmitter was located in a wide side corridor, opposite steel lift doors, as shown in Figure 4.2. Measurements were taken over a small area in a lecture theatre, with the receiver moved randomly between each of 9 measurements within a 5 wavelength radius of the initial point. Rms delay spread values varied between 21 ns and 33 ns, with an average value of 26 ns, and standard deviation of 4 ns. The ray tracing plot from MCS™ is shown in Figure 4.2, and this gave a delay spread of 32 ns,

which was 23% or 6 ns greater than the average measured value of 26 ns

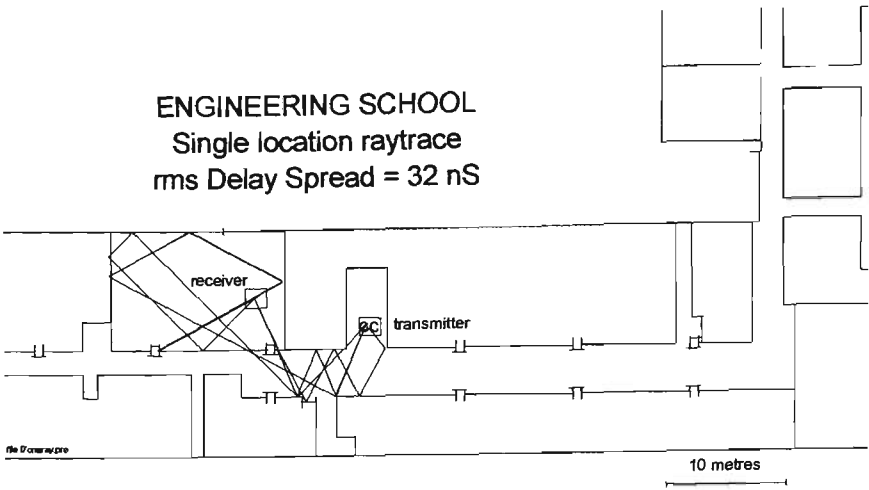


FIGURE 4.2 Single point ray tracing

4. 1.9 Corridor Route

At each measurement point, between 3 and 6 stationary measurements were taken, repositioning the receiver antenna randomly after each measurement within a radius of approximately 2 wavelengths from the initial position. Measurements were done on Sunday evening, when the campus and the building were almost deserted, thus avoiding effects from people moving about.

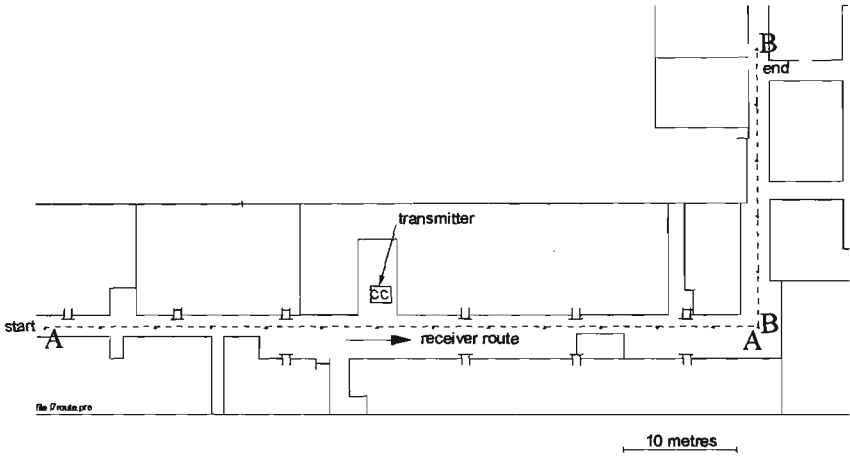


FIGURE 4.3 Receiver route along corridor

Figures 4.3 and 4.4 show the route used for indoor ray tracing simulations, and for measurements. The route distance was 68 metres in the long section of the corridor (AA) and a further 32 metres around the corner into the shorter section of corridor (BB), for a total route distance of 100 metres. *X-Ray* simulations were done for a number of combinations of reflections, wall transmissions and diffractions. Not all desired combinations could be simulated because of the tendency of the software to freeze with more demanding sets of parameters. This work was done in 1996 when *X-Ray* was experimental research code. Since then *Uni-*



versity of Bristol researchers have evolved improved ray tracing software packages, but the improved versions were not available for this study

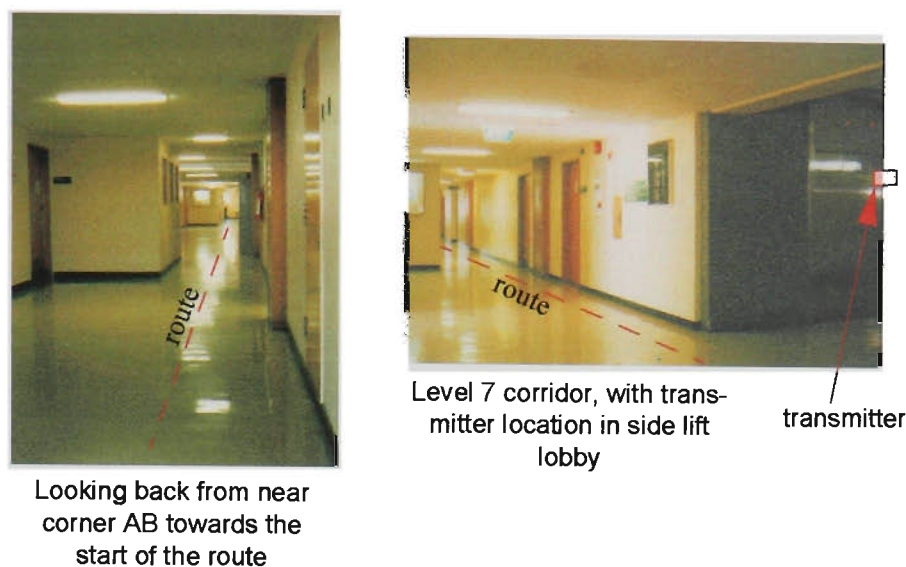


FIGURE 4.4 D Block Level 7 corridor

4. 1.9.1 Convergence of X-Ray Simulations - Power

As the number of reflections, wall transmissions, and diffractions is increased, it would be expected that a ray tracing simulation should converge; that is, a stage would be reached where increasing the onward propagating ray limits would make no further significant difference to the propagation solution. For the limited combinations of parameters used, this has not proved to be so, suggesting that a much larger number of reflections, wall transmissions and diffractions is necessary for convergence to occur.

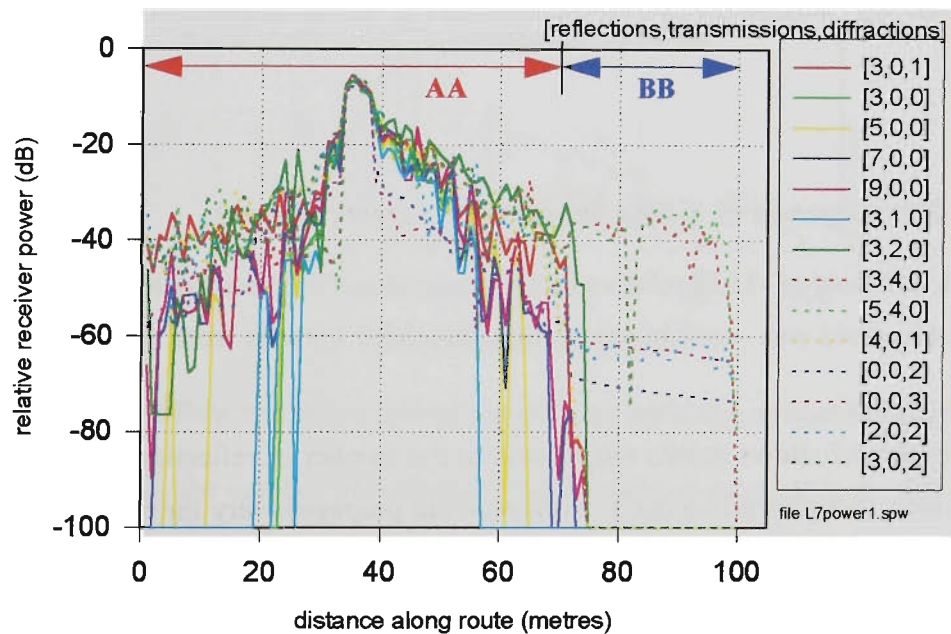
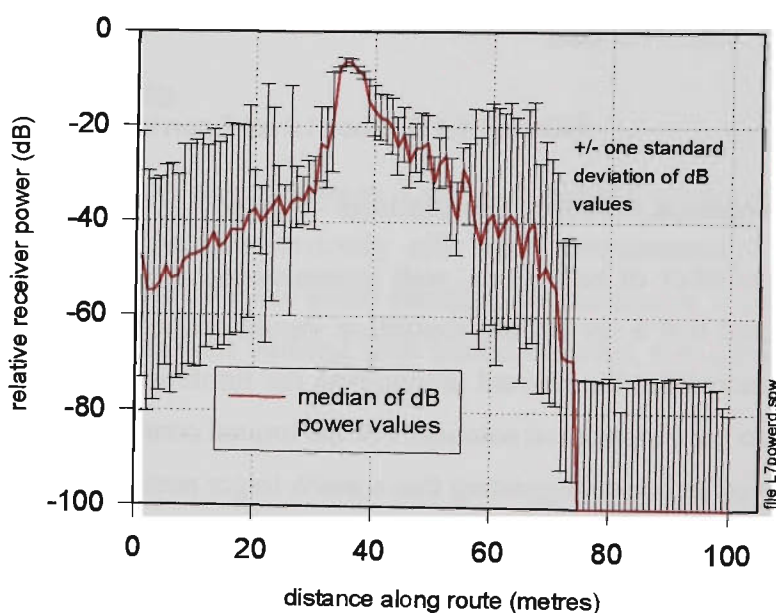


FIGURE 4.5 X-Ray simulated receiver power for various combinations of reflections, wall transmissions, and diffractions

Figure 4.5 shows *X-Ray* simulated relative receiver power values for all the combinations of parameters used. Numbers in square brackets in the legend represent the order of reflections, transmissions and diffractions respectively. Apart from the section of the route between approximately 33 and 40 metres, which corresponds to line of sight (LOS) in close proximity to the transmitter, there is no obvious convergence. Note that for any power to reach very far into the short section of corridor (BB) around the corner, either 4 wall transmissions must be allowed (there are 4 intervening walls), or at least 2 diffractions must be included.

The spread in power values obtained from the *X-Ray* simulations is shown in Figure 4.6, which plots the median of the dB powers, and shows  $\pm$  one standard deviation of dB values at one metre intervals along the route.

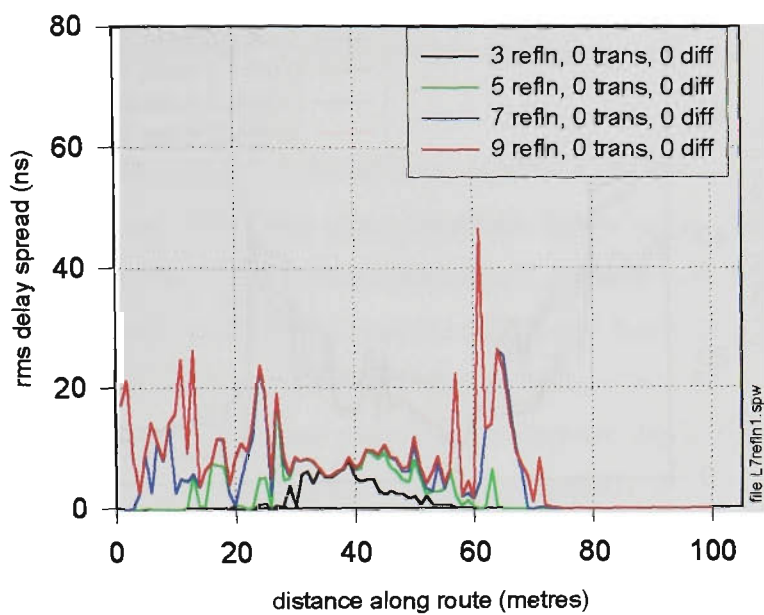


**FIGURE 4.6** Median and standard deviation of *X-Ray* simulated receiver power in dB for all combinations of parameters used

#### 4. 1.9.2 Convergence of *X-Ray* Simulations - Delay Spread

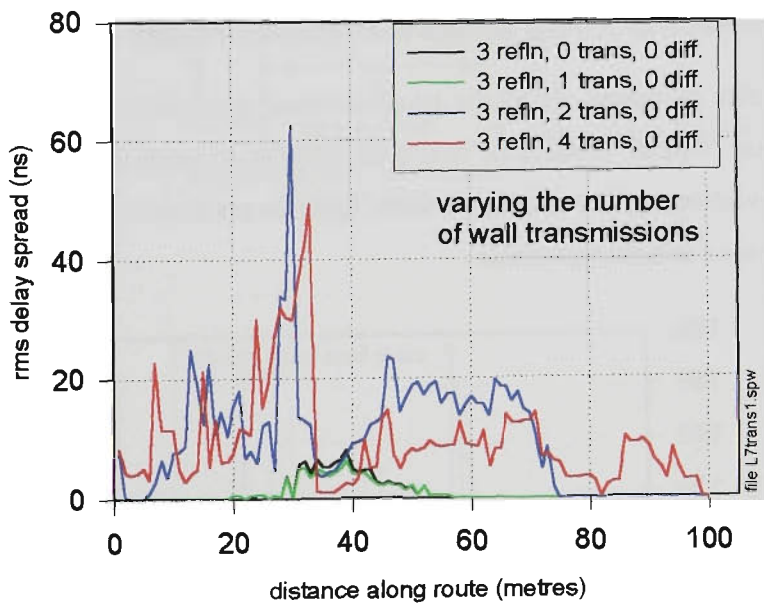
A threshold of -15dB relative to the strongest ray has been set for the *X-Ray* runs, and the same threshold was used in calculating rms delay spreads from measured power delay profiles.

Figure 4.7 shows results when varying the number of reflections, but with zero wall transmissions, and zero diffractions. No power can propagate very far beyond the corner into Section BB (68 to 100 metres) of the corridor. Because power levels in this section are low or zero, no delay spread values are produced.



**FIGURE 4.7 X-Ray rms delay spread for various numbers of reflections**

Rms delay spread values continue to increase in Figure 4.7 over most sections of the route as the number of reflections is increased up to the maximum value of 9 used here. The large change when going from 7 to 9 reflections suggests that even with 9 reflections, the solution is still not converging. .



**FIGURE 4.8 X-Ray rms delay spread for various numbers of wall transmissions**

In Figure 4.8, the number of reflections used is held constant at 3, no diffractions are used, but the number of wall transmissions is varied from zero to 4. Quite different rms delay spreads are obtained when going from 2 to 4 wall transmissions. Note that 4 wall transmissions allows propagation beyond the 74 metre point, into Section BB of the corridor, around the corner.

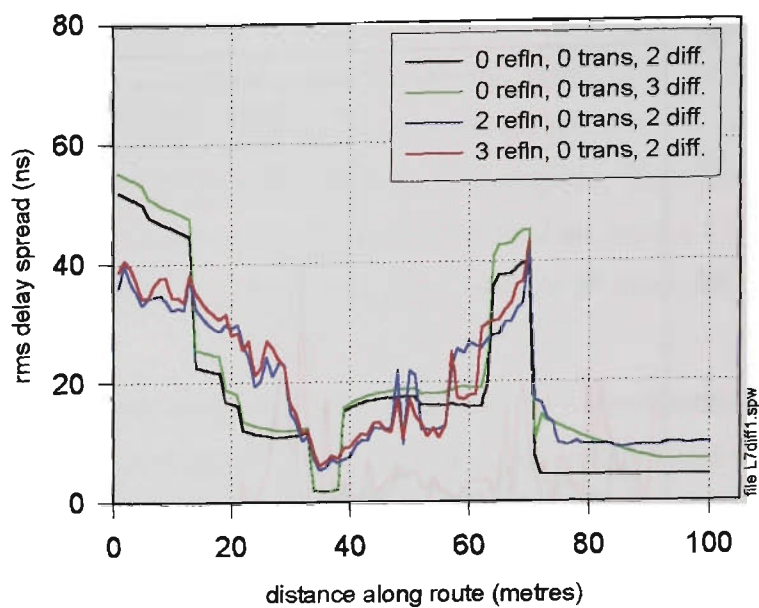


FIGURE 4.9 X-Ray rms delay spread for various numbers of reflections and diffractions

In Figure 4.9, no wall transmissions are allowed, but the number of reflections is either zero, 2, or 3, with either 2 or 3 diffractions. Including diffractions tends to increase the delay spread over most sections of the route, and this was found to improve agreement with measured values (see Figure 4.15, Table 4.2).

4. 1.9.3 Comparison of X-Ray Values with Measurements - Delay Spread

At a series of points along the route, several measurements of instantaneous delay spread were done within a radius of two wavelengths of each nominal position. The mean and standard deviations of the measured delay spreads are shown in Figure 4.10, in comparison with four sets of simulated results..

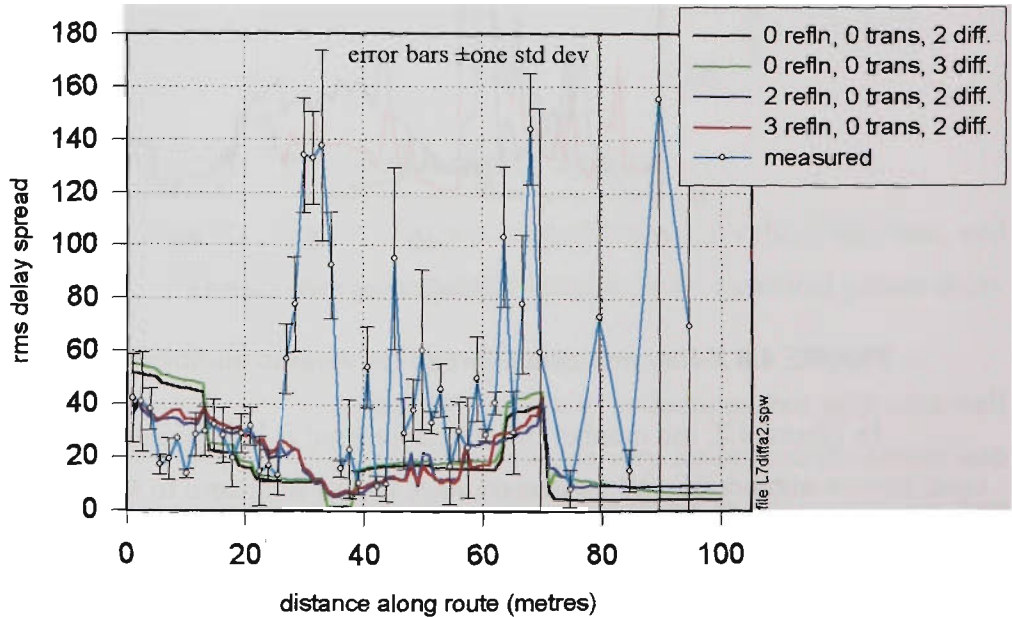
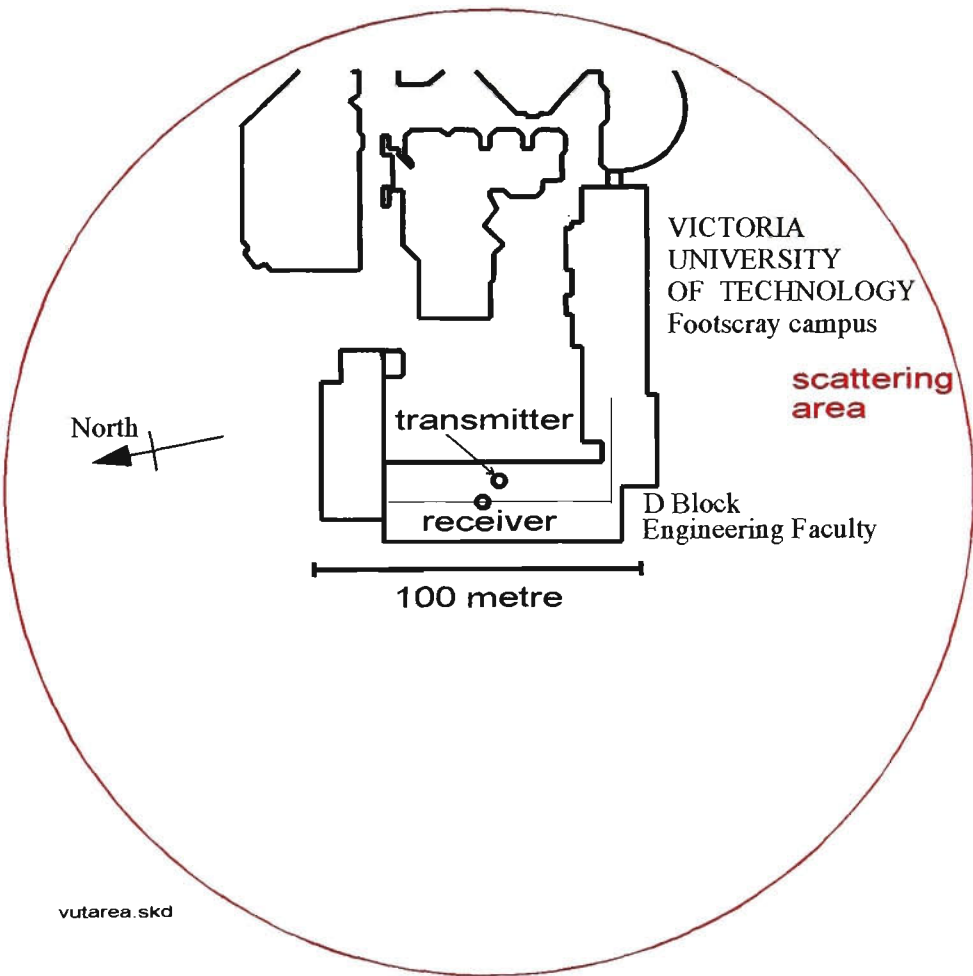


FIGURE 4.10 Measured rms delay spread



It is apparent that the measured delay spreads are much greater over most of the route than any values predicted by *X-Ray*. Particularly past 70 metres, in Section BB beyond the corridor corner, measured values at some points are high, giving a large variation in delay spreads.

Investigating this, measured power delay profiles with high delay spread values were examined to determine the maximum above-threshold excess delay, using a program called ELIPSE.EXE (see Appendix D). With this information, an ellipse can be plotted on the building plan to show the maximum extent of possible reflectors {Ref[4.21]}. In all cases for measurements showing high delay spreads, and also in many cases for more moderate delay spreads, the resulting scattering ellipse extended well beyond the D-Block Engineering Faculty building plan used as the data base for ray tracing simulations.



**FIGURE 4.11 Scattering ellipse for high delay spread measurements**

**4. 1.9.4 High Delay Spread Example**

In Figure 4.11, the scattering ellipse extends beyond the Footscray campus (the ellipse approximates a circle because the foci are relatively close together). In this particular example, the receiver is located at 28.5 metres along the route, just obscured from the transmitter by an internal corner, but both transmitter and receiver have a clear view of exterior

buildings at approximately the right distance to give the measured excess delay path of 860 ns. Figure 4.13, covering Section AA of the corridor, shows the group of rays at 860 ns excess delay, scattered from outside the building. This excess delay is represented by the ellipse in Figure 4.11.

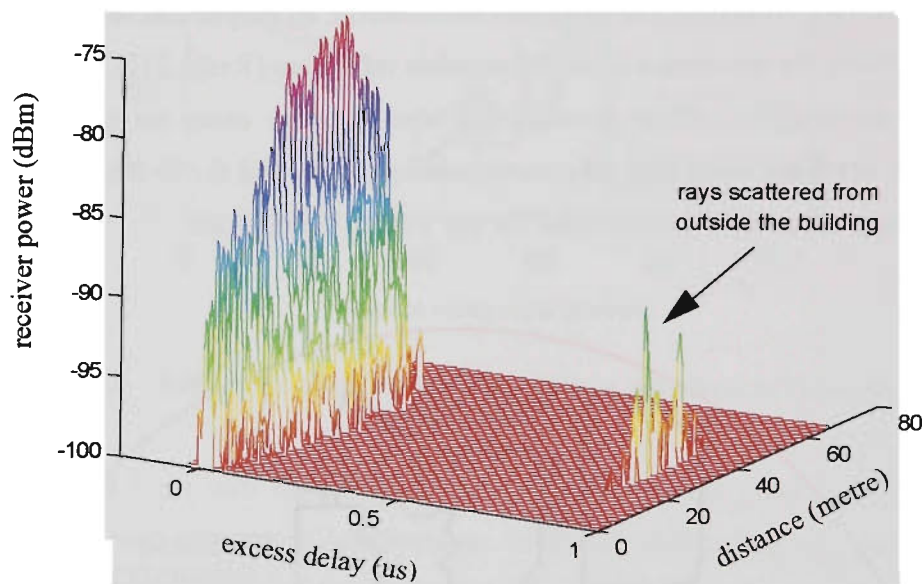


FIGURE 4.12 Measured average PDPs along corridor AA

4. 1.9.5 Medium Delay Spread Example

At a point 46.8 metres along the route, the four measurements taken gave an average delay spread of 30 ns, but maximum excess path length varied over individual measurements from 38 metres to 110 metres. Corresponding scattering ellipses are shown in Figure 4.13.

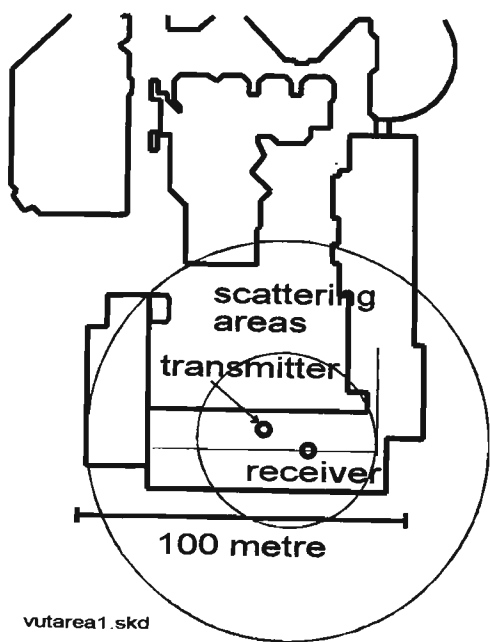


FIGURE 4.13 Scattering ellipses for medium delay spread example

The smaller (blue) ellipse corresponds to a maximum excess path of 38 metres, which indicates scattering within the building (because the ellipse does not include any external buildings or objects). Intersecting external buildings, the larger (red) ellipse shows that external scattering may be occurring, although multiple reflections within the building are another but less likely possibility.

This demonstrates that the building data base used for indoor ray tracing simulations must extend far beyond the plan of the building being studied, to include scattering from external objects and adjacent buildings.

4. 1.9.6 Applying a Range Limit

To exclude rays arriving from scatterers outside the building, and beyond the area of the data base plan used for ray tracing, a range limit has been applied, and the delay spread values recalculated. A maximum range of 450 ns excess delay has been imposed, with all PDP values beyond this range set to zero. The excess half path corresponding to 450 ns is 75 metre, which should allow most ray paths within the building to be included. PDPs with the range limit imposed, are shown in Figure 4.14. With the range limit applied, measured values show much better agreement with the best *X-Ray* configuration, and also with *MCS*<sup>TM</sup> over most of the route. This is illustrated in Figure 4.15, which shows the average measured delay spread value along the route, in comparison with the best *X-Ray* parameter configuration found, and with *EDX MCS*<sup>TM</sup>

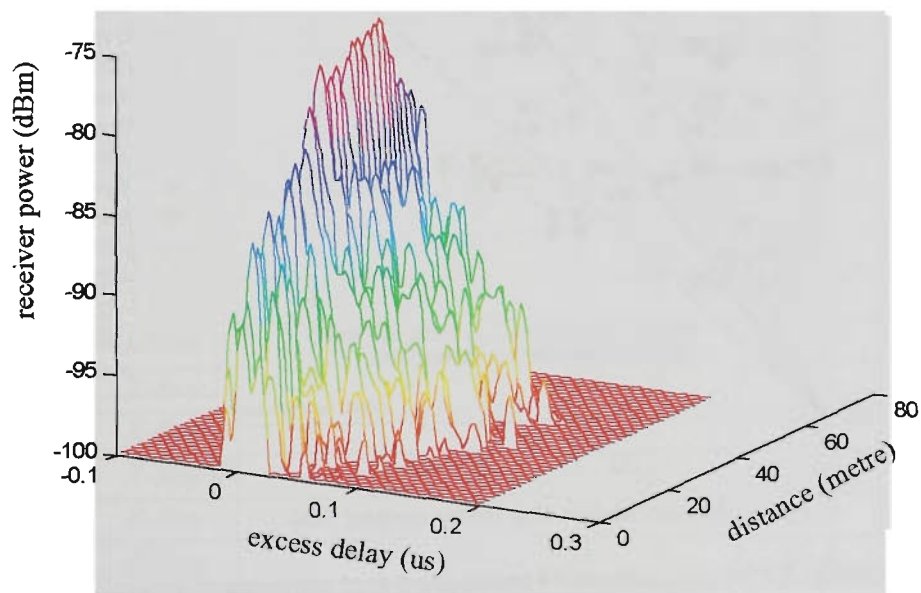


FIGURE 4.14 Measured average PDPs (Section AA) after range limit application

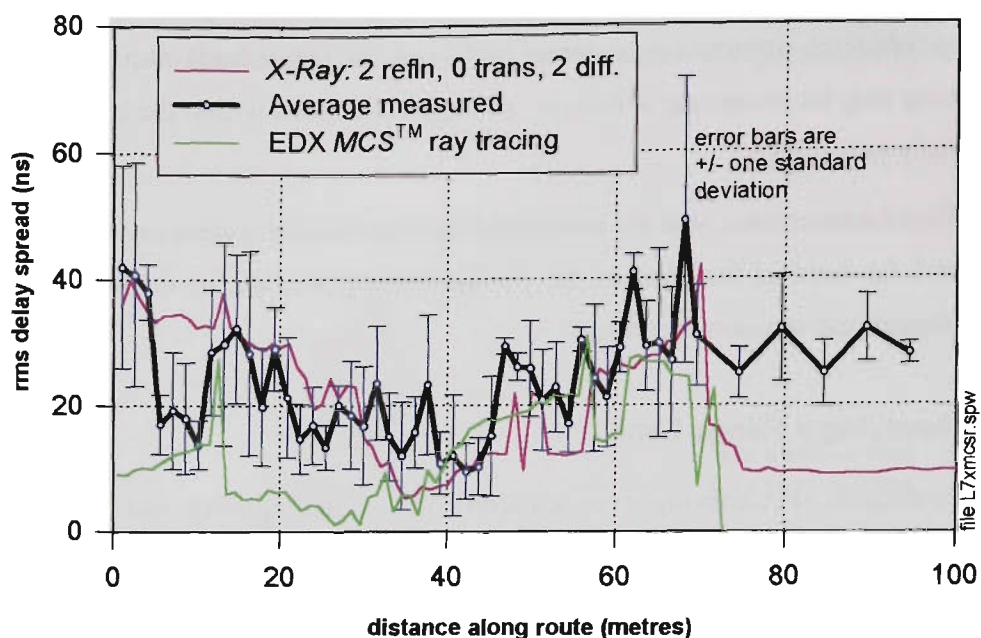


FIGURE 4.15 Delay spread from measurement and ray tracing

Note that rays generated by MCS™ do not reach around the corridor corner into Section BB beyond 73 metre, so no delay spread value are generated for this section of the route (Figure 4.15)..

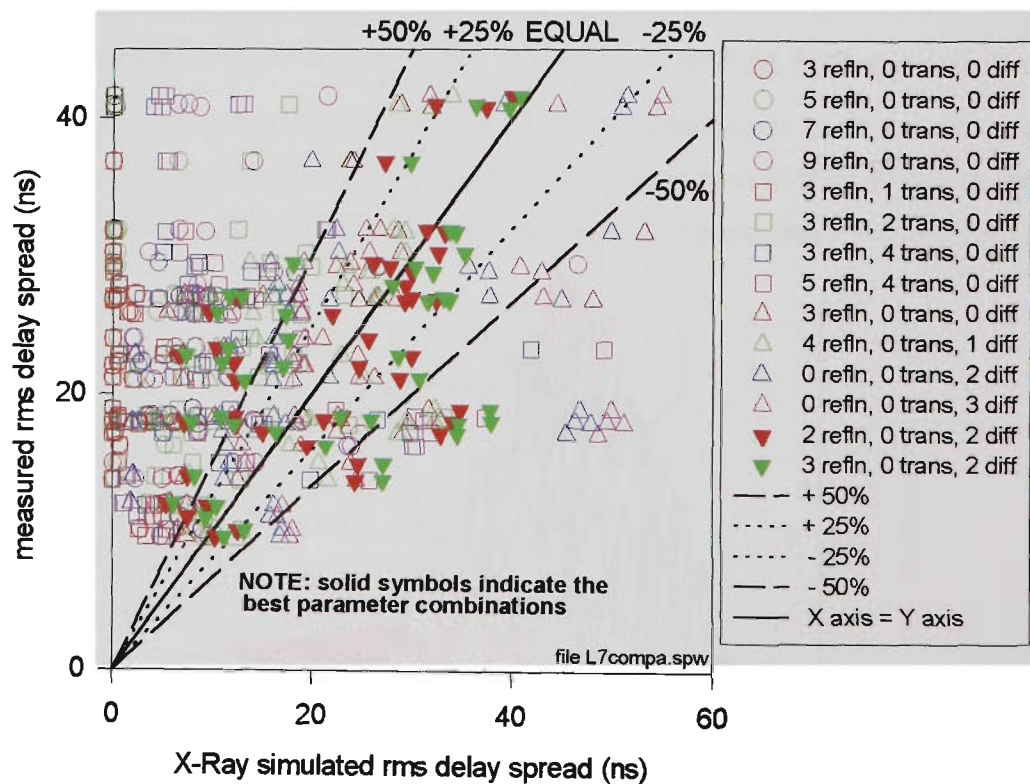


FIGURE 4.16 Comparison of measured and simulated rms delay spreads

Figure 4.16 shows a plot of each measurement point as an XY coordinate, where the *X axis* value is the *X-Ray* simulated delay spread, and the *Y axis* value is the average measured delay spread for the same point.

Points where the measured and simulated values agree lie on a 45 degree line. Points above the line represent locations with a measured value greater than the simulated value; conversely points below the line occur when the measured value is less than the simulated value.

All *X-Ray* parameter values used are represented in Figure 4.16. The best parameter combinations, [2 reflections, 0 transmissions, 2 diffractions] and [3 reflections, 0 transmissions, 2 diffractions], are plotted with solid colour red and green symbols respectively, and cluster around the 45° line. The tendency for the simulated values to underestimate measured values for other parameter combinations is evident.

To investigate the comparison in a quantitative way, an rms error measure is defined in EQ4.1. A similar mean square error is used in Ref[4.2].

$$\text{error}_{rms} = \sqrt{\frac{\sum_1^m (ds_{measured} - ds_{XRay})^2}{m}}$$

(EQ 4.1)

where  $ds_{measured}$  and  $ds_{XRay}$  are the respective measured and *X-Ray* simulated delay spreads over  $m$  measurement positions

**TABLE 4.2 rms error over measured route for various *X-Ray* configurations, and for EDX MCS™ sorted from best to worst**

Simulator	number of reflections	number of transmissions	number of diffractions	rms error (ns)
<i>X-Ray</i>	2	0	2	8.5
<i>X-Ray</i>	3	0	2	9.3
<i>X-Ray</i>	3	0	1	9.3
<i>X-Ray</i>	4	0	1	9.4
<i>X-Ray</i>	0	0	2	12.6
MCS™	4	1	1	13.2
<i>X-Ray</i>	0	0	3	13.3
<i>X-Ray</i>	9	0	0	15.7
<i>X-Ray</i>	3	2	0	16.2
<i>X-Ray</i>	5	4	0	17.0
<i>X-Ray</i>	3	4	0	17.4
<i>X-Ray</i>	7	0	0	18.1
<i>X-Ray</i>	5	0	0	21.7
<i>X-Ray</i>	3	0	0	23.3
<i>X-Ray</i>	3	1	0	23.4

The best ray tracing configuration on this basis from the available choices, is *X-Ray* with 2 reflections, 0 transmissions and 2 diffractions, with an rms error of 8.5 ns (Table 4.2). The average delay spread over the full measured route is 23.9 ns, and the average for the route in the long straight corridor (AA) is 23.3 ns. Ray tracing, using the “best” configuration (2



reflections, 2 diffractions) gives a mean delay spread in the long straight corridor (AA) of 21.8 ns, only 6.5% lower than the measured average. The ray tracing rms error is 8.5 ns, or 36% of the measured mean.

Cumulative distributions of delay spread do not provide any information relating to particular points on the measurement route, but do give a picture of the range and distribution of delay spreads over the entire route. Cumulative distribution function (CDF) plots for the long corridor Section AA for average measured rms delay spread, for the two best *X-Ray* configurations, and for *EDX MCS<sup>TM</sup>*, are shown in Figure 4.17. Below 90% probability, the maximum difference between the measured and *X-Ray* distributions is 5ns, while above 90% the difference reaches 9ns. For *EDX MCS<sup>TM</sup>* below 90% CDF, the maximum difference between the measured and *MCS<sup>TM</sup>* distributions is 11ns, while above 90% the difference reaches 18ns.

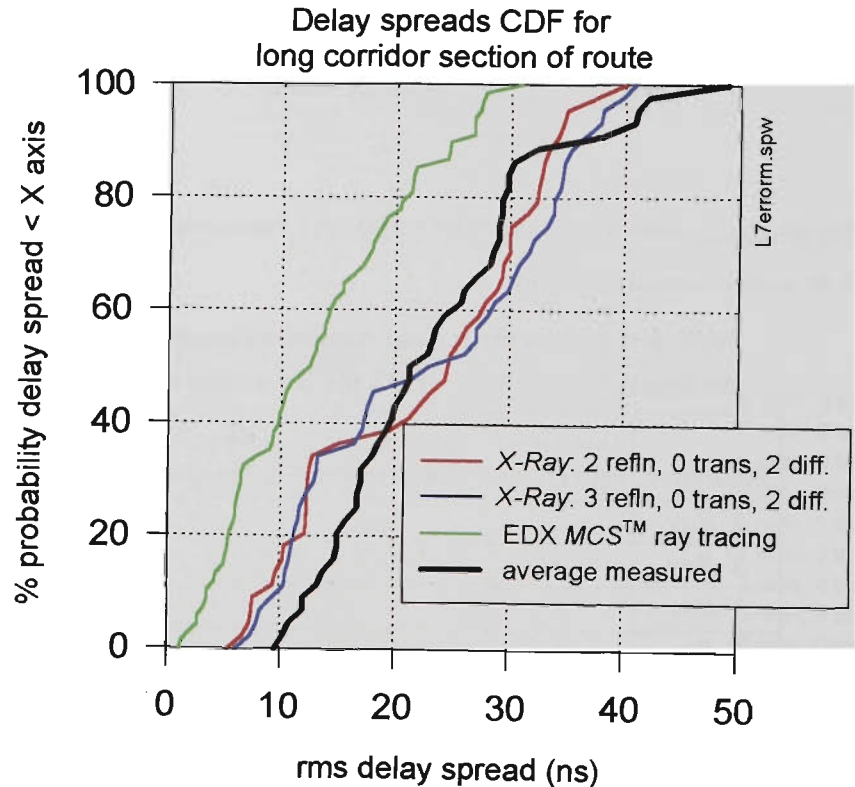


FIGURE 4.17 Distributions of average measured, *X-Ray* best configurations, and *MCS<sup>TM</sup>* in the long corridor Section AA of route.

4. 1.10 Campus Courtyard Measurements

Outdoor measurements were undertaken on the university campus, in a large courtyard area, completely surrounded by irregular shaped buildings, and complicated by sloping ground levels, various elevated pedestrian bridges, trees, and irregular roof profiles and heights. None of these factors could be included in the 2D ray tracing data bases used by *MCS<sup>TM</sup>* and *X-Ray*.

The two receiver routes, denoted *nv* and *m*, are shown in Figure 4.18. Some significant reinforced concrete elevated pedestrian walkways and supporting pillars, shown in Figures 4.19 and 4.20, have been omitted from the ray trace database. Apart from the pillars, the 2D ray tracing software cannot cope with the elevated structures. The under-surface of these is between 4 and 5 metres above ground level, but because of the change in ground level, is only about 2 metres in elevation above the transmitter. At the start of route *nv*, ground level is 3 metres below ground level at the transmitter, and gradually rises along the route. The early part of the route is most influenced by the elevated walkways and lower ground level; in fact the route passes underneath one elevated concrete walkway, and terminates within view of a new campus building to the east, which has not been included in the data base. A plantation of trees, also not included in the ray tracing data base, obstructs the path over most of the route.

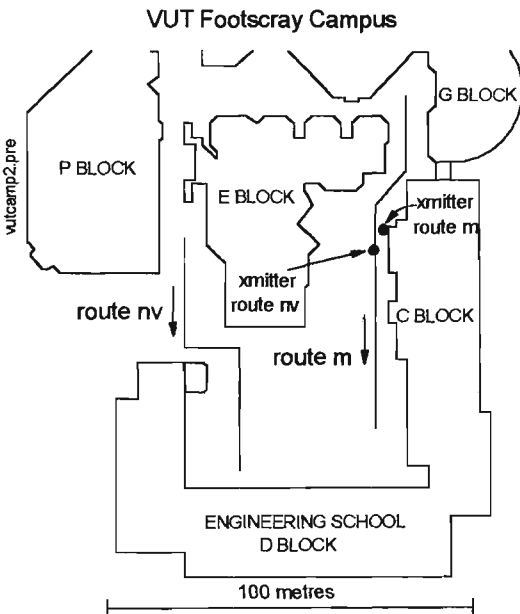


FIGURE 4.18 Campus plan, showing two outdoor routes in the courtyard area

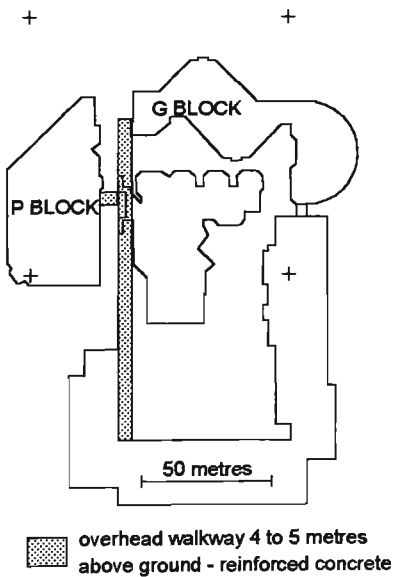
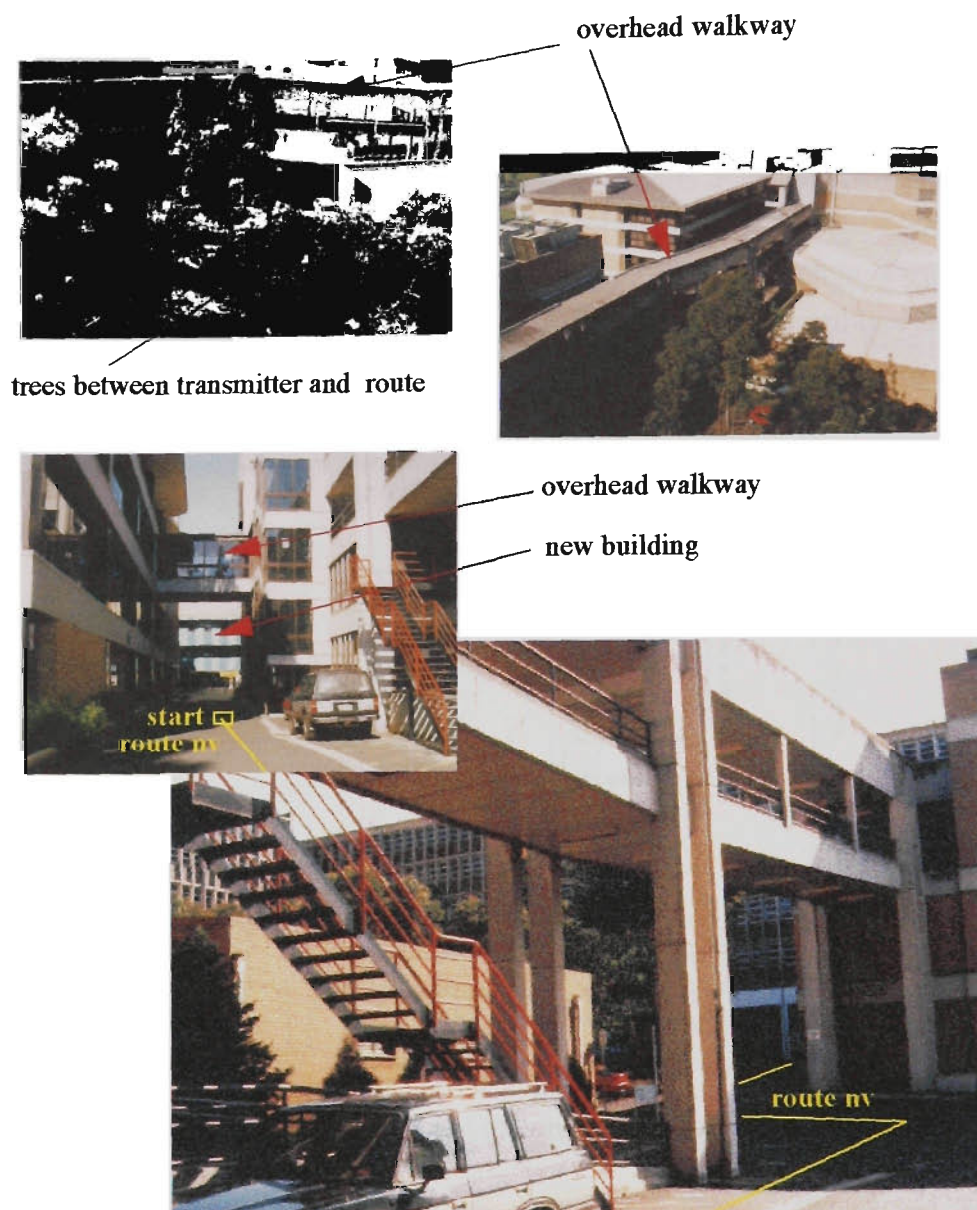


FIGURE 4.19 VUT Campus showing overhead walkways

Photos depicting the elevated structures suspected of increasing measured delay

spreads, are shown in Figure 4.20. These photos show how the real environment has been very simplified in the 2D raytracing plan shown in Figure 4.18.



**FIGURE 4.20** Victoria University of Technology campus route *nv*, showing overhead structures

#### 4. 1.10.1 Convergence of X-Ray Simulations on Route *nv* - Power

Difficulties with the *X-Ray* program restricted simulations for this route to just three runs, with parameter combinations of [reflections,transmissions,diffractions] equal to [3,0,0], [3,2,0], and [3,0,1].

Resulting simulated power values along the route are shown in Figure 4.21.



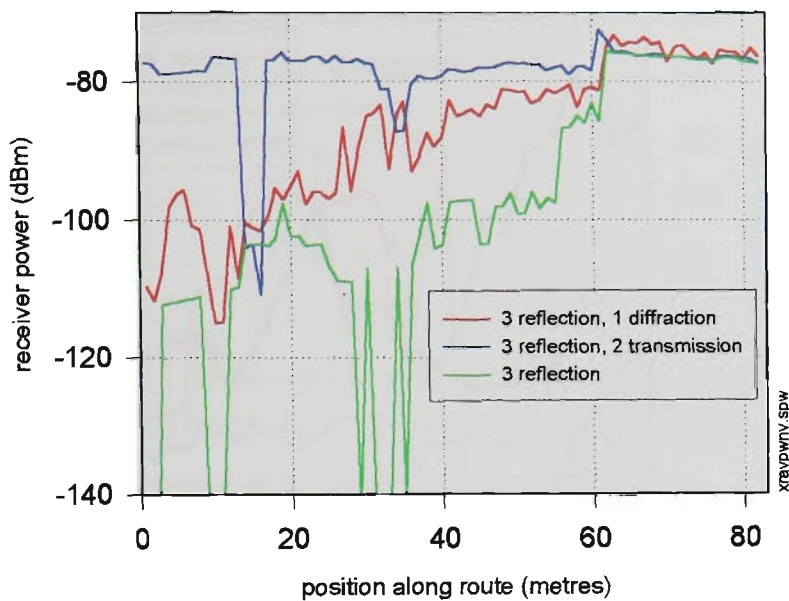


FIGURE 4.21 X-Ray simulated receiver power for route *nv*

In the ray tracing plan, all walls have been assigned a nominal thickness of 0.3 metre. Where buildings are simply shown as an outline plan with no internal structure, which is the case in this study (see Figure 4.18), *X-Ray* treats the building as hollow and empty, and the additional path loss for transmission through the entire building is calculated as two wall losses. The start of route *nv* is separated from the transmitter position by two walls, so the simulation which includes two wall transmissions shows a high power level for the initial part of the route. This over-estimate is a result of simplification of the building data base, resulting in buildings being treated as empty hollow shells. Rays will pass through such buildings if two wall transmissions are allowed. Introducing internal walls would prevent this.

Insufficient combinations of parameters are available to draw any conclusions about convergence. However, including one order of diffraction fills in the power drop-outs which occur for the [3,0,0] case.

4. 1.10.2 X-Ray Simulations on Route *nv* - Delay Spread

The general trend for *X-Ray* configuration [3,0,1] follows measured values over the second half of the route (Figure 4.22), but deviates considerably at the start of the route, where overhead structures which were not included in the 2D ray tracing data base intrude into the propagation environment. Trees obscure most of the route, but have also not been included in the ray tracing plan.

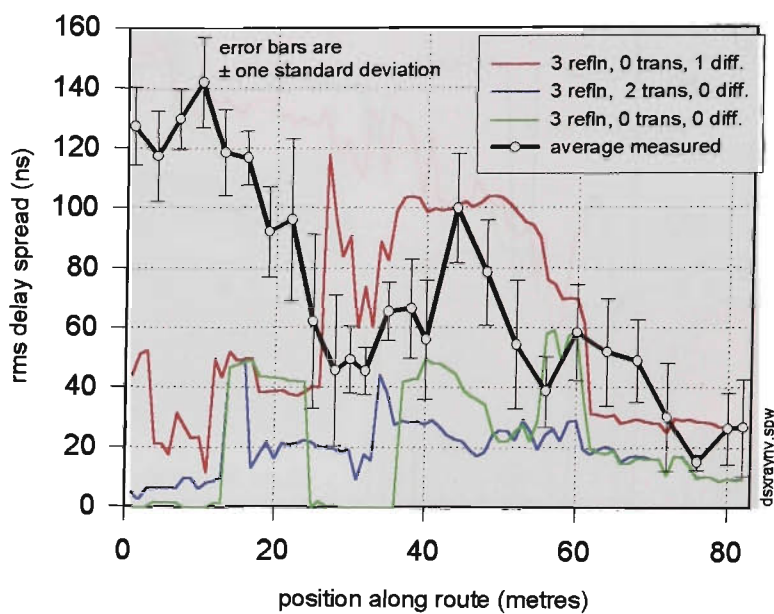


FIGURE 4.22 *X-Ray* and measured rms delay spread for route *nv*

4. 1.10.3 MCS™ Simulations on Route *nv* - Delay Spread

*MCS™* predicts the measured delay spread well over the last third of the route (Figure 4.23), but underestimates the earlier sections, as *X-Ray* also does.

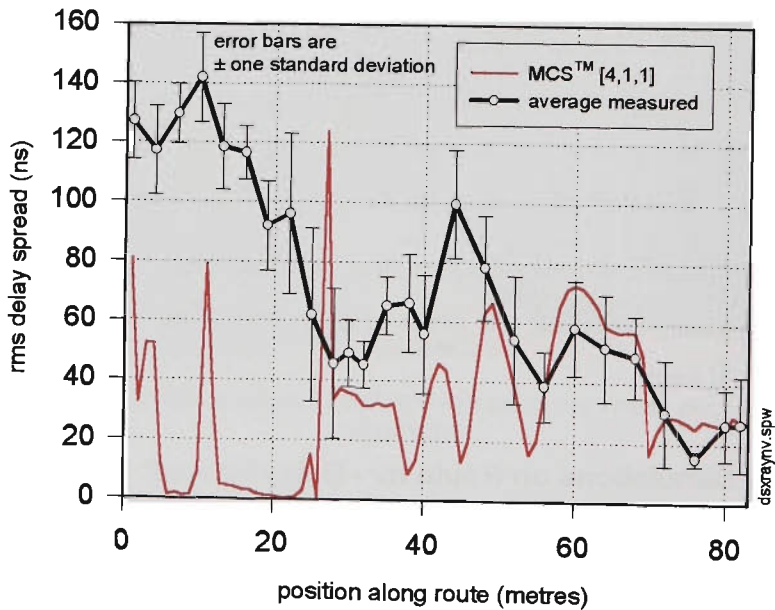


FIGURE 4.23 *MCS™* and measured rms delay spread for route *nv*

The rms error measure defined in EQ.4.1 has been used to compare measured and simulated delay spreads, with the result shown in Table 4.3. The average of all measured delay spread values over the whole route is 100.9 ns, and the best rms error value of 53.7 ns, obtained with *X-Ray* [3,0,1], is 53% of the overall average.

TABLE 4.3 rms error values for route *nv*

Ray tracing simulation	rms error (ns)
<i>X-Ray</i> [3,0,1]	53.7
<i>MCS</i> <sup>TM</sup> [4,1,1]	62.4
<i>X-Ray</i> [3,2,0]	66.0
<i>X-Ray</i> [3,0,0]	67.6

Finally, the overall route delay spread CDFs are compared in Figure 4.24, and on this basis, together with the rms error values shown in Table 4.3, the *X-ray* [3,0,1] simulation is judged to be the best approximation to the measured values.

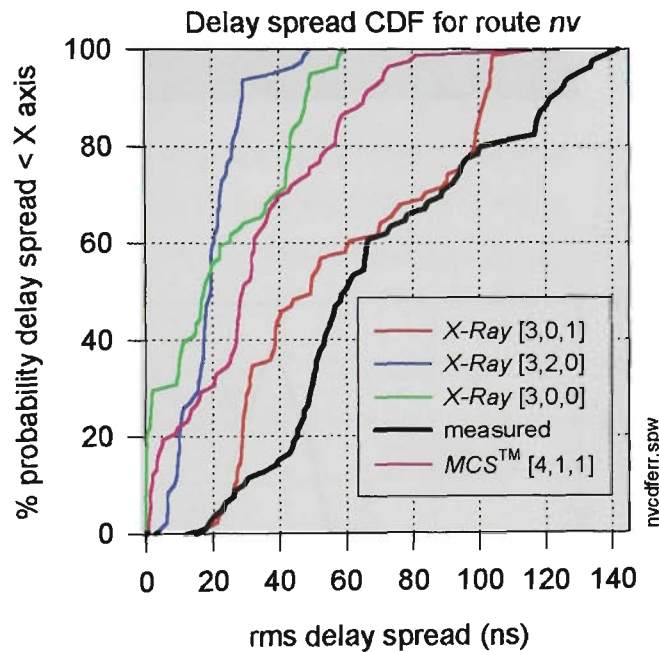


FIGURE 4.24 Distributions of average measured, *X-Ray* and *MCS*<sup>TM</sup> ray tracing delay spreads for route *nv*

4. 1.10.4 Convergence of *X-Ray* Simulations on Route *m* - Power

Parameter combinations of [3,0,0], [3,1,0], and [3,0,2] were used in *X-Ray* simulations for route *m*, with results depicted in Figure 4.26. All of route *m* is LOS, and agreement between the power simulations with different parameter combinations is better than 1 dB over the first half of the route, and within  $\pm 4$  dB over the remainder of the route. At position 42 metres, a power peak occurs as the receiver passes close to the transmitter.

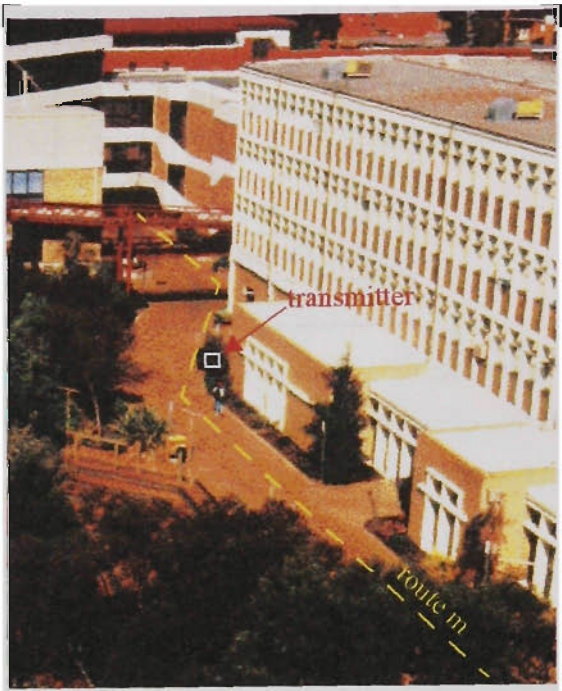


FIGURE 4.25 The location of route *m*

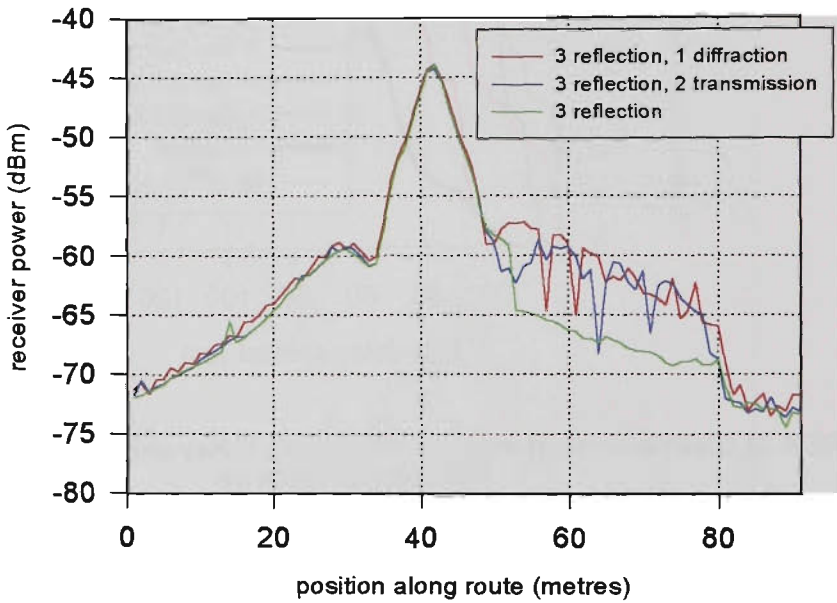


FIGURE 4.26 X-Ray simulated receiver power for route *m*

4. 1.10.5 X-Ray Simulations on Route *m* - Delay Spread

This route is all LOS, and passes close to the transmitter at the 43 metre point.

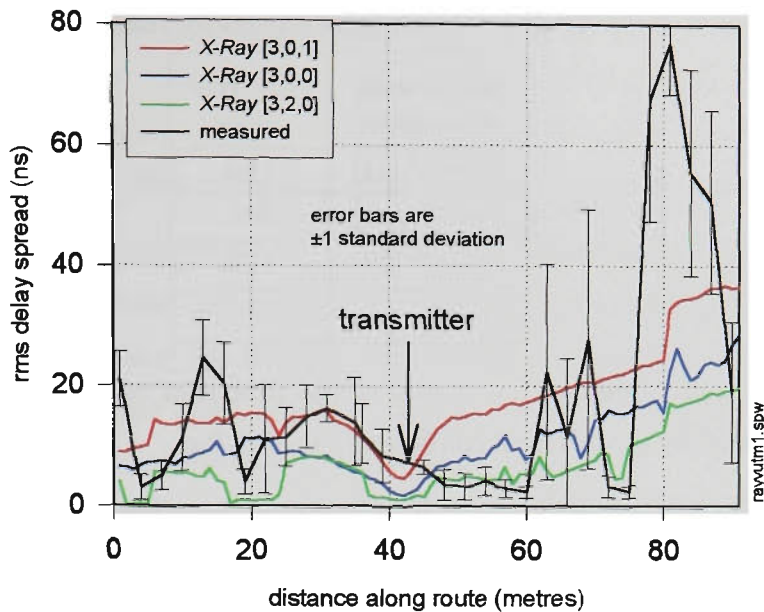


FIGURE 4.27 X-Ray and measured rms delay spread for route *m*

The *X-Ray* simulation with 3 reflections and one diffraction [3,0,1] tracks measured values, except for the section of route just after the transmitter (46 to 62 metres), and the section around 80 metres where the average measured delay spread peaks to 77 ns (Figure 4.27).

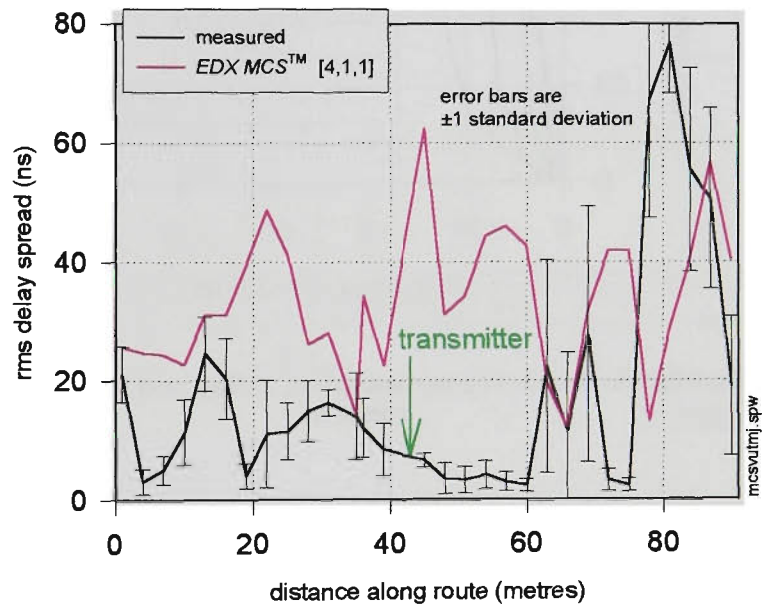


FIGURE 4.28 MCS™ and measured rms delay spread for route *m*

Figure 4.28 above, shows little apparent agreement between MCS™ and measured delay spread values.

Table 4.4 gives the rms error (defined in EQ4.1) based on all measured values. On this test, the best result is produced by *X-Ray* with the [3,0,1] configuration, with an rms error of 18.4 ns. The average of all measured delay spreads for the entire route is 17.9 ns, and in comparison to this, the rms error values for all ray tracing attempts are large. The rms error



value for *X-Ray* [3,0,1] is 103% of the whole route average measured delay spread.

TABLE 4.4 rms error values for route *m*

Ray tracing simulation	rms error (ns)
<i>X-Ray</i> [3,0,1]	18.4
<i>X-Ray</i> [3,2,0]	20.0
<i>X-Ray</i> [3,0,0]	21.6
<i>MCS</i> <sup>TM</sup> [4,1,1]	30.1

It is also noticeable that ray tracing results produced by *MCS*<sup>TM</sup> differ dramatically from those produced by the different configurations of *X-Ray*.

The CDFs of delay spreads over the whole route have been plotted in Figure 4.35.

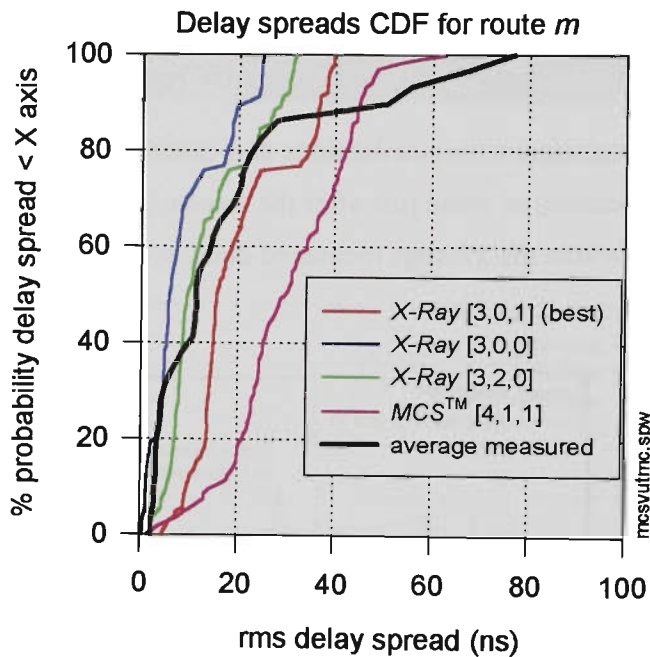


FIGURE 4.29 Distributions of average measured, *X-Ray* and *MCS*<sup>TM</sup> delay spreads over route *m*.

## 4. 2 Multipath Propagation Between Floors

### 4. 2.1 Introduction

For this section, the transmitter was situated on the top floor (Level 7) of the *Engineering Faculty* D Block building, located in a large lecture room, one metre inside a row of east facing outside windows with a view to adjacent campus buildings. Propagation between floors in D Block via reflected paths from other campus buildings was thus a possibility. A plan of the campus is shown in Figure 4.18, and a plan of Level 7 Building D, indicating the

new transmitter location and the receiver route is shown in Figure 4.30.

Lower floors of the building (Levels 5, 4 and 3) have the same corridor plan, and measurement locations on these levels were confined to the central corridor. The transmitter remained in the same position on Level 7 for all measurements on lower floors. An open doorway connected the lecture room housing the transmitter with the central corridor.

Measured PDPs were processed to identify the individual rays, within the resolution of the sounder (see programs *RAYS*, *RAYSORT* and *RAYBIN* in Appendix D). The distribution of rms delay spreads was found to be quite different for the transmitter floor, compared with the lower floors, where delay spreads were up to 8 times as large. On the lower floors, typically a number of rays arrived ahead of the strongest ray.

Distributions of the number of rays per PDP for different thresholds are given for each floor. The average total number of resolvable rays per PDP was found to be proportional to the threshold, and this held for all floors, although the constant of proportionality varied, with up to 2.5 times as many rays per PDP on the lower floors, compared with Level 7.

The distribution of rays in time and amplitude bins is also shown for each floor.

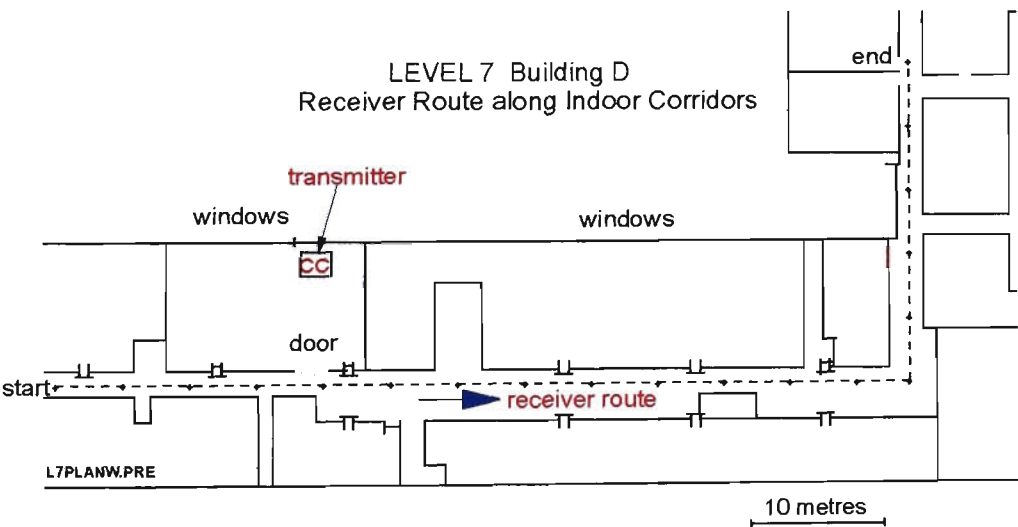


**FIGURE 4.30 Level 7 route, showing transmitter location near windows**

Figure 4.31 gives the cumulative distribution of delay spreads on Level 7, for the two different transmitter locations; the window location used for this section, and the lift lobby location used for the ray tracing validation measurements in the previous section. The distributions are very similar apart from the high delay spread tail, where the lift lobby location gives higher values.

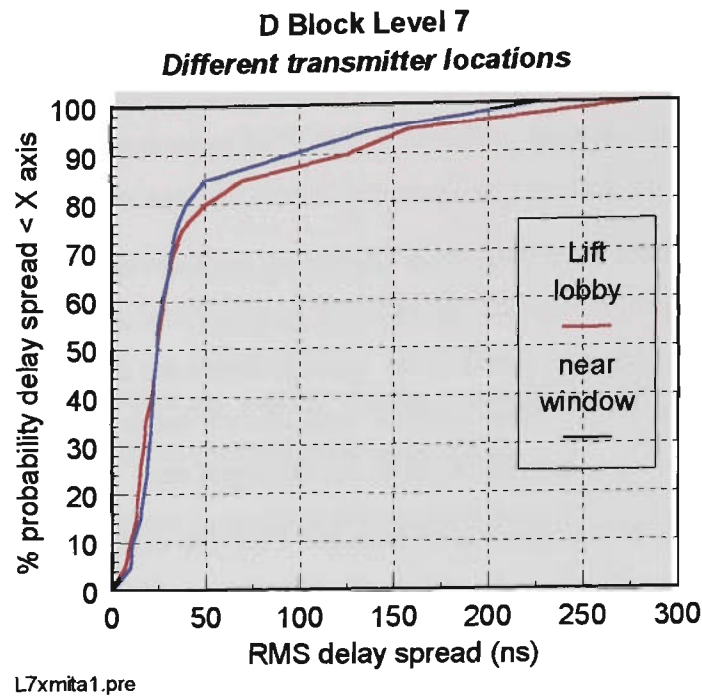


**FIGURE 4.31** Delay spread CDFs for different transmitter locations - Level 7

Cumulative distributions of delay spread for the four different floors are shown in Figure 4.32. Curves for the lower floors, Levels 3, 4, and 5 are broadly similar, and exhibit much higher values of delay spread (approximately 8 times as high), than for Level 7, the floor where the transmitter is located.

**TABLE 4.5** Delay spread on different floors, with transmitter on Level 7

rms delay spread (ns)				
	Level 7	Level 5	Level 4	Level 3
median	24	260	210	180
< 95%	135	430	440	290

The worst case on Level 5 has a delay spread of 475 ns, and the PDP for this delay spread shows a 0 dB path delayed by 1  $\mu$ s. A 1  $\mu$ s delay requires a return path length difference of 300 metre, corresponding to a reflection from an external object at 150 metre. Such paths have already been discussed in Section 4.1.9.3. For comparison, measurements in three different high rise buildings are discussed in Ref[4.22], with overall median delay spreads in the range 70 to 90 nS, and maximum rms delay spreads of 440, 507 and 1470 ns. In all cases these maximums also occurred when the transmitter and receiver were on different floors.



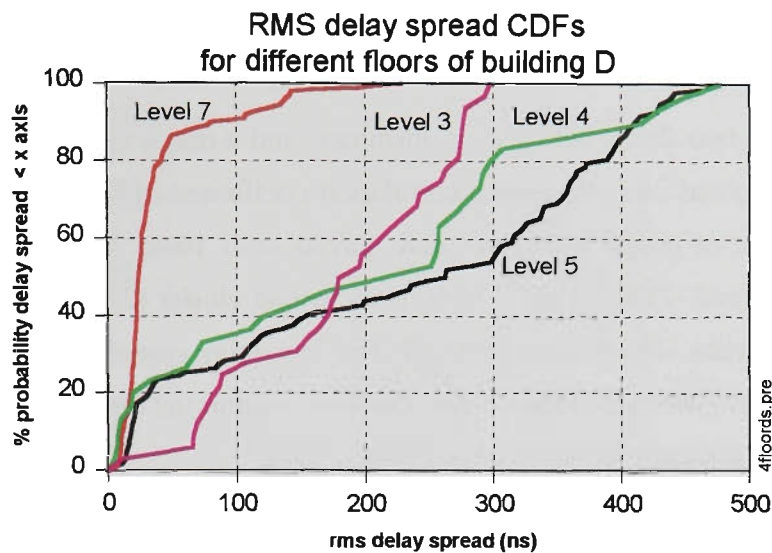


FIGURE 4.32 Delay spread CDFs for different floors of building

4. 2.2 Delay Spread Versus Path Loss

Figures 4.33 and 4.34 plot the logarithm of delay spread versus *path loss factor* for Levels 7 and 5. The *path loss factor* is the attenuation required in series with a back-to-back cable connection between the transmitter output and receiver input to achieve the same strongest-path power at the receiver output. Hence it is related to path loss, but does not include allowance for antenna gains.

A general trend for delay spread to increase with path loss factor is evident, but is weakly correlated.

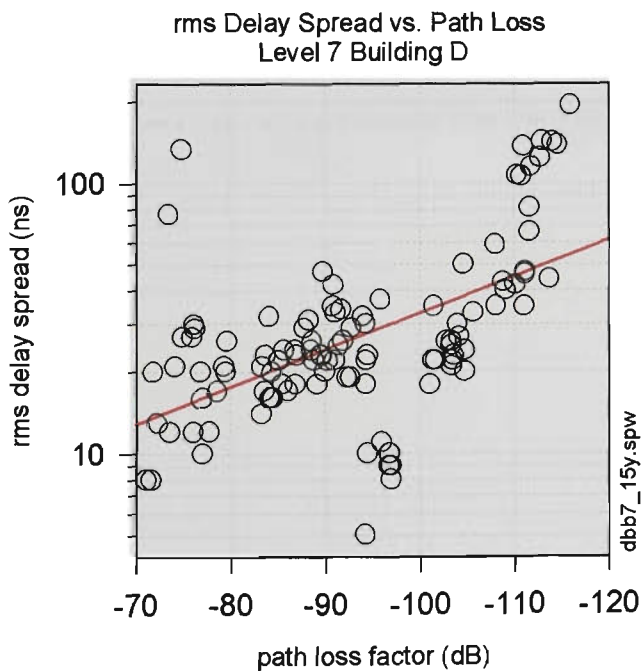
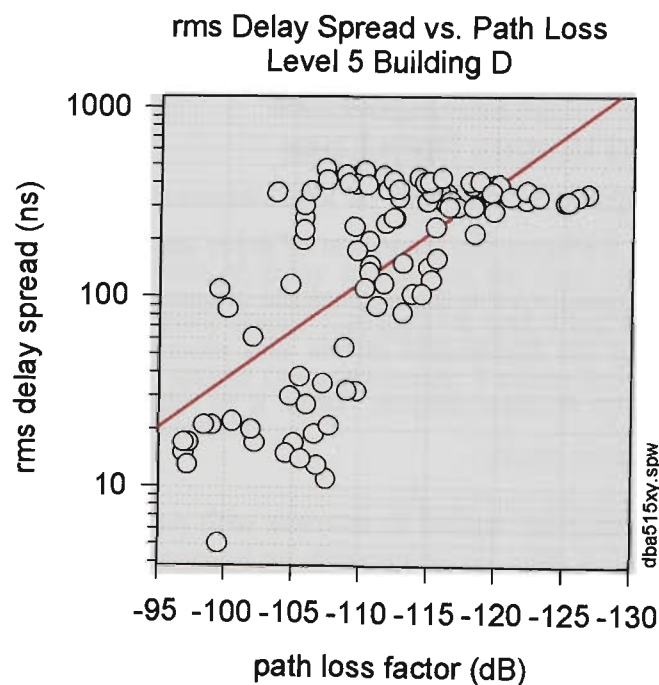


FIGURE 4.33 Delay spread versus path loss factor - Level 7 with transmitter on the same floor

For Level 7, where the transmitter and receiver were on the same floor (median delay spread 24 ns), the linear regression correlation factor between the common logarithm of delay spread and dB path loss factor is a low 0.3 (Figure 4.33).

Level 5, two floors below the transmitter, and a much more dispersive environment (median delay spread 260 ns) gives a correlation coefficient of 0.47. The plot (Figure 4.34) features a cluster of points with low delay spread from 10 to 30 ns, and path loss factors between -95 dB and -110 dB, and a high delay spread cluster (200 to 500 ns) at higher path loss factors, between -105 dB and -130 dB. The low delay spread cluster are likely to represent rays travelling through floors or via stair wells within the building, while the high delay spread cluster represent scatterers outside the building.



**FIGURE 4.34** Delay spread versus path loss factor - Level 5 with transmitter two floors above

### 4. 2.3 Average Delay versus Delay Spread

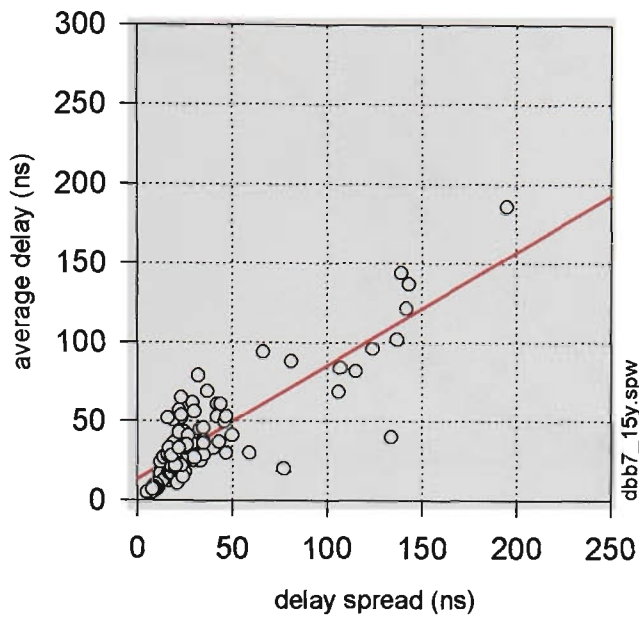


**FIGURE 4.35 Average delay versus delay spread - Level 7**

Average delay and delay spread tend to be related {Ref[4.23]}. For the same floor, Level 7 (Figure 4.35), a linear regression with a correlation coefficient of 0.7 has the equation:

$$D_{avg} = 14 + 0.72 \, ds_{rms} \text{ nanoseconds}$$

(EQ 4.2)

where  $D_{avg}$  is the average excess delay and  $ds_{rms}$  is the rms delay spread

For the more dispersive Level 5, two floors below the transmitter, average delay is not even approximately linearly related to delay spread. The linear regression line on Figure 4.36 has a low correlation coefficient of 0.32.

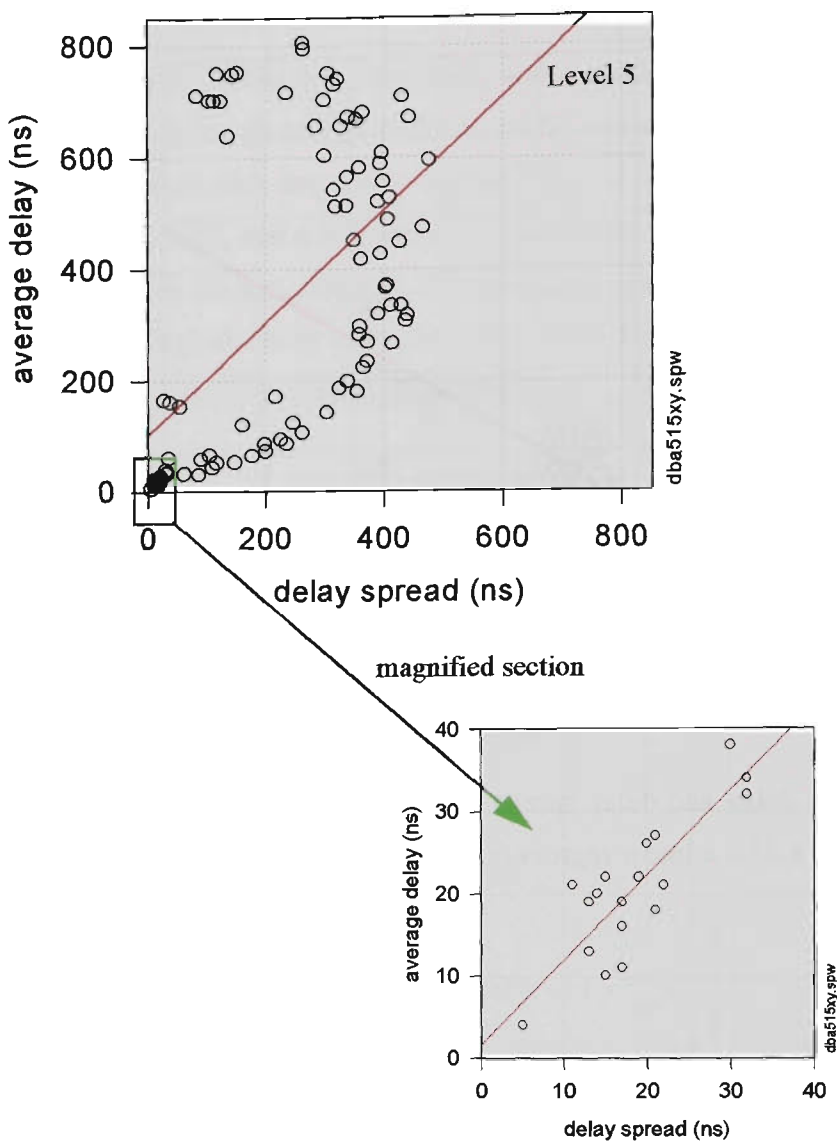


**FIGURE 4.36 Relation between average delay and delay spread - Level 5**

However, the cluster of points near the origin (Figure 4.36) does follow a linear trend, with a correlation coefficient of 0.71, given by the equation:

$$D_{avg} = 1.7 + 1.03 ds_{rms} \text{ nanoseconds} \tag{EQ 4.3}$$

These rays are likely to be short path through-floor or stairwell rays, as discussed earlier.

What sort of PDP results in an average delay several times greater than the delay spread, such as shown in Figure 4.36? The following example provides one answer.

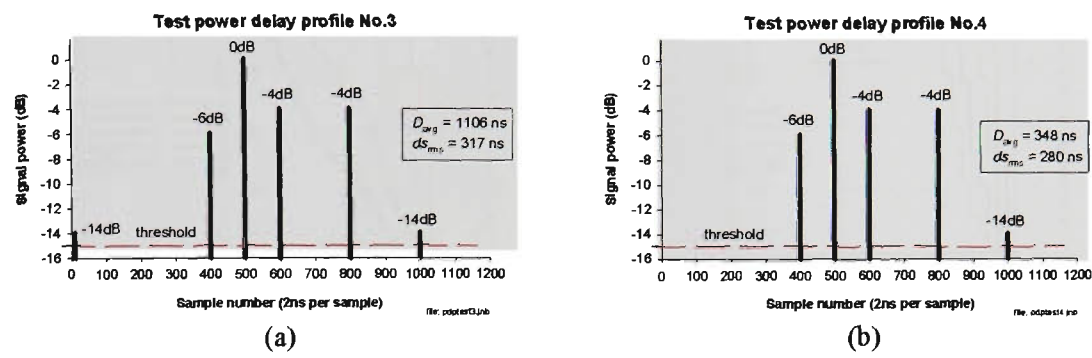


FIGURE 4.37 Illustrating a PDP with high  $D_{avg}/ds_{rms}$  ratio

For the calculation of average delay, the first above-threshold ray (threshold = -15dB) is taken as the zero time origin. In Figure 4.37(a), the -14dB ray at sample 1 becomes the time reference, and the average delay value is high because of the powerful cluster of rays between samples 500 and 800. However the early -14dB ray does not have much influence on the delay spread, because of the concentration of strong rays around sample 500. The average delay is 1106 ns, and the rms delay spread is 317 ns, a ratio of 3.49. Figure 4.37(b) is the same as (a) except for the disappearance of the early -14dB ray; now the -6dB ray at sample 400 becomes the time origin for the average delay calculation, which reduces markedly, to 348 ns. The delay spread falls a little, to 280 ns, giving a ratio of 1.24.

A characteristic of propagation to Level 5 is the presence of a number of rays preceding the strongest ray, giving PDPs of the type typified by Figure 4.37(a). Propagation on Level 7 (the same floor as the transmitter) or in typical outdoor situations, gives PDPs more like Figure 4.37(b), where the first arriving ray is generally also the strongest ray.

### 4. 2.4 Number of Rays in Each Power Delay Profile

A path or ray is defined as any sample in the profile with two prior monotonically increasing samples, and two monotonically decreasing samples following. The total number of paths (within the 10ns time resolution of the channel sounder) between -1μs and +5μs, including the strongest path, are counted for threshold levels of -5, -10, -15, -25 and -30dB, and plotted as cumulative distributions in Figure 4.38 for Levels 7, 5, 4, and 3. If the noise floor for a particular PDP is higher than the threshold level chosen, then only rays above the noise floor have been counted. Median and maximum numbers of rays are tabulated in Table 4.6.

A similar approach to this has been applied to outdoor propagation in Ref[4.24].

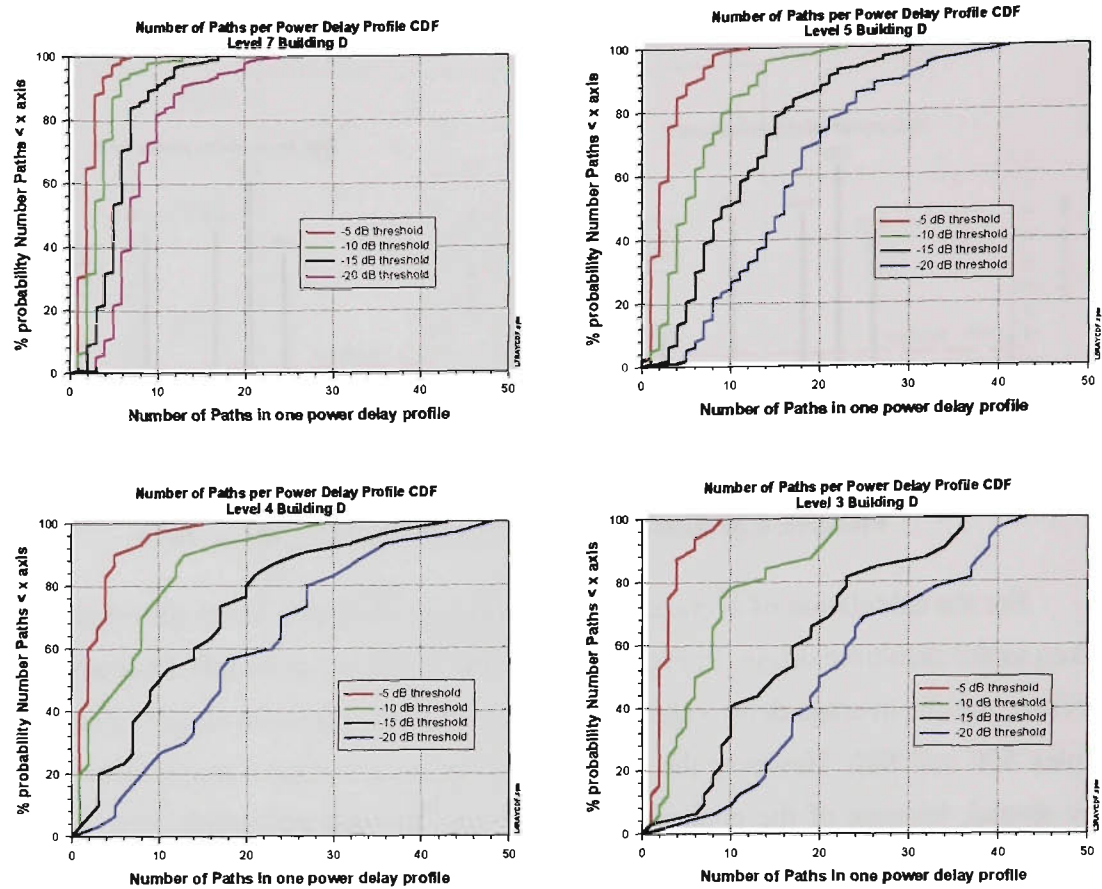


FIGURE 4.38 CDF of number of rays in one PDP on Levels 7, 5, 4 and 3

Table 4.6 summarises some statistics for numbers of rays at different thresholds, and on different floors.

TABLE 4.6 Number of rays per PDP

	Level 7	Level 5	Level 4	Level 3
-5dB median	2	2	2	2
-10dB median	3	5	6	6
-15dB median	5	10	10	15
-20dB median	7	16	17	20
-5dB maximum	7	12	15	9
-10dB maximum	13	23	29	22
-15dB maximum	17	30	43	36
-20dB maximum	24	41	48	43

Plotting the average total number of above-threshold rays per PDP, as a function of threshold level, and as a function of the floor or level in the building, gives Figure 4.39. As the threshold is reduced, the number of rays comprising the PDP increases because weaker rays are being added to the aggregate.



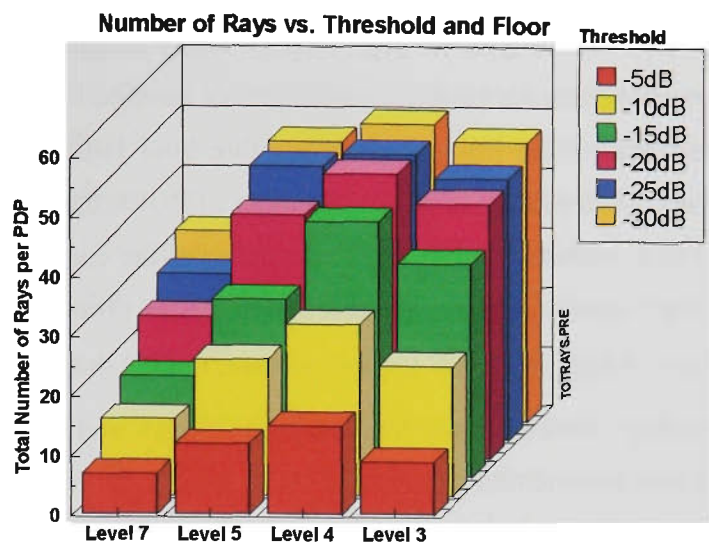


FIGURE 4.39 Average total rays per PDP vs. threshold, and building floor

Figure 4.39 suggests that for the higher thresholds (-5dB, -10dB, etc.) the average total number of rays per impulse response is proportional to the dB threshold value. Replotting the data in Figure 4.40 shows this more clearly:

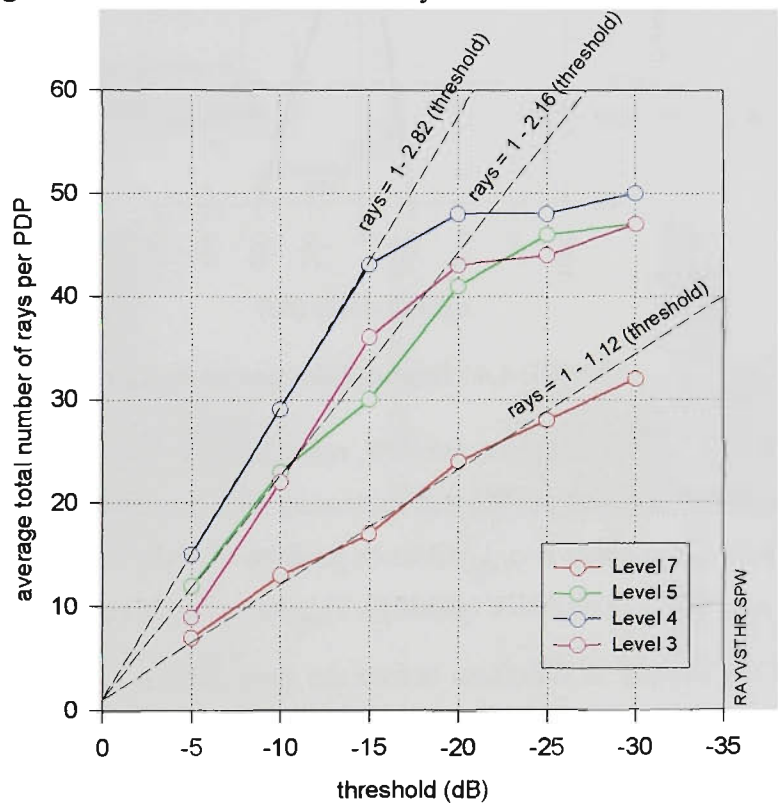


FIGURE 4.40 Approximations to average total rays per PDP

With 0dB threshold, one ray (the 0dB ray) will always be present. *Level 7* shows a close approximation to a linear relationship, and with lower floors the relationship is approximately linear down to thresholds in the -15dB to -20dB area, but with a steeper slope. The linear approximation for *Level 5* is accurate to within 1.4dB down to -20dB threshold, and *Level 3* is within 1.1dB down to -20dB. The *Level 4* approximation is a close fit to -15dB, but departs by 3.3dB at -20dB.

When searching for rays in the PDP, a noise threshold is applied, based on an estimate of the actual noise in the profile, plus a safety factor margin. Rays with power values below the noise threshold are not counted, which places an upper limit on the total number of valid rays in a particular PDP, reached when the threshold falls to the noise floor. As the threshold hits the noise floor for an increasing number of PDPs, the mean total number of rays per PDP will tend to a saturation value; this is the cause of the curves in Figure 4.40 tending to flatten out at high numbers of rays. The effect is more pronounced for building levels below the transmitter, where the signal level is weaker, raising the relative noise floor.

Proportionality between mean total number of rays and threshold implies that the PDP shape is a falling exponential in terms of linear power, or linear in terms of dB power, and that the average number of rays per unit excess delay is constant.

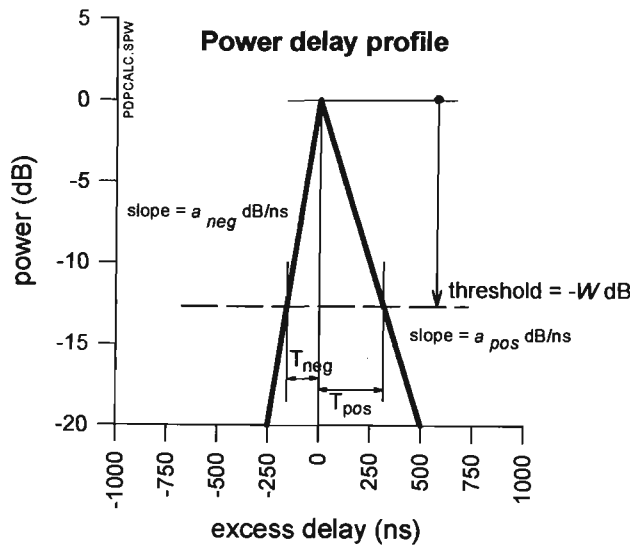


FIGURE 4.41 Exponential power delay profile

Figure 4.41 shows a continuous PDP, made up of a conglomerate of uniformly time-spaced rays, and with a power profile that increases, then decreases, exponentially. The slope for the rising part of the curve is  $a_{neg}$  dB/ns (a positive quantity), while the slope for the falling portion is  $a_{pos}$  dB/ns (a negative quantity).  $T_{neg}$  has a negative value.

If the ray density is  $r$  rays/ns before the peak, and  $p$  rays/ns after the peak, for a threshold of  $-W$  dB (where  $W$  is positive):

$$\text{total number of rays} = -rT_{neg} + pT_{pos} \quad (\text{EQ 4.4})$$

$$\text{but} \quad T_{neg} = -\frac{W}{a_{neg}} \quad \text{and} \quad T_{pos} = \frac{W}{a_{pos}}$$

$$\text{hence} \quad \text{total number of rays} = W \left( \frac{r}{a_{neg}} + \frac{p}{a_{pos}} \right) \quad (\text{EQ 4.5})$$

showing that the total number of rays is proportional to  $W$ , the dB threshold.



### 4.2.5 Number of Paths Sorted Into Power and Time Bins

Each ray found is sorted into a time and power bin. Each time bin is 200 ns wide, with four time bins preceding the strongest ray (the time reference), and six time bins following the strongest ray. Note that the strongest ray (0 ns, 0dB), to which the PDP is normalized, is excluded from the count. All other rays within the section of the PDP between -400 ns and +1200 ns (relative to the 0dB ray), are included.

Because the time bins are much larger than the resolution of the sounder, it is possible for more than one ray to be sorted into each bin. Each time bin is subdivided into four 5dB wide power bands; 0 to  $\geq -5$  dB,  $< -5$  dB to  $\geq -10$  dB, etc. down to -20 dB. This gives a total of 40 bins, and each ray can only be counted in one bin.

Histograms of the average number of rays or paths per PDP in each bin are shown in Figure 4.42. Significant numbers of rays arrive ahead of the strongest path, especially on the lower floors, because of attenuated wall and floor transmission rays arriving ahead of stronger rays from outdoor reflectors or diffractors. In outdoor propagation measurements, it is unusual to see much activity prior to the strongest path.

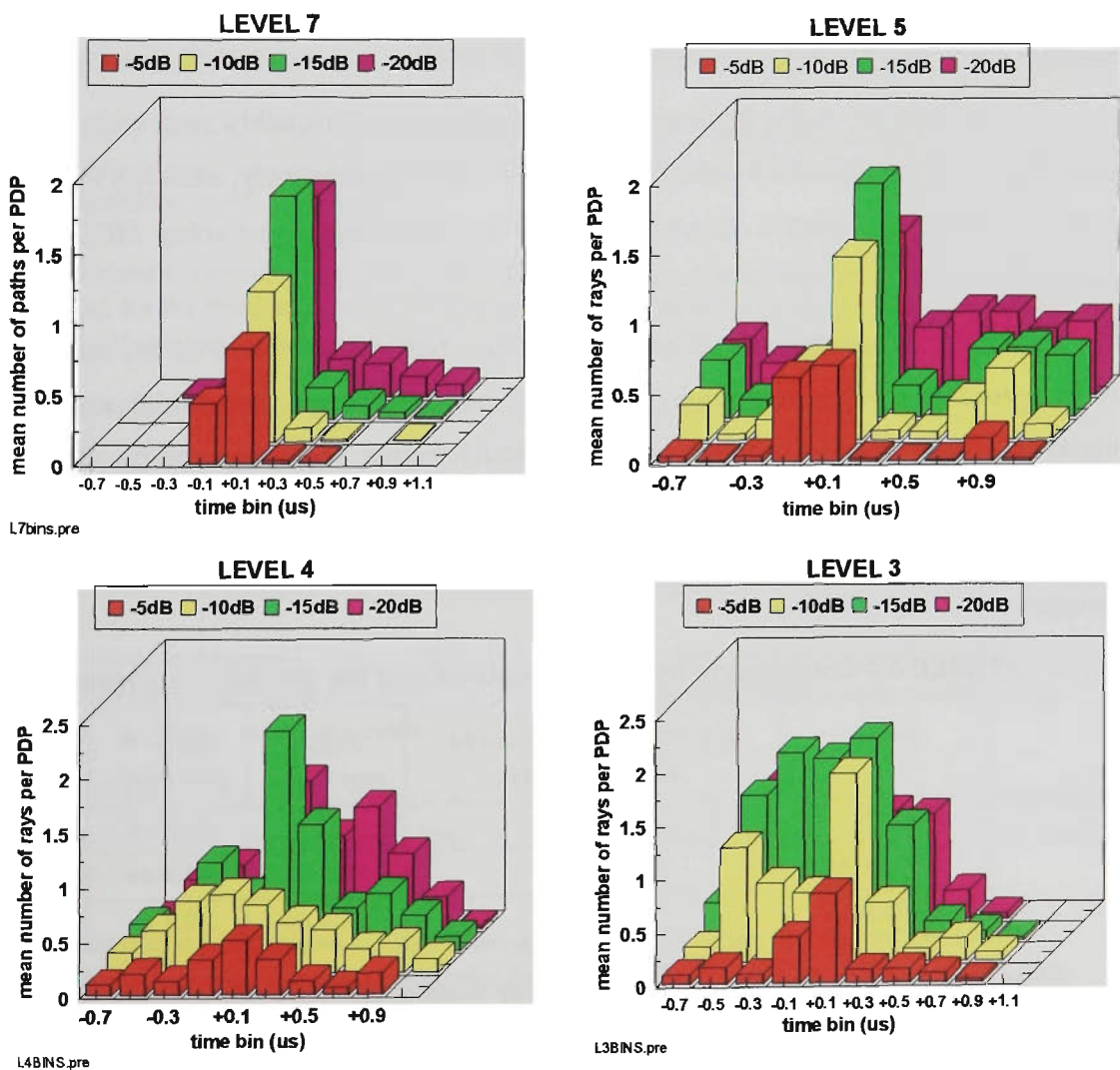


FIGURE 4.42 Average number of rays per PDP sorted by power and delay

### 4.3 Conclusions

The ray tracing model *X-Ray* was tested over an indoor route, and two outdoor courtyard routes, using different combinations of numbers of reflections, wall transmissions and diffractions. Testing with all combinations of these parameters was not possible because of software limitations. For the indoor route, fourteen different combinations were used, while only three combinations were used for each outdoor route. Over LOS sections of the routes, simulated receiver power values converged well, to within several dB, irrespective of the parameter combination used. Over NLOS sections of routes, simulated receiver power varied by large amounts, typically 20 to 30 dB, but much greater at some points. Signals did not reach into the end section of the indoor route (BB, Figure 4.3) which is around two 90° corners from the transmitter, unless 2 diffractions, or 4 wall transmissions were included.

Measured delay spreads were compared with *X-Ray* and *MCS*<sup>TM</sup> (v1.0) simulated values, using an rms error measure, and using plots of cumulative distributions. Measurements indoors revealed scattering originating outside the building, giving high values of delay spread. Ray tracing simulations were confined by the building plan to internal scattering. By applying a range limit to the measured signals, good agreement with *X-Ray* was obtained provided that 2 diffractions and 2 or 3 reflections were used.

Delay spreads on the outdoor LOS route *m* agreed reasonably well with the *X-Ray* model using 1 diffraction and 3 reflections. *MCS*<sup>TM</sup> performed poorly, although the problem of not being able to define a threshold window makes comparisons using *MCS*<sup>TM</sup> almost meaningless.

Most of the outdoor route *nv* was NLOS. Over the last 65% of the route, delay spreads agreed well with *X-Ray* using 3 reflections and 1 diffraction. The initial portion of the route gave measured delay spreads consistently much higher than simulated ray tracing values. The area contained complex structures which could not be included in the ray tracing plan, and this combined with intervening trees and foliage provides a possible reason for the discrepancy.

**TABLE 4.7 Comparison between measured and ray tracing delay spreads**

route	average of all measured delay spreads	<i>X-Ray</i> rms error	<i>MCS</i> <sup>TM</sup> rms error
indoor	24 ns	8.5 ns	13.2 ns
outdoor <i>nv</i>	101 ns	53.7 ns	62.4 ns
outdoor <i>m</i>	18 ns	18.4 ns	30.1 ns

For best results, it has been found that ray tracing models must utilise 2 to 3 reflections, and 1 or 2 onward -propagating orders of diffraction. If ray tracing models are applied indoors, the database plan should extend well beyond the building, to include external scatterers.

In view of the uncertainty in the estimates used for building material electrical properties, simplifications and omissions made with ray tracing plans, and the 2D limitation of the ray tracing software, it is perhaps surprising that ray tracing simulations can produce useful estimates of delay spreads.

Propagation measurements between floors of a multi-floor building show a marked increase (approximately eight-fold) in delay spread values on floors other than the transmitter floor. On other floors there is also an increase in the number of rays, and a tendency for attenuated rays to arrive ahead of the strongest ray. The early attenuated rays are postulated to be fairly direct internal rays arriving through floors or via stairwells, while the strongest ray arrives via reflection or diffraction external to the building.

The number of rays in a PDP was found to be proportional to the threshold used, implying that on average the PDP is exponential with a uniform number of rays per unit excess delay.

## 4.4 References - Chapter 4

- [4.1] Ulrich Dersch & E.Zollinger, "Propagation Mechanisms in MicroCell and Indoor Environments", IEEE Trans. on Vehicular Technology, Vol.43, No.4, November 1994, pp.1-23.
- [4.2] Scott Y.Seidel, Theodore S.Rappaport, "Site-Specific Propagation Prediction for Wireless In-Building Personal Communication System Design", IEEE Trans. on Vehicular Technology, Vol.43, No.4, November 1994, pp.874-891.
- [4.3] Michael C.Lawton, J.P.McGeehan, "The Application of a Deterministic Ray Launching Algorithm for the Prediction of Radio Channel Characteristics in Small-Cell Environments", IEEE Trans. on Vehicular Technology, Vol.43, No.4, November, 1994, pp.955-969.
- [4.4] Harry R.Anderson, "A Second Generation 3-D Ray-Tracing Model Using Rough Surface Scattering", Proc. IEEE 46th.Vehicular Technology Conference, Atlanta USA, April-May 1996, pp.46-50.
- [4.5] Zhongrong Liu, Wolf Mende, "Modelling Microcellular Radio Wave Propagation", Proc. IEEE 46th. Vehicular Technology Conference, Atlanta USA, April-May 1996, pp1278-1282.
- [4.6] Walter Honcharenko, Henry L.Bertoni, J.L.Dailing, J.Qian, H.D.Yee, "Mechanisms Governing UHF Propagation on Single Floors in Modern Office Buildings", IEEE Trans. on Vehicular Technology, Vol.41, No.4, November 1992, pp.496-504.
- [4.7] G.E.Athanasiadou, A.R.Nix, J.P.McGeehan, "A Ray Tracing Algorithm for Microcellular Wideband Propagation Modelling", Proc. IEEE 45th. Vehicular Technology Conference, Vol.1, July 1995, pp.261-264.
- [4.8] Reinaldo A.Valenzuela, "A Ray Tracing Approach to Predicting Indoor Wireless Transmission", Proc. IEEE 43rd. Vehicular Technology Conference, May 1993, pp.214-218.
- [4.9] Dieter J.Cichon, Torsten C. Becker, Martin Dottling, "Ray Optical Prediction of Outdoor and Indoor Coverage in Urban Macro- and Micro-Cells", Proc. IEEE 46th Vehicular Technology Conference, Atlanta USA, April-May 1996, pp.41-45.

- 
- [4.10] Kurt R.Schaubach, Nathaniel J.Davis IV & Theodore S.Rappaport, "A Ray Tracing Method for Predicting Path Loss and Delay Spread in Microcellular Environments", Proc. IEEE 42nd. Vehicular Technology Conference, 1992, pp.932-942.
- [4.11] Scott Y.Seidel, Kurt R.Schaubach, Thomas T.Tran & Theodore Rappaport, "Research in Site-Specific Propagation Modeling for PCS System Design", Proc. IEEE 43rd.Vehicular Technology Conference, May 1993, pp.261-264.
- [4.12] Jeane-Pierre Rossi and Armand J.Levy, "Propagation Analysis in Cellular Environment with the Help of Models Using Ray Theory and GTD", Proc. IEEE 43rd.Vehicular Technology Conference, May 1993, pp.253-256.
- [4.13] K.Rizk, A.Mawira, J.-F.Wagen,F.Gardiol, "Propagation in Urban Microcells with High Rise Buildings", Proc. IEEE 46th. Vehicular Technology Conference, Atlanta USA, April-May 1996, pp.859-863.
- [4.14] EDX Engineering Inc., "User's Manual for Program *MCST*<sup>TM</sup>"
- [4.15] A.Nix, "X-Ray User Manual v1.1" , December 1995
- [4.16] K.J.Gladstone and J.P.McGeehan, "Computer simulation of multipath fading in the land mobile radio environment", IEE Proceedings. Pt.G, December 1980, pp.323-330.
- [4.17] K.J.Gladstone and J.P.McGeehan, "A computer simulation of the effect of fading on a quasi-synchronous sideband diversity AM mobile radio scheme", IEEE Journal on Selected Areas of Communications, SAC-2, January 1984, pp.191-203.
- [4.18] M.C.Lawton, R.L.Davies & J.P.McGeehan, "An Analytical Model for Indoor Multipath Propagation in the Picocellular Environment", Proc. IEE 6th. Int. Conf. Mobile Radio and Personal Communications UK, December 1991, pp.1-8.
- [4.19] M.C.Lawton and J.P.McGeehan, "The Application of GTD and Ray Launching Techniques to Channel Modelling for Cordless Radio Systems", IEEE Proc. 42nd. Vehicular Technology Conference, Denver, USA, May 1992, pp.125-130.
- [4.20] S.Jenvey, "Ray Optics Modelling for Indoor Propagation at 1.8 GHz", Proc. IEEE 44th. Vehicular Technology Conference, Vol.3, 1994, pp.1750-1753.
- [4.21] J.D.Parsons, "The Mobile Radio Propagation Channel", Pentech Press, London, 1992, pp.161-164.
- [4.22] Scott Y.Seidel, Theodore S.Rappaport, Martin J.Feuerstein, Kenneth L.Blackard & Limond Grindstaff, "The Impact of Surrounding Buildings on Propagation for Wireless In-Building Personal Communications System Design", IEEE JSAC Special Issue on Wireless Personal Comms, 1992, pp.1-35.
- [4.23] J.D.Parsons & J.G.Gardiner, "Mobile Communications Systems", Blackie, Glasgow and London, 1989, pp.59-63.
- [4.24] Jeffery A.Wepman, J.Randy Hoffman & Lynette H.Loew, "Analysis of Impulse Response Measurements for PCS Channel Modelling Applications", IEEE Trans. on Vehicular Tech., Vol.44, No.3, August 1995, pp.613-621.
- [4.25] Theodore S.Rappaport, Joseph C.Liberti, Kenneth L.Blackard & Bruce Tuch, "The Effects of Antenna Gains and Polarization on Multipath Delay Spread and Path Loss at 918 MHz on Cross-campus Radio Links", IEEE VTC, 1992, pp.550-553.

- 
- [4.26] C.M.Peter Ho, Theodore S.Rappaport and M.Prabhakar Koushik, "Antenna Effects on Indoor Obstructed Wireless Channels and a Deterministic Image-Based Wide-Band Propagation Model for In-Building Personal Communication Systems", *Int .Journal of Wireless Information Networks*, Vol.1, No.1, 1994, pp.61-76.
- [4.27] University of Bristol (A.Nix), "Information paper on ACTS AWACS", ETSI Broadband Radio Access Networks No.1, April 1997, pp.1-12.
- [4.28] G.T. Martin and M. Faulkner, "Wide Band Propagation Measurements and Ray Tracing Simulations at 1890 MHz.". Published in the Proceedings 4th IEEE International Conference on Universal Personal Communications (ICUPC'95), November 6-10,1995 Tokyo Japan, pages 283-287
- [4.29] G.T. Martin, M. Faulkner and M.A.Beach\*, "Comparison of Delay Spread Measurements with Ray Tracing Simulations at 1890 MHz.". Published in the Proceedings of the 6th. IEEE International Conference on Personal, Indoor and Mobile Communications (PIMRC'95), September 27-29, 1995 Toronto Canada. (\* *University of Bristol*). Volume 3, pages 1156-1160.
- [4.30] G.T. Martin and M. Faulkner, "PCS Ray Characteristics Between Multiple Floors of a Concrete Building". Published in the Proceedings of the 47th. International IEEE Conference on Vehicular Technology (VTC'97), Phoenix USA, May 1997, Volume 3, pages 1400-1404.
- [4.31] G.T. Martin and M. Faulkner, "Wideband Propagation at 1890 MHz. in an Indoor Multistorey Concrete Building". Presented at the Workshop on Applications of Radio Science (WARS'95), June 25-27, 1995, Canberra, Australia.

# Chapter 5: Outdoor Measurements

## 5. INTRODUCTION

An outdoor wideband multipath propagation measurement program at 1.89GHz under Australian conditions was the major motivation and objective of the original proposal for this thesis project. At that stage (1992) no other Australian wideband outdoor propagation data had been published, and this is still believed to be the case at the completion of the research (June 2000).

Initial results of measurements covered in this chapter were presented at the *IEEE 44th. International Vehicular Technology Conference VTC'94, Stockholm, Sweden*, in June 1994 {Ref[5.1]}, and a complete summary was presented at the *IEE 10th. International Conference on Antennas and Propagation ICAP'97, Edinburgh, UK*, in April 1997 {Ref[5.2]}. The concept of *Propagation Signatures* introduced in this chapter will be presented at the *10th. Virginia Tech Symposium on Wireless Personal Communications, Blacksburg Virginia, USA*, in June 2000 {Ref[5.3]}.

Following on from the work on indoor measurements presented in Chapter 4, this chapter describes outdoor wideband propagation measurements at 1890 MHz undertaken in the Australian capital cities of Adelaide, Melbourne, Canberra and Sydney. Various environments within these cities were measured, and both high and low transmitter antenna positions have been used. The portability feature of the backpack channel sounder receiver has been exploited to gain access to shopping arcades and narrow pedestrian lanes in Melbourne, where vehicles are prohibited, and trolley mounted test equipment would be too unwieldy.

The channel sounder has been used in the *outdoor* resolution mode, with a chip rate of 25 MHz, and bandwidth of 50 MHz, giving a resolution of 40 ns, equivalent to a path length difference of 12 metres. Omnidirectional vertically polarised antennas were used, in most cases with a discone as the transmitting antenna and a halfwave antenna for the receiver {see Appendix C: *Antennas*}.

The receiver was carried either in a car, or on foot in backpack mode. During each measurement, the receiver was stationary. At most measurement locations, several measurements were obtained, with small random changes (of a few wavelengths) in position between each measurement.

Detailed maps and tables showing all measurement locations may be found in Appendix E: *Measurement Locations*.

Multipath effects can be summarised in a number of different ways, as discussed and defined in Chapter 2. The parameters used in this chapter are the *rms delay spread*, *mean delay*, the *maximum delay* or *15dB delay window*, and the *K factor*.

Noise and low level spurious signals distort the calculation of time dispersion parameters {see Chapter 2, section 2.8}, and to avoid this an arbitrary amplitude threshold is applied, where all samples less than the threshold are set to zero. The threshold chosen is -15 dB relative to the strongest ray.

Probability distributions for the *rms delay spread*, the *average delay*, the *15dB delay window*, and *K factor*, are presented. Median rms delay spread values ranging from 52 to 1200 ns have been found.

A novel graphic summary of the distribution of multipath rays over power and excess delay bins, termed the *Propagation Signature*, is introduced in this chapter. This shows a vivid pictorial fingerprint or signature of the multipath propagation excess delay statistics for a particular environment.

## 5.1 Adelaide

Adelaide has a population of over one million, and is the capital of the state of South Australia. It is situated on the flat alluvial plains of the Torrens River, with the Adelaide Hills to the east.

Measurements were performed in the downtown city area, which consists of a rectangular grid of wide tree-lined streets with medium to high buildings, and also in North Adelaide, a suburban area with predominantly single storey buildings. North Adelaide measurements were centred on the six storey Hotel Adelaide.

One set of tests at the Hotel Adelaide was done with the transmitter antenna protruding from a first floor window facing south. Although this would function as a low antenna from the viewpoint of a receiver to the north of the hotel, the aspect across the Torrens valley to the south and the downtown area was quite elevated, so this case has been classed as a high antenna. Measurements were also done with the transmitter on the flat roof of the hotel, six storeys up, with unobstructed views in all directions and clearly falling into the high antenna category. In the city centre, the transmitter was set up in Victoria Square, with the antenna on a 5 metre tripod mast, amongst taller trees. Victoria Square is a large tree covered garden square at the intersection of King William Street running north-south, and Wakefield Street running east-west. Measurements were confined to the vicinity of these two streets. Apart



from obstruction by trees, line of sight conditions existed in the north-south direction, but not in the east-west direction, because the transmitter was in the north section of the Square and offset from Wakefield Street.



**FIGURE 5.1 Victoria Square transmitter site**

### **5. 1.1 Hotel Adelaide, First Floor**

Measurements were made between the Torrens River and the Hotel Adelaide, with the transmitter antenna protruding from a first floor window on the south side of the building. Additional measurement positions were located in the downtown city area, using the same transmitter site.

### **5. 1.2 Hotel Adelaide, Sixth Floor Roof**

The roof of the hotel is flat, apart from a small services structure in the central part, and a low parapet around the edge. Cellular base station antennas, and other point-to-point microwave antennas are located on the roof. Hotel Adelaide is the highest building in the vicinity, with a commanding outlook over the flat terrain, and over buildings of one to three floors, to the northern sector. To the south, the ground falls away to the Torrens Lake, then rises to the northern edge of the downtown city business area.

### **5. 1.3 Adelaide - Victoria Square**

Measurements extended along King William Street, both north and south of Victoria



Square, and east of the Square along Wakefield Street. The transmitter antenna was on a 5 metre mast amongst taller trees, in Victoria Square {Figure 5.1}.

### 5.1.4 Adelaide - Results

#### 5.1.4.1 rms Delay Spread

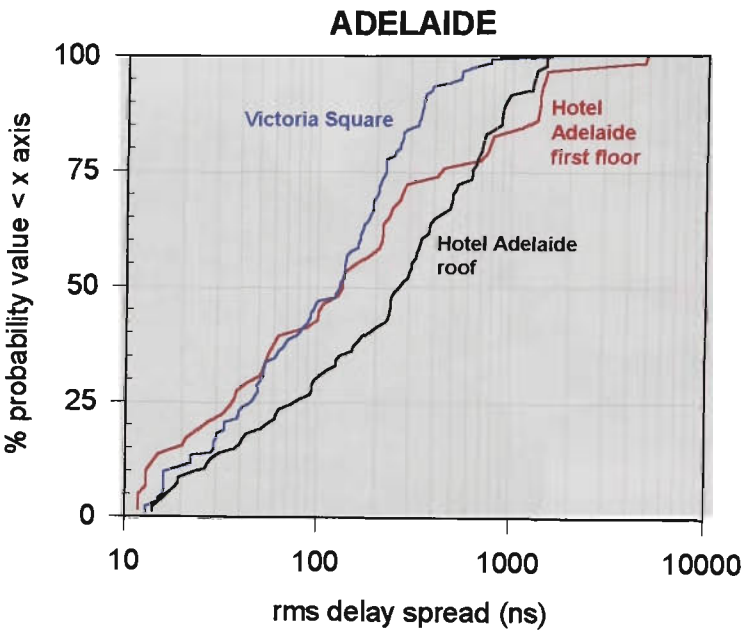


FIGURE 5.2 Adelaide - CDFs of rms delay spread

Cumulative distributions functions (CDFs) of rms delay spread are shown in Figure 5.2. Whilst the Victoria Square site gives the highest median value, the first floor transmitter location exhibits a small group of measurements with high value delay spreads.

#### 5.1.4.2 Average Delay

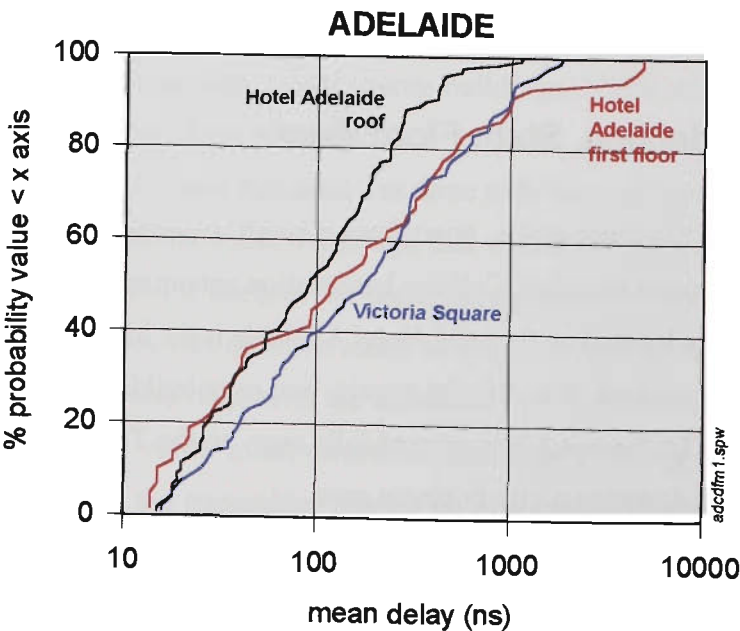


FIGURE 5.3 Adelaide - CDFs of average delay

5. 1.4.3 15dB Delay Window

The 15dB delay window was introduced in Chapter 2 as a measure of time dispersion, and is the time between the first and last rays in the power delay profile (PDP) which are greater than or equal to  $-15\text{dB}$ . This is similar to the 10dB power window.

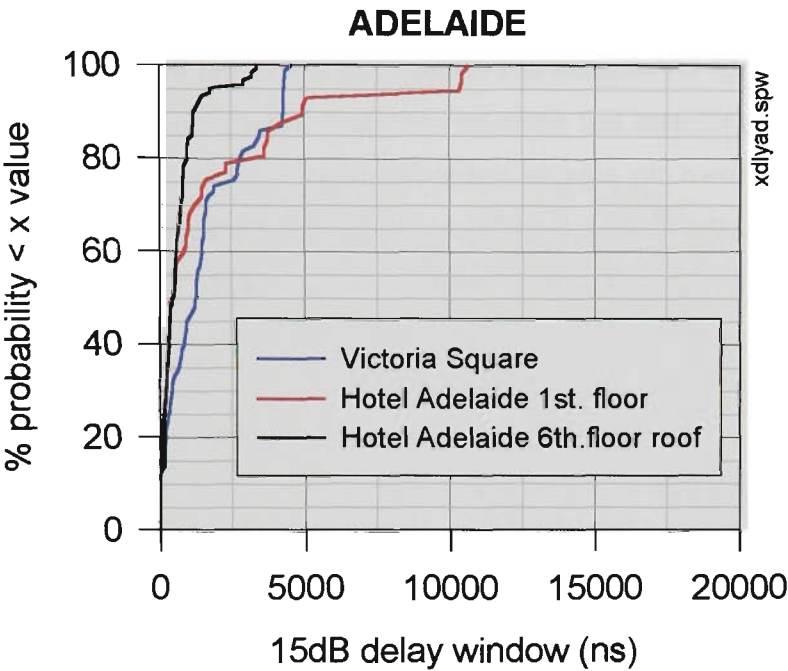


FIGURE 5.4 Adelaide - 15dB delay window

5. 1.4.4 K Factor

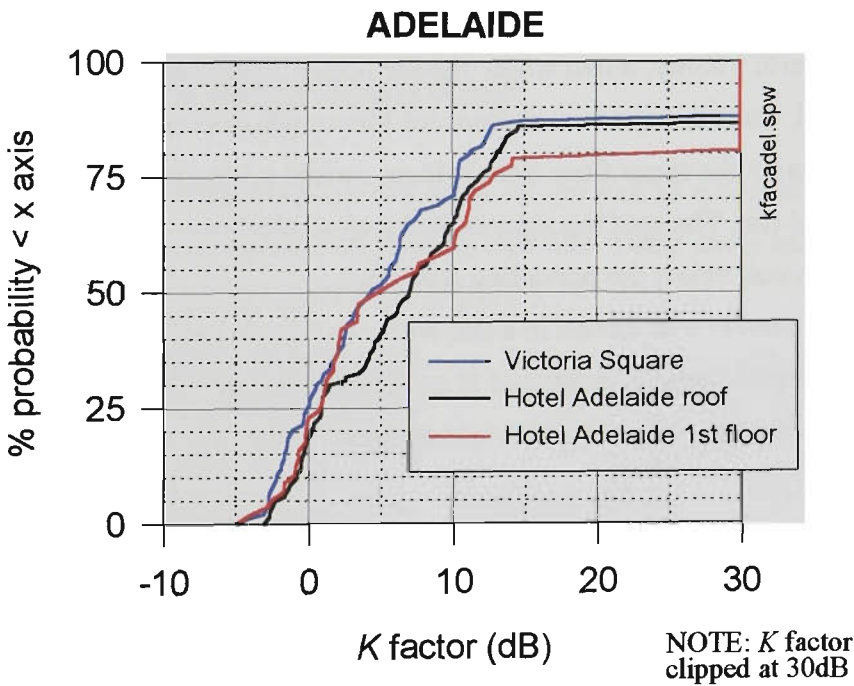


FIGURE 5.5 Adelaide - CDFs of K factor

## 5.2 Melbourne

Melbourne is the capital of the state of Victoria, and with a population of over three million is the second largest city in Australia. The city centre is laid out with wide boulevards on a square quarter mile grid, with a “little” street midway along each block. Narrow lanes and a number of indoor arcades further subdivide the grid. Buildings are a mix of the old, only a few floors high and constructed of masonry and brick, and the recent, towering to over fifty storeys, and built of steel and concrete and glass. Measurements in central Melbourne were done in the downtown city area, in pedestrian malls, lanes, and indoor arcades, using the portability offered by the backpack sounder. Further measurements were done three kilometres from the centre, in North Fitzroy, an inner suburban area with 19th. century residential terrace housing comprising a mix of one and two storey dwellings.

In the city centre, soundings were done in the Bourke Street Mall area, and in two indoor street level shopping arcades, each about one hundred and twenty metres long. For the arcade measurements, the transmitter was in a car boot with the car at a kerbside parking meter, approximately one hundred and fifty metres to the side of the arcade entrances. The transmitter antenna was mounted on a towbar mast, three metres above ground level. The car mounted transmitter, in a different location, was also used for Bourke Street measurements. A university building in Flinders Street was used for the third set of city measurements, with the transmitter on a 13th. floor balcony. While this was above many of the roof tops of older buildings, it was still well below many nearby high buildings. The concrete canyons of small streets and lanes below were all non-line of sight, but with scope for roof top diffraction.

In North Fitzroy, a two storey terrace house located in Delbridge Street near the top of a slight hill, was used as a base station site. One series of soundings was done with the transmitter antenna on the upper floor front balcony, while a 3 metre mast on the roof top was used for the second run. The roof top antenna had a clear view over all nearby roofs, while the balcony location was below the prevailing roof lines.

The receiver was carried in a car, with a half wave roof-mounted antenna. The car was stationary for each measurement, and at each position several power delay profiles separated by a few wavelengths were logged. Measurements in the other cities were all car based.

### 5.2.1 Melbourne - Bourke Street Mall, and Flinders Street

The receiver was carried as a backpack, and all measurements were obtained on footpaths, or in narrow laneways with no vehicle access, and in building recesses.

### 5.2.2 Melbourne - City Arcades

Using the receiver in the backpack configuration allowed access to two typical city

shopping arcades, consisting of indoor ground floor shops. The arcades have large open entrances to Bourke Street, and extend for the length of half a city block.

### 5.2.3 Melbourne - Delbridge Street Balcony

The antenna projected from a residential balcony at first floor level, below the surrounding roof lines (Figure 5.6). The receiver was carried in a car, with the halfwave antenna about 300 mm. above the vehicle roof.



FIGURE 5.6 Antenna on Delbridge Street balcony, looking north east

### 5.2.4 Melbourne - Delbridge Street Roof

The antenna was mounted on a 3 metre mast, on the roof of a two storey residential building, placing the antenna above the surrounding roof line. Three and a half kilometres to the south, high city office buildings were visible (Figure 5.7).

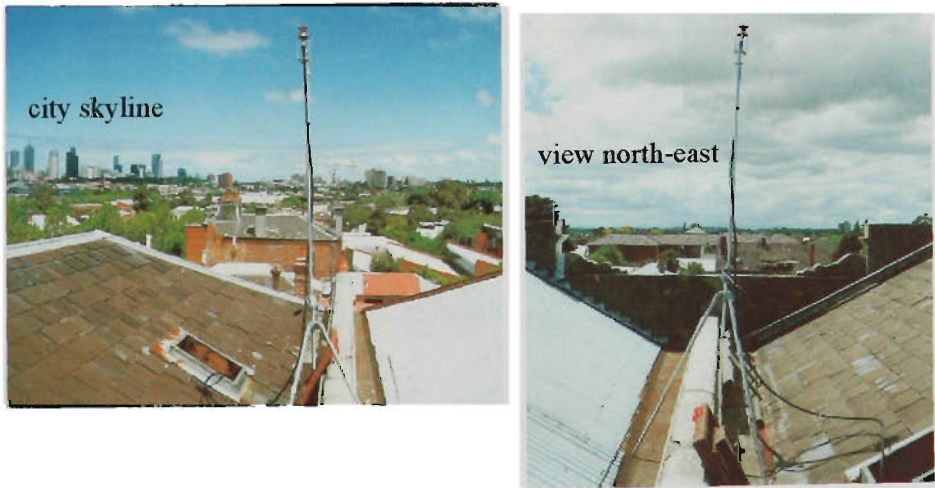


FIGURE 5.7 Roof antenna at Delbridge Street

## 5.2.5 Melbourne - Results

### 5.2.5.1 rms Delay Spread

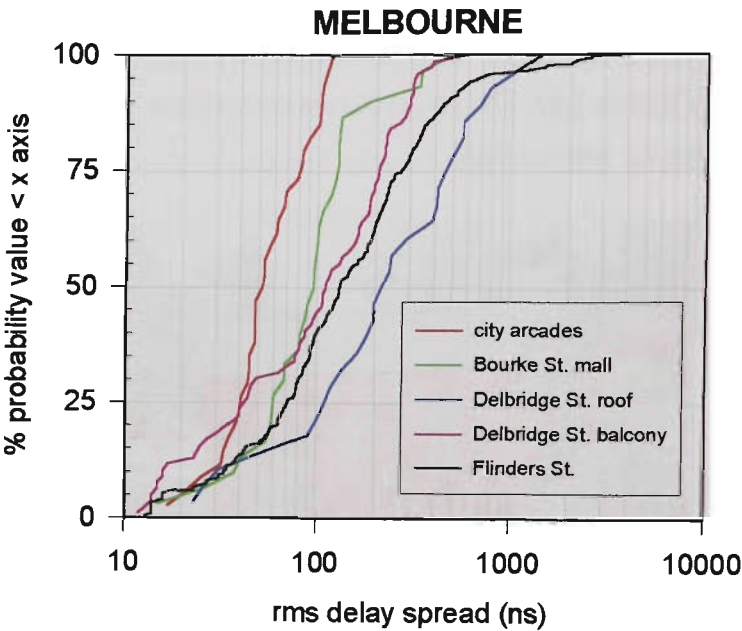


FIGURE 5.8 Melbourne - CDFs of rms delay spread

### 5.2.5.2 Average Delay

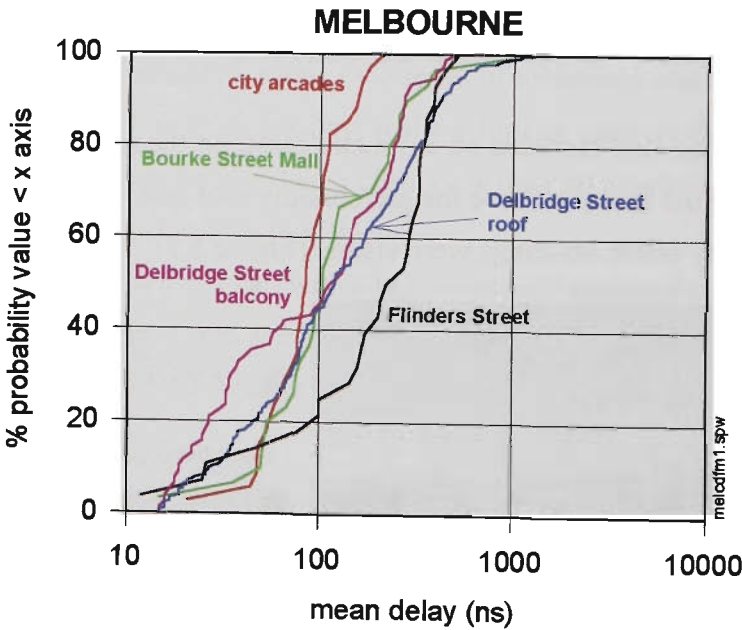


FIGURE 5.9 Melbourne - CDFs of average delay



5. 2.5.3 15dB Delay Window

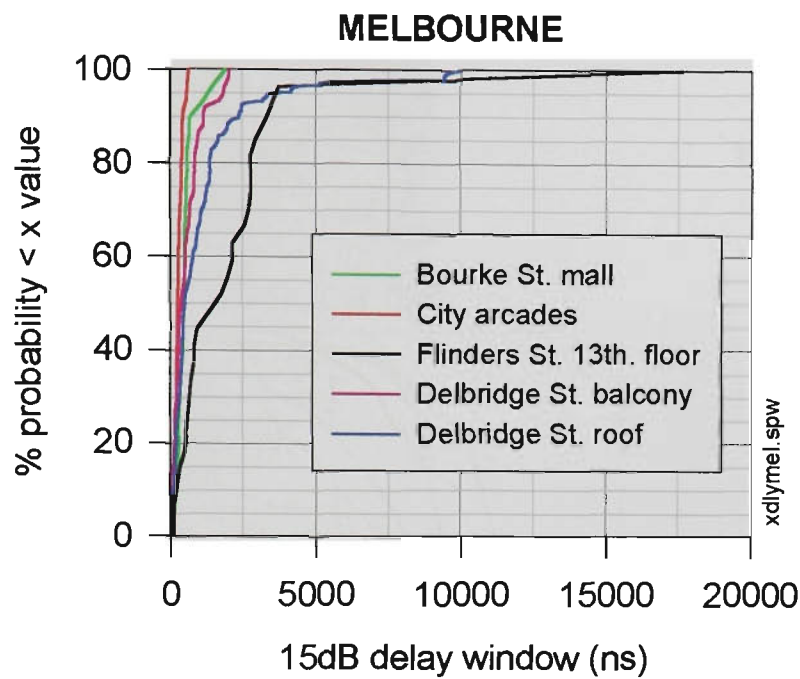


FIGURE 5.10 Melbourne - 15dB delay window, showing long delays

High antenna positions produce high 15dB delay window values for a small percentage of the PDPs, up to 9.9  $\mu$ s for the Delbridge Street roof transmitter site, and 17.6  $\mu$ s for the Flinders Street thirteenth floor site (Figure 5.10)

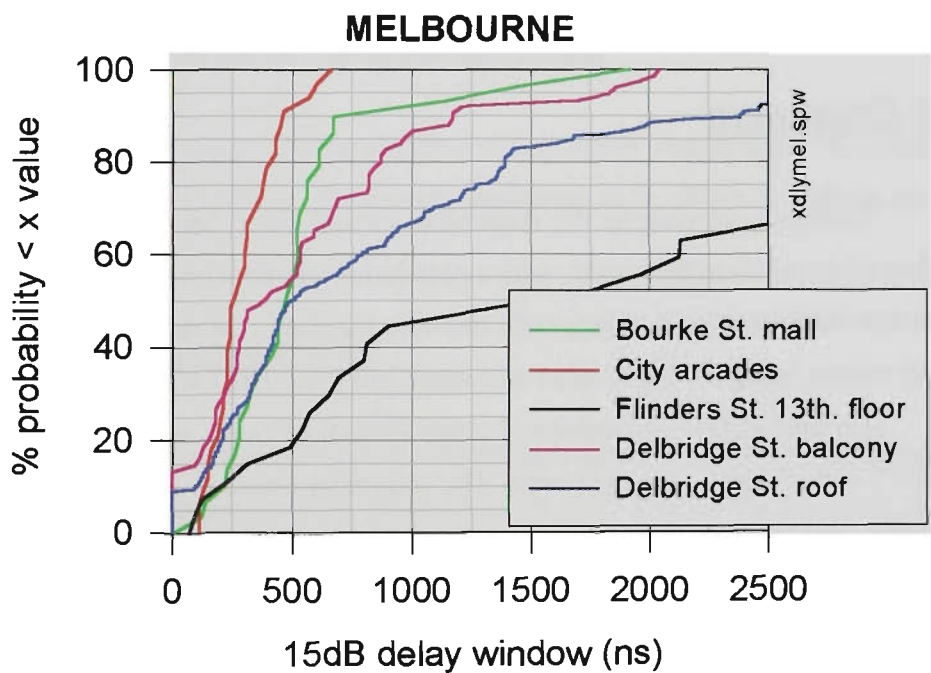


FIGURE 5.11 Melbourne 15dB delay window with detail at lower delays

The distributions for these sites indicate longer delays at all probability levels greater than 50%, compared with the low antenna measurements. More detail at lower delays is shown in Figure 5.11, where the time axis is expanded. City arcades show the lowest delays at prob-

abilities over 30%, and also exhibit the lowest delay spreads of all the Melbourne measurements. The majority of city arcade PDPs show a 15dB delay window between 200ns to 300ns, corresponding to excess path lengths between 66 and 100 metres, which is of the same order as the size of the arcades.

5. 2.5.4 K Factor

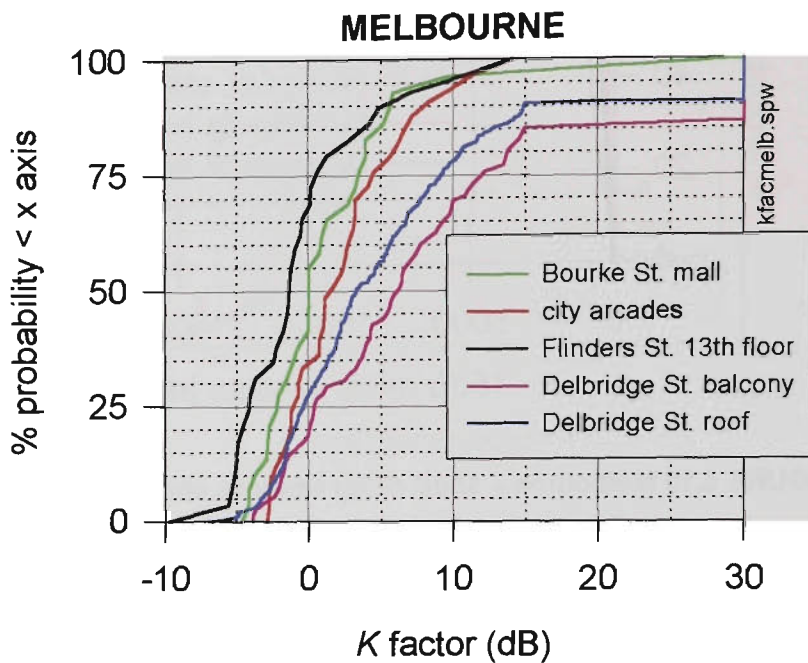


FIGURE 5.12 Melbourne - CDFs of K factor

5. 3 Canberra

Canberra, serving as the Australian capital since being established in 1927, is the smallest of the cities in this study, with a population of about one quarter of a million. The city centre has wide tree-lined streets with low rise buildings. Measurements were performed in the city centre, using a 5 metre mast on a small hill (City Hill) at the edge of the area surveyed.

A suburban low rise industrial estate (Dundas Court), and a hilly suburban residential area (O'Connor) were also measured. The industrial estate is located on flat ground, ringed with hills, and the transmitter antenna was sited on a 4 metre mast, on the flat roof of a two storey building, overlooking all the adjacent roof tops.

Figure 5.13 shows the transmitter site at City Hill.

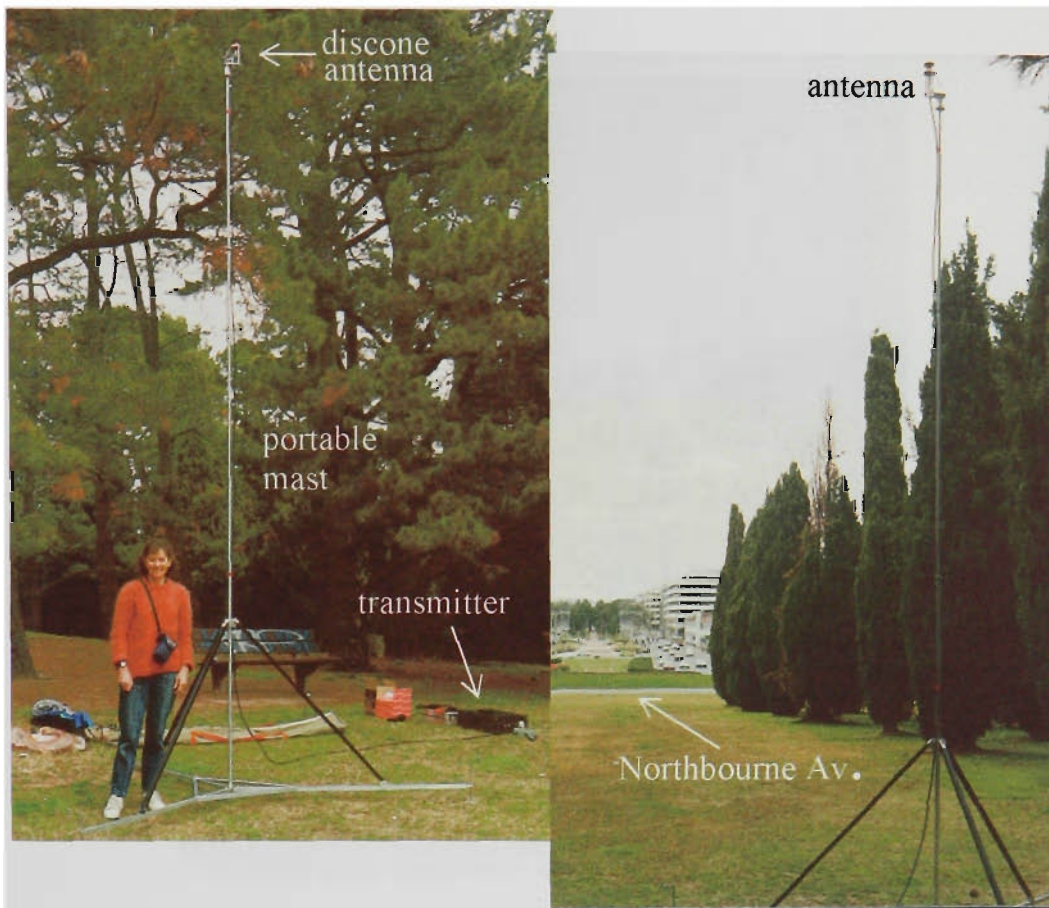


**FIGURE 5.13** City Hill transmitter site

### 5.3.1 Canberra - O'Connor Residential Area

O'Connor has undulating winding streets, predominantly single storey detached housing, and many street and garden trees. The suburb is adjacent to the Black Mountain nature reserve to the west.

### 5.3.2 Canberra - Dundas Court

Dundas Court is within a small light industrial and commercial area with a regular grid of streets, covering an area approximately 500 metres by 1000 metres. To the north, across a main road, a similar size shopping centre and car park is located. These areas are on flat ground, in a valley running north-south. Surrounding residential estates, and open grassland rise up the sides of the valley to the west and east.

The flat roof of a two storey computer company was used as the transmitter site, with the antenna on a 4 metre mast (Figure 5.14). Other buildings in the industrial estate had similar roof lines, giving the antenna a clear view of surrounding housing areas and the hills beyond. Nearby streets in the industrial estate were shadowed by buildings.





FIGURE 5.14 Roof-top antenna - Dundas Court

5. 3.3 Canberra - Results

5. 3.3.1 rms Delay Spread

Cumulative distributions for the three measurement sites are given in Figure 5.15.

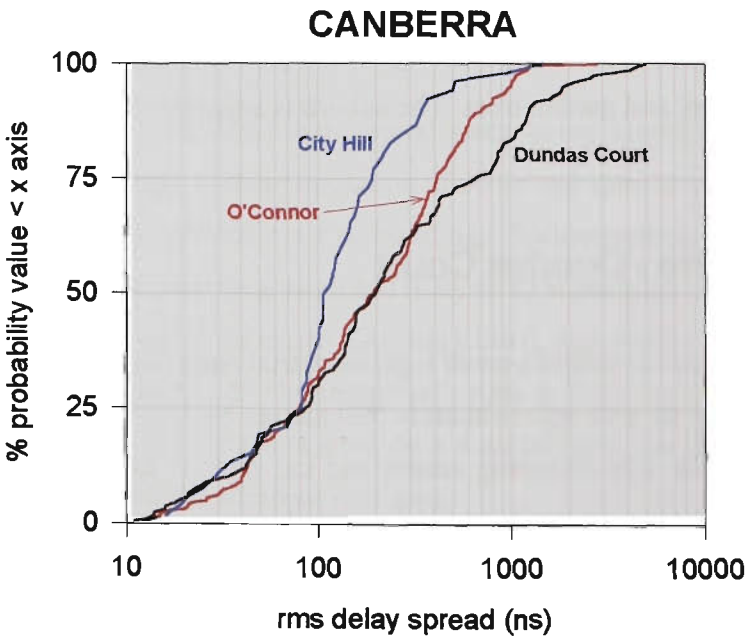


FIGURE 5.15 Canberra - CDFs of rms delay spread

5. 3.3.2 Average Delay

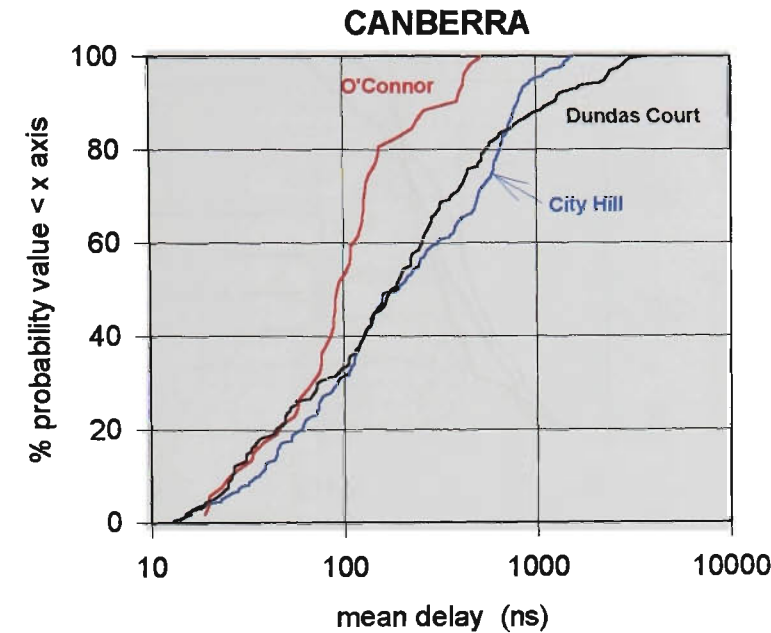


FIGURE 5.16 Canberra - CDFs of average delay

5. 3.3.3 15dB Delay Window

The 15dB delay window distributions are given in Figure 5.17.

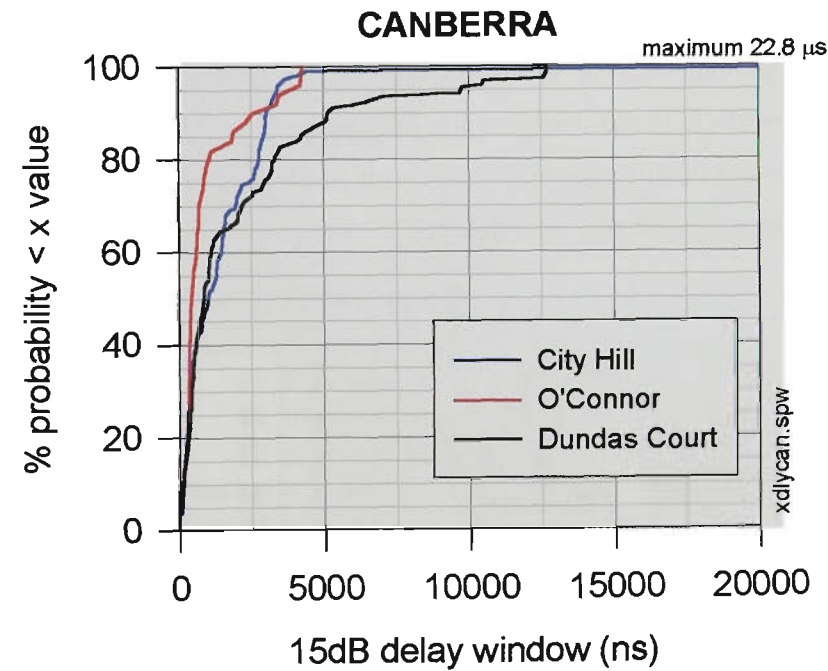


FIGURE 5.17 Canberra - CDFs of 15dB delay window

5. 3.3.4 K Factor

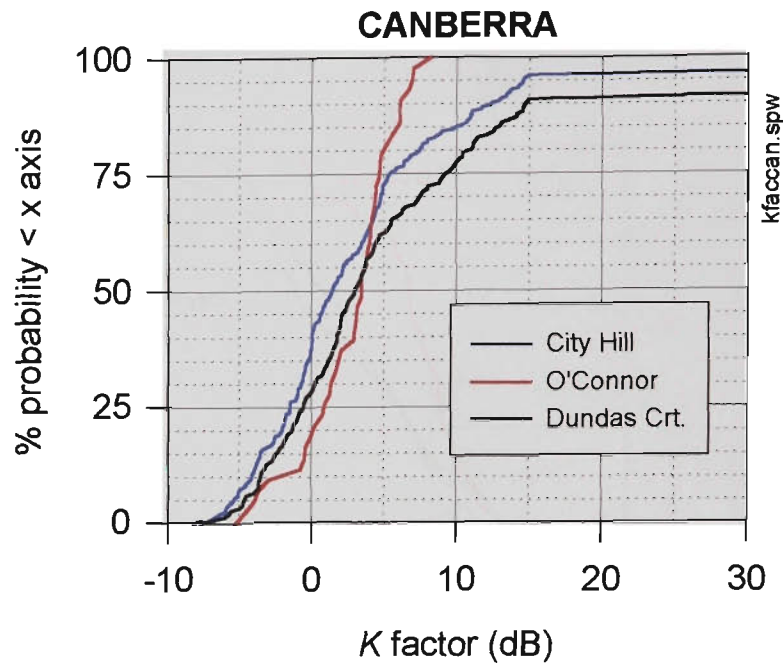


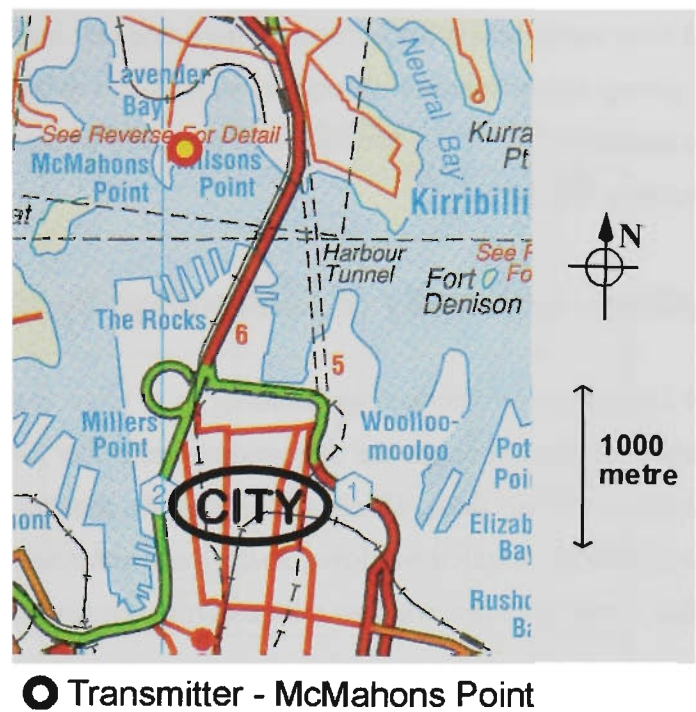
FIGURE 5.18 Canberra - CDFs of K factor

5. 4 Sydney

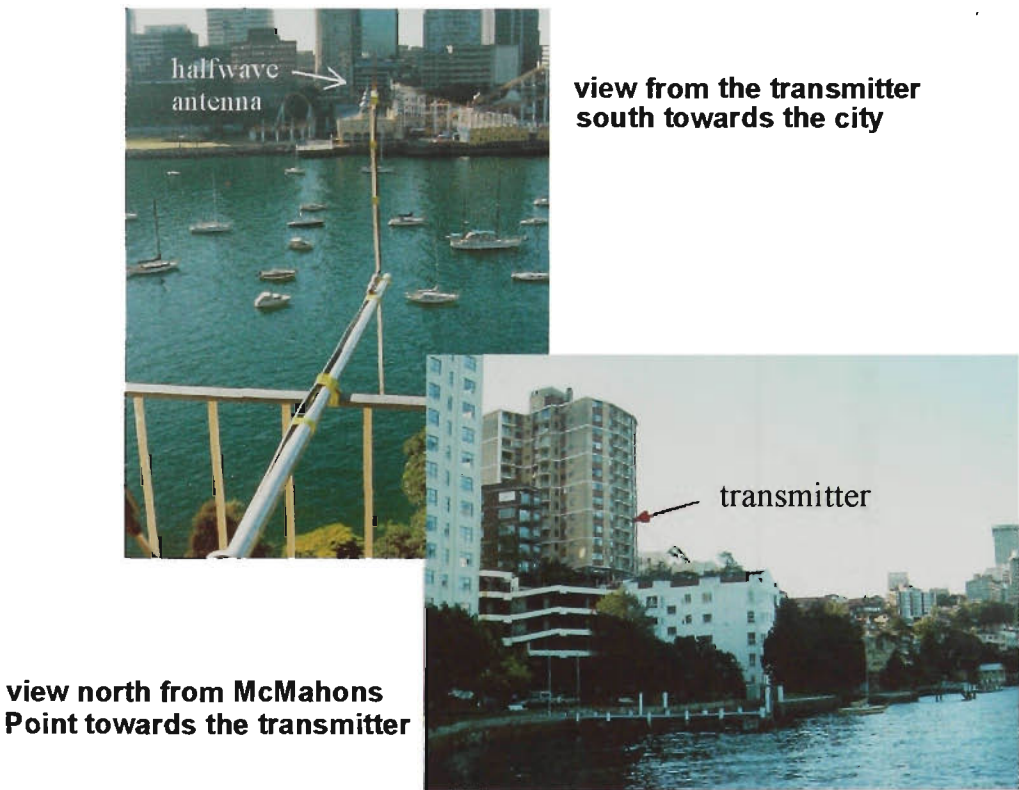
Sydney measurements were done on the north side of Sydney Harbour at McMahons Point, a hilly area suffering strong reflections from distant city buildings across the harbour, and in the main city area with the transmitter looking toward the city from the 23rd. floor of the *University of Technology Sydney*, a prominent high building south of the city centre. The north side of the harbour situation in Sydney is unusual. The topography is steep and hilly, even including sections of cliff, and it is possible to have receiver locations which, although close to the transmitter, are deeply shadowed, but with good visibility to the high rise city skyline across the harbour, giving strong rays delayed by 5  $\mu$ s to 10  $\mu$ s.



FIGURE 5.19 View from North Sydney (McMahons Point) across Sydney Harbour to the high-rise city.



**FIGURE 5.20 McMahon's Point transmitter site in relation to the city**



**FIGURE 5.21 McMahon's Point transmitter site, on 4th. floor balcony**

At McMahon's Point, the transmitter antenna projected from the fourth floor balcony of an elevated apartment building, with commanding views to the east and the south across water to the Sydney Harbour bridge, and the city business centre with numerous high rise buildings. Steep terrain below the transmitter together with other buildings, heavily shadowed the



direct path for close receiver positions near the water edge. In these cases, both transmitter and receiver had clear views across the harbour to high-rise city buildings, approximately 1 to 1.5 km. distant, giving strong specular reflections with excess delays in the range  $5\mu\text{s}$  to  $10\mu\text{s}$ .

The relationship of the McMahons Point area to the main city business district is shown by the map in Figure 5.20.

### 5.4.1 Sydney - University of Technology Sydney

The *University of Technology* building is a large multi-storey (approximately 30 floors) structure which dominates the surrounding area. The *Department of Electrical Engineering* occupies the 23rd. floor, which was used as the transmitter site for this measurement session. The building has sealed windows, so the transmitter halfwave antenna was situated in a vacant office, close to a glass window with a north view towards the central city area.

### 5.4.2 Sydney - Results

#### 5.4.2.1 rms Delay Spread

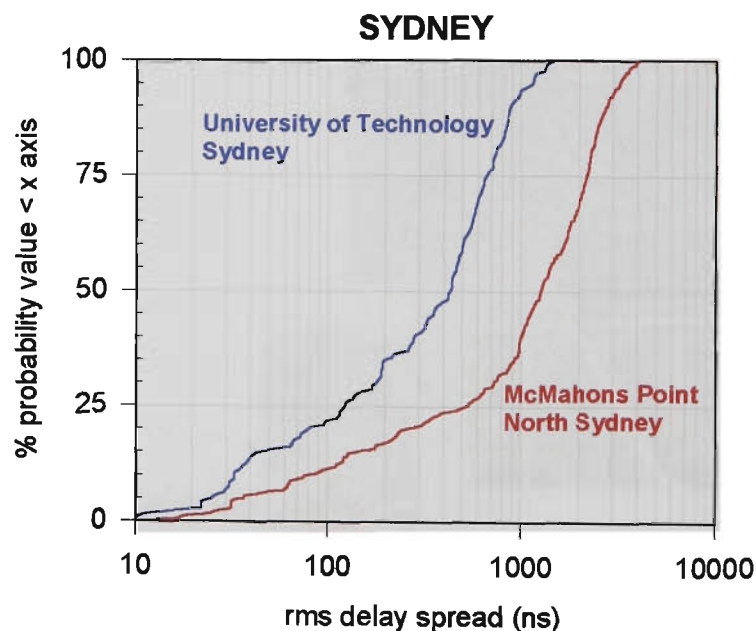


FIGURE 5.22 Sydney CDFs of rms delay spread

5. 4.2.2 Average Delay

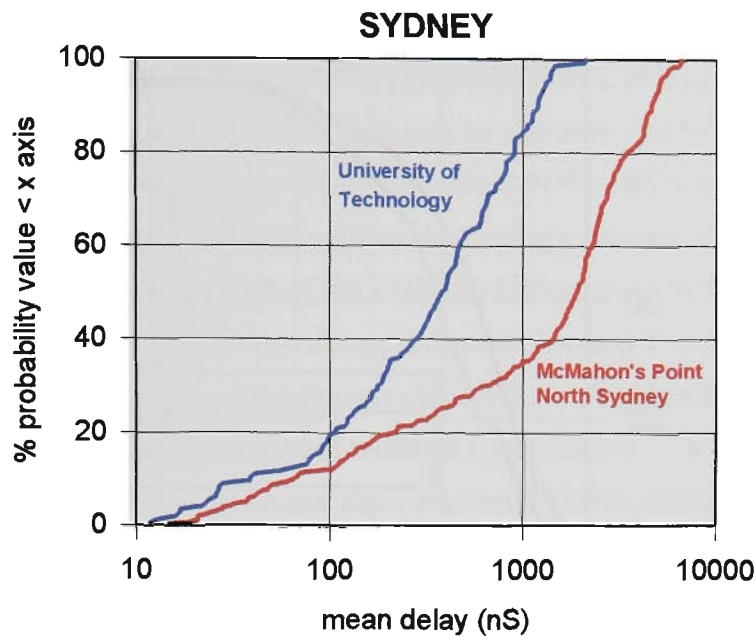


FIGURE 5.23 Sydney CDFs of average delay

5. 4.2.3 15dB Delay Window

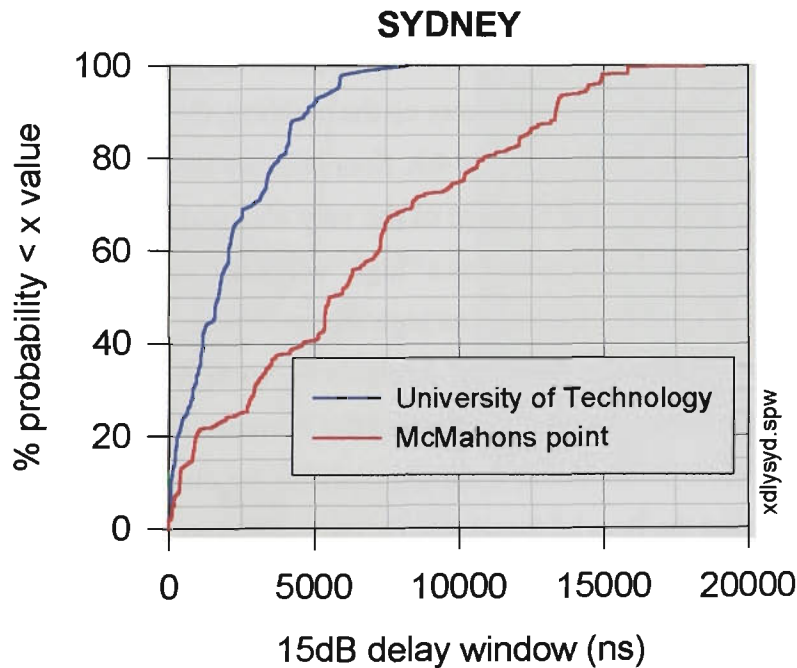


FIGURE 5.24 Sydney CDFs of 15dB delay window

5. 4.2.4 K Factor

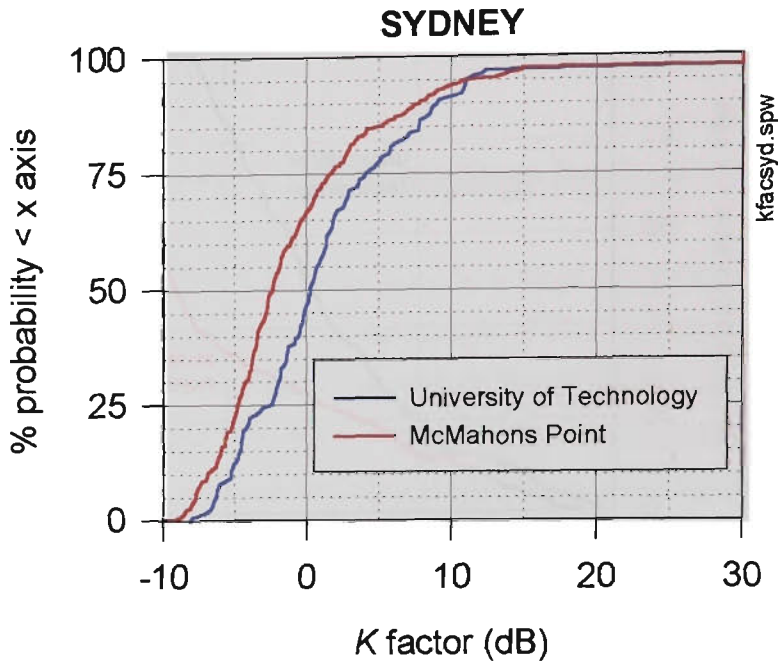


FIGURE 5.25 Sydney CDFs of K factor

5. 5 High And Low Antennas

Transmitter antennas are categorized as “high” or “low”, a relative term depending on whether the antenna is above or below the prevailing roof levels in the area. Some cases are not clear cut, for example, the building at 300 Flinders Street in Melbourne. Although the antenna was on the 13th. floor and above some roof levels, it was also below others. Also because of the south-facing balcony location part way up the building, the antenna was shadowed to the north by the building itself. In Sydney, the 4th. floor balcony location at McMahon's Point was only part way up the building, but because of the very elevated outlook to the south and east across the harbour, this has been classed as a “high” antenna (see Figure 5.21). Thus all of the Sydney measurements have been classed as high antenna cases.

The 1st. floor antenna in the Hotel Adelaide in North Adelaide has been classed as a “high” antenna because to the south it overlooked the Torrens valley and the city. On the other hand, for locations close to the hotel, it should probably be classified as a low antenna. The Bourke Street Mall and the Bourke Street Arcade measurements used a low antenna, approximately 3 metres above ground. Victoria Square in central Adelaide is also a low antenna case.

## 5. 6 A Novel Graphic Propagation Environment Signature

### 5. 6.1 The Presentation Problem

Presentation of the large amount of data collected during propagation measurement sessions poses a dilemma. Each environment area may be characterised by hundreds of PDPs, which show wide individual variations. While individual PDPs are interesting to examine, these scarcely convey the overall statistical picture. Averaging a number of profiles to produce an average PDP over an area loses a lot of the available information. Single parameter measures, such as *rms delay spread*, *average delay*, *delay window* and *K factor*, provide useful summaries of signal time dispersion. Distribution plots of these single parameter measures, as shown in earlier sections of this chapter, give a valuable quantitative picture of the area statistics, and the spread and maximum values of these measures. But in addition, there remains a need to present a concise picture of multipath activity.

### 5. 6.2 The Propagation Signature

A novel graphic summary of the distribution of multipath rays over power and excess delay bins is introduced in this section. This gives a vivid pictorial signature or fingerprint of the multipath propagation excess delay statistics for a particular environment. Akin to a contour map, an example of the *Propagation Signature* is shown below in Figure 5.26(b).

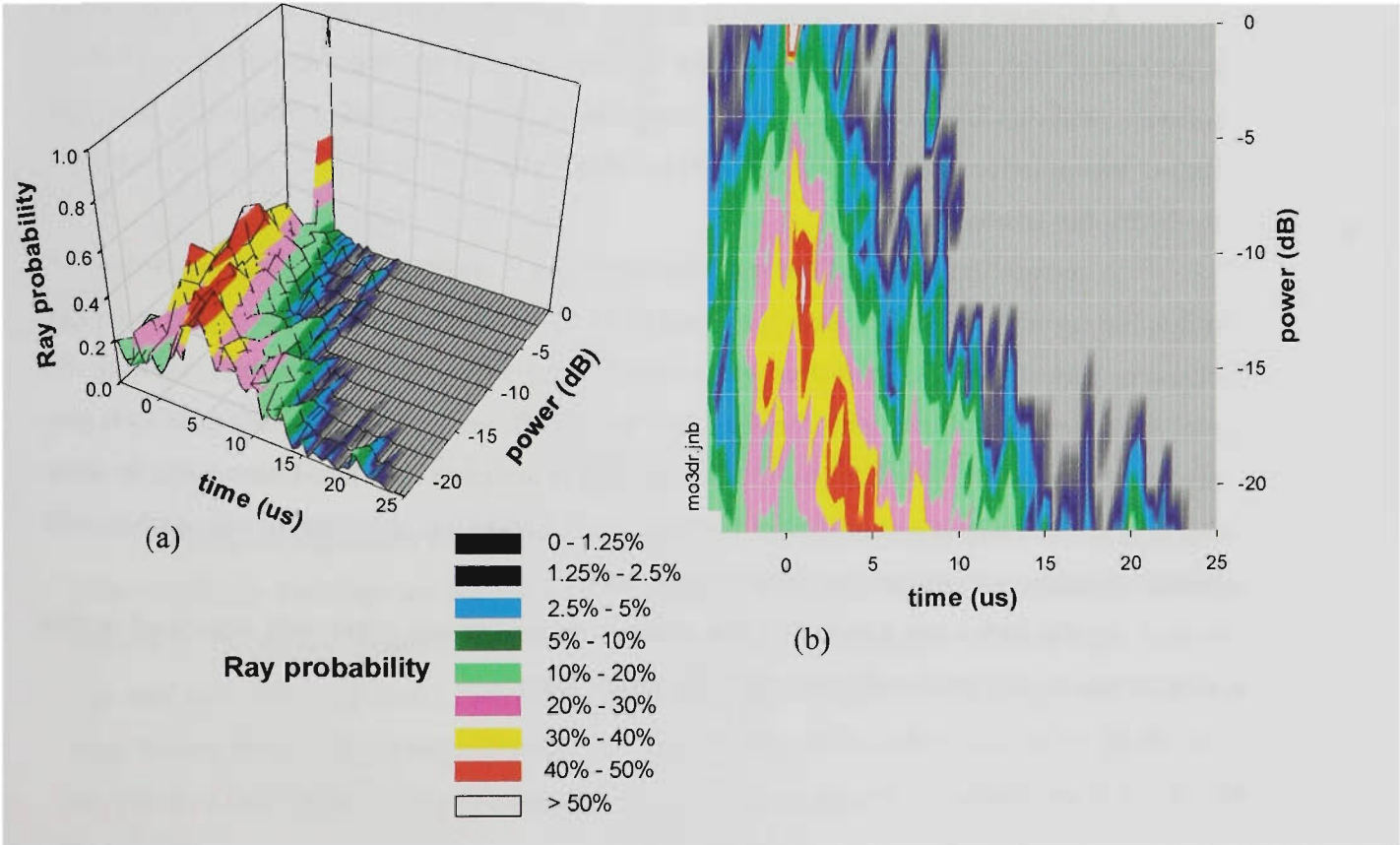


FIGURE 5.26 Presentation example - distribution of rays over time and power bins



Normalized PDPs are analysed using *RAYSORT* (see Appendix D: *Software Summary*). Individual rays are identified, and sorted into both power and excess delay bins. The time bins are  $0.5\mu\text{s}$  wide, and range from  $-4.5\mu\text{s}$  to  $+25\mu\text{s}$ . Power bins are 2dB wide, and extend from 0dB to -30dB. Thus there are 59 time bins and 15 power bins, giving a matrix of 885 bins. Not all PDPs acquired during a measurement campaign have 30dB dynamic range, so to allow more of the measured data to be utilised, the power range has been reduced to 24dB (12 bins 2dB wide), resulting in 708 bins. Profiles with less than 24dB dynamic range are discarded. Other measures calculated in this chapter (*rms delay spread*, etc.), which used a threshold of -15dB, included some noisier profiles which have been excluded from the *signatures*.

Rays from each PDP analysed accumulate in the appropriate bins. Finally, the number of rays in each bin is divided by the total number of PDPs, giving the average number of rays per PDP in each bin. Prior to identifying rays and sorting these into bins, each PDP had been normalised to the strongest ray, which furnished the origin for power (0dB) and excess delay time (0  $\mu\text{s}$ ). Of course, the strongest ray may not be the first to arrive, so the normalisation scheme can result in rays with negative excess delays. Remember that the time scale is relative to the strongest ray, not the direct path. By definition, the [0 to  $0.5\mu\text{s}$ , 0 to -2dB] bin will have an average number of rays/bin of  $\geq 1$ . The average number of rays/bin can be interpreted as the probability of a ray occurring in that particular bin. If the 'probability' exceeds 1, this simply implies more than 1 ray/bin on average. Even though the channel sounder allows up to twelve resolvable rays per  $0.5\mu\text{s}$  time bin, apart from the origin bin, cases of more than one ray/bin on average have seldom been found.

A 3D mesh plot of ray probability ( $z$  axis) versus the power, time bin matrix ( $xy$  axes) is generated, with  $z$  ranges depicted with a diffused colour band legend. The graph plotting software performs linear interpolations between bins, and colour diffusion effectively provides further interpolation. Data for power bin [0 to -2dB] is labeled "0dB" etc., with the final [-22 to -24dB] bin labeled "-22dB".

A conventional view of the resulting mesh plot is shown in Figure 5.26(a). Notice the origin bin ray with value  $z=1$  (this is clipped to 1). The conventional oblique 3D view always obscures part of the plot, no matter which viewing angles are chosen. However, viewing the plot from vertically above, with "perspective" turned off, results in the contour map style presentation shown in Figure 5.26(b). Colour banding is assigned on a non-linear scale, to show more detail for low ray probabilities. The result is a distinctive, informative and aesthetically pleasing signature of the propagation environment.

In the following figures, all the outdoor measurements previously described in this chapter are re-presented in *Propagation Signature* form.

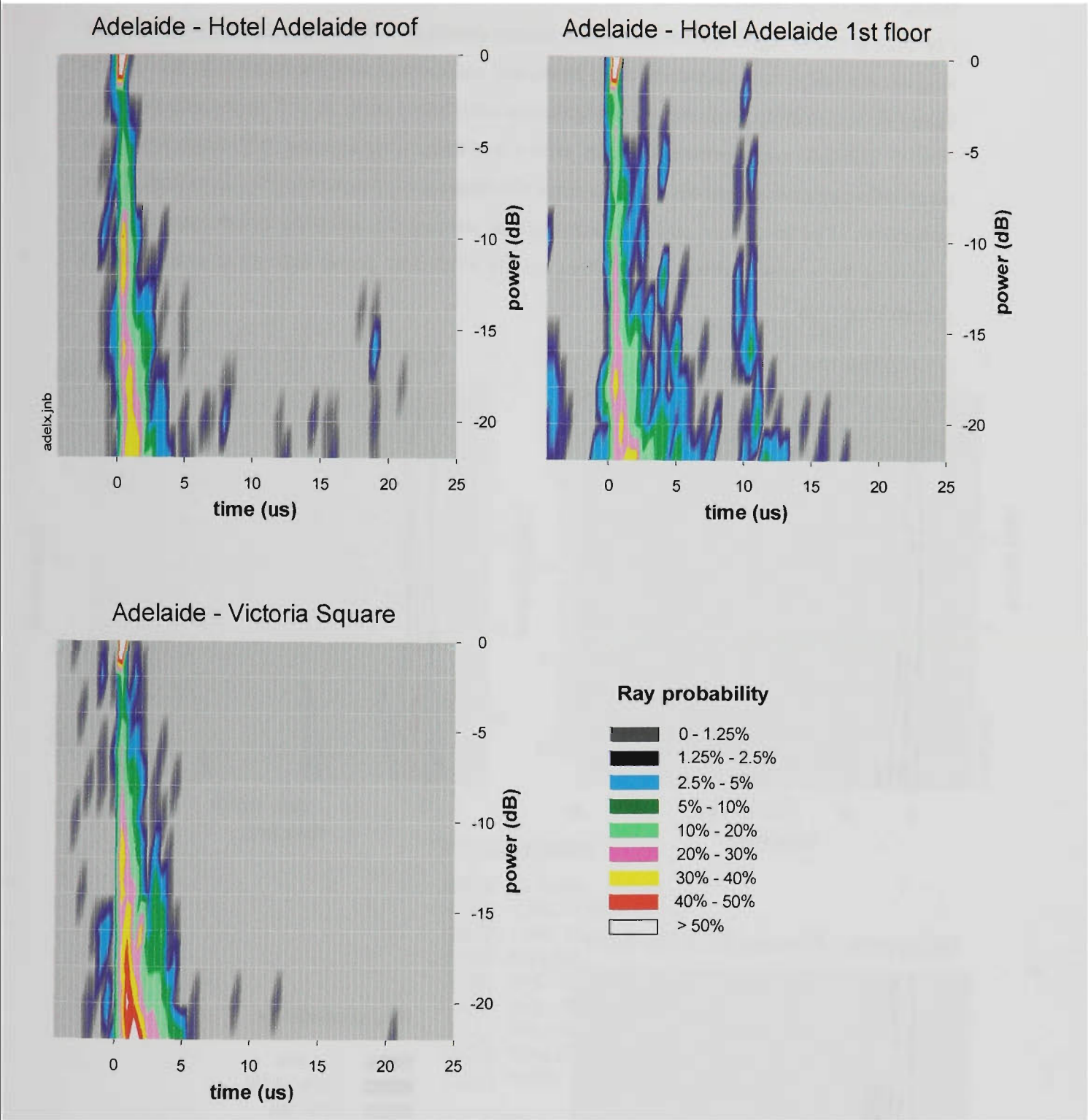


**FIGURE 5.27 Adelaide propagation signatures**

Adelaide signatures are shown in Figure 5.27. From the Adelaide Hotel transmitter locations, tall city buildings are from 1.4 km to 3.5 km (4.5  $\mu$ s to 11.5  $\mu$ s) to the south. With the antenna on the roof, measurements were made to the north of the hotel, moving away from the city, and also in the city itself. The strong direct path predominates, with no powerful paths at large excess delays. Some activity occurs at 3  $\mu$ s, -10dB, some at 8  $\mu$ s, at -16 to -22dB, at 19  $\mu$ s, and at -12 to -24dB. All these excess delays may be explained by reflections from tall city buildings.

Locating the transmitter antenna protruding from a 1st floor window on the south (city

facing) side of the hotel, and with the receiver moving through the Torrens valley and into the city area, gives strong multipath activity at excess delays of 2.5  $\mu$ s, 4  $\mu$ s, and 10 to 12  $\mu$ s. The long excess delays range between -2 to -24dB, and could occur with the receiver in the Torrens valley via a reflection from the north edge of the city. Some paths at -4.5  $\mu$ s are also present.

The final measurement location, with a low transmitter antenna in Victoria Square, is notable for negative excess delay paths, some at relatively high power levels, up to 0dB. These range from -1  $\mu$ s to -3.5  $\mu$ s, and represent the first arriving ray, showing that the strongest ray is arriving by a more indirect path. There is only slight low power activity at excess delays greater than 6  $\mu$ s

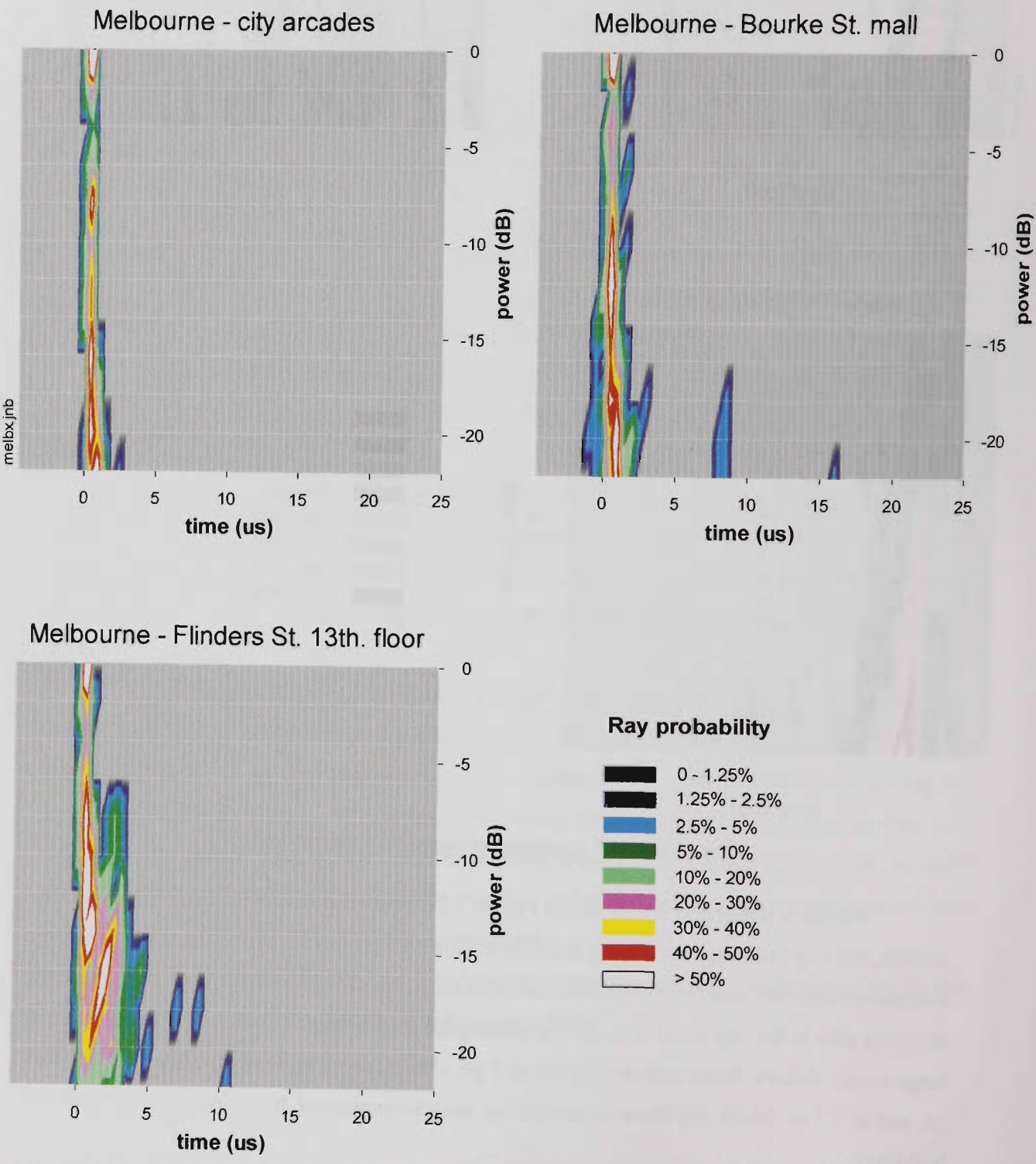
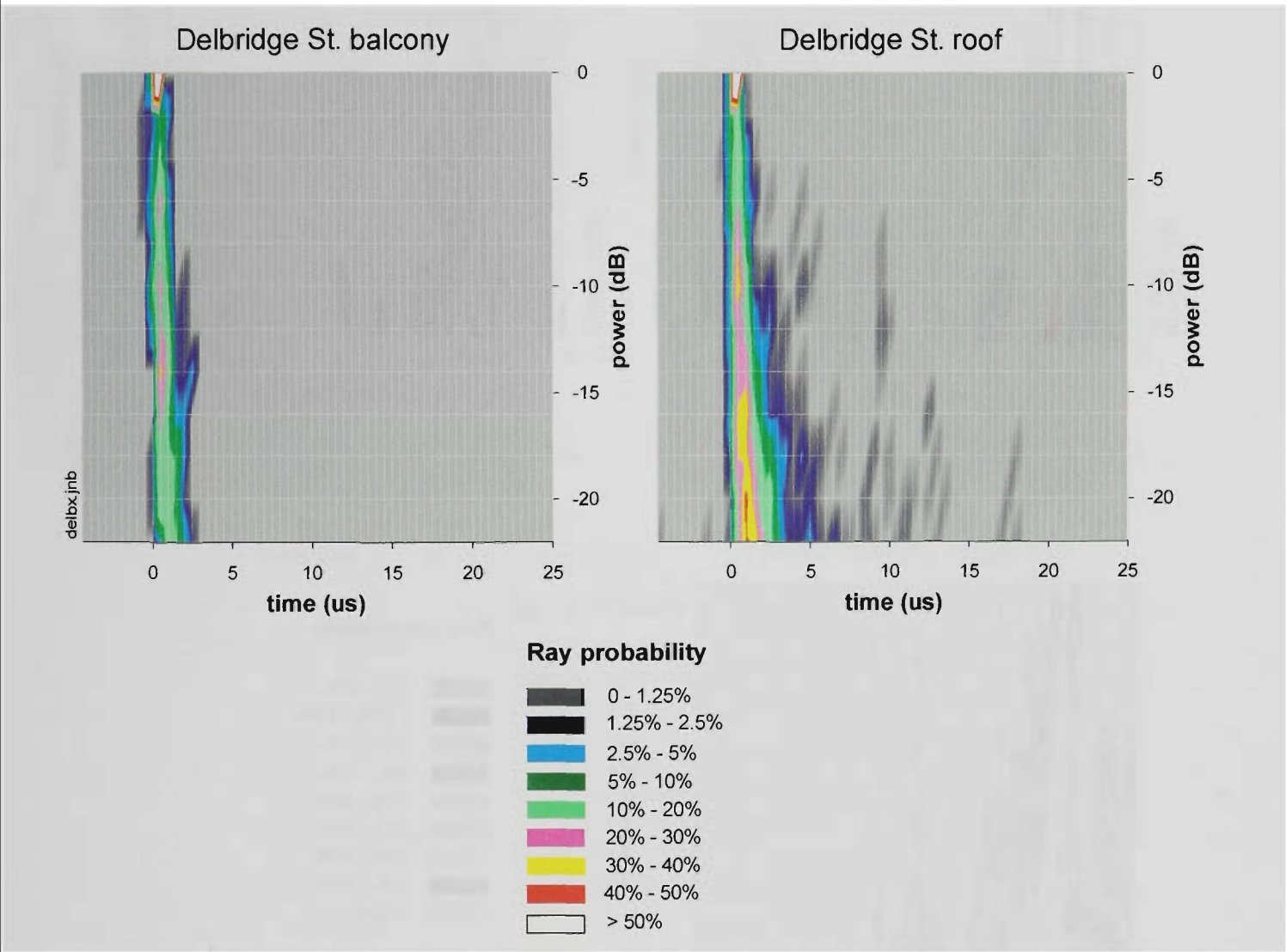


FIGURE 5.28 Melbourne City propagation signatures

Figure 5.28 shows signatures for Melbourne city. The city arcade measurements display little time dispersion, similar to indoor environments, which in effect the arcades are.

Bourke Street Mall measurements, with a very low transmitter antenna, indicate some strong paths at up to  $1.5\ \mu\text{s}$  (excess path of 450 metres), and lower power paths at  $8\ \mu\text{s}$  (-16dB to -24dB) and  $15.5\ \mu\text{s}$  (-22dB). Flinders Street measurements, with the transmitter antenna high above street level (13th floor) but still below many city rooftops, show time dispersion of approximately  $5\ \mu\text{s}$ , with some low power paths up to  $10\ \mu\text{s}$ .



**FIGURE 5.29 Melbourne suburban propagation signatures**

Inner suburban measurements based in Delbridge Street (see Figures E.9 and E.10, Appendix E) gives a signature with little dispersion and no large excess delays with the below-rooftop low transmitter antenna (balcony). Raising the transmitter antenna above rooftop level increases time dispersion markedly (Figure 5.29). Rays are present at  $9.5\ \mu\text{s}$  (-8dB), equivalent to an excess path of 2.9 km, and at  $13.5\ \mu\text{s}$  and  $18\ \mu\text{s}$ . The straight line distance from the Delbridge Street transmitter to the corner of Lonsdale and Swanston Streets in the city area, is 3.1 km. For a receiver location in Johnston Street, the excess path to city buildings in Lonsdale



Street is 3.3 km, equivalent to 11  $\mu$ s. Excess paths across the whole city may produce excess delays over a range of approximately 5  $\mu$ s to 22  $\mu$ s. The city skyline (see Figure 5.7) is thus at the correct distance to explain rays at long delays in the Delbridge Street roof signature.

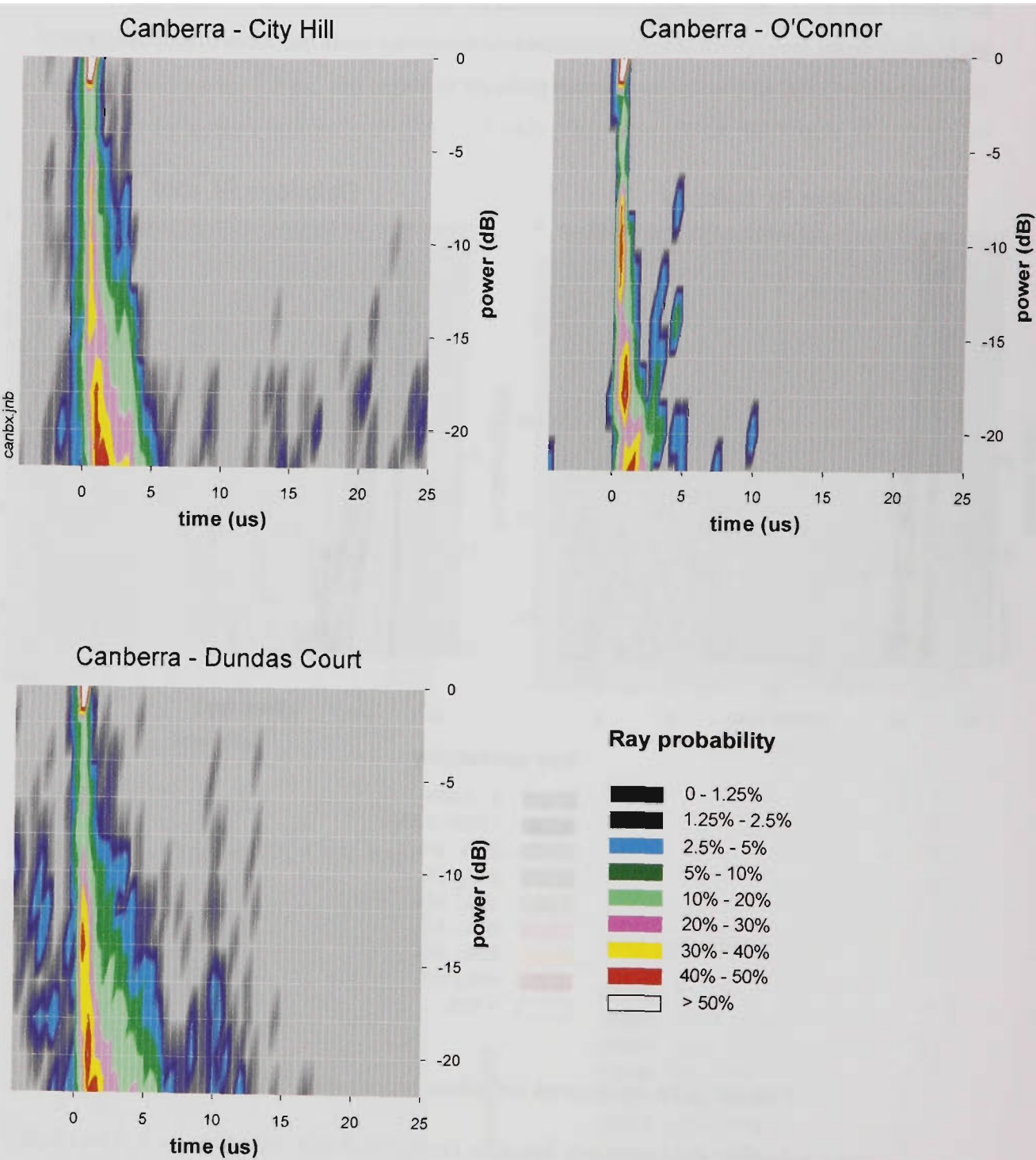


**FIGURE 5.30 Canberra propagation signatures**

Figure 5.30 illustrates signatures resulting from Canberra measurements. The City Hill signature shows cases where the first arriving ray is not the strongest. Some rays with excess delays to 25  $\mu$ s are present at powers up to -16dB, and at -10dB with excess delay of 22.5  $\mu$ s. A map of the measurement locations is shown in Figure E.11, Appendix E. O'Connor (see Fig-

ure E.12, Appendix E) is a hilly suburban area. Rays are evident at 5  $\mu$ s (-8dB) and 10  $\mu$ s (-20dB) with nothing at longer excess delays, although this signature has been formed from a small number of PDPs, and may not be fully representative of the area.

The Dundas Court signature represents a valley hemmed by hills, and shows some strong rays at up to 13  $\mu$ s excess delay. The signature also displays cases where the strongest ray is not the earliest arrival. Figure E.13 Appendix E, shows the measurement locations.

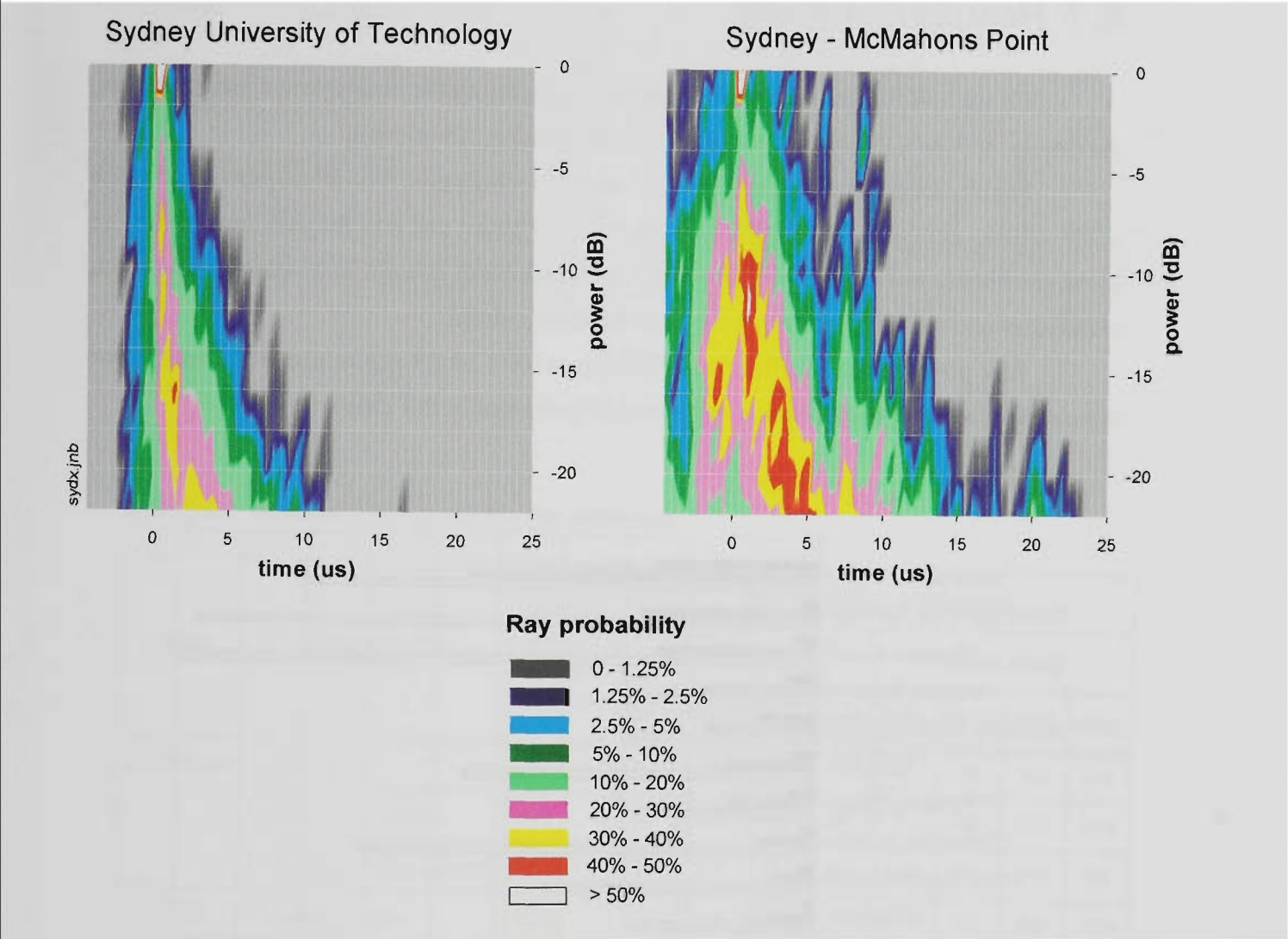


**FIGURE 5.31 Sydney propagation signatures**

The McMahons Point signature comprises measurements clustered around Blues Point, shadowed below cliffs from the elevated 4th floor McMahons Point transmitter location (see Figures 5.19, 5.21). Because of the heavy shadowing, many of the reflected paths are as strong or stronger than the direct ray. Specular reflectors abound, including the metal Sydney Harbour bridge structure, Luna Park across Lavender Bay, and high-rise city buildings on the south shore of the harbour. The signature shows strong rays between 0 and 4.5  $\mu$ s, with the longer delays corresponding to the north end of the bridge, about 700 metres distant. There are other rays at 8  $\mu$ s (-1dB to -6dB), 9.5  $\mu$ s, 10  $\mu$ s, 11  $\mu$ s, 12 $\mu$ s, 13  $\mu$ s, 17.5  $\mu$ s and 20  $\mu$ s.

The excess path corresponding to the northern edge of the high-rise city on the south side of the harbour is approximately 10  $\mu$ s. The south edge of the city (*University of Technology Sydney* building, just south of the downtown city area) could give excess paths ranging up to about 26  $\mu$ s, so any rays with excess paths in the range 10  $\mu$ s to 26  $\mu$ s may be caused by high-rise city buildings. This environment is the most dispersive of any measured in Australia, and there is considerable evidence that in many cases, the strongest ray is not the first arrival.

## 5.7 Results Summary

Figure 5.32 illustrates *rms delay spread* values for all the measurement areas. Median, maximum, and the value not exceeded in 90% of locations are plotted.

Results are summarised in Tables 5.1 and 5.2, which give *rms delay spread*, and *mean delay* values, not exceeded in 25%, 50% and 90% of cases, and also the maximum values of these parameters observed during the tests. The maximum straight line separation between transmitter and receiver for each transmitter location is listed.

Any power delay profiles not exhibiting at least 20 dB signal above the noise floor were discarded prior to calculation of the results presented in this chapter.

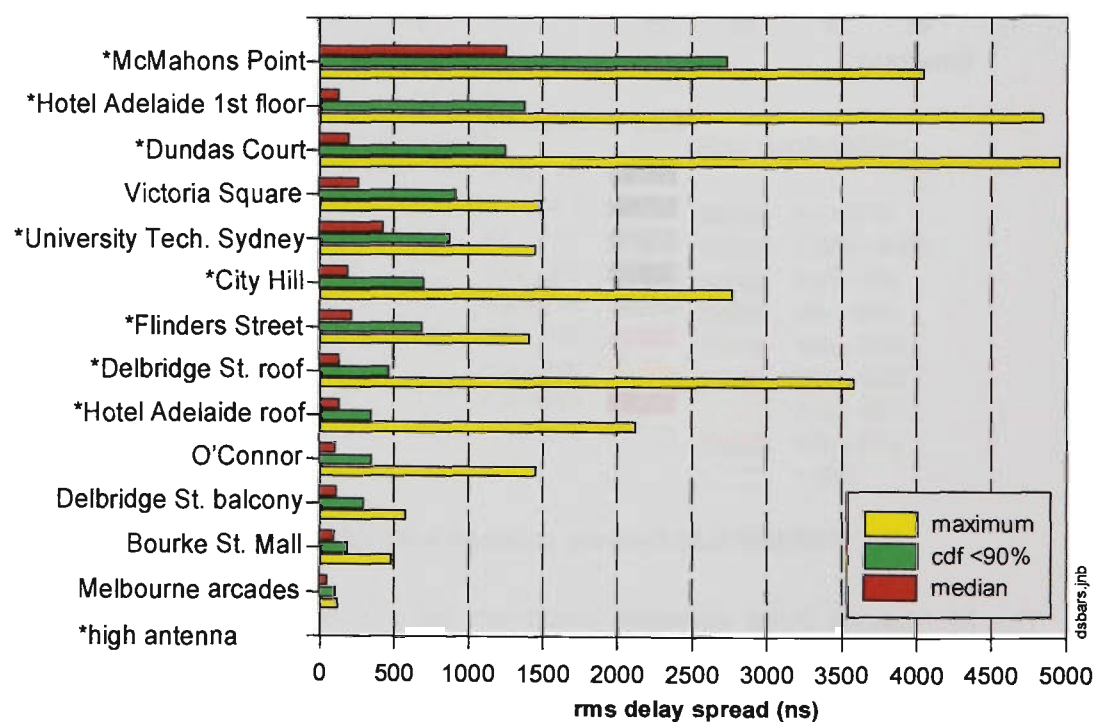


FIGURE 5.32 Comparison of delay spread statistics



TABLE 5.1 Summary of results for high antennas

CITY	LOCATION	Largest Range used (metres)	% probability < value(ns)							
			rms delay spread				mean delay			
			25%	50%	90%	max	25%	50%	90%	max
Melbourne	Flinders Street	500	110	215	690	1410	100	220	390	510
	Delbridge Street roof	1200	70	130	470	3600	60	118	420	1540
Adelaide	Hotel Adelaide 1st floor	2000	37	134	1380	4840	33	117	1000	4860
	Hotel Adelaide roof	2500	44	130	350	2130	36	92	360	1140
Canberra	City Hill	1500	79	193	700	2770	75	190	800	1520
	Dundas Court		85	197	1250	4950	53	176	1200	3750
Sydney	McMahons Point	1600	517	1260	2740	4050	364	1880	4620	6560
	University of Tech. Sydney	1800	123	430	880	1450	138	380	1190	2110

TABLE 5.2 Summary of results for low antennas

CITY	LOCATION	Largest Range used (metres)	% probability < value(ns)							
			rms delay spread				mean delay			
			25%	50%	90%	max	25%	50%	90%	max
Melbourne	Arcades	300	40	52	100	120	62	85	160	210
	Bourke Street Mall	800	60	96	180	480	75	104	280	1260
	Delbridge Street balcony	650	42	110	300	580	33	112	270	490
Adelaide	Victoria Square	1500	76	263	920	1490	54	173	980	1830
Canberra	O'Connor	1400	81	110	350	1450	58	93	390	530

5.8 Conclusions

Results presented in this chapter cover the outdoor measurement program in Australia, which has constituted a major objective of this thesis research project.

As no other wideband measurements for Australia have been published to date, an attempt will be made in this section to put measured results into context by surveying published

overseas measurements.

Tables 5.3 and 5.4 summarize a range of published overseas results, sorted approximately into order of increasing *rms delay spread*. Table 5.5 explains the abbreviations used in the preceding tables. Results from this chapter, highlighted with red outlines, have been inserted into the tables in positions according to median delay spread values.

Several problems arose in this attempt to summarize other published work. Methods and equipment used varied widely, and have not always been fully described. In most cases, full distributions of delay spread values were not given. In some cases, only median (50% CDF) values have been given; in other cases 90% CDF values were given, or maximum values, or a range of values were listed. Because the shape of the delay spread distribution is environment-dependent and quite variable (as is evident from distributions presented in this chapter), it is difficult to do more than very approximately sort measurements which are based on different statistics.

Most of the published measurements were made using omnidirectional vertically polarised antennas. However, in some cases, one of the antennas (transmitter or receiver) was directional in the horizontal plane, which would tend to reduce the influence of multipath effects, leading to smaller values of delay spread. Some measurements were also obtained using omnidirectional antennas with gain in the vertical plane, and a downtilted pattern {Ref[5.9]}.

The most serious inconsistency in the published results is the variation of threshold level used when calculating delay spreads. This topic was covered in detail in Chapter 2 (see section 2.8.1, *rms Delay Spread Sensitivity to Threshold*). In a few cases the threshold is specified relative to the strongest ray {Ref[5.2], Ref[5.10], Ref[5.12], Ref[5.25], Ref[5.30]}. In many other cases, the threshold is related in some way to the noise floor, making delay spread values equipment-dependent. Some authors indeed fail to mention a threshold, introducing even more uncertainty into the question of how delay spreads were calculated. The -15dB threshold adopted in this thesis precludes the very high values of maximum delay spread reported in some publications. In spite of these problems, the reported measurements have been ranked approximately in order of increasing delay spread. The Australian measurements reside in the centre half of the list, displaying neither very small nor very large extremes of delay spread.

Melbourne and Canberra measurements made using a low antenna fit into the second quarter of the list (median delay spreads between 52 and 118 ns), amongst measurements in overseas cities in urban microcells using low antennas. The remaining Melbourne and Canberra measurements, made with high antennas, and the high antenna Adelaide measurements (median delay spreads between 130 and 215 ns) are comparable with urban area high antenna measurements from a group of cities including San Francisco, Brooklyn, Cleveland, The Hague, and Tokyo. Victoria Square Adelaide measurements (median delay spread 263 ns), although classified here as a low antenna case, also fit into this area.

With a median delay spread of 430 ns, *Sydney University of Technology* results group

with other high antenna urban measurements made in cities such as Bristol, Dublin, Cleveland, and Ottawa. The most dispersive Australian location, Sydney Harbour (median delay spread 1.26  $\mu$ s) is comparable with results from New York, Aalborg, Birmingham, Vancouver, and Swiss cities with adjacent mountains.

The work presented in this chapter has described an extensive outdoor measurement program undertaken in four Australian cities, under a variety of propagation environments. Comparing these results with published measurements for a variety of overseas cities and conditions, places the Australian results within the middle region of delay spread values.

A new method of summarizing data to illustrate the time dispersive nature of a propagation environment, the *Propagation Signature* {ref[5.3]}, has been introduced, and applied to the Australian measurements. The propagation signature has been used to explain excess delay paths in relation to scattering objects in the measurement environment.

TABLE 5.3 Australian measurements compared with other published results

Author	Ref	Freq MHz	Ant (m)	W dB	rms delay spread			City	Environment	Dir Ant	Rng max (m)	Res (ns)
					50%	90%	max					
					(ns)	(ns)	(ns)					
Wepman	5.25	1850	8.7	-20	20		2000	Denver	flat rural cell		5000	100
Arowjolu	5.24	1800	5	ns	21		219	Liverpool	LOS microcell dense urban		ns	ns
Arowjolu	5.24	1800	7	ns	22		224	Liverpool	LOS microcell dense urban		ns	ns
Furuno	5.20	2600	low	ns			200		NLOS rectilinear streets		ns	ns
Arowjolu	5.24	1800	7	ns	29		276	Liverpool	NLOS microcell dense urban		ns	ns
Davies	5.19	1870	low	NF+		90		Bristol	chemistry quadrangle microcell		ns	50
Davies	5.19	1870	low	NF+		110		Bristol	Woodland Rd. microcell		ns	50
Davies	5.19	1870	low	NF+		120		Bristol	Tyndall Av. microcell		ns	50
Moriyama	5.17	2600	9	ns	36		190	Mushashino	dense residential 2 storey		500	40
Arowjolu	5.24	1800	5	ns	36		94	Liverpool	NLOS microcell dense urban		ns	ns
Davies	5.19	1870	high	NF+		210		Bristol	suburban residential		ns	50
Kausche	5.21	1800	6	ns	51		216	Munster	LOS, microcell urban, 3-5 storey buildings		ns	ns
Kausche	5.22	1800	6	ns	51		216	Munster	LOS, microcell urban, 3-5 storey buildings		ns	ns
MARTIN	5.2	1890	low	-15	52	100	120	Melbourne	inside city arcades		300	40
MARTIN	5.2	1890	low	-15	96	180	480	Melbourne	Bourke St. Mall, urban highrise		800	40
MARTIN	5.2	1890	low	-15	110	350	1450	Canberra	O'Connor suburban, hilly		1400	40
MARTIN	5.2	1890	low	-15	110	300	580	Melbourne	Delbridge St. balcony, urban/suburban		650	40
Ichitsubo	5.31	2598	7	ns	118	160		Yokosuka	LOS street microcell residential		400	33
Furuno	5.20	2600	low	ns			300		LOS rectilinear streets		ns	ns
Nche	5.27	1800	20	ns	120		700	Liverpool	urban microcell, 9 storey buildings		200	33
MARTIN	5.2	1890	high	-15	130	470	3600	Melbourne	Delbridge St. roof, suburban, distant skyscrapers		1200	40
MARTIN	5.2	1890	high	-15	130	350	2130	Adelaide	Hotel Adelaide roof, urban highrise skyline		2500	40
MARTIN	5.2	1890	high	-15	134	1360	4840	Adelaide	Hotel Adelaide 1st floor, urban highrise skyline		2000	40
Devasirvatham	5.16	850	6	ns	135		243	Brooklyn	urban microcell, buildings to 4 storeys		200	25
Blackard	5.15	1900	3.7	ns	137		1012	SanFrancisco	LOS microcell		ns	ns
Feuerstein	5.29	1900	3.7	ns	137		1012	SanFrancisco	urban microcell		1300	100
Devasirvatham	5.16	1900	6	ns	140		233	Brooklyn	urban microcell, buildings to 4 storeys		200	25
Jorgensen	5.30	1900	ns	-14	160			Cleveland	rural		ns	200
Ichitsubo	5.31	2598	7	ns	160	240		Tokyo	LOS street microcell urban		300	33
Devasirvatham	5.7	850	9	ns	175		640	Red Bank	suburban microcell, 3 storey, distant 10 storey		800	25
Feuerstein	5.29	1900	8.5	ns	177		732	SanFrancisco	urban microcell		1200	100
Van Rees	5.6	910	50	fixed	190		900	The Hague	suburban		2200	200
MARTIN	5.2	1890	high	-15	193	700	2770	Canberra	City Hill, urban, 4 storey		1500	40
MARTIN	5.2	1890	high	-15	197	1250	4950	Canberra	Dundas Court, commercial, suburban, nearby hills			40
Ichitsubo	5.31	2598	30	ns	200	330		Tokyo	LOS street microcell urban		300	33
MARTIN	5.2	1890	high	-15	215	690	1410	Melbourne	Flinders St. city highrise		500	40
Blackard	5.15	1900	13.3	ns	258		1859	SanFrancisco	LOS microcell		ns	ns
MARTIN	5.2	1890	low	-15	263	920	1490	Adelaide	Victoria Square, city highrise		1500	40
de Weck	5.9	1050	210	NF+6		800		Lucerne	mountainous		5600	200
Feuerstein	5.29	1900	13.3	ns	276		1860	SanFrancisco	urban microcell		2000	100
Sousa	5.28	910	high	var	310		6300	Toronto	suburban		2000	100
Davies	5.19	1870	high	NF+		1000		Bristol	urban city centre		ns	50
Jorgensen	5.30	1900	ns	-14	350			Cleveland	suburban		ns	200
Salous	5.32	1808	ns	ns	353		1120	Dublin	urban city centre		ns	14
Seidel	5.13	942	var	var	400		19000	4 cities	urban		6500	500

(continued)

TABLE 5.4 Australian measurements compared with other published results (continued)

Author	Ref	Freq MHz	Ant (m)	W dB	rms delay spread			City	Environment	Dir	Rng	Res
					50%	90%	max			Ant	max (m)	(ns)
					(ns)	(ns)	(ns)					
MARTIN	5.2	1890	high	-15	430	880	1450	Sydney	University of Technology 23rd floor, city highrise		1800	40
Bultitude	5.10	910	4.8	-25	460		2130	Ottawa	urban		ns	ns
Bultitude	5.10	910	8.2	-25	490		2940	Ottawa	urban		ns	ns
Bultitude	5.10	910	6.5	-25	530		2150	Ottawa	urban		ns	ns
Takeuchi	5.8	400	27	ns	560		1680	Kyoto	urban	dir	960	600
Jorgensen	5.30	1900	ns	-14	600			Cleveland	urban city centre		ns	200
Bultitude	5.10	910	3.7	-25	670		1230	Ottawa	urban		ns	ns
Sousa	5.28	910	high	var	710		2600	Toronto	urban		1000	100
Turkmani	5.14	880	35	ns	750		6000	Liverpool	urban		ns	100
Wepman	5.25	1850	103	-20	750		1700	Denver	urban high rise cell		5000	100
Bajwa	5.5	436	36	ns	815		1800	Birmingham	suburban		3000	100
Rappaport	5.11	892	10	var	1000		25500	San Francisco	urban, surrounding hills		5000	500
Seidel	5.13	942	20	ns			2900	Frankfurt	urban, skyscrapers		ns	ns
Morgensen	5.12	910	50	-20	1000		4800	Aalborg	urban, 6 storey buildings	dir	3000	1000
Jorgensen	5.30	1900	ns	-14	1000			Cleveland	urban		ns	200
Ichitsubo	5.31	2598	30	ns	1000	2700		Yokosuka	urban circular microcell		1000	33
Ichitsubo	5.31	2598	30	ns	1000	1800		Tokyo	urban circular microcell		1000	33
Morgensen	5.12	910	32	-20	1100		4300	Aalborg	urban, 6 storey buildings	dir	3000	1000
Cox	5.4	910	120	ns	1200		3300	New York	urban macrocell, skyscrapers		2500	100
Seidel	5.13	942	23	ns			5400	Stuttgart	suburban, some 4 storey, distant hills		ns	ns
MARTIN	5.2	1890	high	-15	1260	2740	4050	Sydney	McMahons Point, city highrise across harbour		1600	40
Morgensen	5.12	910	24	-20	1300		5500	Aalborg	urban, 6 storey buildings	dir	3000	1000
Mohr	5.26	2000	28	ns	1320		1600	Munich	NLOS urban macrocell, roof level antenna		ns	100
de Weck	5.9	1050	360	NF+6		4000		Stockmatt	mountainous	dir	7000	200
Driessen	5.18	910	ns	var	1480		23000	Vancouver	urban, surrounding high mountains		ns	100
Bajwa	5.5	436	28	ns	1500		2600	Birmingham	urban		3000	100
de Weck	5.9	1050	140	NF+6		4600		Yvome	mountainous		4600	200
de Weck	5.9	850	80	NF+6		4900		Berne	mountainous		5500	150
Rappaport	5.11	892	21	var	2000		7000	Greenbelt	residential multistorey, office, hilly		4000	500
Mohr	5.26	2000	28	ns	2020		2800	Munich	receiver rural next to freeway		ns	100
de Weck	5.9	1050	210	NF+6		6100		Lucerne	mountainous	dir	5600	200
de Weck	5.9	1050	110	NF+6		7100		Stans	mountainous		7000	200
de Weck	5.9	1050	140	NF+6		7700		Yvome	mountainous	dir	4600	200
Rappaport	5.11	892	35	var	2500		7500	Washington	urban		ns	500
Rappaport	5.11	892	43	var	2500		13500	Oakland	urban, surrounding mountains		12000	500
Mohr	5.26	2000	60	ns	2590		3200	Munich	NLOS urban to 6 storeys, distant high buildings		ns	100
de Weck	5.9	850	170	NF+6		9100		Krattigen	mountainous		6500	150
de Weck	5.9	1050	ns	NF+6		10000		Geneva	mountainous	dir	4600	200
de Weck	5.9	1050	220	NF+6	3600	10000		Vevey	mountainous	dir	12900	200
Driessen	5.18	910	ns	var	6800		21000	Vancouver	bdge, surrounding high mountains		ns	100
de Weck	5.9	900					100	COST 207	rural			
de Weck	5.9	900					1000	COST 207	typical urban			
de Weck	5.9	900					2500	COST 207	typical poor urban			
de Weck	5.9	900					5000	COST 207	typical poor hilly and mountainous			

TABLE 5.5 Explanation of abbreviations used in Tables 5.3 and 5.4

Table entry	Meaning
Ref	reference (see section 5.10)
Ant	transmitter antenna height (metres)
	high = above surrounding roof levels
	low = below surrounding roof levels
W dB	threshold in dB relative to strongest path (eg. -15), or as otherwise shown
	ns = not specified
	NF+ = noise floor plus a margin
	NF+6 = noise floor plus 6 dB
	var = variable, usually related to the noise floor
Dir Ant	dir = antenna(s) directional in azimuth.
	no entry = omnidirectional antennas (may have gain in the vertical plane)
Rng max (m)	maximum distance from transmitter to receiver (metres)
Res (ns)	channel sounder time resolution in nanoseconds

---

## 5.9 References

- [5.1] G.T.Martin and M.Faulkner, "Delay Spread Measurements at 1890 MHz in Pedestrian Areas of the Central Business District in the City of Melbourne", Proceedings IEEE 44th. Vehicular Technology Conference VTC'94, Stockholm, Sweden, Vol.1, June 1994, pages 145-149.
- [5.2] G.T.Martin and M.Faulkner, "Wide Band Propagation Measurements in Four Australian Cities", Proceedings IEE 10th. International Conference on Antennas and Propagation ICAP'97, Vol.2, April 1997, pages 2.199-2.203.
- [5.3] G.T.Martin, "Propagation Signatures to Characterize Wideband Environments", 10th. Virginia Tech Symposium on Wireless Personal Communications, Blacksburg Virginia, USA, June 2000.
- [5.4] Donald C.Cox, Robert P.Leck, "Distributions of Multipath Delay Spread and Average Excess Delay for 910-MHz Urban Mobile Radio Paths", IEEE Transactions on Antennas and Propagation, Vol.AP-23, No.2, March 1975, pages 206-213.
- [5.5] A.S.Bajwa, J.D.Parsons, "Small-area Characterisation of UHF Urban and Suburban Mobile Radio Propagation", IRE Proceedings Part F, Vol.129, No.2, April 1982, pages 102-109.
- [5.6] Jan Van Rees, "Measurements of the Wide-Band Radio Channel Characteristics for Rural, Residential, and Suburban Areas", IEEE Transactions on Vehicular Technology, Vol.36, No.1, February 1987, pages 2-6.
- [5.7] David M.Devasirvatham, "Radio Propagation Studies in a Small City for Universal Portable Communications", IEEE Vehicular Technology Conference VTC'88, Philadelphia USA, June 1988, pages 100-104.
- [5.8] Tsutomu Takeuchi, Fumjo Ikegami, Susumu Yoshida, Nobuyoshi Kikuma, "Comparison of Multipath Delay Characteristics with BER Performance of High Speed Digital Mobile Transmission", IEEE Vehicular Technology Conference VTC'88, Philadelphia USA, June 1988, pages 119-126.
- [5.9] Jean-Paul de Weck, Peter Merki and Rudolf Werner Lorenz, "Power Delay Profiles Measured in Mountainous Terrain", IEEE Vehicular Technology Conference VTC'88, Philadelphia USA, June 1988, pages 105-112.
- [5.10] R.J.C.Bultitude, G.K.Bedal, "Propagation Characteristics on Microcellular Urban Mobile Radio Channels at 910 MHz", IEEE Journal on Selected Areas in Communications, Vol.7, No.1, January 1989, pages 31-39.
- [5.11] T.S.Rappaport, S.Y.Seidel, "Path Loss and Multipath Delay Statistics in Four European Cities for 900 MHz", Electronic Letters, Vol.26, No.20, September 1990, pages 1713-1715.
- [5.12] Preben Elgaard Mogensen, Patrick Eggers, Jan Elling, "Propagation Measurements in City Area for GSM Small Cells", Proceedings 4th. Nordic Seminar on Digital Mobile Radio Communications, DMR IV, Oslo, Norway, June 1990, pages 1-8.
- [5.13] Scott Y.Seidel, Theodore S.Rappaport, Sanjiv Jain, Michael L.Lord & Rajendra Singh, "Path Loss, Scattering, and Multipath Delay Statistics In Four European Cities for Digital Cellular and Microcellular Radiotelephone", IEEE Transactions on Vehicular Technology, Vol.40, No.4, November 1991, pages 721-730.
- [5.14] A.M.D.Turkmani, D.A.Demery & J.D.Parsons, "Measurement and Modelling of Wideband Mobile Radio Channels at 900 MHz", IEE Proceedings-I, Vol.138, No.5, October 1991, pages 447-457.



- [5.15] Kenneth L.Blackard, Martin J.Feuerstein, Theodore S.Rappaport, Scott Y.Seidel, Howard H.Xia, "Path Loss and Delay Spread Models as Functions of Antenna Height for Microcellular System Design", IEEE 42nd. Vehicular Technology Conference VTC'92, Denver USA, May 1992, pages 333-337.
- [5.16] D.M.J.Devasirvatham, C.Banerjee, R.R.Murray, D.A.Rappaport, "Two-Frequency Radiowave Propagation Measurements in Brooklyn", IEEE International Conference on Universal Personal Communications, ICUPC'92, Dallas, USA, Sept. 1992, pages 23-27.
- [5.17] Eimatsu Moriyama, Mitsuhiko Mizuno, Yoshinori Nagata, Yukitsuna Furuya, Isamu Kamiya & Seiji Hattori, "2.6 GHz Band Multipath Characteristics Measurement in a Residential Area for Micro-cellular Systems", IEEE Vehicular Technology Conference VTC'92, Denver USA, May 1992, pages 423-426.
- [5.18] Peter F.Driessen, "Multipath Delay Characteristics in Mountainous Terrain at 900 MHz", IEEE Vehicular Technology Conference VTC'92, Denver USA, May 1992, pages 520-523.
- [5.19] R.L. Davies, "The Measurement and Application of Multipath Propagation in the Microwave Frequencies Around 1.8 GHz", PhD Thesis, University of Bristol, UK., July 1992.
- [5.20] Tatsuo Furuno, Tokio Taga, "Time Delay Spread for Low Antenna Height Microcellular System", Asia-Pacific Conference on Communications, APCC'93, Taejon, Korea, August 1993, pages 125-128.
- [5.21] U. Kausche, "Measurements of Power Delay Profiles and Linked Simulations for DECT in Urban Roads with Antennas Placed Below Rooftops", COST 231 Technical Document No.100, Limerick, September 1993.
- [5.22] U. Kausche, "Wideband Pathloss and Delay Spread Measurements in a NLOS Situation", COST 231 Technical Document No.97, Limerick, September 1993.
- [5.23] A.M.D. Turkmani, A.A. Arowojolu, "Microcellular Propagation for PCN Networks - A Review", Proceedings International Conference on Universal Personal Communications, ICUPC'94, SanDiego, USA, Sept./Oct. 1994, pages 171-177.
- [5.24] A.A. Arowojulu, A.M.D. Turkmani, J.D. Parsons, "Time Dispersion Measurements in Urban Microcellular Environments", IEEE 44th. Vehicular Technology Conference VTC'94, Stockholm, Sweden, June 1994, pages 150-154.
- [5.25] Jeffrey A.Wepman, J. Randy Hoffman, Lynette H.Loew, "Characterization of Macrocellular PCS Propagation Channels in the 1850-1900 MHz Band", IEEE International Conference on Universal Personal Communications ICUPC'94, SanDiego, USA, September 1994, pages 165-170.
- [5.26] Werner Mohr, "Radio Propagation for Local Loop Applications at 2 GHz", IEEE International Conference on Universal Personal Communications ICUPC'94, SanDiego, USA, September 1994, pages 119-123.
- [5.27] C.Nche, D.G.Lewis, A.M.D.Turkmani, "Wideband Characterisation of Mobile Radio Channels at 1.8 GHz", IEEE Vehicular Technology Conference VTC'94, Stockholm, Sweden, June 1994, pages 1775-1779.
- [5.28] Elvinao S.Sousa, Vladan M.Jovanovic, Christian Daigneault, "Delay Spread Measurements for the Digital Cellular Channel in Toronto", IEEE Transactions on Vehicular Technology, Vol.43, No.4, November 1994, pages 837-847.
- [5.29] Martin J.Feuerstein, Kenneth L.Blackard, Theodore S.Rappaport, Scott Y.Seidel, Howard H.Xia, "Path Loss, Delay Spread, and Outage Models as Functions of Antenna Height for Microcellular System Design", IEEE Transactions on Vehicular Technology, Vol.43, No.3, August

1994, pages 487-498.

[5.30] Jeffrey Jorgensen, Ivica Kostanic and William Foose, "Application of Channel Sounding to CDMA PCS Design at 1900 MHz", IEEE Vehicular Technology Conference VTC'97, Phoenix, USA, Vol.3, May 1997, pages 1937-1941.

[5.31] Shinichi Ichitsubo, Tatsua Furuno, Ryoji Kawasaki, "A Statistical Model for Microcellular Multipath Propagation Environment", IEEE Vehicular Technology Conference VTC'97, Phoenix, USA, Vol.1, May 1997, pages 61-66.

[5.32] S.Salous, N.Bajj, "Urban Wideband Measurements at 1.8 GHz with Different Chirp Bandwidths", IEEE Vehicular Technology Conference VTC'98, Ottawa, Canada, Vol.2, May 1998, pages 697-701.



# Chapter 6: RAKE Diversity

## 6. INTRODUCTION

Measured propagation data may be employed to answer questions of system performance in real radio environments, without the limitation of simplifying assumptions inherent to a lesser or greater extent in analysis using channel models.

In this chapter, some of the measurements described in Chapter 4 and Chapter 5 are applied to provide insights into choosing the diversity order for code division multiple access (CDMA) systems.

Based on wideband propagation measurements in three different outdoor environments, and indoor measurements in a multi-floor building, the relationship between the number of RAKE receiver {Ref[6.18]} ‘branches’, ‘fingers’ or ‘tines’ and the proportion of the total incident time-dispersed signal power utilised in the receiver is examined, for various system bandwidths.

Wide band propagation measurement data with a resolution of 40 ns for the outdoor environments, is filtered to produce channel sounding power delay profiles corresponding to system RF bandwidths of 1.25, 2.5, 5, 8, and 16 MHz. Indoor measurement data with a higher resolution of 10 ns is filtered to equivalent RF bandwidths of 5, 10, 20, 30 and 50 MHz.

The number and power levels of all resolvable rays are found, and the aggregate power in the strongest  $n$  rays, where  $n$  ranges from 1 to 10, is calculated as a fraction of the total profile power. Results show how much received power is discarded as a result of using a limited number of tines, providing a guide for choosing the optimum number of tines for wideband systems.

A simple empirical model is proposed, which shows that the effective number of RAKE tines or branches is proportional to the square root of the system bandwidth, and proportional to the square root of the median instantaneous rms delay spread. A pre-publication copy of the author’s paper on this work {Ref[6.11]} was sent in March 1997 to Jan-Erik Berg at *Eric-*

*son Radio Systems AB*, Stockholm, prompting a theoretical simulation study in Sweden {Ref[6.13]} which showed broad agreement with the author's conclusions, and became an input document to *EURO-COST 259 (European Cooperation in the Field of Scientific and Technical Research)*, and possibly contributed to the choice of wideband CDMA as a third generation system. The *Ericsson* group also applied a similar analysis to some of their own propagation measurements {Ref[6.14]}.

Papers on aspects of this chapter were presented by the author at the *8th. IEEE International Symposium on Personal, Indoor and Mobile Radio Communications PIMRC'97, Helsinki, Finland, September 1997* {Ref[6.11]}, and at the *3rd. ACTS Mobile Communications Summit, Rhodes, Greece, in June 1998* {Ref[6.15]}. Ideas described in this chapter have also led to publications by Ericsson research staff {Ref[6.13], Ref[6.14]}.

## 6.1 Multipath Diversity

In free space, only a tiny fraction of a communications system's radiated power is intercepted by the receiver antenna, with the rest being lost in other directions. Typical mobile radio Personal Communication Systems (PCS) operate in a cluttered urban environment where propagation conditions are far removed from the free space case, and where multipath propagation is the norm. Indeed, without multipath effects, cellular mobile communication systems could not function. Often no line of sight path (LOS) exists, and the receiver depends upon the multipath signal consisting of time-dispersed rays arriving via reflection, refraction and diffraction mechanisms.

Indoor PCS or Wireless Local Area Network (WLAN) radio systems operate in an enclosed environment, with windows to external scatterers. If no LOS path exists, the receiver relies on multipath signals from inside the building, or from outside scatterers.

## 6.2 RAKE Receivers

Wide band CDMA systems using RAKE receivers {Ref[6.18]} are able to exploit multipath propagation to benefit from path diversity. Using more than one path, or ray, increases the signal power available to the receiver and, with suitable combining, improves the received signal-to-noise power ratio, reduces fading, and eases the power control problem.

RAKE receivers also offer other attractive possibilities, such as macrodiversity (the ability to access two base stations simultaneously) which allows soft handover to be implemented, greatly reducing the likelihood of dropped calls {Ref[6.16]}.

Third generation mobile systems approaching standardisation include CDMA technology with RF bandwidths ranging from 1.25 MHz to 20 MHz. { Ref[6.1]}. In the USA, the IS-95 standard (1.25 MHz) is established, and is now being installed in Australia. In Europe, examples of wide band CDMA research have included the UK Department of Trade and Industry/Engineering and Physical Sciences Research Council DTI/EPSRC LINK-CDMA project (8 MHz) which resulted in a working test-bed {Ref[6.2]}, and the *Research and Development in Advanced Communications Technologies in Europe* (RACE) CoDiT project, subsequently further developed into a mobile test-bed. Recently, wideband CDMA known as WCDMA, has been selected by the *European Telecommunications Standards Institute* (ETSI) as the basic radio access system for third generation *Universal Mobile Telecommunications Standard* (UMTS) services {Ref.[6.3]}. The basic chip rate for WCDMA is 4.096 MHz, with carrier spacing of 5 MHz.

RAKE receivers suffer from high complexity, which increases with the number of tines utilised. How does the designer choose the best number of tines, bearing in mind increasing complexity and cost, and the trend to diminishing benefit, as the number is increased? This chapter studies one aspect of the question, by examining the utilisation of the available signal power as the number of tines is increased.

As system bandwidth is increased, the time resolution ability increases, showing more detail in the power delay profile. Each resolvable time bin becomes more deterministic with increasing bandwidth, because the number of interfering rays contributing to the bin reduces; in the limit with infinite bandwidth (such as can be simulated using a ray tracing approach) each bin contains a single ray, and small scale fading vanishes, leaving only large scale fading (see Chapter 2, Section 2.1). Ref[6.8] models fading reduction with bandwidth increase using ray tracing simulation. The topic is also treated in Ref[6.5], Ref[6.6], Ref[6.7], Ref[6.9], Ref[6.10], and Ref[6.12]. For example, as the bandwidth increases from 1.25 MHz to 20 MHz, Ref[6.10] shows an increase in  $K_{factor}$  from -6 dB to 6.7 dB in the dominant branch. Later branches or rays show a smaller increase in  $K_{factor}$ . Fading reduction as bandwidth increases is further improved by exploiting internal diversity, where the strongest time bins undergo maximal ratio combining.

## 6.3 Propagation Data

Measured wideband propagation data is used for this analysis. Outdoor data was obtained in the cities of Adelaide, Melbourne and Sydney. A full description of these measurements is given in Chapter 5 and Appendix E. Indoor measurements were made in the *Victoria University of Technology* Engineering building known as 'D' Block. Measurements made in this building are described in detail in Chapter 4.

Omnidirectional vertically polarised antennas were used, usually with a discone as the transmitting antenna and a halfwave antenna for the receiver.

## 6. 4 Measurement Environments

Adelaide measurements were done in North Adelaide, a suburban area with predominantly single storey buildings. The transmitter was located on the flat roof of the Hotel Adelaide, six storeys high, with unobstructed views in all directions.

Melbourne measurements were done three kilometres from the city centre, in North Fitzroy, an inner suburban area with residential terrace housing, comprising a mixture of one and two storey dwellings. A two storey terrace house near the top of a slight hill was used as a base station site, with the transmitter antenna on the upper front balcony, and below the prevailing roof lines.

Sydney measurements were done in the main city area with the transmitter overlooking the city from the 23rd. floor of the *University of Technology Sydney*, a prominent high building to the south of the city centre.

Indoor measurements were performed in the *Victoria University of Technology* engineering building, known as D block. This building has been well described in Chapter 4.

## 6. 5 Receiver

For all outdoor measurements, the receiver was carried in a car, with a half wave omni-directional roof mounted antenna. The car was stationary for each measurement, at locations scattered throughout the measured area, rather than following an equally spaced measurement route.

Indoor measurements were performed with the receiver on a stationary trolley, moved along a route between measurements. Instantaneous impulse responses were used for all results presented in this chapter (and for all results in this thesis unless otherwise indicated), without any averaging. Table 6.1 shows a summary of outdoor propagation data.

Table 6.1 Outdoor propagation data

City	Location	Max. Range (metres)	% probability < value (ns)							
			rms delay spread				average delay			
			25%	50%	90%	Max.	25%	50%	90%	Max.
Melbourne	Delbridge St. (balcony)	650	42	110	300	580	33	112	270	490
Adelaide	Hotel Adelaide (roof)	2500	44	130	350	2130	36	92	360	1140
Sydney	University of Tech. Sydney	1800	123	430	880	1450	138	380	1190	2110

## 6. 6 Filtering

Filtering data collected using a wideband channel sounder is equivalent to repeating the measurements several times using a series of sounders with reduced bandwidths, but with

the advantage that the channel has not altered between bandwidth changes.

A channel impulse response measured with infinite bandwidth would show every possible ray arriving at the receiver. As the bandwidth is restricted, the peaks of the impulse response broaden, and each resolved ray consists of the three dimensional vector addition of an increasing number of closely spaced paths. The measured baseband wideband impulse response in-phase and quadrature components, appended with zero samples before and after, are filtered in the time domain using a maths software package (*MATLAB®*). The *filtfilt* function {Ref[6.17]} is used with a 2-pole Butterworth lowpass filter. This function performs digital filtering with zero phase or time shifts, by running the data through the filter in the forward direction, then reversing the filtered sequence and running it back through the filter. This process doubles the filter order, and cancels any phase or time shifts. After filtering, the power delay profile (PDP) is calculated, and the peak power is normalised to 0 dB. The system RF bandwidth as defined by this filtering process is twice the low pass filter cutoff frequency. All bandwidths referred to in this chapter are RF system bandwidths.

Figure 6.1 shows part of an *outdoor mode* PDP before additional filtering, and with filtering, for system bandwidths of 1.25 MHz and 8 MHz.

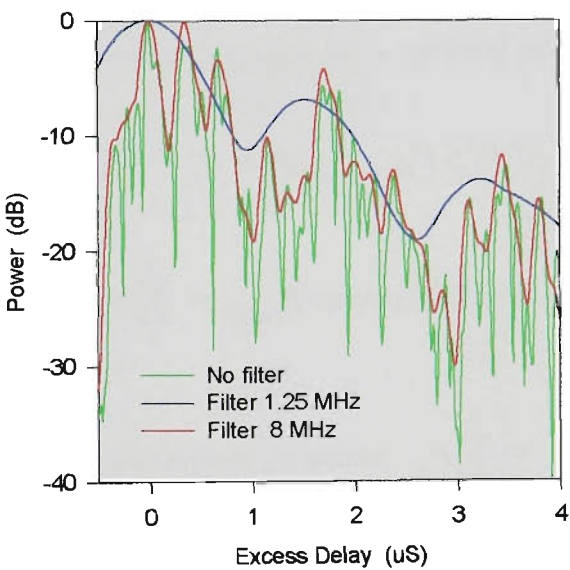


FIGURE 6.1 Filtered power delay profile (file sydb18)

### 6.7 Thresholds

Filtering reduces the dynamic range of the signal, because of a reduction in processing gain, so prior to filtering, a threshold is applied to I and Q values in the following way:

(i) the PDP using unfiltered data is formed, and a threshold is applied. (ii) then any power samples below the threshold are used to identify the constituent I and Q components, which are set to zero prior to the filtering process. (iii) a second threshold is then applied to the filtered PDP.

Generally both thresholds have been set at -20dB relative to the strongest ray. Conse-

quently, any ray contributing less than 1% of the strongest ray power is discarded. This affects the calculation of both total power and the cumulative power of  $n$  rays, but as the work in this chapter is based on a level of -1dB, or 79.4% of the total power, the effect of the thresholds is insignificant.

## 6.8 Tine Power and Total Power

Impulse response excess delay is measured between -1  $\mu$ s and +25  $\mu$ s relative to the strongest peak. Dynamic range of the measurement before filtering, that is, the power difference between the peak power and the noise floor, is typically between 30 dB and 40 dB. Data with insufficient dynamic range is discarded. All  $j$  peaks in the filtered power delay profiles are identified. A peak is defined as a sample preceded by two increasing samples, and followed by two decreasing samples.

After the PDP has been reduced to a list of peak values, the total profile power  $P_{total}$  is calculated as the sum of all peak powers. The strongest  $n$  peaks are identified, and the cumulative sum of these peak powers is calculated for values of  $n$  between 1 and 10. The sum of peak powers in the strongest  $n$  peaks is called the tine power  $P_n$  where  $n$  is the number of tines, and results are given in terms of the ratio of tine power to total power,  $P_{used}$ .

$$\text{if } P_i \leq P_{threshold} \text{ then } P_i = 0$$

$$\text{total PDP power } P_{total} = \sum_1^j P_i \quad (\text{EQ 6.1})$$

$$\text{tine power } P_n = \sum_1^n P_s \quad \text{where } P_s \text{ are the strongest peaks in descending order}$$

$$\text{receiver power utilised is the ratio } P_{used} = \frac{P_n}{P_{total}} \quad (\text{EQ 6.2})$$

## 6.9 Outdoor Results

Results for two of the three different environments are plotted in Figures 6.2 to 6.5, as cumulative distributions at two different bandwidths, 1.25 MHz and 8 MHz. The axes have been kept the same for this family of plots, to facilitate comparison.

The vertical axis gives the probability that the power ratio  $P_{used}$  is greater than the  $P_{used}$  value on the horizontal axis. A family of curves for the first ten strongest rays,  $n=1$  to  $n=10$  is shown. The  $n=3$  curve, for example, is the curve for three tines, using the combined power of the three strongest rays.

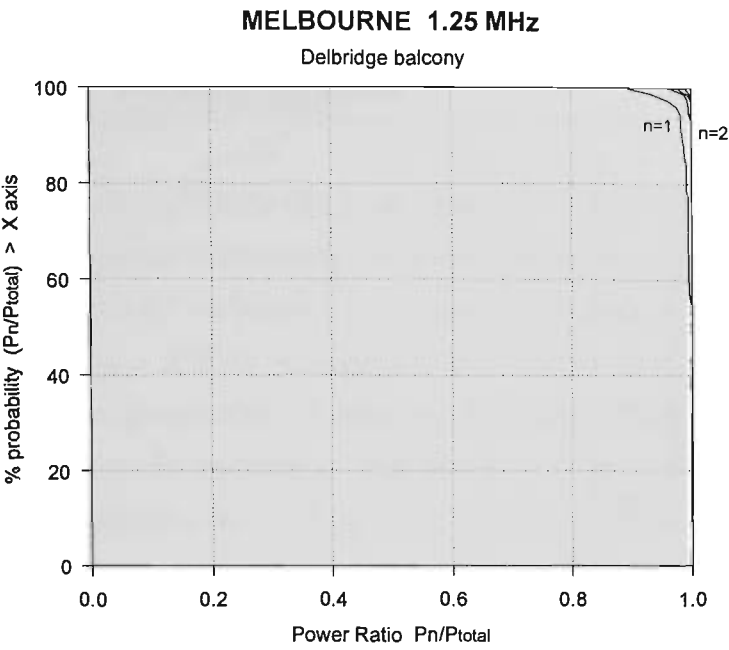


FIGURE 6.2 Melbourne - 1.25 MHz bandwidth

At 1.25 MHz bandwidth, Figure 6.2 shows (for example) 95% probability that more than 95% of the total power is contained in just one tine.

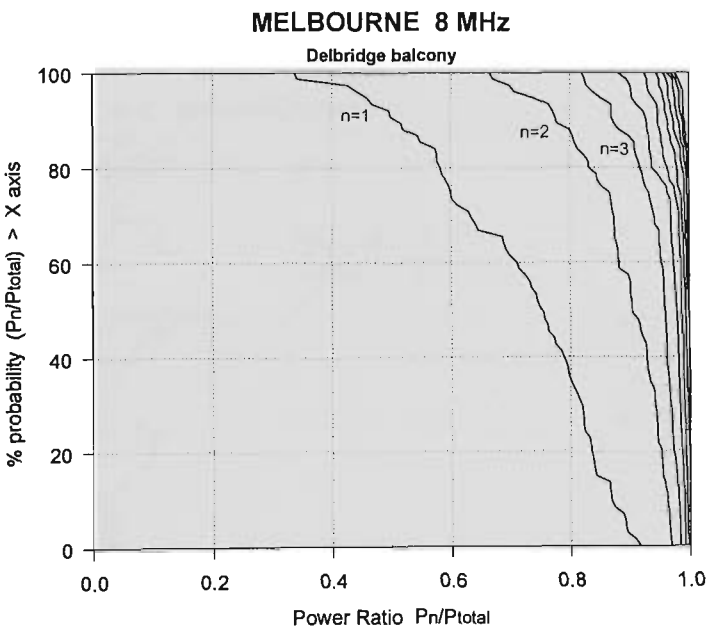


FIGURE 6.3 Melbourne - 8 MHz bandwidth



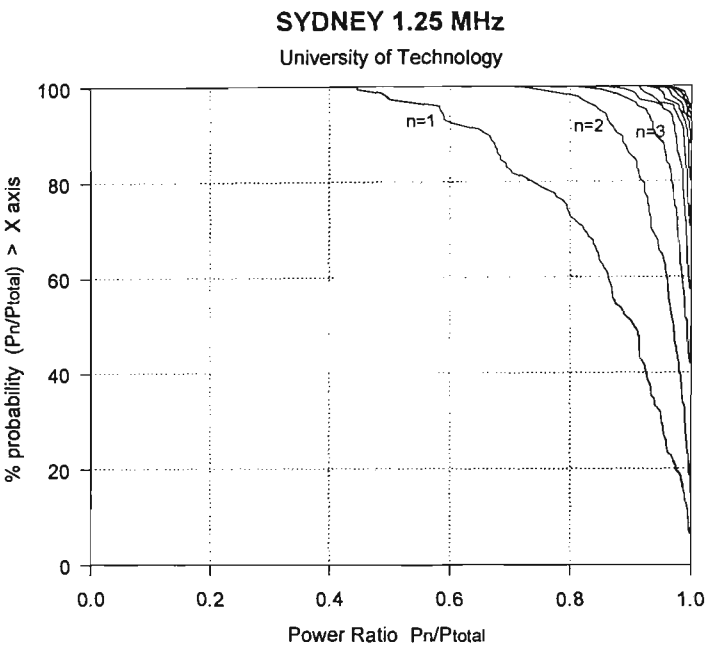


FIGURE 6.4 Sydney - 1.25 MHz bandwidth

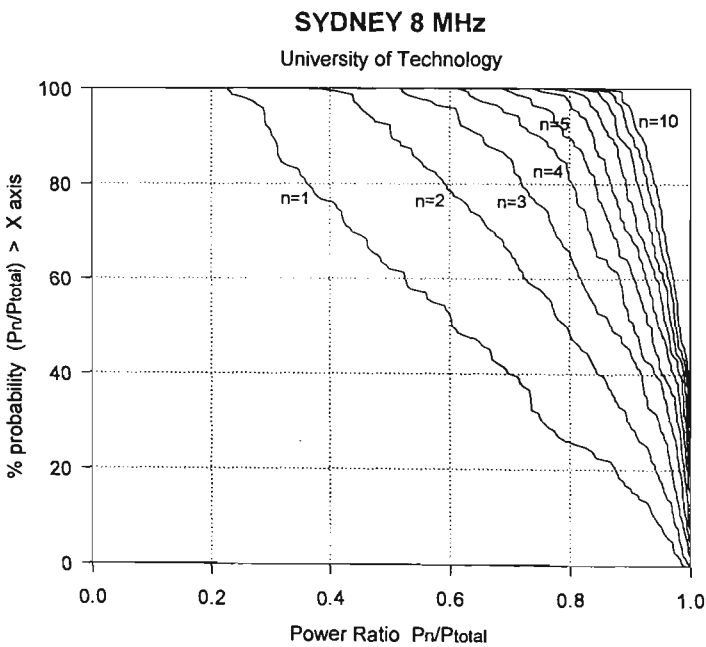


FIGURE 6.5 Sydney - 8 MHz bandwidth

Comparing Figures 6.2 and 6.3 shows that as the bandwidth increases, more tines must be utilised to capture the same proportion of the total profile power. Figure 6.3 (8 MHz bandwidth) shows 95% probability that more than 95% of the total power is contained in the 6 strongest tines, compared with 1 tine for 1.25 MZ bandwidth. Similarly, the much more dispersive Sydney environment shown in Figures 6.4 and 6.5 shows that the total power is

spread over an even higher number of tines.

### 6. 10 Number of Tines Plots

To illustrate the effect of bandwidth more clearly, the data for the three different outdoor measurement environments is plotted in a different manner in the following graphs, Figure 6.6 (Melbourne), Figure 6.7 (Adelaide) and Figure 6.8 (Sydney). These plots show the worst case power ratio  $P_{used}$  at 95% of locations, or in other words for 95% of the power delay profile data,  $P_{used}$  is greater than or equal to the values plotted. The plots are constructed from data shown on the cumulative distribution plots, such as Figure 6.2 to Figure 6.5. On the graphs in Figures 6.6 to 6.8,  $P_{used}$  is expressed in decibels, where 0 dB corresponds to complete utilisation of the profile power, and -1dB corresponds to utilisation of 79.4% of the profile power.

The other variables are bandwidth, with values of 1.25 MHz, 2.5 MHz, 4 MHz, 8 MHz and 16 MHz, and the number of tines used, ranging between 1 and 10.

The graphs clearly illustrate the increase in the number of tines required for a fixed power ratio  $P_{used}$  as the system bandwidth is increased. This comes about from the increase in time resolution in the power delay profile of the channel impulse response with greater system bandwidths. Melbourne and Adelaide results are similar, which is in line with the similar rms delay spreads obtained with these measurements. Sydney is a much more dispersive case, with rms delay spreads over three times greater, and this is reflected in Figure 6.8.

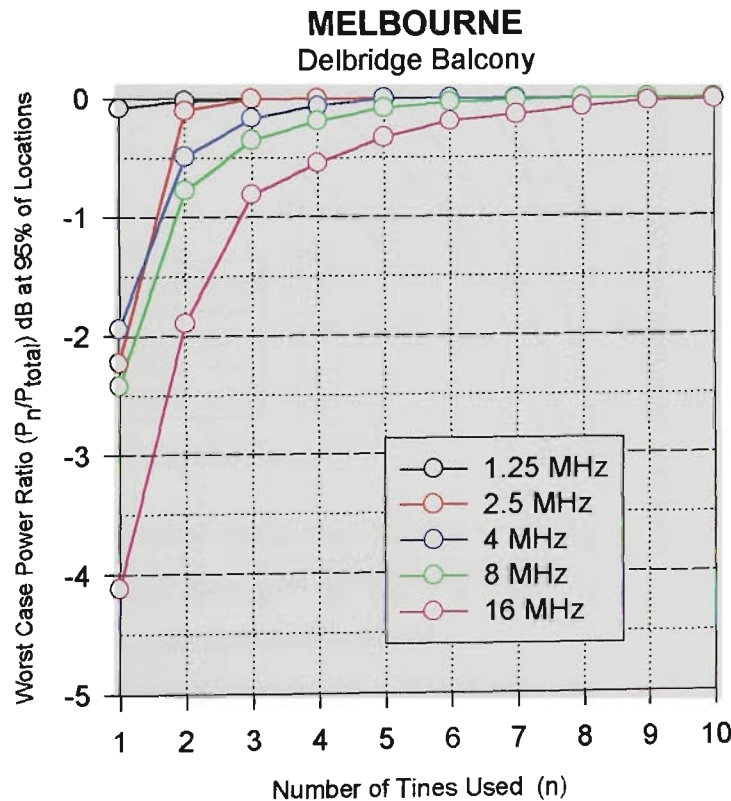


FIGURE 6.6 Number of tines - Melbourne

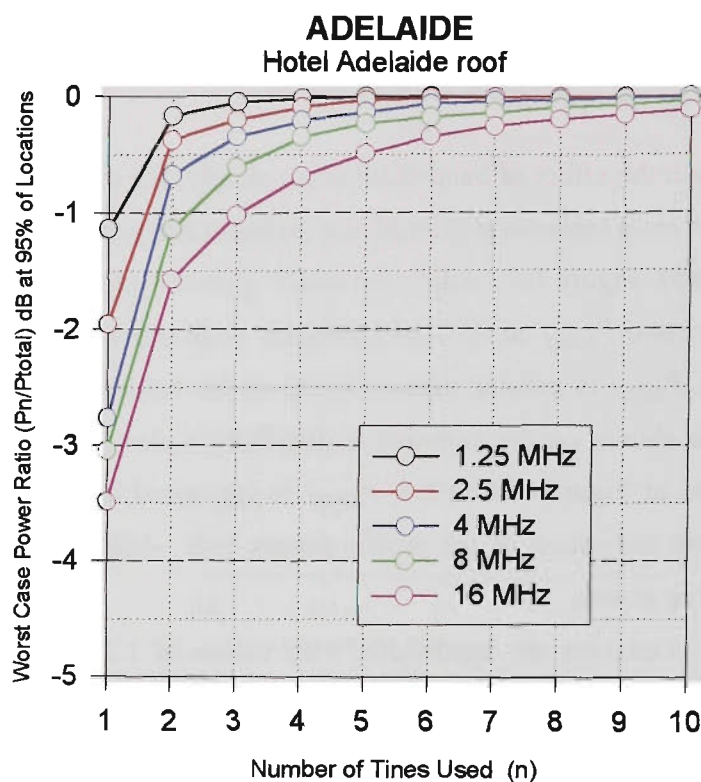


FIGURE 6.7 Number of tines - Adelaide

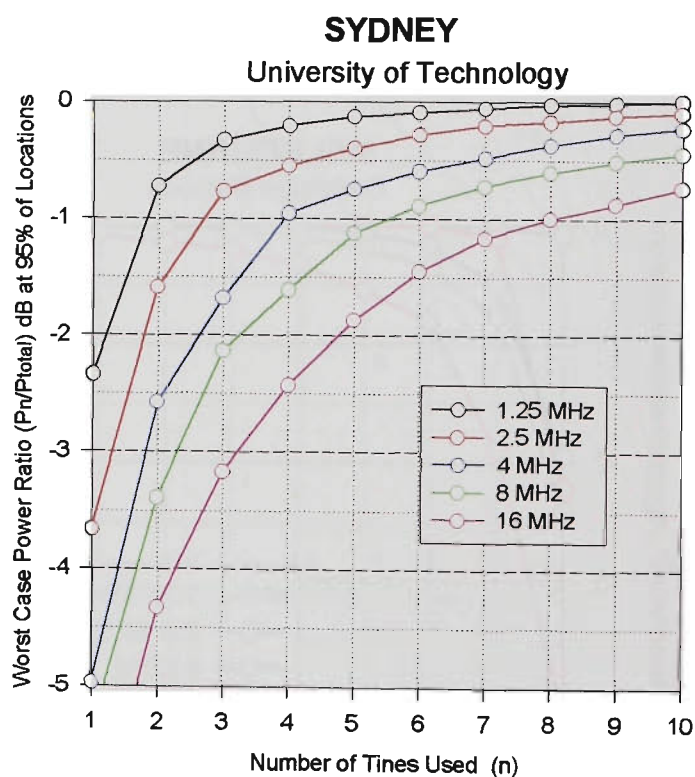


FIGURE 6.8 Number of tines - Sydney

The number of variables involved, and wide variations in the channel impulse response, complicates the presentation of results in a meaningful way. Environmental factors are very evident, with the results for the Sydney measurements being noticeably different,

with a much higher number of rays with significant power, compared with the less dispersive Melbourne and Adelaide data. Figures 6.6, 6.7 and 6.8, based on the 95% cumulative distribution level, give clear insight into the effect of bandwidth.

$P_{used}$  values presented here will only be worse (i.e. less) in 5% of cases. A similar presentation is used by *Allpress* {Ref[6.7]}, who describes repeated measurements with a variable chipping rate sounder over short sections of three streets in central Bristol, UK. Chip rate was set at 1.25 MHz, 2.5 MHz, 5 MHz, 10 MHz and 20 MHz, with the measurements repeated at each rate. A graph is presented based on the average of measured data, showing the percentage of total multipath power used, as a function of combined diversity order, and shows that a maximum of three tines utilised 80% or more of the total power even at the highest chip rate. Overall conclusions in Ref[6.7], based on the sounding work, and studies using a CDMA testbed, suggest that with chip rates below 5 MHz there is little advantage in using multipath diversity, and that to benefit from multipath diversity, chip rates should be 10 MHz or greater. However, the Bristol work was based on a limited set of measurement locations, all performed in a similar propagation environment.

## 6. 11 Initial Tine Number Model - Outdoor

Tabulating the -1 dB level from Figures 6.6, 6.7, and 6.8 to give the number of tines required to keep  $P_{used}$  greater than -1 dB (or 79% of total profile power) in 95% of cases, results in Table 6.2.

Table 6.2 Number of tines versus bandwidth - outdoor data

Number of tines required to give $P_{used} \geq -1$ dB in 95% of cases					
Propagation Location	System Bandwidth				
	1.25 MHz	2.5 MHz	4 MHz	8 MHz	16 MHz
Melbourne	1	2	2	2	3
Adelaide	1	2	2	3	3
Sydney	2	3	4	6	8

A very simple empirical model results from the above table, and serves as guideline for the number of tines which should be considered for internal diversity in a CDMA RAKE receiver in outdoor environments.

Where  $\alpha$  is an environment factor, with  $\alpha = 1$  for medium dispersion environments, such as suburban areas, and  $\alpha = 2$  for higher dispersion channels, such as downtown high-rise city areas with a high base station antenna, and  $BW_{MHz}$  is the system RF bandwidth in MHz, the number of tines  $N_{tines}$  (rounded to the nearest integer) is given by:

$$N_{tines} = \alpha \cdot \sqrt{BW_{MHz}}$$

(EQ 6.3)

Applying Eq.6.3 gives the results shown in Table 6.3, comparing the number of tines calculated from the model, with (in square brackets) the number derived from measured data.

Table 6.3 Number of tines from the model compared with outdoor data

<i>NOTE: square brackets [ ] show measured results</i>	$N_{tines}$ number of tines from Simple Model				
	1.25 MHz	2.5 MHz	4 MHz	8 MHz	16 MHz
Melbourne $\alpha = 1$	1 [1]	2 [2]	2 [2]	3 [2]	4 [3]
Adelaide $\alpha = 1$				3 [3]	
Sydney $\alpha = 2$	2 [2]	3 [3]	4 [4]	6 [6]	8 [8]

6. 12 Indoor Results

A similar approach to the outdoor work was used. Impulse responses were measured in *indoor mode* at the much higher resolution of 10 ns, and the propagation measurement data was filtered to produce channel sounding power delay profiles corresponding to system RF bandwidths of 5, 10, 20, 30, and 50 MHz. The power delay profiles cover the excess delay range of -1  $\mu$ s to +5  $\mu$ s (Remember that negative excess delay simply means that the strongest ray is not the first).

The measurement data was found to fall into two broadly similar groups, which have been called Group 1 and Group 2.

### 6.12.1 Group 1 Plot

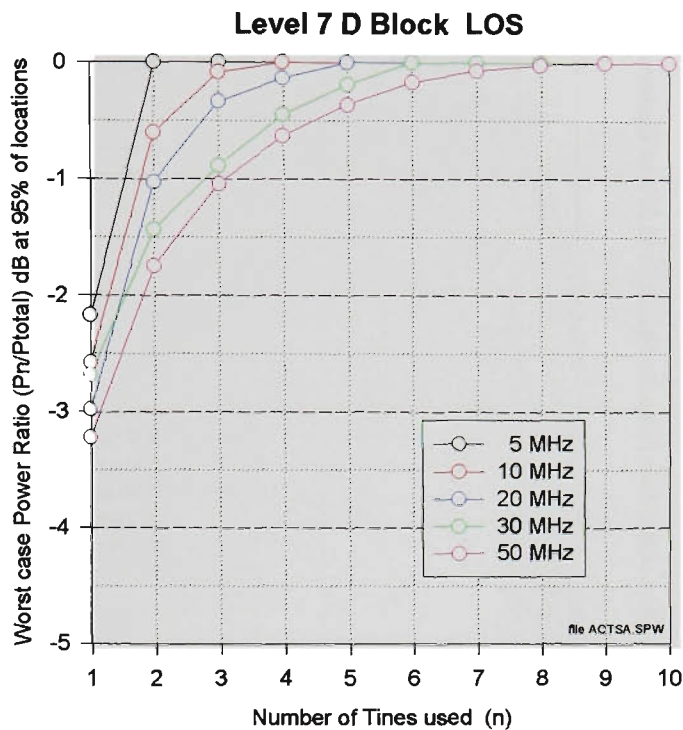


FIGURE 6.9 Level 7 D Block - LOS

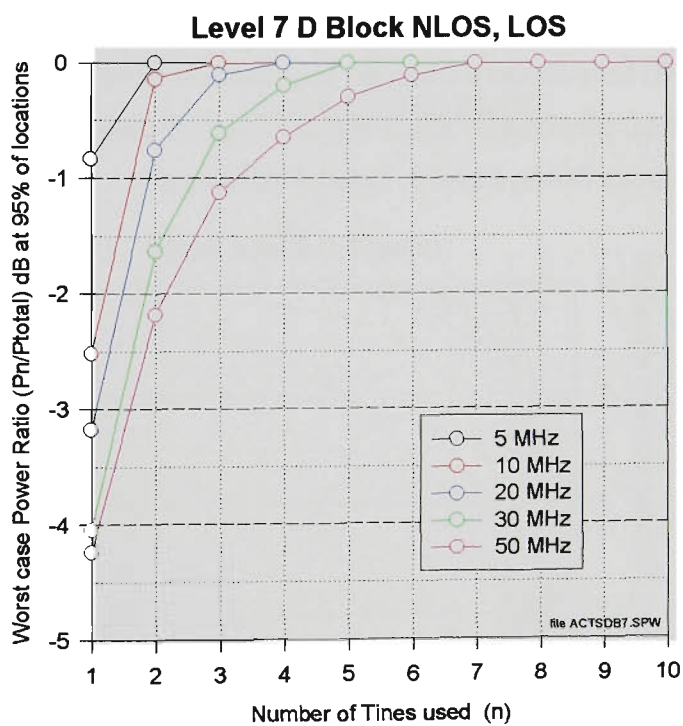


FIGURE 6.10 Level 7 D Block - NLOS and LOS

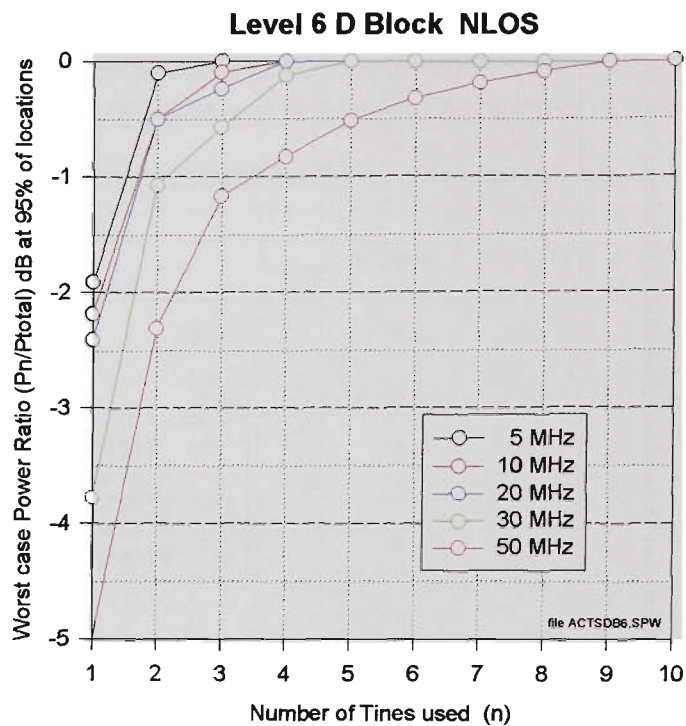


FIGURE 6.11 Level 6 D Block - NLOS

Group 1 plots include all Level 7 (same floor as the transmitter) and all Level 6 (the floor below the transmitter ) measurements. Some measurements on Level 7 are LOS, some are NLOS, and a third group are mixed NLOS and LOS. All measurements on lower floors are of course NLOS, because the transmitter remained on Level 7.

Group 2 plots, which show much higher values of time dispersion, include all measurements from the lower floors, Level 5, Level 4 and Level 3.

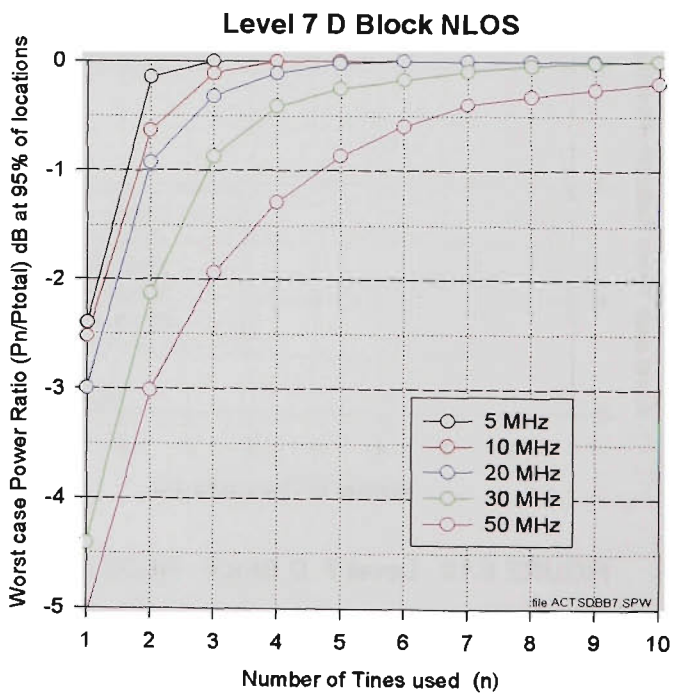


FIGURE 6.12 Level 7 D Block - NLOS



6.12.2 Group 2 Plots

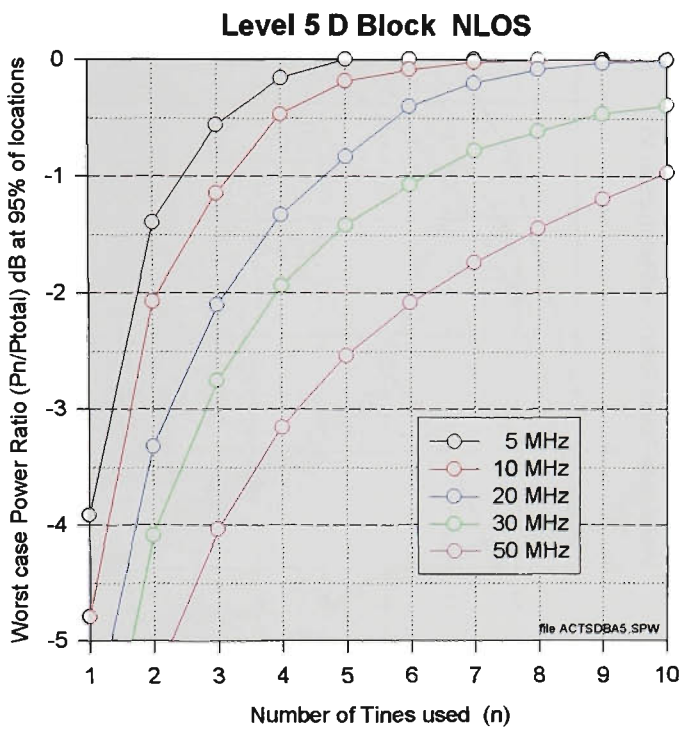


FIGURE 6.13 Level 5 D Block - NLOS

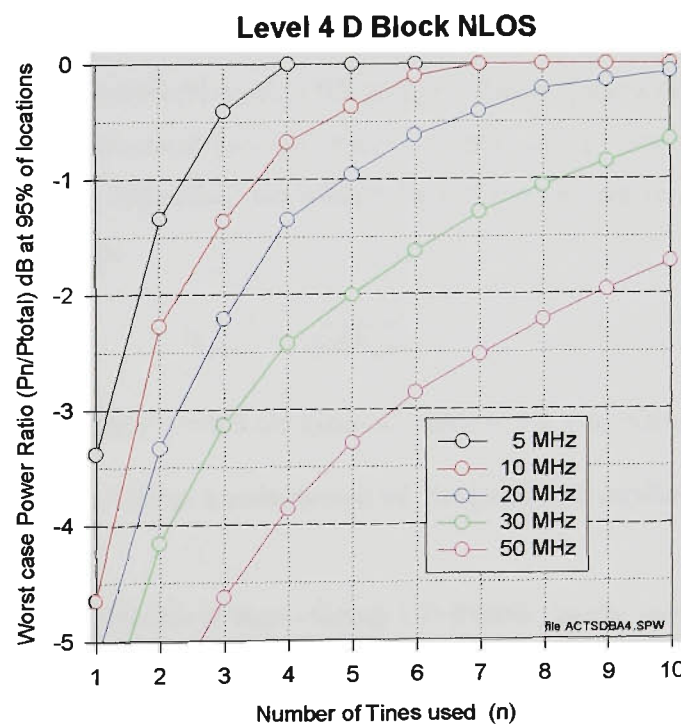


FIGURE 6.14 Level 4 D Block - NLOS

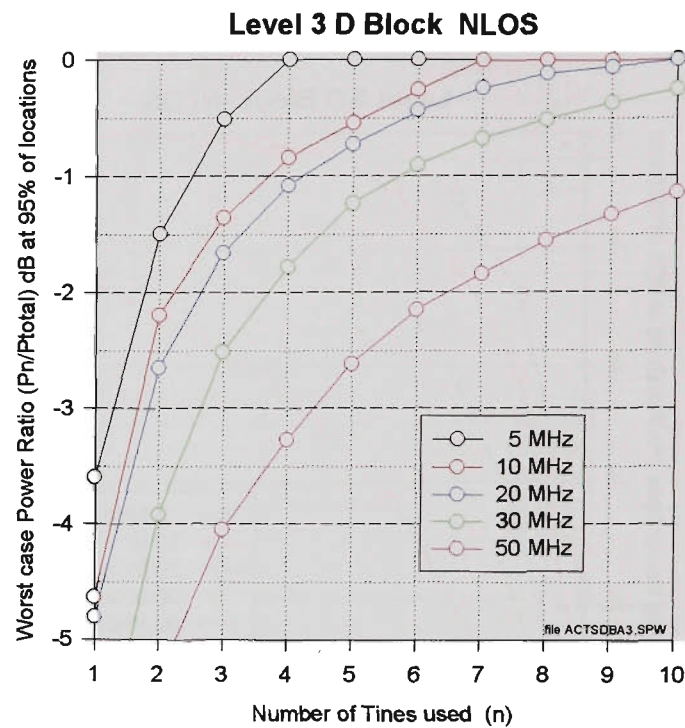


FIGURE 6.15 Level 3 D Block - NLOS

6. 13 Initial Tine Number Model - Indoor

The two groupings of similar data indicate that a model with two environment value constants should be sought. Figure 6.16 is used to obtain the environment constant values.

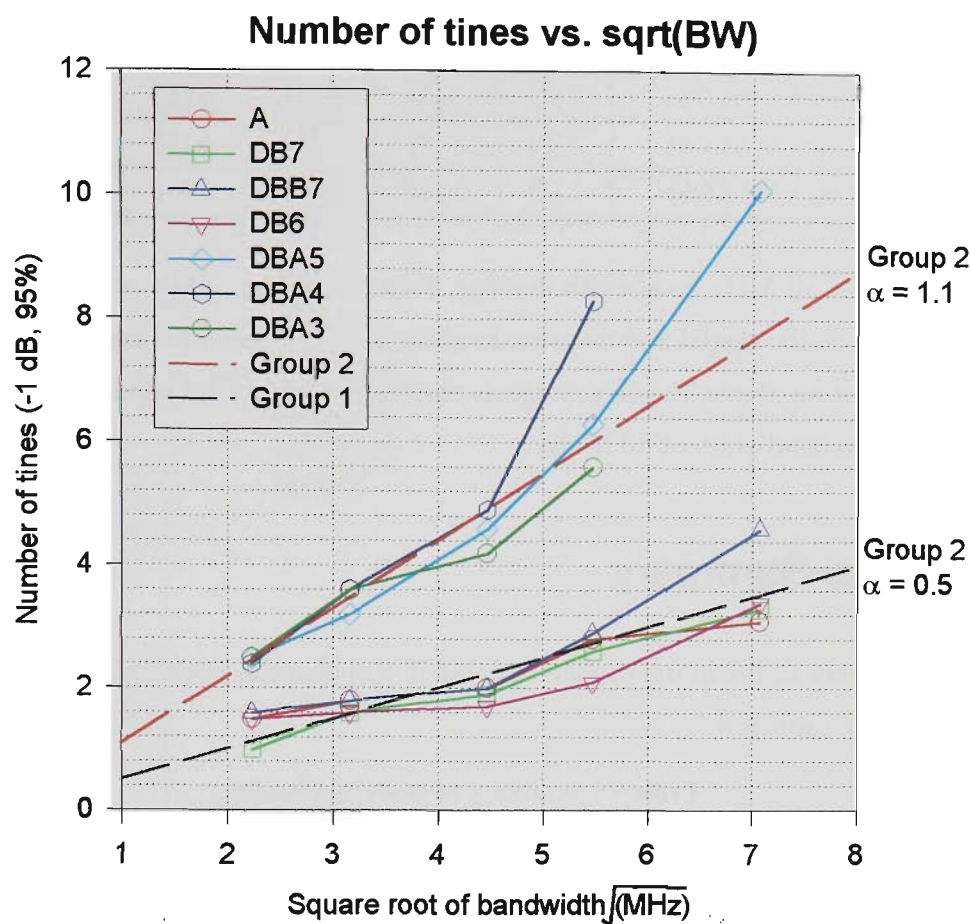


FIGURE 6.16 Finding environment constants for the indoor model

Figure 6.16, where the number of times is plotted against the square root of the bandwidth, illustrates how the measured results fall into two distinct groupings. The straight lines of best fit give values for the environment constants. Some leeway exists because the number of times must be an integer, and values calculated from the model are rounded up or down.

The indoor model is:

$$N_{tines} = \alpha \sqrt{BW_{MHz}}$$

(EQ 6.4)

where  $\alpha = 0.5$  for Group 1, and  $\alpha = 1.1$  for Group 2

Tables 6.4, and 6.5 show a comparison of the predicted number of times with the measured data.

Table 6.4 Number of times - Group 1 INDOOR - model [measured]

Group 1	System bandwidth (MHz)				
Measurement	5MHz	10MHz	20MHz	30MHz	50MHz
Level 7 (LOS)	1 [1]	2 [2]	2 [2]	3 [3]	4 [3]
Level 7 (NLOS, LOS)	1 [1]	2 [2]	2 [2]	3 [3]	4 [3]
Level 7 (NLOS)	1 [2]	2 [2]	2 [2]	3 [3]	4 [5]
Level 6 (NLOS)	2 [2]	2 [2]	2 [2]	3 [2]	4 [3]

Table 6.5 Number of tines - Group 2 INDOOR - model[measured]

Group 2	System bandwidth (MHz)				
Measurement	5MHz	10MHz	20MHz	30MHz	50MHz
Level 5 (NLOS)	2 [2]	3 [3]	5 [5]	6 [6]	8 [10]
Level 4 (NLOS)	2 [2]	3 [4]	5 [5]	6 [8]	8 [13]
Level 3 (NLOS)	2 [2]	3 [4]	5 [4]	6 [6]	8 [11]

Results at 50 MHz bandwidth diverge from the model, while at lower bandwidths, agreement between the model and measured values is within one tine (except for Level 4, 30 MHz). The departure above 30 MHz suggests that the simple model should be restricted to a maximum system bandwidth of 30 MHz.

6.14 Model Summary

A summary of the initial models derived in this chapter, with their ranges of application, are given in Table 6.6.

Table 6.6 Summary of model application

Model	Bandwidth Range	Environment	median rms delay spread
$N_{tines} = 0.5 \sqrt{BW_{MHz}}$	1MHz - 30MHz	Indoor - same floor or adjacent floor, LOS and NLOS	24 ns
$N_{tines} = 1.0 \sqrt{BW_{MHz}}$	1MHz - 16MHz	Outdoor - suburban/urban with moderate dispersion, median rms delay spread 120 ns	124 ns
$N_{tines} = 1.1 \sqrt{BW_{MHz}}$	1MHz - 30MHz	Indoor - location $\geq$ two floors from transmitter, NLOS, scattering from outside structures.	103 ns
$N_{tines} = 2.0 \sqrt{BW_{MHz}}$	1MHz - 16MHz	Outdoor - urban high rise with high dispersion, median rms delay spread 430 ns	437 ns

6.15 Incorporating Delay Spread

Combining the instantaneous rms delay spread values within each environment group results in the distribution plots shown in Figure 6.17 (below). Median values are listed in Table 6.6.

It may be observed from Table 6.6 that an approximate relationship is apparent between the environment factor  $\alpha$  and the overall median instantaneous rms delay spread  $ds_{median}$  in nanoseconds, namely:

$$\alpha = 0.1 \sqrt{ds_{median}}$$

(EQ 6.5)

The form of EQ.6.5 is chosen in the spirit of an approximate relationship which ties in with the initial models developed so far (hence the square root), and which is easy to remember and apply (hence the 0.1 coefficient), in order to satisfy the requirements of a “rule-of-thumb” model. It will be demonstrated shortly that in spite of these liberties, the final model gives results of useful accuracy, especially considering the statistical basis of the model and the wide spread of measurement conditions used to obtain input data

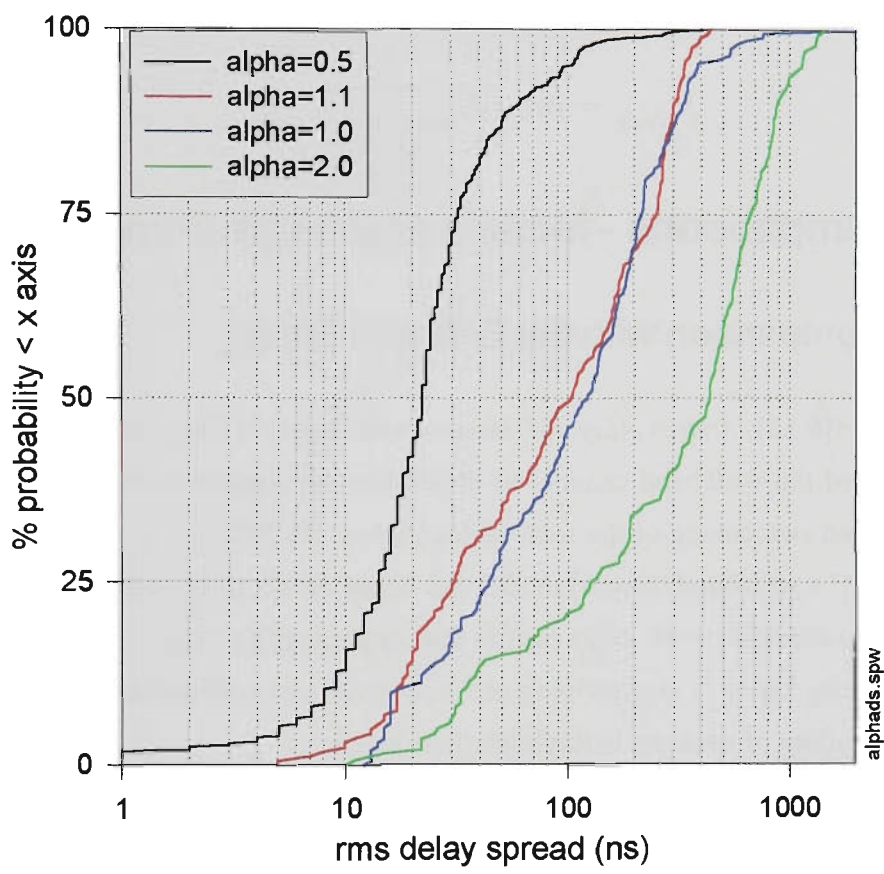


FIGURE 6.17 Distribution of rms delay spreads for each model environment factor

.Comparing the values given by EQ.6.5 with the original empirical values gives agreement

Table 6.7 Comparison of  $\alpha$  values from EQ.6.5 with empirical values

<i>ds<sub>median</sub></i>	$\alpha$ empirical	$\alpha$ from EQ.6.5	% difference
24 ns	0.5	0.49	-2%
124 ns	1.0	1.11	+11%
103 ns	1.1	1.01	-9%
437 ns	2.0	2.09	+4.5%

equal to or better than 11% (Table 6.7), although there is an anomaly around the 100 ns region.

## 6.16 Final Tine Number Model

Combining the initial outdoor and indoor tine number models, together with EQ.6.5, gives a single model which covers all the environments, both indoor and outdoor, considered in this chapter.

The final model, expressing the number of tines required to utilise power to within -1 dB of the total profile power in 95% of locations, in terms of median rms delay spread in nanoseconds, and system bandwidth in MHz, is given by EQ.6.6:

$$N_{tines} = 0.1 \sqrt{ds_{median} BW_{MHz}} \quad (\text{EQ 6.6})$$

## 6.17 Comparisons - Models and Measurements

### 6.17.1 Comparison with the Ericsson Model

In Ref[6.12], *Andres Alayon-Glazunov and Jan-Erik Berg (Ericsson Radio Systems)* have simulated the wideband channel to determine the number of RAKE fingers needed to capture a given percentage of the total signal power, for different delay spreads and system bandwidths. The wideband channel model was based on the following assumptions:

- (i) the average power delay profile falls exponentially with increasing excess delay
- (ii) delay times of rays arriving at the receiver are exponentially distributed
- (iii) fading of each tap is Rayleigh distributed
- (iv) the phase of arriving rays is uniformly distributed

They found that the number of fingers or tines required is a function of the product of delay spread and system bandwidth, and to capture 80% (or -1 dB) of the profile power, the number of fingers required is (equation 3.6 in Ref[6.12]):

$$N_{lines} = 0.0386 (ds_{rms} BW_{MHz})^{0.595} \quad (\text{EQ 6.7})$$

The original equation has been adjusted to put the delay spread in units of nanoseconds, and to use the nomenclature of this chapter. Comparing this equation with EQ.6.6 shows that they are quite similar, differing by less than one tine up to  $N_{tines} = 20$ , as illustrated in Figure 6.18.

When comparing these models, some differences in the way the parameters are defined should be kept in mind. Delay spreads in the simulations {Ref[6.12]} appear to be single values, with the simulations averaged over a set of power delay profiles with the same delay spread, while the *Martin model* proposed in this chapter is based on the median delay spread of a collection of measurements with a widely varying range of delay spreads, calculated using a -15 dB threshold (see Chapter 2, Section 2.8). The proposed *Martin model* is



also based on worst case power ratios at 95% of locations.

Perhaps of more interest than the good agreement in  $N_{tines}$  between the models, is the fact that the curves (Figure 6.18) show the same general shape, indicating that the dependence on the square root of the product of delay spread and system bandwidth proposed in the *Martin model*, is supported by the theoretical model using widely employed wideband channel assumptions.

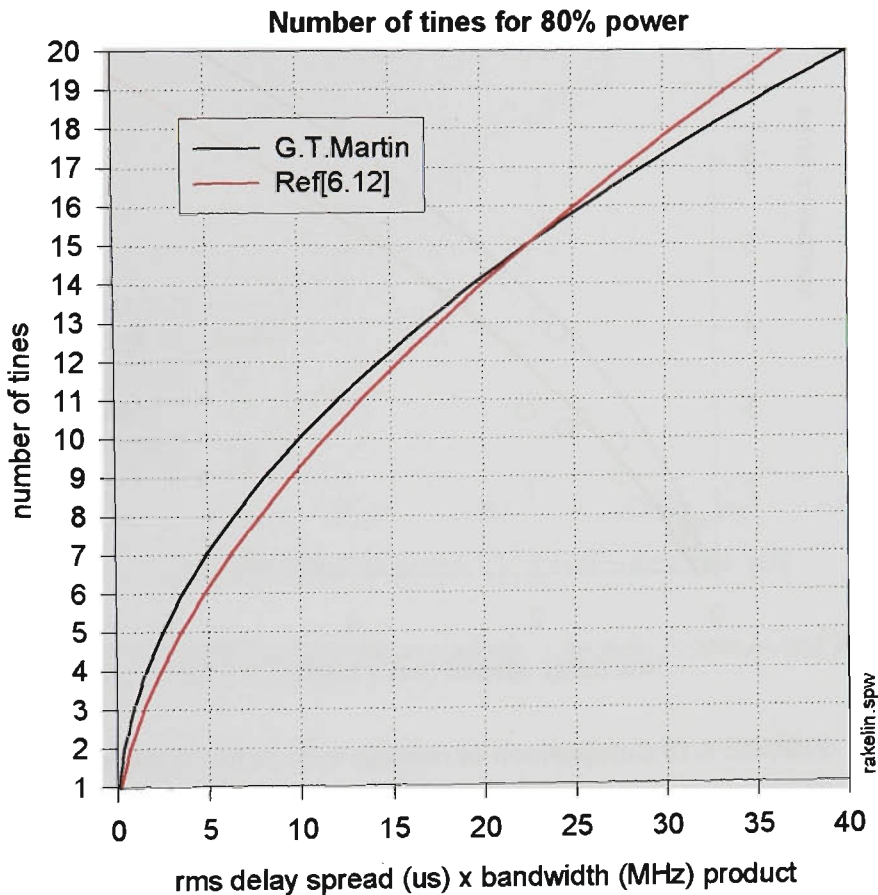


FIGURE 6.18 Comparison of *Martin* and *Ericsson* models

6. 17.2 Comparison of Models with Outdoor Measured Data

Figure 6.19 compares the measured outdoor Adelaide, Melbourne and Sydney results with the *Martin model* and the *Ericsson model*. In the region around 2 to 3 times, the *Ericsson model* looks better, although when rounded to the nearest integer, the difference between both models and measurements is a maximum of one time. At higher tine numbers, the *Martin model* gives better agreement with the (Sydney) measurements.

Six single measurement results are given in Ref[6.14], at bandwidths of 1.25 MHz and 5 MHz, for rms delay spreads of 230 ns, 760 ns, and 6050 ns, and are compared with the *Ericsson model* in the same paper. These do not agree with either model, giving a number of times approximately half that predicted by the models. Delay spread was calculated with a threshold “set to about 6 dB above the noise level”, which would be expected to give higher



delay spreads than with a -15 dB threshold (which the *Martin model* is based on). To obtain a meaningful comparison, a large number of measurements should be used, rather than just six.

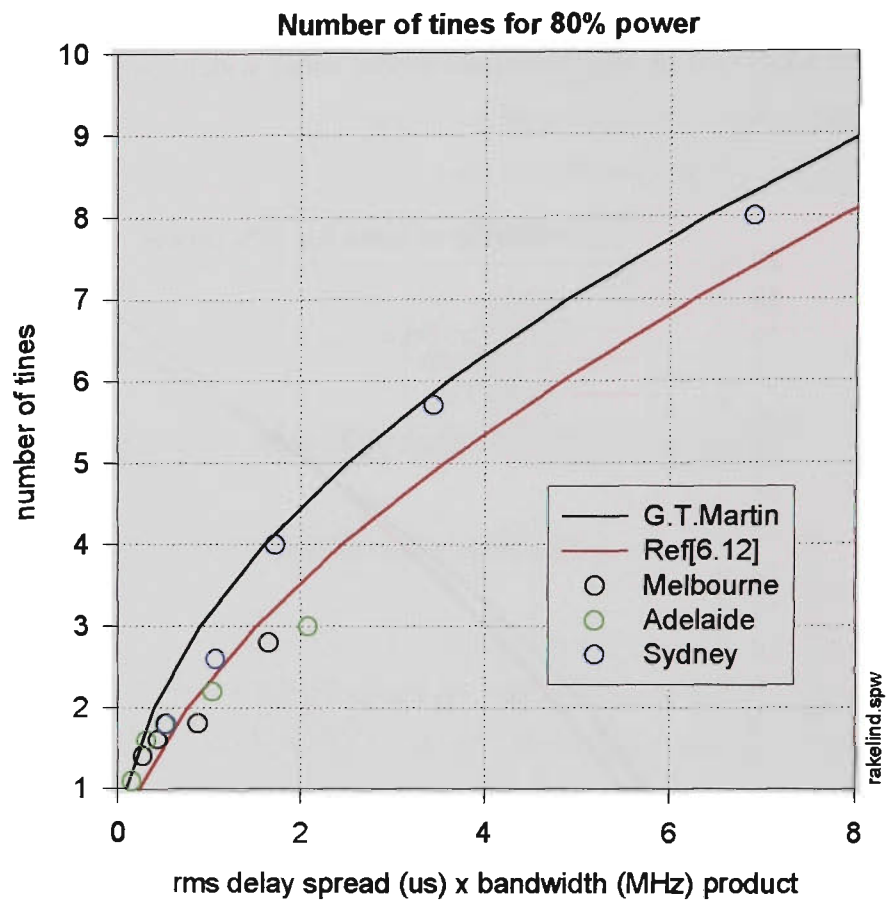


FIGURE 6.19 Comparison of models with outdoor measured data

### 6. 17.3 Comparison of Models with Indoor Measured Data

Figure 6.20 shows the comparison between indoor measured results and the models. The measured points show good agreement with the *Martin model*, with the *Ericsson model* underestimating the number of tines required. Points for 24 ns, 50 MHz, Group 1, ( $x$  axis = 1.2) are diverging from the model, but by restricting the model to a maximum bandwidth of 30 MHz (see section 6.12) these points are excluded. Group 2, 103 ns, 50 MHz points also diverge from the model, but are excluded by the 30 MHz restriction.

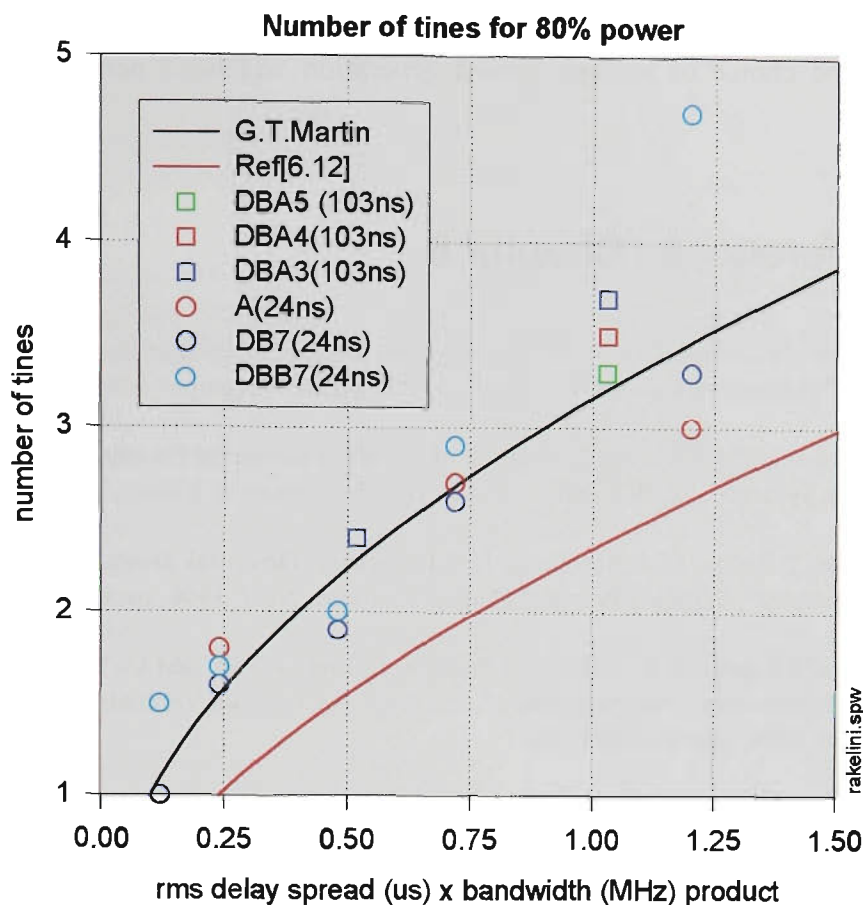


FIGURE 6.20 Comparison of models with indoor measured data

## 6. 18 Conclusions

A very simple empirical model has been found to give a good match to the measured results, and serves as a guideline for the number of times which should be utilised for internal diversity in a CDMA system.

The number of times required is proportional to the square root of the product of median instantaneous rms delay spread and system bandwidth. The model agrees well with both indoor and outdoor measurements made under a variety of propagation conditions, with median rms delay spreads varying from 24 ns to 437 ns, and at system bandwidths up to 16 MHz in the outdoors and 30 MHz for the indoor case.

In the propagation environments studied in this chapter, it appears that there is no benefit in using multi-path diversity with narrow band 1.25 MHz CDMA systems. To benefit from diversity, bandwidths of at least 4 MHz are indicated. This may not be the case in some urban environments (e.g. some USA cities), where very high rms delay spreads of the order of 10µS have been reported, and where multipath diversity may benefit even narrow band 1.25MHz CDMA systems. However, even though urban Sydney looks very similar to a typical high-rise American city, the Australian measurements used in this paper have not produced rms delay spreads greater than approximately 2µs.

The *Martin model* proposed in this chapter has triggered further study and simulation work at *Ericsson Radio Systems* (Stockholm), which has generated publications to ETSI influencing the choice of emerging third generation wideband personal communications standards.

## 6. 19 References - Chapter 6

[6.1] Akio Sasaki, "A Perspective of Third Generation Mobile Systems in Japan", Proceedings of the ACTS Mobile Telecommunications Summit, Granada, Spain, November 1996.

[6.2] S.C.Swales et al, "A Rigorous Evaluation of CDMA Techniques for future European Personal Communication Systems", LINK Final project Report, University of Bristol, U.K., February 1996.

[6.3] S.C.Swales, T.Busby, M.A.Beach and J.P.McGeehan, "Downlink Design for a Wideband DS-CDMA Demonstrator", *Wireless Personal Communications*, No.7, 1998, pages 275-301.

[6.4] E.Dahlman, J.Knutsson, F.Oversjo, M.Persson, C.Roobol, "WCDMA - The Radio Interface for Future Mobile Multimedia Communications", *IEEE Transactions on Vehicular Technology*, Vol.47, No.4, November 1998, pages 1105-1118.

[6.5] S.A.Allpress, M.A.Beach, J.P.McGeehan and A.Hammer, "Diversity Signal Processing Requirements of Direct Sequence CDMA Networks in Cellular & Micro-Cellular Environments", Proceedings of the IEE Sixth International Conference on Radio and Personal Communications, Warwick, U.K., December 1991, pages 68-73.

[6.6] S.A.Allpress, M.A.Beach, G.Martin and C.M.Simmonds, "An Investigation of Rake Receiver Operation in an Urban Environment for Various Spreading Bandwidth Allocations", Proceedings of the IEEE 41st. Vehicular Technology Conference, VTC'92, Denver, USA, May 1992, pages 506-510.

[6.7] Stephen Alan Allpress, "Optimising Signalling Rate and Internal Diversity Order for Mobile Cellular DS-CDMA Systems", PhD. Thesis, University of Bristol, U.K., December 1993.

[6.8] H.R.Anderson and J.P.McGeehan, "Assessing the Effect of DS-CDMA Chip Rate on RAKE Branch Statistics Using a Ray-Tracing Propagation Model", Proceedings of the IEEE International Symposium on Personal, Indoor and Mobile Radio Communications, PIMRC'94, 1994, pages 33-37.

[6.9] Shigeru Kozono, "Received Signal-Level Characteristics in a Wide-Band Mobile Radio Channel", *IEEE Transactions on Vehicular Technology*, Vol.43, No.3, Part I, August 1994, pages 480-486.

[6.10] M.A. Beach and S.A. Allpress, "Propagation Aspects of Mobile Spread-spectrum Networks", Chapter 12, "Propagation of Radiowaves", Editors M.P.M. Hall, L.W.Barclay, M.T.Hewitt, The Institution of Engineers, U.K. 1996, ISBN 0852968191.

[6.11] G.T.Martin and M.Faulkner, "1.9 GHz Measurement-based Analysis of Diversity Power versus the Number of RAKE Receiver Tines at Various System Bandwidths", Proceedings of the 8th. IEEE International Symposium on Personal, Indoor and Mobile Radio Communications, PIMRC'97, Helsinki, Finland, Vol.3, September 1997, pages 1069-1073.

[6.12] Henrik Asplund and Jan-Erik Berg, "An Investigation of Measured Wideband Channels at 1880 MHz with Applications to 1.25 MHz and 5 MHz CDMA Systems", European Cooperation in the Field of Scientific and Technical Research, COST 259 TD(97)026, Turin, Italy, 26-28 May, 1997.

- 
- [6.13] Andres Alayon-Glazunov and Jan-Erik Berg, "CDMA RAKE Receivers Performance Evaluation Using a Wideband Channel Model", European Cooperation in the Field of Scientific and Technical Research, COST 259 TD(97) 64 Rev.1, Bern, Switzerland, 2-4 February, 1998.
- [6.14] Henrik Asplund, Andres Alayon-Glazunov and Jan-Erik Berg, "An Investigation of Measured and Simulated Wideband Channels with Applications to 1.25 MHz and 5 MHz CDMA Systems", Proceedings of the 48th. Vehicular Technology Conference, VTC'98, Ottawa, Canada, Vol.1, May 1998, page 562-566.
- [6.15] Gregory T.Martin and Michael Faulkner, "Useable CDMA Diversity Order at Various System Bandwidths for In-building Propagation", 3rd. ACTS Mobile Communication Summit, Rhodes, Greece, Vol2, June 1998, pages 892-896.
- [6.16] Jerry D. Gibson, "The Mobile Communications Handbook", pages 257, 441. CRC Press published in cooperation with IEEE Press, USA, 1996. ISBN 0-8493-8573-3.
- [6.17] "MATLAB Signal Processing Toolbox User's Guide", January 199, page 2-102. Published by The MathWorks, Inc. Massachusetts, USA.
- [6.18] Theodore S.Rappaport, "Wireless Communications Principles and Practice", IEEE Press, Piscataway USA, 1996, ISBN 0-7803-1167-1(IEEE), Chapter 6.
-

# Chapter 7: Conclusions and Future Work

## 7.1 Conclusions

Each chapter has ended with discussion and conclusions, so these will not be restated here. The channel sounder developed for this project has proved to work well. The back-to-back tests, and comparisons with the sliding correlator simulations described in Chapter 3 demonstrate the performance of the sounder.

Originally this project was envisaged to comprise the development of a channel sounder, and a program of outdoor measurements to characterise the virgin Australian propagation environment at around 2GHz. These goals were successfully met some time ago, and since then interesting side issues have been pursued, such as the sliding correlator simulation in Chapter 3, the concept of propagation signatures in Chapter 5, and the interesting relationship between the number of usable RAKE tones, the system bandwidth and the median instantaneous rms delay spread discussed in Chapter 6.

## 7.2 Future Work

The immediate plan is to move the channel sounder to the 2.4GHz ISM band, as the spectrum used to date is now being auctioned at very high prices.

Based on experience gained with the original sounder, together with the proliferation of RF parts now available to work around 2.4GHz, it would be possible to build a much smaller and lighter sounder to continue to exploit the advantages of portability. GPS conditioned clocks which surpass even rubidium oscillators in stability offer interesting scope for outdoor measurements with high long term stability.

To support work in our research group on smart antennas and space-time processing, there is a need to obtain angle of arrival data in the Melbourne environment. An attractive method is to use a rotating narrow beam directional antenna as done elsewhere (e.g. Nortel in the UK, Ref[7.1]), and ideas for building such a system are progressing.

Multiple-input multiple-output (MIMO) high data rate indoor systems offer rich scope for propagation work, together with novel solutions for antenna arrangements to measure the correlation between permutations of antenna pairs.

## 7.3 References

[7.1] C. Ward, M. Smith, A. Jeffries, D. Adams and J. Hudson, "Characterising the Radio Propagation Channel for Smart Antenna Systems", IEE Electronics & Communication Engineering Journal, Vol.8, No.4, August 1996, pages 191-200.

# Appendix A: Transmitter Hardware

## A. INTRODUCTION

In this appendix, details of the *channel sounder* transmitter hardware design and development are documented.

Some of the hardware is similar for both the transmitter and the receiver. For example, interdigital bandpass filters, frequency synthesized sources, rubidium oscillators, and pseudo-noise (PN) generators, are used in both the transmitter and receiver, although the frequency synthesizers operate at different frequencies.

Local oscillator synthesizers, rubidium oscillators, and PN generators will be covered in this appendix. Bandpass filters are covered in Appendix B - *Receiver Hardware*. Antennas are covered in Appendix C - *Antennas*.

These appendices include detailed circuit schematics, and a description of the development and characterization of the hardware blocks which comprise the *channel sounder* instrumentation.

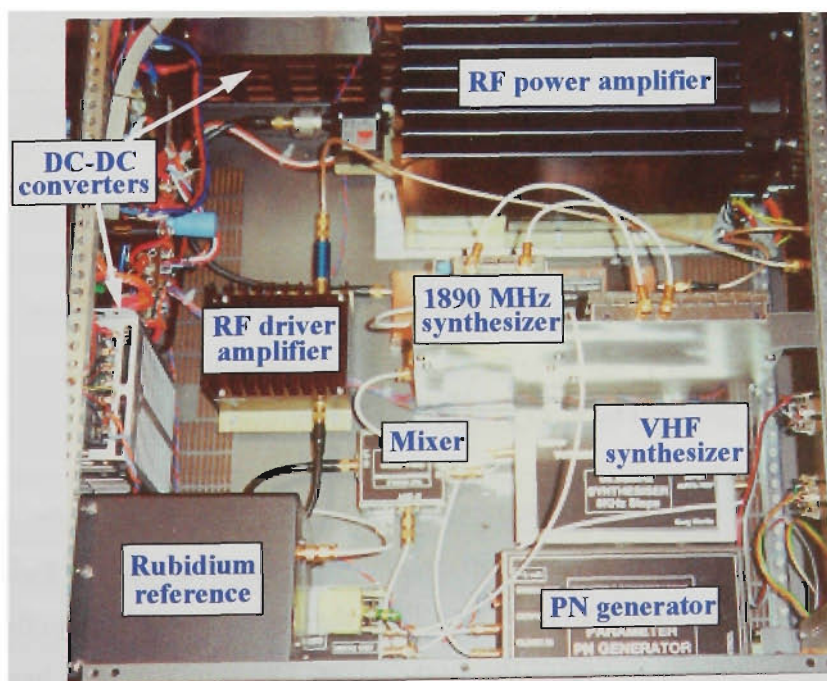


FIGURE A.1 Transmitter electronics

## A.1 Frequency Standards

Rubidium oscillators are used in the transmitter and the receiver to provide very stable atomic frequency standards, sufficiently stable to allow both units to stay synchronized for several hours. The oscillators are made by the *Ball Efratom Division*, part of *Ball Aerospace Systems Group*, Colorado USA. The model used is the *M-100* Military Rubidium Oscillator. Being a military specification model, the unit is rugged and well suited to portable field use. The specifications are summarised in Table A.1:

TABLE A.1 M-100 rubidium oscillator specifications

Parameter	Specification
Output	sinewave 0.5V,+30%,-10% V <sub>rms</sub>
Frequency	10 MHz ± 5E-11
Input Power	18W at 26V DC, 25°C ambient, after warm-up
Input Voltage	22.5V to 32V DC
Warm-up time	<10 minutes at 25°C ambient
Warm-up current	
Input Voltage Sensitivity	<1E-11 for ±10% supply voltage change
Short-Term Stability (Allen Variance)	3E-11 τ 1 second
	1E-11 τ 10 second
	3E-11 τ 100 seconds
Long Term Drift	approx. 2E-10 per year
Phase Noise	-130 dBc/Hz at 100 Hz offset
	-140 dBc/Hz at 1kHz offset
Harmonics	< -30 dBc
Spurious (non-harmonic)	< -80 dBc
Adjustment Range	3E-9
Size	3.94x3.90x4.81 inches
Weight	4 lbs.(1.81 kgm.) without heatsink

## A.2 UHF Frequency Synthesizers

In the transmitter a signal source at 1890 MHz, phase locked to the 10 MHz frequency reference, is required to serve as the carrier, and in the receiver a phase locked source at 1690 MHz is required as the first local oscillator. Both these sources are built to the same design, the only difference being the setting of the loop divider. The synthesizer is based on a design for a low noise single loop synthesizer described in Ref[A.1]. This design claims a novel feature, using an additional op-amp ahead of the normal active loop filter. The extra opamp converts



the differential phase-frequency comparator (PFC) output to single ended, and allows the active filter op-amp to be used single-ended with the non-inverting input grounded. Claimed advantages are: (a) eliminates noise pick-up and feedforward via the high impedance non-inverting input of the active filter which is now grounded, (b) added reference frequency suppression because of cancellation in the differential amplifier, (c) more flexible design, by introducing an extra degree of freedom; the loop gain can be altered without altering the active filter parameters, and (d) improved buffering between the PFC and the active filter and the low driving point impedance seen by the active filter input, allowing lower impedance active filter components.

Advanced CMOS 74AC logic devices are claimed to have the best low noise characteristics of available logic families {Ref[A.1]}, and are used for the dividers and the PFC.

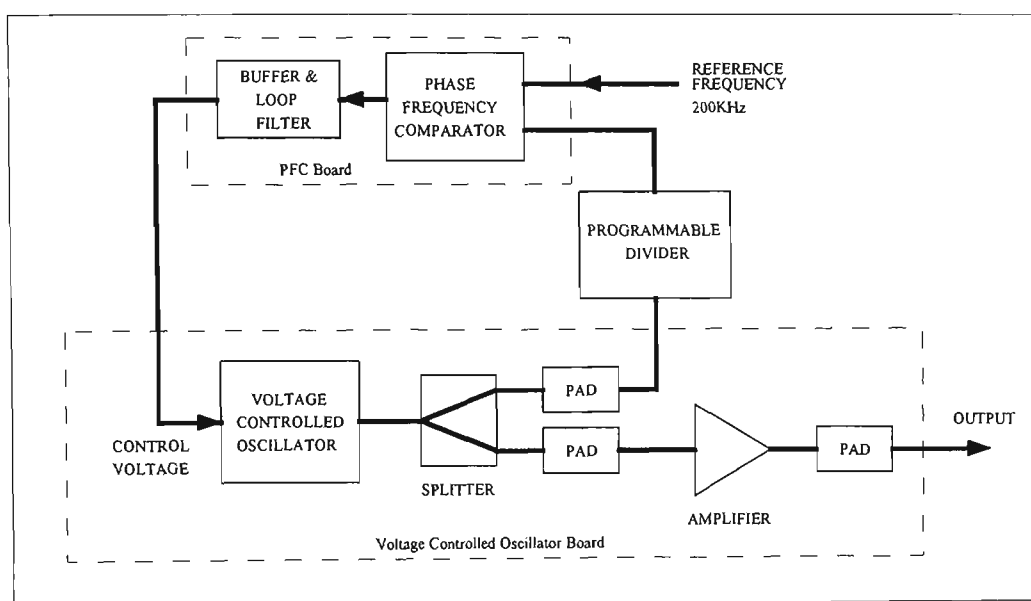


FIGURE A.2 Phase lock loop block diagram

### A.2.1 Loop Bandwidth and Phase Noise

Inside the loop bandwidth, negative feedback action of the phase lock loop (PLL) acts to counteract phase jitter, and tends to keep the voltage controlled oscillator (VCO) phase constant, reducing phase noise to an extent limited by PFC phase noise, reference frequency source phase noise, and noise contributions by other circuitry in the PLL. Outside the loop bandwidth, the PLL is too slow to improve the VCO phase noise, which remains the same as for an unlocked VCO. So for low phase noise, a high loop bandwidth is desirable, up to the point where the residual PLL phase noise becomes greater than the inherent phase noise of the VCO.

The tradeoff is that a wide loop bandwidth reduces attenuation of comparison frequency noise, giving larger spurs at  $\pm$  the comparison frequency (and harmonics) in the output spectrum. In some applications, other factors such as loop lock time, will influence the choice of loop bandwidth. Phase noise and spurious signals (principally sidebands at the phase comparison frequency), are the major issues with PLL spectral purity.

## A.2.2 Prescalers

Programmable divider speed is limited by currently available technology, which will not operate fast enough to count at 1890 MHz, so for any UHF synthesiser, a prescaler divider is required. These are now available at low cost in silicon, for input frequencies up to beyond 2.5 GHz. The prescaler divides by a fixed ratio, or in the case of the dual-modulus prescaler, by either  $P$  or  $(P+1)$  depending on the logic level applied to a mode-select pin. Dual-modulus prescalers are available in various  $P/(P+1)$  ratios, including  $8/9$ ,  $10/11$ ,  $16/17$ ,  $32/33$ ,  $64/65$ , and  $128/129$ .

## A.2.3 Fixed Prescaling

If the PLL output frequency is  $f_{VCO}$ , the phase-comparison frequency is  $f_{comp}$ , the reference frequency is  $f_{ref}$ , the synthesiser frequency step size is  $f_{step}$ , and the reference divider ratio is  $R$ , the prescaler ratio is  $P$  and the programmable divider ratio is  $M$ , then:

$$f_{comp} = \frac{f_{ref}}{R} \quad (\text{EQ A.1})$$

$$f_{VCO} = PMf_{comp} \quad (\text{EQ A.2})$$

as  $M$  can increment in steps of 1, then the frequency step size is given by:

$$f_{step} = Pf_{comp} \quad (\text{EQ A.3})$$

For example, if  $f_{VCO} = 1890$  MHz, and  $f_{step} = 0.2$  kHz, with  $P = 64$ , then the phase comparison frequency  $f_{comp}$  equals  $\frac{1}{P}f_{step}$  or 3.125 kHz.

## A.2.4 Dual-Modulus Prescaling

Two programmable counters,  $M$  and  $A$  operate in parallel, and count to  $M$  and  $A$ . With  $A < M$ , the dual modulus prescaler divides by  $(P+1)$  initially, until the  $A$  counter fills, when the prescaler switches to divide by  $P$  for the remaining  $(M-A)$  counts. So the overall division ratio is  $B$  where:

$$B = (P+1)A + (M-A)P$$

$$\text{hence } B = PM + A \quad (\text{EQ A.4})$$

$$\text{So } f_{VCO} = (PM + A)f_{comp} \quad (\text{EQ A.5})$$

$A$  can increment in steps of  $1 \times f_{comp} = f_{step}$  which for the example values, gives a phase comparison frequency of 0.2 MHz. This illustrates the advantage of the dual-modulus scheme in giving a  $f_{comp}$  value equal to  $f_{step}$ , and  $P$  times greater than with a fixed prescaler, for

example 200 kHz instead of 3.125 kHz in the above example (Section A.2.3). For a given loop bandwidth and step size, better attenuation of phase comparison frequency sidebands by the loop filter will occur.

If  $A=0$ , the prescaler ratio is  $P$  at all times, and if  $A=M$ , the prescaler ratio is  $(P+1)$  at all times. These values represent the usable lower and upper limits for  $A$ . Each value of  $M$  gives a range of  $(P+1)$  frequency steps, from which one is chosen by the ‘fine tuning’ action of the  $A$  value. When  $M>P$ , some of the values in adjacent ranges are repeated, increasingly so as  $M$  becomes greater. For example if the desired output frequency is 1882 MHz with  $f_{comp}=0.2$  MHz, this can be obtained with either  $M=147$  and  $A=2$ ,  $M=146$  and  $A=66$ , or  $M=145$  and  $A=130$ . While the scheme works for values of  $A$  up to  $A=M$ , there is no point in providing more capacity in the  $A$  counter than for a maximum value  $A=P-1$ , which would then restrict the possibilities for 1882 MHz to  $M=147$ ,  $A=2$ . For  $P=64$ , the  $A$  counter needs 6 bits. Because programmable counter integrated circuits come in 4 bit blocks, in this design both  $A$  and  $M$  counters are 8 bits in length.

## A.2.5 Minimum Divider Ratio

A minimum value  $M = M_{minimum}$  exists, below which not all frequency step values will be obtainable.

The top frequency of the lowest range occurs when:

$$B_1 = PM_{minimum} + A_{maximum} = PM_{minimum} + M_{minimum}$$

The bottom frequency of the next range up occurs when the divider ratio is:

$$B_2 = P(M_{minimum} + 1) \quad \text{as } A = 0$$

we want one count increment between these two values, that is:  $B_2 - B_1 = 1$ , giving:

$$PM_{minimum} + M_{minimum} + 1 = P(M_{minimum} + 1)$$

hence

$$M_{minimum} = P - 1 \tag{EQ A.6}$$

giving a minimum divide ratio of:

$$B_{minimum} = P(P - 1) \tag{EQ A.7}$$

## A.2.6 Loop Design

The design of PLLs is well covered in the literature, with some of the most useful information condensed in semiconductor company application notes {Ref[A.2], Ref[A.3], Ref[A.4], Ref[A.5]}. The standard loop is the second order loop, although most second order

loops (including the design used here) are only approximately so because of one or more further-out high frequency poles, either intentionally introduced to reduce phase comparator spurs, or simply due to stray capacitance.

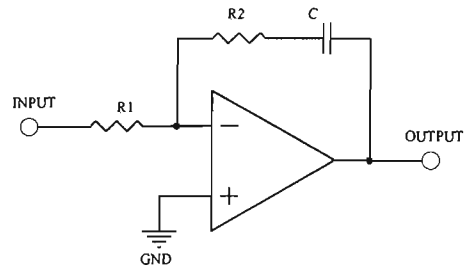


FIGURE A.3 Loop filter

If  $K_\phi$  volt/radian is the PFC gain,  $K_{VCO}$  radian/sec/volt is the VCO gain,  $K_{amp}$  is the buffer amplifier voltage gain, and  $R1, R2, C$  are the loop filter components shown above, then:

$$R1 = \frac{K_\phi K_{VCO} K_{amp}}{B \omega_n^2 C}$$

(EQ A.8)

$$R2 = \frac{2\zeta}{\omega_n C}$$

(EQ A.9)

$$\omega_n = \sqrt{\frac{K_\phi K_{VCO} K_{amp}}{B C R1}}$$

(EQ A.10)

$$\zeta = \frac{\omega_n R2 C}{2}$$

(EQ A.11)

where  $\omega_n$  is the loop natural frequency in radian/second,  $\zeta$  is the damping factor, and  $B$  is the loop divider ratio. Using these equations, the 1890 MHz design summary (derived from a spreadsheet calculation) is shown below:

Loop Filter Design Greg Martin 29/3/94 file PLLFILT.WKS	
PARAMETER	VALUE
This section calculates natural frequency and damping factor for an existing design	
Kvco rad/sec/volt	584000000
Kphi phase detector	0.8
Kamp amplifier gain	10
Output Freq (Hz)	1.89E+09
Reference Freq (Hz)	200000
Ratio N	9450
Capacitor C nF	1000
Input R (R1) ohm	560
Feedback R (R2) ohm	68
Fn loop natural freq (Hz)	4729.0558
Damping factor	1.0102304

FIGURE A.4 Loop filter design at 1.89 GHz

The same components and loop filter are used for the 1690 MHz design employed in the receiver, but because of the different loop divider ratio, loop parameters are slightly different.

TABLE A.2 PLL parameters

	PLL Frequency	
	1.69 GHz	1.89 GHz
Natural Frequency $\omega_n$	4.7 kHz	5.0 kHz
Damping Factor $\zeta$	1.01	1.07

A.2.7 Open Loop Bode Plot

Using a linear model for the phase lock loop, and analysis with *SPICE*, the open loop Bode plot including all the significant higher frequency poles can be obtained, and from this the phase margin is found. The VCO input capacitance is specified as < 50 pF, and this will only have a minor effect as it is shunted with 1330 pF (see Figures A.8 and A.9).

The phase margin at 1890 MHz is 37° and at 1690 MHz it is 33°. Without the *LC* low pass filter which adds a double pole at 67 kHz, the *RC* filter (3.9K and 1330 pF) which has a pole at 30.7 kHz, and the pole at 142 kHz due to the 2.2 nF in the buffer amplifier, the phase margins would increase to 80° and 81° respectively. However, some sacrifice in phase margin is worthwhile as a tradeoff to reduce phase comparison frequency spurs, and the final circuit values are the result of extensive experiment and testing to reduce noise and spurious output.

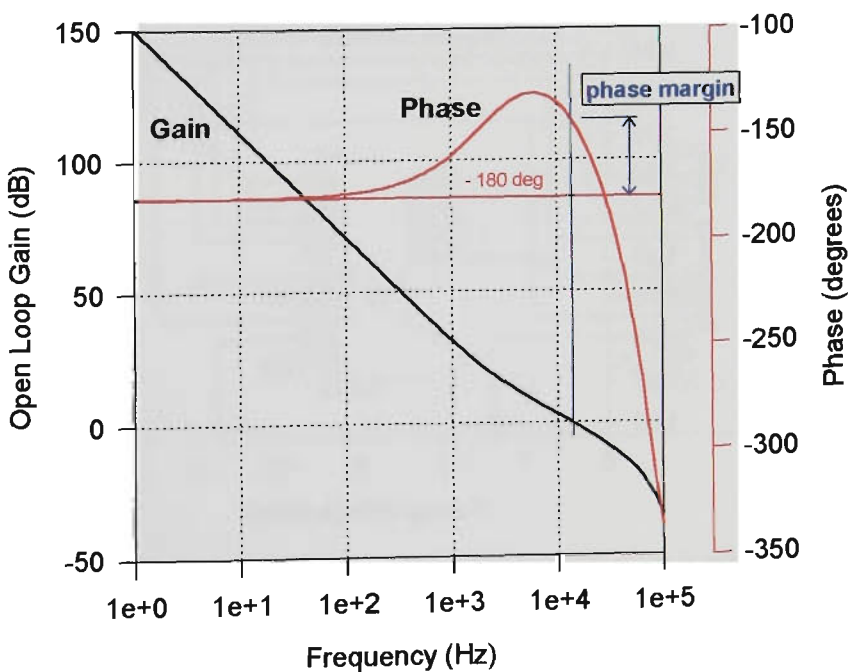


FIGURE A.5 Open loop Bode plot for 1890 MHz phase locked loop

A.2.8 Voltage Controlled Oscillator

A commercial surface mount wideband VCO, model *C-600M* manufactured by *Z Communications, Inc. USA*. is used. Specifications are given in Table A.3.

:

TABLE A.3 VCO specifications

Parameter	Value
Tuning range	1200 MHz - 2400 MHz
Phase noise @ 10 kHz offset	-98 dBc/Hz
Harmonics (typical)	-10 dBc
Power out into 50Ω	+10 ± 2.5 dBm
Tuning voltage	0 to 26 volt
Supply voltage	5 volts
Supply current	35 mA

During the development of the synthesizer, a problem occurred with the VCO. Over part of the tuning range, a strong subharmonic appeared, at half of the frequency, but almost the same power as the normal output. To prevent this happening, the output must feed via the minimum possible length of microstrip into a 50Ω T pad. Grounding of the package is important, and it is flow-soldered to the ground plane, with numerous surrounding through-pins to the underside ground plane.

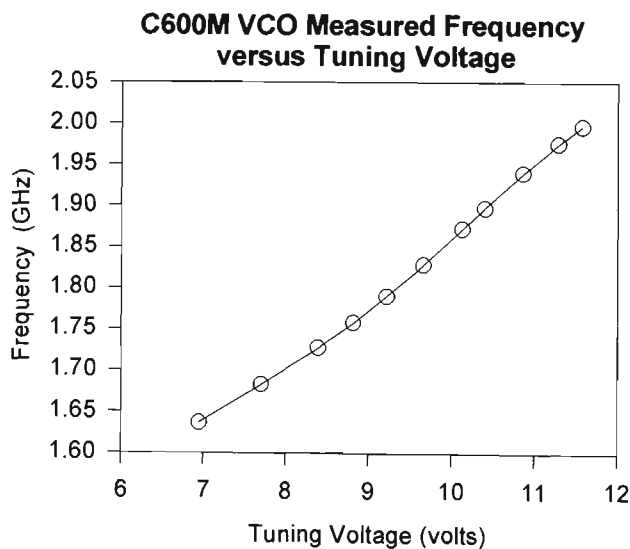


FIGURE A.6 Z-Com C-600M measured VCO transfer function

A.2.9 Circuit Schematics

As indicated in the block diagram (Figure A.2), the synthesiser is built on three sepa-

rate circuit boards, and also housed in three separate tinned steel boxes, interconnected with coaxial cable. Separate boxes proved necessary to reduce spurious components to below -60 dBc.

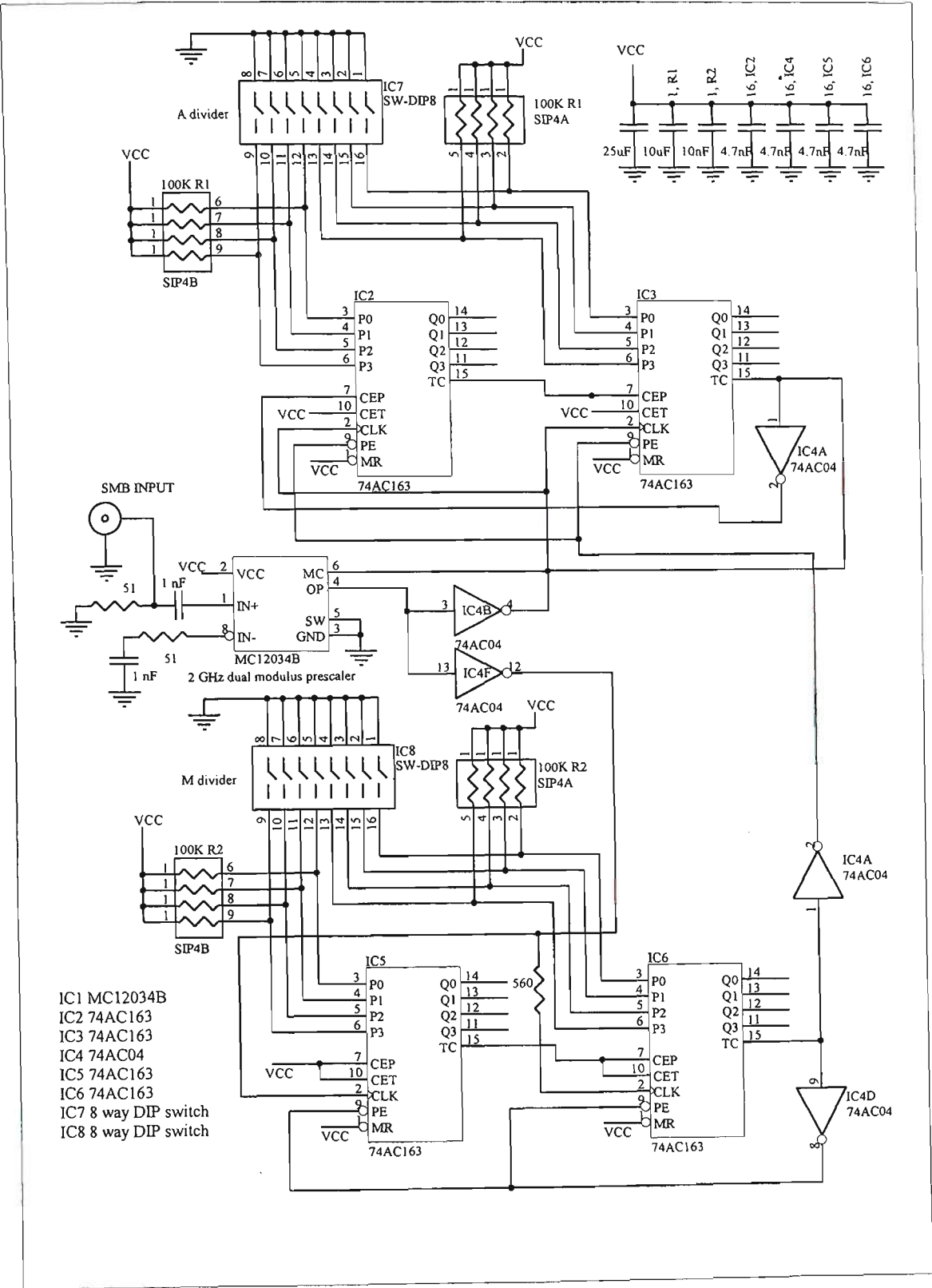


FIGURE A.7 PLL programmable counter schematic



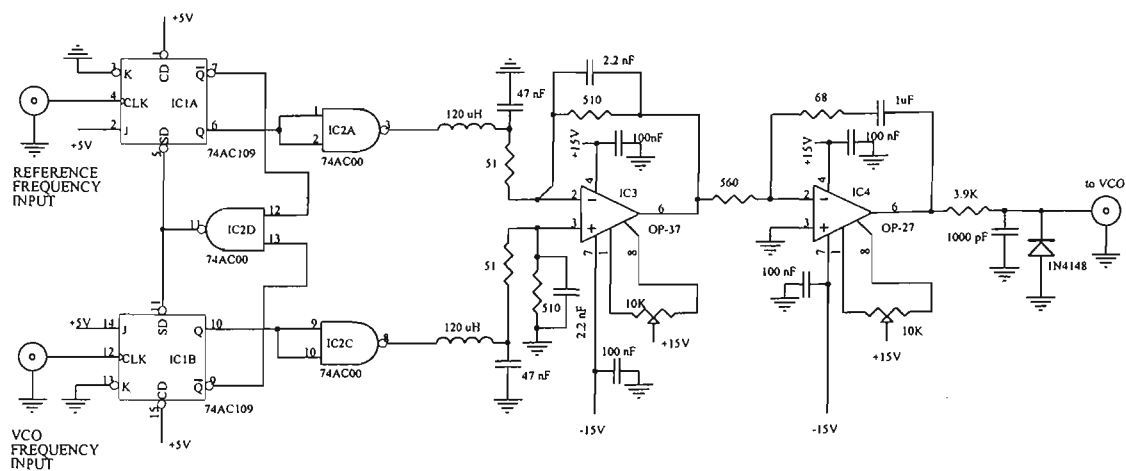


FIGURE A.8 Phase frequency comparator and loop filter

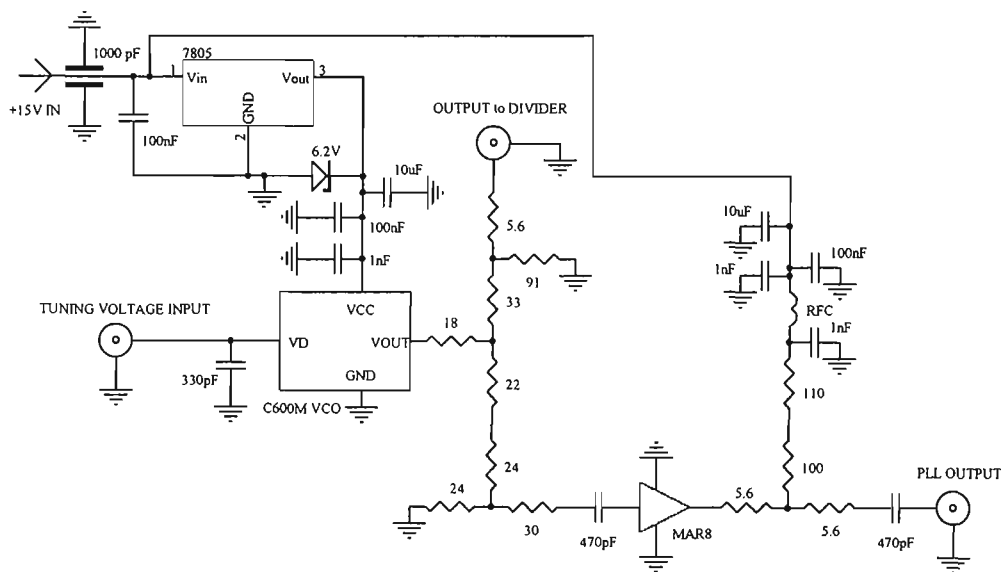


FIGURE A.9 VCO and output amplifier

A.2.10 Synthesizer Performance

In this section the performance of the synthesizers is shown, in terms of phase noise and spectrum plots.

TABLE A.4 UHF synthesiser performance

Parameter	Value
Phase noise at < 200 Hz to 5 kHz offset	-76 dBc/Hz
Phase noise at 50 kHz offset	-98 dBc/Hz
PFC frequency spurs at ± 200 kHz	-70 dBc
Other non-harmonic spurious	< -80 dBc
Output power into 50Ω	5 dBm ± 2 dBm

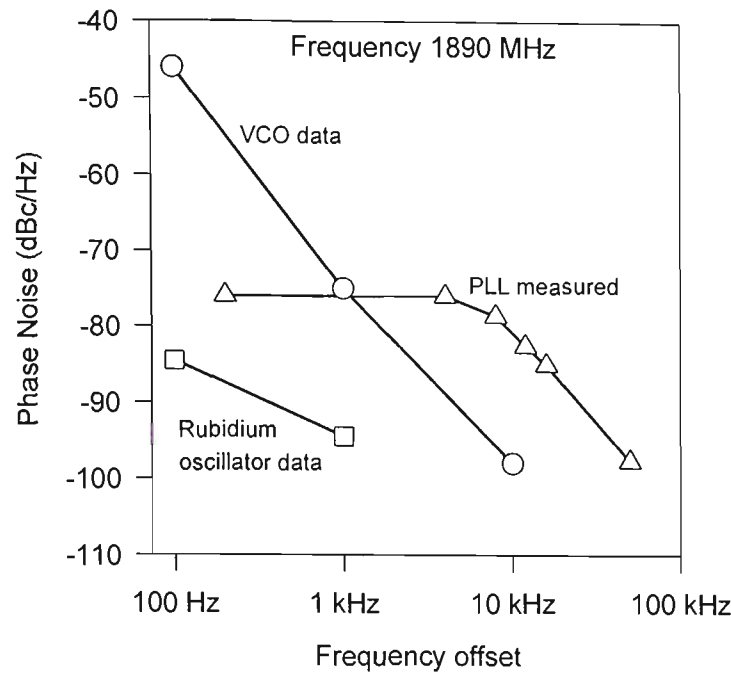


FIGURE A.10 PLL phase noise

Measured PLL single sideband phase noise was obtained from a spectrum analyser plot (Figure A.12) and corrected for a bandwidth change of 100 Hz to 1 Hz by adding -20 dB, to give dBc/Hz values. This is not an accurate measurement, but gives a guideline figure {Ref[A.6]}. Attempts to measure the VCO phase noise yielded values 30 to 40 dB worse than the manufacturer’s data, but it is likely that the tuning voltage used was noisy and drifting, making the measurement invalid. The VCO data curve plotted above (Figure A.10), is from the manufacturer’s specifications. Taking the manufacturer’s specification for the rubidium oscillator phase noise, and correcting this for the frequency scale-up factor of 1890/10 by adding 45.5 dB, gives a lower bound for PLL noise performance, which can never be better than the reference frequency noise. Phase jitter introduced by the frequency divider, which divides the 10 MHz reference down to 200 kHz before it is applied to the loop, plus jitter from the dividers within the loop, the phase noise contribution from the PFC, and noise from the loop op-amps, will all contribute to the final phase noise characteristic.

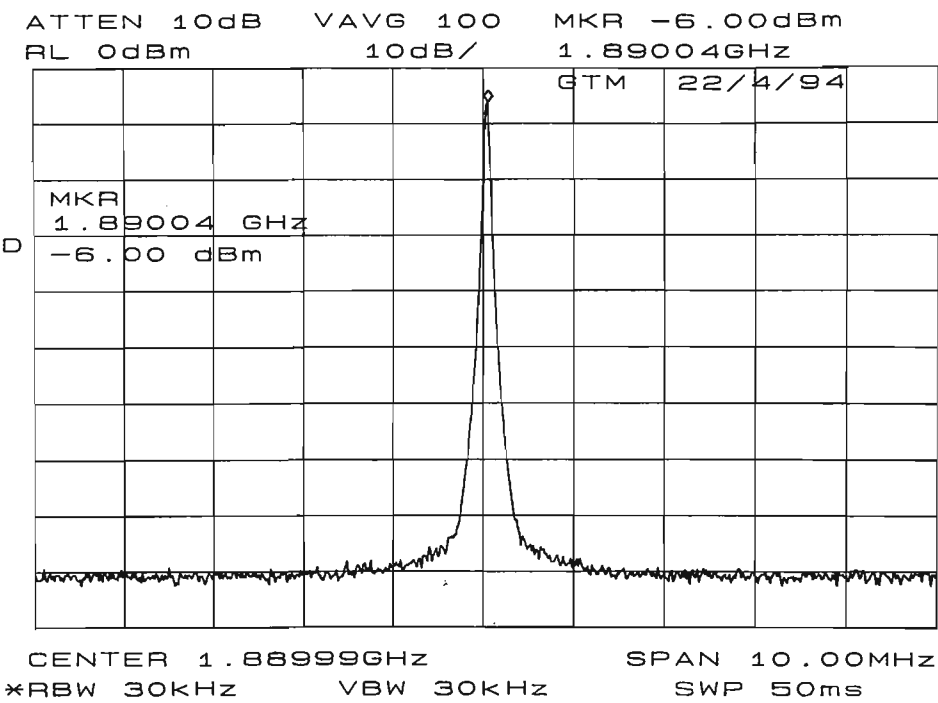


FIGURE A.11    Spectrum of 1890 MHz synthesizer at 10 MHz span

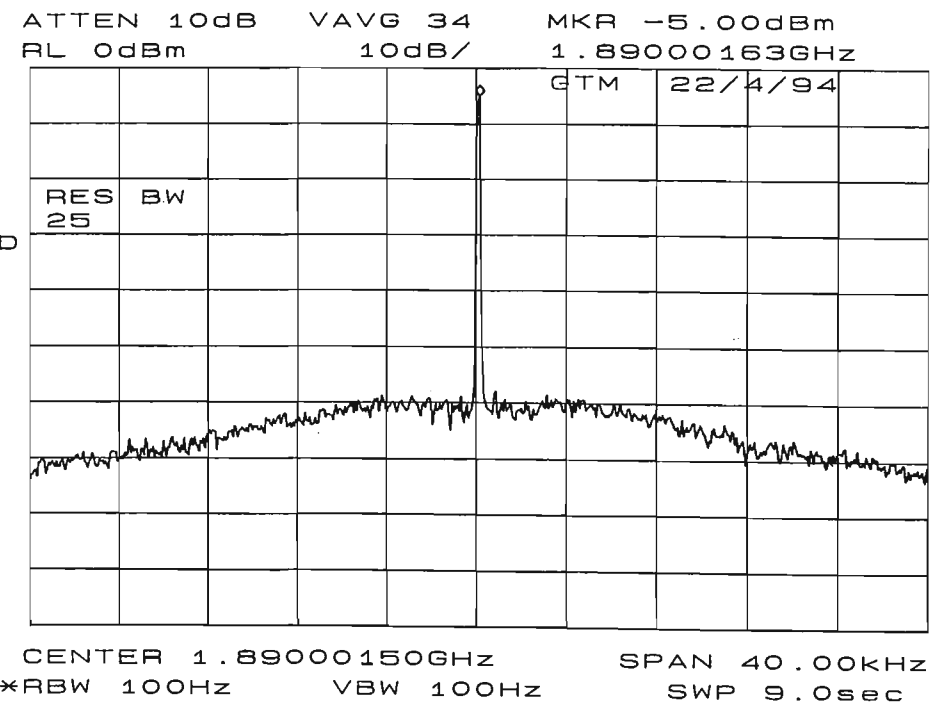


FIGURE A.12    Spectrum of 1890 MHz synthesizer at 40 kHz span

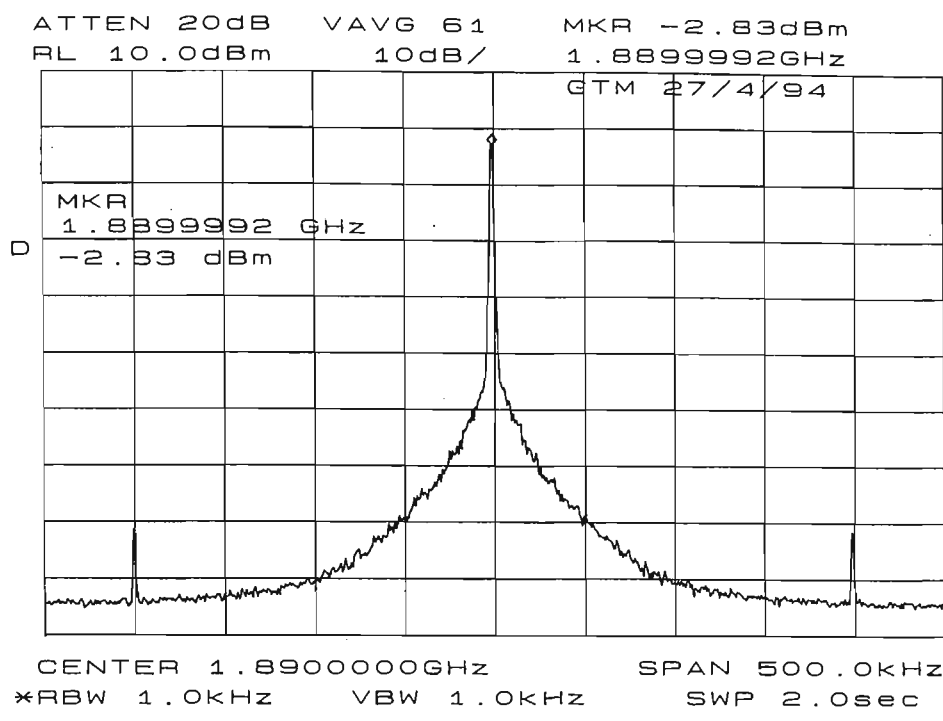


FIGURE A.13 Spectrum at 1890 MHz showing  $\pm 200$  kHz spurs

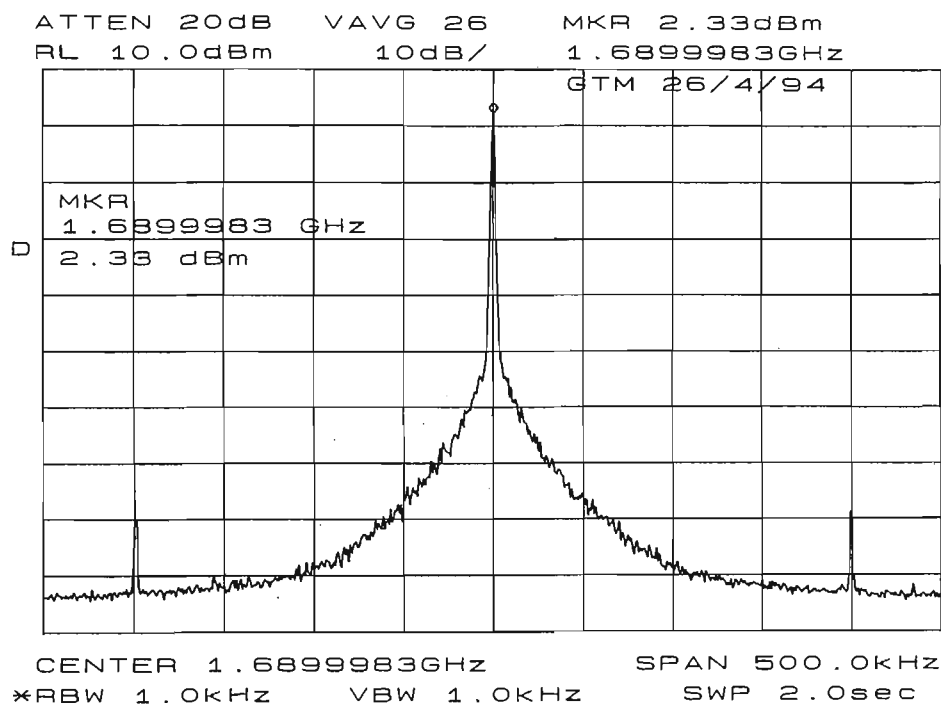


FIGURE A.14 Spectrum at 1690 MHz showing  $\pm 200$  kHz spurs

A.2.11 Future Improvements

Although the performance of these signal sources has been adequate for all *channel sounder* measurements (demonstrated in *back-back* evaluation; see Chapter 3) to date, with experience gained developing the synthesizers it has become apparent that an improved design

would be possible.

These are essentially fixed frequency sources (unless a substantial move to a different part of the band is wanted), so a 200 kHz step size is unnecessarily small. A larger step size would ease the problem with PFC frequency spurs, and would reduce (or eliminate) logic noise in dividing down from the 10 MHz rubidium oscillator. A 10 MHz step size should be used, provided the PFC will operate at this speed.

Since these synthesizers were built, low cost synthesiser chips have appeared on the market with inbuilt dual-modulus prescalers. A good example is the *National Semiconductor PLLatinum™* family, including the LMX2320 (2 GHz) and LMX2325 (2.5 GHz) devices. The addition of a loop filter and a VCO, and some method of serial programming the divider settings at each power-up, results in a complete PLL. These chips have an inbuilt reference divider with a minimum divide ratio of 3, so a 2.5 MHz step size (reference divide ratio of 4) is the maximum possible using a 10 MHz reference, still a big increase on 0.2 MHz.

Having an inbuilt prescaler is a significant advantage, because the problem of prescaler modulus switching delays has been solved within the chip. The modulus change must happen in less than one clock period of the VCO frequency, or in less than 0.6 nanoseconds at 1890 MHz.

A better VCO is another area for major improvement. The octave bandwidth of the C-600M is not required. Generally, narrow band VCOs have lower phase noise than wide band types, because higher Q reactive networks can be used. The measured sensitivity of the C-600M of approximately 93 MHz/volt, means that 100 Hz change in output frequency occurs with a tuning voltage change of just 1.1 microvolts, so very low loop noise voltage levels must be maintained. Narrow band VCO circuits at 1890 MHz, using high Q ceramic or coaxial transmission line resonators can be built with a tuning range of the order of 20 MHz for a tuning voltage change of 20 volts, or 1 MHz/volt sensitivity, and such VCOs would be much more appropriate in this application.

## A.3 VHF Synthesizer

Sliding correlation requires two pseudo-noise (PN) sequences clocked at slightly different rates. The receiver clock at 100 MHz is generated by multiplying the 10 MHz reference. The other clock has a slight frequency offset, for example 100.02 MHz, and is produced by a VHF synthesizer locked to the 10 MHz reference. At the time of development, it was thought that the multiplier would be simpler and use less power than the synthesizer, and so the multiplier was used in the portable receiver.

A *Motorola* CMOS type MC145152 parallel input PLL is the basis of the synthesizer, and allows the frequency to be set with a single 8 pole DIP (dual in-line package) switch. The VCO uses a MC1648 ECL (emitter-coupled logic) oscillator chip with an LC (inductance-capacitance) tank circuit, and a MC12017 dual modulus 64/65 divider acts as a prescaler. The

reference frequency is divided down to 40 kHz (see Figure A.19) externally, then divided further by 8 to give a PFC frequency, and a step size, of 5 kHz. The DIP switch allows setting of the synthesizer frequency in 5 kHz steps in the vicinity of 100 MHz. For *outdoor mode* measurements with a 25MHz chip rate, the synthesizer is set to 100.02 MHz, ( $M=312, A=36$ ) which after division by 4 gives a chip rate of 25.005 MHz. *Indoor mode* measurements are done with the synthesizer set to 100.005 MHz ( $M=312, A=33$ ).

Loop Filter Design	
PARAMETER	VALUE
This section calculates natural frequency and damping factor for an existing design	
Kvco rad/sec/volt	33000000
Kphi phase detector	0.8
Kamp amplifier gain	1
Output Freq (Hz)	1E+08
Reference Freq (Hz)	5000
Ratio N	20004
Capacitor C nF	150
Input R (R1) ohm	22000
Feedback R (R2) ohm	15000
Fn loop natural freq (Hz)	100.6513
Damping factor	0.711441

FIGURE A.15 PLL design parameters

In addition to the active lead-lag loop filter, a higher frequency pole is contributed by the  $RC$  lowpass filter. The poles formed by the 0.1 uF capacitor (C13) across the op-amp output, and by the 100 k $\Omega$  together with the VCO varicap capacitance are at over 100 kHz, and so have a negligible effect. See Figure A.17. A *SPICE* analysis of the open loop transfer function gives the Bode plot shown in Figure A.16, with a loop phase margin of 66°.

The output from the VCO is attenuated by a capacitive divider, giving -16 dBm into a 50 $\Omega$  load.

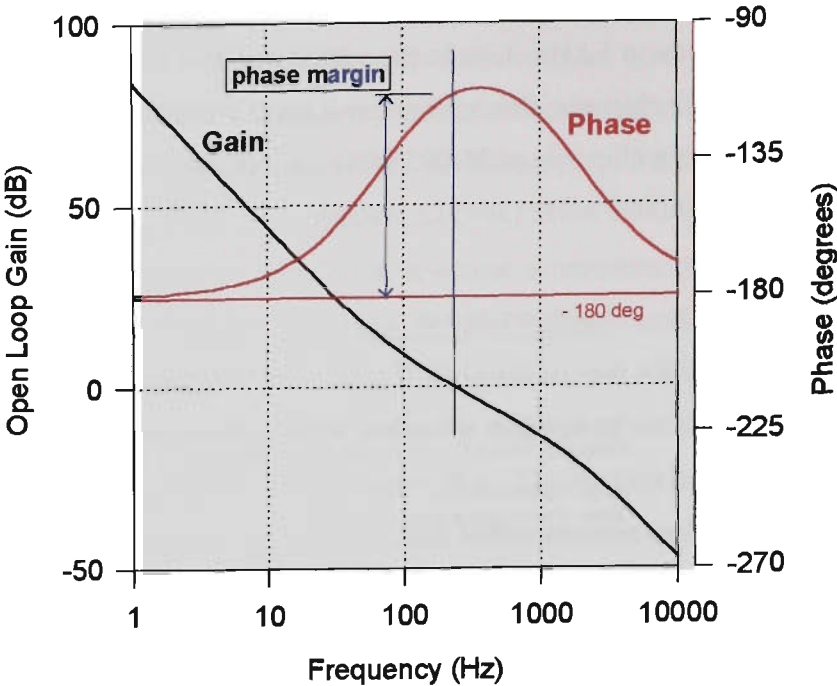


FIGURE A.16 Open loop Bode plot for 100 MHz phase locked loop

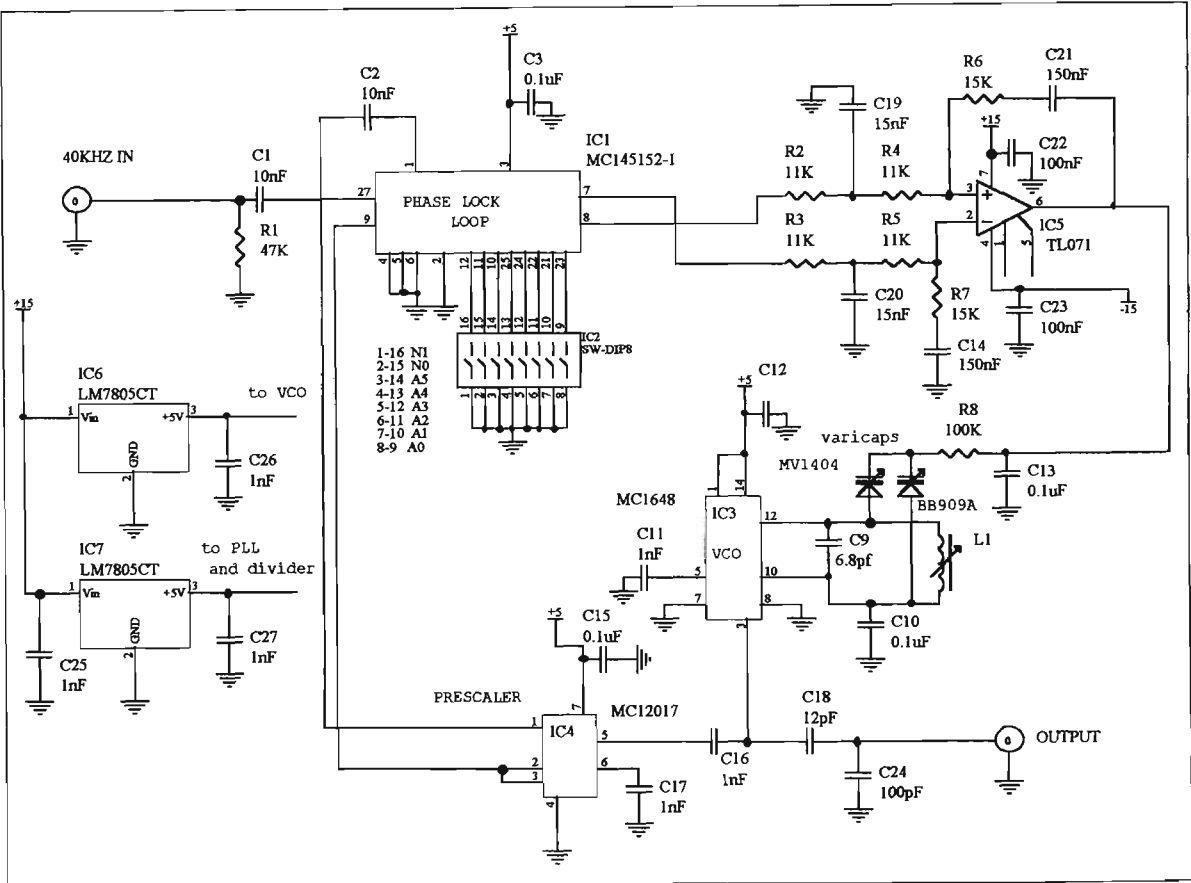


FIGURE A.17 VHF Synthesizer circuit schematic



### A.3.1 Performance

Measuring the output spectrum on an HP3589A analyser, and correcting for the resolution bandwidth, gives an estimate for the single sideband phase noise as a function of offset frequency, and a plot of this is shown below (Figure A.18).

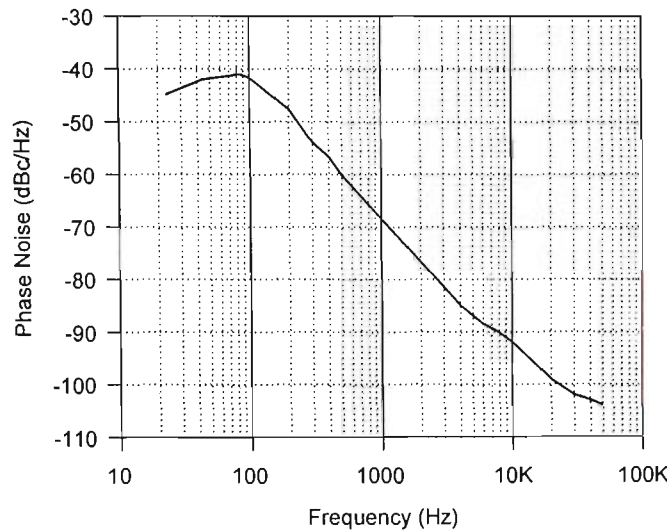
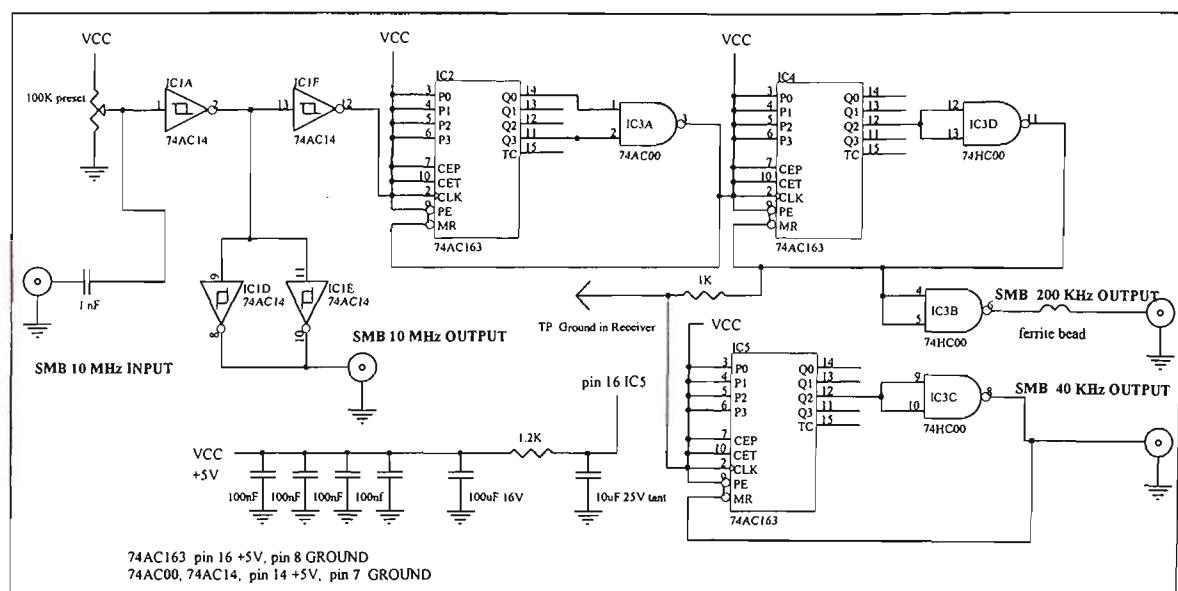


FIGURE A.18 VHF synthesizer single sideband phase noise

The first reference frequency spurs, at 5 kHz offset, are at -43 dBc. Other spurious signals in the frequency offset range >5 kHz up to 50 kHz, are at < -62 dBc. Lower spur and spurious levels would be desirable. In a future improved version of the hardware, use of a voltage controlled crystal oscillator as the VCO will be investigated. To change the offset frequency when switching *channel sounder* modes, two separate PLL sources are proposed.

### A.4 Frequency Dividers

Reference frequencies of 200 kHz and 40 kHz are required for the synthesizers, and these are obtained by dividing the 10 MHz rubidium oscillator output by 50 and 250 respectively. At the input the sinusoidal 10 MHz signal is AC coupled, and then level shifted by adding a positive DC voltage to bring it into the operating range of the Schmitt trigger inverter IC1A (Figure A.19). Low noise advanced CMOS series 74AC logic is used. The divider is housed in a tinplate steel box, with its own (external) 5V linear regulator. In the receiver, the 40 kHz output is not required, and this stage of the divider is disabled.



**FIGURE A.19** Frequency divider circuit schematic

## A.5 PN Generator

### A.5.1 Design

The PN generator has the following features:

1. Operates with a low level clock of non-critical waveshape.
2. Maximum chip rate is over 100 MHz.
3. The chip rate is switchable to equal the input clock rate, or  $1/2$ ,  $1/4$ ,  $1/8$ , or  $1/16$  of the input clock rate.
4. The sequence length is switchable between 2047, 1023, 511, or 255 bits.
5. Logic is included to prevent lock-up in the all zero state.
6. A trigger pulse output is generated for each completed sequence, and this automatically adjusts as the sequence length is changed.
7. A start pulse input allows the option of starting the sequence in a known state, for synchronising the sequence with another PN generator, or for using a windowed portion of the sequence.

Parameters are varied by altering the circuit configuration using fast multiplexers. Hence parameters may be switched by switching address logic to the multiplexers, over non-critical long cables, without degrading the circuit speed.

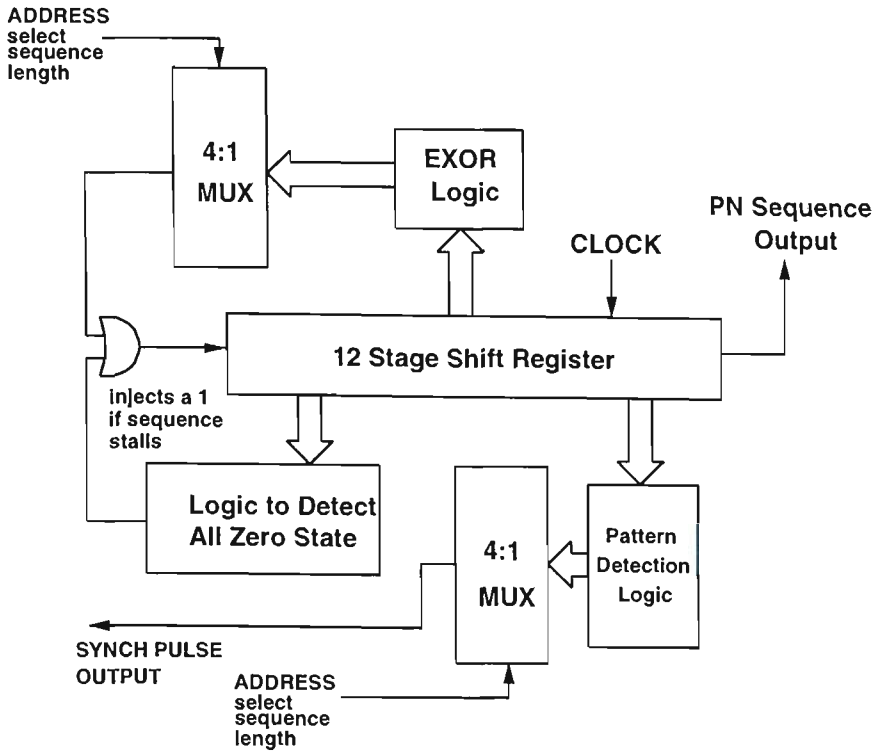


**FIGURE A.20 Variable length PN generator - block diagram**

Clock breakthrough, resulting in spectral lines at multiples of the clock frequency sitting in the nulls of the spectrum, can be a problem with PN generators.

### A.5.2 Circuit Techniques

Maximal length PN sequences are generated by a binary shift register with the input provided by the modulo-2 addition of two or more outputs from shift register stages. Only certain feedback connections generate maximal length sequences, and tables of these connections are available {Ref [A.7]}. Three different circuit arrangements are possible:

1. Simple type, as described above.
2. Modular type, where the modulo-2 adders are inserted between shift register stages.
3. Syncopated register generators.

The shortest period possible for the PN chip is equal to the sum of the toggle time of a register stage plus gate delays in the modulo-2 adder plus any feedback path delay. For two feedback taps, the simple shift register generator with one modulo-2 adder is the fastest possible configuration. When the number of feedback taps exceeds two, extra layers of modulo-2 adders are required, adding extra delay in the feedback path and reducing the maximum speed. In this case, the modular type is a better choice, because the maximum adder delay with multiple feedback taps is equivalent to a single modulo-2 adder. The syncopated generator uses modulo-2 addition of two half-rate sequences, clocked with clocks 180° out of phase. The idea can be extended to more than two sequences. Speed is limited by register rise and fall times, and the performance of the final modulo-2 adder.

The syncopated generator is a way of squeezing more speed out of marginal technology, but a better solution is simply to use faster integrated circuits. The ever increasing speed of *ASIC* (application-specific integrated circuit) chips is becoming attractive for the realisation of a single chip PN generator. Already devices with maximum clock speed over 100 MHz are available at low cost.

### A.5.3 Logic

With high speed as a goal, it is sensible to use the fastest available logic family. Emitter-coupled logic (ECL) is still the fastest available, although it is both difficult to obtain and expensive in small quantities. *Motorola* MECL10KH series ECL is used in the PN generator.

Typical gate propagation delay is 1 ns, with rise and fall times of 1.5 ns, with a maximum toggle frequency of 250 MHz (faster ECL families are also available). Outputs are open emitter and can be wire-ored. External pull-down resistors are required, and help reduce chip heating by taking some dissipation off the chip. Supply voltages of -5.2 volt and -2 volt are used. Complementary outputs are available, and may simplify some logic designs. Noise margins are small (150 mV) so overshoot and ringing must be well controlled to avoid glitches.

### A.5.4 ECL Techniques

The high speed of ECL logic signals has several implications for layout and circuit techniques adopted. Time delays through the interconnecting wiring can become significant. Sixty millimetres of track on epoxy board is equivalent to one gate delay, so tracks should be kept short and direct. The interconnecting tracks behave as transmission lines, and if these are not properly terminated, multiple reflections will result in severe ringing which may cause multiple triggering, or glitches, in subsequent gates. Crosstalk between tracks can also be a problem. RF layout techniques with a ground plane should be used. Interconnecting tracks are designed as microstrip transmission lines. The open emitter outputs of ECL have an impedance of about 7 ohms when high, and a high impedance, determined by the pull-down resistor, when low. Several approaches can be taken to the problem of terminating the transmission lines between gates. The gate outputs may be terminated at the chip at the input of the transmission line, or at the input of the driven gate at the output end of the line, or at both ends {Ref[A.3]}.

The generator described here is built on double-sided epoxy circuit board, with the component side used entirely as a ground plane. Tracks are designed as 100 ohm microstrip, and kept as short as possible. All single interconnections are terminated at the far end with a pull-down resistor of 100 ohms, going to -2 volts. This voltage is used rather than -5 volts, to reduce power consumption and chip dissipation. Where an inter-connection goes to more than one input, if the connections are sequential, only the far end of the line is pulled down with 100 ohms. Where, for layout convenience, a line goes off in two different directions, each end is

terminated with a 220 ohm pull-down. This is a compromise, but works well enough. Some inter-connections cannot be routed on the single layer, and are wired with a “*Vero*” pen (point-point wiring). The numerous pull-down resistors are wired to a -2 volt bus, which is constructed using stick-on microstrip (effectively forming a third layer), on the track side of the board.

### A.5.5 Power Supplies

The PN generator was originally designed to run from -8 volts, with inbuilt linear regulators to supply -5.2 and -2 volts. However, in the *channel sounder*, the PN generators are operated from -5 volts provided by a DC converter. The -5.2 volt internal regulator is bypassed, but the -2 volt regulator is retained. Total supply current at -5 volts is 0.92 amps.

### A.5.6 Feedback Paths

The simple shift register generator circuit configuration is used. Each sequence length other than 255, can be produced with one modulo-2 addition, or a single two-input EXOR gate. The 255 sequence needs two layers of gates.

An 11 stage shift register is used, long enough to generate the longest sequence. Feedback paths for the shorter sequences are tapped off earlier stages. Tappings used are shown below:.

TABLE A.5 PN generator feedback tappings

Sequence Length	Number of Registers	Feedback from Stages	MC10H174P MUX input pin	MUX Address		Switch Position
				A	B	
2047	11	9, 11	10	1	1	1
1023	10	7, 10	12	1	0	2
511	9	5, 9	11	0	1	3
255	8	2, 3, 4, 8	13	0	0	4

A multiplexer selects the feedback path, thus determining the sequence length generated. For the shorter sequences, the later stages of the shift register merely add a constant time delay, allowing the output to always be taken from the last stage of the register. ECL chips containing 4 shift register stages (MC10H141P) are available, so to obtain 11 stages, three integrated circuits must be used. The twelfth stage is used as an output buffer.

### A.5.7 Address Switching

To select different sequence lengths, the address lines of the multiplexer in the feedback path are switched. Required addresses for the particular multiplexer inputs used are given

in Table A.5. A switch wiring scheme using a 2-pole 4-position switch is shown in the main circuit schematic (Figure A.25). As ECL inputs include 50 K $\Omega$  pull-down resistors on the chip, open-circuited inputs are low. An 1N4148 diode to ground produces a voltage level of about -0.8 volt (the forward voltage drop of the diode), and this serves as an ECL high signal.

### A.5.8 Input Clock

Input clock signal amplitude and waveshape are not critical. The clock is produced by either a synthesizer or a multiplier, and is not ECL compatible, so the input clock signal is conditioned by a preamplifier to interface with the ECL stages. This design uses a *Plessey* SL952 amplifier/limiter followed by a DC level shift to interface the input clock.

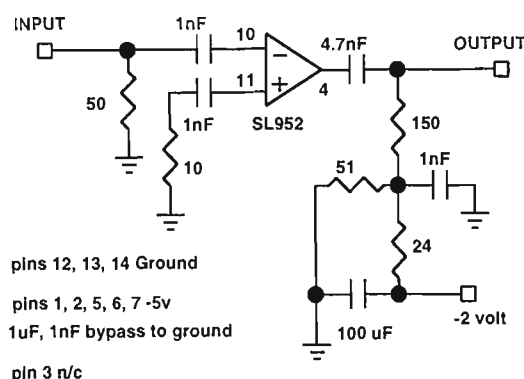


FIGURE A.21 Clock preamplifier and ECL translator

The schematic for this chip is not available, but it is believed to be a balanced differential amplifier with series/shunt feedback stages, followed by emitter follower buffers. Normally this IC operates from +5 volts, but by grounding the 5 volt rail, and connecting all the ground connections to -5 volt, the output can be made almost ECL compatible. The bandwidth of the device is approximately 1 GHz, so stability may be a problem, and layout is critical. One side of the differential input (pin 11) is grounded via a 10 ohm damping resistor, recommended in a *Plessey* Application Note to improve stability with an unbalanced source. The circuit of the SL952 preamplifier is shown in Figure A.21. Tests using a 20 MHz sinusoidal input source at -22 dBm gave an approximately square wave output, with a high level of -1.1 volt, and a low of -2.4 volt. Increasing the input level to -10 dBm gives an output swing from -1.0 to -2.7 volts, and 0 dBm input gives -0.9 to -2.9 volt. This signal will drive some ECL chips directly, but is not reliable with all devices, so a DC level shifting network has been added at the output.

### A.5.9 Variable Chip Rate

The chip rate is variable under control of a front panel switch. After preamplification by the SL952, the clock signal goes to a 4-stage binary counter (MC10178P), and the divided outputs, plus the input, are taken to an MC10H164P 8-line multiplexer. Multiplexer outputs

are selected by switching the address lines. If the input is 100 MHz, this gives 100, 50, 25, 12.5, and 6.25 MHz selectable chip rates. A block diagram is shown in Figure A.22.

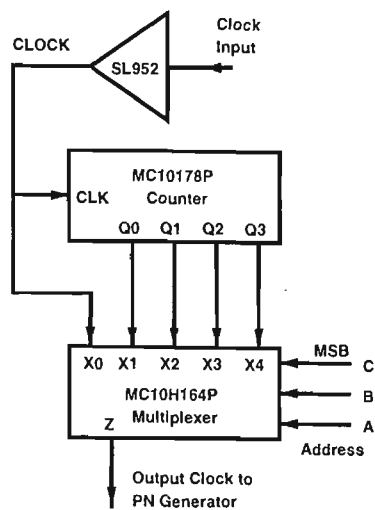


FIGURE A.22 Block diagram - variable clock

A.5.10 All Zero State

Past experience with a simple PN generator showed that sequence dropout, caused by the register getting into the *all-zero* state did happen occasionally, and was very inconvenient, requiring manual resetting. In this design, if the *all-zero* state occurs, a 1 is added into the feed-back path to restart the sequence. Combinational logic is used to detect the *all-zero* state.

There are other ways of detecting the *all-zero* state and restarting. If a counter equal in length to the number of shift register stages is incremented on every clock pulse, and reset each time the PN output is “1”, the counter will never fill unless the PN generator falls into the *all-zero* state. Then the counter output can be used to preset one or more of the PN shift register stages, or inject a “1” into the feedback path to restart the PN sequence. Another method is to drive a diode charge pump and RC network from the PN output. If the *all-zero* condition occurs, the capacitor will discharge, hence the sequence can be restarted. The occurrence of an *all-zero* state will necessarily disrupt synchronism of the PN generator if it has been started simultaneously with another PN generator.

A.5.11 Synchronisation Pulse

A synch pulse is produced with a length equal to the sequence length, and the leading edge coincides with one unique pattern of the sequence. The synch pulse is automatically adjusted if the sequence length is altered, using another multiplexer. The unique state detected to produce the synch pulse is shown in Table A.6, and has been chosen to allow some of the logic, already in place to detect the all zero state, to contribute to synch pulse generation, re-



ducing the hardware outlay.

TABLE A.6 PN Generator Synch Patterns

Sequence Length	Number of Register Stages	Synch Pattern
2047	11	11110000000
1023	10	11100000000
511	9	1100000000
255	8	10000000

A.5.12 Start Pulse

The MC10H141P four bit universal shift register is controlled by the S1 and S2 inputs, to either shift right, shift left, load parallel data from the D inputs, or stop shifting. The normal operating condition in this design is shift left, with S1 *high*, and S2 *low*. To start, or restart, from a known initial condition, S1 is taken *low* for more than one clock period, presetting the register with whatever data is present on the D (preset) lines, which can be hard wired in any desired state. When S1 goes *high*, the sequence will start from the preset state. For example, if all the D inputs are *high*, the sequence will start from the *all-ones* state on the next positive clock edge after S1 goes *high*.

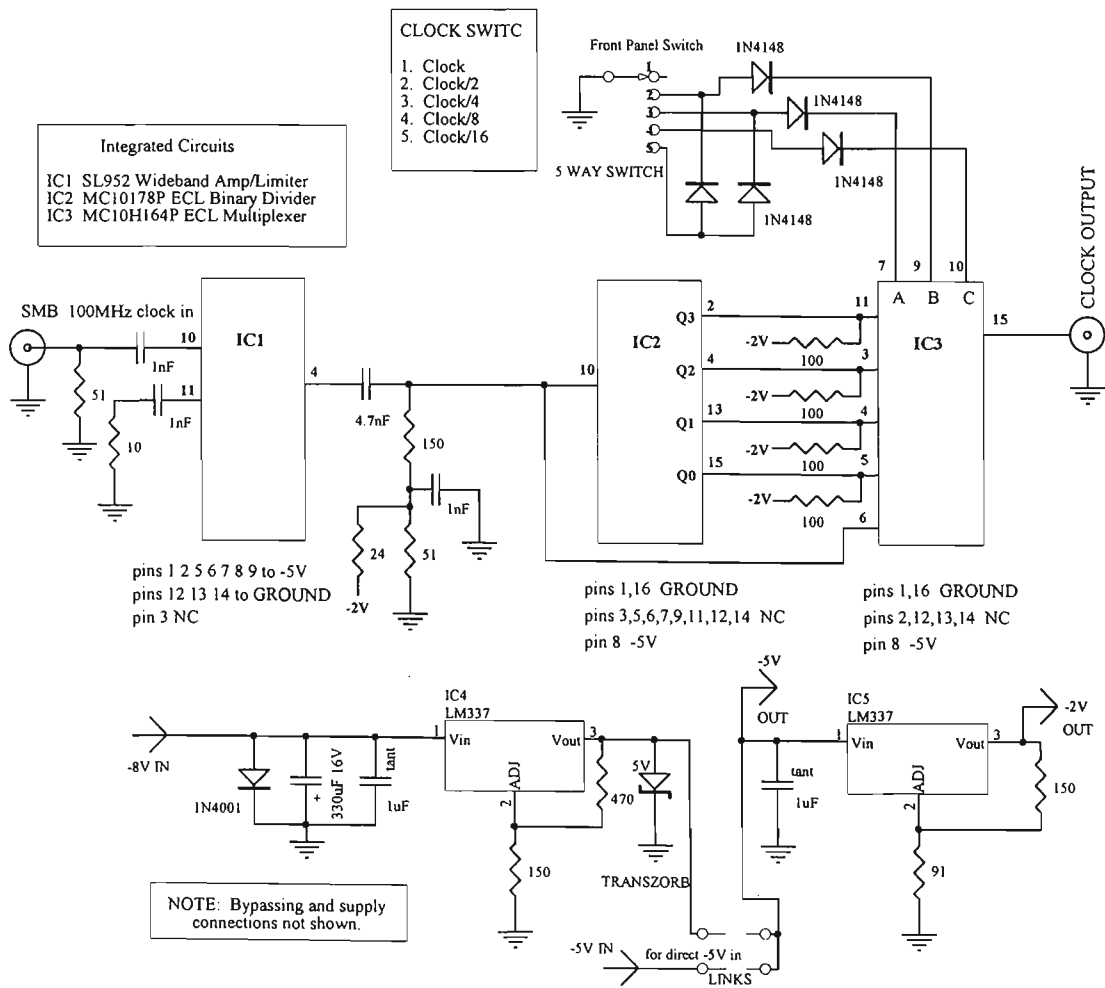


FIGURE A.23 PN generator clock and power supply schematic



Firstly, examine the overall spectrum. With a 25 MHz chipping rate, and using a *HP 8562B Spectrum Analyser*, suitable instrument settings are: Start Frequency= 0 MHz, Stop Frequency =100 MHz, Video Bandwidth =1 kHz, Averaging OFF, Attenuation= -40 dB, Relative Level =-10 dB, Vertical Scale=10 dB/division. The display should look much like Figure A.24, with nulls at 25, 50, 75, 100, 125 MHz, and with a smooth envelope which does not alter from sweep to sweep. Next, the fine detail of the spectrum is examined. The envelope is actually made up of a series of spectral lines, at frequency intervals given by the chipping frequency divided by the sequence length. Examine the middle portion of the main lobe, and set the spectrum analyser to: Start Frequency 10 MHz, Stop Frequency 10.2 MHz; all other settings remain as previously specified. Over a small portion of the main lobe, the envelope amplitude will be nearly constant, and the spectrum will appear as a series of peaks, as shown below in Figure A.26:

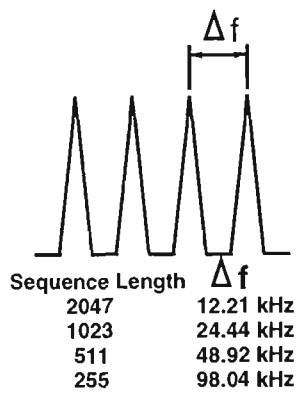


FIGURE A.26 PN spectrum fine detail

The frequency spacing between peaks is constant, with the values given. If the frequency spacing is greater than these values, it indicates that the sequence is not maximal length. With this design, another method of checking that the sequence is maximal length is to accurately measure the length of the synch pulse. For the 2047 sequence at 25 MHz, this should be 81.88 microseconds.

### A.5.14 Clock BreakThrough

The appearance of spectral lines at multiples of the chipping frequency, and sitting right in the spectral nulls, is a commonly encountered problem. *Dixon* {Ref[A.7]} calls this effect “code imbalance”, or “code-rate spurious signals”. This fault is caused by an imbalance between the weighted values of the *high* and *low* output signals, which can be caused by unequal durations of the *high* and *low* states, unequal rise and fall times, and unequal ringing (overshoot and undershoot) on the rise and fall edges of the output waveform.

For code balance, the following equation must be true:

$$A_{high} \int_0^{\tau_1} G_{high}(c) dt = A_{low} \int_{\tau_1}^{\tau_2} G_{low}(c) dt \quad (\text{EQ A.12})$$

where  $A_{high}$  and  $A_{low}$  are the amplitudes of the high and low signals respectively, and the  $G(c)$  are signal envelopes,  $\tau_1$  is the duration of a *high* and  $\tau_2 - \tau_1$  is the duration of a *low*.

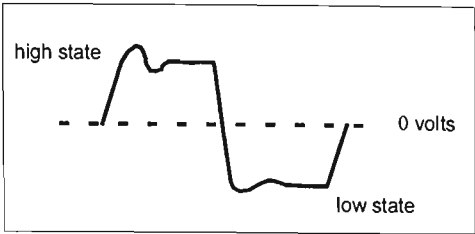


**FIGURE A.27 PN output waveform**

Ringling is influenced by the quality of the matching of the final shift register stage to the output transmission line, and if the matching is improved and the ringling reduced, the clock spurs will diminish. Using an additional register stage as a buffer is an advantage, as the output does not need to drive any other logic gates, but just the output line. In this design, up to eleven register stages are needed, whereas twelve are available in the three MC10H141P 4-bit registers used, allowing the twelfth stage to be used solely to buffer the output. The output is AC coupled, and the resistor configuration in the output network is chosen for minimum ringling without sacrificing much output voltage swing, with the output connected via coaxial cable to the 50Ω input of a 500 MHz oscilloscope (*HP-183A*). The edges appear slightly over-damped, with no overshoot, but with a small amount of ripple following transitions.

As the chipping frequency goes up, the clock spur problem gets worse, because rise and fall time imbalance is relatively more important, and any ringling also becomes more significant relative to the chip period. The final output network is shown in Figure A.25. Note that the DC blocking capacitors insert a notch in the spectrum near zero frequency.

Clock break through is so dependent on second order effects that the two nominally identical PN generators built for this project, showed different performance figures (Table A.7) for this effect.

TABLE A.7 Measured clock break-through

Clock break-through harmonic number	PN Generator, and clock frequency			
	No. 1		No. 2	
	20 MHz	80 MHz	20 MHz	80 MHz
1	-37.2 dB	-11.0 dB	-18.6 dB	-12.3 dB
2	-25.5 dB	-13.4 dB	-28.3 dB	-9.3 dB
3	-24.1 dB	-20.7 dB	-24.6 dB	-8.3 dB
4	-30.3 dB	-10.0 dB	-20.0 dB	-7.5 dB
5	-20.0 dB	-26.0 dB	-17.0 dB	-27.2 dB

Measurements were done at 20 and 80 MHz, rather than the 25 and 100 MHz clock frequencies finally chosen for *channel sounder* operation. Values in dB are relative to the maximum value of the main spectrum lobe. For the 20 MHz clock, the clock break through harmonic 1 refers to the spur at 20 MHz, harmonic 2 means 40 MHz, etc. For these tests, the clock input signal was a sinusoidal signal supplied by a high quality signal generator. The clock break through values were the same for both the case where (a) the clock signal was divided by the ECL binary divider, and (b) the clock signal bypassed the divider. For example, the results did not alter if the clock input was 80 MHz not divided, or 160 MHz divided by 2; or in the case of the lower frequency clock, 20 MHz not divided, or 80 MHz divided by 4.

Plotting clock break through in the first null as a function of clock frequency for PN Generator No.1 gives the curve shown below in Figure A.28:

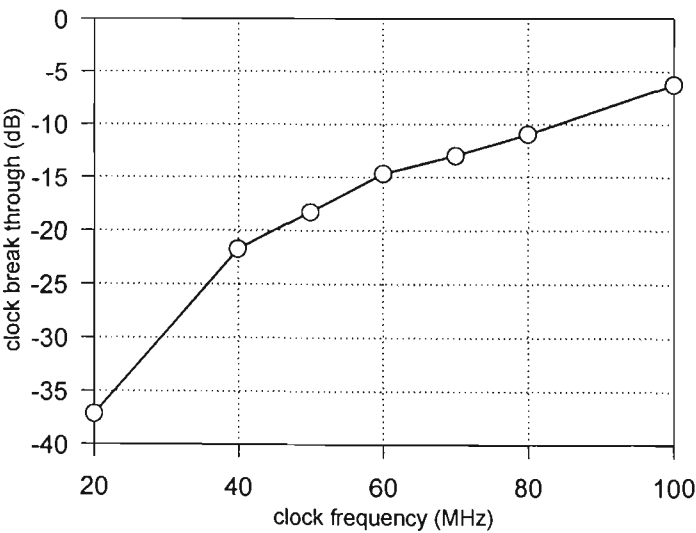


FIGURE A.28 Clock break through at first null - PN generator No.1

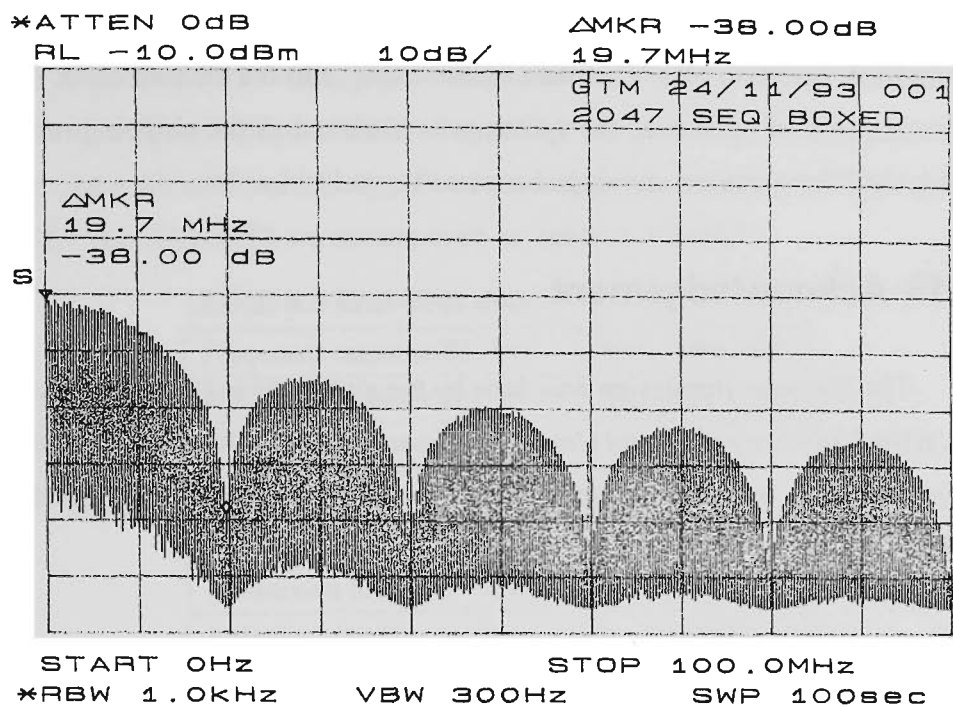


FIGURE A.29 PN generator No.1 spectrum with 20 MHz clock

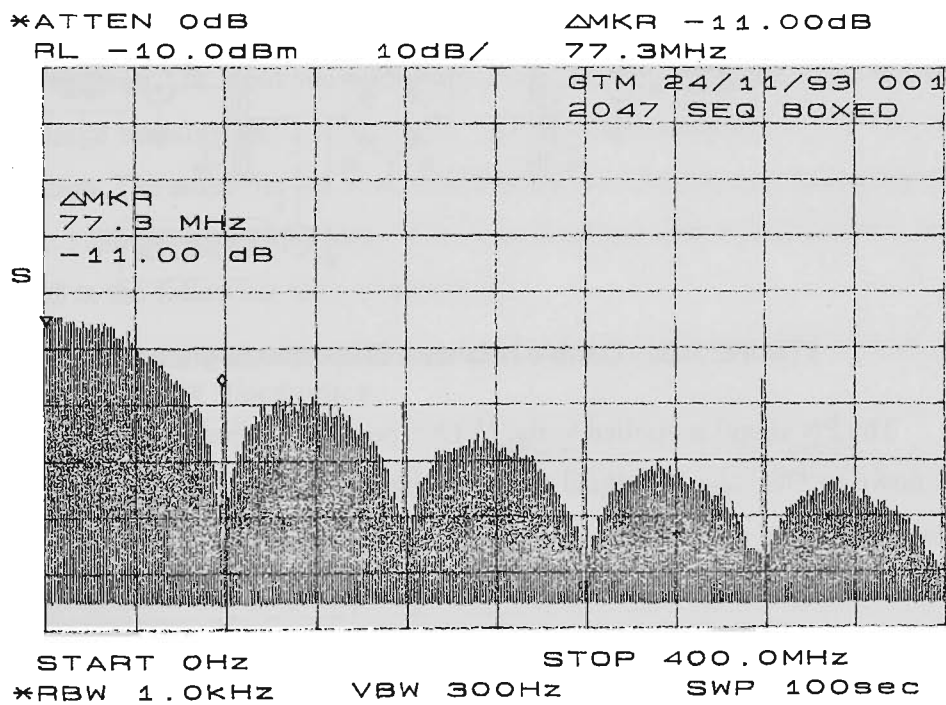


FIGURE A.30 PN generator No.1 spectrum with 80 MHz clock

A.5.15 Maximum Chip Rate

The maximum speed of operation depends on wiring and gate delays. This design operates to chipping rates of just over 100 MHz, before the shortest sequence (length 255) ceases to function. This sequence uses an extra layer of gates, and so would be expected to be the first

to fail. Other sequence lengths operate to over 120 MHz. The multiplexer used to give the variable sequence length feature of course adds delay and limits performance, as also does the *OR gate* used for insertion of a ‘1’ if the sequence falls into the all-zero state. To determine the maximum speed of operation, the spectrum is observed as the chipping rate is gradually increased, until the spectrum envelope becomes ragged and erratic.

A.5.16 Acknowledgement

The PN generator design was done by the author during a period of sabbatical leave in 1991, at the *University of Bristol Centre for Communication Research*. The variable parameter feature was used by other researchers at the *University of Bristol* {Ref[A.8], Ref[A.9], Ref[A.10]}.

A.6 Mixer

*Mini-Circuits* SRA-2000 mixers are used as a bi-phase modulator in the transmitter, and as a down-converting mixer in the receiver.

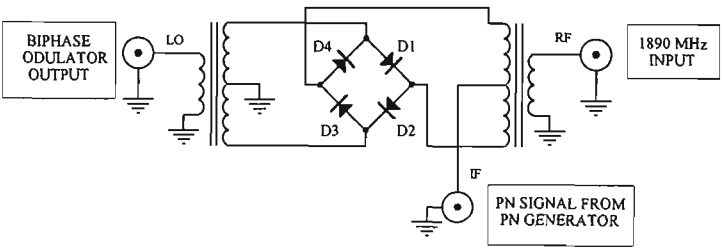


FIGURE A.31 Double balanced SRA-2000 bi-phase modulator

The PN signal is applied to the *IF Out* port, as the frequency response of this port extends down to DC. The PN signal turns on alternate pairs of diodes, swapping the electrical connections of the two centre-tapped transformer windings, and so switching the phase by 180°. This action is illustrated below:

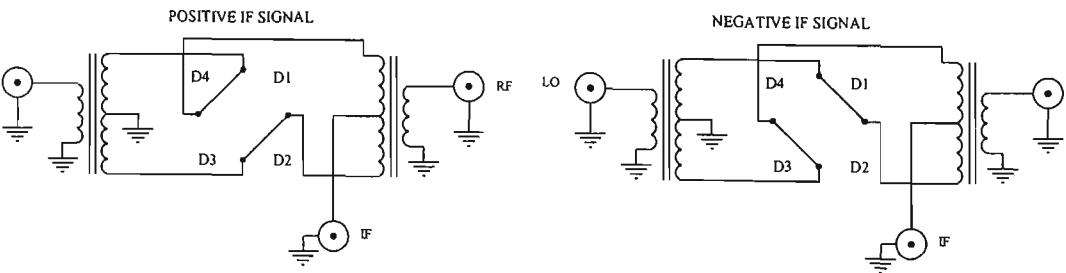


FIGURE A.32 Bi-phase modulation action

In the receiver, the circuit connections follow the port names, with the 1890 MHz



spread signal applied to the *RF Port*, the 1690 MHz synthesiser signal applied to the *LO Port*, and the 200 MHz centre frequency IF signal taken from the *IF Port*. The mixer is mounted on a small piece of circuit board with a ground plane, and mounted in a 50 mm x 50 mm tinned steel box, with short lengths of coax connecting to SMA connectors. The mixer case is soldered to the ground plane. Manufacturer's specifications and typical performance figures in the 1890 MHz region for the SRA-2000 are summarised in Table A.8 below:

TABLE A.8 SRA-2000 data

Frequency response RF, LO	100 - 2000 MHz
Frequency response IF	DC - 600 MHz
VSWR RF	< 2.5
VSWR LO	< 2.0
VSWR IF	< 1.5
Conversion loss LO = 4 dBm	7.9 dB
Isolation LO - IF	> 30 dB

## A.7 Power Amplifier

The power amplifier is a custom-built commercial unit manufactured by *WESSEX Electronics*, Bristol, U.K. It is a Class A amplifier with 10 watts (40 dBm) output, with very low spurious content. The input and output are protected with circulators, and the amplifier incorporates a large heatsink and a cooling fan. The device operates from 12V DC, which suits battery operation. The amplifier has been modified by the manufacturer to operate over the frequency range 1790 MHz to 1990 MHz. The specifications and manufacturer's test sheet results are listed in the following table (Table A.9):

TABLE A.9 RF Power amplifier specifications, model No. ANP-0113S, serial No. 4310, *WESSEX Electronics*.

Parameter	Specification	Test Result
case temperature	35+/-5°C	32°C
gain	40 dB min	43.0 dB
gain variation with frequency	1.0 dB pp max.	0.9 dB pp.
input return loss	20.8 dB min.	21 dB
output return loss	20.8 dB min.	21.0 dB
output power @P(-1dB) GCP	+40 dBm	+40.9 dBm
frequencies. power)		1.99 GHz
DC current @P(-1dB) GCP	7.5A max.	5.9A
2nd harmonic	-50 dBc (min. freq)	-70 dBc across band
3rd harmonic	-50 dBc (min. freq)	-70 dBc across band
spurious signals	-80 dBc	-80 dBc noise floor
DC supply		+12V

## A.8 Power Supplies - Transmitter

The rubidium oscillator requires a supply voltage of 22.5V to 32V DC, dictating the choice of battery arrangement as two 12 volt lead-acid batteries in series. One of these also supplies the 12 volt high current (up to 8 amp) requirement of the RF power amplifier, and is of larger capacity. A low dropout voltage, high current linear regulator is used to ensure that the RF power amplifier supply voltage will not exceed the specified value of 12 volts, even if the battery voltage exceeds 12 volts. Other voltages required by the transmitter electronics include -5 volt (PN generator),  $\pm 15$  volts (UHF synthesiser), +15 volts (RF driver amplifier), +5 volts (reference frequency divider). These voltages are provided by a commercial DC-DC converter, a step-up switching regulator, and linear regulators. Front panel LEDs monitor the various supply voltages, and will fade and then extinguish if supplies drop below preset thresholds.

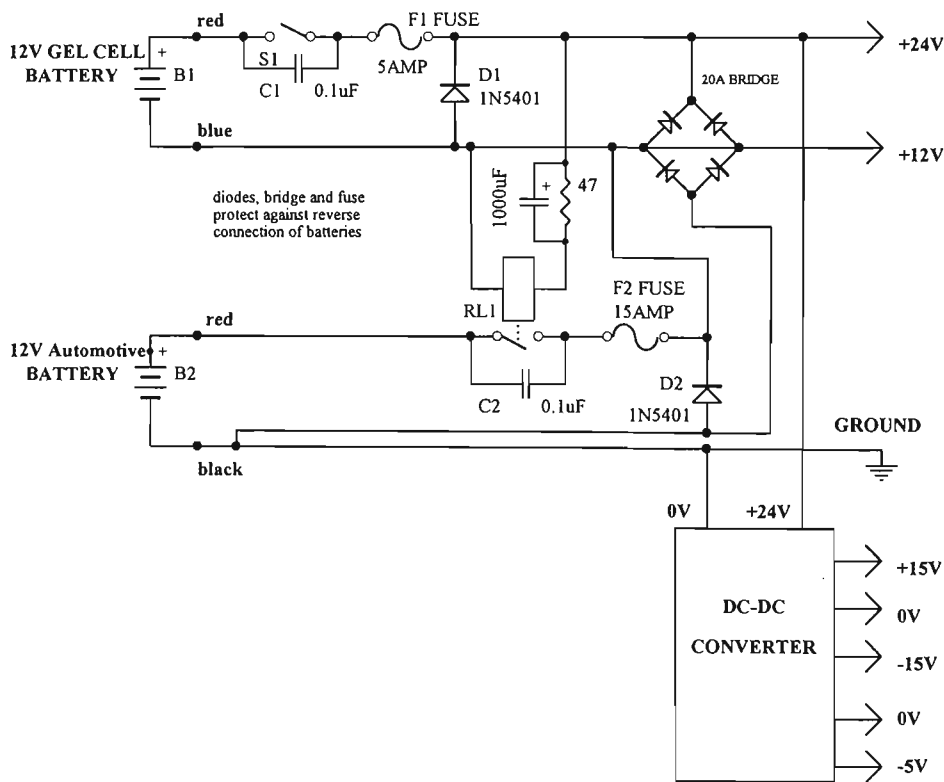


FIGURE A.33 Transmitter power arrangements

S1 is the main power switch, with the high current supply switched by the relay RL1, controlled by S1. RL1 is a heavy duty automotive horn relay, with hold-in current reduced from the normal 0.5A to 0.2A by a 47Ω series resistor. A 1000μF capacitor provides a low impedance path for the initial pull-in current.

Fuses, and a 20A bridge connected as series-parallel diodes, protect against inadvertent reverse polarity connection of either battery. Batteries available to power the transmitter are listed in Table A.10.

**TABLE A.10 Batteries - transmitter**

	Make	Model	Capacity
Low capacity	Yuasa	NP7-12	7 AH
High capacity (one used)	Yuasa	NPC38-12	38 AH
	Yuasa	NP65-12	65 AH
	Bosch	SP360	340 CCA
	Bosch	P450C	420 CCA

### A.8.1 Step-up Regulator For Driver Amplifier

RF amplifier *Mini-Circuits* ZHL-1724HLN is used as a driver amplifier, and is specified for a power supply of 15 volts at up to 725 mA. This is supplied by a step-up switching regulator running from 12 volts. The regulator includes a crowbar over-voltage protection circuit to protect the load. The crowbar triggers at 16.6 volts when the SCR (S1) clamps the output to ground and blows fuse F1. Short fast over-voltage transients are clamped by the 16 volt zener at the output. An *LC* output filter reduces switching noise on the output to  $< 40\text{mV}$  peak-peak. The regulator is housed in a tinplate steel box, with feed-through capacitors on the input and output lines. Input current at 12 volt is 0.9A.

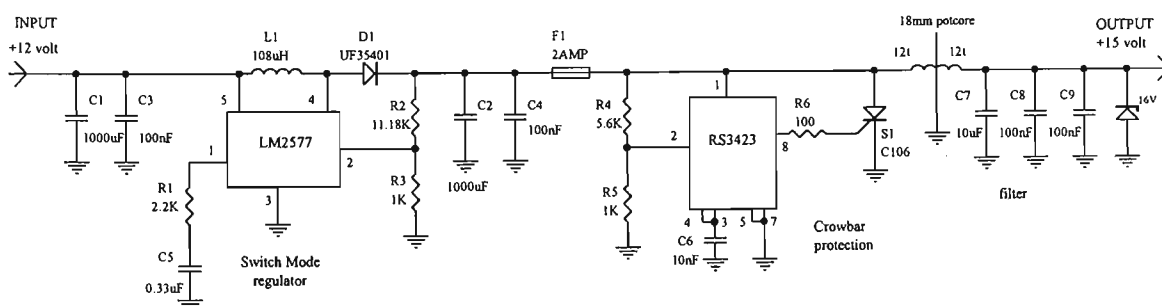
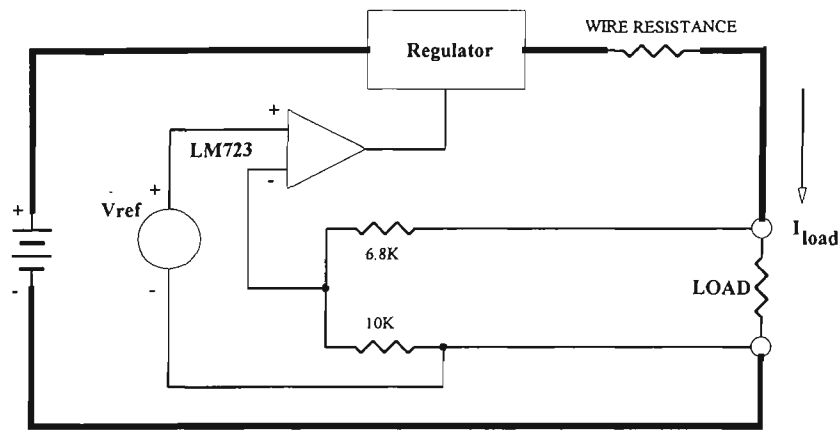


**FIGURE A.34** Step-up switching regulator for the RF driver amplifier

### A.8.2 Low Dropout +12 volt Regulator

A low-dropout voltage linear regulator ensures that the supply to the expensive RF power amplifier does not exceed the specified 12 volt level. Parallel power FETs with a low individual “on” resistance of 40mΩ are used as the series regulator element, controlled by an LM723 regulator. When dealing with high currents and low voltage drops, wiring resistance becomes significant, so to obtain good regulation, a 4-wire arrangement is used, with low current voltage-sensing leads wired directly to the load, allowing the regulator to compensate for wiring voltage drops. The circuit arrangement is shown in Figures A.35, and A.36.



HIGH CURRENT REGULATOR VOLTAGE SENSING

FIGURE A.35 High current regulator block diagram

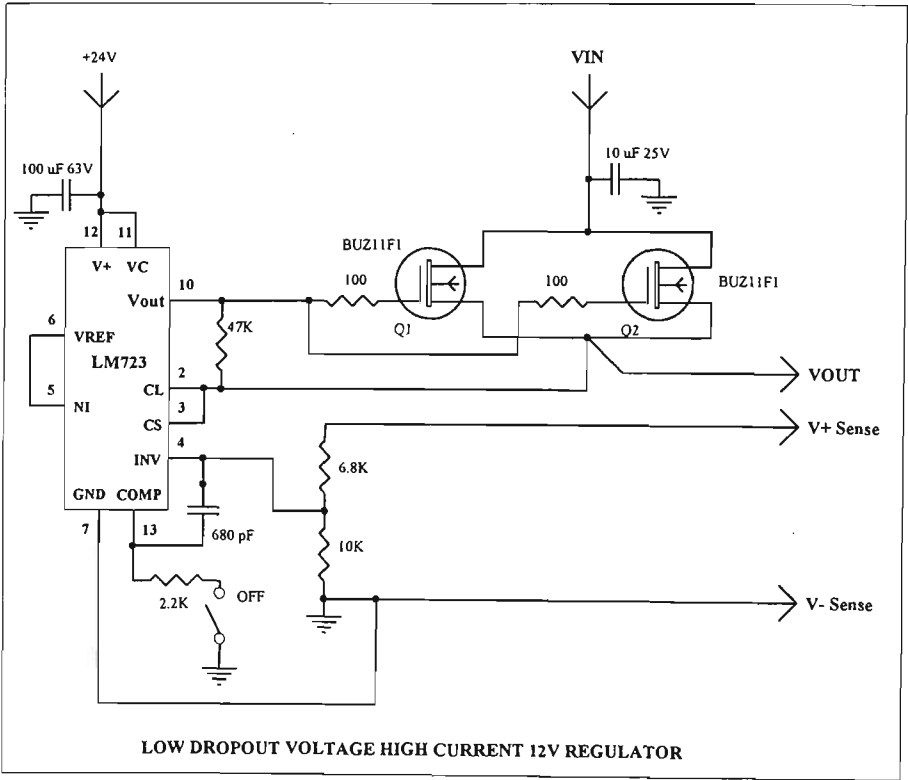


FIGURE A.36 High current 12V regulator

Measured regulator performance is shown in Figure A.37. At 4 amp load, the dropout voltage is 100mV, and at 10 amp load the dropout voltage rises to 600mV. Provided the dropout voltage is exceeded, the load regulation is excellent, with an output voltage variation of less than 10mV for load variation between 0 and 10 amp.

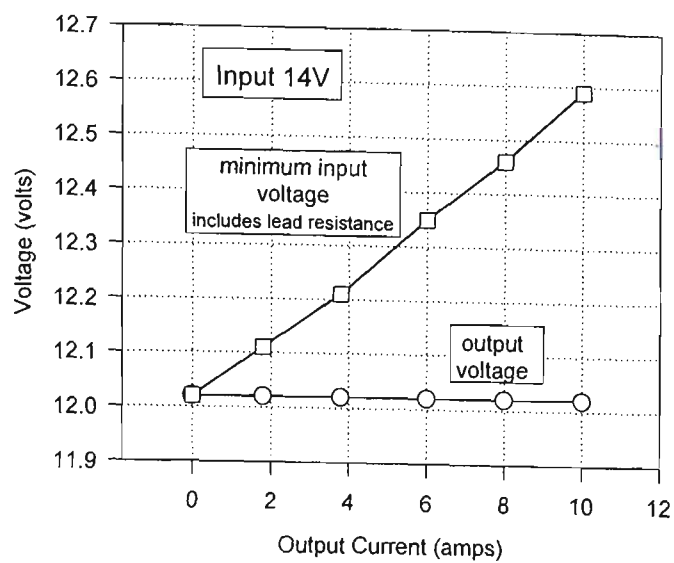


FIGURE A.37 Low-dropout regulator performance

If the input voltage falls below the minimum input voltage shown on the above graph, then the output voltage will fall correspondingly.

A.8.3 Supply Supervision

Front panel LEDs monitor the health of the various supply voltages:

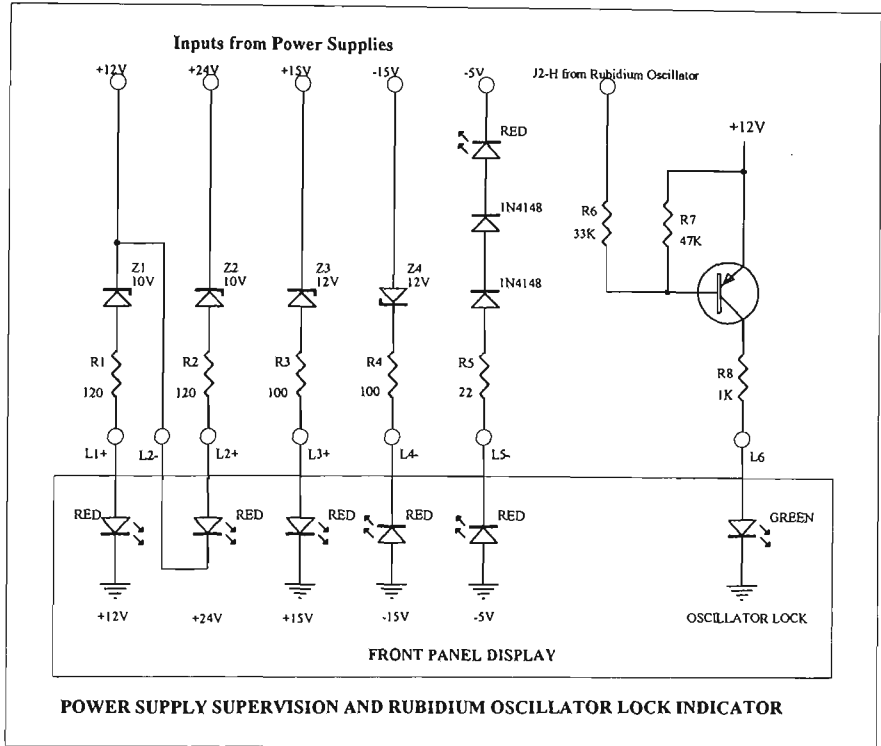


FIGURE A.38 Power supply supervision LEDs

---

## A.9 References - Appendix A

- [A.1] M.V. Harris, "A 1.8GHz Synthesiser for Use in Mobile Radio", IEE 6th. International Conference. Mobile Radio and Personal Communications, Warwick, U.K, 9-11 December 1991, pages 136-142.
- [A.2] Floyd M. Gardner, "Phaselock Techniques", 2nd. Ed. John Wiley & Sons, 1979.
- [A.3] Motorola, "MECL Data", DL122/D Rev.5, 1993.
- [A.4] GEC Plessey, "Professional Products IC Handbook", GEC Plessey Semiconductors Publication HB2480-2.0, June 1994.
- [A.5] Cynthia L. Barker, "Introduction to Single Chip Microwave PLLs", National Semiconductor Application Note 885, March 1993.
- [A.6] Hewlett Packard, Product Note 11729B-1.
- [A.7] Robert C. Dixon, "Spread Spectrum Systems with Commercial Applications", John Wiley & Sons, Inc, 1994.
- [A.8] S.A.Allpress, M.A.Beach, G.Martin & C.M.Simmonds, "An Investigation of RAKE Receiver Operation in an Urban Environment for Various Spreading Bandwidth", IEEE VTC, 1992, 506-510.
- [A.9] S. A. Allpress, "Optimising Signalling Rate and Internal Diversity Order for Mobile Cellular DS-CDMA Systems", PhD Thesis, University of Bristol, U.K., December 1993.
- [A.10] M.A. Beach and S.A. Allpress, "Propagation Aspects of Mobile Spread-spectrum Networks", Chapter 12, "Propagation of Radiowaves", Editor: M.P.M. Hall, The Institution of Engineers, UK, 1996.

# Appendix B: Receiver Hardware

## B. INTRODUCTION

This appendix contains detailed documentation of the design and characterization of the *channel sounder* receiver electronics (Figure B.1), and also serves as a handbook for the receiver.

Some of the receiver electronics has already been covered in Appendix A - *Transmitter Hardware*; namely, rubidium oscillators, UHF frequency synthesizers, and PN generators. These components are used in both the transmitter and the receiver.

Appendix B documents the design of the remaining sections of the receiver, including the low loss interdigital bandpass filters (also used in the transmitter), a low noise amplifier, the frequency multiplier electronics, *Bessel* lowpass active filters, and power supply arrangements.

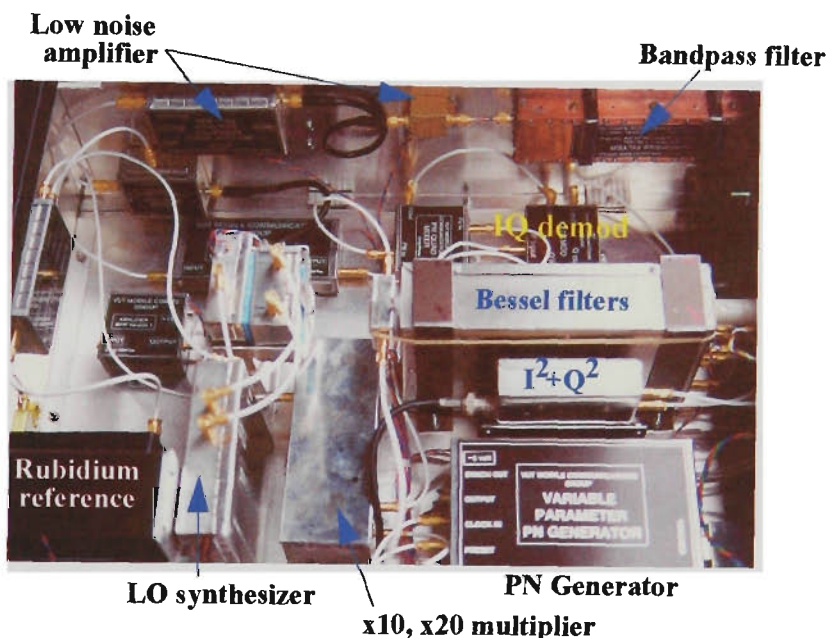


FIGURE B.1 Receiver electronics

### B.1 Receiver Portability

The *VUT channel sounder* has been designed to be self contained and portable, giving great flexibility for use in pedestrian and indoor/outdoor areas such as city arcades and shopping centres. The portability feature has been described in Chapter 3 - *Channel Sounding*. Pictures of the receiver in backpack configuration are shown in Figure B.2. Since these early



photos of the *channel sounder*, the antenna has been lowered to just above head level.

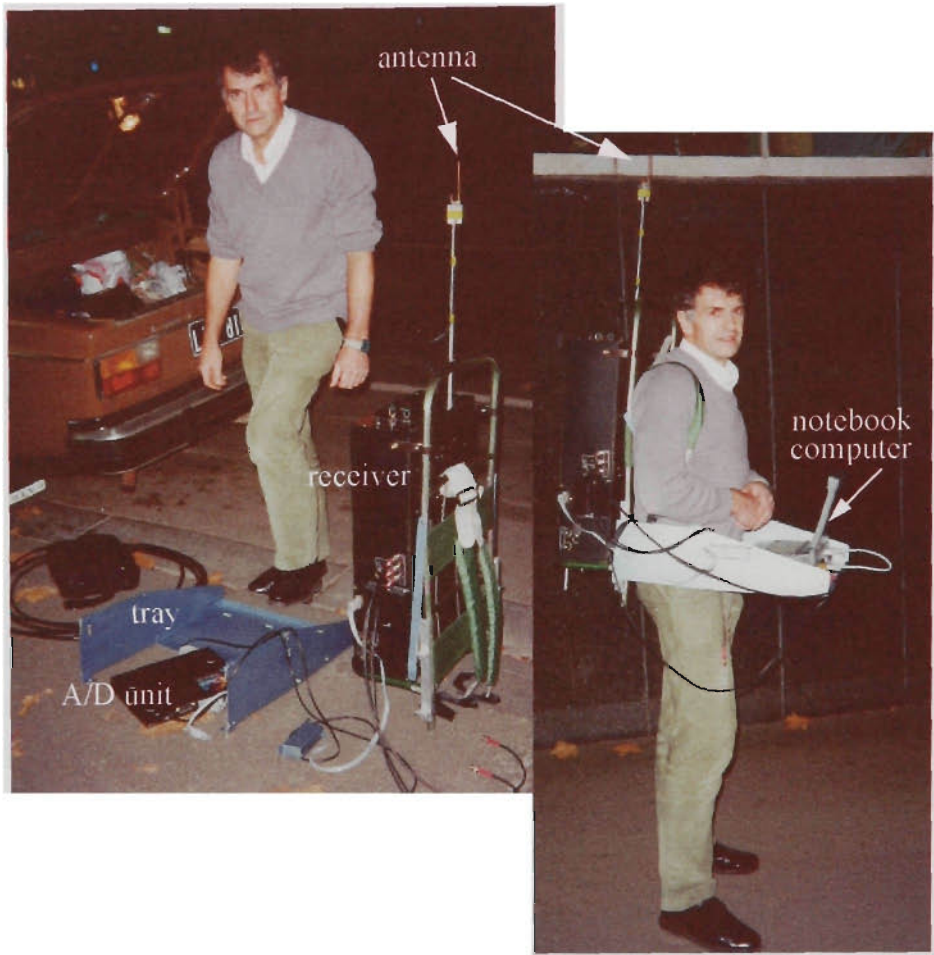


FIGURE B.2 VUT *channel sounder* receiver and data acquisition equipment in portable backpack configuration

## B.2 Bandpass Filter

At the input to the receiver, immediately following the antenna, a bandpass filter is required to band-limit the input signal for the wideband low noise amplifier, to reduce the risk of overload by strong out-of-band signals with consequent intermodulation distortion.

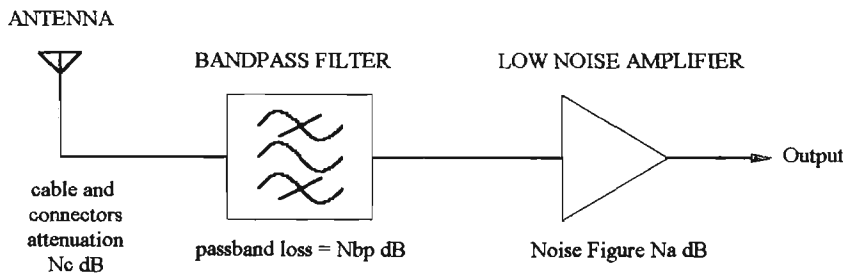


FIGURE B.3 Front end noise considerations

The total receiver noise figure  $N_{receiver}$  is the sum of the input amplifier noise figure and the insertion losses ahead of the amplifier,

$$N_{receiver} = N_c + N_{bp} + N_a$$

(EQ B.1)

hence for a low noise figure it is important to keep the insertion loss  $N_{bp}$  of the band-pass filter as low as possible, and this is a primary design goal.

B. 2.1 Losses

Bandpass filters consist of a cascade of coupled resonators. Insertion loss is dependent on the unloaded Q of the resonators, which is proportional to the ratio of stored to dissipated energy in the filter reactive elements. Energy is lost as heat in dissipative dielectrics, and in resistive losses in conductors. Dielectric loss can be eliminated by doing away with the lossy dielectric, using air instead.

Resistive losses can be minimised by using high conductivity metals. Resistivities of several metals are given in Table B.1 below {from Ref[B.1]}.

:

TABLE B.1 Resistivity of metals

Material	Composition % weight	resistivity (annealed) μΩmetre	% increase relative to silver
silver (pure)	Ag 99.999+	0.0147	0%
silver (normal)	Ag 99.325 Au 0.675	0.0150	2.04%
copper	Cu 99.99+	0.0158	7.48%
copper (oxygen-free)	Cu 99.95	0.0153	4.08%
gold	Au 99.999+	0.0219	48.98%
aluminium		0.0274	86.4%

Examination of this table should dispel the popular notion that gold is a better conductor than copper. The physical state of the metal is also important. For example, the resistivity of hard-drawn copper is about 2.6% greater than that of annealed copper, and electroplated metals have higher resistivities still.

B. 2.1.1 Skin Effect

In a round conducting wire, flux generated by current flow forms concentric circles centered on the axis of the wire. The inner flux circles link less of the total current than flux circles close to the surface, so inductance due to flux linkage is greater at the centre of the wire than near the surface. At high frequencies, this effect concentrates current flow near the surface of the conductor, producing the *skin effect*. The skin depth is the penetration depth where the current density has reduced to  $\frac{1}{e}$  of the surface value. Skin depth  $\delta$  is proportional to the square root of the resistivity, and for copper at frequency  $f$  Hz is given by Ref[B.2]:

$$\delta = 66040 \sqrt{\frac{1}{f}} \quad \text{microns} \quad (\text{EQ B.2})$$

At 1890 MHz, the skin depth is a mere 1.52 microns, so the current is concentrated very close to the surface. High frequency resistance is much higher than the DC resistance because only a small portion of the conductor cross-section is used. For a long straight circular conductor of diameter  $d$ , the high frequency resistance is given by:

$$R_{ac} = \frac{d}{4\delta} R_{dc} \quad (\text{EQ B.3})$$

#### 2.1.1.0.1 Surface Roughness

If the high frequency surface currents have to traverse rough ridges, akin to a ploughed field, the effective resistivity is increased. For an rms surface roughness of  $\Delta_{rms}$  the effective resistivity  $\rho_{eff}$  is given by Ref[B.3]:

$$\frac{\rho_{eff}}{\rho} = 1 + \frac{2}{\pi} \operatorname{atan} \left( 1.4 \frac{\Delta_{rms}}{\delta} \right) \quad (\text{EQ B.4})$$

If  $\Delta_{rms} > \delta$  then  $\rho_{eff} \rightarrow 2\rho$  for rough surfaces. For example, if the rms roughness is 2.2 times the skin depth, then the effective resistivity reaches 90% of the maximum given by EQ B.4.

#### 2.1.1.0.2 Electroplated Finishes

Silver plating is often specified for conductors carrying RF current in the belief that this will reduce losses and raise the circuit unloaded Q, because at room temperature silver has the highest conductivity of any material. However, the opposite result is more likely, with RF losses increasing. Pure silver has a DC conductivity only about 5% higher than pure copper, and as the RF resistance is proportional to the square root of the DC value, the advantage at best is only 2.5%, a minor gain. Plated deposits can have quite different physical properties from those of the pure wrought metal, and generally have much higher resistivities. Resistivity values for plated silver in the range 0.0159 to 1.3 micro-ohm metre have been reported {Ref[B.4]}. Commercial silver plating processes aim to produce a bright deposit requiring no further buffing, and so use brightening or grain-refining agents in the plating solution. These compounds are deposited with the silver, reducing the conductivity. The crystal structure, banding or layering of the deposit, and internal stresses in the plated film, all tend to reduce the conductivity.

Atmospheric sulphides tarnish the silver plate, so it is common practise to add a final protective layer, such as a very thin flash layer of gold or rhodium, as these materials do not oxidise. At microwave frequencies, the skin depth is so small that most of the RF current will flow in the protective flash coating rather than in the underlying silver. If a protective coating is used, a low-loss insulating varnish is preferable. The best material for RF conductors, apart from pure silver, is pure annealed copper, polished to a smooth surface finish, and not plated.

B. 2.1.2 Radiation

Another filter loss mechanism is radiation, where unshielded filter resonators may act as an antenna array, increasing the filter insertion loss. A shielded structure can overcome this loss mechanism.

2. 1.2.0.1 Losses versus Filter Order

Bandpass filter insertion loss  $IL_{dB}$  in dB as a function of loaded  $Q$  ( $Q_l$ ), resonator unloaded  $Q$  ( $Q_u$ ), and filter order  $N_{order}$ , is given by Ref[B.5] :

$$IL_{dB} = \frac{4.34Q_l}{Q_u} \sum_{n=1}^{n=N_{order}} g_n$$

(EQ B.5)

The  $g_n$  values (Figure B.4) are normalised parameters for a prototype low pass filter of order  $N_{order}$  with a cutoff frequency of 1 radian and terminations of 1 ohm, and give inductance values in henries and capacitance values in farads. Tables of  $g$  values can be found in filter design handbooks.

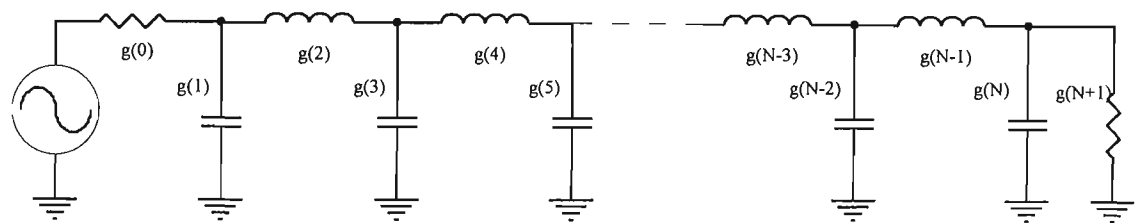


FIGURE B.4 Prototype low pass filter parameters

For Butterworth filters of up to order  $N_{order}=10$ ,  $g$  values {Ref[B.6]} are listed in Table B.2 below:

TABLE B.2 Butterworth low pass parameters  $g(0)=g(N+1)=1$

N	$g(1)$	$g(2)$	$g(3)$	$g(4)$	$g(5)$	$g(6)$	$g(7)$	$g(8)$	$g(9)$	$g(10)$	$\Sigma g$
2	1.4142	1.4142	1								2.8284
3	1.0000	2.0000	1.0000	1							4.0000
4	0.7654	1.8478	1.8478	0.7654	1						5.2264
5	0.6180	1.6180	2.0000	1.6180	0.6180	1					6.4720
6	0.5176	1.4142	1.9318	1.9318	1.4142	0.5176	1				7.7272
7	0.4450	1.2470	1.8019	2.0000	1.8019	1.2470	0.4450	1			8.9878
8	0.3902	1.1111	1.6629	1.9616	1.9616	1.6629	1.1111	0.3902	1		10.252
9	0.3473	1.0000	1.5321	1.8794	2.0000	1.8794	1.5321	1.0000	0.3473	1	11.518
10	0.3129	0.9080	1.4142	1.7820	1.9754	1.9754	1.7820	1.4142	0.9080	0.3129	12.785

The loaded  $Q$  ( $Q_l$ ) is the ratio of centre frequency to bandwidth .

TABLE B.3 Loaded  $Q$

Centre frequency (MHz)	Bandwidth (MHz)	Loaded $Q$ $Q_l$
1890	50	37.8
	200	9.45

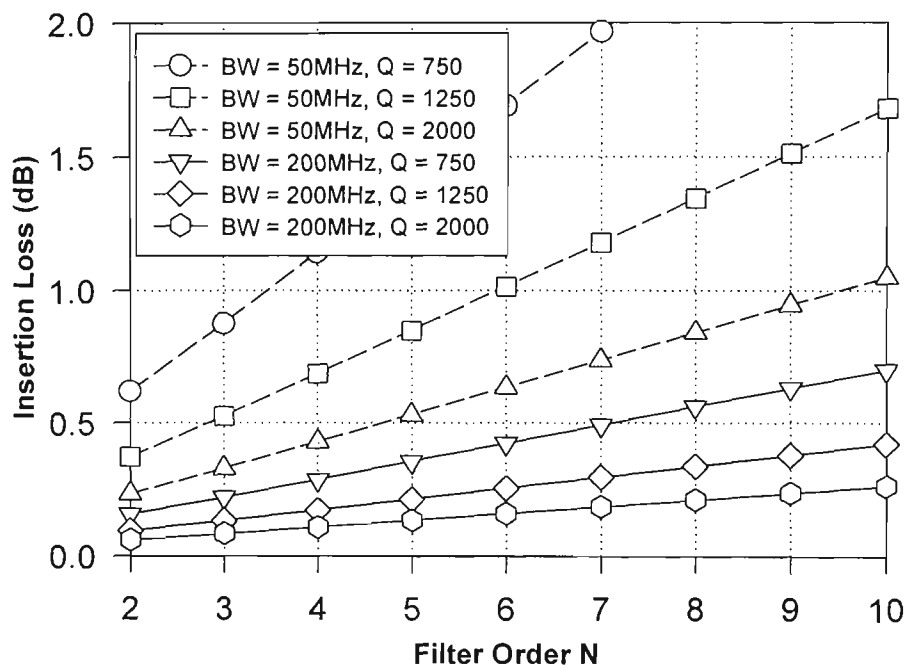


FIGURE B.5 Filter insertion loss versus bandwidth, unloaded  $Q$ , and order  $N_{order}$

The plot in Figure B.5 (from EQ.B.5) gives useful insights into the requirements for a low insertion loss filter. For example, for a filter of order  $N_{order} = 7$ , and a bandwidth of 50 MHz centered on 1890 MHz, if the insertion loss is required to be less than 1 dB, then resonator unloaded  $Q$ s must be greater than 1457.

B. 2.2 Filter Technologies

Possible technologies for filters at 1890 MHz include:

- (i) ceramic filters
- (ii) microstrip and stripline filters
- (iii) helical filters
- (iv) comb-line filters
- (iv) interdigital filters

If the primary design goal is low insertion loss, filters using solid dielectrics should be avoided, and filter resonators should use the highest conductivity metal available.

### B. 2.2.1 Ceramic Filters

Microwave ceramic dielectrics have low loss and a high dielectric constant, leading to filters of compact size and fairly good efficiency. Unloaded  $Q$  for a quarter wave coaxial ceramic resonator at 2 GHz is typically 600 {Ref[B.7]}, and for a 7th. order filter with bandwidth of 50 MHz and centre frequency 1890 MHz, the insertion loss calculated using EQ.B.5 is 2.5 dB. Specialised manufacturing facilities are required to fabricate these devices. Commercial filters with frequency specifications suitable for the *channel sounder* have an insertion loss of over 2 dB, which is unacceptably high.

### B. 2.2.2 Microstrip and Stripline Filters

Disadvantages of microstrip filters include high insertion loss because of dielectric losses, difficulty in accurately fabricating the narrow gaps required by narrow band designs, and the problems of radiation and proximity effects. If sufficiently accurate etching or milling facilities are available, the filters are easy to produce. However the filters generally are fixed once constructed, and cannot easily be fine-tuned for optimum response. To be practicable, the filter must be housed in a shielded enclosure, as some of the field exists in the space above the board, and this complicates the design.

Microstrip filters with suitable parameters for the *channel sounder* have been found to have insertion loss in the region of 4 dB. In Ref [B.8], *Cohn* describes a design method for edge-coupled bandpass stripline filters, which eases gap tolerance requirements compared with end-coupled filters. An example of a 6 resonator filter centred on 1200 MHz with 200 MHz bandwidth is given. A prototype constructed using stripline, with 0.5 inch spacing between ground planes, polystyrene dielectric and copper foil strip resonators was described. After some trial-and-error adjustment of resonator lengths by cutting foil, the final filter had a centre frequency of 1207 MHz and an insertion loss of 0.7 dB. This class of filter, using half wave resonators, will produce narrow spurious passbands at twice the frequency of the first passband centre frequency, with even slight mistuning, which is a further disadvantage {Ref [B.9]}.

### B. 2.2.3 Helical Filters

These filters use transmission line type resonators in the form of helical coils, grounded at one end, and loaded with an adjustable variable capacitance screw at the open end. The resonators are mounted in cavities (usually square), and are coupled via apertures in the shielded enclosure, with the coupling factor depending on the size, shape and position of the aperture. Adjustment screws may also be used for fine adjustment of the apertures. The input and output ports are coupled to the end-most helices using either magnetic loops, capacitive coupling or direct taps. Helical filters are compact and provide low-loss performance in the range 30 MHz to 1GHz, although commercial versions are also manufactured for higher frequencies.

One problem is susceptibility to mechanical vibration, because the helix is attached

at one end only, and behaves like a long spring. The addition of dielectric supports can improve the rigidity, but introduces the penalty of dielectric losses {Ref [B.3]}.

#### B. 2.2.4 Compline Filters

Compline and interdigital filters are families of coupled resonant line filters, with some attractive advantages. The comb-line filter consists of a series of rectangular or round transmission line resonators, with the same short-circuit and open-circuit reference planes. If the resonators are 90 degrees or quarter wavelength in length, the magnetic and electric fields coupling adjacent resonators cancel, resulting in an “all-stop” filter. By reducing the length of the resonators, and loading the open ends with lumped capacitance, the fields are unbalanced and magnetic coupling occurs.

The resonators may be reduced in length to 45 degrees, or even 30 degrees, resulting in a physically smaller filter, but with a decrease in unloaded  $Q$ , and increased insertion loss. A reduction from 90 to 45 degrees results in halving the effective unloaded resonator  $Q$ . An advantage of shorter resonators is to move the first spurious passband further out, to four times the design passband in the case of  $\frac{\lambda}{8}$  resonators. Alternatively, quarter wave resonators may be used with aperture coupling. *Kurzrok* {Ref [B.11]} gives graphs showing the coupling effects of different apertures. *Matthaei* {Ref[B.12]} gives a design method for bandwidths of up to 15%, and *Pregla* {Ref[B.13]} discusses filters which add some lumped capacitive coupling between resonators.

#### B. 2.2.5 Interdigital Filters

Interdigital filters consist of TEM-mode quarter wave resonators between ground planes. The structure is similar to the compline filter, but with the important difference that every alternate resonator is grounded at the opposite end. This alternation of the sense of the resonators results in strong coupling, allowing larger spacings between resonators, easing manufacturing tolerances, and also allowing wide bandwidth filters to be realised. Resonators are 90 degrees in length, and do not require capacitive loading, resulting in high unloaded  $Q$  values, and low insertion loss. In practice, the resonators may be shortened slightly (10% to 15%), and a small amount of adjustable capacitive loading added, to allow fine-tuning. Both compline and interdigital filters suit self-supporting construction without using a solid dielectric, eliminating dielectric losses. They also allow larger diameter resonators and larger spacing between resonators and ground planes (compared with say microstrip filters), and these factors also contribute to higher unloaded  $Q$  and lower insertion loss {Ref[B.14]}. An exact analysis of interdigital and related filters is given in Ref[B.15], while Ref[B.16] and Ref[B.17] present approximate design methods.

## B. 2.3 Filter Design

After reviewing the various filter possibilities, the interdigital filter configuration was selected as the best solution for the *channel sounder* filters, for the following reasons:

- (i) rigid self-supporting structure not requiring dielectric support, eliminating dielectric losses.
- (ii) fully enclosed shielded structure, eliminating radiation losses, EMC problems, and proximity effects.
- (iii) transmission line resonators may be made with a large diameter and with large ground plane spacing, increasing the unloaded  $Q$ .
- (iv) manufacturable with normal machine shop tooling, without needing specialised facilities.
- (v) a high manufacturing tolerance is not required.
- (vi) fine-tuning adjustments can be easily incorporated, allowing tuning for optimum performance.
- (vii) the first spurious passband is at over 3 times the design centre frequency, and usually well into the stop-band of amplifiers following the filter.

The design method used is based on *Dishal's* approximate method, described in Ref[B.17]. This paper simplifies earlier design methods in two significant areas; (a) all resonator rods are of the same diameter, and (b) instead of using two extra non-resonant rods to couple the input and output, direct tapplings near the ground ends of the first and last resonators are used.

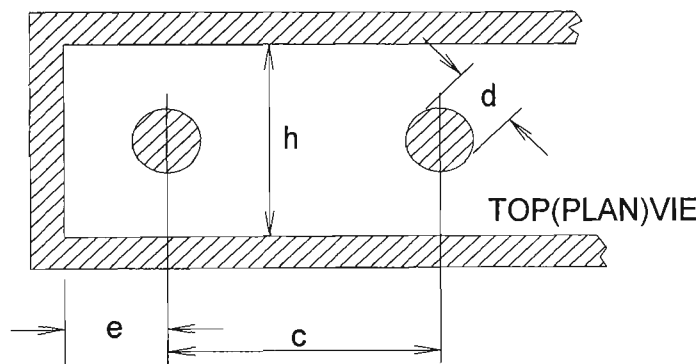


**FIGURE B.6 Plan view showing filter dimensions**

The design problem is to determine the filter dimensions required to give a certain coefficient of coupling  $K$  between adjacent rod resonators. *Dishal* uses *Honey's* approximation {Ref[B.18]} for the narrow band case (bandwidth < 10%) for coupling between two rods:

$$K = \frac{4}{\pi} \left[ \frac{\ln \coth \left( \frac{\pi C}{2h} \right)}{\ln \coth \left( \frac{\pi d}{4h} \right)} \right] \quad (\text{EQ B.6})$$

where the dimensions are defined in Figure B.6, with  $d$  the rod diameter,  $h$  the enclosure width and  $C$  the axial spacing between adjacent parallel resonator rods. The ratio  $d/h$  is



called the normalised rod diameter, and  $C/h$  is the normalised rod spacing, and  $K$  is almost a linear function of both these ratios. This linear approximation is:

$$\log K = -1.37 \left( \frac{C}{h} \right) + 0.91 \left( \frac{d}{h} \right) - 0.048 \quad (\text{EQ B.7})$$

and from this the resonator spacing  $C$  is given by:

$$C = \frac{h}{1.37} \left( 0.91 \left( \frac{d}{h} \right) - 0.048 - \log K \right) \quad (\text{EQ B.8})$$

if  $k$  is the normalised coefficient of coupling,  $f_0$  is the centre frequency, and the bandwidth is  $BW_{3dB}$  then  $K$  is given by:

$$K = k \left[ \frac{BW_{3dB}}{f_0} \right] \quad (\text{EQ B.9})$$

For normalised end wall spacing  $e/h < 0.7$ , the impedance  $Z_0$  of the end resonators, ignoring the effect of the adjacent rod, is given closely for small percentage bandwidths, by:

$$Z_0 = 1.38 \log \left[ \frac{4}{\pi} \left( \frac{h}{d} \right) \tanh \left( \frac{\pi e}{h} \right) \right] \quad (\text{EQ B.10})$$

The tanh term may be evaluated as a function of exponential terms:

$$\tanh z = \frac{\exp(z) - \exp(-z)}{\exp(z) + \exp(-z)} \quad (\text{EQ B.11})$$

Filter design data gives the normalised  $q$  values for the resistively loaded first and last resonators. These  $q$  values are denormalised to give values:

$$Q = q \left( \frac{f_0}{BW_{3dB}} \right) \quad (\text{EQ B.12})$$

Tapping a resistive load  $R$  distance  $l$  from the grounded end of a resonator length  $L$  ( $L = \pi/4$ ) where  $l < 0.2L$  results in a singly-loaded  $Q$  value given by:

$$Q = \frac{\pi}{4} \left( \frac{R}{Z_0} \right) \frac{1}{\sin^2 \left( \frac{\pi l}{2L} \right)} \quad (\text{EQ B.13})$$

rearranging to give  $l$ :

$$\frac{l}{L} = \frac{2}{\pi} \arcsin \sqrt{\frac{\pi R}{4 Z_0 Q}} \quad (\text{EQ B.14})$$

## B. 2.4 Filter Design Parameters:

A seventh order ( $N_{order} = 7$ ) Butterworth filter response has been chosen, as a compromise between skirt steepness, and size, complexity and insertion loss. Tables of the normalised  $k$  and  $q$  parameters for various filter responses are given in Ref[B.19], and the relevant values are reproduced below (Table B.4). Note the symmetry, with  $q_1 = q_7$ ,  $k_{12} = k_{67}$ ,  $k_{23} = k_{56}$  and  $k_{34} = k_{45}$  which results in physical symmetry about the centre line of the filter.

TABLE B.4 Butterworth normalised parameters  $N_{order}=7$

	k <sub>12</sub>	k <sub>23</sub>	k <sub>34</sub>	k <sub>45</sub>	k <sub>56</sub>	k <sub>67</sub>	
	1.34	0.669	0.528	0.528	0.669	1.34	
q <sub>1</sub>	q <sub>2</sub>	q <sub>3</sub>	q <sub>4</sub>	q <sub>5</sub>	q <sub>6</sub>	q <sub>7</sub>	q <sub>8</sub>
0.445	∞	∞	∞	∞	∞	∞	0.445

## B. 2.5 Filter Design:

The filter enclosure width is nominally one quarter wavelength of the centre frequency, and the resonators are made 90% of a quarter wavelength. The 10% gap allows for brass screws to provide fine tuning by adjustable capacitive loading to the ends of the resonators. To calculate filter dimensions, the design steps are as follows:

1. Decide on the filter order  $N$ , and response type (e.g. Butterworth, Chebyshev...)
2. From filter tables {Ref.[B.19]}, determine the normalised values for  $k$  and  $q$ .
3. Enclosure width  $L$  equals the centre frequency quarter wavelength.
4. Resonator rod length equals  $0.9L$ .
5. Calculate the fractional bandwidth  $BW' = (BW_{3dB}/f_0)$
6. Choose a resonator rod diameter  $d$ .
7. Choose the enclosure depth  $h$ . Keep  $(d/h) < 0.5$ .
8. Denormalise  $k$  to give  $K$  (EQ.9)
9. Denormalise the end resonator  $q$  to give  $Q$  (EQ. 12)
10. Calculate inter-rod spacing  $C$ , using EQ.8. Repeat for other  $k$  values.
11. Choose the end wall spacing  $e$ .
12. Calculate  $Z_0$  from EQ.10
13. Calculate  $l$ , the tap position from ground, using EQ.14. For a  $50\Omega$  system,  $R = 50$

Note that imperial rather than metric units are used, because copper stock is still manufactured and sold in imperial sizes. These design steps are easily performed by setting up a spreadsheet with the formulas required.

B. 2.6 Experimental Filters

A number of filters were manufactured and tested to determine corrections necessary to the approximate design method, and to experiment with some of the practical aspects of manufacture and feed arrangements. Filters were made with copper rod, tube, sheet and bar, tin-plated steel sheet, and copper-clad epoxy circuit board. Resonators ranged in diameter from 0.083 inches to 0.5 inches, and filter orders  $N_{order}$  of 5, 7, and 8 were tried. Magnetic loop and direct tapping feed arrangements were tried.

B. 2.6.1 Tinplate Filter

An  $N_{order} = 5$  filter was made using copper wire (diameter 0.083 inch) for the resonators, and folded and soldered tinplate (tin plated steel) for the box. Tools required were a sheet metal guillotine and a bender, an electric drill, and a heavy-duty soldering iron. No great precision was used. This filter performed well considering the crude construction, and could be tuned to the correct centre frequency, with passband flatness better than 0.4 dB (Figure B.7). Bandwidth shrinkage of 16% occurred, with a measured bandwidth of 33.5 MHz, compared with the design value of 40 MHz. The insertion loss was 2.3 dB, attributed at the time to the lossy tinplate steel used for the enclosure. Later experiments with feed arrangements suggest that perhaps the filter loss could have been improved by using a different feed tapping position.

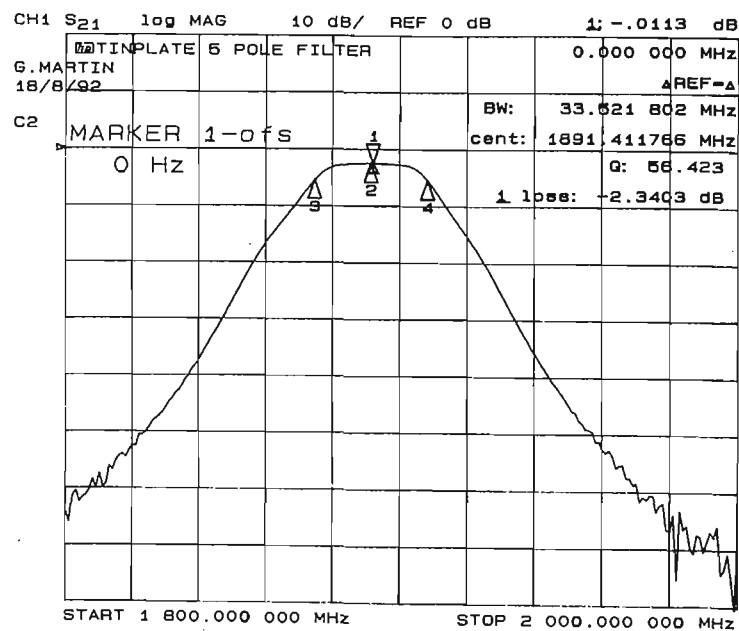


FIGURE B.7 Tinplate experimental filter

B. 2.6.2 Circuit Board Filter

A filter was made using single-sided epoxy circuit board for the enclosure, and 5/16 inch copper tube for the resonators. The circuit board was cut in a guillotine, and then soldered together, with the copper side innermost, to form the enclosure. Because of differential expansion, considerable distortion of the circuit board occurred during soldering. The resulting 5th.

order filter had an insertion loss of  $< 0.7$  dB, but it was not possible to tune for a flat passband, and this construction method was abandoned, because of circuit board warping.

### B. 2.7 Centre Frequency

*Dishal's* approximate design method stipulates that the enclosure width should be a quarter wavelength at the centre frequency, and the resonator length be 90% of the enclosure width. It was found that while this worked with small diameter resonators (diameter = 0.083 inches, length = 1.405 inches, length/diameter ratio = 12.6 ), when using large diameter resonators (for example, diameter = 0.5 inches, length = 1.405 inches, length/diameter ratio = 2.8 ) the centre frequency was markedly reduced.

The effect is shown for four different resonator diameters in Figure B.8, which plots the ratio of the quarter wavelength frequency for the actual resonator length, to the measured centre frequency with the filter tuned for the best bandpass response shape, against the resonator rod diameter .

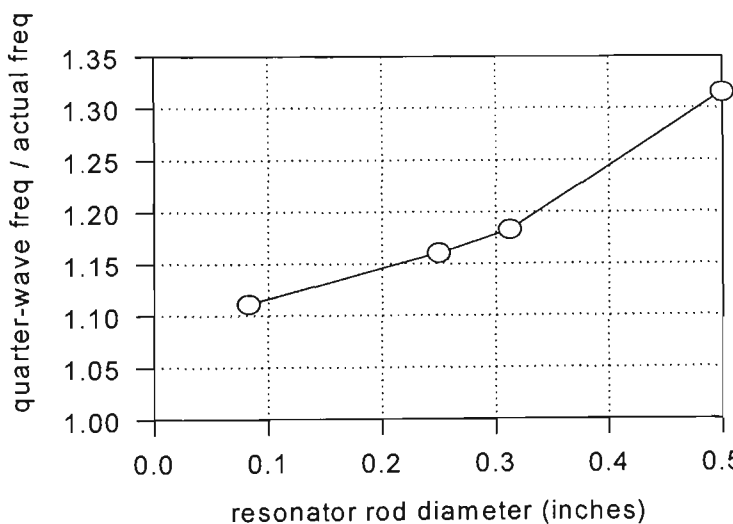


**FIGURE B.8 Effect of resonator rod diameter**

For the smallest diameter rod, the ratio is equal to the expected 111% (reciprocal of 90%), but as the rod diameter increases, a further correction to the length is required to obtain the desired centre frequency. For the 0.3125 inch rod (  $5/16''$  ), the ratio from the graph is 1.183, so for the correct centre frequency the rod length should be  $1/1.183$  or 84.5% of the enclosure width. This is a further reduction of 6.1% from the nominal 90% length. The effect may be considered as an end effect, or as increased capacitive loading because of the larger end area.

### B. 2.8 Other Effects - Bandwidth Shrinkage

Some bandwidth shrinkage, where the measured bandwidth is less than the design bandwidth, was found to occur, and seems to depend on all filter variables. *Matthaei* {Ref[B.9]} mentions bandwidth shrinkage, and attributes it to the various approximations

used in deriving design equations, stating a figure of 7% from experience. An empirical correction adjusts for this effect.

## B. 2.9 Other Effects - Tap Position

The feed point has a strong effect on both the insertion loss, and the ability to tune the filter to give a flat passband response. Experiments with prototype filters show that the optimum tap position occurs further up the end resonator ( a larger  $l$  value ) than given by EQ.B.14. If the tapping method changes the feed impedance from 50 ohms, a different tapping position would be required to give the best match.

## B. 2.10 Filter Tuning

Each resonator has a 6BA brass tuning screw aligned with the axis of the resonator, with the position of the screw altering the capacitance between the open end of the rod and ground. Using these, the centre frequency of the filter can be pulled a long way, up to 165 MHz in the case of one of the 7 resonator  $5/16''$  rod experimental filters. At the lower end of the centre frequency range, both passband response shape and insertion loss are worse, and the tuning adjustment also becomes more critical.

Best performance is obtained when the filter dimensions are such that the wanted centre frequency can be set with minimum protrusion of the capacitive tuning screws into the filter enclosure. Under these conditions, screw settings are much less touchy, because one screw pitch is a relatively smaller percentage of the total screw to resonator gap than is the case when the screws are very close to the resonators.

Screws run in threads tapped into the copper enclosure frame, and external lock-nuts are provided. After final tuning, and with lock-nuts tightened, quick-drying lacquer (nail varnish) is used to seal the screw positions.

After some practice, with a network analyser displaying the frequency response, tuning is not difficult, even though all the tuning adjustments interact. A systematic tuning method is described by Dishal {Ref[B.20 ]}, but is not necessary if modern instrumentation is available.

## B. 2.11 Filter Construction

Filters are constructed using high conductivity annealed copper. Such material is difficult to solder, as it conducts heat away from the heat-source very effectively. Most of the construction problems which had to be solved were related to assembly techniques, and soldering methods, which would work without causing heat distortion and misalignment of filter parts.

Side frames for the enclosure were made from  $5/8''$  by  $3/16''$  rectangular copper bar.

Top, bottom and ends were made as four separate pieces. The top and bottom pieces were drilled right through to take the resonator rods before assembly. End pieces were attached with brass screws, using tapped holes in the ends of the top and bottom pieces, and then soldered.

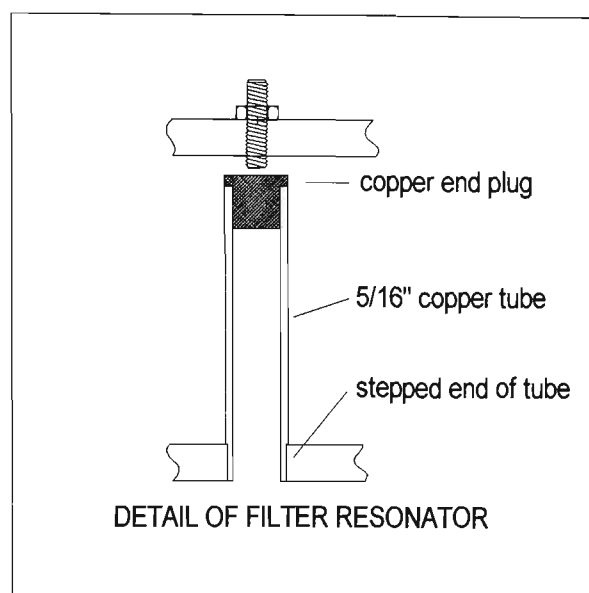


**FIGURE B.9 Filter construction detail**

Resonator rods were made from  $5/16''$  copper tube. The bottom  $3/16''$  of each piece of tube was turned down to remove 10 thou. (0.01 inch) of material, forming a stepped cylinder with a tight push fit into the enclosure bars. The step prevents the tube falling through the bar during soldering when clearances increase. Copper end plugs were made for each tube, also stepped so that the visible part of the plug was the same diameter as the outside of the tube (Figure B.9). Using tube rather than rod for the filter reduces the filter weight, and makes soldering easier by reducing the heatsink effect. With solid rod, it is almost impossible to solder input and output tapings to the end resonators.

End bars were drilled to take SMA stub contact panel jacks (such as *Radio Spares* part RS111-526) and four holes were drilled and tapped for 2 mm. mounting screws. Before the SMA connectors were finally mounted, the protruding dielectric was trimmed to be flush with the inner surface of the enclosure. To connect from the SMA centre conductor to the tapping point on the resonator, a 5 mm wide strip of thin soft copper sheet, tapered at the SMA end, was soldered using a high-capacity iron (such as an arc-heated "Scope" soldering iron). The SMA connector is best positioned slightly closer to the ground end of the resonator than the tapping point.

Soldering of the filter components was done using an oxy-acetylene torch, and a low melting point silver solder. Figures B.11 and B.12 show detail of the construction.

Assembly steps are as follows:

1. solder the end plugs into the resonator tubes.
2. solder tubes into the top and bottom bars.
3. do a preliminary polish of the tubes and inner surface of bars.
3. screw end bars to top and bottom bars.
4. solder joints between bars.
5. clean and polish joints.
6. solder a piece of copper sheet to one side of the enclosure frame.
7. drill and tap closely spaced 2 mm. holes to attach copper sheet to other side of enclosure frame.
8. polish interior of the filter.
9. mount SMA connectors, solder feed taps.
10. install tuning screws.
11. screw side plate on, and tune and test filter.
12. if desired, the second side plate can also be soldered before the final tune.

B. 2.12 50 MHz Filter

FILTER DESIGN	G.T.Martin			
Bandpass Filter Design - Round Rods, Butterworth				
	k12	k23	k34	k45
centre freq.MHz	1890.0000	1890.0000	1890.0000	1890.0000
width of box L inch	1.5613	1.5613	1.5613	1.5613
rod length inch	1.4051	1.4051	1.4051	1.4051
bandwidth 3dB MHz.	55.0000	55.0000	55.0000	55.0000
rod diameter d inch	0.3125	0.3125	0.3125	0.3125
box depth h inch	0.6250	0.6250	0.6250	0.6250
norm. coupling k	1.3400	0.6690	0.5280	0.5280
denorm. K	0.0390	0.0195	0.0154	0.0154
rod spacing c inch	0.8285	0.9661	1.0130	1.0130
end spacing e inch	0.5000			
Zo	55.2333			
norm. q of end rod	0.6180			
denormalised Q	21.2367			
tap length l inch	0.1829			
THIS IS A 7 POLE DESIGN FOR 50 OHMS, AND IS SYMMETRICAL.				
q1=q7, k12=k67, k23=k56, k34=k45				
Filter uses 5/16 inch rod.				
NOTE: width reduced 6% to 1.47 inch, and rod length reduced 6% to 1.32 inch.				

FIGURE B.10 Filter design spreadsheet - 50 MHz bandwidth

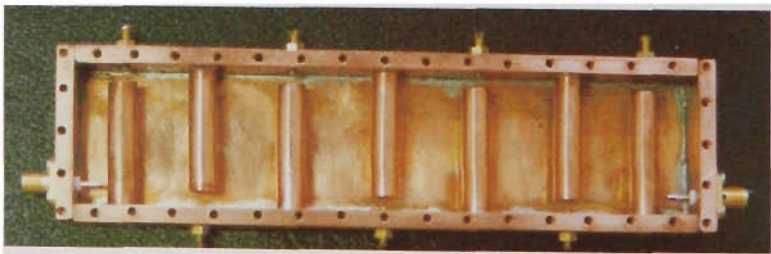


FIGURE B.11 Filter with top plate removed (connector taps incomplete)

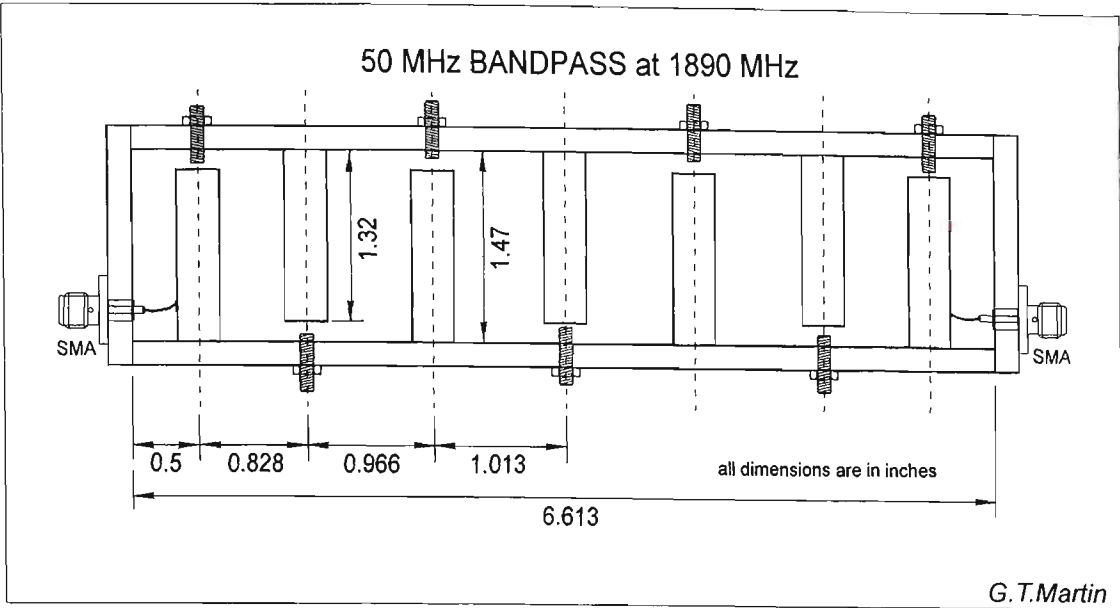


FIGURE B.12 Side elevation of 50 MHz filter, showing dimensions

B. 2.13 200 MHz Filter

FILTER DESIGN	G.T.Martin			
Bandpass Filter Design - Round Rods, Butterworth				
	k12	k23	k34	k45
centre freq.MHz	1890.0000	1890.0000	1890.0000	1890.0000
width of box L inch	1.5613	1.5613	1.5613	1.5613
rod length inch	1.4051	1.4051	1.4051	1.4051
bandwidth 3dB MHz.	210.0000	210.0000	210.0000	210.0000
rod diameter d inch	0.3125	0.3125	0.3125	0.3125
box depth h inch	0.6250	0.6250	0.6250	0.6250
norm. coupling k	1.3400	0.6690	0.5280	0.5280
denorm. K	0.1489	0.0743	0.0587	0.0587
rod spacing c inch	0.5630	0.7006	0.7475	0.7475
end spacing e inch	0.5000			
Zo	55.2333			
norm. q of end rod	0.6180			
denormalised Q	5.5620			
tap length l inch	0.3634			
THIS IS A 75 POLE DESIGN FOR 50 OHMS, AND IS SYMMETRICAL.				
q1=q7, k12=k67, k23=k56, k34=k45				
Filter uses 5/16 inch rod.				
NOTE: width reduced 6% to 1.47 inch, and rod length reduced 6% to 1.32 inch.				

FIGURE B.13 Design spreadsheet for the 200 MHz filter



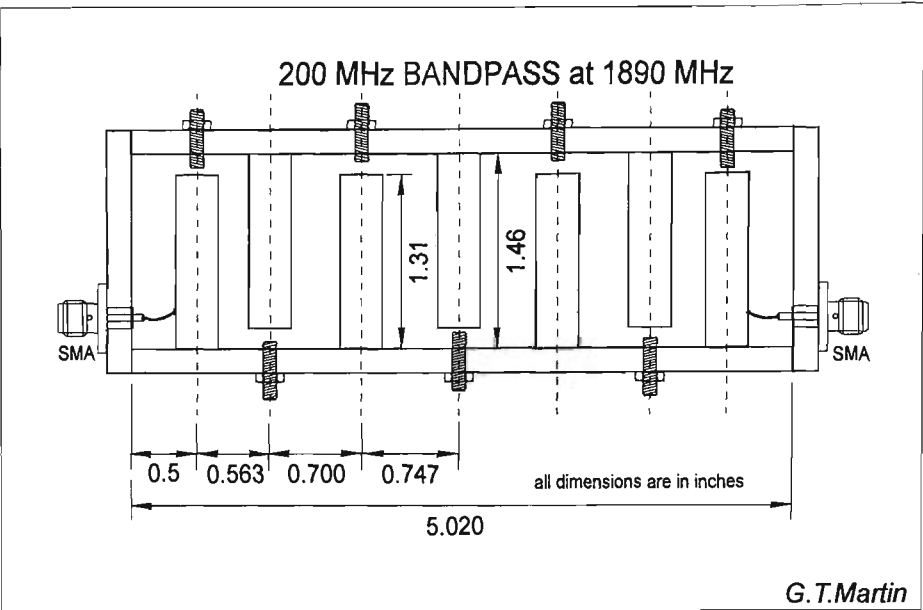


FIGURE B.14 Side elevation of the 200 MHz filter

Figure B.13 shows the design spreadsheet for 200 MHz filters. The spreadsheet contains the design formulas and correction factors, allowing new designs to be rapidly generated. Figure B.14 shows a dimensioned drawing of the filter.

B. 2.14 Measured Performance for 50 MHz Filter

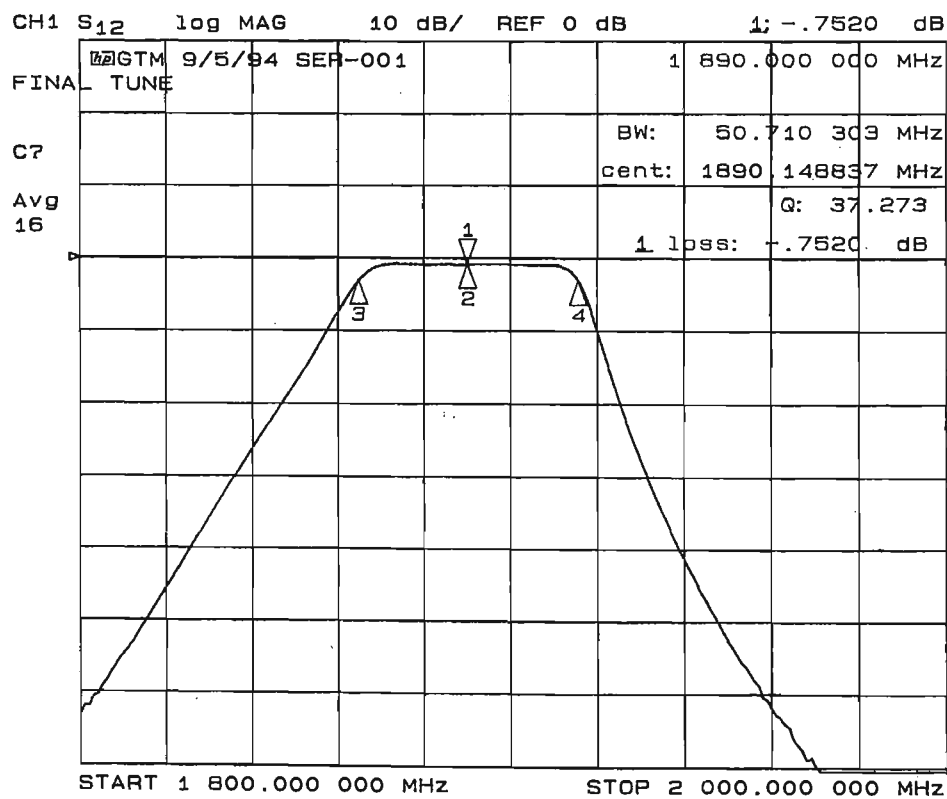


FIGURE B.15 Measured frequency response for 50 MHz filter (serial 001)

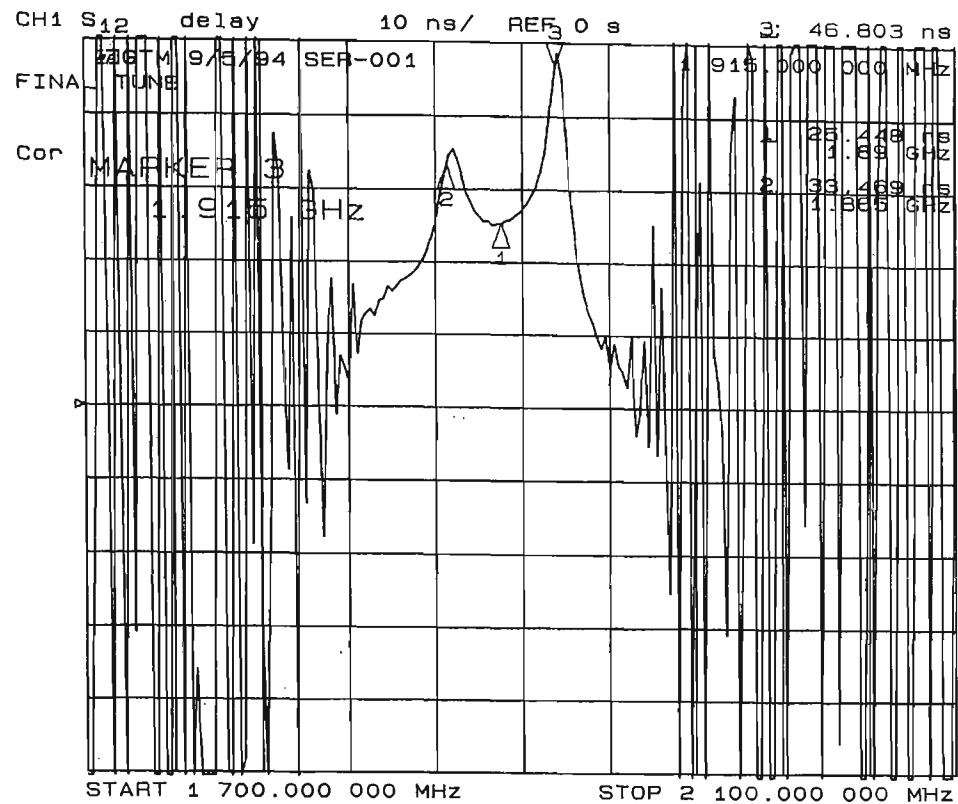


FIGURE B.16 Group delay for 50 MHz filter (serial 001)

B. 2.15 Group Delay

The group delay  $t_{delay}$  of a network with a phase shift  $\phi$  at frequency  $f$  is:

$$t_{delay} = - \frac{\partial \phi}{\partial f}$$

(EQ B.15)

If phase increases linearly with frequency, the group delay is constant and the network is described as *linear-phase*. A linear-phase filter in the time domain causes a constant signal delay, but there is no distortion of the waveform shape. In the channel sounder, any variation of group delay across the passband will blur the resolution in the time domain.

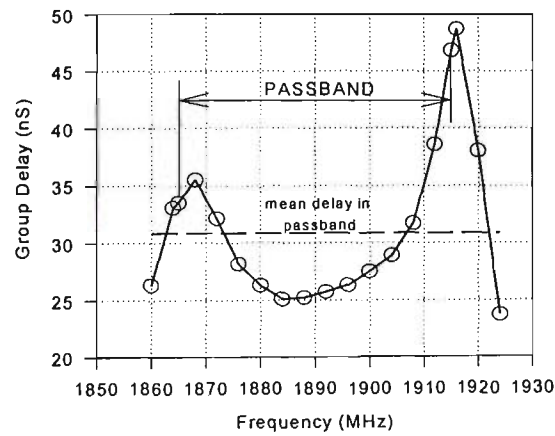


FIGURE B.17 Measured passband group delay for 50 MHz filter (serial 001)

The passband is defined as 50 MHz (1865 MHz to 1915 MHz) because the first spectrum nulls in the pseudo noise signal with a 25 MHz chipping rate are at these frequencies. Group delay tends to peak in the vicinity of the cutoff frequencies (Figure B.16), and the more abrupt the cutoff, the worse the group delay characteristic becomes. The shape of the bandpass group delay response is proportional to the dissipative insertion loss as a function of frequency {Ref [B.5]}. Average group delay in the passband is 30.9 ns, with a standard deviation or rms delay of 6.2 ns. Maximum peak-peak group delay or maximum differential group delay is 21.7 ns over the whole passband, reducing to 5 ns over the central 2/3 of the band (Figure B.17). As the differential group delay across the passband is only a little over half the inherent resolution of the channel sounder, the resolution should not be noticeably degraded.

See Chapter 3 for characterisation of the time domain impulse response of the band-pass filters, and an evaluation of the effect on *channel sounder* performance.

B. 2.16 Measured Performance for 200 MHz Filter

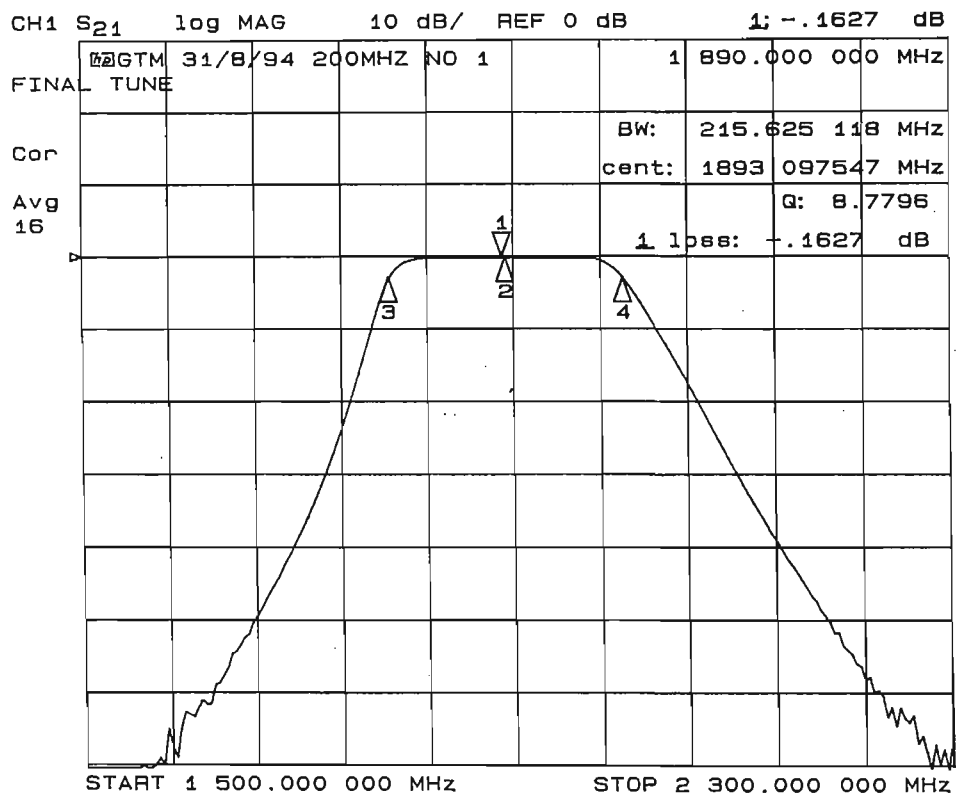


FIGURE B.18 Measured frequency response for 200 MHz filter (serial 001)

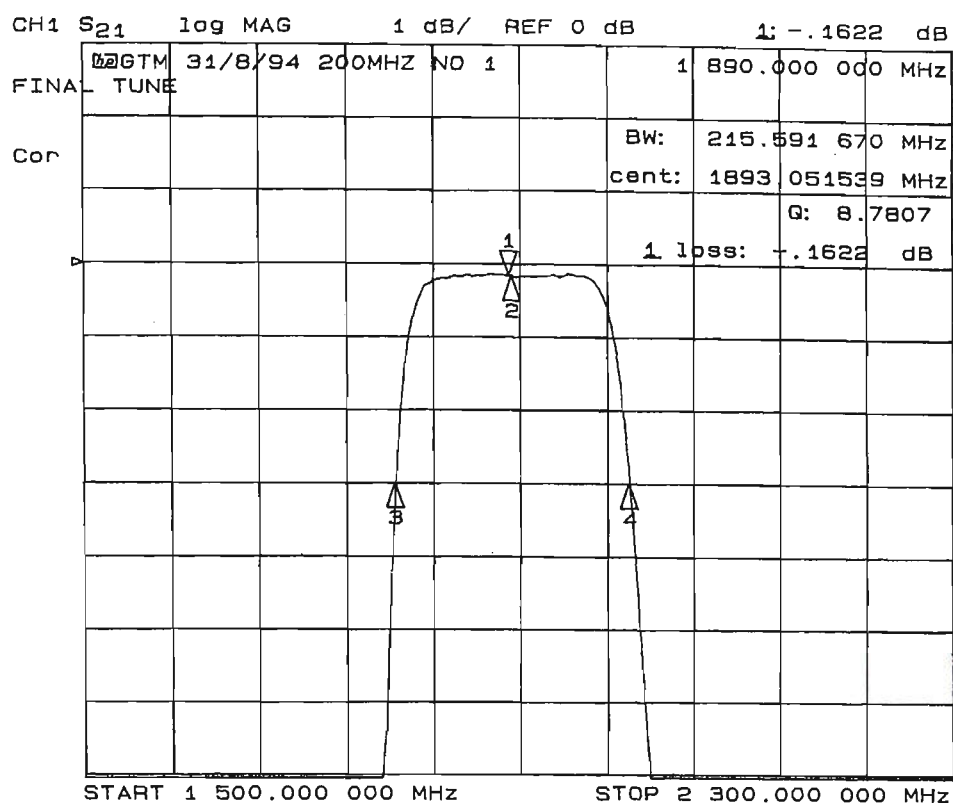


FIGURE B.19 Passband detail (1 dB/division) for 200 MHz filter (serial 001)

B. 2.17 Summary of Measured Filter Performance

TABLE B.5 Measured filter performance

Filter	Serial No.	Centre Frequency (MHz)	Bandwidth (MHz)	Insertion Loss (dB)	Average Group Delay (ns)	Differential Group Delay (ns)	rms Group Delay (ns)
50 MHz	001	1890.1	50.7	0.75	30.9	21.7	6.2
	002	1890.1	49.8	0.76	30.9	21.5	6.1
200 MHz	001	1893.1	215.6	0.16	-	-	-
	002	1893.7	204.4	0.68	8.1	3.4	1.1

The group delay for the first 200 MHz filter (serial 001) was not measured. The first (serial 001) 200 MHz filter shows excellent performance, with a very flat passband and low insertion loss of 0.16 dB (Figures B.18 and B.19). The second version of this filter was nominally identical, but had a higher insertion loss. The reason for this is not known, but may possibly be a poor solder joint, or a tooling mark. However, to keep these figures in perspective, the insertion loss is still low at 0.68 dB. The lower loss filter is used in the receiver front end, which is the more critical location because of the effect on noise figure, while the serial 002 version is used in the transmitter prior to the final power amplifier, where the insertion loss does not matter greatly.

## B.3 Low Noise Amplifiers

### B. 3.1 Stage One

A commercial wide band low noise amplifier model ZEL-1724LN manufactured by *Mini-Circuits* is used as the front end amplifier .

TABLE B.6 ZEL-1724LN specifications

Frequency range (MHz)	1700 - 2400
Noise Figure (max) (dB)	1.5
Gain (minimum) (dB)	20 ± 1.0
Maximum output power (dBm) 1dB comp.	+ 10
Maximum no-damage input power (dBm)	+ 13
Intercept point (dBm)	+ 22
Input VSWR	2.5
Output VSWR	2.5
DC voltage (volts)	15
DC current (mA)	70

Measured frequency response of the particular unit used is shown below (Figure B.20).

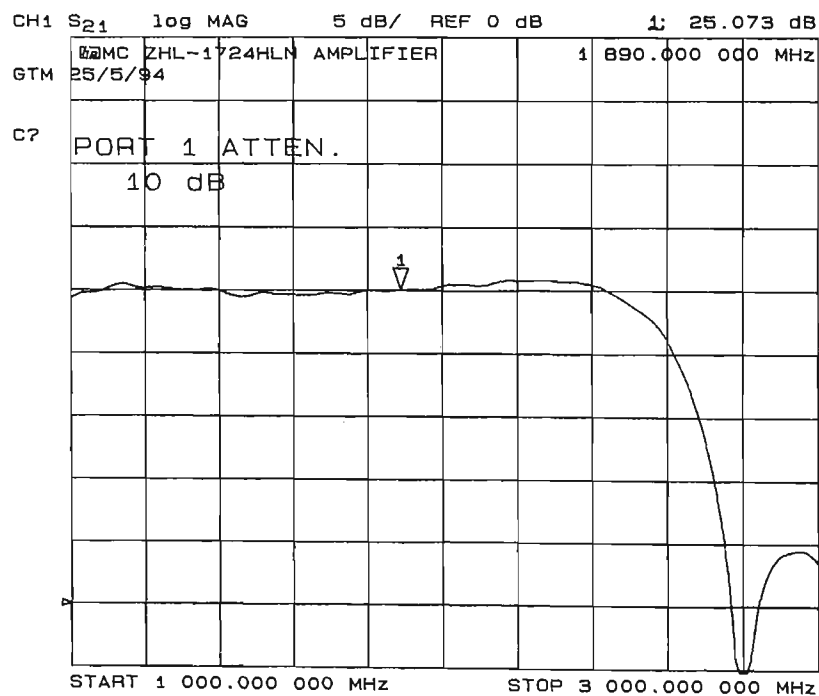


FIGURE B.20 Frequency response of ZEL-1724LN low noise amplifier

A 10 dB attenuator was used before the amplifier during measurement to prevent amplifier overload. The measured gain at 1890 MHz is 25.1 dB. Gain flatness is better than 0.1 dB over a 200 MHz band centered on 1890 MHz (Figure B.20).

B. 3.2 Stage Two

Stage two of the RF amplifier uses two MMICs, an HP INA0-3184, followed by a *MiniCircuits* MAR-6. The circuit schematic is shown in Figure B.21.

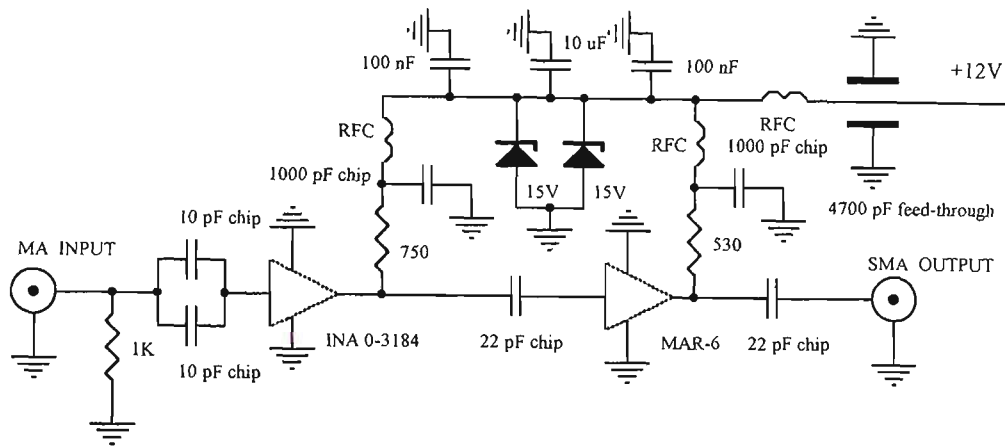


FIGURE B.21 Circuit schematic of low noise amplifier

When the ground plane surface-mount board was tested, the frequency response was well behaved, with gain decreasing slowly with frequency. However, after the board was installed in a tinplate steel box, the frequency response became very peaky, indicating a tendency to instability caused by coupling from output to input, in the context of the high wide band gain of 40dB. Considerable experimentation with shielding and grounding was needed to solve this problem, and restore the boxed frequency response to be the same as it had been for the bare circuit board. An internal tinplate cover was soldered to the ground plane to completely enclose the first stage, and the location of earth braid straps between the circuit board ground plane and the main box was found to be important. Measured response of the final boxed amplifier is shown below (Figure B.22).

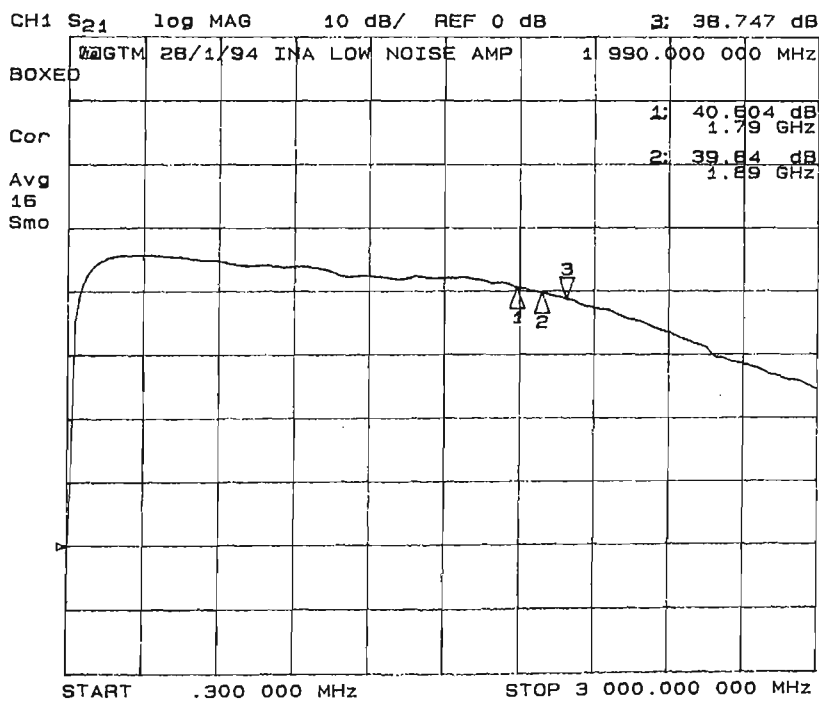


FIGURE B.22 Measured response of boxed INA low noise amplifier

Gain at 1890 MHz is 39.8 dB, gain at 1790 MHz is 0.8 dB higher, and at 1990 MHz gain is 1.1 dB lower. The INA-03184 noise figure is specified as < 3 dB at 1.9 GHz. This has a negligible effect on the system noise figure, because of gain from the previous stage.

## B.4 Frequency Multiplier

In the receiver, a signal source at 100 MHz is required to serve as the PN generator clock, and a source at 200 MHz is required as a second local oscillator to translate the IF signal down to baseband. Both these sources have to be phase-locked to the 10 MHz rubidium reference, and low phase noise and low spurious content is also desirable. The 10 MHz reference has very low phase noise (see Appendix A.1), and by multiplying this signal, the phase noise, although increased by the multiplication factor, will still be better than is possible with a synthesizer. With a synthesizer, the reference phase noise is also multiplied by the same amount, and in addition VCO phase noise is added, and is likely to be the major component. A synthesizer using a very high Q (and hence narrowband) VCO, such as a crystal VCO would be an alternative solution, with the benefit of low spurious output.

A drawback of the multiplier approach is that it is hard to suppress harmonics, and sub-harmonics, of the output frequency. The multiplier solution has been adopted in the *channel sounder* receiver. Multiplier action is based on operating a transistor in a non-linear mode (Class-C is used here), which generates a harmonic comb of the input frequency. Tuned amplifiers then select the desired harmonic. A balanced configuration which tends to cancel even harmonics is used to multiply by an odd integer, and single ended circuits which suppress odd harmonics are used for frequency doubling {Ref [B.21]}. A block diagram of the multiplier is shown below, followed by the complete circuit schematic (Figures B.23, B.24).

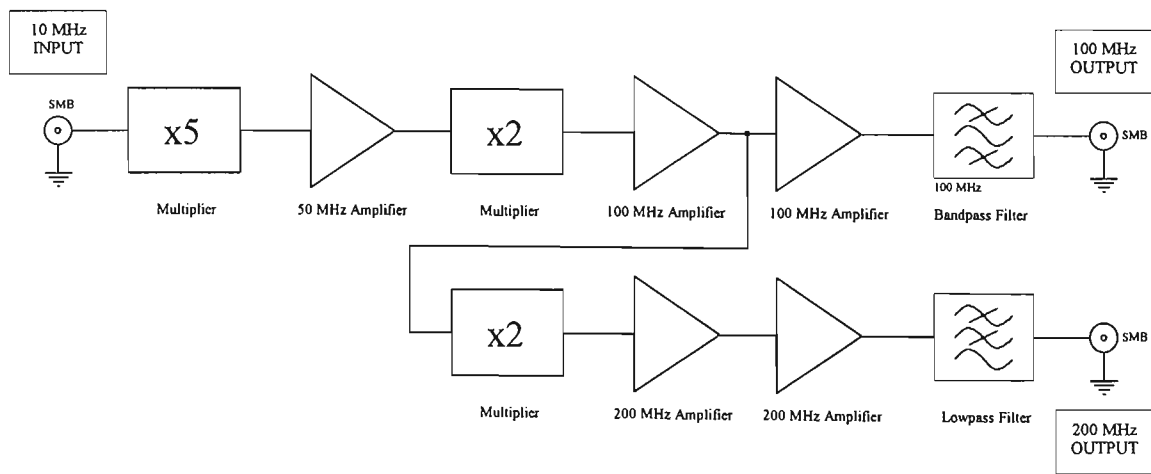


FIGURE B.23 Multiplier block diagram

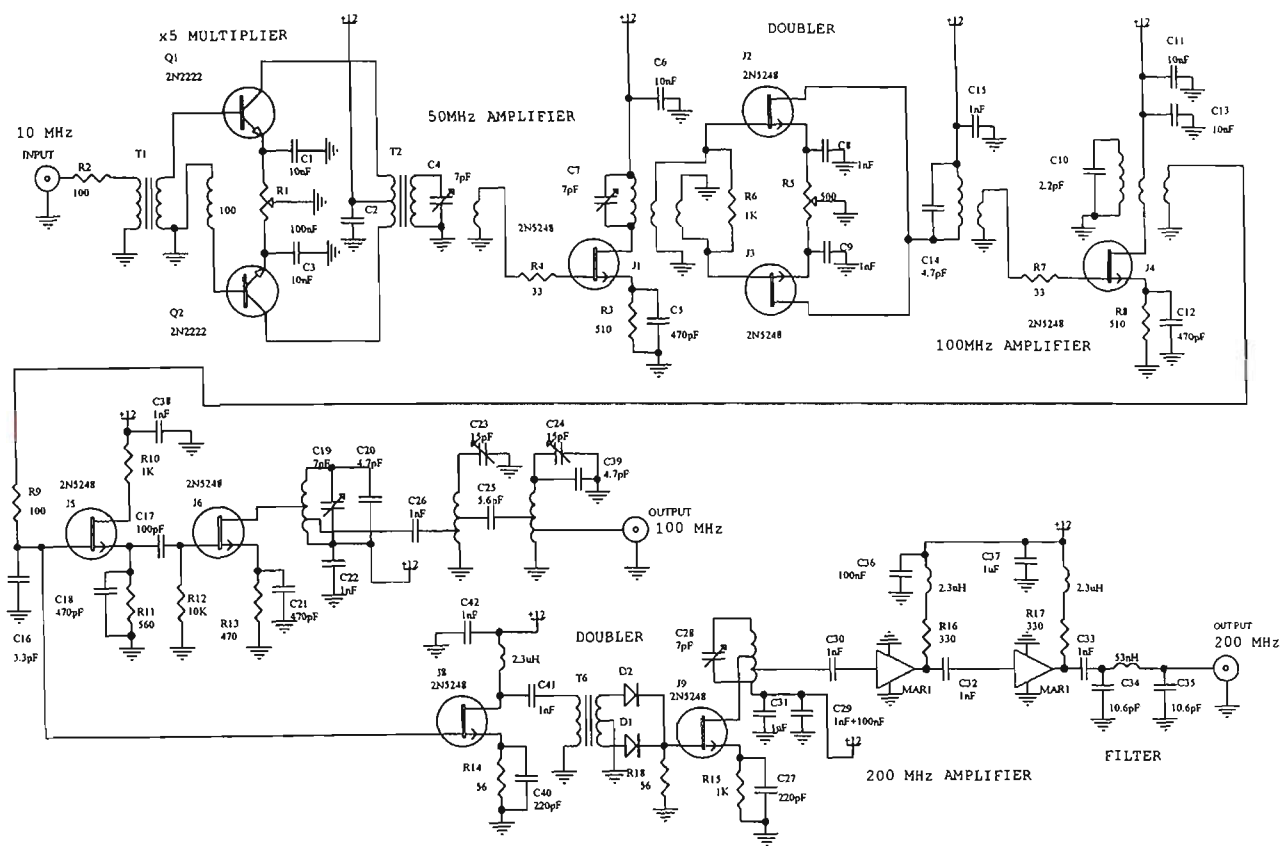


FIGURE B.24 Multiplier 100 MHz and 200 MHz - circuit schematic

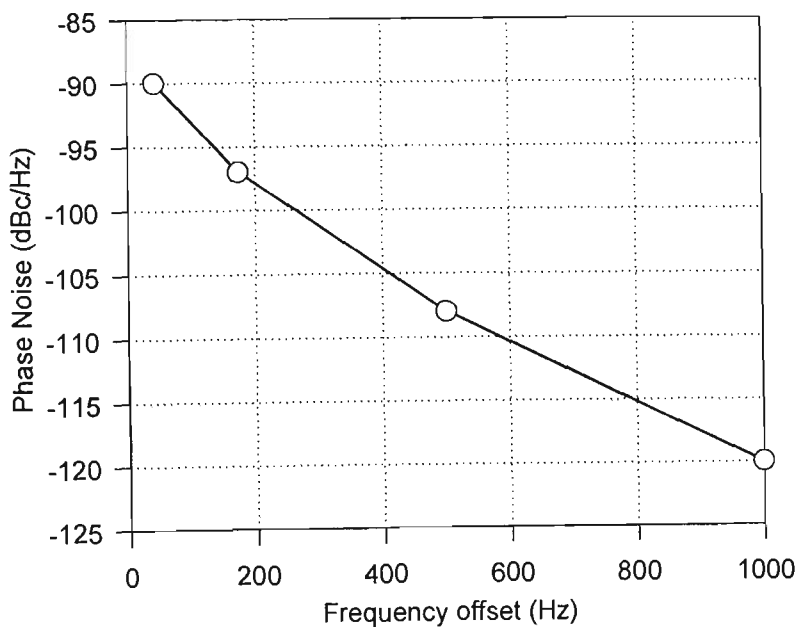


FIGURE B.25 Phase noise versus frequency offset at 200 MHz

Phase noise measured close to the 200 MHz output signal is plotted in Figure B.25. The method of measurement, from a spectrum analyser plot, is only approximate. The rubidium frequency standard 10 MHz output has a phase noise specification of -130 dBc/Hz at 100 Hz offset. The above curve gives -93 dBc/Hz at 100 Hz offset. Allowing a factor of 13 dB



increase in phase noise for multiplication by 20, makes the rubidium standard phase noise equivalent to -117 dBc/Hz for 100 Hz offset at 200 MHz. Measured multiplier phase noise is 24 dB worse. Part of this is phase noise contributed by the multiplier and amplifier stages, and part may be due to the approximate measurement method. Spurious and unwanted harmonic output levels are shown in Table B.7.

TABLE B.7 Multiplier spurious outputs

Harmonics	100 MHz	200 MHz
2	-29 dBc	-26 dBc
3	-57 dBc	-45 dBc
other spurious	< -41 dBc	< -46 dBc

B.5 Bessel Integrators

Low pass filters are used to integrate the I and Q signals, following the mixers where the cross correlation of the delayed received signal with the slow PN sequence occurs. *Bessel* filters have the property of constant group delay in the pass band, and are chosen for the integration role, to avoid distortion of time information in the received signal . In the frequency domain, *Bessel* filters have a gradual roll-off, a trade-off for the desirable linear phase property.

To act effectively as antialiasing filters for the following analogue to digital conversion, 8 pole filters are used. The role and performance of these filters has been covered in detail in Chapter 3, section 3.2.10. The 8 pole filters are designed as a cascade of four 2- pole *Sallen-Key* non-inverting active filter stages, built around the low noise TL074 quad op-amp integrated circuit. This type of filter was also used in the *University of Bristol* channel sounder.

To suit different possible chip rates, five filters were built for each channel, with nominal -3dB cutoff frequencies of 15 kHz, 3 kHz, 1.5 kHz, 750 Hz and 187 Hz. All these filters are fed in parallel from a 60 dB gain stage, which uses a low noise NE5534 operational amplifier.

All filter outputs are multiplexed via an analogue multiplexer, and the desired output is selected by addressing the multiplexer using a binary code selected with a five position front panel rotary switch.

Each output drives two unity gain buffers. One buffer output goes to the data logging equipment, and the other drives the  $I^2+Q^2$  circuit. The full circuit schematic is shown below (Figure B.26).

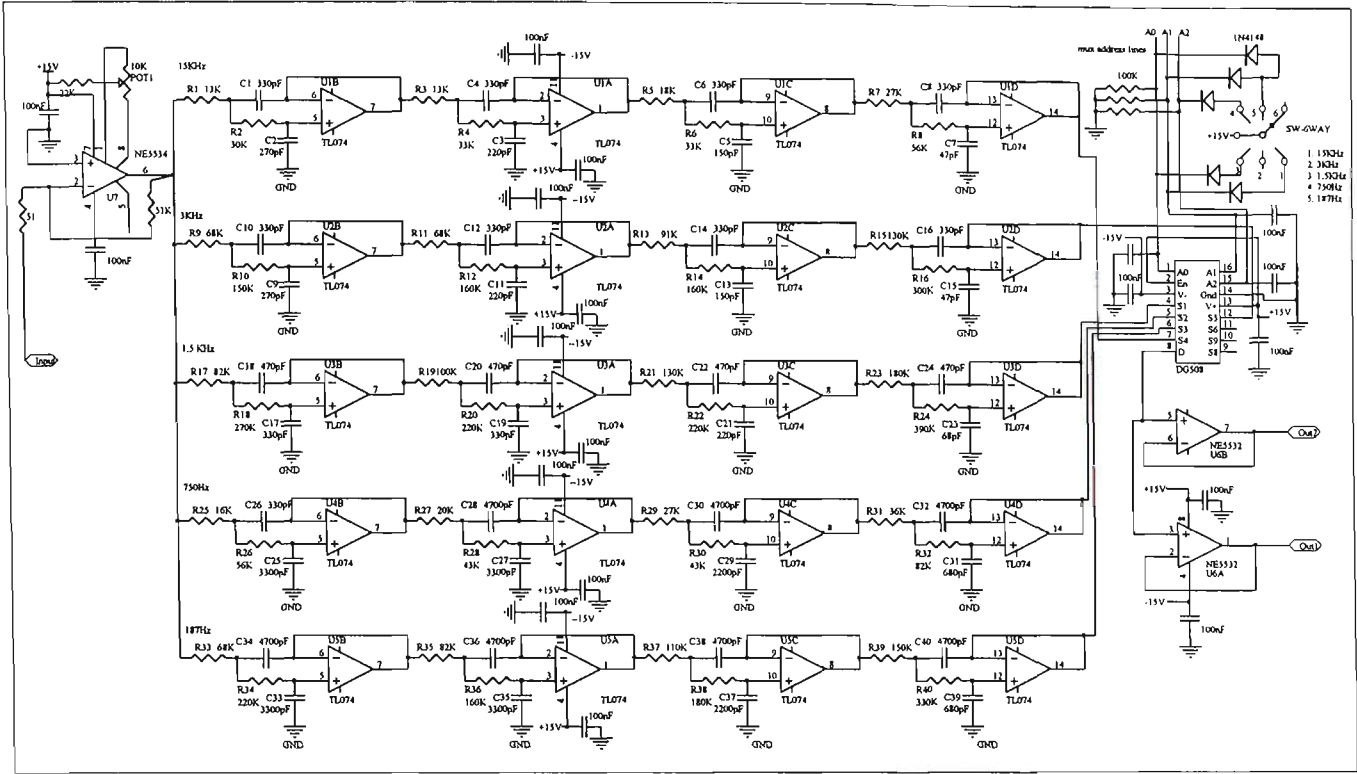


FIGURE B.26 Bessel integrators circuit schematic

B. 5.1 Design of Bessel filters

Pole pairs for an 8 pole Bessel filter are given in Table B.8 {Ref[B.22]}

TABLE B.8 8 pole Bessel/ filter parameters

$\omega_0$	Q
5.655	0.506
5.825	0.560
6.210	0.711
6.959	1.226

For an 8 pole filter, 1% deviation of group delay from the zero frequency value occurs at a frequency  $\omega=5.22$ , and the -3 dB frequency is  $\omega=3.17$ . If the -3 dB frequency is 3 kHz, frequency must be scaled by  $\frac{3000 \times 2\pi}{3.17} = 5946$  and then 1% group delay deviation will occur at 4.94 kHz.

The design steps are as follows:

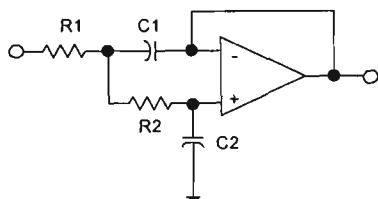
- 1. For each stage, look up  $\omega_0$  and Q values (Table B.8)
- 2. Scale (denormalise)  $\omega_0$
- 3. Choose C2

4. Calculate  $C1 \geq 4C2Q^2$ , then choose C1

5. Solve for R2; where 
$$R2 = \frac{\frac{C1\omega_0}{Q} \mp \sqrt{\left[\frac{C1\omega_0}{Q}\right]^2 - 4C1C2\omega_0^2}}{2C1C2\omega_0^2}$$

6. Solve for R1; where 
$$R1 = \frac{1}{R2C1C2\omega_0}$$

7. Repeat for the other 3 stages.



Sallen-Key 2 pole active filter stage

Component values may easily be calculated with a short spreadsheet program, giving design values and nearest preferred values. The results are shown in Table B.9.

Figures B.27, 28, 29, and 30 show simulated performance for the exact design component values, and performance using nearest preferred component values.

TABLE 9. Bessel filter component values

Stage	Freq(Hz)	C1( pF)	C2( pF)	R1(KΩ)	R2(KΩ)	R1(KΩ)	R2(KΩ)
				design values		nearest preferred 5%	
1	15,000	330	270	13.0	30.53	13	30
2	15,000	330	220	13.95	32.92	13	33
3	15,000	330	150	18.17	32.61	18	33
4	15,000	330	47	26.04	57.84	27	56
1	3,000	330	270	65.02	152.65	68	150
2	3,000	330	220	69.76	164.58	68	160
3	3,000	330	150	90.89	163.07	91	160
4	3,000	330	47	130.2	289.2	130	300
1	1,500	470	330	83.7	272.5	82	270
2	1,500	470	330	102.3	210.18	100	220
3	1,500	470	220	133.1	213.2	130	220
4	1,500	470	68	185.3	394.4	180	390
1	750	4700	3300	16.74	54.5	16	56
2	750	4700	3300	20.46	42.04	20	43
3	750	4700	2200	26.62	42.63	27	43
4	750	4700	680	37.1	78.9	36	82
1	187	4700	3300	67.0	218.0	68	220
2	187	4700	3300	81.5	167.4	82	160
3	187	4700	2200	106.5	170.6	110	180
4	187	4700	680	148.3	315.6	150	330

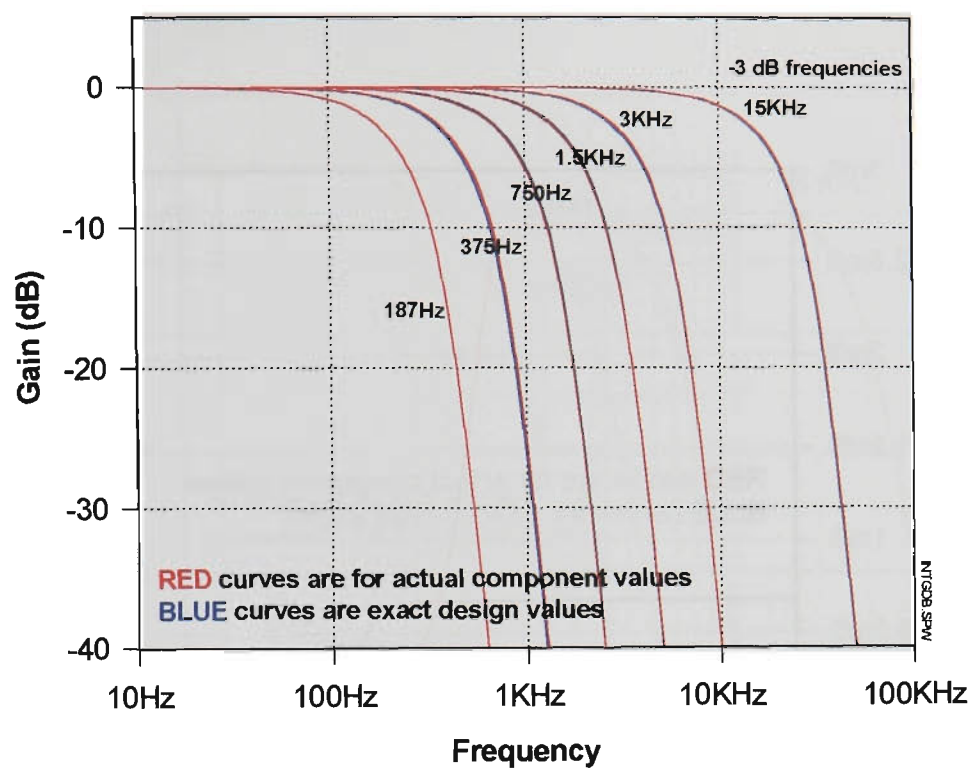


FIGURE B.27 Bessel integrators frequency response (SPICE simulations)

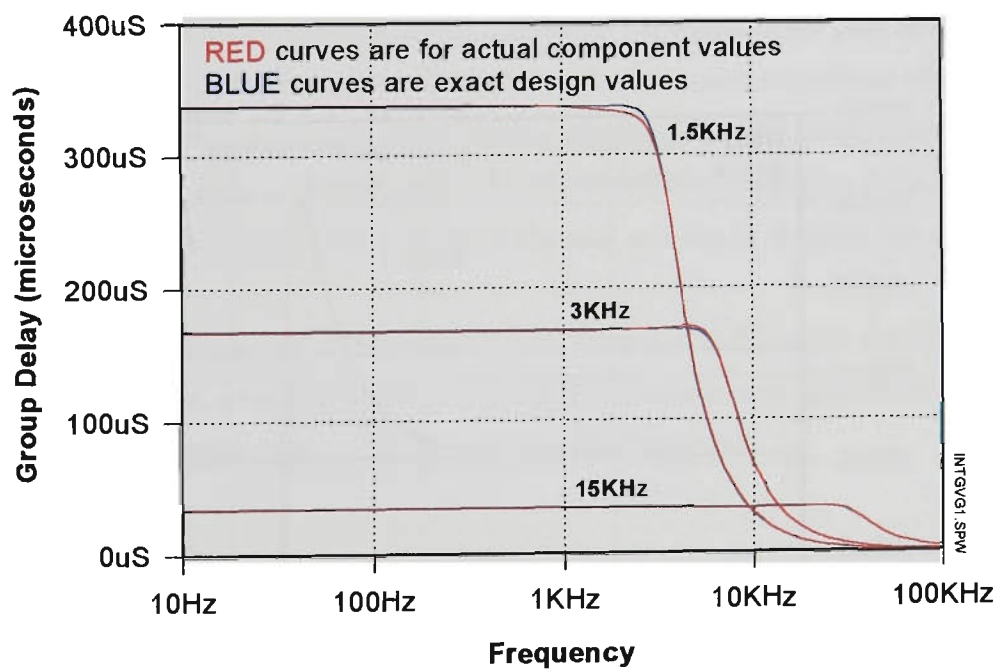


FIGURE B.28 Bessel integrators group delay (SPICE simulations)

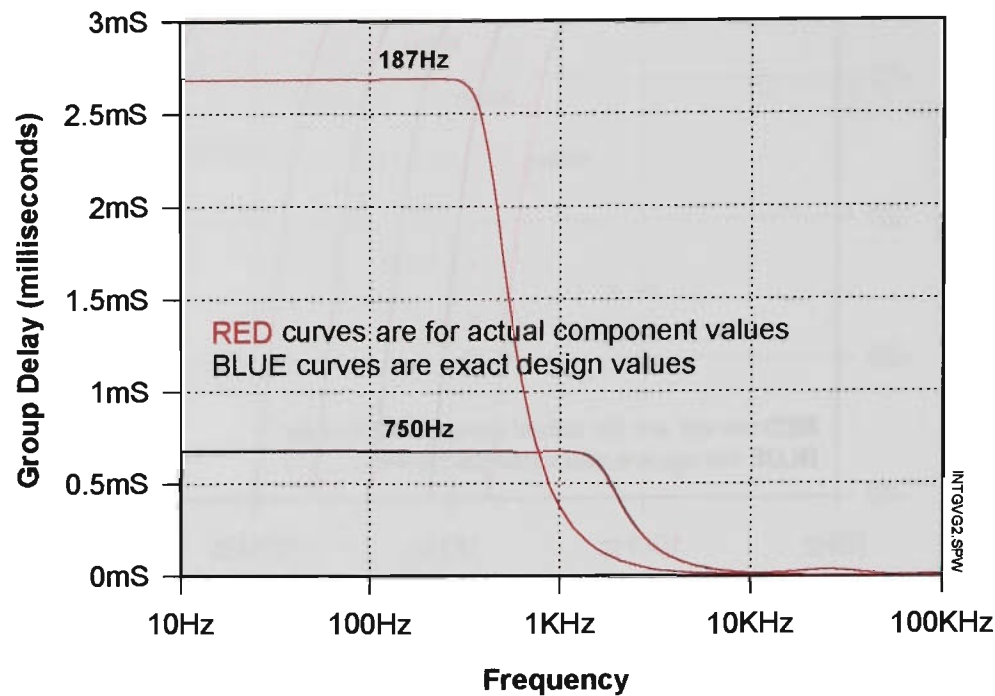


FIGURE B.29 Bessel integrators group delay (SPICE simulations)

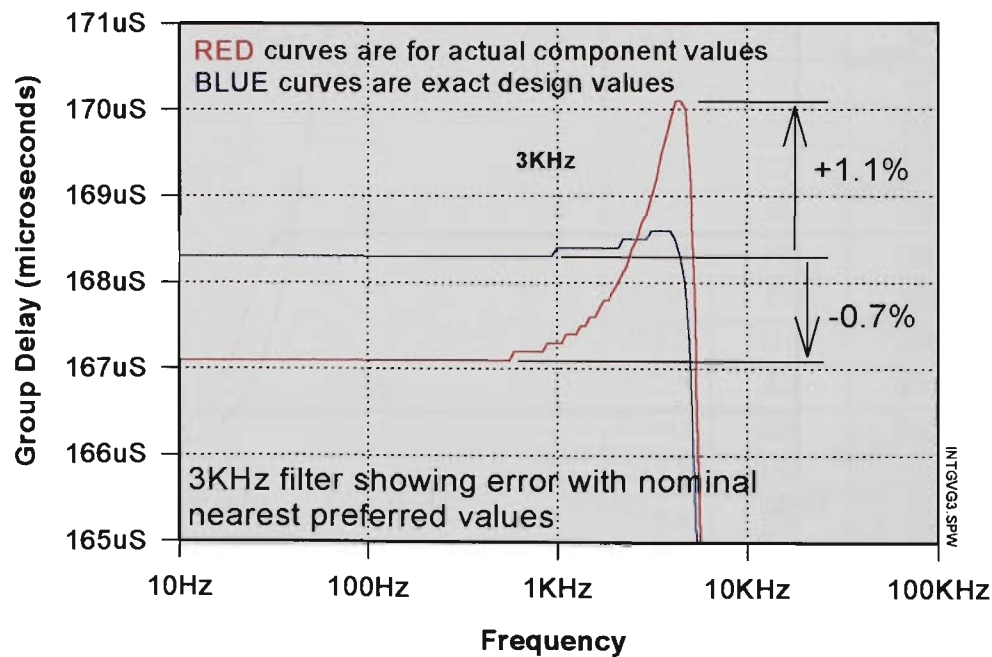


FIGURE B.30 Group delay error with nearest preferred value components for 3 kHz filter

B. 5.2 Frequency Response and Gain Matching

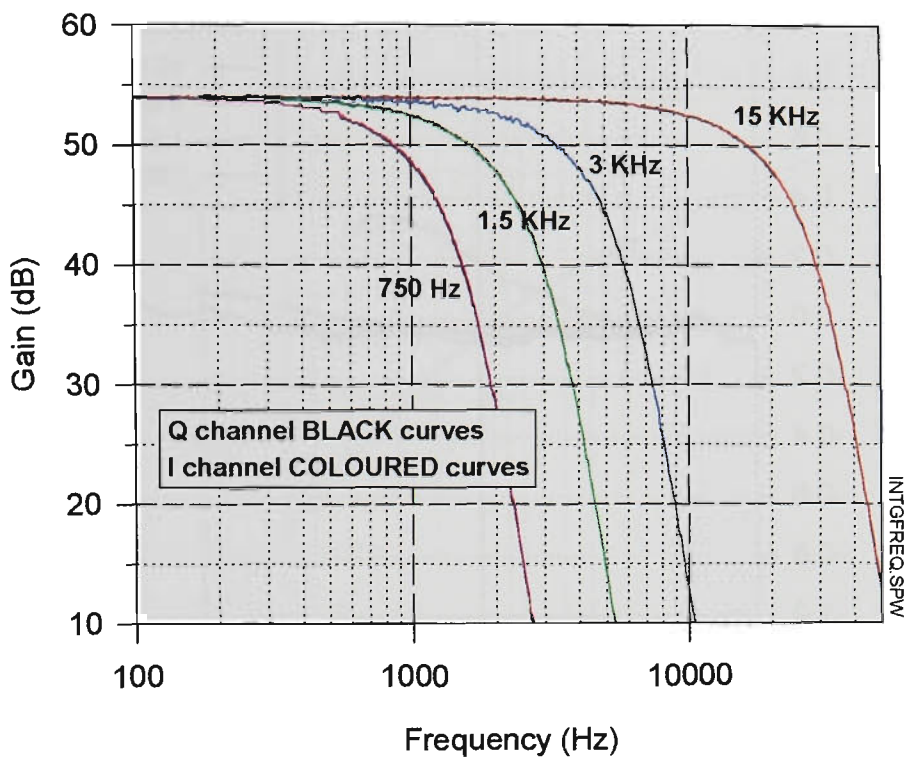


FIGURE B.31 *Bessel* integrators measured frequency response

A HP3589A Network Analyser allowed the performance of the baseband amplifier and *Bessel* filters to be measured sufficiently accurately to compare the gain and group delay matching of the I and Q channel filters. The analyser had a source impedance of 50Ω, and allowing for the 50Ω input resistance of the baseband amplifier, the expected passband gain was 60dB - 6 dB = 54 dB. Measured frequency responses are shown in Figure B.31.

The difference in the dB gain of the I channel and the Q channel, for each filter, is shown in Figure B.32.

All gain difference curves lie within +0.15 dB and -0.1 dB inside the filter passband, and for the 3 kHz filter, which is the filter used for all measurements presented in this thesis, the gain matching is better than ±0.04 dB over the filter passband.

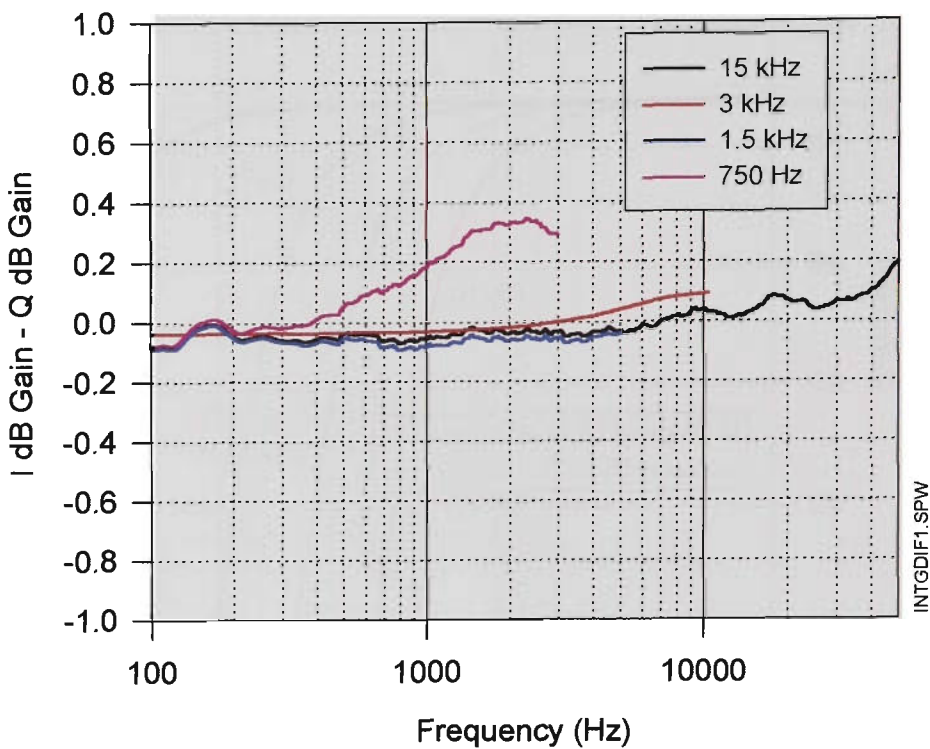


FIGURE B.32 Measured difference in dB gains, I Channel - Q Channel

B. 5.3 Group Delay

A linear phase or constant group delay response in the filter passband is desirable to avoid signal distortion in the time domain. To preserve fidelity of the complex signal, good matching of group delay between the I and Q channels is required. Tabulated measurements for all filters are presented in Table B.10, together with curves of group delay matching, and phase matching, for the 3 kHz filters (the filters used for all the channel sounding measurements to date.

TABLE B.10 Measured filter group delay

Filter	I Channel		Q Channel		Difference
	Group Delay	Frequency	Group Delay	Frequency	
1.5 kHz	341.6 uS	1509 Hz	342.5 uS	1509 Hz	-0.26%
3 kHz	176.7 uS	3020 Hz	177.5 uS	3020 Hz	-0.41%
15 kHz	35.94 uS	15070 Hz	36.29 uS	15070 Hz	-0.97%

Group delay is substantially constant to well beyond the nominal filter -3 dB frequency, for example to 6 kHz for the 3 kHz cut-off filters. Measured group delays show small rapid variations with frequency, but these are an artifact of the measurement setup. The phase varies smoothly with frequency, and so it follows that the group delay must also be a continuous and slowly varying function of frequency. In the plot below (Figure B.33), showing percentage dif-



ference of group delay between channels, a running average with 8% aperture has been used to remove the small rapid erratic fluctuations of delay difference.

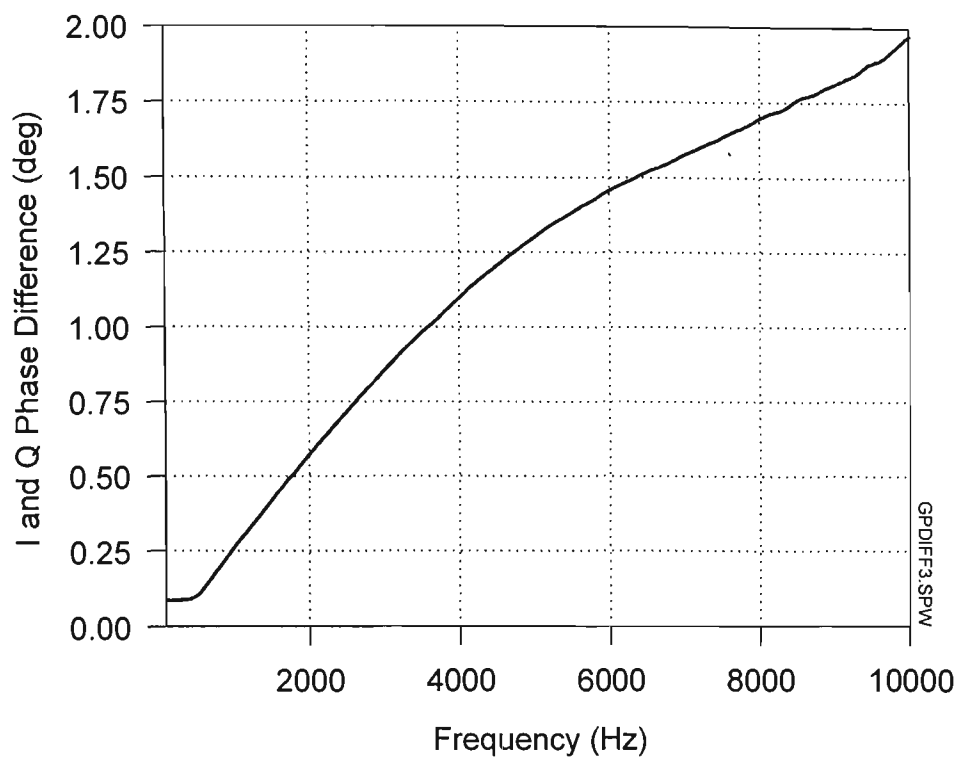


FIGURE B.33 3 KHz filters, measured phase difference I and Q channels

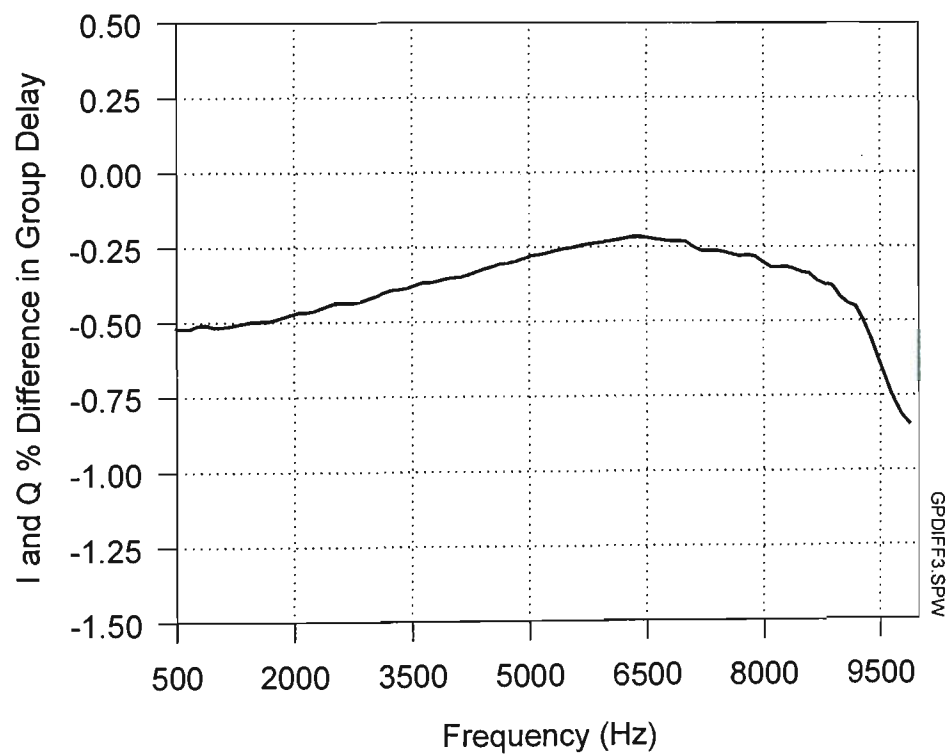


FIGURE B.34 3 kHz filters, measured % delay difference I and Q channels



## B.6 $I^2 + Q^2$ Display

A squarer and adder circuit produces an  $I^2 + Q^2$  output from the receiver I and Q signals, and allows the channel power delay profile to be displayed on a portable oscilloscope during a measurement session, or for demonstration purposes. Two multiplier integrated circuits type SG1495 are used, each with the X and Y inputs tied together to produce  $X^2$ . The squared signals are added and converted to a single-ended output with an op-amp. Plotting the output from this circuit on a log scale against input on a log scale, results in a characteristic which is linear over three decades of output voltage (10mV to 10V), but departs from linear behaviour over the next two lower decades (0.1mV to 10mV). However, this is of little concern for display purposes. The circuit schematic is shown in Figure B.36, and measured performance is shown in Figure B.37.

The fact that the power display is linear is a drawback, because in practise only about 20 dB dynamic range can be seen on the oscilloscope. An improved design using more accurate squarers, and a log summing circuit to give a logarithmic output, has been designed, but not yet implemented.

Another useful way of displaying the receiver output on an oscilloscope is to form a XY polar display with the I and Q outputs. Overload of either the I or Q channel is immediately obvious, and the display gives an indication of the extent of multipath activity.

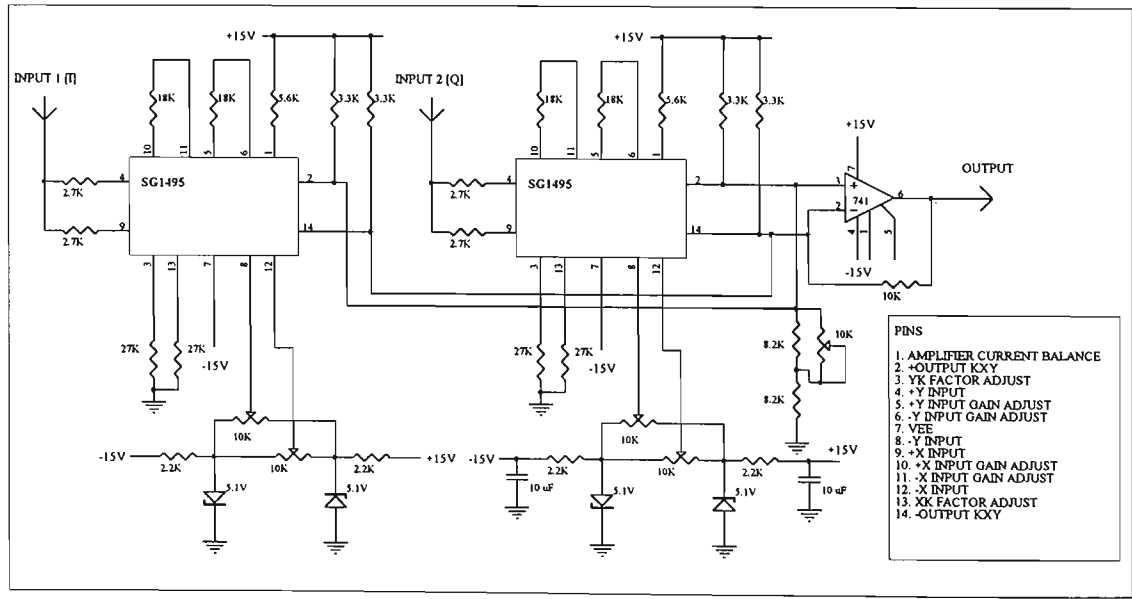


FIGURE B.35  $I^2 + Q^2$  squarer and adder circuit

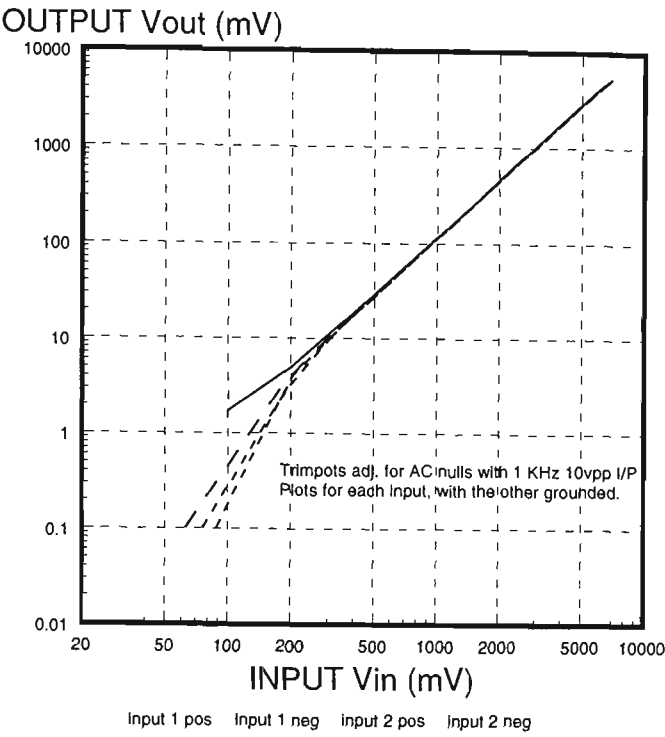


FIGURE B.36  $I^2+Q^2$  squarer and adder performance

B.7 Power Supplies - Receiver

As with the transmitter, the 24 volt requirement of the rubidium oscillator is met by using two 12 volt sealed lead-acid batteries (SLA) in series to power the receiver. Two *Yuasa* NP7-12 7 amp-hour batteries are mounted in a compartment in the base of the receiver box. A 3-pin DIN socket allows connection of an external battery charger, without removing the batteries.

Other voltages required in the receiver are produced by a step-down switching regulator (+12 volts), and two commercial DC-DC converters. A ZUS152405 provides -5 volts, and a ZUW252415 gives  $\pm 15$  volts.

A fear with switching supplies is that harmonics of the switching noise will interfere with sensitive RF or IF stages in the receiver. To reduce this possibility, all the switching supplies are housed in a heavy gauge tinned steel box, with additional extensive LC low-pass filtering added on the input side, and on all outputs. No evidence of problems with noisy supplies have been found while using the *channel sounder*. Details of the filtering are shown below in Figure B.37.

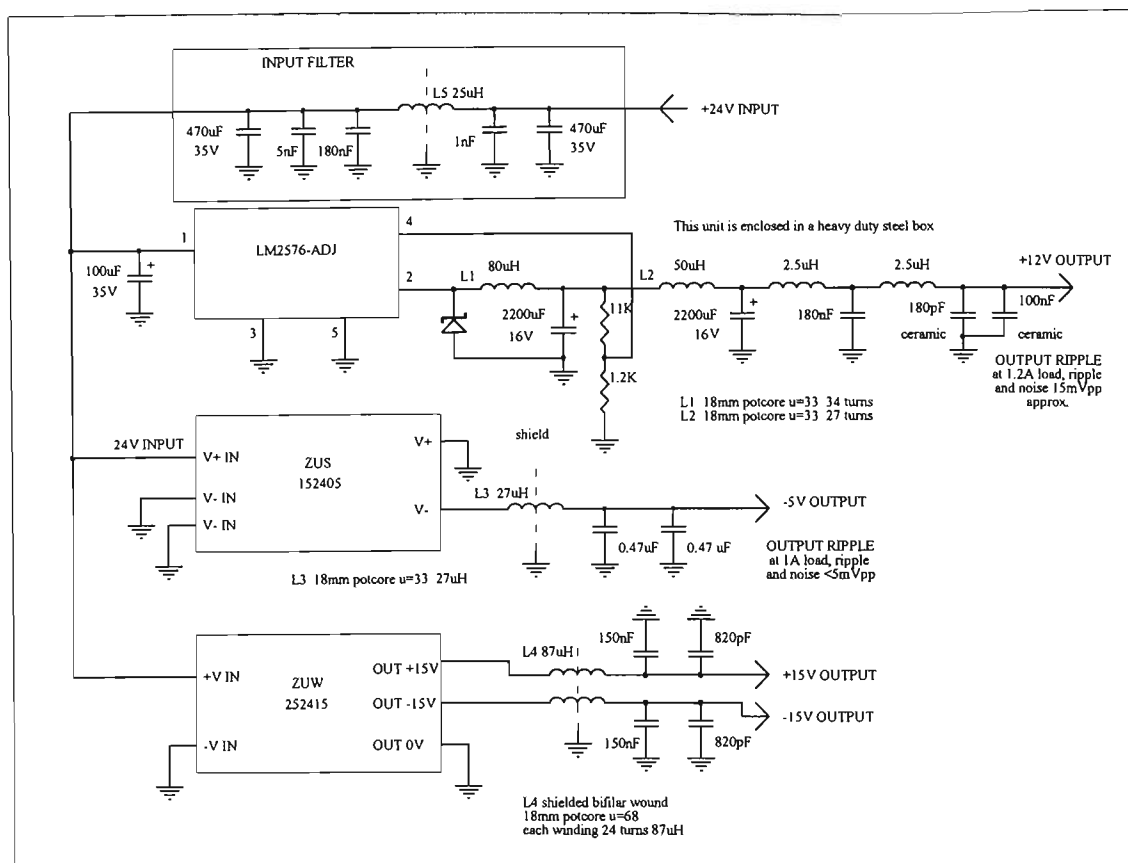


**FIGURE B.37 Receiver switching supplies**

The 12 volt supply powers the analogue to digital data acquisition *DaqBook100* unit, while maintaining equal load on the two batteries. Peak-peak ripple and noise on the 12 volt output with 0.6A load is <10mV, and <15mV with 1.2A load, while for the -5V supply at 1A load the figure is <5mV.

A panel of indicator LEDs monitors the level of the various supply voltages. The circuit schematic is the same as for the transmitter (see Figure A.38, Appendix A).

Figures B.38 and B.39 show the general power supply arrangement for the receiver. Fuses and diodes are included to protect against inadvertent incorrect reverse polarity connection of the 12 volt SLA batteries.

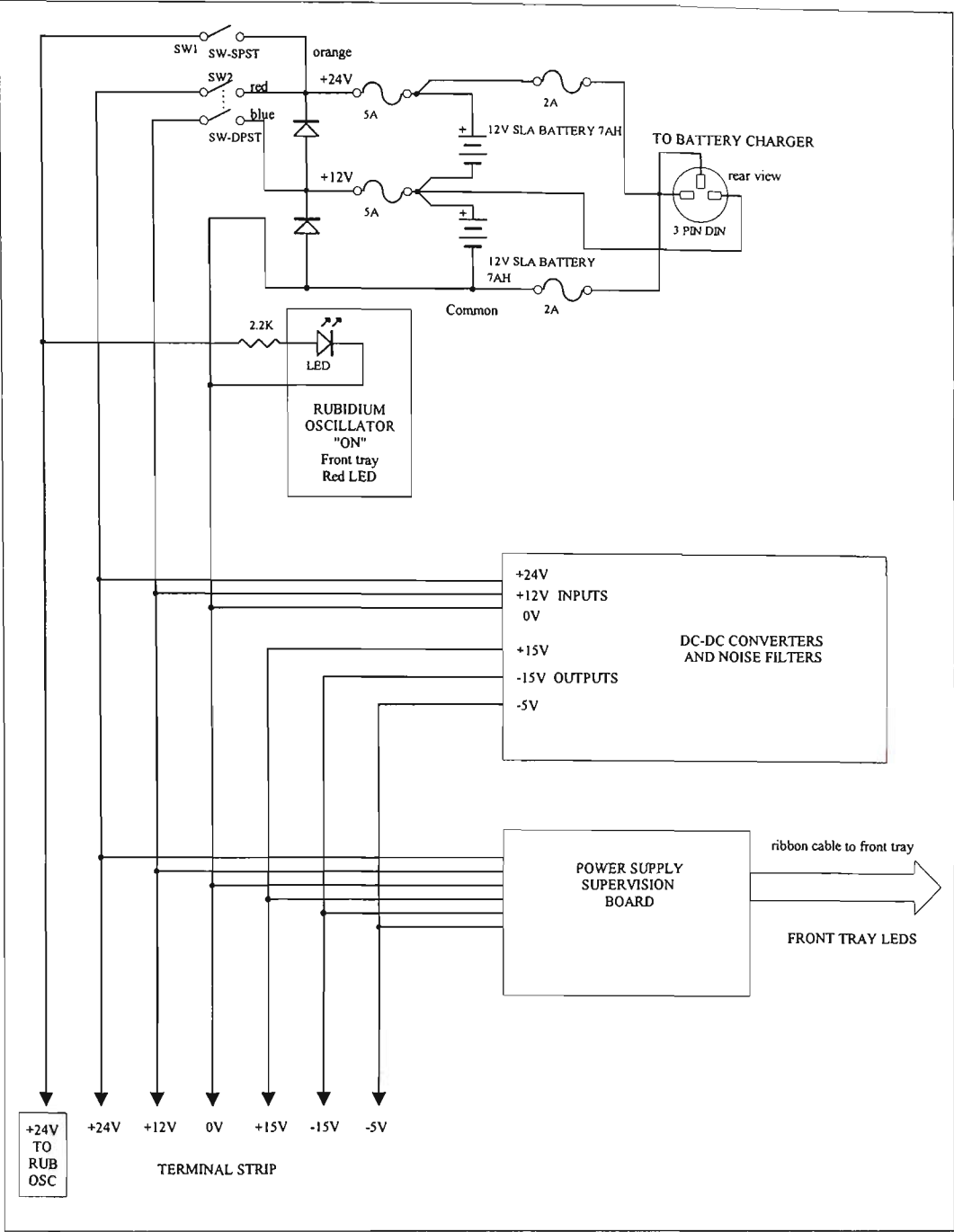


FIGURE B.38 Receiver power supply arrangement

Switch-on is controlled by two toggle switches. SW1 switches power to the rubidium oscillator which is switched on first to allow warm-up, taking 3 to 5 minutes. After the frequency reference is locked, indicated by a LED illuminating, the rest of the receiver is switched on using SW2.

During a measurement session, the main receiver can be switched off (provided the system is being used in a mode not requiring PN synchronisation) to conserve battery power while moving between different measurement regions, leaving the rubidium oscillator running.

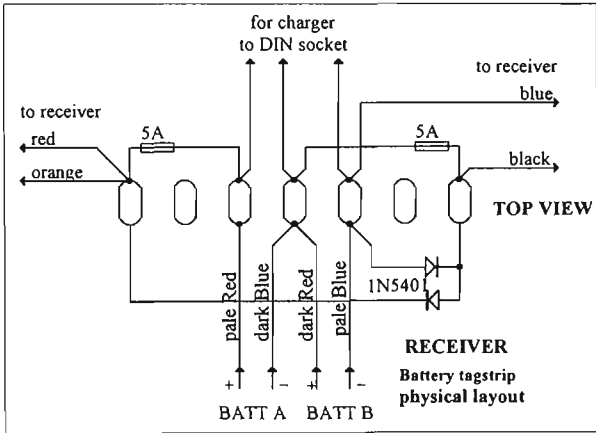


FIGURE B.39 Receiver power supply tagstrip

When using the receiver in a vehicle, the battery charger plug may be used to connect an additional set of external batteries in parallel with the internal batteries, to increase the operating time.

B.8 Modifications to Synchronise PN Sequences

B. 8.1 Introduction

If the PN sequences in the transmitter and receiver are initially synchronised, a time reference point for the commencement of the impulse response measurement is available. To synchronise the sequences, a cable is connected between the two PN generators, which are held in the “all ones” state until a synchronous start signal via the cable. Subsequently the cable may be removed, and the sequences will continue to have a defined timing relationship.

As already discussed in Chapter 3, the synchronising scheme adopted here resets both PN sequences periodically, with the reset period less than the sliding correlation time for the whole sequence length. This reset process is syncopated by the rubidium clocks, and occurs after a preset number of clock pulses, determined by switch settings on programmable counters.

Resetting before the correlator slides through the entire sequence length effectively “windows” the measurement time, allowing the impulse response measurement repetition rate to be increased (almost up to the reciprocal of the window time span), but retains the ambiguity time of the full PN sequence length. Each time the PN sequence is reset, a new time origin is created, allowing absolute path delays to be measured.

The modification requires the addition of a TTL to ECL interface to the PN generators, and provision of programmable counters, clocked by the rubidium frequency sources, in both transmitter and receiver. Provision for a synchronising cable, and a reset switch is also made.

Adding a distance-measuring wheel allows impulse response measurement data to be collected automatically at fixed increments of route distance. Making the wheel shaft encoder

counter adjustable allows the choice of various distance increments for gathering data.

In this section, circuit schematics of the counters, and other additions to the electronics, are documented and described.

### B. 8.2 PN Counter

The schematic is shown in Figure B.40. A cascade of 74F163 16-bit counters give a minimum count of 256, corresponding to a period of 25.6μs with the 100ns clock. By setting DIP switches to increase the count, the output period can be increased to 1.678 seconds, in steps of 25.6μs.

The counter output from the final stage is taken from the ripple carry out (RCO) pin. The RCO signal is not designed to function as a counter output, and is plagued with glitches. To eliminate these, the RCO pulse is NOR gated with the clock pulse in IC12A, giving a 50ns wide output pulse coinciding with the low half of the clock pulse. A D-flipflop (IC10B) is clocked by the RCO output pulse, with the D input set by the wheel trigger electronics. The output of this goes high on the next RCO pulse after the wheel trigger signal, and triggers a monostable (IC11), which generates a 20μs (approximately) output pulse, used to trigger the data acquisition system

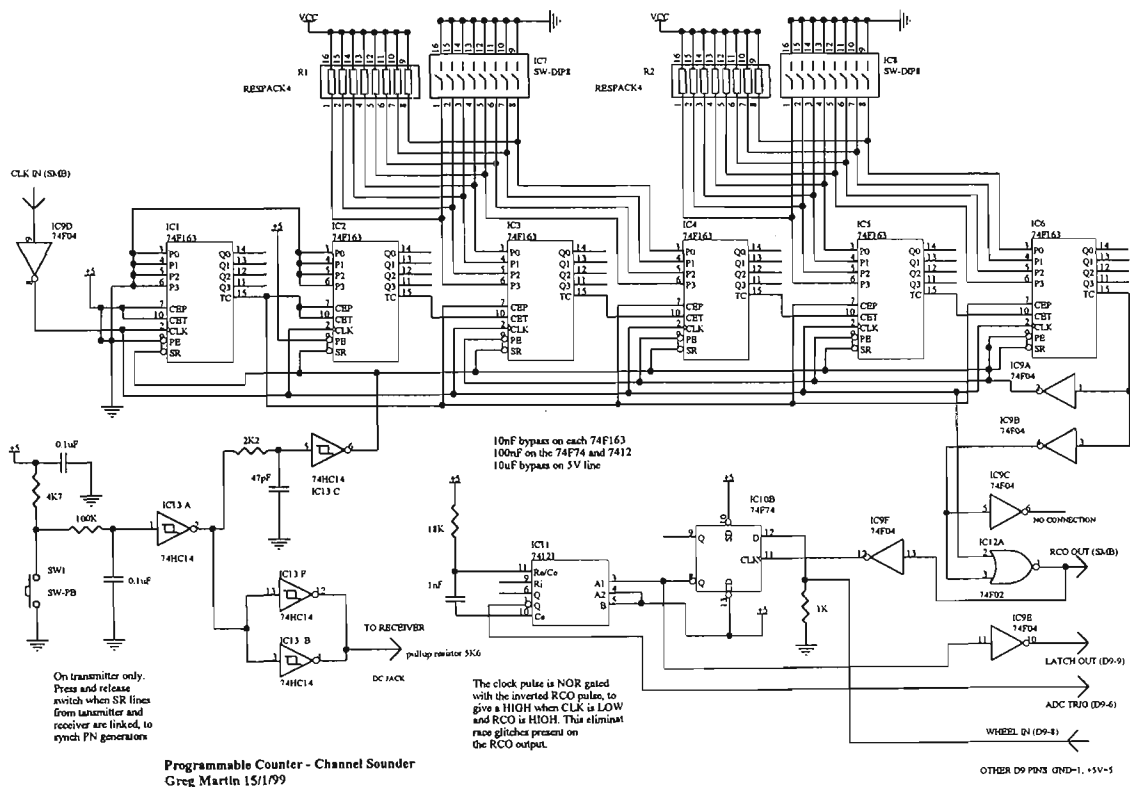
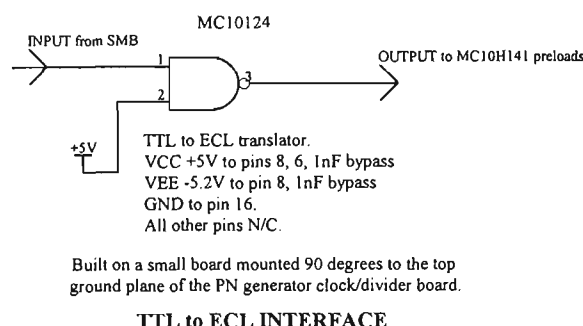


FIGURE B.40 PN counter

### B. 8.3 PN Preset

The RCO out pulse (50ns wide) goes via a TTL to ECL interface (Figure B.41), and

asynchronously presets all the shift register stages of the PN generator to “1”. When the pulse is removed, the PN generator restarts from the “all ones” state on the next clock edge. This restart will happen simultaneously in the transmitter and the remote receiver, within the limitations of rubidium clock drift, and phase differences of the PN counter clocks, and the PN generator clocks.



**FIGURE B.41 TTL to ECL interface for presetting PN generator**

## B. 8.4 Reset Switch

During development of the PN synchronisation modification, a problem became apparent. Originally, the reset was intended to be synchronous for both PN generators. But with the phase variation between the rubidium clocks, it was possible for the transmitter sequence to start before the receiver sequence, placing the main correlation peak prior to and outside the correlation window. Even if the peak was initially just within the window, rubidium clock drifts may eventually move it outside the window. Path delay pushes the correlation peak into the window, but for indoor measurements where path delays are small, the problem had to be overcome.

The solution was to introduce a small delay of approximately 70ns to the transmitter reset, which ensured that the correlation peak of the shortest path always fell within the correlation window, even at one metre transmitter-receiver spacing. The delay is provided by an RC network (4.7K $\Omega$  and 47pF) followed by a Schmitt trigger buffer. A similar network, with a longer time constant, eliminates switch contact bounce.

## B. 8.5 Other Modifications

The PN counters require buffered 10MHz rubidium clocks, so additional buffered clock outputs have been provided. See Figures B.42 and B.43.

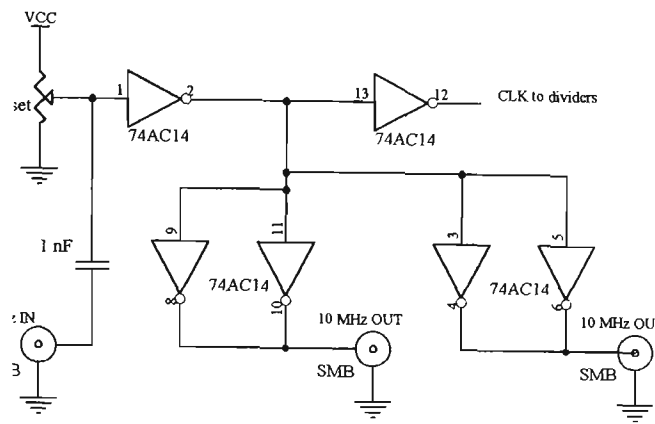
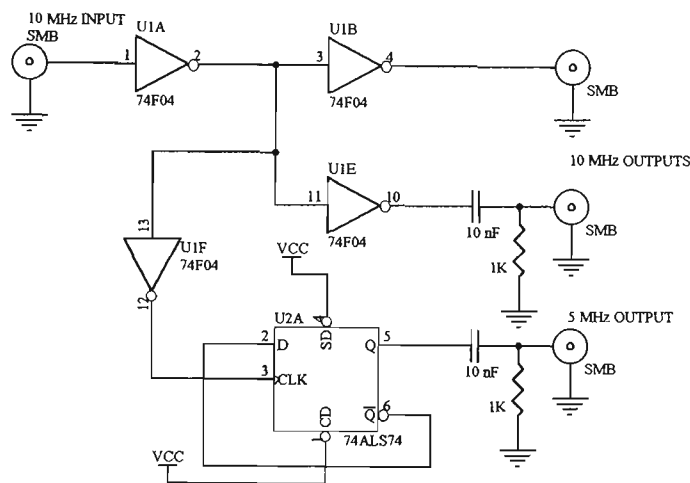


FIGURE B.42 Modified receiver divider



10 MHz BUFFER and DIVIDE BY 2

NOTE: A 74AC04 is used in the receiver instead of the 74F04, to provide sufficient drive for the multiplier circuit.

FIGURE B.43 10MHz buffer

B. 8.6 Wheel Trigger

A 12 inch BMX type bicycle wheel is connected to an optical encoder, which produces 147 pulses for each metre of travel. The pulses are counted, and counter outputs can be decoded for different count lengths by altering DIP switches. Nineteen bits of counter output are available on a DB25 connector, with the 2-way toggle switch set on “manual”. A circuit schematic is shown in Figure B.44.

Using the wheel trigger, measurements may be automatically initiated at precisely fixed increments of distance as the receiver moves along a route. Figure B.45 depicts the equipment in operation.



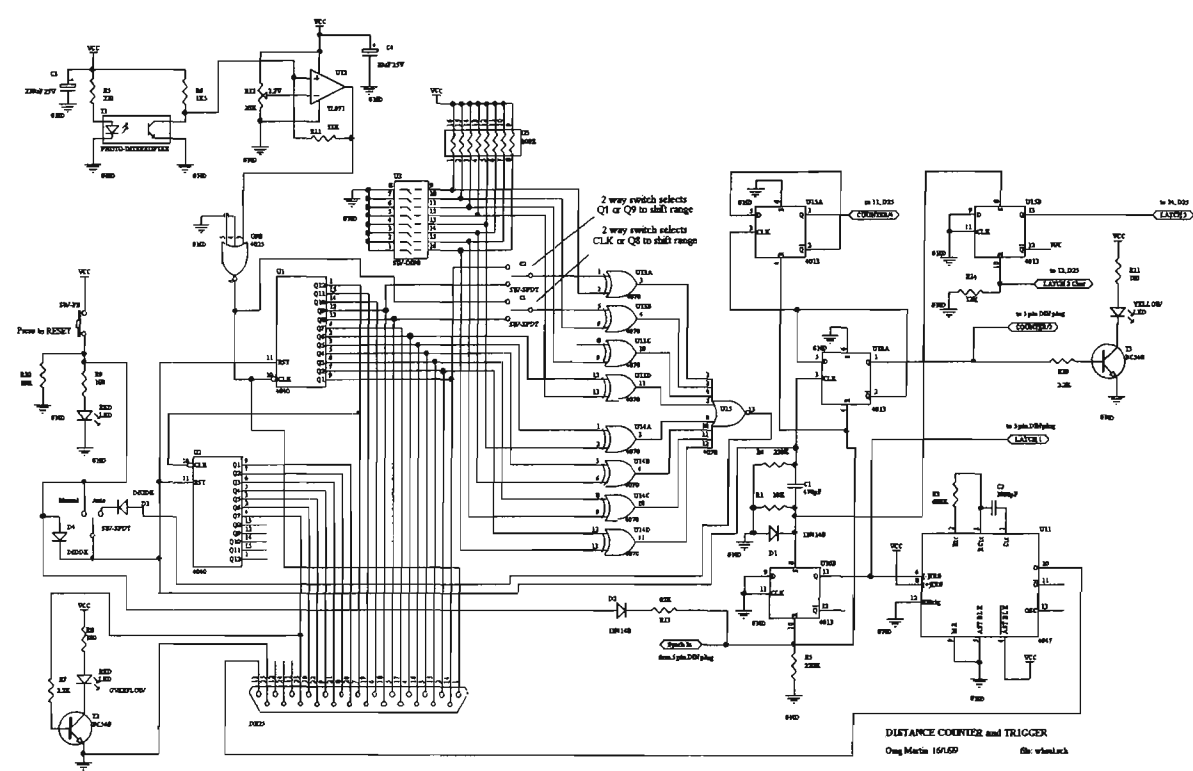


FIGURE B.44 Wheel trigger electronics



FIGURE B.45 Receiver on a trolley - with wheel trigger

B. 8.6.1 Auto Setting

With the toggle switch on “auto”, the counter is reset after a count length determined by DIP switch settings.

Counter reset causes the following operations to occur:

- 8. Sets the RS latch U10B (LATCH 1), which triggers monostable U11, giving an output pulse on pin 13 (DB25). The latch output is available on a 5 pin DIN socket, and the reset line to all latches is also brought out to the 5 pin DIN.
- 9. Clocks a divide-by-2 stage U10A; the output of this is a square wave and appears on the 5 pin DIN, and also operates a yellow LED indicator on the front panel of the wheel trigger unit. This output pulse is used to initiate data acquisition from the *channel sounder*.
- 10. The divide-by-2 stage clocks a further divide-by-2, and the output of this appears on pin 11 (DB25).
- 11. Sets U15B (LATCH 2), and the output of this is on pin 12 (DB25). LATCH 2 stays set until a high reset signal is applied to pin 12 (DB25), or until the front panel reset push button is pressed.

The front panel reset push button does the following:

- 1. operates a red LED on the front panel
- 2. resets LATCH 1 (U10B)
- 3. resets the divide-by-2 and divide-by-4 stages (U10A and U15A)
- 4. resets both binary counters (U1 and U2)

B. 8.6.2 Manual Setting

With the toggle switch on “manual”, the counters continue to count until a manual re-set occurs. Counter capacity allows approximately 3.6 km of travel before the counter fills. When output Q7 of the second counter (U2) goes high, a red front panel “overflow” LED lights. In manual mode, the divide-by-2 and divide-by-4 stages (U10A, U15A) are not operated. LATCH 1 and LATCH 2 are not operated. This setting allows distance to be logged if required.

B. 8.6.3 Wheel Counter Settings (Auto)

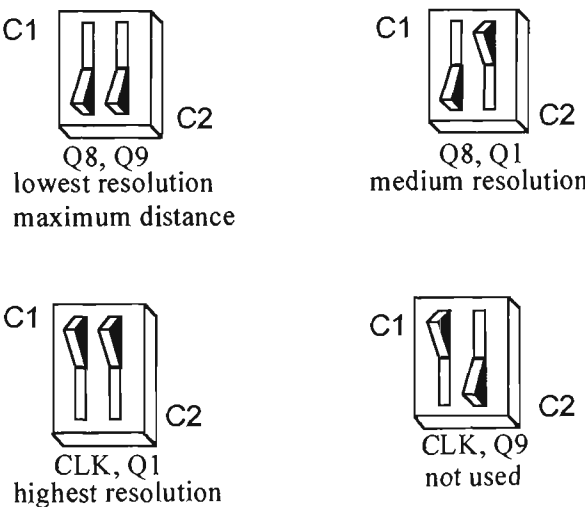


FIGURE B.46 Range switch (C1, C2) settings

TABLE B.11 DIP switch aliases for C1, C2 settings

Resolution	8 POLE DIP SWITCH							
	8	7	6	5	4	3	2	1
high	Q1	CLK	Q7	Q6	Q5	Q4	Q3	Q2
medium	Q1	Q8	Q7	Q6	Q5	Q4	Q3	Q2
low	Q9	Q8	Q7	Q6	Q5	Q4	Q3	Q2

NOTE: The “OFF” DIP switch setting corresponds to “1”

B. 8.6.4 Examples

To set the trigger distance to approximately 50 mm, note that one wheel clock pulse corresponds to 6.8 mm of travel. So to get 50 mm increments, the required divide ratio is  $50/6.8 = 7.3$ . Choose the nearest divide ratio of 8, which will give a distance increment of  $6.8 \times 8 = 54$  mm. Because of the divide-by-two stage, the DIP switches are set to divide by 4 to give a total divide ratio of 8. The divide by 2 stage can be taken into account by basing the calculation on a step increment of 13.6 mm. For a divide ratio of 4, set the DIP switch to 11111101; position 2 is the only switch set to “0”.

TABLE B.12 Example DIP switch settings

Distance step (mm)	Divide by	Resolution	DIP SWITCH							
			8	7	6	5	4	3	2	1
13.6	1	high	Q1	CLK	Q7	Q6	Q5	Q4	Q3	Q2
			on	off	on	on	on	on	on	on
54.4	4	medium	Q1	Q8	Q7	Q6	Q5	Q4	Q3	Q2
			on	on	on	on	on	on	off	on
108.8	8	medium	Q1	Q8	Q7	Q6	Q5	Q4	Q3	Q2
			on	on	on	on	on	off	on	on
1006.4	74	medium	Q1	Q8	Q7	Q6	Q5	Q4	Q3	Q2
			off	on	on	off	on	on	off	on
10009.6	736	low	Q9	Q8	Q7	Q6	Q5	Q4	Q3	Q2
			off	on	off	off	off	on	on	on

B. 8.7 PN Preset Counter

This has a fixed minimum divide ratio of 256, multiplied by a programmable divide ratio of 16 bits or in other words 65536, giving a maximum divide ratio of 16777216. With the 10 MHz input clock, the maximum output divide period is 1.6777216 seconds.

To program the counter, divide the desired ratio by 256, convert the result to binary, and set the DIP switches accordingly (switch “ON” gives a “1”).

Note that the least significant bit is at the left hand end of each switch, the reverse of the way binary numbers are normally written.

**Example:**

Divide by  $524288/256 = 2048 = 0000\ 1000\ 0000\ 0000$

Switch settings for this example are shown below in Table B.13.

**TABLE B.13 PN counter DIP switch settings**

L S B							M S B	L S B							M S B
1	2	3	4	5	6	7	8	1	2	3	4	5	6	7	8
0	0	0	0	0	0	0	0	0	0	0	1	0	0	0	0

**B.9 References - Appendix B**

[B.1] L.J. Giacoletto, “Electronics Designers’ Handbook”, 2nd. Edition, McGraw-Hill,1977, page 2.20.

[B.2] Peter A. Rizzi, “Microwave Engineering Passive Circuits”, Prentice-Hall, Inc., 1988, page 44.

[B.3] Randall W. Rhea, “HF Filter Design and Computer Simulation”, McGraw-Hill, 1995, page 57.

[B.4] A.M. Fowler, “Radio Frequency Performance of Electroplated Finishes”, Proceedings Institution of Radio and Electronics Engineers”, May 1970, pp.148-164.

[B.5] Randall W. Rhea, “HF Filter Design and Computer Simulation”, McGraw-Hill, 1995, page 197.

[B.6] Randall W. Rhea, “HF Filter Design and Computer Simulation”, McGraw-Hill, 1995, page 47.

[B.6] Trans-Tech, Inc., “Coaxial Transmission Line Elements”, Publication No. 50030170, Rev.2, August 1992.

[B.8] Seymour B.Cohn, “Parallel-Coupled Transmission Line Resonator Filters”, IRE Trans. Microwave Theory and Techniques, Vol.MTT-6, No.2, April 1958.

[B.9] George L.Matthaei, “Interdigital Band-Pass Filters”, IRE Trans. on Microwave Theory and Techniques, Vol.10, No.6, November 1962.

[B.10] Randall W. Rhea, “HF Filter Design and Computer Simulation”, McGraw-Hill,1995, page 123.

[B.11] R.M. Kurzrok, “Design of Comb-Line Band-Pass Filters”, IEEE Trans. Microwave Theory and Techniques, Vol.MTT-14, No.7, July 1966, pp.351-353.

[B.12] George L.Matthaei, “Comb-Line Band-Pass Filters of Narrow or Moderate Bandwidth”, The Microwave Journal, August 1963, pp.82-91.

[B.13] R. Pregla, “Microwave Filters of Coupled Lines and Lumped Capacitances”, IEEE Trans. Microwave Theory and Techniques, Vol.MTT-18, May 1970, pp.278-280.

[B.14] Randall W. Rhea, “HF Filter Design and Computer Simulation”, McGraw-Hill,1995, page 337.

[B.15] R.J.Wenzel, “Exact Theory of Interdigital Band-Pass Filters and Related Structures”, IEEE Trans. Microwave Theory and Techniques, Vol.MTT-13, No.5, September 1965, pp.559-575.

- 
- [B.16] George L. Matthaei, "Interdigital Band-Pass Filters", IRE Trans. on Microwave Theory and Techniques, Vol.10, No.6, November 1962.
- [B.17] M. Dishal, "A Simple Design Procedure for Small Percentage Bandwidth Round-rod Interdigital Filters", IEEE Trans. on Microwave Theory and Techniques, Vol. MTT-13, No.5, September 1965,
- [B.18] J.T. Bolljahn and G.L. Matthaei, "A Study of the Phase and Filter Properties of Arrays of Parallel Conductors Between Ground Planes", Proceedings Institute of Radio Engineers, March 1962, pages 299-311.
- [B.19] International Telephone and Telegraph Corporation (ITT), "Reference Data for Radio Engineers", 5th. Edition, Howard W. Sams & Co., Inc., 1969, page 8.25.
- [B.20] Milton Dishal, "Alignment and Adjustment of Synchronously Tuned Multiple-Resonant-Circuit Filters", Electrical Communication, June 1952, pp.154-164.
- [B.21] The American Radio Relay League, "The ARRL Handbook", 73rd. Edition, 1996,
- [B.22] M.E. Van Valkenburg, "Analog Filter Design", Holt, Rinehart and Winston, New York, 1982, page 289.

# Appendix C: Antennas

## C. INTRODUCTION

Two different types of vertically polarized antenna have been constructed for the channel sounding measurement program:

1. discone omnidirectional
2. halfwave (ground independent) omnidirectional

Dimensioned drawings, measured impedance matching plots, and measured polar patterns are shown in this appendix.

Polar patterns were measured in an anechoic chamber at the *Centre for Communications Research, University of Bristol*. Thanks are due to Dr. Geoff Hilton of the *University of Bristol*, for developing the excellent automated antenna measurement system in use at Bristol, and for instruction and assistance in making the measurements.

### C. 1 Discone Antenna

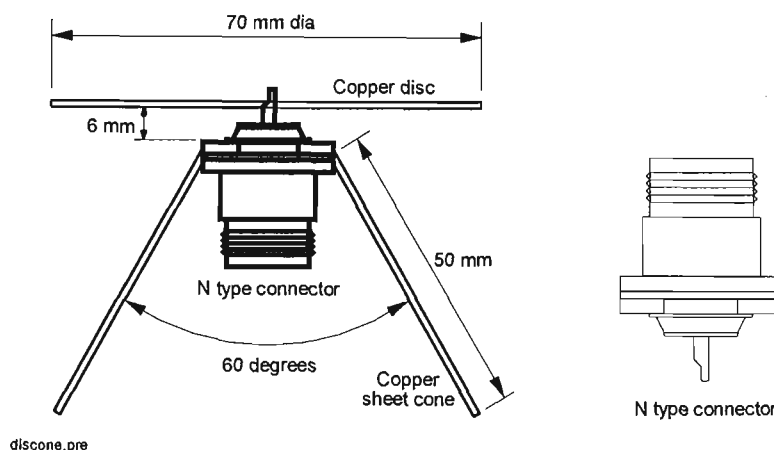


**FIGURE C.1 Discone antenna - cross section view**

Discone antennas provide good matching over a very wide bandwidth, and a close approximation to an ideal omnidirectional pattern. The antenna is ground-independent, and has the same gain as a halfwave dipole. Construction is not difficult, apart from the fabrication of a cone from copper sheet. The design was based on equations and information from Ref.[C.1], [C.2], [C.3], [C.4]. The antenna was built on a panel-mounting N-type 50 $\Omega$  connector (see Figure C.1), with the spacing between the truncated cone and the disc determined

empirically to give the best match over frequencies around 1.9 GHz. This construction method is a convenient technique patented by T.Rappaport and described in Ref.[C.5], although at the time this antenna was developed, the author was unaware of Rappaport’s previous work.

C.1.1 Discone Antenna Matching

The wide matching bandwidth of the discone is illustrated by the measured VSWR plot shown in Fig C.2. VSWR is <1.5 between 1.5GHz and 3GHz, and at 1.89GHz, the VSWR<1.1

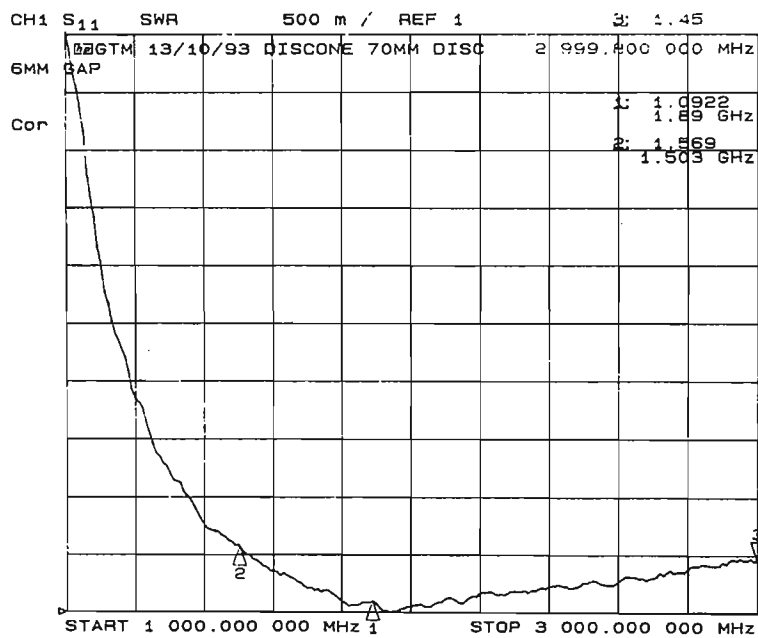


FIGURE C.2 Discone - measured VSWR

C.1.2 Discone Antenna - Polar Pattern in Azimuth

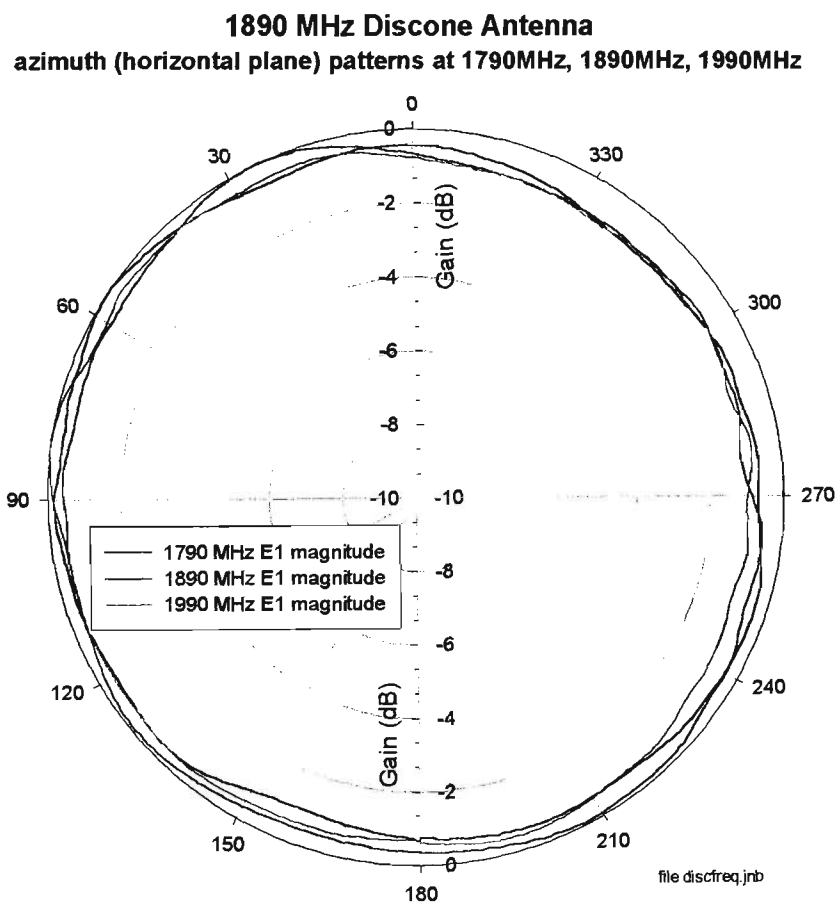


FIGURE C.3 Discone azimuth polar pattern at three frequencies

Figure C.3 shows that the horizontal pattern is omnidirectional within  $\pm 0.5\text{dB}$  over a 200MHz bandwidth (1790MHz to 1990MHz), which is the bandwidth of the sounder in *indoor* mode. Part of this variation is caused by the measurement setup. In elevation (Figure C.4), the pattern maximum is close to the horizontal, and deep nulls occur vertically above and below the antenna. The slight asymmetry below the antenna is thought to be due to the coaxial feed cable, and the support structure used during testing.

Measured at 1890 MHz, the discone gain was  $2.5 \pm 0.5\text{ dBi}$ . A thin halfwave dipole has a theoretical gain of 2.15 dBi. The gain measurement was done in the anechoic chamber by comparing the discone with a calibrated horn.



C.1.3 Discone Antenna - Polar Pattern in Elevation

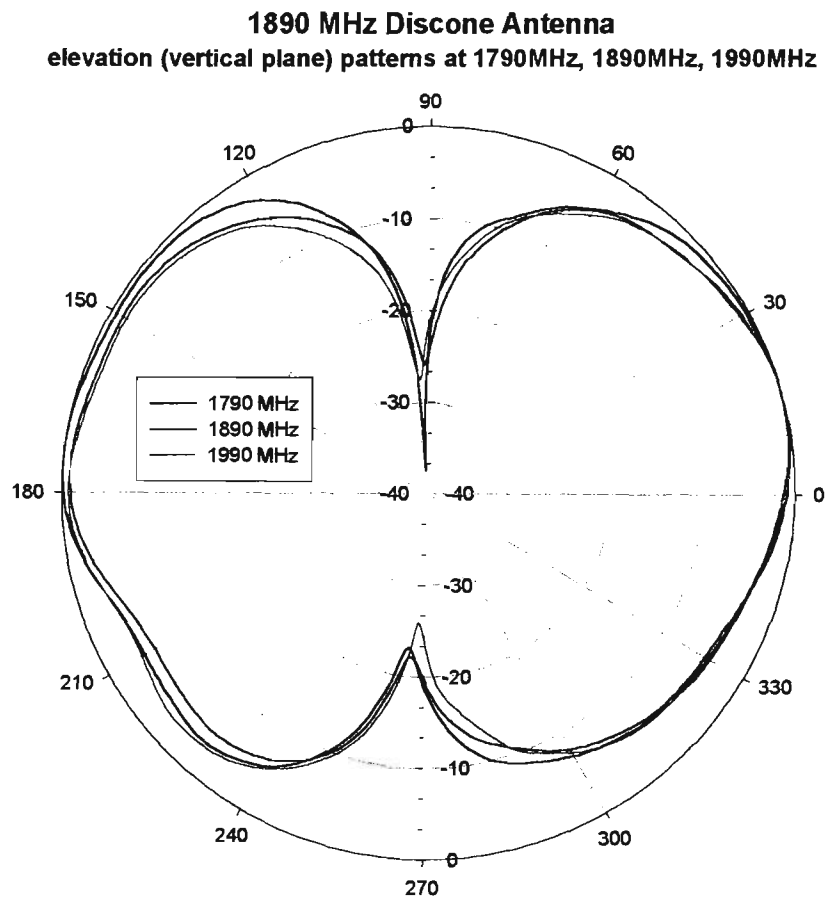


FIGURE C.4 Discone elevation pattern at three frequencies



FIGURE C.5 Discone on test in the anechoic chamber at the *University of Bristol*

## C. 2 Halfwave J Antennas

A vertical halfwave antenna, fed from a shorted quarter wave open wire section, forms the omnidirectional ground-independent “J antenna”, described in Ref.[C.6]. The feed point along the quarter wave line is adjusted to give a good match at the operating frequency.

A balun should be used for the transition from coax to the quarter wave matching section, but in the antennas built for this project the balun was omitted. The coaxial feeder is connected directly to the quarter wave section, using small copper clamps. Adjusting the position of the clamps alters the shunt capacitance between them, and gives further fine adjustment of matching (Figure C.6).

The polar pattern varies from omnidirectional by up to  $\pm 3\text{dB}$ , probably because of the unbalanced feed arrangement.

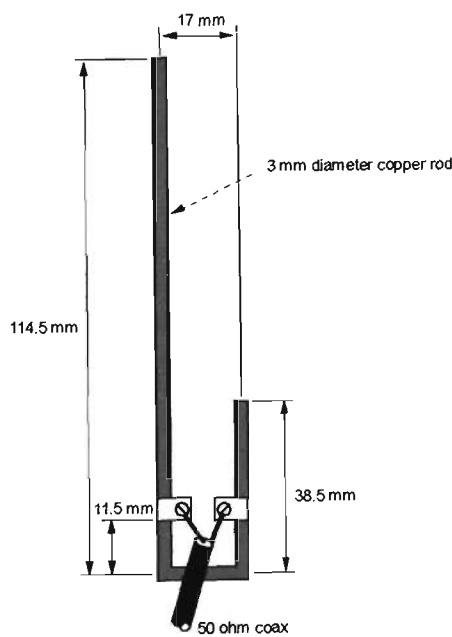


FIGURE C.6 Halfwave 1890MHz J antenna

### C.2.1 Halfwave J Antenna Matching

Figure C.7 shows measured matching, with the  $VSWR < 2$  from 1860MHz to 2095MHz. Slight retuning was required to move this down to cover 1.79GHz to 1.99GHz.

Two of these antennas are in use. One is mounted in a section of plastic plumbing pipe and fitted with a magnetic base, for use on the roof of a car (see Figure C.9). The other is used on the receiver with the backpack or the trolley, but has also been used as the transmitter antenna in Sydney, for the McMahon's Point and the *University of Technology Sydney* measurements.

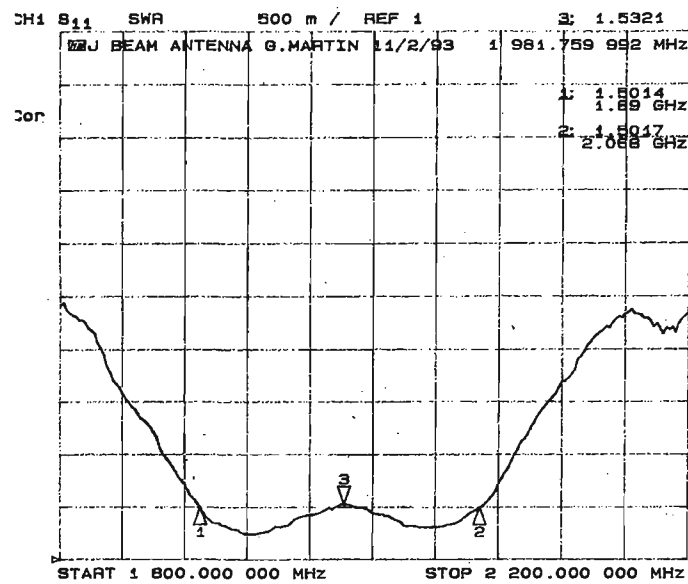


FIGURE C.7 Halfwave J antenna - measured VSWR

C.2.2 Halfwave Antenna - Polar Pattern in Azimuth

1890 MHz Roof Mount Half Wave Antenna  
azimuth (horizontal plane) patterns at 1865MHz, 1890MHz, 1915MHz

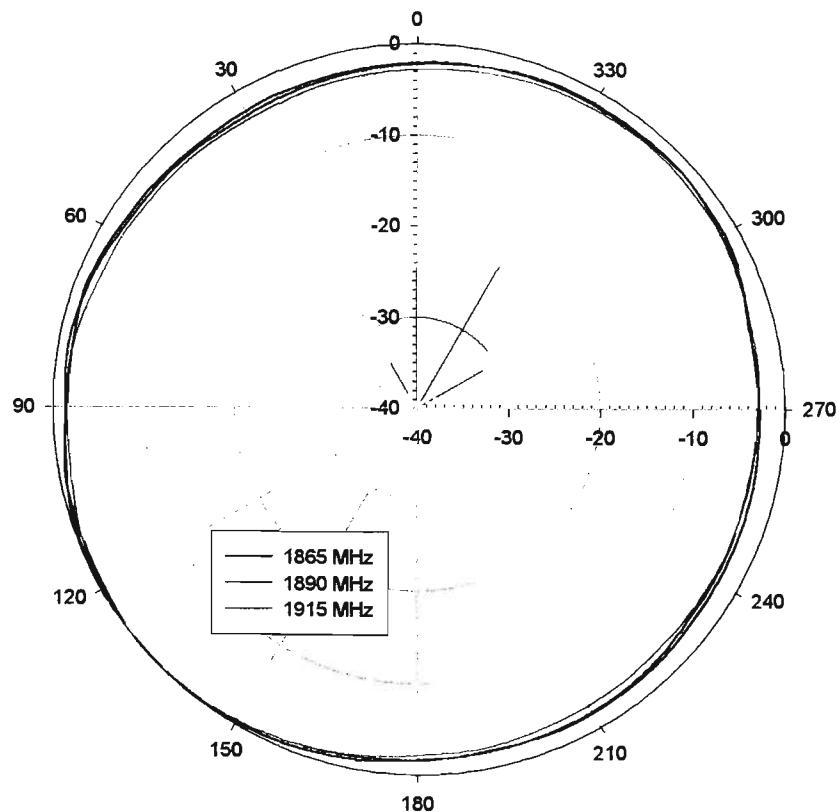


FIGURE C.8 J antenna azimuth polar pattern at three frequencies - roof mount model in plastic tube

Over the 50MHz bandwidth required for the sounder in outdoor mode, the roof mount model is omnidirectional within  $\pm 1.5\text{dB}$ . In elevation, both J antennas show maximum gain in the horizontal direction.

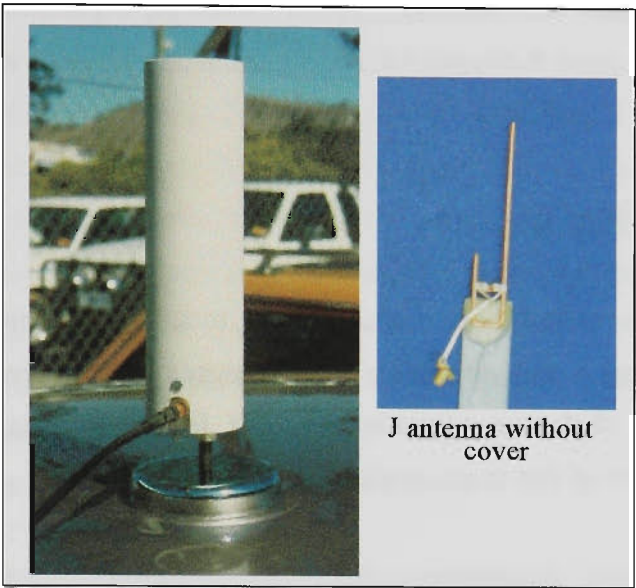


FIGURE C.9 J antenna - roof mount version

### C. 3 Antenna Mounting

Various mounting arrangements for the transmitter and receiver antennas have been used during the measurement program. The discone antenna has an offset mounting bracket, with a stepped-diameter aluminium socket, allowing it to mount on any diameter tube used with the tow bar mount, or the portable mast. The bracket offset allows the stiff low-loss coaxial cable to run vertically below the antenna, without the need for sharp bends.

#### C.3.1 Backpack Receiver Unit

A halfwave J antenna attached to an aluminium tube clips to the side of the receiver housing, placing the antenna just above head level (see Figure B.2, Appendix B).

#### C.3.2 Vehicle Roof Mount - Magnetic Base

Initially, vehicle based measurements used a halfwave J antenna mounted on an aluminium tube attached to the rear door of the car and protruding vertically through the open window, to position the antenna just above roof level. Later the magnetic base halfwave J antenna has been used, mounted on the car roof (Figure C.9).

### C.3.3 Camera Tripod Mount

A 2 metre length of aluminium tube was adapted to attach to a camera tripod, providing a mounting for the transmitter antenna. The tube may be positioned horizontally, to protrude out of hotel windows, or over the edge of balconies, to position the antenna outside the building line (see Chapter 5, Figure 5.6 and Figure 5.21), or used vertically to form a short mast (see Chapter 5, Figure 5.7).

### C.3.4 Car Tow Bar Mount

A fitting was made to bolt to a car tow bar, to attach aluminium tubing to form a two section telescoping mast with adjustable height ranging from approximately 2 to 4 metres. This has been used with the transmitter in a car boot, for low antenna city measurements.

An illustration of this in use is shown in Figure C.10 below.



**FIGURE C.10 Tow bar mount in use**

### C.3.5 Portable Mast

A lightweight portable mast was designed and built specifically for use with the channel sounder. The mast disassembles into lengths of aluminium tube and angle, and packs into a 2 metre long canvas “cricket bag” which is easily carried. Assembly of the mast using wing-nuts may be done in a few minutes, without tools. Foot pads on each leg are adjustable in height over a range of approximately 250 mm, to level the mast.

Initially the mast consisted of three sections of telescoping aluminium tube, achieving a height of approximately 5.6 metres. Later an additional section was added, allowing antenna heights of up to 7.5 metres. The mast may use one, two, three or four of the 2 metre sections, giving a range of heights.

Small sandbags are available to weight the outer ends of the tripod legs to improve stability in windy conditions.

This mast has been used extensively (see Chapter 5, Figures 5.1, 5.13, 5.14)

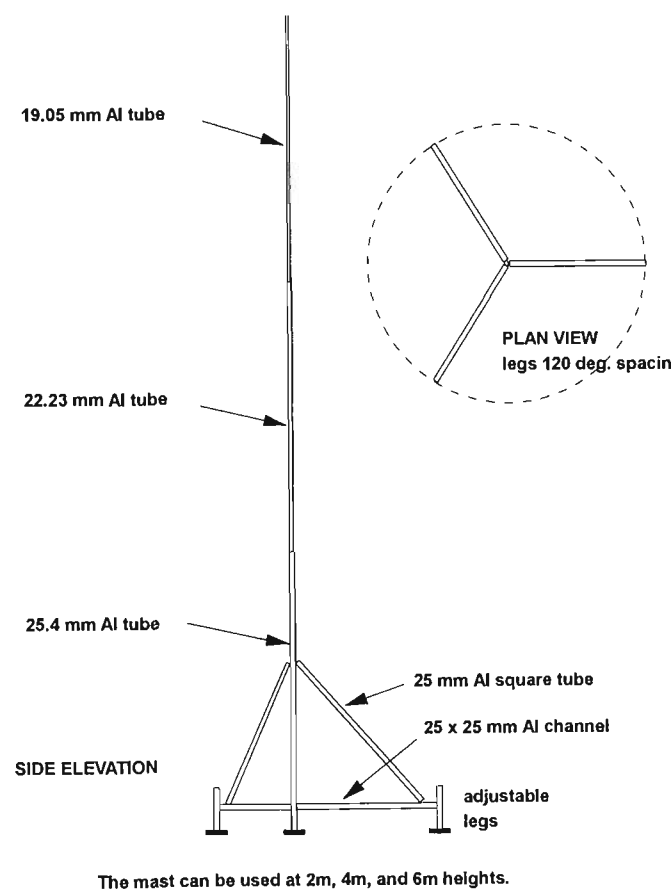


FIGURE C.11 Portable light weight mast

---

## C. 4 References - Appendix C

[C.1] A.G. Kandoian, "Three New Antenna Types and Their Applications", Proc. IRE, Vol.34, February 1946, pages 70-75.

[C.2] "The ARRL Antenna Book", Section 7-17, 1994, The American Radio Relay League.

[C.3] D.S.Evans, G.R.Jessop, "VHF-UHF Manual", Section 7.28, 3rd. Ed., 1982, Radio Society of Great Britain.

[C.4] "Reference Data for Radio Engineers", Section 25-10, 5th. Ed., 1969, Howard Sams & Co., Inc.

[C.5] Theodore S. Rappaport, "Wide-Band Test Antennas", RF Design, April 1988, pages 37-41.

[C.6] "The ARRL Antenna Book", Section 16-21, 1994, The American Radio Relay League.

# Appendix D: Software

## D. INTRODUCTION

A number of Pascal software programs and MATLAB scripts have been written in the course of this project, to collect channel sounder measurements, then to process, sort, filter, summarise, and model propagation parameters. Some of this software is summarised and described in this appendix. Where a program has evolved through a number of versions, only the latest or the most representative is described, although in some cases other versions are summarised in brief tabular form, where these versions serve a different purpose. This appendix also serves as a handbook for using the software.

Software listings are not included, because to do so even using small 8 point type would require over 70 additional pages.

### D.1 DAQ3

TABLE D.1 DAQ3

Program Name	DAQ3
Purpose	Driver for DaqBook A to D unit, to collect I and Q data from the channel sounder.
Revision date	10/11/94
Input files	-
Input file directory	-
Input information	filebase, start number, samples/second/channel, number of samples/channel(12,000 maximum). Hit the ENTER key to initiate the measurement.
Output files	filebaseS.BIN (S is the file number, which automatically increments)
Output directory	C:\greg\prop



## D.2 CONVRTG2

TABLE D.2 CONVRTG2

Program Name	CONVRTG2
Purpose	removes DC offsets from I and Q values. Finds the largest power sample, then stores this as I,Q sample pair 500. Takes 499 sample pairs before sample 500, and 2500 after.
Revision date	1/11/94
Input files	filebaseS.BIN (S is the file number)
Input file directory	C:\greg\prop
Input information	filebase, start number, number of files.
Output files	filebaseS.DAT (S is the file number)
Output directory	C:\greg\process

## D.3 DELAYG4

TABLE D.3 DELAYG4

Program Name	DELAYG4
Purpose	Calculates average delay and rms delay spread for each PDP. Operates on a batch of files. Skips missing files.
Revision date	20/8/96
Input files	filebaseS.DAT (S is the file number)
Input file directory	C:\greg\process
Input information	filebase, start file number, final file number, sample time (ns), threshold before peak: dB relative to 0dB (-dB), threshold after peak: dB relative to 0dB (-dB), range after peak (nS),
Output files	filebase.RMS
Output directory	C:\greg

## D.4 AVERAGEG, AVERAGEA

### D.4.1 AVERAGEG

The output file **@filebaseN.DAT** is a binary file in the same format as other **.DAT** files, with 3000 pairs of I,Q values, except that the square root of the average power value at each normalised sample time is stored in the I value, with the corresponding Q value set to zero. The word **filebase** refers to any chosen generic name for a family of files. In this program the name must be no longer than 6 characters to stay within the *DOS* requirement of filenames no longer than 8 characters. A text output file **@filebaseN.ASC** is also produced for plotting the average PDP. This file has 3000 rows and two columns of numbers, the first

column being time in  $\mu\text{s}$  in increments of the sample time, and the second column is power values normalised to 0dB. The file is normalised so the maximum ray (0 dB) occurs at zero time in row 500. During one run of AVERAGEG, a number of batches of .DAT files can be separately averaged, and the output files produced are numbered consecutively N=1, N=2, etc.

TABLE D.3A AVERAGEG

Program Name	AVERAGEG
Purpose	averages PDPs (linear power values are averaged). Output amplitudes are normalised relative to 0dB.
Revision date	23/3/96
Input files	filebaseS.DAT (S is the file number)
Input file directory	*\greg\process * means specify drive letter
Input information	filebase, start number, final number, sample time(nS)
Output files	@filebaseN.DAT (N is sequence number of the output file, incremented by 1 for each group of files averaged during one session) @filebaseN.ASC (text file for plotting PDP graph)
Output directory	*\greg\process *\greg\graph

D.0.1 AVERAGEA

This differs from AVERAGEG in requiring a *Gain Factor* to be entered before each batch of .DAT files is averaged. Amplitude and power values in the output files are then given in absolute rather than normalised terms, with values that relate to the path loss. This allows groups of PDP measurements all taken in nominally the same location to be averaged, and compared with the average PDP in another location where the *Gain Factor* used during the measurements may be different.

The *Gain Factor* is defined as:

$$Gain\ Factor = -130 + Xmitter\ Atten. + Rec\ Gain\ Factor$$

*Xmitter Atten* is the setting in dB of the switched attenuator preceding the Transmitter RF power amplifier, and the *Rec Gain Factor* is 0 for 60 dB receiver baseband gain, 10 for 50 dB and 20 for the 40 dB setting. The *Gain Factor* added to the amplitude of the strongest ray in dBV gives a *Path Loss Factor*, which is related to the path loss, but does not include antenna gains

TABLE D.4 AVERAGEA

Program Name	AVERAGEA
Purpose	averages PDPs (linear power values are averaged). Output amplitudes are in <i>Gain Factor</i> terms
Revision date	13/8/96
Input files	filebaseS.DAT    (S is the file number)    skips missing files
Input file directory	*\greg\process       * means specify drive letter
Input information	filebase, start number, final number, sample time(ns), gain factor
Output files	&filebaseN.DAT    (N is sequence number of the output file, incremented by 1 for each group of files averaged during one session) &filebaseN.ASC    (text file for plotting PDP graph)
Output directory	*\greg\process *\greg\graph

D.1 PLOTG2

The PLOTG series of programs allow rapid plotting of a sequence of PDPs on the screen, to quickly review a set of measurements. The option of generating a text file to use in a graph plotting program or spreadsheet is provided. PLOTG plots from 0 to -50 dB on the vertical axis, and from sample 1 to sample 3000 on the horizontal axis (blue curve). The amplitude of the peak ray (which is normalised to 0 dB) is listed in dBV, and an indication of the noise floor is given.

PLOTG2 adds a second curve in a contrasting colour (magenta) which shows an expanded section of the PDP from sample 400 to sample 1000. PLOTG3 plots the part of the PDP between sample 475 and 625. PLOTG4 plots from sample 475 to 625 but with a linear vertical axis from -5 volt to +5 volt. Both the I channel (blue curve) and the Q channel (red curve) are plotted. PLOTG5 is the similar to PLOTG4, but is designed to work with data produced by a different A to D unit (*Pico* ADC100). Finally, PLOTG6 is similar to PLOTG3, except that the horizontal axis is scaled from -50 ns to 250 ns, assuming 2 ns/sample.

TABLE D.5 PLOTG2

Program Name	PLOTG2
Purpose	plots a PDP graph on screen from 0 dB to -50 dB and from sample 1 to sample 3000 (blue curve), and also an expanded section of the PDP from sample 400 to sample 1000 (magenta curve). Normalised data with 0 dB at sample 500.
Revision date	1/11/94
Input files	.DAT files. Will do a sequence of files
Input file directory	C:\greg\process
Input information	filebase, starting file number, number of files
Output files	.ASC text file for plotting a graph (optional)
Output directory	C:\greg\propgraf

D.2 RAYS, RAYS1, RAYS20

RAYS searches through the entire PDP and identifies all resolvable signal paths or rays. Operating on the  $I^2+Q^2$  PDP, a ray is defined as a localised peak in the curve, where the preceding two samples are monotonically increasing, and the following two samples are monotonically decreasing. This gives a minimum interval between successive peaks or rays, of four sample intervals. Indoor measurements (chip rate 100 MHz) with a theoretical resolution of 10 ns have been recorded at 2 ns/sample, so four sample intervals equals 8 ns, while outdoor measurements (chip rate 25 MHz) with a theoretical resolution of 40 ns have been done at 10 ns/sample, and four sample intervals equals 40 ns. On the assumption that the first and last sections of the data file are likely to be noise, the linear power average of the first 100 samples is calculated, and this is also done for the last 100 samples. The lower of the two power averages is taken as a “noise floor”. An arbitrary noise floor threshold of five times the noise floor (or 6.9 dB greater) is used to allow for impulsive noise, and any power sample less than this threshold is set to zero. A higher threshold can be added when the program is run.

D.2.1 .PTH File

Each input file produces a **filebaseS.PTH** file, which lists all the “negative” rays (those arriving before normalised time zero) and all the “positive rays” (those arriving after time zero), in terms of normalised time, and normalised power. A coarse histogram of ray parameters follows. Each column is a time bin of width 100 samples, starting at bin-4 and going to bin+6. Bin -4 covers samples  $\geq 100 < 200$ . Column 5 is time bin+1, which covers  $> 500 < 600$  and omits the normalised zero time 0 dB ray. Row 1 covers the power bin of  $\geq -5\text{dB}$ , row 2 covers  $< -5\text{dB} \geq -10\text{dB}$ , row 3 covers  $< -10\text{dB} \geq -15\text{dB}$ , and row 4 covers

$< -15\text{dB} \geq -20\text{dB}$ , all relative to the strongest ray which is normalised to 0dB. This is followed by a table which sorts rays into amplitude bins, irrespective of time, where each bin is 5 dB wide. The final table sorts rays into time bins, irrespective of amplitude, where each bin is 100 samples wide, that is 200 ns for 2 ns/sample, or 1 us wide for 10 ns/sample. Note that RAYS20 does not produce .PTH files.

## D.2.2 .RAY File

**filebase.RAY** summarises ray powers for each file, without regard to excess delay. Each row of data represents one PDP file. All power levels are normalised so the strongest ray is 0 dB. The first 6 columns give the number of rays  $\geq -5$  dB,  $\geq -10$  dB,  $\geq -15$  dB,  $\geq -20$  dB,  $\geq -25$  dB,  $\geq -30$  dB respectively.

The second 6 columns give the number of rays between the power intervals of  $\leq 0$  to  $\geq -5$  dB,  $< -5$  to  $\geq -15$  dB,  $< -15$  to  $\geq -25$  dB,  $< -20$  to  $\geq -25$  dB,  $< -25$  to  $\geq -30$  dB respectively.

## D.2.3 .STS File

**filebase.STS** is a summary of statistics for all input files, in a table with 16 rows and 6 columns. Row 6 represents the strongest ray, with all quantities for this ray normalised to zero. Row 5 represents the first “negative” ray, that is, the first ray adjacent to, but arriving before, the strongest ray. Moving further into negative time, the next resolvable ray is called the second “negative ray”, and is summarised in row 3. Rows 1 and 2 give data for the 5th. and 4th. negative rays. Row 7 has data for the first “positive” ray (the first resolvable ray arriving after the strongest ray), and the remaining rows cover the next nine “positive” rays.

The first column is the standard deviation of the excess delay for all rays of the same type, e.g. first “positive” ray, across all the input files. Column 2 is the average excess delay, and column 3 the average power in dB (where the linear normalised powers of all the individual rays of the same type are averaged then converted to a dB value).

Column 4 is equal to column 3 plus 25 dB. Columns 5 and 6 give standard deviation values for ray power, calculated two different ways:

### Column 5:

$$\text{standard deviation in dB} = 10 \cdot \log_{10} \cdot \left( 1 + \frac{\text{linear power standard deviation}}{\text{linear power mean}} \right) \quad (\text{EQ D.1})$$

### Column 6:

$$\text{standard deviation in dB} = 10 \cdot \log_{10} \cdot (\text{linear power standard deviation}) \quad (\text{EQ D.2})$$

TABLE D.6 RAYS

Program Name	RAYS
Purpose	identifies and sorts rays in the PDP
Revision date	13/1/97
Input files	filebaseS.DAT      (S is the file number)      skips missing files limited to a maximum of 200 files
Input file directory	*:\greg\process      * means specify drive letter
Input information	filebase, start number, final number, sample time(nS), ray threshold relative to 0dB (-dB)
Output files	filebaseS.PTH   list of rays in each PDP filebase.PKE filebase.PT   average and std.dev of times for positive rays filebase.PA   average and std.dev of amplitudes for positive rays filebase.NT   average and std.dev of times for negative rays filebase.NA   average and std.dev of amplitudes for negative rays filebase.STS   summary of ray statistics filebase.RAY   summary of numbers of rays above various power thresholds, and between power thresholds, for each file.
Output directory	*:\greg\rays

D.2.4 Example of a filebaseS.PTH Output File

positive rays		negative rays	
TIME	Power	TIME	Power
us	dB	us	dB
0.000	0.0	0.016	-2.4
0.016	-3.4	-0.094	-35.8
0.032	-6.6	0.162	-35.3
0.048	-4.9	-0.188	-38.9
0.074	-5.6	0.460	-36.3
0.098	-13.4	-0.542	-37.9
0.142	-7.0	-0.686	-33.6
0.190	-29.4	-0.702	-33.2
0.228	-16.9	-0.786	-33.0
0.260	-20.8	-0.824	-28.1
0.288	-19.6	-0.840	-27.3
0.324	-18.7	-0.854	-28.6
0.354	-29.7	-0.870	-33.4
0.378	-19.9	-0.884	-37.2
0.394	-25.5	-0.940	-37.0
0.418	-37.0	-0.958	-32.7
0.438	-32.5		
0.492	-34.9		
0.528	-32.8		
0.828	-36.0		
0.844	-32.2		
0.942	-28.0		
0.954	-27.6		
0.974	-28.2		
1.028	-37.0		
1.066	-35.0		
1.082	-35.6		
1.330	-37.1		
1.386	-37.0		
1.906	-35.9		
3.440	-37.9		

0	0	0	1	2	0	0	0	0	0
0	0	0	0	3	0	0	0	0	0
0	0	0	0	1	0	0	0	0	0
0	0	0	0	0	4	0	0	0	0

this is a coarse histogram of ray parameters. Each column is a time bin of width 100 samples, starting at bin-4 and going to bin+6. Bin-4 covers samples  $\geq 100 < 200$  and going to bin+6. Bin-4 covers samples  $\geq 100 < 200$  and going to bin+6. Bin-4 covers samples  $\geq 100 < 200$  and going to bin+6. Column 5 is time bin+1, which covers  $> 500 < 600$  and omits the normalised zero time 0 dB ray. Row 1 covers the power bin of  $\geq -5$ dB, row 2 covers  $< -5$ dB  $\geq -10$ dB, row 3 covers  $< -10$ dB  $\geq -15$ dB, and row 4 covers  $< -15$ dB  $\geq -20$ dB, all relative to the strongest ray which is normalised to 0dB.

no.paths > -5dB = 4  
no.paths > -10dB = 3  
no.paths > -15dB = 1  
no.paths > -20dB = 4  
no.paths > -25dB = 1  
no.paths > -30dB = 9

sorts rays into amplitude bins, irrespective of time, where each bin is 5 dB wide.

no.paths in time bin -1 = 1  
no.paths in time bin +1 = 7  
no.paths in time bin +2 = 7  
no.paths in time bin +3 = 0  
no.paths in time bin +4 = 0  
no.paths in time bin +5 = 3  
no.paths in time bin +6 = 0  
no.paths in time bin +7 = 0  
no.paths in time bin +8 = 0  
noise floor = -39.14 dB

sorts rays into time bins, irrespective of amplitude, where each bin is 100 samples wide, that is 200 ns for 2 ns/sample, or 1 us wide for 10 ns/sample.

Filename c:\greg\rays\db71.pth

### D.2.5 Example of a filebase.PKE Output File

0	0	0	50	114	0	0	0	0	0
0	0	0	36	213	0	0	0	3	0
2	0	4	17	305	3	0	0	26	0
9	15	29	29	340	35	3	5	49	5

this is a coarse histogram of ray parameters. Each column is a time bin of width 100 samples, starting at bin-4 and going to bin+6. Bin-4 covers samples  $\geq 100 < 200$ . Column 5 is time bin+1, which covers  $> 500 < 600$  and omits the normalised zero time 0 dB ray. Row 1 covers the power bin of  $\geq -5$ dB, row 2 covers  $< -5$ dB $\geq -10$ dB, row 3 covers  $< -10$ dB $\geq -15$ dB, and row 4 covers  $< -15$ dB $\geq -20$ dB, all relative to the strongest ray which is normalised to 0dB.

0.00	0.00	0.00	0.29	0.65	0.00	0.00	0.00	0.00	0.00
0.00	0.00	0.00	0.21	1.22	0.00	0.00	0.00	0.02	0.00
0.01	0.00	0.02	0.10	1.74	0.02	0.00	0.00	0.15	0.00
0.05	0.09	0.17	0.17	1.94	0.20	0.02	0.03	0.28	0.03

this is a repeat of the above table, but with each figure divided by the number of files.

no.paths > -5dB = 338  
no.paths > -10dB = 252  
no.paths > -15dB = 362  
no.paths > -20dB = 638  
no.paths > -25dB = 977  
no.paths > -30dB = 1226

no.paths in time bin -1 = 206  
no.paths in time bin +1 = 1395  
no.paths in time bin +2 = 334  
no.paths in time bin +3 = 34  
no.paths in time bin +4 = 20  
no.paths in time bin +5 = 332  
no.paths in time bin +6 = 25  
no.paths in time bin +7 = 21  
no.paths in time bin +8 = 34

### D.2.6 Example of Part of a filebase.RAY Output File

2	4	8	11	23	25	2	2	4	3	12	2
2	7	11	18	47	47	2	5	4	7	29	0
2	5	8	16	36	38	2	3	3	8	20	2
3	5	5	13	41	41	3	2	0	8	28	0
1	4	5	11	33	56	1	3	1	6	22	23
6	8	11	31	45	45	6	2	3	20	14	0
3	6	10	35	40	40	3	3	4	25	5	0
3	5	6	23	28	28	3	2	1	17	5	0
1	4	6	18	54	54	1	3	2	12	36	0
2	4	8	34	41	41	2	2	4	26	7	0
4	5	6	15	31	31	4	1	1	9	16	0
2	4	8	17	29	29	2	2	4	9	12	0
2	3	4	6	14	14	2	1	1	2	8	0
6	8	11	31	32	32	6	2	3	20	1	0
2	2	4	7	36	37	2	0	2	3	29	1
3	7	10	34	35	35	3	4	3	24	1	0

filename c:\greg\rays\db7.ray

Each row of data represents one PDP file. The first 6 columns give the number of rays  $\geq -5$  dB,  $\geq -10$  dB,  $\geq -15$  dB,  $\geq -20$  dB,  $\geq -25$  dB,  $\geq -30$  dB. The second 6 columns give the number of rays between the power intervals of  $\leq 0$  to  $\geq -5$  dB,  $< -5$  to  $\geq -15$  dB,  $< -15$  to  $\geq -25$  dB,  $< -20$  to  $\geq -25$  dB,  $< -25$  to  $\geq -30$  dB respectively. Any ray with power less than the “noise floor” is ignored. Apart from this, all rays are counted; the threshold level specified does not apply for this output file.



D.2.7 Example of a filebase.STS Output File

Time std.dev. us	Time average us	Power average dB	Power avg+25dB dB	Power std.dev std.dev	Power std.dev relative	
0.192	-0.562	-15.1	9.9	2.7	-15.8	fifth "negative" ray
0.238	-0.415	-17.5	7.5	1.6	-21.1	fourth "negative" ray
0.256	-0.280	-11.8	13.2	3.8	-10.4	third "negative" ray
0.137	-0.114	-7.8	17.2	3.9	-6.1	second "negative" ray
0.109	-0.066	-5.4	19.6	3.0	-5.5	first "negative" ray
0.000	0.000	00.0	25.0	0.0	0.0	strongest ray (normalised to time=0, power=0 dB)
0.007	0.021	-5.0	20.0	2.5	-6.0	first "positive" ray
0.088	0.050	-8.2	16.8	3.3	-7.7	second "positive" ray
0.121	0.080	-9.8	15.2	3.2	-9.4	third "positive" ray
0.220	0.124	-11.5	13.5	3.7	-10.2	fourth "positive" ray
0.597	0.271	-12.6	12.4	4.5	-10.1	fifth "positive" ray
0.612	0.356	-13.6	11.4	3.3	-12.9	sixth "positive" ray
0.753	0.434	-15.0	10.0	3.1	-14.8	seventh "positive" ray
0.486	0.461	-14.9	10.1	3.2	-14.5	eighth "positive" ray
0.834	0.705	-14.9	10.1	2.6	-15.7	ninth "positive" ray
1.318	1.231	-16.0	9.0	3.1	-15.8	tenth "positive" ray
filename c:\greg\rays\db7.sts						
actual number of files = 175						

D.2.8 Example of part of a filebase.PA Output File

-6.8	-4.4	-5.7	-7.7	-2.6	-10.4	-14.8	-15.8	-19.0	-19.8	first 10 "positive" rays for file 166
-5.5	-13.6	-15.9	-19.5	-16.1	-17.1	-17.4	-19.2	-16.7	-15.2	first 10 "positive" rays for file 167
-16.7	-6.6	-12.6	-15.4	-10.6	-9.4	-17.6	-16.4	-18.7	-20.0	etc.
-7.0	-12.7	-13.0	-2.3	-16.6	-17.6	-19.3	-18.6	-19.9	-17.1	
-1.8	-14.4	-8.6	-16.1	-17.3	-17.3	-17.2	-18.9	-17.9	-18.7	
-12.1	-18.7	-9.8	-11.3	-13.4	-17.2	-19.8	-19.3	-12.0	-19.0	
-6.5	-18.2	-13.4	-20.0	0.0	0.0	0.0	0.0	0.0	0.0	
-3.7	-8.7	-11.9	-6.5	-1.6	-4.5	-15.2	-15.8	-13.6	-16.4	
-1.7	-14.5	-16.3	-10.9	-16.5	0.0	0.0	0.0	0.0	0.0	
-3.2	-0.9	-12.3	-6.2	-7.2	-6.3	-6.7	-18.6	-15.6	-15.7	first 10 "positive" rays for file 175
-5.0	-8.2	-9.8	-11.5	-12.6	-13.6	-15.0	-14.9	-14.9	-16.0	average power for all files
2.5	3.3	3.2	3.7	4.5	3.3	3.1	3.2	2.6	3.1	standard deviation of power for all files
-6.0	-7.7	-9.4	-10.2	-10.1	-12.9	-14.8	-14.5	-15.7	-15.8	relative standard deviation of power for all files
-6.8	-10.5	-11.9	-13.8	-15.1	-15.3	-16.4	-16.3	-16.0	-17.1	
4.5	4.6	4.3	4.2	3.9	3.6	3.1	3.2	2.9	2.7	
0.989	0.989	0.949	0.870	0.797	0.638	0.452	0.288	0.186	0.124	
filename c:\greg\rays\db7.pa										
actual number of files = 175										

### D.2.9 Example of Part of a filebase.PT Output File

0.020	0.030	0.040	0.072	0.090	0.108	0.134	0.154	0.308	0.454	first 10 "positive" rays for file 166
0.010	0.078	0.106	0.114	0.166	0.368	0.828	1.696	1.712	2.244	first 10 "positive" rays for file 167
0.020	0.030	0.044	0.056	0.068	0.084	0.106	0.154	0.616	3.038	etc.
0.018	0.050	0.058	0.078	0.114	0.140	0.186	0.600	1.122	1.224	(NOTE: all times in $\mu$ s)
0.010	0.028	0.038	0.052	0.072	0.090	0.104	0.250	0.812	3.026	
0.024	0.036	0.058	0.084	0.122	0.302	0.374	0.756	0.972	1.592	
0.024	0.040	0.092	0.104	0.000	0.000	0.000	0.000	0.000	0.000	
0.012	0.028	0.042	0.054	0.066	0.080	0.110	0.136	0.146	0.264	
0.028	0.064	0.072	0.088	0.118	0.000	0.000	0.000	0.000	0.000	
0.018	0.030	0.044	0.060	0.084	0.112	0.120	0.220	0.292	0.306	first 10 "positive" rays for file 175
0.021	0.050	0.080	0.124	0.271	0.356	0.434	0.461	0.705	1.231	average times for each ray
0.007	0.088	0.121	0.220	0.597	0.612	0.753	0.486	0.834	1.318	standard deviation for each ray
filename c:\greg\rays\db7.pt										
actual number of files = 175										

### D.2.10 Example of Part of a filebase.NA Output File

-19.5	-19.4	-19.1	0.0	0.0	file 166, power of first 5 "negative" rays
-1.4	-2.4	-5.3	-19.0	-18.5	file 166, power of first 5 "negative" rays
-5.7	-20.0	-19.3	-16.4	0.0	etc.
-9.1	-12.0	-19.3	-17.1	-10.6	
-2.9	-0.9	-15.8	-19.7	0.0	
-6.3	-0.7	-17.9	0.0	0.0	
-2.4	0.0	0.0	0.0	0.0	
-3.1	-4.9	-19.8	-17.8	-16.6	
-18.4	0.0	0.0	0.0	0.0	
-15.5	-15.0	-17.4	-14.1	-14.5	file 175, power of first 5 "negative" rays
-5.4	-7.8	-11.8	-17.5	-15.1	average power for all files
3.0	3.9	3.8	1.6	2.7	standard deviation of power for all files
-5.5	-6.1	-10.4	-21.1	-15.8	relative standard deviation of power for all files
-8.9	-12.7	-15.2	-17.8	-16.3	
6.6	6.7	5.0	1.6	3.0	
0.616	0.232	0.107	0.056	0.034	
filename c:\greg\rays\db7.na					
actual number of files = 175					

D.2.11 Example of Part of a filebase.NT Output File

-0.238 -0.400 -0.728 0.000 0.000

-0.014 -0.036 -0.044 -0.334 -0.786

-0.014 -0.116 -0.514 -0.714 0.000

-0.028 -0.042 -0.166 -0.224 -0.288

-0.028 -0.052 -0.066 -0.822 0.000

-0.020 -0.034 -0.238 0.000 0.000

-0.008 0.000 0.000 0.000 0.000

-0.020 -0.036 -0.144 -0.244 -0.730

-0.394 0.000 0.000 0.000 0.000

-0.020 -0.100 -0.684 -0.708 -0.718

first 5 "negative" rays for file 166

first 5 "negative" rays for file 167

first 5 "negative" rays for file 168

etc.

(NOTE: all times in  $\mu$ s)

first 5 "negative" rays for file 166

-0.066 -0.114 -0.280 -0.415 -0.562

0.109 0.137 0.256 0.238 0.192

average times for each ray

standard deviation of time for each ray

filename c:\greg\rays\db7.nt  
actual number of files = 175

TABLE D.7 RAYS1

Program Name	RAYS1
Purpose	identifies and sorts rays in the PDP. Based on RAYS but modified to produce a .DMD file with data for trial model.
Revision date	4/2/97
Input files	filebaseS.DAT (S is the file number) skips missing files limited to a maximum of 200 files
Input file directory	*:\greg\process * means specify drive letter
Input information	filebase, start number, final number, sample time(ns), ray threshold relative to 0dB (-dB)
Output files	filebaseS.PTH list of rays in each PDP filebase.PKE filebase.PT average and std.dev of times for positive rays filebase.PA average and std.dev of amplitudes for positive rays filebase.NT average and std.dev of times for negative rays filebase.NA average and std.dev of amplitudes for negative rays filebase.STS summary of ray statistics filebase.RAY filebase.DMD
Output directory	*:\greg\rays

TABLE D.8 RAYS20

Program Name	RAYS20
Purpose	identifies and sorts rays in the PDP. Based on RAYS1 but modified to use the first 10 negative rays (instead of 5), and the first 20 positive rays (instead of 10).
Revision date	27/3/97
Input files	filebaseS.DAT      (S is the file number)      skips missing files limited to a maximum of 170 files
Input file directory	*:\greg\process      * means specify drive letter
Input information	filebase, start number, final number, sample time(nS), ray threshold relative to 0dB (-dB)
Output files	Note: .PTH files are not produced filebase.PKE filebase.PT2   average and std.dev of times for positive rays filebase.PA2   average and std.dev of amplitudes for positive rays filebase.NT2   average and std.dev of times for negative rays filebase.NA2   average and std.dev of amplitudes for negative rays filebase.STS   summary of ray statistics filebase.RAY filebase.DM2
Output directory	*:\greg\rays

D.3 RAYSORT

RAYSORT sorts a number of power delay profiles (PDP) into an array of time and power bins. This allows a three dimensional plot with axes of power, time, and the average number of rays per PDP in each bin.

Input consists of standard .DAT 3000 sample PDP files, and the program looks for these files in the directory \*:\greg\process where the drive letter \* (e.g. C or D) must be specified when the program starts. The input filebase name must be specified, together with the initial file number, and the final file number. A power level threshold must also be specified.

Output consists of a single file called **filebase.SUR** and written to C:\greg\rays. This is a text file in array form with 60 rows and 17 columns. Each row is a time bin, with the first column giving the upper time label in microseconds for that bin. Each time bin covers 50 samples. Thus if samples are in 2ns steps, each time bin is 100ns or 0.1µs, and the first bin covers -1.0µs to -0.9µs. The eleventh bin covers 0 to +0.1µs, and always includes the normalised 0dB ray at zero time for each PDP. There are 60 time bins. Each column after the first represents a power bin in 2dB steps. There are 15 bins ranging from [0dB to -2dB] to [-28dB to -30dB]. The seventeenth column counts all the samples below the threshold or below

-30db, whichever is higher.

TABLE D.9 RAYSORT

Program Name	RAYSORT
Purpose	Identifies rays and sorts these into power and time bins, for a number of normalised PDPs.
Revision date	30/1/97
Input files	filebaseS.DAT      (S is the file number)      skips missing files
Input file directory	*:\greg\process
Input information	filebase, start number, final number, sample time(nS), ray threshold relative to 0dB (-dB)
Output files	filebase.SUR
Output directory	*:\greg\rays

D.4 RAYBIN, RAYBIN1

RAYBIN finds all the rays in a PDP, then sorts these into time bins which are 20 samples wide, and calculates statistics for each time bin. A total of 30 time bins are used, so only the central portion of the PDP is covered.Sorts rays into 20 sample wide time bins, with 10 time bins before zero time, and 20 bins after. RAYBIN also calculates power and time averages and standard deviations for the average ray in each time bin, and the probability of a ray being present in the time bin.

BIN NUMBER	SAMPLES	TIME( $\mu$ s)	TIME( $\mu$ s)	
		2 ns/sample	10 ns/sample	
Time Bin 1	001 to 319	-1.00 to -0.36	-5.00 to -1.80	includes all initial samples
Time Bin 2	320 to 339	-0.36 to -0.32	-1.80 to -2.00	
Time Bin 3	340 to 359	-0.32 to -0.28	-2.00 to -2.20	
Time Bin 4	360 to 379	-0.28 to -0.24	-2.20 to -2.40	
.....	.....	.....	.....	
Time Bin 10	480 to 499	-0.04 to 0.00	-0.20 to 0.00	sample 500 is not included
Time Bin 11	501 to 519	0.00 to 0.04	0.00 to 0.20	
Time Bin 12	520 to 539	0.04 to 0.08	0.20 to 0.40	
.....	.....	.....	.....	
Time Bin 27	820 to 839	0.64 to 0.68	3.20 to 3.40	includes all remaining samples
Time Bin 28	840 to 859	0.68 to 0.72	3.40 to 3.80	
Time Bin 29	860 to 879	0.72 to 0.76	3.80 to 4.00	
Time Bin 30	880 to 3000	0.76 to 5.00	4.00 to 25.00	

- NOTE:
- 1. The normalised 0 dB strongest ray (sample 500) is not included.
  - 2. The first time bin also includes all earlier rays.
  - 3. The last time bin also includes all later rays.
  - 4. Time bins are 40 ns wide for *Indoors*, and 200 ns wide for *Outdoors*.
  - 5. The bins do not overlap; times have been rounded in the above table for simplicity.

### D.4.1 .TBN File

**filebase.TBN** is the output file, and can be used as an input data file for channel modelling programs such as RMSIM20. The file contains one row for each of the 30 time bins, and a row for the zero time normalised 0 dB strongest ray. The first column is the power of the average ray, followed by columns for the standard deviation of power, excess delay time of the average ray, the standard deviation of this delay, and finally, the probability of a ray occurring in the time bin. The probability of ray occurrence is calculated by dividing the total number of rays found in a time bin, by the total number of PDPs. If the “probability” is greater than 1, this means that on average, there is more than one ray per PDP in that particular time bin. Only rays greater than the user specified threshold, or the noise threshold, whichever is greater, are included. If no rays occur in a time bin, the average power is listed as -99 dB.

### D.4.2 RAYBIN1

With RAYBIN, time bins 1 and 30 are “catch-all” bins for all rays outside the time bin range. If many such rays exist, the average power in bins 1 and 30 can be high. RAYBIN1 covers a wider section of the PDP by using time bins which are 50 samples wide (100 ns for indoor measurements, and 500 ns for outdoor measurements). The 10 negative time bins now cover all the samples in the negative time region, and the 20 positive bins cover to an excess delay of 2  $\mu$ s (indoor), or 10  $\mu$ s (outdoor). Time bin 30 is still a catch-all bin for all further rays. The output file has the same form as the .TBN files, but uses a different extension, **filebase.TBC**

TABLE D.10 RAYBIN

Program Name	RAYBIN
Purpose	Sorts rays into 20 sample wide time bins, with 10 time bins before zero time, and 20 bins after. Calculates power and time averages and standard deviations for the average ray in each time bin, and the probability of a ray being present in the time bin.
Revision date	29/4/97
Input files	filebaseS.DAT            (S is the file number)   skips missing files
Input file directory	*:\greg\process            * means specify drive letter
Input information	filebase, start number, final number, sample time(ns), ray threshold relative to 0dB (-dB)
Output files	filebase.TBN
Output directory	*:\greg\rays

### D.4.3 Example of a filebase.TBN Output File

-8.4	2.8	-880.8	151.1	1.200	Time bin 1
-10.4	3.1	-340.0	14.7	0.150	Time bin 2
-11.0	2.3	-292.0	10.1	0.300	etc.
-11.3	2.0	-261.0	9.2	0.300	
-8.3	3.3	-216.7	7.7	0.150	
-99.0	0.0	0.0	0.0	0.000	
-14.0	0.0	-135.0	1.0	0.100	
-99.0	0.0	0.0	0.0	0.000	
-5.2	2.8	-61.0	11.8	0.500	
-4.7	2.7	-23.7	6.5	0.700	
0.0	0.0	0.0	0.0	1.0	Zero time 0 dB normalised ray
-5.9	3.4	25.8	7.4	1.150	
-7.8	3.4	56.8	11.2	1.100	
-10.9	2.5	94.0	10.7	0.650	
-12.5	0.8	134.0	9.1	0.250	
-11.1	1.6	182.5	8.2	0.200	
-11.1	2.5	222.0	7.1	0.150	
-11.8	0.4	273.0	1.0	0.100	
-11.5	0.0	284.0	0.0	0.050	
-10.1	3.1	352.0	2.0	0.100	
-13.1	0.0	386.0	0.0	0.050	
-12.3	0.0	408.0	0.0	0.050	
-11.7	0.0	448.0	0.0	0.050	
-99.0	0.0	0.0	0.0	0.000	
-99.0	0.0	0.0	0.0	0.000	
-99.0	0.0	0.0	0.0	0.000	
-9.8	2.1	626.0	8.2	0.200	
-8.9	4.1	659.5	13.1	0.400	
-10.4	2.0	698.2	11.5	0.650	
-10.7	2.5	742.0	7.3	0.350	
-8.8	3.7	959.4	70.9	3.350	Time bin 30
filename c:\greg\rays\dba5.tbn					
actual number of files = 20					

**NOTE:** Column 1 is average power in dB  
Column 2 is the standard deviation of power  
Column 3 is the average excess delay  
Column 4 is the standard deviation of excess delay  
Column 5 is the probability of a ray occurring in the time bin

### D.5 ELIPSE

ELIPSE operates on a batch of files, to calculate the maximum above-threshold excess delay half path length in metres for each file. The threshold is specified in dB relative to the strongest ray in the PDP. Standard .DAT input files are used. The output text file lists the input file number, the amplitude of the strongest ray in dBV, the maximum excess delay in ns, and the maximum half excess path in metres. The transmitter and receiver positions form the foci of the scattering ellipse. Knowing these positions, and the half excess path, the scattering ellipse can be plotted.

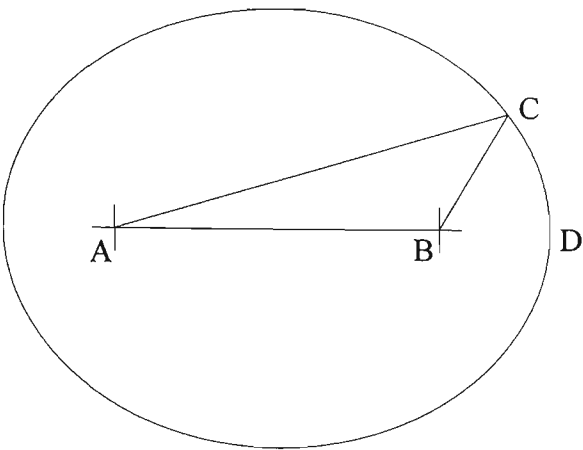


FIGURE E.1 Maximum excess delay scattering ellipse

In Figure E.1, if the transmitter is located at A, with the receiver at B, the shortest path is AB. If the maximum above-threshold path length is  $AC+CB=AD+DB$ , the maximum above-threshold half excess path is BD. Knowledge of the positions of A and B (the foci of the ellipse) and the length BD which locates a point on the ellipse, uniquely defines the ellipse.

TABLE D.10A ELIPSE

Program Name	ELIPSE
Purpose	examines PDPs and finds the first and last above-threshold rays, in effect finding the maximum excess delay for the threshold used. From this the half excess path length in metres is calculated, providing data to plot the maximum excess delay scattering ellipse.
Revision date	27/7/98
Input files	.DAT files. Will do a sequence of files, skips missing files
Input file directory	* :\\greg\\process
Input information	hard drive letter *, filebase, starting file number, final file number, sample time (ns), path threshold relative to 0 dB (dB)
Output files	filebase.ELI, a text file listing file number, strongest ray (dBV), maximum excess delay (ns) and half excess path (metre)
Output directory	* :\\greg\\area

D.1 RMSIM Family

Includes RMSIM(14/1/97), RMSIM2(25/1/97), RMSIM20(28/3/97), RMSIM20A(29/3/97), RMSIM20B(29/3/97), RMSIM20T(1/5/97).

These programs take summarised statistics obtained from measured PDPs (such as produced by RAYS1, RAYS20, RAYBIN and RAYBIN1) and attempt to randomly generate a large number of typical PDPs. If this approach was valid, the cumulative distribution of *rms*



*delay spread* from a large number of simulated PDPs would be expected to match that obtained from a large number of measured results. Many assumptions are built into the simulation programs. Average rays are assumed to have a log normal power distribution, and a normal excess delay distribution. Mean power, and the standard deviation of power, and mean delay and the associated standard deviation, form the input data for random normal distribution generators to produce a ray. Repeating this for the sequence of average rays, or alternatively the average ray from each time bin, produces a Monte Carlo simulation of a PDP. Each ray produced this way is retained or discarded corresponding to the probability of occurrence obtained from the measured data. The *rms delay spread*, and the *average delay*, are then calculated for the simulated PDP. Repeating this a large number of times allows a distribution of simulated *rms delay spreads* to be obtained.

RMSIM2 results from modifying RMSIM so that after the 0 dB ray has been reached, if a ray is discarded by the probability test, no further rays are generated. The procedure called *Delays* used in RMSIM is replaced by a version called *Delays2*. Further versions are summarised in Table 13.

Attempts to use these methods to generate simulated power delay profiles based on statistically condensed parameters derived from measurements were unsuccessful, in the sense that the cumulative distribution function of *rms delay spreads* of simulated PDPs did not give a good match with the distribution of measured delay spreads.

TABLE D.11 SUMMARY OF SIMULATION PROGRAMS

Version	Output Files	Description (unless otherwise noted, changes flow through to later versions)
RMSIM		the original simulation algorithm
RMSIM2	.MC2 .MO2	modified so that following the first positive ray that fails the probability test, all higher number positive rays are set to zero i.e. neglected
RMSIM3	.MC3 .MO3	Works back from positive ray 10 (the ray with the highest delay), until a positive ray is found which passes both the threshold and probability test. Then only earlier rays than this are used in the delay calculations
RMSIM4	.MC4 .MO4	Positive rays are treated as for RMSIM3. To find the first ray, the search is started at the first arriving (i.e. furthest removed from zero time) negative ray, moving forward in time until a ray is found which passes the threshold and probability tests. This is then designated as the first ray, and mean delay and rms delay spread are calculated from this point.
RMSIM20	.MC5 .MO5	Based on 10 negative rays and 20 positive rays
RMSIM20A	.MC5 .MO5	Removes the restriction which prevented simulated negative rays crossing into the positive area, and simulated positive rays moving into the negative area.
RMSIM20B	.MC5 .MO5	Removed the code which neglects further rays once a zero probability ray is found. Otherwise this is the same as RMSIM20B
RMSIM20T	.MC5 .MO5	Based on RMSIM20B, but uses rays data obtained by sorting rays into time bins (data from RAYBIN program). When choosing the first ray to use as the reference for excess delay, probability as well as threshold is considered.

TABLE D.12 RMSIM2

Program Name	RMSIM2 series
Purpose	Uses a Monte Carlo method, using simplified statistics from measured data, to simulate a large number of PDPs.
Revision date	25/1/97
Input files	.DMD, .DM2, .TBN, or .TBC
Input file directory	specified by user
Input information	name for output files
Output files	.MTC power and time for each ray in each simulated PDP .MOD mean delay and rms delay spread for each simulated PDP
Output directory	*:/raymodel * means specify drive letter

## D.2 RAKE Family

This group of *Turbo Pascal* programs and MATLAB scripts allows measured propagation data to be filtered to various narrower RF bandwidths, effectively creating power delay profiles measured with a series of narrower bandwidth channel sounders.

The application of this software is described in detail in Chapter 6.

Power delay profiles are searched to identify all resolvable rays, and then the ratio of the power available in the first  $n$  rays ( $n$  ranging from 1 to 10) to the total power, is calculated. Different versions use either a 3rd order Butterworth filter, or two passes through a 2nd order Butterworth filter using the MATLAB *filtfilt* function. In all cases, the data is padded with leading and trailing zero samples, then following the filtering process the peak value of the PDP is realigned with sample 500, to remove time delays introduced by the filter.

The following tables (TABLES D.14 to D.25) summarise the properties of the RAKE software.

TABLE D.13 RAKE Turbo Pascal FILES SUMMARY

Name	Output Files	Description
BINFILE	.PDP	calculates the PDP $I^2 + Q^2$ from .DAT files, and saves the result in a binary file.
BINFILEM	.SGL	calculates the voltage delay profile $\sqrt{I^2 + Q^2}$ and stores the result in an output file using Turbo Pascal single precision, where each real number uses 4 bytes.
RAKE	.DES .RKE	sorts rays in a PDP into descending order of power, then calculates the total PDP ray power, and the proportion of total power used if 1, 2, 3,.....9, 10 times are used
RAKEMAT	.DES .RKE	processes single precision .FLT filtered files produced by MATLAB and sorts rays in a PDP into descending order of power, then calculates the total PDP ray power, and the proportion of total power used if 1, 2, 3,.....9, 10 times are used.
RAKE-MATX	.RKE	based on RAKEMAT, except that .DES files are not produced, and it will cope with PDPs where the total number of rays < 10
RAKE-MATC	.RKE	modified from RAKEMATX to read files with extension .FIQ produced by MATLAB when filtering I and Q values separately.
ASCMAT	.ASC	takes files with an optional extension (e.g. .FLT or .FIQ) containing $\sqrt{I^2 + Q^2}$ values written in Turbo Pascal single precision real numbers (4 bytes/number) or the equivalent MATLAB float precision, and produces normalised PDP values in an ASCII file suitable for graph plotting.

**TABLE D.14 MATLAB SCRIPTS SUMMARY**

Name	Output Files	Description
gtmfilt.m	.FLT	filters voltage delay profiles with 3rd order Butterworth filter using cutoff frequencies of 0.625, 1.25, 2.5, 4, 8 MHz.
gtmdata.m	.FIQ	filters I and Q samples separately, using a 3rd order Butterworth filter and cutoff frequencies of 0.625, 1.25, 2, 4, 8 MHz.
gtmdatff.m	.FIQ	filters I and Q samples separately, using a 2nd order Butterworth filter and the filtfilt function, effectively giving a 4th order filter. Cutoff frequencies of 0.625, 1.25, 2, 4, 8 MHz. are used.
gtmclean.m	.FIQ	applies a user-specified threshold to the PDP, then filters I and Q samples separately, using a 2nd order Butterworth filter and the filtfilt function, effectively giving a 4th order filter. Cutoff frequencies of 0.625, 1.25, 2, 4, 8 MHz. are used.
gtmhires.m	.FIQ	version of gtmclean.m for indoor measurements, with filter cutoff frequencies of 2.5, 5, 8, 16, 32 MHz.

**TABLE D.15 BINFILEM**

Program Name	BINFILEM
Purpose	calculates the voltage delay profile $\sqrt{I^2 + Q^2}$ and stores the result in a binary output file using Turbo Pascal single precision, where each real number is stored in 4 bytes. This format can be read correctly by MATLAB (Turbo Pascal real numbers normally use 6 bytes/number, and this format cannot be used by MATLAB version 4)
Revision date	21/2/97
Input files	filebaseS.DAT S is the file number (skips missing files)
Input file directory	*:\greg\process * means specify drive letter
Input information	filebase, starting file number, final file number, disc drive letter
Output files	filebaseS.SGL
Output directory	*:\greg/bin

TABLE D.16 RAKE

Program Name	RAKE
Purpose	sorts rays in a PDP into descending order of power, then calculates the total PDP ray power, and the proportion of total power used if 1, 2, 3,.....9, 10 tines are used  copes with a total number of rays less than 10  the threshold value is applied to the .RKE file, but not to the .DES files
Revision date	24/2/97
Input files	filebaseS.DAT    S is the file number    (skips missing files)
Input file directory	*:\greg\process                      * means specify drive letter
Input information	filebase, starting file number, final file number, disc drive letter sample time (ns), path threshold relative to 0 dB
Output files	filebaseS.DES    list of power and times for each ray, for each PDP filebase.RKE    power ratio verses number of tines used
Output directory	*:\greg\rake

TABLE D.17 RAKEMATX

Program Name	RAKEMATX
Purpose	processes single precision .FLT filtered files produced by MATLAB and sorts rays in a PDP into descending order of power, then calculates the total PDP ray power, and the proportion of total power used if 1, 2, 3,.....9, 10 tines are used. Note that .DES files are not produced, and it will cope with PDPs where the total number of rays < 10
Revision date	26/2/97
Input files	NfilebaseS.FLT    N relates to the filter cutoff frequency input files are generated by MATLAB using gtmfilt.m
Input file directory	*:\greg\bin
Input information	filebase, starting file number, final file number, disc drive letter sample time (ns), path threshold relative to 0 dB
Output files	Nfilebase.RKE    N relates to the filter cutoff frequency Note: .DES files are not produced
Output directory	*:\greg\rake

TABLE D.18 RAKEMATC

Program Name	RAKEMATC
Purpose	modified from RAKEMATX to read files with extension .FIQ produced by MATLAB when filtering I and Q values separately.
Revision date	16/8/97
Input files	NfilebaseS.FIQ N relates to the filter cutoff frequency and S is the file number input files are generated by MATLAB using either gtmdata.m, gtmdataff.m, gtmclean.m, or gtmhires.m
Input file directory	*:\greg\bin
Input information	filebase, starting file number, final file number, disc drive letter sample time (ns), path threshold relative to 0 dB
Output files	Nfilebase.RKE N relates to the filter cutoff frequency Note: .DES files are not produced
Output directory	*:\greg\rake

TABLE D.19 ASCMAT

Program Name	ASCMAT
Purpose	takes files with an optional extension (e.g. .FLT or .FIQ) containing $\sqrt{I^2 + Q^2}$ values written in Turbo Pascal single precision real numbers (4 bytes/number) or the equivalent MATLAB float precision, and produces normalised PDP values in an ASCII file suitable for graph plotting time values (us) are in column 1, power values (dB) in column 2
Revision date	24/2/97
Input files	NfilebaseS.* N relates to the filter cutoff frequency and S is the file number
Input file directory	*:\greg\bin
Input information	filebase, starting file number, final file number, disc drive letter
Output files	filebaseS.ASC
Output directory	*:\greg\ascii

TABLE D.20 gtmfilt.m (MATLAB script)

Program Name	gtmfilt.m
Purpose	filters voltage delay magnitude profiles with 3rd order Butterworth filter using cutoff frequencies of 0.625, 1.25, 2.5, 4, 8 MHz.
Revision date	26/2/97
Input files	filebaseS.SGL    S is the file number    (skips missing files)
Input file directory	C:\greg\bin
Input information	filebase, starting file number, final file number
Output files	NfilebaseS.FLT        S is the input file number N=1 filter cutoff frequency of 0.625 MHz, RF bandwidth 1.25 MHz N=2 filter cutoff frequency of 1.25 MHz, RF bandwidth 2.5 MHz N=3 filter cutoff frequency of 2.5 MHz, RF bandwidth 5.0 MHz N=4 filter cutoff frequency of 4.0 MHz, RF bandwidth 8.0 MHz N=5 filter cutoff frequency of 8.0 MHz, RF bandwidth 16 MHz
Output directory	C:\greg\bin

TABLE D.21 gtmdata.m (MATLAB script)

Program Name	gtmdata.m
Purpose	filters I and Q samples separately, using a 3rd order Butterworth filter and cutoff frequencies of 0.625, 1.25, 2, 4, 8 MHz.
Revision date	16/8/97
Input files	filebaseS.DAT    S is the file number    (skips missing files)
Input file directory	C:\greg\process
Input information	filebase, starting file number, final file number
Output files	NfilebaseS.FIQ        S is the input file number N=1 filter cutoff frequency of 0.625 MHz, RF bandwidth 1.25 MHz N=2 filter cutoff frequency of 1.25 MHz, RF bandwidth 2.5 MHz N=3 filter cutoff frequency of 2.0 MHz, RF bandwidth 4.0 MHz N=4 filter cutoff frequency of 4.0 MHz, RF bandwidth 8.0 MHz N=5 filter cutoff frequency of 8.0 MHz, RF bandwidth 16 MHz
Output directory	C:\greg\bin

TABLE D.22 `gtmdatff.m` (MATLAB script)

Program Name	<code>gtmdatff.m</code>
Purpose	filters I and Q samples separately, using a 2nd order Butterworth filter and the <i>filtfilt</i> function, which gives two passes through the 2nd order filter. cutoff frequencies of 0.625, 1.25, 2, 4, 8 MHz. are used.
Revision date	20/8/97
Input files	filebaseS.DAT    S is the file number    (skips missing files)
Input file directory	C:\greg\process
Input information	filebase, starting file number, final file number
Output files	NfilebaseS.FIQ        S is the input file number N=1 filter cutoff frequency of 0.625 MHz, RF bandwidth 1.25 MHz N=2 filter cutoff frequency of 1.25 MHz, RF bandwidth 2.5 MHz N=3 filter cutoff frequency of 2.0 MHz, RF bandwidth 4.0 MHz N=4 filter cutoff frequency of 4.0 MHz, RF bandwidth 8.0 MHz N=5 filter cutoff frequency of 8.0 MHz, RF bandwidth 16 MHz
Output directory	C:\greg\bin

TABLE D.23 `gtmclean.m` (MATLAB script)

Program Name	<code>gtmclean.m</code>
Purpose	applies a user-specified threshold to the PDP, then filters I and Q samples separately, using a 2nd order Butterworth filter and the <i>filtfilt</i> function, which gives two passes through the 2nd order filter. cutoff frequencies of 0.625, 1.25, 2, 4, 8 MHz. are used.
Revision date	26/8/97
Input files	filebaseS.DAT    S is the file number    (skips missing files)
Input file directory	C:\greg\process
Input information	filebase, starting file number, final file number
Output files	NfilebaseS.FIQ        S is the input file number N=1 filter cutoff frequency of 0.625 MHz, RF bandwidth 1.25 MHz N=2 filter cutoff frequency of 1.25 MHz, RF bandwidth 2.5 MHz N=3 filter cutoff frequency of 2.0 MHz, RF bandwidth 4.0 MHz N=4 filter cutoff frequency of 4.0 MHz, RF bandwidth 8.0 MHz N=5 filter cutoff frequency of 8.0 MHz, RF bandwidth 16 MHz
Output directory	C:\greg\bin



TABLE D.24 gtmhires.m (MATLAB script)

Program Name	gtmhires.m
Purpose	applies a user-specified threshold to the PDP, then filters I and Q samples separately, using a 2nd order Butterworth filter and the <i>filtfilt</i> function, which gives two passes through the 2nd order filter. cutoff frequencies of 2.5, 5, 8, 16, 32 MHz. are used, intended for use with high resolution indoor measurements
Revision date	26/8/97
Input files	filebaseS.DAT    S is the file number    (skips missing files)
Input file directory	C:\greg\process
Input information	filebase, starting file number, final file number
Output files	NfilebaseS.FIQ        S is the input file number N=1 filter cutoff frequency of 2.5 MHz, RF bandwidth 5.0 MHz N=2 filter cutoff frequency of 5.0 MHz, RF bandwidth 10.0 MHz N=3 filter cutoff frequency of 8.0 MHz, RF bandwidth 16.0 MHz N=4 filter cutoff frequency of 16.0 MHz, RF bandwidth 32.0 MHz N=5 filter cutoff frequency of 32.0 MHz, RF bandwidth 64.0 MHz
Output directory	C:\greg\bin

---

# Appendix E: Measurement Locations

## E - INTRODUCTION

All outdoor measurement locations are documented in this appendix. In many cases, maps show transmitter and receiver positions for the various measurement sessions.

Often, several impulse response measurements were made in the close vicinity of each nominal receiver position, randomly moving the receiver a few wavelengths between each measurement. Listings document each of these measurements, and also give an indication of the received signal strength, and values for the instantaneous rms delay spread, and for the average delay.

Maps have been scanned from sections of street directory and motoring club maps.

## E.1 Adelaide - Victoria Square

**Transmitter Location:** Victoria Square, in the city centre.  
**Transmitter Antenna:** portable mast, approx. 5m above ground, discone antenna.  
**Receiver:** in a car with halfwave antenna above roof level  
**Sample time:** 10 ns, **Threshold:** -15 dB, **Range:** 25  $\mu$ s

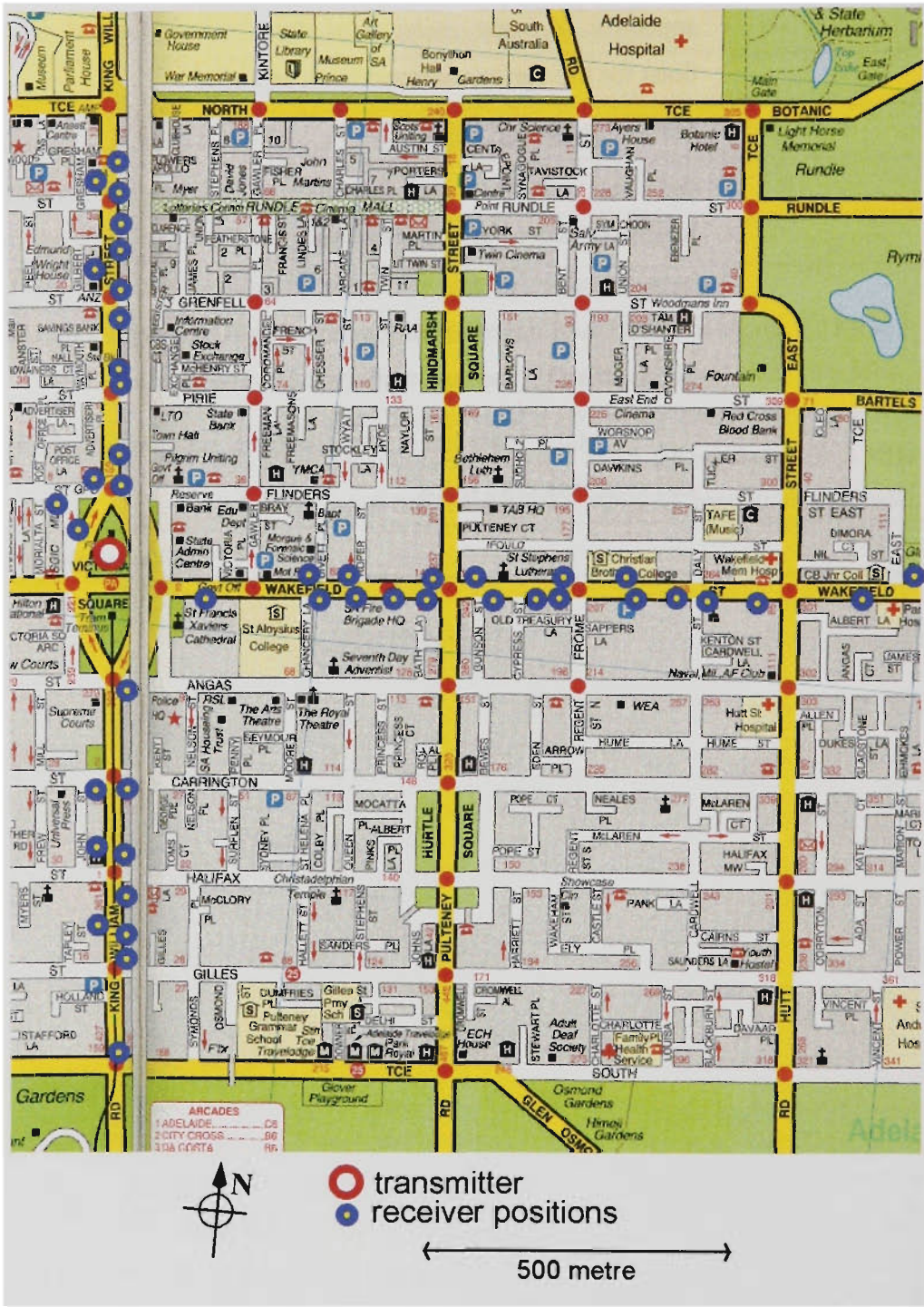


FIGURE E.1 Adelaide - Victoria Square site, showing receiver locations

TABLE E.1 Adelaide - Victoria Square - filebase ad

file	dBV	rms delay (ns)	avg delay (ns)	gain factor (dB)	location of measurement
1	15.5	41	37	-125	Adelaide VicSq pos1 Wakefield opp Chancery La
2	14.9	55	40	-125	Adelaide VicSq pos1 Wakefield opp Chancery La
3	8.7	486	301	-125	Adelaide VicSq pos2 Wakefield Street
4	12.2	80	67	-125	Adelaide VicSq pos2 Wakefield Street
5	2.1	478	463	-125	Adelaide VicSq pos3 Wakefield W of Putney
6	4.0	373	310	-125	Adelaide VicSq pos3 Wakefield W of Putney
7	4.1	627	496	-130	Adelaide VicSq pos4 Wakefield E of Putney
8	1.7	614	607	-130	Adelaide VicSq pos4 Wakefield E of Putney
9	1.3	323	149	-130	Adelaide VicSq pos5 Wakefield W of Frome
10	0.3	437	248	-130	Adelaide VicSq pos5 Wakefield W of Frome
11	1.3	518	277	-130	Adelaide VicSq pos6 Wakefield E of Frome
12	0.6	496	301	-130	Adelaide VicSq pos6 Wakefield E of Frome
13	-1.4	8749	15161	-130	Adelaide VicSq pos7 Wakefield E of East Trc
14	-1.2	8659	15035	-130	Adelaide VicSq pos7 Wakefield E of East Trc
15	2.2	8570	14602	-130	Adelaide VicSq pos8 Wakefield SE East Trc
16	3.6	8685	15395	-130	Adelaide VicSq pos8 Wakefield SE East Trc
17	1.2	8816	14475	-130	Adelaide VicSq pos9 Wakefield SW East Trc
18	0.4	9005	15298	-130	Adelaide VicSq pos9 Wakefield SW East Trc
19	-0.1	873	774	-130	Adelaide VicSq pos10 Wakefield W of Hutt
20	-0.7	712	910	-130	Adelaide VicSq pos10 Wakefield W of Hutt
21	1.4	963	1049	-130	Adelaide VicSq pos11 Wakefield E of Cardwell
22	1.5	888	980	-130	Adelaide VicSq pos11 Wakefield E of Cardwell
23	1.7	932	1350	-130	Adelaide VicSq pos12 Wakefield W of Cardwell
24	3.0	877	636	-130	Adelaide VicSq pos12 Wakefield W of Cardwell
25	-0.0	1313	1031	-130	Adelaide VicSq pos13 Wakefield Street
26	-1.5	1483	1456	-130	Adelaide VicSq pos13 Wakefield Street
27	0.1	1265	1140	-130	Adelaide VicSq pos14 Wakefield SE of Frome
28	-0.6	1303	1029	-130	Adelaide VicSq pos14 Wakefield SE of Frome
29	0.4	625	466	-130	Adelaide VicSq pos15 Wakefield 50m W of Frome
30	1.7	721	756	-130	Adelaide VicSq pos15 Wakefield 50m W of Frome
31	0.6	677	807	-130	Adelaide VicSq pos16 Wakefield SW cnr Cypress
32	0.0	695	581	-130	Adelaide VicSq pos16 Wakefield SW cnr Cypress
33	4.6	496	301	-130	Adelaide VicSq pos17 Wakefield W of Pulteney
34	2.6	658	769	-130	Adelaide VicSq pos17 Wakefield W of Pulteney
35	13.0	37	27	-130	Adelaide VicSq pos18 Wakefield Street
36	10.3	187	92	-130	Adelaide VicSq pos18 Wakefield Street
37	9.4	31	37	-120	Adelaide VicSq pos19 Wakefield opp Roper
38	9.5	26	28	-120	Adelaide VicSq pos19 Wakefield opp Roper
39	12.6	28	29	-120	Adelaide VicSq pos20 Wakefield E of Chancery
40	11.8	151	52	-120	Adelaide VicSq pos20 Wakefield E of Chancery
41	11.4	19	18	-100	Adelaide VicSq pos21 E of King William
42	12.5	19	18	-100	Adelaide VicSq pos21 E of King William
43	3.5	203	222	-120	Adelaide VicSq pos22 SE cnr Angas & King William
44	2.2	291	259	-120	Adelaide VicSq pos22 SE cnr Angas & King William
45	1.2	238	200	-125	Adelaide VicSq pos23 SE cnr Carrington & KingW
46	-2.3	526	478	-125	Adelaide VicSq pos23 SE cnr Carrington & KingW
47	-3.5	797	535	-125	Adelaide VicSq pos24 KingW N of Halifax
48	-5.0	905	636	-125	Adelaide VicSq pos24 KingW N of Halifax
49	1.6	223	137	-125	Adelaide VicSq pos25 KingW S of Halifax
50	4.1	169	72	-125	Adelaide VicSq pos25 KingW S of Halifax
51	2.4	22	24	-125	Adelaide VicSq pos26 KingW N of Gilles
52	0.7	379	111	-125	Adelaide VicSq pos26 KingW N of Gilles
53	-1.9	703	376	-125	Adelaide VicSq pos27 NE cnr KingW & Gilles
54	0.1	667	292	-125	Adelaide VicSq pos27 NE cnr KingW & Gilles
55	-6.9	1249	1834	-125	Adelaide VicSq pos28 in RH turn lane KW at SouthTrc
56	-6.3	1285	1594	-125	Adelaide VicSq pos28 in RH turn lane KW at SouthTrc
57	9.5	1489	984	-130	Adelaide VicSq pos29 W side KW 50m N of Gilbert
58	3.0	1479	1788	-130	Adelaide VicSq pos29 W side KW 50m N of Gilbert
59	9.5	130	75	-130	Adelaide VicSq pos30 W side KW 20m N of Sturt
60	13.4	91	42	-130	Adelaide VicSq pos30 W side KW 20m N of Sturt
61	8.4	882	365	-130	Adelaide VicSq pos31 W side KW 10m S of Wright
62	9.7	234	90	-130	Adelaide VicSq pos31 W side KW 10m S of Wright

TABLE E.1 Adelaide - Victoria Square - filebase ad (continued)

file	dBV	rms delay (ns)	avg delay (ns)	gain factor (dB)	location of measurement
63	0.8	247	122	-100	Adelaide VicSq pos32 W side Victoria Square
64	1.9	162	78	-100	Adelaide VicSq pos32 W side Victoria Square
65	6.9	16	19	-100	Adelaide VicSq pos33 NW of Victoria Square
66	7.2	14	16	-100	Adelaide VicSq pos33 NW of Victoria Square
67	-5.4	295	269	-100	Adelaide VicSq pos34 NW cnr KW & Franklin
68	1.1	94	60	-100	Adelaide VicSq pos34 NW cnr KW & Franklin
69	3.2	51	35	-100	Adelaide VicSq pos34 NW cnr KW & Franklin
70	-1.4	239	186	-130	Adelaide VicSq pos35 KW 20m S of Gilbert Pl
71	-2.0	336	274	-130	Adelaide VicSq pos35 KW 20m S of Gilbert Pl
72	-1.7	73	60	-130	Adelaide VicSq pos36 KW 20m N of Hindley
73	-1.6	61	41	-130	Adelaide VicSq pos36 KW 20m N of Hindley
74	-4.8	343	205	-130	Adelaide VicSq pos37 KW cnr Apollo Pl
75	-1.1	125	90	-130	Adelaide VicSq pos37 KW cnr Apollo Pl
76	-1.2	94	104	-130	Adelaide VicSq pos38 KW NE cnr Rundle Mall
77	1.9	18	22	-130	Adelaide VicSq pos38 KW NE cnr Rundle Mall
78	0.5	43	39	-130	Adelaide VicSq pos38 KW NE cnr Rundle Mall
79	-2.4	304	179	-130	Adelaide VicSq pos39 KW SE cnr Rundle Mall
80	-1.9	332	173	-130	Adelaide VicSq pos39 KW SE cnr Rundle Mall
81	2.0	153	117	-130	Adelaide VicSq pos40 King William St
82	1.9	125	65	-130	Adelaide VicSq pos40 King William St
83	9.4	60	45	-130	Adelaide VicSq pos41 KW NE cnr Grenfell
84	9.7	40	35	-130	Adelaide VicSq pos41 KW NE cnr Grenfell
85	7.9	63	56	-130	Adelaide VicSq pos41 KW NE cnr Grenfell
86	9.9	27	26	-130	Adelaide VicSq pos41 KW NE cnr Grenfell
87	-1.0	321	306	-130	Adelaide VicSq pos42 KW 20m S of Grenfell
88	-1.5	399	336	-130	Adelaide VicSq pos42 KW 20m S of Grenfell
89	11.1	232	168	-130	Adelaide VicSq pos43 KW 40m N of Pirie
90	9.1	273	219	-130	Adelaide VicSq pos43 KW 40m N of Pirie
91	13.6	263	138	-130	Adelaide VicSq pos44 KW 20m N of Pirie
92	9.4	306	211	-130	Adelaide VicSq pos45 NE cnr Pirie & KW
93	9.2	375	303	-130	Adelaide VicSq pos45 NE cnr Pirie & KW
94	9.4	103	59	-120	Adelaide VicSq pos46 KW near Town Hall
95	8.4	112	65	-120	Adelaide VicSq pos46 KW near Town Hall
96	9.6	96	59	-120	Adelaide VicSq pos46 KW near Town Hall
97	8.7	237	127	-120	Adelaide VicSq pos46 KW near Town Hall
98	3.8	14	16	-100	Adelaide VicSq pos47 KW 40m N of Flinders
99	6.3	17	20	-100	Adelaide VicSq pos47 KW 40m N of Flinders
100	5.2	15	17	-100	Adelaide VicSq pos47 KW 40m N of Flinders



## E.2 Adelaide - Hotel Adelaide First Floor

**Transmitter Location:** Hotel Adelaide, Brougham Place, North Adelaide.  
**Transmitter Antenna:** on a boom outside 1st. floor window, facing south. Discone antenna.  
**Receiver:** in a car with halfwave antenna above roof level.  
**Sample time:** 10 ns, **Threshold:** -15 dB, **Range:** 25  $\mu$ s

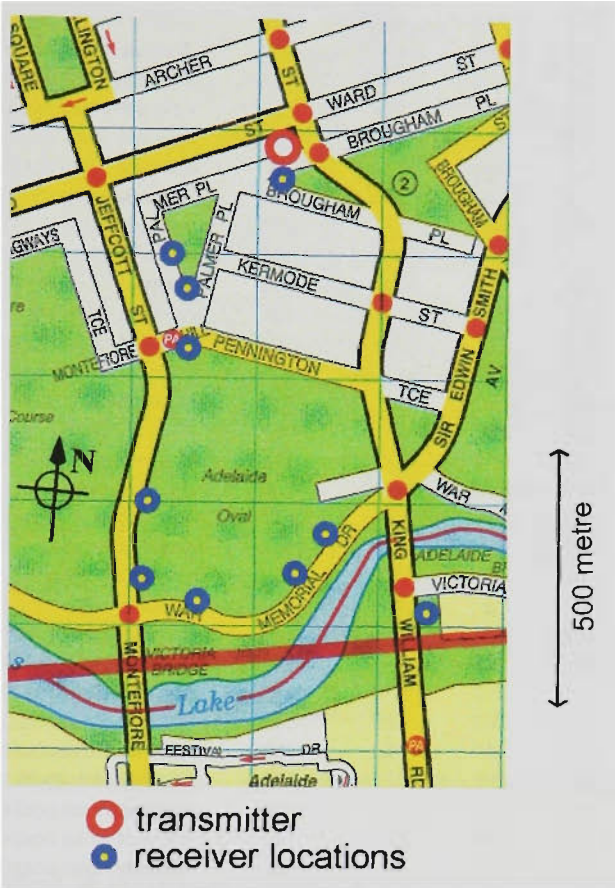


FIGURE E.2 Hotel Adelaide - transmitter on first floor (map 1)

TABLE E.2 Adelaide - Hotel Adelaide first floor - filebase aq

file	dBV	rms delay (ns)	avg delay (ns)	gain factor (dB)	location of measurement
1	8.8	21	22	-90	Adelaide Hotel pos1 Brougham Place
2	7.5	60	37	-90	Adelaide Hotel pos1 Brougham Place
3	1.5	288	397	-130	Adelaide Hotel pos2 Palmer Place
4	2.1	264	361	-130	Adelaide Hotel pos2 Palmer Place
5	-2.5	1381	451	-130	Adelaide Hotel pos3 Palmer 20m N Pennington
6	-0.9	1460	511	-130	Adelaide Hotel pos3 Palmer 20m N Pennington
7	6.4	4841	4385	-130	Adelaide Hotel pos4 Montefiore Hill
8	8.1	4711	3797	-130	Adelaide Hotel pos4 Montefiore Hill
9	5.9	14	18	-130	Adelaide Hotel pos5 Montefiore Rd
10	4.6	12	14	-130	Adelaide Hotel pos5 Montefiore Rd
11	5.1	13	15	-130	Adelaide Hotel pos5 Montefiore Rd
12	5.7	13	15	-130	Adelaide Hotel pos5 Montefiore Rd
13	0.4	53	33	-130	Adelaide Hotel pos6 20m N War Memorial Drv
14	1.1	1366	427	-130	Adelaide Hotel pos6 20m N War Memorial Drv
15	6.2	107	93	-130	Adelaide Hotel pos7 War Memorial Drv
16	6.9	101	92	-130	Adelaide Hotel pos7 War Memorial Drv
17	4.4	43	41	-130	Adelaide Hotel pos8 War Memorial Drv
18	4.7	27	26	-130	Adelaide Hotel pos8 War Memorial Drv

**TABLE E.2 Adelaide - Hotel Adelaide first floor - filebase aq** (continued)

<b>file</b>	<b>dBV</b>	<b>rms delay (ns)</b>	<b>avg delay (ns)</b>	<b>gain factor (dB)</b>	<b>location of measurement</b>
19	6.6	1332	886	-130	Adelaide Hotel pos9 War Mem Drv E Stadium
20	6.5	1389	958	-130	Adelaide Hotel pos9 War Mem Drv E Stadium
21	4.0	1411	1031	-130	Adelaide Hotel pos9 War Mem Drv E Stadium
22	5.8	1492	1266	-130	Adelaide Hotel pos9 War Mem Drv E Stadium
23	1.7	690	4861	-130	Adelaide Hotel pos10 King William S river
24	1.3	743	4844	-130	Adelaide Hotel pos10 King William S river
25	1.6	797	643	-130	Adelaide Hotel pos11 Festival Theatre
26	3.0	771	562	-130	Adelaide Hotel pos11 Festival Theatre
27	2.4	448	294	-130	Adelaide Hotel pos12 KW 30m N North Trc
28	2.4	413	283	-130	Adelaide Hotel pos12 KW 30m N North Trc
29	5.2	207	117	-130	Adelaide Hotel pos13 KW 10m N North Trc
30	4.8	234	115	-130	Adelaide Hotel pos13 KW 10m N North Trc
31	6.7	55	39	-130	Adelaide Hotel pos14 KW 30m S North Trc
32	7.1	51	34	-130	Adelaide Hotel pos14 KW 30m S North Trc
33	6.4	35	29	-130	Adelaide Hotel pos15 King William St
34	6.1	63	43	-130	Adelaide Hotel pos15 King William St
35	6.6	57	30	-130	Adelaide Hotel pos16 NE cnr KW & Rundle
36	7.3	20	22	-130	Adelaide Hotel pos16 NE cnr KW & Rundle
37	3.2	24	21	-130	Adelaide Hotel pos17 King William St
38	1.4	38	41	-130	Adelaide Hotel pos17 King William St
39	-1.2	214	179	-130	Adelaide Hotel pos18 SW cnr KW & Hindley
40	0.4	1121	1000	-130	Adelaide Hotel pos18 SW cnr KW & Hindley
41	6.2	12	14	-130	Adelaide Hotel pos19 Hindley opp Blyth
42	6.9	12	15	-130	Adelaide Hotel pos19 Hindley opp Blyth
43	-0.2	37	179	-130	Adelaide Hotel pos20 Hindley at Rosina
44	0.2	32	172	-130	Adelaide Hotel pos20 Hindley at Rosina
45	4.6	88	54	-130	Adelaide Hotel pos21 Hindley St
46	4.1	100	71	-130	Adelaide Hotel pos21 Hindley St
47	1.5	240	373	-130	Adelaide Hotel pos22 Hindley 10m E Montefiore
48	0.0	273	532	-130	Adelaide Hotel pos22 Hindley 10m E Montefiore
49	5.1	134	150	-130	Adelaide Hotel pos23 Montefiore
50	6.8	126	125	-130	Adelaide Hotel pos23 Montefiore
51	6.5	217	231	-130	Adelaide Hotel pos24 North Trc under Overpass
52	7.2	216	225	-130	Adelaide Hotel pos24 North Trc under Overpass
53	12.0	13	14	-125	Adelaide Hotel pos25 Nth Trc 20m E Montefiore
54	11.0	15	18	-125	Adelaide Hotel pos25 Nth Trc 20m E Montefiore
55	-1.1	138	105	-125	Adelaide Hotel pos26 North Trc Casino
56	-1.3	134	93	-125	Adelaide Hotel pos26 North Trc Casino
57	1.1	183	324	-125	Adelaide Hotel pos27 North Trc Parliament
58	3.2	157	324	-125	Adelaide Hotel pos27 North Trc Parliament

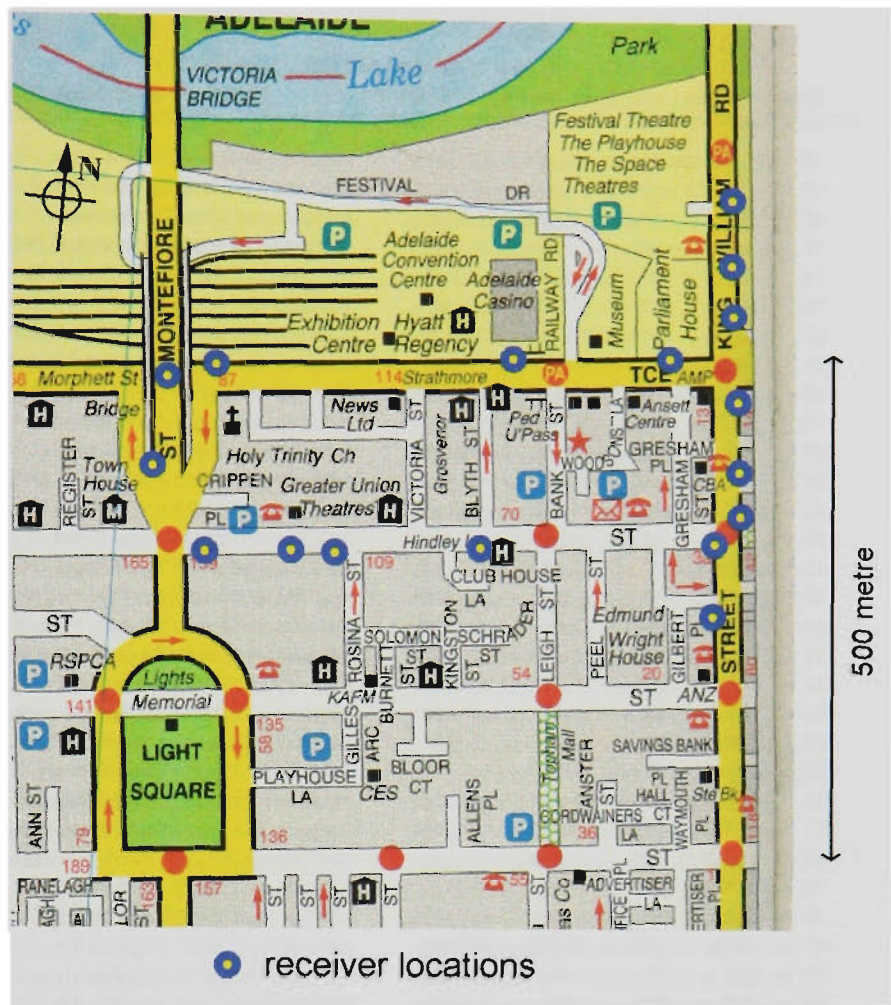


FIGURE E.3 Hotel Adelaide - transmitter on first floor (map 2)

### E.3 Adelaide - Hotel Adelaide Roof

**Transmitter Location:** Hotel Adelaide, Brougham Place, North Adelaide  
**Transmitter Antenna:** 3m above flat roof, 7th. floor level. Discone antenna.  
**Receiver:** in a car, with halfwave antenna above roof level.  
**Sample time:** 10 ns, **Threshold:** -15 dB, **Range:** 25  $\mu$ s

TABLE E.3 Adelaide - Hotel Adelaide roof - filebase an

file	dBV	rms delay (ns)	avg delay (ns)	gain factor (dB)	location of measurement
1	11.3	349	1123	-110	Adelaide roof pos1 O'Connell St 10m S Archer
2	9.6	343	1141	-110	Adelaide roof pos1 O'Connell St 10m S Archer
3	5.3	22	20	-110	Adelaide roof pos2 cnr O'Connell & Chapel
4	5.5	19	20	-110	Adelaide roof pos2 cnr O'Connell & Chapel
5	9.0	16	20	-110	Adelaide roof pos3 cnr O'Connell & Tynte
6	10.4	16	18	-110	Adelaide roof pos3 cnr O'Connell & Tynte
7	3.7	205	142	-110	Adelaide roof pos4 O'Connell Street
8	3.2	198	127	-110	Adelaide roof pos4 O'Connell Street
9	-1.2	272	277	-110	Adelaide roof pos5 SW cnr O'Connell & Gover
10	-0.5	247	192	-110	Adelaide roof pos5 SW cnr O'Connell & Gover
11	4.9	49	36	-110	Adelaide roof pos6 O'Connell Street
12	4.9	39	29	-110	Adelaide roof pos6 O'Connell Street
13	12.3	13	16	-125	Adelaide roof pos7 Terrace West



**TABLE E.3 Adelaide - Hotel Adelaide roof - filebase an** (continued)

file	dBV	rms delay (ns)	avg delay (ns)	gain factor (dB)	location of measurement
14	12.5	13	15	-125	Adelaide roof pos7 Terrace West
15	6.7	131	89	-125	Adelaide roof pos8 Terrace West
16	5.6	138	107	-125	Adelaide roof pos8 Terrace West
17	5.3	129	92	-125	Adelaide roof pos9 cnr Travers & Terrace West
18	5.5	96	63	-125	Adelaide roof pos9 cnr Travers & Terrace West
19	-0.3	60	67	-125	Adelaide roof pos10 Wellington Square N
20	-1.5	69	75	-125	Adelaide roof pos10 Wellington Square N
21	-2.0	192	165	-125	Adelaide roof pos11 Wellington Square
22	-2.2	192	169	-125	Adelaide roof pos11 Wellington Square
23	-0.2	192	138	-125	Adelaide roof pos12 Tynte Street
24	0.2	161	125	-125	Adelaide roof pos12 Tynte Street
25	3.1	165	277	-125	Adelaide roof pos13 cnr Tynte St & Tynte Pl
26	3.1	161	269	-125	Adelaide roof pos13 cnr Tynte St & Tynte Pl
27	12.1	13	15	-110	Adelaide roof pos14 Tynte Street
28	11.5	16	18	-110	Adelaide roof pos14 Tynte Street
29	5.8	47	69	-110	Adelaide roof pos15 Nth Adel Primary School
30	7.1	38	69	-110	Adelaide roof pos15 Nth Adel Primary School
31	-1.1	223	209	-120	Adelaide roof pos16 Tynte Street
32	-0.8	219	192	-120	Adelaide roof pos16 Tynte Street
33	8.9	84	85	-120	Adelaide roof pos17 cnr Tynte & Lefevre
34	8.6	88	92	-120	Adelaide roof pos17 cnr Tynte & Lefevre
35	10.9	53	36	-120	Adelaide roof pos18 Lefevre Street
36	10.7	49	36	-120	Adelaide roof pos18 Lefevre Street
37	0.5	210	209	-120	Adelaide roof pos19 Lefevre opp Archer St
38	-0.1	223	239	-120	Adelaide roof pos19 Lefevre opp Archer St
39	8.8	54	37	-120	Adelaide roof pos20 Ward Street
40	7.9	63	46	-120	Adelaide roof pos20 Ward Street
41	10.2	338	262	-120	Adelaide roof pos21 Kingston Trc
42	7.1	82	54	-120	Adelaide roof pos21 Kingston Trc
43	6.5	67	51	-120	Adelaide roof pos21 Kingston Trc
44	11.3	16	18	-120	Adelaide roof pos22 Jerningham Street
45	11.2	15	17	-120	Adelaide roof pos22 Jerningham Street
46	2.9	539	425	-120	Adelaide roof pos23 Finnis St opp Edith Pl
47	3.4	546	456	-120	Adelaide roof pos23 Finnis St opp Edith Pl
48	4.0	168	282	-120	Adelaide roof pos24 SE cnr Frome & Finnis
49	3.7	180	261	-120	Adelaide roof pos24 SE cnr Frome & Finnis
50	9.7	92	135	-120	Adelaide roof pos25 S cnr Edwin Smith Av & Frome
51	9.2	92	129	-120	Adelaide roof pos25 S cnr Edwin Smith Av & Frome
52	-0.8	166	235	-120	Adelaide roof pos26 ESmith just S Pennington
53	-0.8	171	238	-120	Adelaide roof pos26 ESmith just S Pennington
54	5.2	204	146	-120	Adelaide roof pos27 War Memorial Drive
55	6.1	184	119	-120	Adelaide roof pos27 War Memorial Drive
56	9.2	16	19	-120	Adelaide roof pos28 King William Street
57	9.3	16	19	-120	Adelaide roof pos28 King William Street
58	-1.6	288	239	-120	Adelaide roof pos29 North Terrace
59	-2.1	329	267	-120	Adelaide roof pos29 North Terrace
60	2.6	54	43	-130	Adelaide roof pos30 E side Gawler Pl
61	1.9	51	40	-130	Adelaide roof pos30 E side Gawler Pl
62	2.8	52	35	-130	Adelaide roof pos31 W side Gawler Pl
63	2.0	53	36	-130	Adelaide roof pos31 W side Gawler Pl
64	-0.5	124	163	-130	Adelaide roof pos32 SW cnr North Trc & Gawler
65	-0.8	124	161	-130	Adelaide roof pos32 SW cnr North Trc & Gawler
66	2.5	100	70	-130	Adelaide roof pos33 King William at Pirie
67	3.6	90	55	-130	Adelaide roof pos33 King William at Pirie
68	5.7	16	19	-130	Adelaide roof pos34 King William at Flinders
69	5.3	172	181	-130	Adelaide roof pos35 King William & Weymouth
70	4.4	33	25	-130	Adelaide roof pos35 King William & Weymouth
71	7.2	22	22	-130	Adelaide roof pos36 King William S Curie
72	7.3	22	23	-130	Adelaide roof pos36 King William S Curie
73	6.1	44	37	-130	Adelaide roof pos37 King William N Curie
74	7.3	39	32	-130	Adelaide roof pos37 King William N Curie
75	9.2	29	26	-130	Adelaide roof pos38 KW 20m N of Curie
76	7.1	46	36	-130	Adelaide roof pos38 KW 20m N of Curie
77	4.5	62	43	-130	Adelaide roof pos38 KW 20m N of Curie

**TABLE E.3 Adelaide - Hotel Adelaide roof - filebase an** (continued)

file	dBV	rms delay (ns)	avg delay (ns)	gain factor (dB)	location of measurement
78	8.2	28	26	-130	Adelaide roof pos38 KW 20m N of Curie
79	8.6	30	27	-130	Adelaide roof pos38 KW 20m N of Curie
80	8.1	29	25	-130	Adelaide roof pos38 KW 20m N of Curie
81	8.8	15	18	-130	Adelaide roof pos38 KW 20m N of Curie
82	9.6	29	26	-130	Adelaide roof pos38 KW 20m N of Curie
83	9.5	33	26	-130	Adelaide roof pos38 KW 20m N of Curie
84	8.7	30	25	-130	Adelaide roof pos38 KW 20m N of Curie
85	8.6	33	28	-130	Adelaide roof pos38 KW 20m N of Curie
86	3.7	245	169	-130	Adelaide roof pos39 Montefiore overpass
87	4.1	223	156	-130	Adelaide roof pos39 Montefiore overpass
88	6.3	138	54	-130	Adelaide roof pos40 Festival Drive
89	5.4	137	55	-130	Adelaide roof pos40 Festival Drive
90	3.0	97	54	-130	Adelaide roof pos41 War Memorial Drive
91	5.2	41	29	-130	Adelaide roof pos41 War Memorial Drive
92	7.4	269	113	-130	Adelaide roof pos42 War Memorial Drive
93	7.6	270	114	-130	Adelaide roof pos42 War Memorial Drive
94	10.2	223	127	-130	Adelaide roof pos43 Main North Road
95	10.4	213	121	-130	Adelaide roof pos43 Main North Road
96	12.3	137	80	-130	Adelaide roof pos44 Main North Road
97	12.4	148	96	-130	Adelaide roof pos44 Main North Road
98	2.7	188	238	-130	Adelaide roof pos45 Main North & Thorngate
99	2.1	205	278	-130	Adelaide roof pos45 Main North & Thorngate
100	-0.9	261	183	-130	Adelaide roof pos46 Main North & Carter
101	-1.4	262	197	-130	Adelaide roof pos46 Main North & Carter
102	-0.6	766	417	-130	Adelaide roof pos47 Main North & Penn PI
103	-0.5	764	418	-130	Adelaide roof pos47 Main North & Penn PI
104	1.9	329	183	-130	Adelaide roof pos47 Main North & Penn PI
105	0.8	475	245	-130	Adelaide roof pos47 Main North & Penn PI
106	-1.6	545	333	-130	Adelaide roof pos47 Main North & Penn PI
107	-0.7	630	356	-130	Adelaide roof pos47 Main North & Penn PI
108	5.0	139	99	-130	Adelaide roof pos47 Main North & Penn PI
109	5.2	130	88	-130	Adelaide roof pos47 Main North & Penn PI
110	1.8	78	44	-130	Adelaide roof pos48 Main North & Gloucester
111	1.4	71	125	-130	Adelaide roof pos48 Main North & Gloucester
112	-1.4	350	439	-130	Adelaide roof pos49 Main North & Charlbury
113	-1.3	348	439	-130	Adelaide roof pos49 Main North & Charlbury
114	0.4	381	550	-130	Adelaide roof pos49 Main North & Charlbury
115	-0.5	388	559	-130	Adelaide roof pos49 Main North & Charlbury
116	-1.9	357	856	-130	Adelaide roof pos49 Main North & Charlbury
117	-1.4	2126	420	-130	Adelaide roof pos49 Main North & Charlbury
118	-0.9	341	190	-130	Adelaide roof pos49 Main North & Charlbury
119	2.9	140	65	-130	Adelaide roof pos49 Main North & Charlbury
120	2.3	141	72	-130	Adelaide roof pos49 Main North & Charlbury
121	3.4	49	38	-130	Adelaide roof pos49 Main North & Charlbury

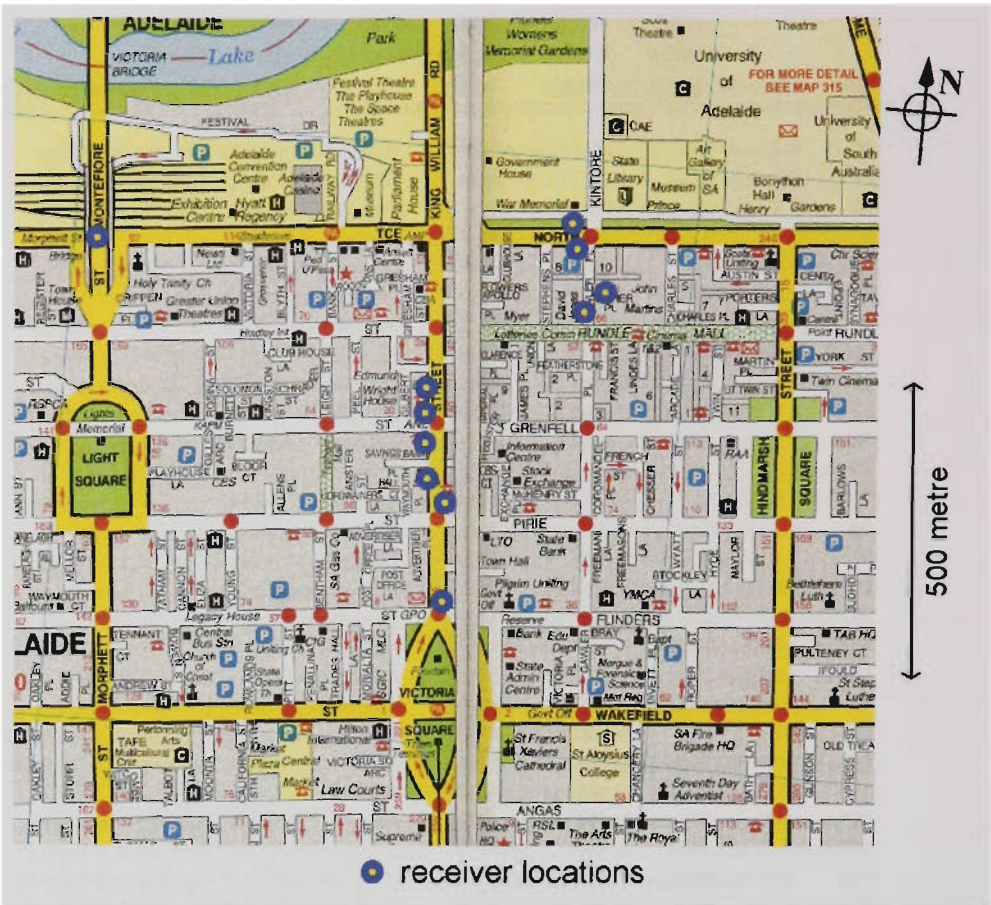


FIGURE E.4 Hotel Adelaide - transmitter on roof (map 1)

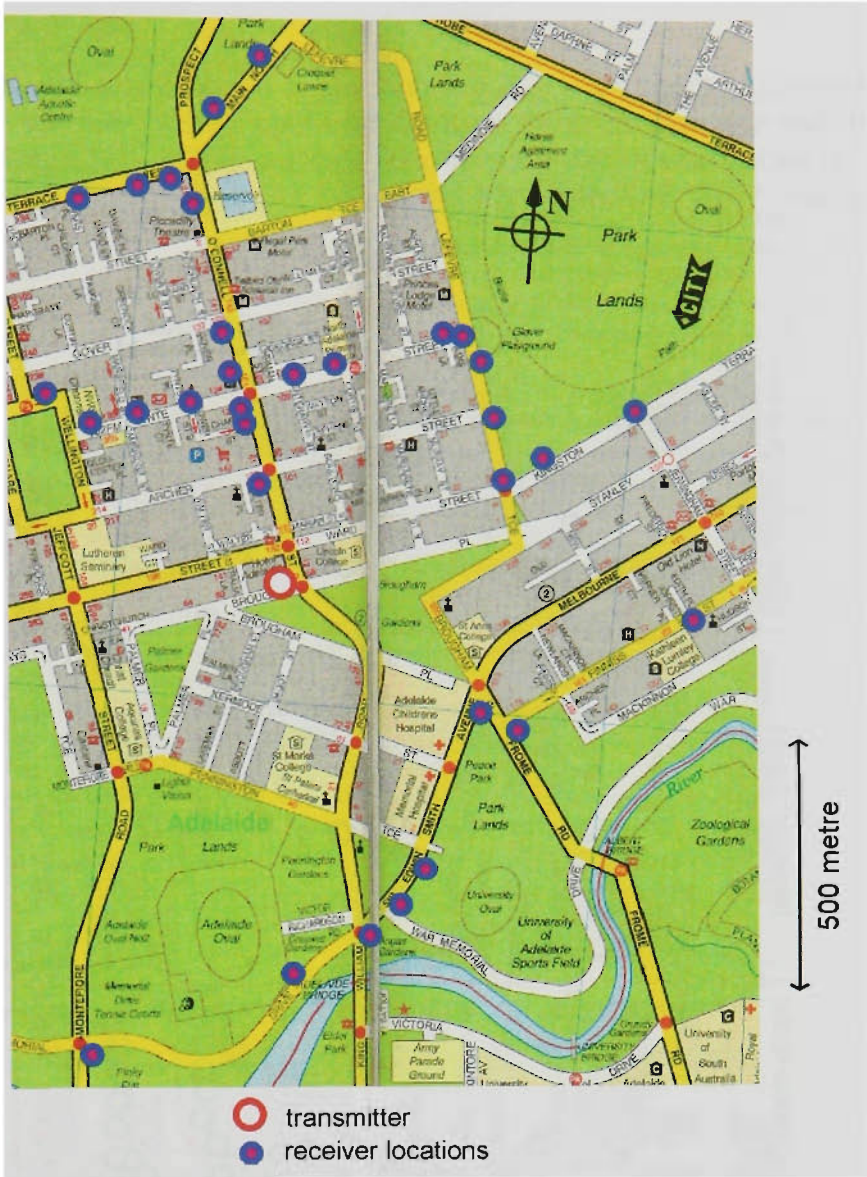


FIGURE E.5 Hotel Adelaide - transmitter on roof (map 2)

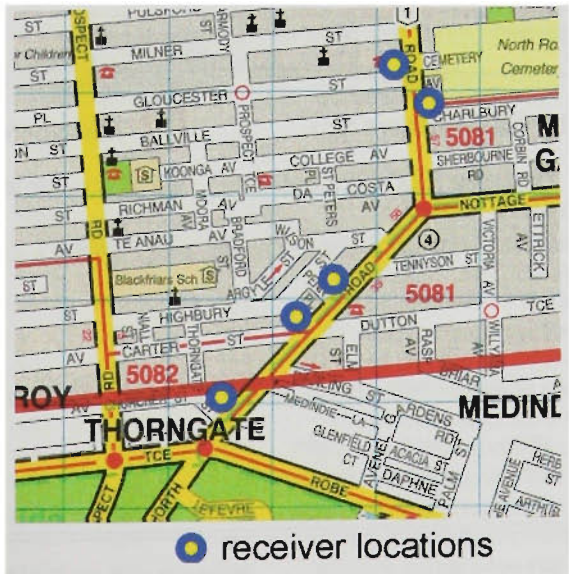


FIGURE E.6 Hotel Adelaide - transmitter on roof (map 3)



E.4 Melbourne - Bourke Street Mall

**Transmitter Location:** in car boot on north side of Bourke Street, 20m east of Queen Street.  
**Transmitter Antenna:** 2m mast on car towbar fitting. Discone antenna.  
**Receiver:** backpack unit with halfwave antenna 0.3m above head height  
**Sample time:** 10 ns, **Threshold:** -15 dB, **Range:** 25  $\mu$ s

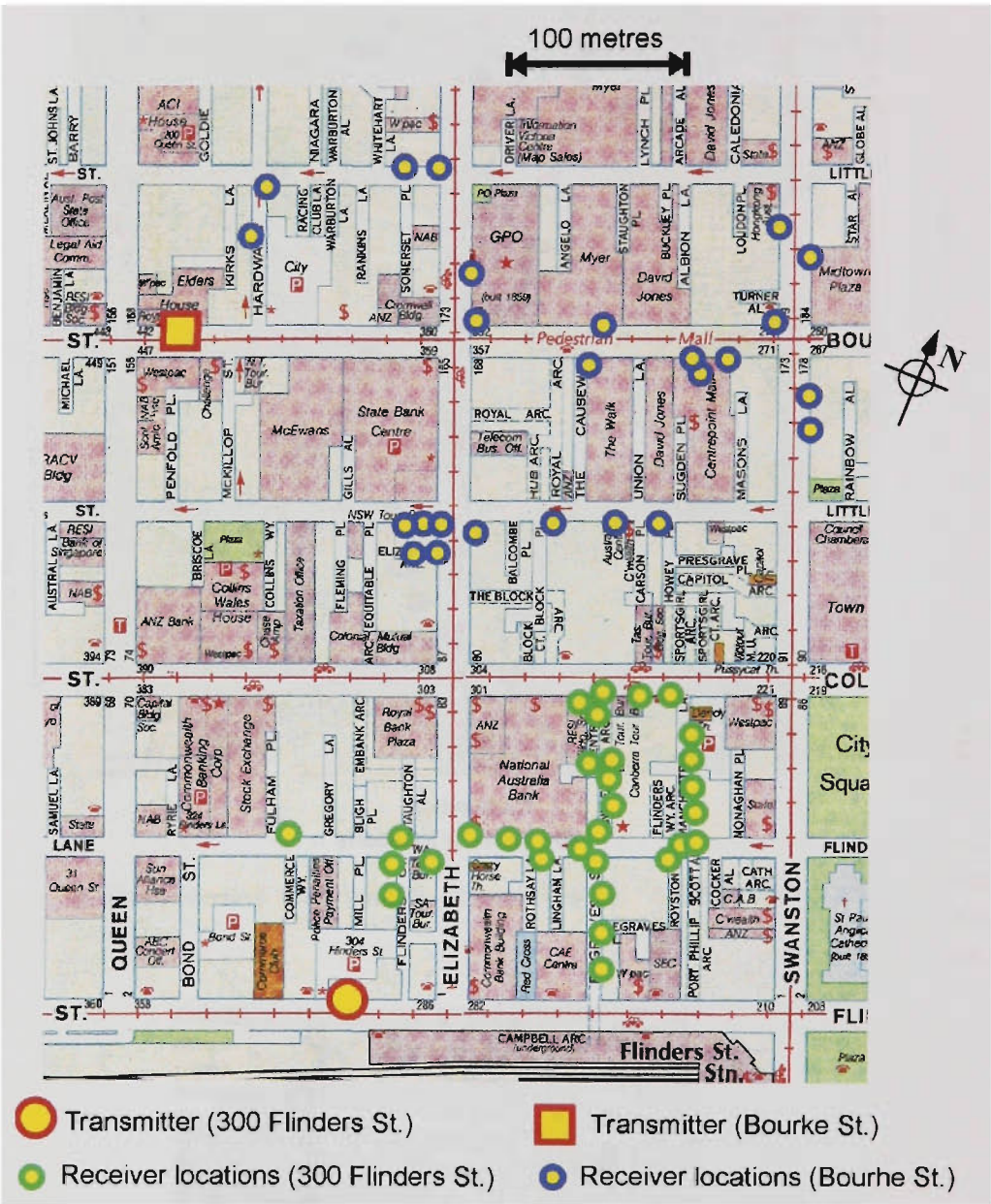


FIGURE E.7 Melbourne - Bourke Street mall, and Flinders Street transmitter sites

TABLE E.4 Melbourne - Bourke Street mall - filebase bmr

file	dBV	rms delay (ns)	avg delay (ns)	gain factor (dB)	location of measurement
1	13.4	59	94	-119	Bourke St pos1 Hardware Street
2	7.3	123	75	-119	Bourke St pos2 cnr Hardware & Lt Bourke
3	5.7	183	283	-125	Bourke St pos3 Lt Bourke 20m W Elizabeth
4	16.2	26	52	-125	Bourke St pos4 NW cnr Lt Bourke & Eliz
5	13.7	81	51	-125	Bourke St pos5 GPO arcade 50m N Mall

TABLE E.4 Melbourne - Bourke Street mall - filebase bmr (continued)

file	dBV	rms delay (ns)	avg delay (ns)	gain factor (dB)	location of measurement
6	14.2	58	54	-119	Bourke St pos6 GPO arcade cnr Mall
7	13.4	68	68	-119	Bourke St pos7 Mall recess W door Myer
8	12.0	15	15	-119	Bourke St pos8 Mall 5m into lane opp Myer
9	7.0	101	111	-119	Bourke St pos9 Mall Hungry Jacks recess
10	13.0	60	50	-119	Bourke St pos10 Mall David Lawrence
11	9.9	87	76	-119	Bourke St pos11 NW cnr Mall & Swanston
12	-3.1	90	117	-125	Bourke St pos12 Swanston W 100m N Mall
13	1.3	55	104	-125	Bourke St pos13 Swanston E 70m N Mall
14	1.3	68	80	-125	Bourke St pos14 Swanston 50m S Mall
15	-1.2	117	183	-125	Bourke St pos15 Swanston mid Mall & Lt Collins
16	-2.6	37	36	-128	Bourke St pos16 Lt Collins 150m W Swanston
17	-4.7	334	1264	-128	Bourke St pos17 Lt Collins mid Eliz & Swanston
18	-1.3	479	388	-128	Bourke St pos18 Lt Collins 150m E Elizabeth
19	6.5	341	356	-128	Bourke St pos19 SE cnr Lt Collins & Eliz
20	9.1	82	228	-125	Bourke St pos20 SW cnr Lt Collins & Eliz
21	13.6	41	95	-119	Bourke St pos21 Eliz 50m S Mall in Galeria recess
22	8.7	96	255	-119	Bourke St pos22 Eliz 10m S Mall
23	8.7	96	255	-119	Bourke St pos22 Eliz 10m S Mall
24	13.7	106	201	-119	Bourke St pos23 Galeria plaza W of Eliz
25	13.9	100	89	-119	Bourke St pos23 Galeria plaza W of Eliz
26	8.3	132	225	-119	Bourke St pos23 Galeria plaza W of Eliz
27	12.2	128	104	-119	Bourke St pos23 Galeria plaza W of Eliz
28	12.2	128	104	-119	Bourke St pos23 Galeria plaza W of Eliz
29	15.0	98	120	-119	Bourke St pos23 Galeria plaza W of Eliz
30	12.9	129	125	-119	Bourke St pos23 Galeria plaza W of Eliz

E.5 Melbourne - 300 Flinders Street, 13th. Floor

Transmitter Location: on 13th. floor outside balcony, facing south.  
Transmitter Antenna: 3m mast on balcony. Discone antenna.  
Receiver: backpack unit with halfwave antenna 0.3m above head height.  
Sample time: 10 ns, Threshold: -15 dB, Range: 25 μs

See Figure E.7 above for the transmitter and receiver locations.

TABLE E.5 Melbourne - Flinders Street - filebase fsr

file	dBV	rms delay (ns)	avg delay (ns)	gain factor (dB)	location of measurement
1	6.0	118	158	-119	Flinders pos1 Flinders & Flinders Lane
2	11.1	90	77	-119	Flinders pos2 SW cnr Eliz & Flinders Lane
3	7.3	53	47	-119	Flinders pos3 Degraives 30m N Flinders
4	5.9	26	25	-119	Flinders pos4 Degraives 100m N Flinders
5	9.8	31	26	-125	Flinders pos5 Degraives 50m S Flinders Ln
6	2.3	110	271	-125	Flinders pos6 Degraives & Flinders Ln
7	-1.2	161	220	-125	Flinders pos7 Flinders Ln & Degraives
8	-6.1	215	351	-125	Flinders pos8 Centre Place 2m from Fl Ln
9	-9.7	8213	10143	-128	Flinders pos9 Centre Place 30m from Fl Ln
10	-10.7	240	325	-128	Flinders pos10 Centre Place steps
11	-9.8	415	303	-128	Flinders pos10 Centre Place steps
12	-10.0	1773	515	-128	Flinders pos10 Centre Place steps
13	-6.2	412	289	-128	Flinders pos11 Centre Way Collins end
14	-6.9	565	352	-128	Flinders pos11 Centre Way Collins end
15	-4.5	773	513	-128	Flinders pos12 Collins near Center Way

TABLE E.5 Melbourne - Flinders Street - filebase fsr (continued)

file	dBV	rms delay (ns)	avg delay (ns)	gain factor (dB)	location of measurement
16	-1.1	290	202	-128	Flinders pos13 Collins at QTB
17	-4.0	686	440	-128	Flinders pos13 Collins at QTB
18	-2.9	1037	992	-128	Flinders pos14 Collins & Manchester Ln
19	-1.9	134	100	-128	Flinders pos15 Manchester 100m N FI Ln
20	-4.1	180	165	-128	Flinders pos15 Manchester 100m N FI Ln
21	-5.7	497	323	-128	Flinders pos16 Manchester 80m N FI Ln
22	-3.8	558	391	-128	Flinders pos17 Manchester 10m N FI Ln
23	0.9	195	100	-128	Flinders pos18 Manchester 5m N FI Ln
24	-0.5	389	331	-125	Flinders pos19 Flinders Ln opp Royston Pl
25	1.2	236	283	-125	Flinders pos20 Flinders Ln & Royston
26	0.4	197	205	-125	Flinders pos21 Flinders Ln 50m E Eliz
27	-3.1	453	326	-125	Flinders pos22 Flinders Ln 40m E Eliz
28	3.5	100	173	-119	Flinders pos23 NE cnr FI Ln & Eliz
29	12.9	23	12	-119	Flinders pos24 FI Ln & Staughton Alley
30	-4.7	1410	385	-119	Flinders pos25 Flinders Court

E.6 Melbourne - City Arcades

Transmitter Location: in car boot in Bourke Street, 100m east of Russell Street.  
Transmitter Antenna: on car towbar fitting, 2.5m above ground. Discone antenna.  
Receiver: backpack unit with halfwave antenna 0.3m above head height  
Sample time: 10 ns, Threshold: -15 dB, Range: 25 μs

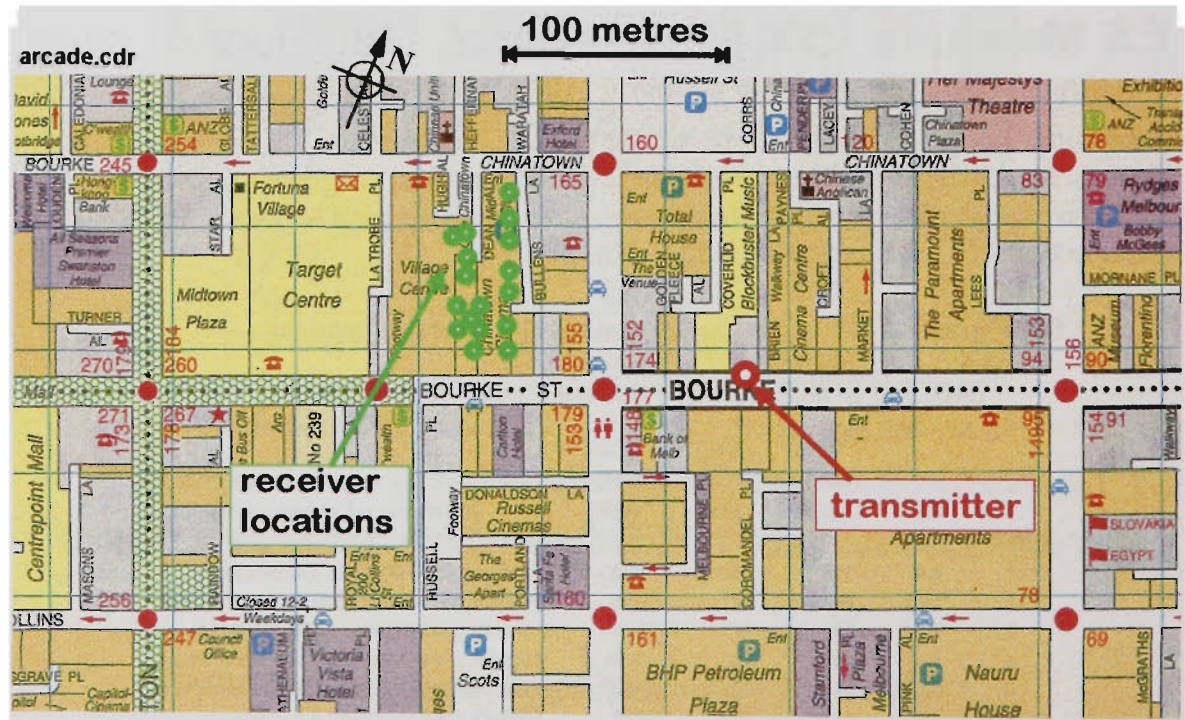


FIGURE E.8 Melbourne - city arcades, showing measurement locations

TABLE E.6 Melbourne - city arcades - filrbase acr

file	dBV	rms delay (ns)	avg delay (ns)	gain factor (dB)	location of measurement
1	7.1	103	159	-119	Melbourne pos1 Mid City Arcade 20m N Bourke
2	4.4	117	153	-119	Melbourne pos1 Mid City Arcade 20m N Bourke
3	0.0	83	111	-119	Melbourne pos2 Mid City Arcade 30m N Bourke
4	1.1	61	67	-119	Melbourne pos3 Mid City Arcade 40m N Bourke
5	0.6	41	85	-119	Melbourne pos4 Mid City Arcade 50m N Bourke
6	0.3	48	77	-119	Melbourne pos5 Mid City Arcade 60m N Bourke
7	-1.8	68	77	-119	Melbourne pos5 Mid City Arcade 60m N Bourke
8	0.2	44	98	-119	Melbourne pos5 Mid City Arcade 60m N Bourke
9	5.2	104	209	-119	Melbourne pos6 SW cnr Lt Bourke & Russell
10	-4.8	90	86	-125	Melbourne pos6 Village Arcade 15m N Bourke
11	1.7	45	53	-125	Melbourne pos7 Village Arcade 20m N Bourke
12	-4.1	82	178	-125	Melbourne pos8 Village Arcade 25m N Bourke
13	-2.3	62	79	-125	Melbourne pos8 Village Arcade 25m N Bourke
14	9.1	21	56	-125	Melbourne pos8 Village Arcade 25m N Bourke
15	-0.0	35	103	-125	Melbourne pos8 Village Arcade 25m N Bourke
16	7.3	48	91	-125	Melbourne pos8 Village Arcade 25m N Bourke
17	8.2	53	64	-125	Melbourne pos8 Village Arcade 25m N Bourke
18	7.3	48	48	-125	Melbourne pos8 Village Arcade 25m N Bourke
19	8.7	32	108	-125	Melbourne pos8 Village Arcade 25m N Bourke
20	2.0	106	137	-125	Melbourne pos8 Village Arcade 25m N Bourke
21	2.7	45	93	-119	Melbourne pos9 Village Arcade 40m N Bourke
22	-0.4	101	166	-119	Melbourne pos9 Village Arcade 40m N Bourke
23	10.3	17	59	-119	Melbourne pos9 Village Arcade 40m N Bourke
24	10.6	25	21	-119	Melbourne pos10 Village Arcade 30m N Bourke
25	4.3	78	104	-119	Melbourne pos10 Village Arcade 30m N Bourke
26	6.0	52	48	-119	Melbourne pos10 Village Arcade 30m N Bourke
27	8.9	33	81	-119	Melbourne pos10 Village Arcade 30m N Bourke
28	4.2	67	82	-119	Melbourne pos10 Village Arcade 30m N Bourke
29	13.7	38	73	-119	Melbourne pos11 Village Arcade 25m N Bourke
30	9.0	57	103	-119	Melbourne pos11 Village Arcade 25m N Bourke
31	9.8	53	44	-119	Melbourne pos11 Village Arcade 25m N Bourke
32	9.2	112	111	-119	Melbourne pos12 Village Arcade 15m N Bourke
33	13.5	40	49	-119	Melbourne pos12 Village Arcade 15m N Bourke
34	11.8	48	85	-119	Melbourne pos12 Village Arcade 15m N Bourke

E.7 Melbourne - North Fitzroy Balcony

**Transmitter Location:** 27 Delbridge Street, North Fitzroy.

**Transmitter Antenna:** on boom over edge of 1st. floor balcony, about 5m above ground, halfwave antenna.

**Receiver:** in a car with halfwave magnetic base antenna on roof.

**Sample time:** 10 ns, **Threshold:** -15 dB, **Range:** 25  $\mu$ s

TABLE E.7 Melbourne - North Fitzroy balcony - filebase delbc

file	dBV	rms delay (ns)	avg delay (ns)	gain factor (ns)	location of measurement
1	5.6	70	57	-97	Fitzroy balcony pos1 cnr Delbridge & Park Pl
2	7.5	24	22	-97	Fitzroy balcony pos1 cnr Delbridge & Park Pl
3	5.2	49	33	-97	Fitzroy balcony pos1 cnr Delbridge & Park Pl
4	-2.2	42	33	-97	Fitzroy balcony pos1 cnr Delbridge & Park Pl
5	1.2	87	66	-97	Fitzroy balcony pos1 cnr Delbridge & Park Pl



**TABLE E.7 Melbourne - North Fitzroy balcony - filebase delbc** (continued)

<b>file</b>	<b>dBV</b>	<b>rms delay (ns)</b>	<b>avg delay (ns)</b>	<b>gain factor (ns)</b>	<b>location of measurement</b>
6	-2.9	163	199	-107	Fitzroy balcony pos2 cnr Delbridge & Rowe
7	-0.3	82	64	-107	Fitzroy balcony pos2 cnr Delbridge & Rowe
8	5.2	40	33	-107	Fitzroy balcony pos2 cnr Delbridge & Rowe
9	3.2	46	34	-107	Fitzroy balcony pos2 cnr Delbridge & Rowe
10	4.3	33	37	-107	Fitzroy balcony pos2 cnr Delbridge & Rowe
11	5.3	16	19	-117	Fitzroy balcony pos3 NE cnr Delbridge & Falconer
12	9.9	16	19	-117	Fitzroy balcony pos3 NE cnr Delbridge & Falconer
13	11.5	14	16	-117	Fitzroy balcony pos3 NE cnr Delbridge & Falconer
14	10.9	15	18	-117	Fitzroy balcony pos3 NE cnr Delbridge & Falconer
15	-1.0	106	41	-117	Fitzroy balcony pos3 NE cnr Delbridge & Falconer
16	-10.4	374	494	-117	Fitzroy balcony pos4 Rowe St near Michael
17	-12.6	307	437	-117	Fitzroy balcony pos4 Rowe St near Michael
18	-6.9	280	142	-117	Fitzroy balcony pos4 Rowe St near Michael
19	-6.4	225	146	-117	Fitzroy balcony pos4 Rowe St near Michael
20	-6.8	298	283	-117	Fitzroy balcony pos4 Rowe St near Michael
21	-7.8	130	101	-117	Fitzroy balcony pos5 Rowe just NE Michael
22	-3.8	15	18	-117	Fitzroy balcony pos5 Rowe just NE Michael
23	0.2	13	15	-117	Fitzroy balcony pos5 Rowe just NE Michael
24	0.5	77	38	-117	Fitzroy balcony pos5 Rowe just NE Michael
25	-1.0	45	30	-117	Fitzroy balcony pos5 Rowe just NE Michael
26	5.3	17	20	-117	Fitzroy balcony pos6 McKean N of Michael
27	1.8	40	34	-117	Fitzroy balcony pos6 McKean N of Michael
28	-4.4	111	133	-117	Fitzroy balcony pos6 McKean N of Michael
29	-6.2	112	120	-117	Fitzroy balcony pos6 McKean N of Michael
30	-1.0	107	112	-117	Fitzroy balcony pos6 McKean N of Michael
31	-6.0	133	135	-117	Fitzroy balcony pos7 Michael E of Howe
32	-11.3	116	145	-117	Fitzroy balcony pos7 Michael E of Howe
33	-9.5	320	198	-117	Fitzroy balcony pos7 Michael E of Howe
34	-14.9	581	395	-117	Fitzroy balcony pos7 Michael E of Howe
35	-5.8	153	137	-117	Fitzroy balcony pos7 Michael E of Howe
36	-6.1	181	106	-117	Fitzroy balcony pos8 NE cnr Michael & Queens Pd
37	-9.1	388	274	-117	Fitzroy balcony pos8 NE cnr Michael & Queens Pd
38	-3.6	162	94	-117	Fitzroy balcony pos8 NE cnr Michael & Queens Pd
39	-7.9	288	226	-117	Fitzroy balcony pos8 NE cnr Michael & Queens Pd
40	-1.7	144	90	-117	Fitzroy balcony pos8 NE cnr Michael & Queens Pd
41	-5.6	117	44	-117	Fitzroy balcony pos9 Michael W side Queens Pd
42	-5.3	262	130	-117	Fitzroy balcony pos9 Michael W side Queens Pd
43	-6.6	308	223	-117	Fitzroy balcony pos9 Michael W side Queens Pd
44	-6.7	296	183	-117	Fitzroy balcony pos9 Michael W side Queens Pd
45	-7.8	311	269	-117	Fitzroy balcony pos9 Michael W side Queens Pd
46	-1.6	14	17	-87	Fitzroy balcony pos10 Queens Pd & Delbridge
47	-3.0	37	27	-87	Fitzroy balcony pos10 Queens Pd & Delbridge
48	-5.8	96	58	-87	Fitzroy balcony pos10 Queens Pd & Delbridge
49	-5.8	94	56	-87	Fitzroy balcony pos10 Queens Pd & Delbridge
50	-5.0	44	22	-87	Fitzroy balcony pos10 Queens Pd & Delbridge
51	3.6	77	260	-97	Fitzroy balcony pos11 McKean opp RunScotty
52	3.9	87	255	-97	Fitzroy balcony pos11 McKean opp RunScotty
53	4.2	99	269	-97	Fitzroy balcony pos11 McKean opp RunScotty
54	4.0	107	260	-97	Fitzroy balcony pos11 McKean opp RunScotty
55	4.0	81	273	-97	Fitzroy balcony pos11 McKean opp RunScotty
56	-5.6	208	232	-117	Fitzroy balcony pos12 McKean St 50m N Grant
57	-4.1	195	234	-117	Fitzroy balcony pos12 McKean St 50m N Grant
58	-5.4	196	239	-117	Fitzroy balcony pos12 McKean St 50m N Grant
59	-4.5	169	214	-117	Fitzroy balcony pos12 McKean St 50m N Grant
60	-4.8	187	240	-117	Fitzroy balcony pos12 McKean St 50m N Grant
61	-8.7	233	150	-117	Fitzroy balcony pos13 cnr McKean & Grant
62	-7.3	204	132	-117	Fitzroy balcony pos13 cnr McKean & Grant
63	-8.6	222	170	-117	Fitzroy balcony pos13 cnr McKean & Grant
64	-6.8	159	104	-117	Fitzroy balcony pos13 cnr McKean & Grant
65	-7.7	184	152	-117	Fitzroy balcony pos13 cnr McKean & Grant
66	1.1	217	241	-117	Fitzroy balcony pos14 McKean mid Grant & Delbridge
67	-1.1	221	294	-117	Fitzroy balcony pos14 McKean mid Grant & Delbridge
68	0.3	206	390	-117	Fitzroy balcony pos14 McKean mid Grant & Delbridge
69	1.4	186	430	-117	Fitzroy balcony pos14 McKean mid Grant & Delbridge

TABLE E.7 Melbourne - North Fitzroy balcony - filebase delbc (continued)

file	dBV	rms delay (ns)	avg delay (ns)	gain factor (ns)	location of measurement
70	-0.3	225	253	-117	Fitzroy balcony pos14 McKean mid Grant & Delbridge
71	3.3	23	25	-77	Fitzroy balcony pos15 Delbridge St below xmitter
72	3.0	25	26	-77	Fitzroy balcony pos15 Delbridge St below xmitter
73	2.8	30	27	-77	Fitzroy balcony pos15 Delbridge St below xmitter
74	4.0	27	25	-77	Fitzroy balcony pos15 Delbridge St below xmitter
75	5.3	12	16	-77	Fitzroy balcony pos15 Delbridge St below xmitter
76	2.0	63	35	-77	Fitzroy balcony pos15 Delbridge St below xmitter



FIGURE E.9 Melbourne - Delbridge Street balcony receiver locations

E.8 Melbourne - North Fitzroy Roof

Transmitter Location: 27 Delbridge Street, North Fitzroy.  
Transmitter Antenna: mast 3m above roof level, 2nd.storey. Discone antenna.  
Receiver: in a car with halfwave magnetic base antenna on roof.  
Sample time: 10 ns, Threshold: -15 dB, Range: 25µs



FIGURE E.10 Melbourne - Delbridge Street roof measurement locations

TABLE E.8 Melbourne - Delbridge Street roof - filebase delrf

file	dBV	rms delay (ns)	avg delay (ns)	gain factor (dB)	location of measurement
1	6.8	65	78	-107	Fitzroy roof pos1 Delbridge St & Park Pl
2	9.7	80	128	-107	Fitzroy roof pos1 Delbridge St & Park Pl
3	5.6	93	118	-107	Fitzroy roof pos1 Delbridge St & Park Pl
4	4.9	132	176	-107	Fitzroy roof pos1 Delbridge St & Park Pl
5	4.6	111	119	-107	Fitzroy roof pos1 Delbridge St & Park Pl
6	3.5	34	35	-97	Fitzroy roof pos2 Delbridge St & Rowe St
7	-1.0	57	54	-97	Fitzroy roof pos2 Delbridge St & Rowe St
8	-1.1	76	77	-97	Fitzroy roof pos2 Delbridge St & Rowe St
9	-1.1	77	78	-97	Fitzroy roof pos2 Delbridge St & Rowe St
10	0.5	65	59	-97	Fitzroy roof pos2 Delbridge St & Rowe St
11	6.4	142	120	-97	Fitzroy roof pos3 Del St mid Rowe & Falconer
12	6.7	91	113	-117	Fitzroy roof pos3 Del St mid Rowe & Falconer
13	7.3	89	117	-117	Fitzroy roof pos3 Del St mid Rowe & Falconer
14	6.6	84	143	-117	Fitzroy roof pos3 Del St mid Rowe & Falconer
15	5.2	122	115	-117	Fitzroy roof pos3 Del St mid Rowe & Falconer
16	2.0	13	16	-107	Fitzroy roof pos4 Falconer opp Delbridge
17	2.1	63	51	-107	Fitzroy roof pos4 Falconer opp Delbridge
18	-0.9	67	67	-107	Fitzroy roof pos4 Falconer opp Delbridge
19	-0.2	76	81	-107	Fitzroy roof pos4 Falconer opp Delbridge
20	0.1	78	97	-107	Fitzroy roof pos4 Falconer opp Delbridge
21	-3.3	297	473	-127	Fitzroy roof pos5 Falconer opp Mark
22	-1.3	301	512	-127	Fitzroy roof pos5 Falconer opp Mark
23	0.4	347	550	-127	Fitzroy roof pos5 Falconer opp Mark
24	-2.0	516	358	-127	Fitzroy roof pos5 Falconer opp Mark

**TABLE E.8 Melbourne - Delbridge Street roof - filebase delrf (continued)**

file	dBV	rms delay (ns)	avg delay (ns)	gain factor (dB)	location of measurement
25	-2.5	437	385	-127	Fitzroy roof pos5 Falconer opp Mark
26	10.2	56	53	-127	Fitzroy roof pos6 Alfred Crs near Falconer
27	4.6	181	146	-127	Fitzroy roof pos6 Alfred Crs near Falconer
28	2.5	277	251	-127	Fitzroy roof pos6 Alfred Crs near Falconer
29	3.2	192	252	-127	Fitzroy roof pos6 Alfred Crs near Falconer
30	4.5	128	310	-127	Fitzroy roof pos6 Alfred Crs near Falconer
31	0.5	327	469	-127	Fitzroy roof pos7 Alfred mid Falconer & Rowe
32	2.8	211	346	-127	Fitzroy roof pos7 Alfred mid Falconer & Rowe
33	2.9	245	418	-127	Fitzroy roof pos7 Alfred mid Falconer & Rowe
34	-0.5	280	414	-127	Fitzroy roof pos7 Alfred mid Falconer & Rowe
35	2.2	289	332	-127	Fitzroy roof pos7 Alfred mid Falconer & Rowe
36	8.3	342	270	-127	Fitzroy roof pos8 cnr Alfred Crs & Rowe
37	7.9	516	324	-127	Fitzroy roof pos8 cnr Alfred Crs & Rowe
38	7.0	468	308	-127	Fitzroy roof pos8 cnr Alfred Crs & Rowe
39	6.4	436	281	-127	Fitzroy roof pos8 cnr Alfred Crs & Rowe
40	5.2	518	528	-127	Fitzroy roof pos8 cnr Alfred Crs & Rowe
41	7.9	315	351	-117	Fitzroy roof pos9 Alfred mid Rowe & Grant
42	2.4	424	254	-117	Fitzroy roof pos9 Alfred mid Rowe & Grant
43	-2.4	562	477	-117	Fitzroy roof pos9 Alfred mid Rowe & Grant
44	7.3	54	27	-117	Fitzroy roof pos9 Alfred mid Rowe & Grant
45	1.6	333	302	-117	Fitzroy roof pos9 Alfred mid Rowe & Grant
46	3.8	340	627	-117	Fitzroy roof pos10 cnr Alfred Crs & Grant
47	1.6	368	660	-117	Fitzroy roof pos10 cnr Alfred Crs & Grant
48	2.8	233	515	-117	Fitzroy roof pos10 cnr Alfred Crs & Grant
49	1.9	320	566	-117	Fitzroy roof pos10 cnr Alfred Crs & Grant
50	2.2	230	437	-117	Fitzroy roof pos10 cnr Alfred Crs & Grant
51	6.1	92	63	-117	Fitzroy roof pos11 cnr Alfred Crs & Jamieson
52	5.6	52	38	-117	Fitzroy roof pos11 cnr Alfred Crs & Jamieson
53	5.6	79	68	-117	Fitzroy roof pos11 cnr Alfred Crs & Jamieson
54	5.8	84	61	-117	Fitzroy roof pos11 cnr Alfred Crs & Jamieson
55	6.3	97	87	-117	Fitzroy roof pos11 cnr Alfred Crs & Jamieson
56	6.1	100	94	-127	Fitzroy roof pos12 cnr Jamieson & McKean
57	3.9	209	172	-127	Fitzroy roof pos12 cnr Jamieson & McKean
58	2.6	234	238	-127	Fitzroy roof pos12 cnr Jamieson & McKean
59	6.0	57	119	-127	Fitzroy roof pos12 cnr Jamieson & McKean
60	7.5	121	120	-127	Fitzroy roof pos12 cnr Jamieson & McKean
61	1.3	108	83	-117	Fitzroy roof pos13 cnr McKean & Grant
62	6.8	69	35	-117	Fitzroy roof pos13 cnr McKean & Grant
63	7.2	56	36	-117	Fitzroy roof pos13 cnr McKean & Grant
64	7.9	144	87	-117	Fitzroy roof pos13 cnr McKean & Grant
65	5.4	74	51	-117	Fitzroy roof pos13 cnr McKean & Grant
66	-0.3	87	71	-107	Fitzroy roof pos14 McKean mid Grant & Delbridge
67	-1.4	70	68	-107	Fitzroy roof pos14 McKean mid Grant & Delbridge
68	1.1	70	79	-107	Fitzroy roof pos14 McKean mid Grant & Delbridge
69	4.1	16	21	-107	Fitzroy roof pos14 McKean mid Grant & Delbridge
70	3.4	63	45	-107	Fitzroy roof pos14 McKean mid Grant & Delbridge
71	4.1	92	143	-107	Fitzroy roof pos15 McKean mid Del & Michael
72	0.6	113	167	-107	Fitzroy roof pos15 McKean mid Del & Michael
73	5.0	77	83	-107	Fitzroy roof pos15 McKean mid Del & Michael
74	5.8	38	33	-107	Fitzroy roof pos15 McKean mid Del & Michael
75	5.1	85	81	-107	Fitzroy roof pos15 McKean mid Del & Michael
76	5.1	242	246	-127	Fitzroy roof pos16 cnr Michael & McKean
77	3.8	170	322	-127	Fitzroy roof pos16 cnr Michael & McKean
78	4.6	194	234	-127	Fitzroy roof pos16 cnr Michael & McKean
79	4.6	195	254	-127	Fitzroy roof pos16 cnr Michael & McKean
80	3.6	266	363	-127	Fitzroy roof pos16 cnr Michael & McKean
81	2.5	330	409	-127	Fitzroy roof pos17 Michael mid McKean & Rowe
82	-0.1	293	427	-127	Fitzroy roof pos17 Michael mid McKean & Rowe
83	2.9	358	470	-127	Fitzroy roof pos17 Michael mid McKean & Rowe
84	3.8	362	362	-127	Fitzroy roof pos17 Michael mid McKean & Rowe
85	1.7	301	359	-127	Fitzroy roof pos17 Michael mid McKean & Rowe
86	0.2	245	167	-127	Fitzroy roof pos18 cnr Michael & Rowe
87	5.6	142	86	-127	Fitzroy roof pos18 cnr Michael & Rowe
88	1.8	273	267	-127	Fitzroy roof pos18 cnr Michael & Rowe

**TABLE E.8 Melbourne - Delbridge Street roof - filebase delrf (continued)**

file	dBV	rms delay (ns)	avg delay (ns)	gain factor (dB)	location of measurement
89	-3.5	215	208	-127	Fitzroy roof pos18 cnr Michael & Rowe
90	0.2	202	212	-127	Fitzroy roof pos18 cnr Michael & Rowe
91	-1.6	189	230	-127	Fitzroy roof pos19 Michael opp Woodside
92	3.7	128	157	-127	Fitzroy roof pos19 Michael opp Woodside
93	3.1	131	105	-127	Fitzroy roof pos19 Michael opp Woodside
94	-5.8	247	237	-127	Fitzroy roof pos19 Michael opp Woodside
95	1.7	129	153	-127	Fitzroy roof pos19 Michael opp Woodside
96	-2.1	187	187	-127	Fitzroy roof pos20 cnr Falconer & Michael
97	2.0	151	93	-127	Fitzroy roof pos20 cnr Falconer & Michael
98	1.9	131	81	-127	Fitzroy roof pos20 cnr Falconer & Michael
99	-1.1	331	281	-127	Fitzroy roof pos20 cnr Falconer & Michael
100	-1.4	223	180	-127	Fitzroy roof pos20 cnr Falconer & Michael
101	-2.0	120	186	-127	Fitzroy roof pos21 cnr Scotchmer & Mark
102	2.7	87	94	-127	Fitzroy roof pos21 cnr Scotchmer & Mark
103	-3.1	113	109	-127	Fitzroy roof pos21 cnr Scotchmer & Mark
104	-0.3	145	108	-127	Fitzroy roof pos21 cnr Scotchmer & Mark
105	-1.3	160	168	-127	Fitzroy roof pos21 cnr Scotchmer & Mark
106	2.8	229	216	-127	Fitzroy roof pos22 cnr St Georges & Scotchmer
107	-1.1	579	385	-127	Fitzroy roof pos22 cnr St Georges & Scotchmer
108	-1.2	534	388	-127	Fitzroy roof pos22 cnr St Georges & Scotchmer
109	-1.9	485	364	-127	Fitzroy roof pos22 cnr St Georges & Scotchmer
110	-0.4	132	227	-127	Fitzroy roof pos22 cnr St Georges & Scotchmer
111	-4.7	743	289	-127	Fitzroy roof pos23 cnr Best & St Georges
112	-5.5	883	382	-127	Fitzroy roof pos23 cnr Best & St Georges
113	-4.1	704	277	-127	Fitzroy roof pos23 cnr Best & St Georges
114	-8.0	1192	806	-127	Fitzroy roof pos23 cnr Best & St Georges
115	0.5	95	134	-127	Fitzroy roof pos23 cnr Best & St Georges
116	-4.1	1446	633	-127	Fitzroy roof pos24 cnr Best & Alfred Crs
117	-9.4	2059	1537	-127	Fitzroy roof pos24 cnr Best & Alfred Crs
119	-4.4	1981	1105	-127	Fitzroy roof pos24 cnr Best & Alfred Crs
121	-1.2	2558	844	-127	Fitzroy roof pos25 Alfred Crs near Best
122	-5.1	2493	917	-127	Fitzroy roof pos25 Alfred Crs near Best
123	0.9	85	79	-127	Fitzroy roof pos25 Alfred Crs near Best
124	-4.1	1501	396	-127	Fitzroy roof pos25 Alfred Crs near Best
125	-2.1	1242	328	-127	Fitzroy roof pos25 Alfred Crs near Best
126	7.1	14	16	-117	Fitzroy roof pos26 Brunswick St Cricket Ground
127	8.0	64	43	-117	Fitzroy roof pos26 Brunswick St Cricket Ground
128	5.7	37	26	-117	Fitzroy roof pos26 Brunswick St Cricket Ground
129	6.4	14	17	-117	Fitzroy roof pos26 Brunswick St Cricket Ground
130	4.1	67	46	-117	Fitzroy roof pos26 Brunswick St Cricket Ground
131	9.3	14	16	-127	Fitzroy roof pos27 Newry near Brunswick
132	4.9	54	37	-127	Fitzroy roof pos27 Newry near Brunswick
133	5.5	33	107	-127	Fitzroy roof pos27 Newry near Brunswick
134	5.6	50	80	-127	Fitzroy roof pos27 Newry near Brunswick
135	4.2	96	72	-127	Fitzroy roof pos27 Newry near Brunswick
136	1.4	78	173	-127	Fitzroy roof pos28 Napier St near Newry
137	4.1	66	127	-127	Fitzroy roof pos28 Napier St near Newry
138	3.3	129	79	-127	Fitzroy roof pos28 Napier St near Newry
139	4.5	92	120	-127	Fitzroy roof pos28 Napier St near Newry
140	5.3	91	73	-127	Fitzroy roof pos28 Napier St near Newry
141	8.9	105	204	-127	Fitzroy roof pos29 cnr Napier & Freeman
142	3.9	220	191	-127	Fitzroy roof pos29 cnr Napier & Freeman
143	8.9	90	67	-127	Fitzroy roof pos29 cnr Napier & Freeman
144	6.6	123	195	-127	Fitzroy roof pos29 cnr Napier & Freeman
145	5.2	171	199	-127	Fitzroy roof pos29 cnr Napier & Freeman
146	8.8	31	26	-127	Fitzroy roof pos30 Freeman near Napier
147	11.5	27	28	-127	Fitzroy roof pos30 Freeman near Napier
148	11.5	30	33	-127	Fitzroy roof pos30 Freeman near Napier
149	11.1	26	27	-127	Fitzroy roof pos30 Freeman near Napier
150	8.6	34	35	-127	Fitzroy roof pos30 Freeman near Napier
151	3.9	199	352	-127	Fitzroy roof pos31 Freeman near Brunswick
152	3.7	193	365	-127	Fitzroy roof pos31 Freeman near Brunswick
153	10.4	180	100	-127	Fitzroy roof pos31 Freeman near Brunswick
154	9.5	236	261	-127	Fitzroy roof pos31 Freeman near Brunswick



**TABLE E.8 Melbourne - Delbridge Street roof - filebase delrf (continued)**

file	dBV	rms delay (ns)	avg delay (ns)	gain factor (dB)	location of measurement
155	11.3	180	110	-127	Fitzroy roof pos31 Freeman near Brunswick
156	-0.8	404	293	-127	Fitzroy roof pos32 Brunswick N York
157	7.2	226	94	-127	Fitzroy roof pos32 Brunswick N York
158	4.8	292	153	-127	Fitzroy roof pos32 Brunswick N York
159	3.6	69	36	-127	Fitzroy roof pos32 Brunswick N York
160	-3.2	592	560	-127	Fitzroy roof pos32 Brunswick N York
161	3.2	71	32	-127	Fitzroy roof pos33 Brunswick S Queens Pd
162	2.6	103	49	-127	Fitzroy roof pos33 Brunswick S Queens Pd
163	1.4	160	113	-127	Fitzroy roof pos33 Brunswick S Queens Pd
164	3.3	109	49	-127	Fitzroy roof pos33 Brunswick S Queens Pd
165	2.8	130	72	-127	Fitzroy roof pos33 Brunswick S Queens Pd
166	-3.9	14	17	-127	Fitzroy roof pos34 Westgarth near Young
167	-1.0	44	38	-127	Fitzroy roof pos34 Westgarth near Young
168	-4.6	43	42	-127	Fitzroy roof pos34 Westgarth near Young
169	-2.8	38	32	-127	Fitzroy roof pos34 Westgarth near Young
170	1.3	24	20	-127	Fitzroy roof pos34 Westgarth near Young
171	-4.6	205	185	-127	Fitzroy roof pos35 Cecil St near pool
172	1.6	42	36	-127	Fitzroy roof pos35 Cecil St near pool
173	4.8	59	45	-127	Fitzroy roof pos35 Cecil St near pool
174	-0.1	78	83	-127	Fitzroy roof pos35 Cecil St near pool
175	4.2	80	53	-127	Fitzroy roof pos35 Cecil St near pool
176	-7.3	660	450	-127	Fitzroy roof pos36 Gore St near Cecil
177	1.3	82	63	-127	Fitzroy roof pos36 Gore St near Cecil
178	3.1	27	26	-127	Fitzroy roof pos36 Gore St near Cecil
179	-2.4	414	231	-127	Fitzroy roof pos36 Gore St near Cecil
180	2.5	642	264	-127	Fitzroy roof pos36 Gore St near Cecil
181	-1.3	149	86	-127	Fitzroy roof pos37 Gore St N Cecil
182	4.9	23	20	-127	Fitzroy roof pos37 Gore St N Cecil
183	1.6	215	91	-127	Fitzroy roof pos37 Gore St N Cecil
184	1.8	230	105	-127	Fitzroy roof pos37 Gore St N Cecil
185	3.7	189	87	-127	Fitzroy roof pos37 Gore St N Cecil
186	-0.9	16	19	-127	Fitzroy roof pos38 cnr Gore & Kerr
187	-8.6	294	219	-127	Fitzroy roof pos38 cnr Gore & Kerr
188	-9.8	395	358	-127	Fitzroy roof pos38 cnr Gore & Kerr
189	-5.2	147	74	-127	Fitzroy roof pos38 cnr Gore & Kerr
190	-6.5	3580	1064	-127	Fitzroy roof pos38 cnr Gore & Kerr
191	-1.7	2140	572	-127	Fitzroy roof pos39 cnr Johnston & Smith
192	0.2	119	116	-127	Fitzroy roof pos39 cnr Johnston & Smith
193	1.2	97	150	-127	Fitzroy roof pos39 cnr Johnston & Smith
194	2.6	77	175	-127	Fitzroy roof pos39 cnr Johnston & Smith
195	7.5	198	84	-127	Fitzroy roof pos40 Smith St near Johnston
196	7.5	93	64	-127	Fitzroy roof pos40 Smith St near Johnston
197	8.2	42	38	-127	Fitzroy roof pos40 Smith St near Johnston
198	10.0	23	23	-127	Fitzroy roof pos40 Smith St near Johnston
199	10.8	13	15	-127	Fitzroy roof pos40 Smith St near Johnston
200	11.8	14	17	-127	Fitzroy roof pos40 Smith St near Johnston
201	9.4	36	36	-127	Fitzroy roof pos40 Smith St near Johnston
202	11.3	31	34	-127	Fitzroy roof pos41 Smith just N Argyle
203	10.5	17	19	-127	Fitzroy roof pos41 Smith just N Argyle
204	12.1	40	22	-127	Fitzroy roof pos41 Smith just N Argyle
205	11.6	14	15	-127	Fitzroy roof pos41 Smith just N Argyle
206	13.1	14	16	-127	Fitzroy roof pos41 Smith just N Argyle
207	-0.4	452	285	-127	Fitzroy roof pos41 Smith just N Argyle
208	-2.8	420	315	-127	Fitzroy roof pos42 cnr Smith & Cecil
209	-0.2	384	234	-127	Fitzroy roof pos42 cnr Smith & Cecil
210	-0.2	340	153	-127	Fitzroy roof pos42 cnr Smith & Cecil
211	-2.4	552	383	-127	Fitzroy roof pos42 cnr Smith & Cecil
212	4.1	95	72	-127	Fitzroy roof pos42 cnr Smith & Cecil
213	2.9	160	121	-127	Fitzroy roof pos43 Smith 80m S Queens Pd
214	9.4	16	19	-127	Fitzroy roof pos43 Smith 80m S Queens Pd
215	9.7	39	41	-127	Fitzroy roof pos43 Smith 80m S Queens Pd
216	9.1	43	30	-127	Fitzroy roof pos43 Smith 80m S Queens Pd
217	6.3	116	74	-127	Fitzroy roof pos43 Smith 80m S Queens Pd
218	-3.7	307	300	-127	Fitzroy roof pos44 Hodgkinson near Hilton

**TABLE E.8 Melbourne - Delbridge Street roof - filebase delrf** (continued)

file	dBV	rms delay (ns)	avg delay (ns)	gain factor (dB)	location of measurement
219	4.8	92	49	-127	Fitzroy roof pos44 Hodgkinson near Hilton
220	-2.0	213	168	-127	Fitzroy roof pos44 Hodgkinson near Hilton
221	1.0	129	94	-127	Fitzroy roof pos44 Hodgkinson near Hilton
222	-1.7	182	273	-127	Fitzroy roof pos45 Hodgkinson near Gold
223	0.7	173	381	-127	Fitzroy roof pos45 Hodgkinson near Gold
224	-0.0	190	424	-127	Fitzroy roof pos45 Hodgkinson near Gold
225	2.0	223	295	-127	Fitzroy roof pos45 Hodgkinson near Gold
226	1.7	204	211	-127	Fitzroy roof pos45 Hodgkinson near Gold
227	2.3	197	142	-127	Fitzroy roof pos45 Hodgkinson near Gold
228	-6.0	283	283	-127	Fitzroy roof pos46 North Terrace
229	-4.6	232	311	-127	Fitzroy roof pos46 North Terrace
230	4.4	15	19	-127	Fitzroy roof pos46 North Terrace
231	-4.9	265	391	-127	Fitzroy roof pos46 North Terrace
232	2.0	317	174	-127	Fitzroy roof pos47 North Trc near Hoddle
233	5.4	83	56	-127	Fitzroy roof pos47 North Trc near Hoddle
234	5.9	34	31	-127	Fitzroy roof pos47 North Trc near Hoddle
235	2.9	206	105	-127	Fitzroy roof pos47 North Trc near Hoddle
236	0.5	389	220	-127	Fitzroy roof pos47 North Trc near Hoddle
237	6.3	51	21	-127	Fitzroy roof pos47 North Trc near Hoddle
238	2.2	223	169	-127	Fitzroy roof pos48 North Trc roundabout
239	0.2	349	359	-127	Fitzroy roof pos48 North Trc roundabout
240	-1.4	472	483	-127	Fitzroy roof pos48 North Trc roundabout
241	4.9	220	407	-127	Fitzroy roof pos48 North Trc roundabout
242	4.9	16	20	-127	Fitzroy roof pos49 Gold St mid gardens
243	5.5	112	75	-127	Fitzroy roof pos49 Gold St mid gardens
244	3.3	101	67	-127	Fitzroy roof pos49 Gold St mid gardens
245	2.3	116	82	-127	Fitzroy roof pos49 Gold St mid gardens
246	3.0	180	94	-127	Fitzroy roof pos49 Gold St mid gardens
247	-0.9	98	51	-127	Fitzroy roof pos50 South Terrace W
248	0.8	136	80	-127	Fitzroy roof pos50 South Terrace W
249	0.5	122	60	-127	Fitzroy roof pos50 South Terrace W
250	-2.2	127	61	-127	Fitzroy roof pos50 South Terrace W
251	-5.2	174	144	-127	Fitzroy roof pos50 South Terrace W
252	-5.1	188	132	-127	Fitzroy roof pos51 South Terrace E
253	-4.1	99	79	-127	Fitzroy roof pos51 South Terrace E
254	-1.3	62	69	-127	Fitzroy roof pos51 South Terrace E
255	2.3	63	48	-127	Fitzroy roof pos51 South Terrace E
256	2.1	33	34	-127	Fitzroy roof pos51 South Terrace E

# E.9 Canberra - City Hill

**Transmitter Location:** City Hill. north slope just below summit.

**Transmitter Antenna:** on 5m mast in pine trees. Discone antenna.

**Receiver:** in car with halfwave magnetic base antenna on roof.

**Sample time:** 10 ns, **Threshold:** -15 dB, **Range:** 25  $\mu$ s



**FIGURE E.11** Canberra - City Hill measurement locations



**TABLE E.9 Canberra - City Hill - filebase canc**

file	dBV	rms delay (ns)	avg delay (ns)	gain factor (dB)	location of measurement
1	0.6	1131	928	-120	CANBERRA City Hill pos1 City Hill car park
2	4.0	1225	1170	-120	CANBERRA City Hill pos1 City Hill car park
3	2.1	1261	1485	-120	CANBERRA City Hill pos1 City Hill car park
4	5.9	21	18	-100	CANBERRA City Hill pos2 Northbourne 100m N Alinga
5	5.1	16	14	-100	CANBERRA City Hill pos2 Northbourne 100m N Alinga
6	5.3	30	26	-100	CANBERRA City Hill pos2 Northbourne 100m N Alinga
7	-0.1	11	13	-100	CANBERRA City Hill pos3 cnr Northbourne & Rudd
8	-0.6	22	16	-100	CANBERRA City Hill pos3 cnr Northbourne & Rudd
9	2.1	29	24	-100	CANBERRA City Hill pos3 cnr Northbourne & Rudd
10	1.6	26	23	-100	CANBERRA City Hill pos3 cnr Northbourne & Rudd
11	-5.3	182	214	-130	CANBERRA City Hill pos4 Gould 20m W Northbourne
12	-2.9	160	116	-130	CANBERRA City Hill pos4 Gould 20m W Northbourne
13	-2.3	211	161	-130	CANBERRA City Hill pos4 Gould 20m W Northbourne
14	4.5	75	66	-130	CANBERRA City Hill pos5 cnr Northbourne & Gould
15	5.1	46	32	-130	CANBERRA City Hill pos5 cnr Northbourne & Gould
16	8.2	31	28	-130	CANBERRA City Hill pos5 cnr Northbourne & Gould
17	3.8	15	17	-110	CANBERRA City Hill pos6 Northbourne 100m N Gould
18	-0.3	15	16	-110	CANBERRA City Hill pos6 Northbourne 100m N Gould
19	3.2	14	16	-110	CANBERRA City Hill pos6 Northbourne 100m N Gould
20	-2.6	38	77	-130	CANBERRA City Hill pos7 Greenway 20m W Northbourne
21	-4.3	43	250	-130	CANBERRA City Hill pos7 Greenway 20m W Northbourne
22	-3.3	129	252	-130	CANBERRA City Hill pos7 Greenway 20m W Northbourne
23	-4.1	81	76	-130	CANBERRA City Hill pos8 cnr Wakefield & Northbourne
24	-3.6	67	123	-130	CANBERRA City Hill pos8 cnr Wakefield & Northbourne
25	-8.5	153	106	-130	CANBERRA City Hill pos8 cnr Wakefield & Northbourne
26	-4.2	44	44	-130	CANBERRA City Hill pos9 cnr Wakefield & Northbourne
27	-4.3	50	75	-130	CANBERRA City Hill pos9 cnr Wakefield & Northbourne
28	-5.3	57	61	-130	CANBERRA City Hill pos9 cnr Wakefield & Northbourne
29	-4.2	132	266	-130	CANBERRA City Hill pos10 Elourea 30m E Northbourne
30	-1.1	66	36	-130	CANBERRA City Hill pos10 Elourea 30m E Northbourne
31	-4.0	127	379	-130	CANBERRA City Hill pos10 Elourea 30m E Northbourne
32	-3.7	254	358	-130	CANBERRA City Hill pos11 Cooyong 30m W Mont
33	-9.0	494	607	-130	CANBERRA City Hill pos11 Cooyong 30m W Mont
34	-3.6	272	196	-130	CANBERRA City Hill pos11 Cooyong 30m W Mont
35	-3.2	353	410	-130	CANBERRA City Hill pos12 Mont 100m S Cooyong
36	-3.3	358	311	-130	CANBERRA City Hill pos12 Mont 100m S Cooyong
37	-7.0	323	483	-130	CANBERRA City Hill pos12 Mont 100m S Cooyong
38	1.9	264	723	-130	CANBERRA City Hill pos13 Mont St 20m N Bunda
39	-0.8	291	568	-130	CANBERRA City Hill pos13 Mont St 20m N Bunda
40	-1.1	399	804	-130	CANBERRA City Hill pos13 Mont St 20m N Bunda
41	-0.5	161	150	-130	CANBERRA City Hill pos14 Nangari opp Rabaul
42	-4.0	287	206	-130	CANBERRA City Hill pos14 Nangari opp Rabaul
43	-5.4	320	274	-130	CANBERRA City Hill pos14 Nangari opp Rabaul
44	2.0	129	111	-130	CANBERRA City Hill pos15 Nangari 10m W Rabaul
45	-0.9	185	149	-130	CANBERRA City Hill pos15 Nangari 10m W Rabaul
46	2.8	289	140	-130	CANBERRA City Hill pos15 Nangari 10m W Rabaul
47	9.0	133	127	-130	CANBERRA City Hill pos16 cnr London & Constitution
48	8.2	1040	863	-130	CANBERRA City Hill pos17 carpark opp Constitution
49	4.8	1245	1132	-130	CANBERRA City Hill pos17 carpark opp Constitution
50	10.7	805	502	-130	CANBERRA City Hill pos17 carpark opp Constitution
51	11.0	510	119	-130	CANBERRA City Hill pos17 carpark opp Constitution
52	10.2	735	318	-130	CANBERRA City Hill pos17 carpark opp Constitution
53	6.0	1016	768	-130	CANBERRA City Hill pos17 carpark opp Constitution
54	10.7	42	34	-130	CANBERRA City Hill pos17 carpark opp Constitution
55	13.6	558	185	-130	CANBERRA City Hill pos17 carpark opp Constitution
56	9.6	305	116	-130	CANBERRA City Hill pos17 carpark opp Constitution
57	9.8	371	144	-130	CANBERRA City Hill pos17 carpark opp Constitution
58	7.0	562	1099	-130	CANBERRA City Hill pos17 carpark opp Constitution
59	8.6	554	1407	-130	CANBERRA City Hill pos17 carpark opp Constitution
60	4.4	697	1383	-130	CANBERRA City Hill pos17 carpark opp Constitution
61	7.6	459	1517	-130	CANBERRA City Hill pos17 carpark opp Constitution
62	10.0	347	1322	-130	CANBERRA City Hill pos17 carpark opp Constitution

TABLE E.9 Canberra - City Hill - filebase canc

(continued)

file	dBV	rms delay (ns)	avg delay (ns)	gain factor (dB)	location of measurement
63	10.1	330	140	-130	CANBERRA City Hill pos17 carpark opp Constitution
64	5.6	706	1422	-130	CANBERRA City Hill pos17 carpark opp Constitution
65	8.3	859	814	-130	CANBERRA City Hill pos17 carpark opp Constitution
66	14.2	48	43	-130	CANBERRA City Hill pos18 cnr London & Constitution
67	15.1	40	23	-130	CANBERRA City Hill pos18 cnr London & Constitution
68	14.7	49	39	-130	CANBERRA City Hill pos18 cnr London & Constitution
69	4.6	125	131	-130	CANBERRA City Hill pos19 cnr Alara & Constitution
70	3.8	100	89	-130	CANBERRA City Hill pos19 cnr Alara & Constitution
71	8.0	43	53	-130	CANBERRA City Hill pos20 Constitution 50m W Coranderrk
72	9.2	41	39	-130	CANBERRA City Hill pos20 Constitution 50m W Coranderrk
73	6.4	70	58	-130	CANBERRA City Hill pos20 Constitution 50m W Coranderrk
74	-2.5	466	307	-130	CANBERRA City Hill pos21 Moore 10m S Cooyong
75	-3.7	195	190	-130	CANBERRA City Hill pos21 Moore 10m S Cooyong
76	-7.8	429	373	-130	CANBERRA City Hill pos21 Moore 10m S Cooyong
77	-2.1	398	469	-130	CANBERRA City Hill pos22 Moore 20m N Rudd
78	-2.5	413	468	-130	CANBERRA City Hill pos22 Moore 20m N Rudd
79	-2.3	338	585	-130	CANBERRA City Hill pos22 Moore 20m N Rudd
80	-6.4	1056	928	-130	CANBERRA City Hill pos23 Moore 50m N Alinga
81	-2.2	578	482	-130	CANBERRA City Hill pos23 Moore 50m N Alinga
82	-5.0	599	666	-130	CANBERRA City Hill pos23 Moore 50m N Alinga
83	-2.5	532	693	-130	CANBERRA City Hill pos24 Moore 50m S Alinga
84	-3.5	559	851	-130	CANBERRA City Hill pos24 Moore 50m S Alinga
85	-2.3	582	769	-130	CANBERRA City Hill pos24 Moore 50m S Alinga
86	3.8	455	282	-130	CANBERRA City Hill pos25 cnr Moore & London
87	10.3	59	45	-130	CANBERRA City Hill pos25 cnr Moore & London
88	8.1	103	92	-130	CANBERRA City Hill pos25 cnr Moore & London
89	2.2	642	765	-130	CANBERRA City Hill pos26 carpark City Hill
90	5.7	344	668	-130	CANBERRA City Hill pos26 carpark City Hill
91	4.9	401	624	-130	CANBERRA City Hill pos26 carpark City Hill
92	5.5	250	667	-130	CANBERRA City Hill pos26 carpark City Hill
93	3.9	462	653	-130	CANBERRA City Hill pos26 carpark City Hill
94	0.4	912	993	-130	CANBERRA City Hill pos26 carpark City Hill
95	3.2	650	749	-130	CANBERRA City Hill pos26 carpark City Hill
96	4.5	598	593	-130	CANBERRA City Hill pos26 carpark City Hill
97	3.5	2767	890	-130	CANBERRA City Hill pos26 carpark City Hill
98	13.0	193	436	-130	CANBERRA City Hill pos26 carpark City Hill
99	14.8	134	603	-130	CANBERRA City Hill pos26 carpark City Hill
100	8.6	254	605	-130	CANBERRA City Hill pos26 carpark City Hill
101	12.1	193	798	-130	CANBERRA City Hill pos26 carpark City Hill
102	6.4	314	712	-130	CANBERRA City Hill pos26 carpark City Hill
103	10.0	178	751	-130	CANBERRA City Hill pos26 carpark City Hill
104	8.8	256	817	-130	CANBERRA City Hill pos26 carpark City Hill
105	10.6	137	117	-130	CANBERRA City Hill pos27 carpark Farrell & London
106	8.0	89	129	-130	CANBERRA City Hill pos27 carpark Farrell & London
107	11.4	46	45	-130	CANBERRA City Hill pos27 carpark Farrell & London
108	4.1	151	136	-130	CANBERRA City Hill pos27 carpark Farrell & London
109	7.2	35	33	-130	CANBERRA City Hill pos27 carpark Farrell & London
110	6.0	133	157	-130	CANBERRA City Hill pos27 carpark Farrell & London
111	2.8	120	119	-130	CANBERRA City Hill pos27 carpark Farrell & London
112	9.2	80	54	-130	CANBERRA City Hill pos27 carpark Farrell & London
113	2.7	91	84	-130	CANBERRA City Hill pos27 carpark Farrell & London
114	4.1	129	122	-130	CANBERRA City Hill pos27 carpark Farrell & London
115	9.7	108	73	-130	CANBERRA City Hill pos27 carpark Farrell & London
116	7.9	94	62	-130	CANBERRA City Hill pos27 carpark Farrell & London
117	5.1	944	493	-130	CANBERRA City Hill pos27 carpark Farrell & London
118	4.7	806	385	-130	CANBERRA City Hill pos27 carpark Farrell & London
119	8.2	70	128	-130	CANBERRA City Hill pos27 carpark Farrell & London
120	2.7	620	354	-130	CANBERRA City Hill pos27 carpark Farrell & London
121	1.9	779	393	-130	CANBERRA City Hill pos27 carpark Farrell & London
122	8.9	62	47	-130	CANBERRA City Hill pos27 carpark Farrell & London
123	9.4	37	38	-130	CANBERRA City Hill pos27 carpark Farrell & London
124	3.1	577	246	-130	CANBERRA City Hill pos27 carpark Farrell & London
125	11.2	41	94	-130	CANBERRA City Hill pos27 carpark Farrell & London
126	5.2	88	138	-130	CANBERRA City Hill pos27 carpark Farrell & London

TABLE E.9 Canberra - City Hill - filebase canc

(continued)

file	dBV	rms delay (ns)	avg delay (ns)	gain factor (dB)	location of measurement
127	9.2	85	72	-130	CANBERRA City Hill pos27 carpark Farrell & London
128	10.0	88	109	-130	CANBERRA City Hill pos27 carpark Farrell & London
129	5.9	289	195	-130	CANBERRA City Hill pos27 carpark Farrell & London
130	11.3	32	95	-130	CANBERRA City Hill pos27 carpark Farrell & London
131	10.7	46	32	-130	CANBERRA City Hill pos27 carpark Farrell & London
132	3.7	86	87	-130	CANBERRA City Hill pos27 carpark Farrell & London
133	5.6	98	208	-130	CANBERRA City Hill pos27 carpark Farrell & London
134	9.0	120	107	-130	CANBERRA City Hill pos27 carpark Farrell & London
135	5.6	372	213	-130	CANBERRA City Hill pos27 carpark Farrell & London
136	11.2	40	45	-130	CANBERRA City Hill pos27 carpark Farrell & London
137	4.9	149	159	-130	CANBERRA City Hill pos27 carpark Farrell & London
138	12.8	59	53	-130	CANBERRA City Hill pos27 carpark Farrell & London
139	6.8	137	143	-130	CANBERRA City Hill pos27 carpark Farrell & London
140	-3.4	504	290	-130	CANBERRA City Hill pos28 cnr University & London
141	-3.7	361	263	-130	CANBERRA City Hill pos28 cnr University & London
142	0.2	269	159	-130	CANBERRA City Hill pos28 cnr University & London
143	3.8	153	78	-130	CANBERRA City Hill pos29 Hobart Place
144	10.2	69	46	-130	CANBERRA City Hill pos29 Hobart Place
145	13.8	20	20	-130	CANBERRA City Hill pos29 Hobart Place
146	-3.6	408	641	-130	CANBERRA City Hill pos30 Rudd 20m W Moore
147	-0.5	367	724	-130	CANBERRA City Hill pos30 Rudd 20m W Moore
148	-3.9	368	742	-130	CANBERRA City Hill pos30 Rudd 20m W Moore
149	-5.0	207	378	-130	CANBERRA City Hill pos30 Rudd 20m W Moore
150	-6.9	295	252	-130	CANBERRA City Hill pos31 cnr Rudd & Marcus Clark
151	-4.0	360	652	-130	CANBERRA City Hill pos31 cnr Rudd & Marcus Clark
152	-10.7	528	782	-130	CANBERRA City Hill pos31 cnr Rudd & Marcus Clark
153	-12.3	607	1075	-130	CANBERRA City Hill pos31 cnr Rudd & Marcus Clark
154	-4.5	475	490	-130	CANBERRA City Hill pos31 cnr Rudd & Marcus Clark
155	-3.5	297	523	-130	CANBERRA City Hill pos31 cnr Rudd & Marcus Clark
156	-4.2	297	406	-130	CANBERRA City Hill pos31 cnr Rudd & Marcus Clark
157	-4.3	277	704	-130	CANBERRA City Hill pos32 Rudd 20-80m W Moore
158	-4.2	301	714	-130	CANBERRA City Hill pos32 Rudd 20-80m W Moore
159	-6.0	418	648	-130	CANBERRA City Hill pos32 Rudd 20-80m W Moore
160	2.0	140	711	-130	CANBERRA City Hill pos32 Rudd 20-80m W Moore
161	-1.6	203	555	-130	CANBERRA City Hill pos32 Rudd 20-80m W Moore
162	0.6	233	599	-130	CANBERRA City Hill pos32 Rudd 20-80m W Moore
163	-0.6	284	607	-130	CANBERRA City Hill pos32 Rudd 20-80m W Moore
164	-2.9	440	829	-130	CANBERRA City Hill pos32 Rudd 20-80m W Moore
165	-4.9	484	659	-130	CANBERRA City Hill pos32 Rudd 20-80m W Moore
166	-5.6	512	821	-130	CANBERRA City Hill pos32 Rudd 20-80m W Moore
167	0.2	402	509	-130	CANBERRA City Hill pos32 Rudd 20-80m W Moore
168	0.3	332	540	-130	CANBERRA City Hill pos32 Rudd 20-80m W Moore
169	-1.6	300	633	-130	CANBERRA City Hill pos32 Rudd 20-80m W Moore
170	2.9	347	376	-130	CANBERRA City Hill pos32 Rudd 20-80m W Moore
171	-1.5	413	505	-130	CANBERRA City Hill pos32 Rudd 20-80m W Moore
172	3.2	242	248	-130	CANBERRA City Hill pos33 Rudd 20m E Moore
173	4.0	180	143	-130	CANBERRA City Hill pos33 Rudd 20m E Moore
174	0.9	316	232	-130	CANBERRA City Hill pos33 Rudd 20m E Moore
175	2.4	228	268	-130	CANBERRA City Hill pos33 Rudd 20m E Moore
176	6.4	42	64	-130	CANBERRA City Hill pos34 Gordon W Marcus Clark
177	4.4	107	88	-130	CANBERRA City Hill pos34 Gordon W Marcus Clark
178	4.4	79	92	-130	CANBERRA City Hill pos34 Gordon W Marcus Clark
179	1.3	54	39	-130	CANBERRA City Hill pos34 Gordon W Marcus Clark
180	-2.1	99	63	-130	CANBERRA City Hill pos35 cnr Gordon & McCoy
181	0.8	78	53	-130	CANBERRA City Hill pos35 cnr Gordon & McCoy
182	-4.4	173	155	-130	CANBERRA City Hill pos35 cnr Gordon & McCoy
183	-2.9	144	126	-130	CANBERRA City Hill pos36 McCoy Court
184	0.0	43	28	-130	CANBERRA City Hill pos36 McCoy Court
185	2.0	49	44	-130	CANBERRA City Hill pos36 McCoy Court
186	-2.5	107	72	-130	CANBERRA City Hill pos36 McCoy Court
187	-0.7	108	75	-130	CANBERRA City Hill pos36 McCoy Court
188	-2.7	178	144	-130	CANBERRA City Hill pos36 McCoy Court
189	-1.3	136	114	-130	CANBERRA City Hill pos36 McCoy Court
190	-2.7	173	228	-130	CANBERRA City Hill pos37 cnr Ellery & Liversidge

TABLE E.9 Canberra - City Hill - filebase canc (continued)

file	dBV	rms delay (ns)	avg delay (ns)	gain factor (dB)	location of measurement
191	-1.3	256	223	-130	CANBERRA City Hill pos37 cnr Ellery & Liversidge
192	-0.1	82	110	-130	CANBERRA City Hill pos37 cnr Ellery & Liversidge
193	-4.3	804	493	-130	CANBERRA City Hill pos38
194	6.3	139	115	-130	CANBERRA City Hill pos39 cnr Barry & Northbourne
195	7.1	117	158	-130	CANBERRA City Hill pos39 cnr Barry & Northbourne
196	6.5	100	120	-130	CANBERRA City Hill pos39 cnr Barry & Northbourne
197	13.4	26	29	-115	CANBERRA City Hill pos40 S side City Hill
198	10.0	21	25	-115	CANBERRA City Hill pos40 S side City Hill
199	10.8	13	15	-115	CANBERRA City Hill pos40 S side City Hill
200	6.1	40	46	-115	CANBERRA City Hill pos40 S side City Hill
201	14.6	73	75	-130	CANBERRA City Hill pos41 S side City Hill
202	14.4	67	56	-130	CANBERRA City Hill pos41 S side City Hill
203	6.2	1074	845	-130	CANBERRA City Hill pos41 S side City Hill
204	13.9	1004	547	-130	CANBERRA City Hill pos41 S side City Hill
205	13.2	594	515	-130	CANBERRA City Hill pos41 S side City Hill
206	8.0	961	625	-130	CANBERRA City Hill pos41 S side City Hill
207	12.8	975	485	-130	CANBERRA City Hill pos41 S side City Hill
208	14.7	85	75	-130	CANBERRA City Hill pos41 S side City Hill
209	13.3	409	100	-130	CANBERRA City Hill pos41 S side City Hill
210	13.5	60	37	-130	CANBERRA City Hill pos41 S side City Hill
211	5.7	1014	585	-130	CANBERRA City Hill pos41 S side City Hill
212	14.3	44	40	-130	CANBERRA City Hill pos41 S side City Hill
213	15.8	88	61	-130	CANBERRA City Hill pos41 S side City Hill
214	8.9	306	158	-130	CANBERRA City Hill pos41 S side City Hill
215	11.4	87	115	-130	CANBERRA City Hill pos41 S side City Hill

E.10 Canberra - O'Connor Suburban

Transmitter Location: 17 Nardo Crescent.  
Transmitter Antenna: 3m above 1st. floor balcony. Discone antenna.  
Receiver: in car with halfwave magnetic base antenna on roof.  
Sample time: 10 ns, Threshold: -15 dB, Range: 25  $\mu$ s



FIGURE E.12 Canberra - O'Connor suburban residential area

**TABLE E.10 Canberra - O'Connor suburban - filebase canb**

<b>file</b>	<b>dBV</b>	<b>rms delay (ns)</b>	<b>avg delay (ns)</b>	<b>gain factor (dB)</b>	<b>location of measurement</b>
1	11.1	19	20	-130	Canberra O'Connor pos1 Nardoo & Lomandra
2	-6.6	45	77	-130	Canberra O'Connor pos2 Nardoo opp Quandong
3	-4.6	349	244	-130	Canberra O'Connor pos3 Nardoo & Miller
4	-4.6	1454	400	-130	Canberra O'Connor pos3 Nardoo & Miller
5	1.0	123	91	-130	Canberra O'Connor pos4 Miller & Schrivener
6	-3.1	207	132	-130	Canberra O'Connor pos5 Miller & Clianthus
7	7.7	82	56	-130	Canberra O'Connor pos6 Miller Street
8	1.5	97	138	-130	Canberra O'Connor pos6 Miller Street
9	6.1	87	77	-130	Canberra O'Connor pos6 Miller Street
10	6.0	106	95	-130	Canberra O'Connor pos6 Miller Street
11	0.3	101	103	-130	Canberra O'Connor pos7 Miller & Banksia
12	-0.8	130	149	-130	Canberra O'Connor pos7 Miller & Banksia
13	2.6	82	45	-130	Canberra O'Connor pos7 Miller & Banksia
14	0.5	136	89	-130	Canberra O'Connor pos7 Miller & Banksia
15	1.1	48	34	-130	Canberra O'Connor pos8 MacArthur Av & Wonga
16	1.5	192	86	-130	Canberra O'Connor pos8 MacArthur Av & Wonga
17	-2.0	238	129	-130	Canberra O'Connor pos8 MacArthur Av & Wonga
18	0.2	190	119	-130	Canberra O'Connor pos8 MacArthur Av & Wonga
19	2.4	122	58	-130	Canberra O'Connor pos9 MacArthur Av & Sundew
20	0.1	145	109	-130	Canberra O'Connor pos9 MacArthur Av & Sundew
21	0.9	73	70	-130	Canberra O'Connor pos9 MacArthur Av & Sundew
22	-3.0	320	110	-130	Canberra O'Connor pos10 Wattle St at creek
23	-2.5	268	155	-130	Canberra O'Connor pos10 Wattle St at creek
24	-7.2	958	529	-130	Canberra O'Connor pos10 Wattle St at creek
25	-5.1	517	392	-130	Canberra O'Connor pos11 Wattle & Goodwin
26	-7.0	333	423	-130	Canberra O'Connor pos11 Wattle & Goodwin
27	-8.6	503	459	-130	Canberra O'Connor pos11 Wattle & Goodwin
28	-4.7	87	229	-130	Canberra O'Connor pos12 Wattle & Wandoo
29	-6.3	369	425	-130	Canberra O'Connor pos12 Wattle & Wandoo
30	-5.1	221	266	-130	Canberra O'Connor pos12 Wattle & Wandoo
31	-5.8	146	123	-130	Canberra O'Connor pos13 Wattle & Brigalow
32	-5.1	100	93	-130	Canberra O'Connor pos13 Wattle & Brigalow
34	-4.8	181	192	-130	Canberra O'Connor pos14 Wattle & Correa
35	-1.5	49	38	-130	Canberra O'Connor pos14 Wattle & Correa
36	0.9	16	19	-130	Canberra O'Connor pos14 Wattle & Correa
43	-3.7	163	153	-130	Canberra O'Connor pos16 Dryandra & Yarrow
45	3.0	106	65	-130	Canberra O'Connor pos16 Dryandra & Yarrow
46	-2.3	118	110	-130	Canberra O'Connor pos16 Dryandra & Yarrow
47	-0.5	115	91	-130	Canberra O'Connor pos16 Dryandra & Yarrow
48	1.8	106	82	-130	Canberra O'Connor pos16 Dryandra & Yarrow
49	4.7	21	23	-130	Canberra O'Connor pos16 Dryandra & Yarrow
50	4.2	35	25	-130	Canberra O'Connor pos17 Dryandra & Clianthus
51	1.6	31	33	-130	Canberra O'Connor pos17 Dryandra & Clianthus
54	2.6	81	47	-130	Canberra O'Connor pos17 Dryandra & Clianthus
60	-2.8	156	90	-130	Canberra O'Connor pos19 Dryandra Street
69	-5.5	28	28	-130	Canberra O'Connor pos20 Dryandra & Faunce
70	-8.5	69	59	-130	Canberra O'Connor pos20 Dryandra & Faunce
71	-7.1	25	20	-130	Canberra O'Connor pos20 Dryandra & Faunce
72	-2.2	90	76	-130	Canberra O'Connor pos21 Dryandra Street
73	-6.2	161	129	-130	Canberra O'Connor pos21 Dryandra Street
74	-5.5	106	127	-130	Canberra O'Connor pos21 Dryandra Street
75	-8.7	93	131	-130	Canberra O'Connor pos21 Dryandra Street



E.11 Canberra - Dundas Court

**Transmitter Location:** Total Peripherals, 53 Dundas Court, Woden  
**Transmitter Antenna:** mast 4m above flat 2nd. floor roof.  
**Receiver:** in car with halfwave magnetic base on roof.  
**Sample time:** 10 ns, **Threshold:** -15 dB, **Range:** 25  $\mu$ s

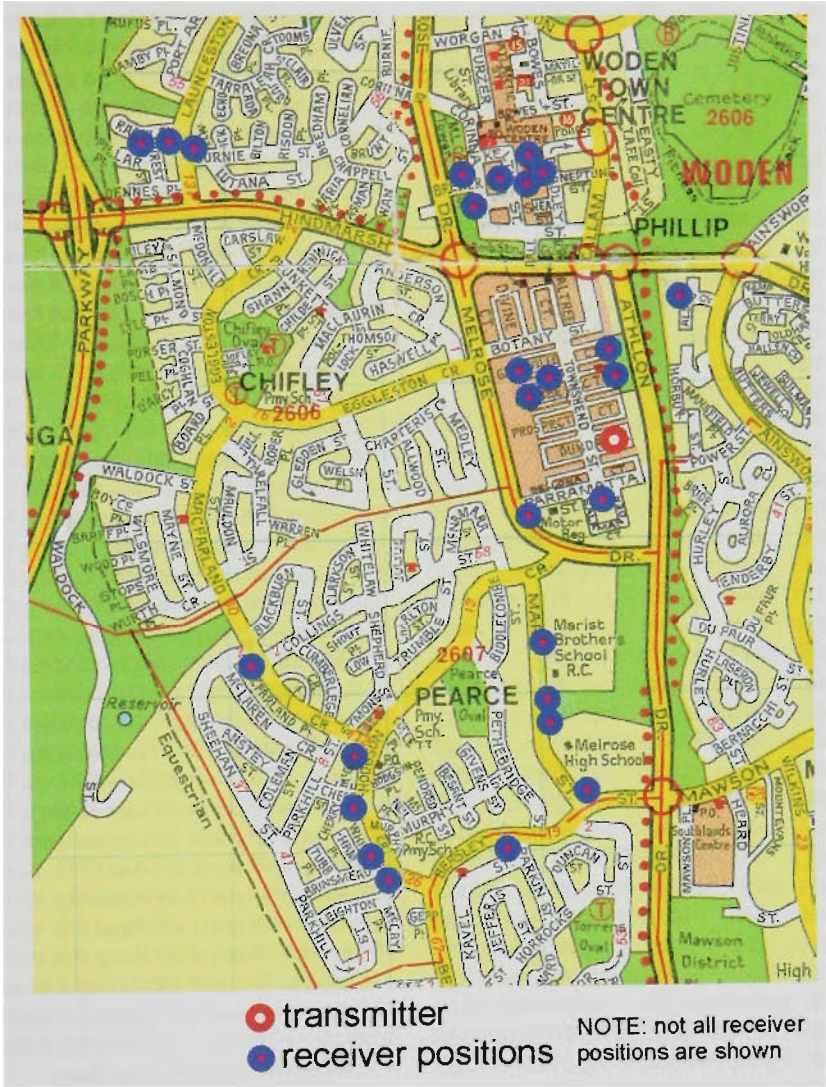


FIGURE E.13 Canberra - Dundas Court light industrial area

TABLE E.11 Canberra - Dundas Court - filebase canbb

file	dBV	rms delay (ns)	avg delay (ns)	gain factor (dB)	location of measurement
1	7.2	39	71	-100	Canberra TP pos1 S end Townshend St
2	7.6	48	27	-100	Canberra TP pos1 S end Townshend St
3	7.6	57	53	-100	Canberra TP pos1 S end Townshend St
4	13.3	125	50	-120	Canberra TP pos2 cnr Melrose & Townshend
5	12.7	14	15	-120	Canberra TP pos2 cnr Melrose & Townshend
6	13.4	142	57	-120	Canberra TP pos2 cnr Melrose & Townshend
7	-5.2	902	317	-120	Canberra TP pos3 Marr Street
8	-3.4	209	73	-120	Canberra TP pos3 Marr Street
9	-11.7	1332	966	-120	Canberra TP pos3 Marr Street
10	-1.9	1581	314	-130	Canberra TP pos4 Marr Street
11	-7.5	4150	2245	-130	Canberra TP pos4 Marr Street

**TABLE E.11 Canberra - Dundas Court - filebase canbb** (continued)

file	dBV	rms delay (ns)	avg delay (ns)	gain factor (dB)	location of measurement
12	-8.1	4954	3037	-130	Canberra TP pos4 Marr Street
13	-2.5	3384	1059	-130	Canberra TP pos5 Marr Street
14	-7.9	4471	2095	-130	Canberra TP pos5 Marr Street
15	-10.5	68	228	-130	Canberra TP pos5 Marr Street
16	-2.3	1789	1282	-130	Canberra TP pos6 cnr Marr & Beasley
17	-1.3	1203	2905	-130	Canberra TP pos6 cnr Marr & Beasley
18	-6.8	1845	2298	-130	Canberra TP pos6 cnr Marr & Beasley
19	-7.4	30	31	-130	Canberra TP pos7 cnr Beasley & Parkin
20	-4.1	14	16	-130	Canberra TP pos7 cnr Beasley & Parkin
22	-0.8	92	57	-130	Canberra TP pos8 cnr Beasley & Brinsmead
23	-6.6	799	224	-130	Canberra TP pos8 cnr Beasley & Brinsmead
24	-2.2	46	50	-130	Canberra TP pos8 cnr Beasley & Brinsmead
25	-3.6	77	73	-130	Canberra TP pos8 cnr Beasley & Brinsmead
26	10.9	18	19	-130	Canberra TP pos9 cnr Hodgson & Murphy
27	1.3	51	31	-130	Canberra TP pos9 cnr Hodgson & Murphy
28	5.5	19	22	-130	Canberra TP pos9 cnr Hodgson & Murphy
29	-1.4	156	114	-130	Canberra TP pos9 cnr Hodgson & Murphy
30	1.3	92	43	-130	Canberra TP pos10 cnr Hodgson & Cherry
31	0.9	136	120	-130	Canberra TP pos10 cnr Hodgson & Cherry
32	-0.0	134	93	-130	Canberra TP pos10 cnr Hodgson & Cherry
33	-2.6	187	138	-130	Canberra TP pos11 cnr Macfarland & Hodgson
34	-1.9	136	155	-130	Canberra TP pos11 cnr Macfarland & Hodgson
35	-12.1	650	501	-130	Canberra TP pos11 cnr Macfarland & Hodgson
36	-1.5	26	27	-130	Canberra TP pos12 cnr Macfarland & Collings
37	-1.6	22	21	-130	Canberra TP pos12 cnr Macfarland & Collings
38	-4.7	49	31	-130	Canberra TP pos12 cnr Macfarland & Collings
39	-4.5	219	196	-130	Canberra TP pos13 cnr Launceston & Bumie
40	-6.2	231	188	-130	Canberra TP pos13 cnr Launceston & Bumie
41	-0.3	89	36	-130	Canberra TP pos13 cnr Launceston & Bumie
42	-0.4	93	53	-130	Canberra TP pos13 cnr Launceston & Bumie
43	-7.6	177	264	-130	Canberra TP pos14 cnr Launceston & Raoul PI
44	-6.9	164	224	-130	Canberra TP pos14 cnr Launceston & Raoul PI
45	-7.2	141	204	-130	Canberra TP pos14 cnr Launceston & Raoul PI
46	6.5	37	29	-130	Canberra TP pos15 cnr Raoul PI & Wrest
47	8.2	50	23	-130	Canberra TP pos15 cnr Raoul PI & Wrest
48	4.3	51	51	-130	Canberra TP pos15 cnr Raoul PI & Wrest
49	-2.9	105	165	-130	Canberra TP pos15 cnr Raoul PI & Wrest
50	-5.9	805	546	-130	Canberra TP pos16 cnr Corinna & Brewer
51	-8.8	899	637	-130	Canberra TP pos16 cnr Corinna & Brewer
52	-1.4	131	143	-130	Canberra TP pos16 cnr Corinna & Brewer
53	-0.0	413	158	-130	Canberra TP pos17 Corinna Street
54	-1.9	856	435	-130	Canberra TP pos17 Corinna Street
55	-0.8	686	259	-130	Canberra TP pos17 Corinna Street
56	-3.4	1067	858	-130	Canberra TP pos18 Corinna Street
57	-2.2	1045	761	-130	Canberra TP pos18 Corinna Street
58	-1.2	1147	795	-130	Canberra TP pos18 Corinna Street
59	-8.3	1223	1275	-130	Canberra TP pos18 Corinna Street
60	2.8	21	25	-130	Canberra TP pos19 Brewer near Corinna
61	2.0	213	48	-130	Canberra TP pos19 Brewer near Corinna
62	-3.6	427	138	-130	Canberra TP pos19 Brewer near Corinna
63	-0.5	1183	1098	-130	Canberra TP pos20 Keltie Street
64	-9.9	1240	1627	-130	Canberra TP pos20 Keltie Street
65	3.1	855	369	-130	Canberra TP pos20 Keltie Street
66	3.5	825	2824	-130	Canberra TP pos21 Woden Centre carpark
67	4.5	1255	2386	-130	Canberra TP pos21 Woden Centre carpark
68	3.4	1213	2370	-130	Canberra TP pos21 Woden Centre carpark
69	6.2	34	35	-130	Canberra TP pos21 Woden Centre carpark
70	1.2	1063	522	-130	Canberra TP pos21 Woden Centre carpark
71	1.0	1144	568	-130	Canberra TP pos21 Woden Centre carpark
72	-7.9	1677	1262	-130	Canberra TP pos22 Ball Street
73	-7.1	2219	2619	-130	Canberra TP pos22 Ball Street
74	-7.3	1846	3746	-130	Canberra TP pos22 Ball Street
75	5.3	996	285	-130	Canberra TP pos23 Botany Street
76	11.8	21	25	-130	Canberra TP pos23 Botany Street

**TABLE E.11 Canberra - Dundas Court - filebase canbb (continued)**

<b>file</b>	<b>dBV</b>	<b>rms delay (ns)</b>	<b>avg delay (ns)</b>	<b>gain factor (dB)</b>	<b>location of measurement</b>
77	9.7	23	26	-130	Canberra TP pos23 Botany Street
78	8.4	856	519	-130	Canberra TP pos24 N end Townshend
79	5.6	835	607	-130	Canberra TP pos24 N end Townshend
80	4.4	776	675	-130	Canberra TP pos24 N end Townshend
81	3.2	561	423	-130	Canberra TP pos25 Grenville Crt
82	4.5	197	299	-130	Canberra TP pos25 Grenville Crt
83	2.7	308	397	-130	Canberra TP pos25 Grenville Crt
84	7.4	437	276	-130	Canberra TP pos25 Grenville Crt
85	2.9	408	395	-130	Canberra TP pos25 Grenville Crt
86	1.0	501	521	-130	Canberra TP pos25 Grenville Crt
87	0.9	516	418	-130	Canberra TP pos25 Grenville Crt
88	12.0	278	168	-130	Canberra TP pos26 E end Grenville
89	12.3	207	89	-130	Canberra TP pos26 E end Grenville
90	8.4	270	132	-130	Canberra TP pos26 E end Grenville
91	4.8	320	639	-130	Canberra TP pos27 Colbee Crt
92	2.6	423	738	-130	Canberra TP pos27 Colbee Crt
93	-1.4	625	1184	-130	Canberra TP pos27 Colbee Crt
94	5.8	263	306	-130	Canberra TP pos28 SW end Colbee
95	0.4	926	538	-130	Canberra TP pos28 SW end Colbee
96	7.4	219	191	-130	Canberra TP pos28 SW end Colbee
97	10.2	151	164	-130	Canberra TP pos28 SW end Colbee
98	7.1	1296	437	-130	Canberra TP pos28 SW end Colbee
99	2.2	1965	917	-130	Canberra TP pos29 W end Colbee
100	0.7	2570	1355	-130	Canberra TP pos29 W end Colbee
101	-2.3	2704	1682	-130	Canberra TP pos29 W end Colbee
102	2.4	426	358	-130	Canberra TP pos30 Colbee mid NW leg
103	5.2	245	355	-130	Canberra TP pos30 Colbee mid NW leg
104	4.9	376	430	-130	Canberra TP pos30 Colbee mid NW leg
105	13.8	102	281	-130	Canberra TP pos30 Colbee mid NW leg
106	12.0	139	199	-130	Canberra TP pos31 Colbee mid NE leg
107	10.3	239	271	-130	Canberra TP pos31 Colbee mid NE leg
108	10.2	240	285	-130	Canberra TP pos31 Colbee mid NE leg
109	16.2	271	167	-130	Canberra TP pos32 NE end Colbee
110	14.7	287	173	-130	Canberra TP pos32 NE end Colbee
111	16.7	277	201	-130	Canberra TP pos32 NE end Colbee
112	9.9	199	569	-130	Canberra TP pos33 Colbee mid SE leg
113	9.9	156	408	-130	Canberra TP pos33 Colbee mid SE leg
114	7.7	224	498	-130	Canberra TP pos33 Colbee mid SE leg
115	2.5	157	114	-130	Canberra TP pos34 cnr Hindmarsh & Ainsworth
116	7.0	56	34	-130	Canberra TP pos34 cnr Hindmarsh & Ainsworth
117	1.1	159	123	-130	Canberra TP pos34 cnr Hindmarsh & Ainsworth
118	10.8	401	120	-130	Canberra TP pos35 cnr Alsop Cl & Ainsworth
119	10.8	55	128	-130	Canberra TP pos35 cnr Alsop Cl & Ainsworth
120	12.3	54	107	-130	Canberra TP pos35 cnr Alsop Cl & Ainsworth
121	14.2	44	45	-130	Canberra TP pos36 W end Alsop Cl
122	14.1	61	50	-130	Canberra TP pos36 W end Alsop Cl
123	8.9	91	95	-130	Canberra TP pos36 W end Alsop Cl
124	15.9	16	19	-120	Canberra TP pos36 W end Alsop Cl
125	16.8	16	18	-120	Canberra TP pos36 W end Alsop Cl
126	14.0	48	27	-120	Canberra TP pos36 W end Alsop Cl
127	11.4	85	40	-120	Canberra TP pos37 Ainsworth opp Horbury
128	11.7	42	26	-120	Canberra TP pos37 Ainsworth opp Horbury
129	13.7	13	15	-120	Canberra TP pos37 Ainsworth opp Horbury
130	2.4	154	243	-130	Canberra TP pos38 Ainsworth opp Power
131	3.7	323	252	-130	Canberra TP pos38 Ainsworth opp Power
132	6.1	100	258	-130	Canberra TP pos38 Ainsworth opp Power
133	7.6	203	72	-130	Canberra TP pos39 Butlers Dv and Sulman PI
134	7.2	25	25	-130	Canberra TP pos39 Butlers Dv and Sulman PI
135	1.3	71	108	-130	Canberra TP pos39 Butlers Dv and Sulman PI
136	6.7	503	316	-130	Canberra TP pos39 Butlers Dv and Sulman PI
137	13.2	380	257	-130	Canberra TP pos40 Sulman PI
138	13.2	381	223	-130	Canberra TP pos40 Sulman PI
139	9.4	316	223	-130	Canberra TP pos40 Sulman PI
140	4.4	108	187	-130	Canberra TP pos41 Ainsworth & Enderby



TABLE E.11 Canberra - Dundas Court - filebase canbb (continued)

file	dBV	rms delay (ns)	avg delay (ns)	gain factor (dB)	location of measurement
141	5.1	82	76	-130	Canberra TP pos41 Ainsworth & Enderby
142	4.2	157	126	-130	Canberra TP pos41 Ainsworth & Enderby
143	11.9	12	14	-130	Canberra TP pos42 Salvation Army carpark
144	9.1	43	24	-130	Canberra TP pos42 Salvation Army carpark
145	5.9	42	33	-130	Canberra TP pos42 Salvation Army carpark
146	4.4	118	138	-130	Canberra TP pos42 Salvation Army carpark
147	7.9	121	105	-130	Canberra TP pos42 Salvation Army carpark
148	6.6	126	130	-130	Canberra TP pos42 Salvation Army carpark
149	2.0	157	176	-130	Canberra TP pos42 Salvation Army carpark
150	5.9	94	141	-130	Canberra TP pos42 Salvation Army carpark
151	7.4	100	44	-130	Canberra TP pos43 Athllon Dr & Melrose
152	7.7	137	67	-130	Canberra TP pos43 Athllon Dr & Melrose
153	8.1	90	33	-130	Canberra TP pos43 Athllon Dr & Melrose
154	7.0	184	107	-110	Canberra TP pos44 Parramatta & Melrose
155	8.0	144	69	-110	Canberra TP pos44 Parramatta & Melrose
156	3.3	228	249	-110	Canberra TP pos44 Parramatta & Melrose
157	12.1	183	98	-110	Canberra TP pos44 Parramatta & Melrose

NOTE: TP = Total Peripherals (company building roof used for transmitter site)

E.12 Sydney - McMahon's Point

**Transmitter Location:** 21 East Crescent, McMahon's Point.  
**Transmitter Antenna:** on boom beyond 4th. floor balcony, overlooking harbour. Halfwave antenna.  
**Receiver:** in car with halfwave magnetic base antenna on roof.  
**Sample time:** 10 ns, **Threshold:** -15 dB, **Range:** 25 μs

TABLE E.12 Sydney - McMahon's Point - filebase syda

file	dBV	rms delay (ns)	avg delay (ns)	gain factor (ns)	location of measurement
1	1.8	1470	2367	-130	SYDNEY McM Pt2 pos1 cnr Blues Pt & Henry Lawson
2	2.3	1259	2705	-130	SYDNEY McM Pt2 pos1 cnr Blues Pt & Henry Lawson
3	0.7	1424	2417	-130	SYDNEY McM Pt2 pos1 cnr Blues Pt & Henry Lawson
4	2.1	1269	2714	-130	SYDNEY McM Pt2 pos1 cnr Blues Pt & Henry Lawson
5	-2.2	2247	3186	-130	SYDNEY McM Pt2 pos2 Henry Lawson Av E end
6	-0.1	1736	2533	-130	SYDNEY McM Pt2 pos2 Henry Lawson Av E end
7	-0.4	2207	2863	-130	SYDNEY McM Pt2 pos2 Henry Lawson Av E end
8	0.6	2002	2846	-130	SYDNEY McM Pt2 pos2 Henry Lawson Av E end
9	-0.2	2228	6492	-130	SYDNEY McM Pt2 pos2 Henry Lawson Av E end
10	0.2	2042	6562	-130	SYDNEY McM Pt2 pos2 Henry Lawson Av E end
11	0.2	2464	3052	-130	SYDNEY McM Pt2 pos2 Henry Lawson Av E end
12	-0.5	2311	2739	-130	SYDNEY McM Pt2 pos2 Henry Lawson Av E end
13	-0.5	2937	3657	-130	SYDNEY McM Pt2 pos2 Henry Lawson Av E end
14	-0.7	2182	3327	-130	SYDNEY McM Pt2 pos2 Henry Lawson Av E end
15	0.4	2400	3266	-130	SYDNEY McM Pt2 pos2 Henry Lawson Av E end
16	2.2	2616	2909	-130	SYDNEY McM Pt2 pos2 Henry Lawson Av E end
17	1.6	2119	2702	-130	SYDNEY McM Pt2 pos2 Henry Lawson Av E end
18	1.4	2344	2475	-130	SYDNEY McM Pt2 pos2 Henry Lawson Av E end
19	2.3	2156	2474	-130	SYDNEY McM Pt2 pos2 Henry Lawson Av E end
20	2.4	2312	2380	-130	SYDNEY McM Pt2 pos2 Henry Lawson Av E end
21	4.6	2849	1594	-130	SYDNEY McM Pt2 pos3 Henry Lawson Av
22	3.6	3004	1792	-130	SYDNEY McM Pt2 pos3 Henry Lawson Av
23	3.1	3383	6559	-130	SYDNEY McM Pt2 pos3 Henry Lawson Av

**TABLE E.12 Sydney - McMahons Point - filebase syda** (continued)

file	dBV	rms delay (ns)	avg delay (ns)	gain factor (ns)	location of measurement
24	1.9	2280	5848	-130	SYDNEY McM Pt2 pos3 Henry Lawson Av
25	1.7	2161	5553	-130	SYDNEY McM Pt2 pos3 Henry Lawson Av
26	2.6	2538	5645	-130	SYDNEY McM Pt2 pos3 Henry Lawson Av
27	3.5	1372	5269	-130	SYDNEY McM Pt2 pos3 Henry Lawson Av
28	12.7	1455	4265	-130	SYDNEY McM Pt2 pos4 McMahons Pt wharf
29	12.3	1662	4332	-130	SYDNEY McM Pt2 pos4 McMahons Pt wharf
30	13.4	1981	3695	-130	SYDNEY McM Pt2 pos4 McMahons Pt wharf
31	12.6	1601	4673	-130	SYDNEY McM Pt2 pos4 McMahons Pt wharf
32	15.3	1425	4190	-130	SYDNEY McM Pt2 pos4 McMahons Pt wharf
33	11.4	1678	4625	-130	SYDNEY McM Pt2 pos4 McMahons Pt wharf
34	11.1	1152	3812	-130	SYDNEY McM Pt2 pos4 McMahons Pt wharf
35	12.9	1029	3920	-130	SYDNEY McM Pt2 pos4 McMahons Pt wharf
36	14.5	1361	4470	-130	SYDNEY McM Pt2 pos4 McMahons Pt wharf
37	13.2	1388	4617	-130	SYDNEY McM Pt2 pos4 McMahons Pt wharf
38	10.5	1649	4844	-130	SYDNEY McM Pt2 pos4 McMahons Pt wharf
39	11.3	1302	4364	-130	SYDNEY McM Pt2 pos4 McMahons Pt wharf
40	12.9	1647	4122	-130	SYDNEY McM Pt2 pos4 McMahons Pt wharf
41	10.0	1227	2727	-130	SYDNEY McM Pt2 pos5 McMahons Pt wharf
42	11.5	875	2612	-130	SYDNEY McM Pt2 pos5 McMahons Pt wharf
43	8.9	1194	4606	-130	SYDNEY McM Pt2 pos5 McMahons Pt wharf
44	9.0	1377	4650	-130	SYDNEY McM Pt2 pos5 McMahons Pt wharf
45	6.9	1467	3175	-130	SYDNEY McM Pt2 pos5 McMahons Pt wharf
46	9.6	1007	2950	-130	SYDNEY McM Pt2 pos5 McMahons Pt wharf
47	10.4	2790	4234	-130	SYDNEY McM Pt2 pos5 McMahons Pt wharf
48	9.7	1074	2524	-130	SYDNEY McM Pt2 pos5 McMahons Pt wharf
49	10.3	864	2503	-130	SYDNEY McM Pt2 pos5 McMahons Pt wharf
50	8.6	1243	2955	-130	SYDNEY McM Pt2 pos5 McMahons Pt wharf
51	14.2	756	4062	-130	SYDNEY McM Pt2 pos6 McMahons Point
52	16.5	1709	4189	-130	SYDNEY McM Pt2 pos6 McMahons Point
53	14.9	2281	3514	-130	SYDNEY McM Pt2 pos6 McMahons Point
54	13.9	1615	4205	-130	SYDNEY McM Pt2 pos6 McMahons Point
55	16.8	1526	4423	-130	SYDNEY McM Pt2 pos6 McMahons Point
56	14.2	1517	4189	-130	SYDNEY McM Pt2 pos6 McMahons Point
57	14.4	1240	4781	-130	SYDNEY McM Pt2 pos6 McMahons Point
58	15.6	1392	4623	-130	SYDNEY McM Pt2 pos6 McMahons Point
59	12.4	1911	4212	-130	SYDNEY McM Pt2 pos6 McMahons Point
60	13.7	963	1846	-130	SYDNEY McM Pt2 pos6 McMahons Point
61	4.0	885	2365	-130	SYDNEY McM Pt2 pos7 Blues Pt Rd harbour end
62	6.2	566	2422	-130	SYDNEY McM Pt2 pos7 Blues Pt Rd harbour end
63	7.5	639	2271	-130	SYDNEY McM Pt2 pos7 Blues Pt Rd harbour end
64	6.0	706	2192	-130	SYDNEY McM Pt2 pos7 Blues Pt Rd harbour end
65	1.1	1019	2110	-130	SYDNEY McM Pt2 pos7 Blues Pt Rd harbour end
66	7.0	712	2336	-130	SYDNEY McM Pt2 pos7 Blues Pt Rd harbour end
67	3.4	1051	2177	-130	SYDNEY McM Pt2 pos7 Blues Pt Rd harbour end
68	3.3	1035	2052	-130	SYDNEY McM Pt2 pos7 Blues Pt Rd harbour end
69	2.6	985	2311	-130	SYDNEY McM Pt2 pos7 Blues Pt Rd harbour end
70	6.9	620	1834	-130	SYDNEY McM Pt2 pos7 Blues Pt Rd harbour end
71	2.6	923	2458	-130	SYDNEY McM Pt2 pos7 Blues Pt Rd harbour end
72	3.0	924	2342	-130	SYDNEY McM Pt2 pos7 Blues Pt Rd harbour end
73	0.7	1387	5580	-130	SYDNEY McM Pt2 pos7 Blues Pt Rd harbour end
74	-0.4	1112	2110	-130	SYDNEY McM Pt2 pos7 Blues Pt Rd harbour end
75	7.0	755	1724	-130	SYDNEY McM Pt2 pos7 Blues Pt Rd harbour end
76	4.5	1037	5055	-130	SYDNEY McM Pt2 pos7 Blues Pt Rd harbour end
77	6.5	988	5143	-130	SYDNEY McM Pt2 pos7 Blues Pt Rd harbour end
78	3.9	1101	5072	-130	SYDNEY McM Pt2 pos7 Blues Pt Rd harbour end
79	4.5	1129	4980	-130	SYDNEY McM Pt2 pos7 Blues Pt Rd harbour end
80	5.1	1081	4779	-130	SYDNEY McM Pt2 pos7 Blues Pt Rd harbour end
81	4.3	991	1421	-130	SYDNEY McM Pt2 pos7 Blues Pt Rd harbour end
82	2.8	1164	1799	-130	SYDNEY McM Pt2 pos7 Blues Pt Rd harbour end
83	2.1	1256	2402	-130	SYDNEY McM Pt2 pos7 Blues Pt Rd harbour end
84	7.0	724	1974	-130	SYDNEY McM Pt2 pos7 Blues Pt Rd harbour end
85	10.2	538	1953	-130	SYDNEY McM Pt2 pos7 Blues Pt Rd harbour end
86	2.5	2101	1174	-130	SYDNEY McM Pt2 pos8 East Crescent
87	1.6	2514	1902	-130	SYDNEY McM Pt2 pos8 East Crescent

TABLE E.12 Sydney - McMahons Point - filebase syda (continued)

file	dBV	rms delay (ns)	avg delay (ns)	gain factor (ns)	location of measurement
88	3.0	2444	2121	-130	SYDNEY McM Pt2 pos8 East Crescent
89	6.5	59	31	-130	SYDNEY McM Pt2 pos8 East Crescent
90	-0.9	2700	3380	-130	SYDNEY McM Pt2 pos8 East Crescent
91	3.8	2231	1571	-130	SYDNEY McM Pt2 pos8 East Crescent
92	2.1	2534	1506	-130	SYDNEY McM Pt2 pos8 East Crescent
93	3.4	2742	2540	-130	SYDNEY McM Pt2 pos8 East Crescent
94	6.5	839	161	-130	SYDNEY McM Pt2 pos8 East Crescent
95	3.5	2809	1882	-130	SYDNEY McM Pt2 pos8 East Crescent
96	6.3	2974	3128	-130	SYDNEY McM Pt2 pos9 cnr Parker & Middle St
97	3.0	2184	1424	-130	SYDNEY McM Pt2 pos9 cnr Parker & Middle St
98	5.7	2825	2440	-130	SYDNEY McM Pt2 pos9 cnr Parker & Middle St
99	3.5	2480	1680	-130	SYDNEY McM Pt2 pos9 cnr Parker & Middle St
100	6.0	2012	948	-130	SYDNEY McM Pt2 pos9 cnr Parker & Middle St
101	-0.9	1324	1672	-130	SYDNEY McM Pt2 pos10 Middle St S end
102	-1.5	914	1348	-130	SYDNEY McM Pt2 pos10 Middle St S end
103	2.3	1254	829	-130	SYDNEY McM Pt2 pos10 Middle St S end
104	0.8	1972	5151	-130	SYDNEY McM Pt2 pos10 Middle St S end
105	-2.4	1294	1440	-130	SYDNEY McM Pt2 pos10 Middle St S end
106	-0.1	1269	1522	-130	SYDNEY McM Pt2 pos10 Middle St S end
107	1.9	284	1759	-130	SYDNEY McM Pt2 pos10 Middle St S end
108	-0.8	1965	1473	-130	SYDNEY McM Pt2 pos10 Middle St S end
109	2.2	728	1646	-130	SYDNEY McM Pt2 pos10 Middle St S end
110	1.1	754	1724	-130	SYDNEY McM Pt2 pos10 Middle St S end

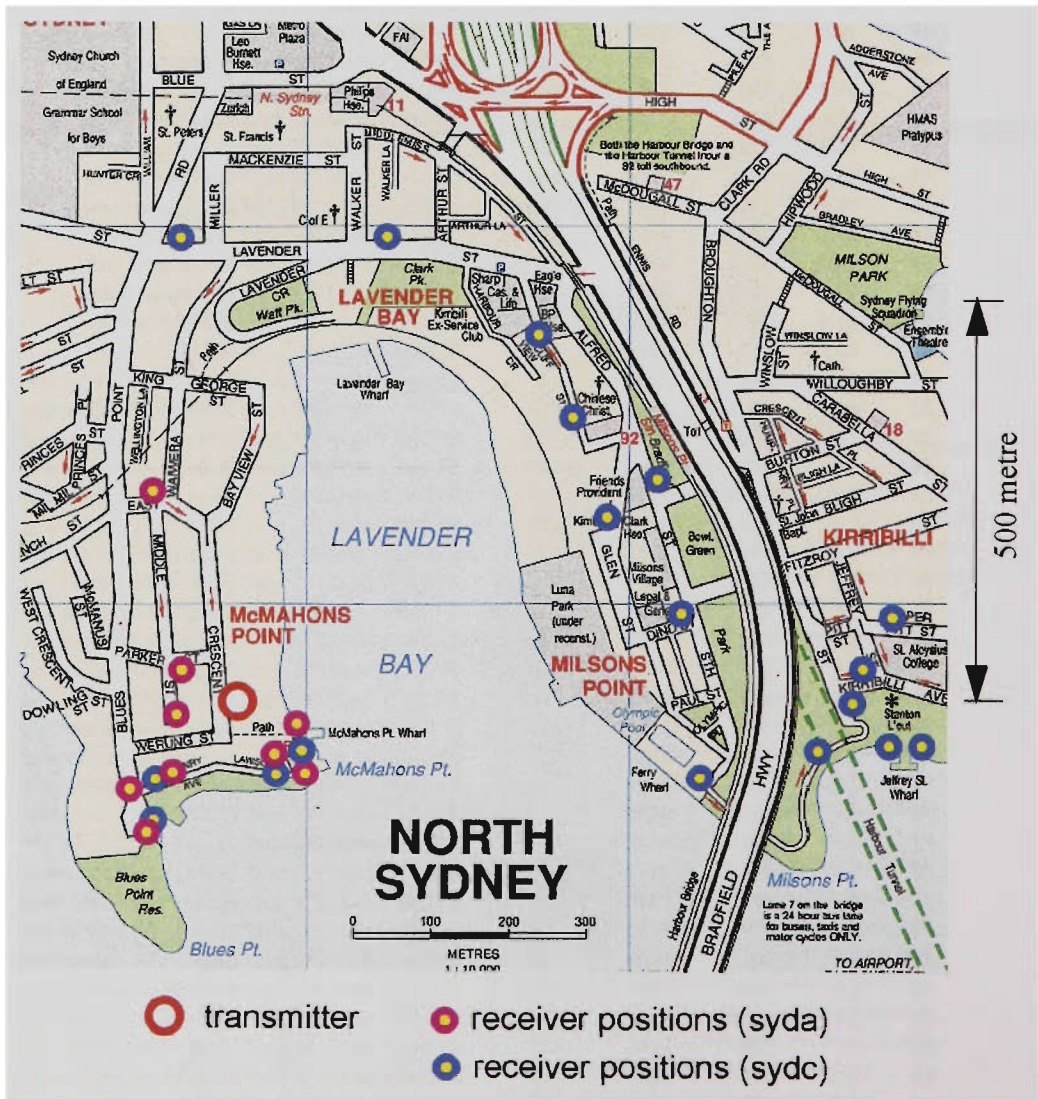


FIGURE E.14 Sydney - McMahons Point, showing measurement locations

E.13 Sydney - McMahon's Point, Second Series

**Transmitter Location:** 21 East Crescent, McMahon's Point.  
**Transmitter Antenna:** on boom beyond 4th. floor balcony, overlooking harbour. Halfwave antenna.  
**Receiver:** in car with halfwave magnetic base antenna on roof.  
**Sample time:** 10 ns, **Threshold:** -15 dB, **Range:** 25  $\mu$ s

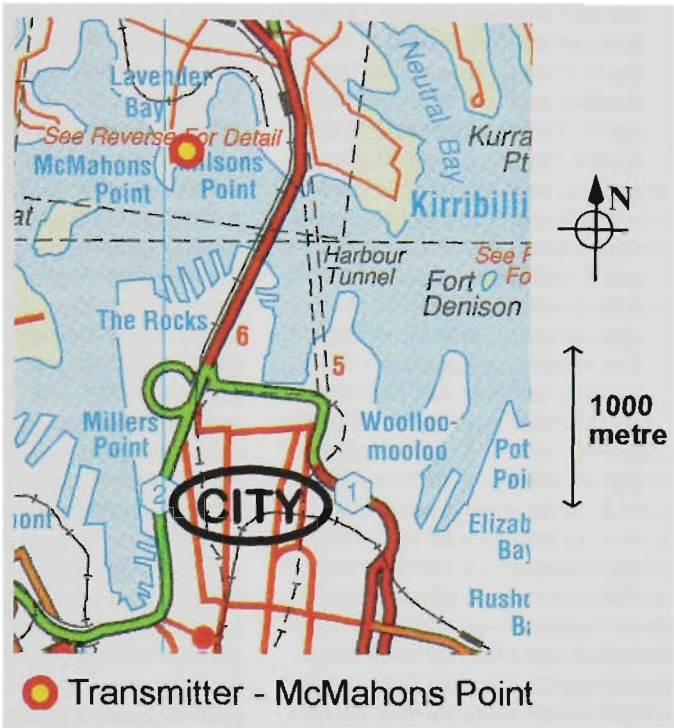


FIGURE E.15 McMahon's Point transmitter site in relation to the city

TABLE E.13 Sydney - McMahon's Point - filebase sydc

file	dBV	rms delay (ns)	avg delay (ns)	gain factor (dB)	location of measurement
1	4.6	2594	2524	-130	SYDNEY McM Pt2 pos1 Henry Lawson Av W end
2	4.4	2433	2186	-130	SYDNEY McM Pt2 pos1 Henry Lawson Av W end
3	4.3	2414	2105	-130	SYDNEY McM Pt2 pos1 Henry Lawson Av W end
4	4.4	2259	2109	-130	SYDNEY McM Pt2 pos1 Henry Lawson Av W end
5	2.6	2240	2567	-130	SYDNEY McM Pt2 pos1 Henry Lawson Av W end
6	2.9	2394	2169	-130	SYDNEY McM Pt2 pos1 Henry Lawson Av W end
7	1.7	2481	2341	-130	SYDNEY McM Pt2 pos1 Henry Lawson Av W end
8	2.0	2623	2777	-130	SYDNEY McM Pt2 pos1 Henry Lawson Av W end
9	2.9	2789	2635	-130	SYDNEY McM Pt2 pos1 Henry Lawson Av W end
10	2.2	2439	4852	-130	SYDNEY McM Pt2 pos1 Henry Lawson Av W end
11	6.2	3230	2735	-130	SYDNEY McM Pt2 pos2 Henry Lawson Av
12	3.9	1709	4320	-130	SYDNEY McM Pt2 pos2 Henry Lawson Av
13	5.2	3603	6374	-130	SYDNEY McM Pt2 pos2 Henry Lawson Av
14	5.5	2146	5020	-130	SYDNEY McM Pt2 pos2 Henry Lawson Av
15	4.6	2207	5122	-130	SYDNEY McM Pt2 pos2 Henry Lawson Av
16	4.4	2320	5029	-130	SYDNEY McM Pt2 pos3 McMahon's Point
17	12.6	3672	4169	-130	SYDNEY McM Pt2 pos3 McMahon's Point
18	11.1	4047	3204	-130	SYDNEY McM Pt2 pos3 McMahon's Point
19	11.5	3924	3009	-130	SYDNEY McM Pt2 pos3 McMahon's Point
20	14.1	3611	2948	-130	SYDNEY McM Pt2 pos3 McMahon's Point
21	10.1	3896	3914	-130	SYDNEY McM Pt2 pos3 McMahon's Point
22	11.1	3061	4309	-130	SYDNEY McM Pt2 pos3 McMahon's Point

**TABLE E.13 Sydney - McMahon's Point - filebase sydc** (continued)

file	dBV	rms delay (ns)	avg delay (ns)	gain factor (dB)	location of measurement
23	5.3	1740	1913	-130	SYDNEY McM Pt2 pos4 Blues Point Rd S end
24	5.1	1857	5440	-130	SYDNEY McM Pt2 pos4 Blues Point Rd S end
25	6.3	1896	2052	-130	SYDNEY McM Pt2 pos4 Blues Point Rd S end
26	5.7	1870	1953	-130	SYDNEY McM Pt2 pos4 Blues Point Rd S end
27	5.4	1767	1846	-130	SYDNEY McM Pt2 pos4 Blues Point Rd S end
28	6.2	1768	2039	-130	SYDNEY McM Pt2 pos4 Blues Point Rd S end
29	6.4	1798	1942	-130	SYDNEY McM Pt2 pos4 Blues Point Rd S end
30	6.3	1781	1628	-130	SYDNEY McM Pt2 pos4 Blues Point Rd S end
31	7.6	2057	2087	-130	SYDNEY McM Pt2 pos4 Blues Point Rd S end
32	8.6	2101	2333	-130	SYDNEY McM Pt2 pos4 Blues Point Rd S end
33	7.9	2043	2051	-130	SYDNEY McM Pt2 pos4 Blues Point Rd S end
34	8.5	1991	2044	-130	SYDNEY McM Pt2 pos4 Blues Point Rd S end
35	9.7	2090	2239	-130	SYDNEY McM Pt2 pos4 Blues Point Rd S end
36	9.4	2106	2392	-130	SYDNEY McM Pt2 pos4 Blues Point Rd S end
37	9.9	1918	1664	-130	SYDNEY McM Pt2 pos4 Blues Point Rd S end
38	3.9	649	364	-130	SYDNEY McM Pt2 pos5 Lavender St 50m E Blues Pt
39	12.3	60	41	-130	SYDNEY McM Pt2 pos5 Lavender St 50m E Blues Pt
40	7.4	616	278	-130	SYDNEY McM Pt2 pos5 Lavender St 50m E Blues Pt
41	11.1	102	71	-130	SYDNEY McM Pt2 pos5 Lavender St 50m E Blues Pt
42	10.4	127	103	-130	SYDNEY McM Pt2 pos5 Lavender St 50m E Blues Pt
43	9.6	174	106	-130	SYDNEY McM Pt2 pos5 Lavender St 50m E Blues Pt
44	5.8	776	448	-130	SYDNEY McM Pt2 pos5 Lavender St 50m E Blues Pt
45	11.4	62	136	-130	SYDNEY McM Pt2 pos5 Lavender St 50m E Blues Pt
46	9.7	208	87	-110	SYDNEY McM Pt2 pos6 Lavender E of Walker
47	4.5	364	337	-110	SYDNEY McM Pt2 pos6 Lavender E of Walker
48	7.8	346	227	-110	SYDNEY McM Pt2 pos6 Lavender E of Walker
49	4.6	379	351	-110	SYDNEY McM Pt2 pos6 Lavender E of Walker
50	9.9	33	38	-110	SYDNEY McM Pt2 pos7 Cliff St S end
51	10.3	37	32	-110	SYDNEY McM Pt2 pos7 Cliff St S end
52	10.1	32	24	-110	SYDNEY McM Pt2 pos7 Cliff St S end
53	2.4	111	151	-110	SYDNEY McM Pt2 pos7 Cliff St S end
54	6.6	32	38	-110	SYDNEY McM Pt2 pos7 Cliff St S end
55	6.8	32	37	-110	SYDNEY McM Pt2 pos7 Cliff St S end
56	11.7	230	139	-130	SYDNEY McM Pt2 pos8 Cliff St BP House
57	7.5	309	285	-130	SYDNEY McM Pt2 pos8 Cliff St BP House
58	7.1	194	320	-130	SYDNEY McM Pt2 pos8 Cliff St BP House
59	1.6	315	446	-130	SYDNEY McM Pt2 pos8 Cliff St BP House
60	5.7	254	434	-130	SYDNEY McM Pt2 pos8 Cliff St BP House
61	7.9	232	227	-130	SYDNEY McM Pt2 pos8 Cliff St BP House
62	8.9	235	221	-130	SYDNEY McM Pt2 pos8 Cliff St BP House
63	3.3	1160	1197	-130	SYDNEY McM Pt2 pos9 Alfred St
64	2.1	1189	1147	-130	SYDNEY McM Pt2 pos9 Alfred St
65	3.8	997	679	-130	SYDNEY McM Pt2 pos9 Alfred St
66	4.4	1118	892	-130	SYDNEY McM Pt2 pos9 Alfred St
67	4.3	1072	857	-130	SYDNEY McM Pt2 pos9 Alfred St
68	3.2	982	827	-130	SYDNEY McM Pt2 pos9 Alfred St
69	2.6	1045	879	-130	SYDNEY McM Pt2 pos9 Alfred St
70	0.0	986	993	-130	SYDNEY McM Pt2 pos9 Alfred St
71	1.3	985	819	-130	SYDNEY McM Pt2 pos9 Alfred St
72	6.3	959	587	-130	SYDNEY McM Pt2 pos9 Alfred St
73	8.8	17	21	-130	SYDNEY McM Pt2 pos9 Alfred St
74	3.7	13	15	-110	SYDNEY McM Pt2 pos10 SW cnr Alfred & Dind St
75	1.7	23	21	-110	SYDNEY McM Pt2 pos10 SW cnr Alfred & Dind St
76	2.7	18	21	-110	SYDNEY McM Pt2 pos10 SW cnr Alfred & Dind St
77	7.9	27	23	-110	SYDNEY McM Pt2 pos11 Glen Street
78	7.4	110	64	-110	SYDNEY McM Pt2 pos11 Glen Street
79	-1.1	218	222	-110	SYDNEY McM Pt2 pos11 Glen Street
80	2.2	120	131	-110	SYDNEY McM Pt2 pos11 Glen Street
81	1.3	121	122	-110	SYDNEY McM Pt2 pos11 Glen Street
82	10.3	126	69	-110	SYDNEY McM Pt2 pos12 Alfred St Olympic pool
83	11.5	94	43	-110	SYDNEY McM Pt2 pos12 Alfred St Olympic pool
84	10.1	90	42	-110	SYDNEY McM Pt2 pos12 Alfred St Olympic pool
85	9.3	121	69	-110	SYDNEY McM Pt2 pos12 Alfred St Olympic pool
86	8.4	180	154	-110	SYDNEY McM Pt2 pos12 Alfred St Olympic pool



**TABLE E.13 Sydney - McMahon's Point - filebase sydc** (continued)

file	dBV	rms delay (ns)	avg delay (ns)	gain factor (dB)	location of measurement
87	9.2	32	28	-110	SYDNEY McM Pt2 pos12 Alfred St Olympic pool
88	6.5	76	60	-130	SYDNEY McM Pt2 pos13 Upper Pitt Street
89	11.7	31	19	-130	SYDNEY McM Pt2 pos13 Upper Pitt Street
90	8.9	64	50	-130	SYDNEY McM Pt2 pos13 Upper Pitt Street
91	9.2	25	26	-130	SYDNEY McM Pt2 pos13 Upper Pitt Street
92	-3.6	517	353	-130	SYDNEY McM Pt2 pos14 cnr Kirribilli & Carabella
93	-3.2	466	327	-130	SYDNEY McM Pt2 pos14 cnr Kirribilli & Carabella
94	-6.2	562	567	-130	SYDNEY McM Pt2 pos14 cnr Kirribilli & Carabella
95	-8.1	537	466	-130	SYDNEY McM Pt2 pos14 cnr Kirribilli & Carabella
96	-7.8	602	698	-130	SYDNEY McM Pt2 pos14 cnr Kirribilli & Carabella
97	-5.2	391	269	-130	SYDNEY McM Pt2 pos14 cnr Kirribilli & Carabella
98	-1.8	86	28	-130	SYDNEY McM Pt2 pos15 cnr Kirribilli & Beulah
99	-5.7	325	180	-130	SYDNEY McM Pt2 pos15 cnr Kirribilli & Beulah
100	-6.4	222	110	-130	SYDNEY McM Pt2 pos15 cnr Kirribilli & Beulah
101	-3.9	241	171	-130	SYDNEY McM Pt2 pos16 Waruda St E end
102	-7.0	484	374	-130	SYDNEY McM Pt2 pos16 Waruda St E end
103	-11.4	2377	1199	-130	SYDNEY McM Pt2 pos16 Waruda St E end
104	-2.5	1797	1076	-130	SYDNEY McM Pt2 pos17 Waruda Street
105	-3.2	1987	1187	-130	SYDNEY McM Pt2 pos17 Waruda Street
106	-2.4	1624	750	-130	SYDNEY McM Pt2 pos17 Waruda Street
107	-4.3	2569	996	-130	SYDNEY McM Pt2 pos17 Waruda Street
108	12.1	37	112	-130	SYDNEY McM Pt2 pos18 Waruda St E end
109	4.0	114	125	-130	SYDNEY McM Pt2 pos18 Waruda St E end
110	1.4	164	166	-130	SYDNEY McM Pt2 pos18 Waruda St E end
111	8.5	43	117	-130	SYDNEY McM Pt2 pos18 Waruda St E end
112	7.8	70	48	-130	SYDNEY McM Pt2 pos18 Waruda St E end
113	6.4	62	54	-130	SYDNEY McM Pt2 pos18 Waruda St E end
114	11.3	46	66	-130	SYDNEY McM Pt2 pos18 Waruda St E end
115	9.9	64	45	-130	SYDNEY McM Pt2 pos18 Waruda St E end
116	0.1	136	135	-130	SYDNEY McM Pt2 pos18 Waruda St E end
117	10.5	74	49	-130	SYDNEY McM Pt2 pos18 Waruda St E end
118	0.2	178	174	-130	SYDNEY McM Pt2 pos18 Waruda St E end
119	1.8	2704	2089	-130	SYDNEY McM Pt2 pos19 cnr Kirribilli & Jeffrey
120	2.1	3200	1775	-130	SYDNEY McM Pt2 pos19 cnr Kirribilli & Jeffrey
121	-3.8	3177	3411	-130	SYDNEY McM Pt2 pos19 cnr Kirribilli & Jeffrey
122	-2.9	3317	2941	-130	SYDNEY McM Pt2 pos19 cnr Kirribilli & Jeffrey
123	1.3	2660	1482	-130	SYDNEY McM Pt2 pos19 cnr Kirribilli & Jeffrey
124	-2.0	3229	2802	-130	SYDNEY McM Pt2 pos19 cnr Kirribilli & Jeffrey
125	-1.8	3549	3119	-130	SYDNEY McM Pt2 pos19 cnr Kirribilli & Jeffrey
126	0.7	2287	1603	-130	SYDNEY McM Pt2 pos20 Broughton St S end
127	6.7	1073	443	-130	SYDNEY McM Pt2 pos20 Broughton St S end
128	2.5	3425	2098	-130	SYDNEY McM Pt2 pos20 Broughton St S end
129	3.5	3263	1269	-130	SYDNEY McM Pt2 pos20 Broughton St S end
130	4.4	2308	606	-130	SYDNEY McM Pt2 pos20 Broughton St S end
131	3.9	3001	1703	-130	SYDNEY McM Pt2 pos21 Jeffrey St S end
132	1.8	2416	2089	-130	SYDNEY McM Pt2 pos21 Jeffrey St S end
133	6.3	1870	1469	-130	SYDNEY McM Pt2 pos21 Jeffrey St S end
134	1.4	1737	1145	-130	SYDNEY McM Pt2 pos22 near Jeffrey St wharf
135	1.9	843	558	-130	SYDNEY McM Pt2 pos22 near Jeffrey St wharf
136	3.8	963	546	-130	SYDNEY McM Pt2 pos22 near Jeffrey St wharf
137	5.5	859	404	-130	SYDNEY McM Pt2 pos22 near Jeffrey St wharf
138	6.2	338	113	-130	SYDNEY McM Pt2 pos22 near Jeffrey St wharf
139	3.2	981	530	-130	SYDNEY McM Pt2 pos23 Olympic Drive
140	6.7	646	201	-130	SYDNEY McM Pt2 pos23 Olympic Drive
141	0.5	1733	1125	-130	SYDNEY McM Pt2 pos23 Olympic Drive
142	4.2	1298	726	-130	SYDNEY McM Pt2 pos23 Olympic Drive

### E.14 Sydney - University of Technology, Broadway

**Transmitter Location:** UTS Broadway, Sydney city area.  
**Transmitter Antenna:** inside fixed glass window, facing north towards city centre.  
**Halfwave antenna.**  
**Receiver:** in car with halfwave magnetic base antenna on roof.  
**Sample time:** 10 ns, **Threshold:** -15 dB, **Range:** 25  $\mu$ s



FIGURE E.16 Sydney - University of Technology Sydney measurement locations

TABLE E.14 Sydney - University of Technology - filebase sydb

file	dBV	rms delay (ns)	avg delay (ns)	gain factor (dB)	location of measurement
1	-0.5	351	1383	-130	Sydney UTS pos1 Thomas St
2	-0.6	389	1382	-130	Sydney UTS pos1 Thomas St
3	-0.4	642	1420	-130	Sydney UTS pos1 Thomas St
4	2.1	270	485	-130	Sydney UTS pos1 Thomas St
5	-0.7	321	1391	-130	Sydney UTS pos1 Thomas St

**TABLE E.14 Sydney - University of Technology - filebase sydb (cont.)**

file	dBV	rms delay (ns)	avg delay (ns)	gain factor (dB)	location of measurement
6	10.8	307	330	-130	Sydney UTS pos1 Thomas St
7	12.7	266	275	-130	Sydney UTS pos2 Thomas St
8	16.5	119	200	-130	Sydney UTS pos2 Thomas St
9	14.9	191	323	-130	Sydney UTS pos2 Thomas St
10	14.8	193	363	-130	Sydney UTS pos2 Thomas St
11	11.1	287	193	-130	Sydney UTS pos3 George St near Pitt St
12	14.9	193	130	-130	Sydney UTS pos3 George St near Pitt St
13	14.9	185	238	-130	Sydney UTS pos3 George St near Pitt St
14	13.7	502	200	-130	Sydney UTS pos4 George St opp Rawson Pl
15	14.2	170	91	-130	Sydney UTS pos4 George St opp Rawson Pl
16	13.9	279	175	-130	Sydney UTS pos4 George St opp Rawson Pl
17	13.9	222	175	-130	Sydney UTS pos4 George St opp Rawson Pl
18	1.9	746	909	-130	Sydney UTS pos5 SW cnr George & Goulburn
19	2.8	817	1205	-130	Sydney UTS pos5 SW cnr George & Goulburn
20	0.7	846	1059	-130	Sydney UTS pos5 SW cnr George & Goulburn
21	5.7	439	450	-130	Sydney UTS pos6 George St World Square
22	9.2	281	234	-130	Sydney UTS pos6 George St World Square
23	7.5	451	376	-130	Sydney UTS pos6 George St World Square
24	-0.4	604	251	-130	Sydney UTS pos7 SW cnr George & Bathurst
25	2.0	191	155	-130	Sydney UTS pos7 SW cnr George & Bathurst
26	-2.5	936	507	-130	Sydney UTS pos7 SW cnr George & Bathurst
27	-2.9	497	303	-130	Sydney UTS pos8 SW cnr George & Druit
28	1.8	82	56	-130	Sydney UTS pos8 SW cnr George & Druit
29	-2.5	792	413	-130	Sydney UTS pos8 SW cnr George & Druit
30	-5.5	1314	1300	-130	Sydney UTS pos9 NE cnr Druit & Kent
31	-6.7	1181	1131	-130	Sydney UTS pos9 NE cnr Druit & Kent
32	-5.5	1327	1060	-130	Sydney UTS pos9 NE cnr Druit & Kent
33	-2.2	600	469	-130	Sydney UTS pos10 NE cnr Sands & Bathurst
34	-0.7	569	400	-130	Sydney UTS pos10 NE cnr Sands & Bathurst
35	-0.1	967	822	-130	Sydney UTS pos10 NE cnr Sands & Bathurst
36	-2.6	22	17	-130	Sydney UTS pos11 Elizabeth St Hyde Park
37	-5.3	31	26	-130	Sydney UTS pos11 Elizabeth St Hyde Park
38	-5.9	26	23	-130	Sydney UTS pos11 Elizabeth St Hyde Park
39	-4.2	40	28	-130	Sydney UTS pos11 Elizabeth St Hyde Park
40	-6.5	33	27	-130	Sydney UTS pos11 Elizabeth St Hyde Park
41	-7.3	22	17	-130	Sydney UTS pos11 Elizabeth St Hyde Park
42	-5.0	11	13	-130	Sydney UTS pos12 Elizabeth St Hyde Park
43	-9.6	42	124	-130	Sydney UTS pos12 Elizabeth St Hyde Park
44	-7.2	29	22	-130	Sydney UTS pos12 Elizabeth St Hyde Park
45	-6.6	33	93	-130	Sydney UTS pos13 Elizabeth S Bathurst
46	-5.9	31	90	-130	Sydney UTS pos13 Elizabeth S Bathurst
47	-5.1	179	730	-130	Sydney UTS pos13 Elizabeth S Bathurst
48	2.1	10	12	-130	Sydney UTS pos14 Elizabeth St
49	-0.1	35	24	-130	Sydney UTS pos14 Elizabeth St
50	0.1	25	78	-130	Sydney UTS pos14 Elizabeth St
51	-5.3	67	133	-130	Sydney UTS pos15 Liverpool St Hyde Park
52	-1.8	22	26	-130	Sydney UTS pos15 Liverpool St Hyde Park
53	-1.4	33	98	-130	Sydney UTS pos15 Liverpool St Hyde Park
54	-5.6	124	121	-130	Sydney UTS pos16 SW cnr Liverpool & Forbes
55	-8.5	170	161	-130	Sydney UTS pos16 SW cnr Liverpool & Forbes
56	-5.0	66	107	-130	Sydney UTS pos16 SW cnr Liverpool & Forbes
57	-0.6	357	311	-130	Sydney UTS pos17 Riley Stopp Warne
58	-8.3	436	649	-130	Sydney UTS pos17 Riley Stopp Warne
59	-7.1	440	602	-130	Sydney UTS pos17 Riley Stopp Warne
60	-4.2	421	450	-130	Sydney UTS pos17 Riley Stopp Warne
61	13.9	329	189	-130	Sydney UTS pos18 NE cnr Riley & Campbell
62	11.5	143	76	-130	Sydney UTS pos18 NE cnr Riley & Campbell
63	11.4	98	64	-130	Sydney UTS pos18 NE cnr Riley & Campbell
64	3.5	370	205	-130	Sydney UTS pos19 E end Reservoir St
65	0.8	595	463	-130	Sydney UTS pos19 E end Reservoir St
66	3.8	319	186	-130	Sydney UTS pos19 E end Reservoir St
67	8.4	39	27	-130	Sydney UTS pos19 E end Reservoir St
68	14.1	30	39	-130	Sydney UTS pos19 E end Reservoir St
69	8.7	49	41	-130	Sydney UTS pos19 E end Reservoir St



**TABLE E.14 Sydney - University of Technology - filebase sydb (cont.)**

file	dBV	rms delay (ns)	avg delay (ns)	gain factor (dB)	location of measurement
70	2.1	125	190	-130	Sydney UTS pos20 E end Ann St
71	2.7	116	164	-130	Sydney UTS pos20 E end Ann St
72	3.4	111	139	-130	Sydney UTS pos20 E end Ann St
73	0.9	73	108	-130	Sydney UTS pos20 E end Ann St
74	2.4	73	166	-130	Sydney UTS pos20 E end Ann St
75	0.8	620	257	-130	Sydney UTS pos21 NE cnr Riley & Albion
76	-2.2	578	352	-130	Sydney UTS pos21 NE cnr Riley & Albion
77	-2.6	1140	610	-130	Sydney UTS pos21 NE cnr Riley & Albion
78	2.8	993	447	-130	Sydney UTS pos22 NE cnr Riley & Fitzroy
79	9.8	64	39	-130	Sydney UTS pos22 NE cnr Riley & Fitzroy
80	2.5	902	417	-130	Sydney UTS pos23 Foveaux opp Bellevue
81	1.2	560	401	-130	Sydney UTS pos23 Foveaux opp Bellevue
82	1.3	418	314	-130	Sydney UTS pos23 Foveaux opp Bellevue
83	2.4	464	366	-130	Sydney UTS pos23 Foveaux opp Bellevue
84	-2.8	684	904	-130	Sydney UTS pos24 Foveaux opp Mary St
85	0.5	639	802	-130	Sydney UTS pos24 Foveaux opp Mary St
86	3.2	564	637	-130	Sydney UTS pos24 Foveaux opp Mary St
87	2.5	423	667	-130	Sydney UTS pos25 cnr Elizabeth & Hay
88	11.4	262	267	-130	Sydney UTS pos25 cnr Elizabeth & Hay
89	6.2	360	476	-130	Sydney UTS pos25 cnr Elizabeth & Hay
90	7.3	513	729	-130	Sydney UTS pos26 NW cnr Eliz & Campbell
91	5.9	501	655	-130	Sydney UTS pos26 NW cnr Eliz & Campbell
92	7.6	476	823	-130	Sydney UTS pos26 NW cnr Eliz & Campbell
93	-1.8	330	786	-130	Sydney UTS pos27 Elizabeth N Goulburn
94	-2.3	461	1264	-130	Sydney UTS pos27 Elizabeth N Goulburn
95	-3.0	480	874	-130	Sydney UTS pos27 Elizabeth N Goulburn
96	-0.0	36	98	-130	Sydney UTS pos28 Elizabeth S Bathurst
97	-0.1	38	100	-130	Sydney UTS pos28 Elizabeth S Bathurst
98	2.5	14	16	-130	Sydney UTS pos28 Elizabeth S Bathurst
99	3.0	578	351	-130	Sydney UTS pos29 NE cnr Sussex & King
100	0.4	706	607	-130	Sydney UTS pos29 NE cnr Sussex & King
101	2.6	489	338	-130	Sydney UTS pos29 NE cnr Sussex & King
102	2.1	879	498	-130	Sydney UTS pos30 SW cnr Sussex & King
103	-1.8	816	598	-130	Sydney UTS pos30 SW cnr Sussex & King
104	1.8	589	328	-130	Sydney UTS pos30 SW cnr Sussex & King
105	2.2	190	151	-130	Sydney UTS pos30 SW cnr Sussex & King
106	0.9	528	618	-130	Sydney UTS pos31 NE cnr Sussex & Druit Pl
107	-0.4	553	651	-130	Sydney UTS pos31 NE cnr Sussex & Druit Pl
108	2.9	440	380	-130	Sydney UTS pos31 NE cnr Sussex & Druit Pl
109	0.9	716	1314	-130	Sydney UTS pos32 NE cnr Sussex & Druit Ln
110	3.2	638	1207	-130	Sydney UTS pos32 NE cnr Sussex & Druit Ln
111	4.9	713	1122	-130	Sydney UTS pos32 NE cnr Sussex & Druit Ln
112	3.3	444	407	-130	Sydney UTS pos33 Sussex St
113	3.9	468	431	-130	Sydney UTS pos33 Sussex St
114	1.5	536	617	-130	Sydney UTS pos33 Sussex St
115	1.0	836	820	-130	Sydney UTS pos34 NE cnr Sussex & Liverpool
116	-0.7	992	913	-130	Sydney UTS pos34 NE cnr Sussex & Liverpool
117	1.6	731	923	-130	Sydney UTS pos34 NE cnr Sussex & Liverpool
118	2.3	870	1005	-130	Sydney UTS pos34 NE cnr Sussex & Liverpool
119	2.3	626	821	-130	Sydney UTS pos34 NE cnr Sussex & Liverpool
120	3.8	671	723	-130	Sydney UTS pos34 NE cnr Sussex & Liverpool
121	10.4	850	768	-130	Sydney UTS pos35 NE cnr Sussex & Goulburn
122	13.3	851	544	-130	Sydney UTS pos35 NE cnr Sussex & Goulburn
123	13.2	777	408	-130	Sydney UTS pos35 NE cnr Sussex & Goulburn
124	14.2	138	84	-130	Sydney UTS pos36 NW cnr Hay & Sussex
125	13.5	214	124	-130	Sydney UTS pos36 NW cnr Hay & Sussex
126	16.6	195	79	-130	Sydney UTS pos36 NW cnr Hay & Sussex
127	-1.4	1347	1113	-130	Sydney UTS pos37 NW cnr Goulburn & George
128	-0.8	1452	1124	-130	Sydney UTS pos37 NW cnr Goulburn & George
129	-1.1	1150	1191	-130	Sydney UTS pos37 NW cnr Goulburn & George
130	4.2	830	907	-130	Sydney UTS pos38 NW cnr Goulburn & Pitt
131	3.2	720	907	-130	Sydney UTS pos38 NW cnr Goulburn & Pitt
132	0.0	868	1223	-130	Sydney UTS pos38 NW cnr Goulburn & Pitt
133	-3.0	1162	1452	-130	Sydney UTS pos39 cnr Pitt & Hay

**TABLE E.14** *Sydney - University of Technology - filebase sydb* (cont.)

file	dBV	rms delay (ns)	avg delay (ns)	gain factor (dB)	location of measurement
134	-2.2	508	1199	-130	Sydney UTS pos40 Mary Ann St
135	-2.2	659	1278	-130	Sydney UTS pos40 Mary Ann St
136	-1.8	745	2076	-130	Sydney UTS pos40 Mary Ann St
137	-3.4	805	2106	-130	Sydney UTS pos40 Mary Ann St
138	-1.1	557	287	-130	Sydney UTS pos40 Mary Ann St
139	0.8	1066	980	-130	Sydney UTS pos41 SW cnr Harris & Mary Ann
140	15.5	134	457	-130	Sydney UTS pos42 Thomas St nr UTS pos gate
141	15.8	116	297	-130	Sydney UTS pos42 Thomas St nr UTS pos gate
142	16.2	95	458	-130	Sydney UTS pos42 Thomas St nr UTS pos gate
143	16.8	78	208	-130	Sydney UTS pos42 Thomas St nr UTS pos gate